NONDESTRUCTIVE EVALUATION AND FLAW CRITICALITY FOR COMPOSITE MATERIALS

R. B. PIPES, *editor*

ASTM STP 696

AMERICAN SOCIETY FOR TESTING AND MATERIALS

NONDESTRUCTIVE EVALUATION AND FLAW CRITICALITY FOR COMPOSITE MATERIALS

A symposium
sponsored by ASTM
Committee D-30 on High Modulus
Fibers and Their Composites
AMERICAN SOCIETY FOR
TESTING AND MATERIALS
Philadelphia, Pa., 10-11 Oct. 1978

ASTM SPECIAL TECHNICAL PUBLICATION 696
R. B. Pipes, University of Delaware, editor
W. R. Scott
S. V. Kulkarni
W. W. Stinchcomb
} coeditors

List price $34.50
04-696000-33

AMERICAN SOCIETY FOR TESTING AND MATERIALS
1916 Race Street, Philadelphia, Pa. 19103

Library of Congress Catalog Card Number: 79-53320

NOTE

The Society is not responsible, as a body,
for the statements and opinions
advanced in this publication.

Printed in Baltimore, Md.
December 1979

Foreword

The symposium on Nondestructive Evaluation and Flaw Criticality for Composite Materials was presented at Philadelphia, Pa., 10-11 Oct. 1978. The American Society for Testing and Materials' Committee D-30 on High Modulus Fibers and Their Composites sponsored the symposium. R. B. Pipes, University of Delaware, presided as symposium chairman and editor of this publication. W. R. Scott, S. V. Kulkarni, and W. W. Stinchcomb presided as session chairmen and coeditors of this publication.

Related ASTM Publications

Advanced Composite Materials—Environmental Effects, STP 658 (1978), $26.00, 04-658000-33

Fatigue of Filamentary Composite Materials, STP 638 (1977), $26.50, 04-638000-33

Nondestructive Testing Standards—A Review, STP 624 (1977), $33.75, 04-624000-22

A Note of Appreciation to Reviewers

This publication is made possible by the authors and, also, the unheralded efforts of the reviewers. This body of technical experts whose dedication, sacrifice of time and effort, and collective wisdom in reviewing the papers must be acknowledged. The quality level of ASTM publications is a direct function of their respected opinions. On behalf of ASTM we acknowledge with appreciation their contribution.

ASTM Committee on Publications

Editorial Staff

Jane B. Wheeler, *Managing Editor*
Helen M. Hoersch, *Associate Editor*
Ellen J. McGlinchey, *Senior Assistant Editor*
Helen Mahy, *Assistant Editor*

Contents

Introduction

The primary goals of the conference and this book are given as follows:

1. To present the state of the art of nondestructive inspection methodologies for composite materials and to assess deficiencies.
2. To evaluate analytical methods for the description of critical flaw geometries and growth phenomena in composite materials.
3. To develop a basic understanding of failure phenomena and to establish methods of fractography for composite materials.
4. To promote an exchange among the traditional disciplines (engineer, materials scientist, and physicist) to develop the unified technology necessary for certification of composite structure.

It is well known that the life of contemporary metallic structure is determined by the nucleation and growth of "crack-like" flaws. The fracture control methodology which has been developed to describe this phenomenon requires the detection of subcritical flaws and the description of the growth process during the life of the material. Fortunately, the various flaw geometrics which occur in metallic materials may be adequately modeled as finite cracks which grow in a self-similar fashion. Hence the development of linear elastic fracture mechanics has adequately served as the basis of this new technology.

Fiber-reinforced composite materials contain multiple defect geometries. In addition, the stiffness and strength properties of composite materials are often highly anisotropic. No unified failure model has emerged to date; rather, a multitude of models is being developed to describe a multimode failure process. When compared with contemporary metallic materials, composite materials have achieved only limited service experience wherein competing failure modes are active. Therefore, certification of composite structure in safety-critical applications will require several specific challenges to be met. First, it will be necessary to develop full-field inspection methodologies for large-scale components. Encouraging initial results have been demonstrated by phased ultrasonic arrays, thermography, acoustic holography, and radiography. Second, analytical models must be developed for determination of criticality of multiple flaws: interlaminar disbond, matrix degradation, fiber degradation, and fiber matrix disbond. Finally, models of the growth and

accumulation of damage in composite materials must be developed which include the deleterious influence of environment.

The papers compiled in this publication treat many aspects of the problem as described in the foregoing. However, certification of composite structure is in a period of evolution. Hence, it is the primary object of this treatment to stimulate work and scientific innovation in this field. Only when a certification methodology has been developed for composites will the true potential for these materials be realized.

This publication is subdivided into three sections—nondestructive evaluation methodology, flaw criticality, and flaw characterization—with separate summaries by Drs. W. R. Scott, S. V. Kulkarni, and W. W. Stinchcomb, respectively, who served as coeditors.

R. B. Pipes

Associate professor, Mechanical and Aerospace Engineering, Center for Composite Materials, University of Delaware, Newark, Del. 19711; editor.

Nondestructive Evaluation Methodology for Composite Materials

T. Liber,[1] *I. M. Daniel,*[1] *and S. W. Schramm*[1]

Ultrasonic Techniques for Inspecting Flat and Cylindrical Composite Specimens

REFERENCE: Liber, T., Daniel, I. M., and Schramm, S. W., **"Ultrasonic Techniques for Inspecting Flat and Cylindrical Composite Specimens,"** *Nondestructive Evaluation and Flaw Criticality for Composite Materials, ASTM STP 696,* R. B. Pipes, Ed., American Society for Testing and Materials, 1979, pp. 5-25.

ABSTRACT: Ultrasonic techniques are discussed for inspection and evaluation of flat and cylindrical composite specimens. Immersion ultrasonic techniques are described using a 5-MHz broad-band focused transducer in the pulse-echo mode. Two types of recording methods are employed, conventional pen-lift C-scanning and analog scanning, augmented with photographs of oscilloscope traces of the pulse at selected locations. The complete scanning system is described, including a fixture for scanning tubular specimens. The techniques discussed are applied to monitoring flaw growth in graphite/epoxy coupons of $[(0/\pm 45/90)_s]_2$ and $[0_2/\pm 45]_{2s}$ layups with four types of initial flaws subjected to fully reversed spectrum fatigue loading. The flaws investigated are (1) circular hole, (2) embedded film patch, (3) internal ply gap, and (4) surface scratches. It was found that, in general, flaw growth is greater in specimens of $[0/\pm 45/90)_s]_2$ layup than in those of $[0_2/\pm 45]_{2s}$ layup. The residual tensile strengths for the preceding specimens, determined after four lifetimes of fatigue testing, are not significantly lower than the initial strengths.

KEY WORDS: nondestructive tests, ultrasonic scanning system, ultrasonic inspection techniques, ultrasonic transducers, pulse-echo, C-scans, composite laminates, graphite/epoxy, flat coupons, cylindrical specimens, critical flaws, flaw growth, spectrum fatigue testing, composite materials

The nondestructive detection, characterization, and evaluation of flaws in laminated composite materials serves many purposes. It can be used to determine material quality, the effects of defects on the performance of the material, the development of accept/reject criteria, and to institute inspection and repair procedures for service-induced flaws.

Various kinds of flaws can be introduced into a fiber-reinforced composite

[1] Senior research engineer, science advisor, and assistant research engineer, respectively, Mechanics and Materials Division, IIT Research Institute, Chicago, Ill. 60616.

laminate during its fabrication and processing. Some of these are contaminants, voids, unpolymerized resin, resin-rich and resin-starved areas, ply gaps, inclusions, delaminations, crazing, and surface scratches. Tight edge delaminations may also develop due to drilling and cutting after laminate cure. Such tight delaminations are generally not detectable by visual inspection but can be discovered by nondestructive inspection (NDI) techniques. Many initial flaws tend to grow under load and service conditions, spreading damage and starting new flaws.

Several techniques exist for nondestructive detection of flaws in materials [*1*].[2] Of interest here is the ultrasonic method as applied to composite materials. The method is often used in the aircraft industry, where many of the techniques for panel inspection have evolved [*2–4*]. Examples of its application in a research environment are inspection of composite tubes and flat coupon specimens for fabrication defects, and for load-induced damage such as delaminations [*5–9*].

Methods and principles for ultrasonic inspection and flaw detection in materials are detailed in the literature [*1,10,11*]. Basically a high-frequency sound (1 to 25 MHz) is emitted in periodic bursts from an ultrasonic transducer through a coupling medium into the specimen being inspected. The resulting attenuated pulse emerging from the specimen is picked up by a receiving transducer; the information from it is electronically processed; and the data are displayed for the evaluation of presence, size, and location of flaws.

The preferred method of flaw indentification is by comparison of pulse information obtained from known flawed and unflawed standard specimens. Appropriate standards, especially in laminated composites, are not always easy to produce and sometimes are not feasible. Alternate pulse processing/identification techniques for ultrasonic inspection, such as frequency and phase shift analysis and adaptive learning techniques, have been proposed and are being developed [*5,12–15*]. Computer-aided data processing is making the required data handling and presentation practical.

The present paper describes an ultrasonic inspection system used for the evaluation of damage growth in initially flawed composite specimens when subjected to successive lifetimes of load and environmental fatigue spectra [*16*]. Four types of initial flaws, designed to simulate service-induced flaws, were investigated: a circular hole, an interply embedded patch, an intraply gap, and surface scratches. Ultrasonic procedures for acquiring the flaw growth data are described. The flaw growth histories of the various specimen types are shown in the form of flaw growth maps. Special fixturing built to expand the system to scan composite tubes is described and some results of tube scanning are presented.

[2]The italic numbers in brackets refer to the list of references appended to this paper.

Ultrasonic Scanning Apparatus

Figure 1 shows the ultrasonic scanning system constructed to perform the nondestructive detection of the flaw growth in composite laminate specimens. The method selected was ultrasonic immersion scanning. The requisites for the system were that it be capable of performing in any of two scan modes, pulse-echo or through transmission, and that the modes be easily interchangeable. The system had to be able to accommodate from a single standard fatigue test coupon to a set of five serially connected test coupons in 152.4-cm-long (60 in.) fatigue test chains used for simultaneous testing of the coupons. In the latter case the mechanical traversing mechanism of the scanning system had to be capable of scanning every specimen without its removal from the chain and to clear the chain when transferring from scanning of one specimen to the next. The outcome of these requirements is a system capable of ultrasonic scanning any size coupon or flat panel up to 33 by 173 cm (13 by 68 in.).

The system, shown in Fig. 1, consists of an all-glass immersion tank 45.7 cm (18 in.) wide, 45.7 cm (18 in.) high, and 183 cm (72 in.) long resting on a support table. The transparent glass tank affords distortion-free visual observation through the tank sides during alignment of specimens and transducers and during scanning. A sturdy steel frame resting on the support table surrounds the glass tank, which is accurately positioned relative to the frame. The frame supports the mechanical system for scanning the specimens.

The mechanical system has a scanning carriage platform with three precision screw drives which move the ultrasonic transducer along three mutually perpendicular axes. It is guided along the tank length on steel shafts attached to the support frame. The platform is elevated above the tank and can be traversed and positioned at any tank location.

Figure 2 shows the motorized screw drive for vertical motion and the vertical scanning arm holding the ultrasonic transducer at its lower end. The drive is capable of moving the arm in up and down scanning strokes of any adjustable length up to 35.6 cm (14 in.) at rates up to 127 cm/min (50 in./min). The strokes are monitored by the cable-type electromechanical position transducer attached to the vertical drive. Figure 2 shows also the horizontal transverse screw drive. It is manually operated and is used only for locating or focusing the ultrasonic transducer each time a new specimen is scanned.

The large tank length made it difficult to provide an accurate position-sensing system for the horizontal longitudinal axis. The problem was solved by a double-drive system. One system is similar to the vertical drive, but uses a reversible stepper motor. It provides longitudinal motion of up to 35.6 cm (14 in.) in step lengths which can be preselected in multiples of 0.0635 mm (0.0025 in.). This drive system is integral with the scanning

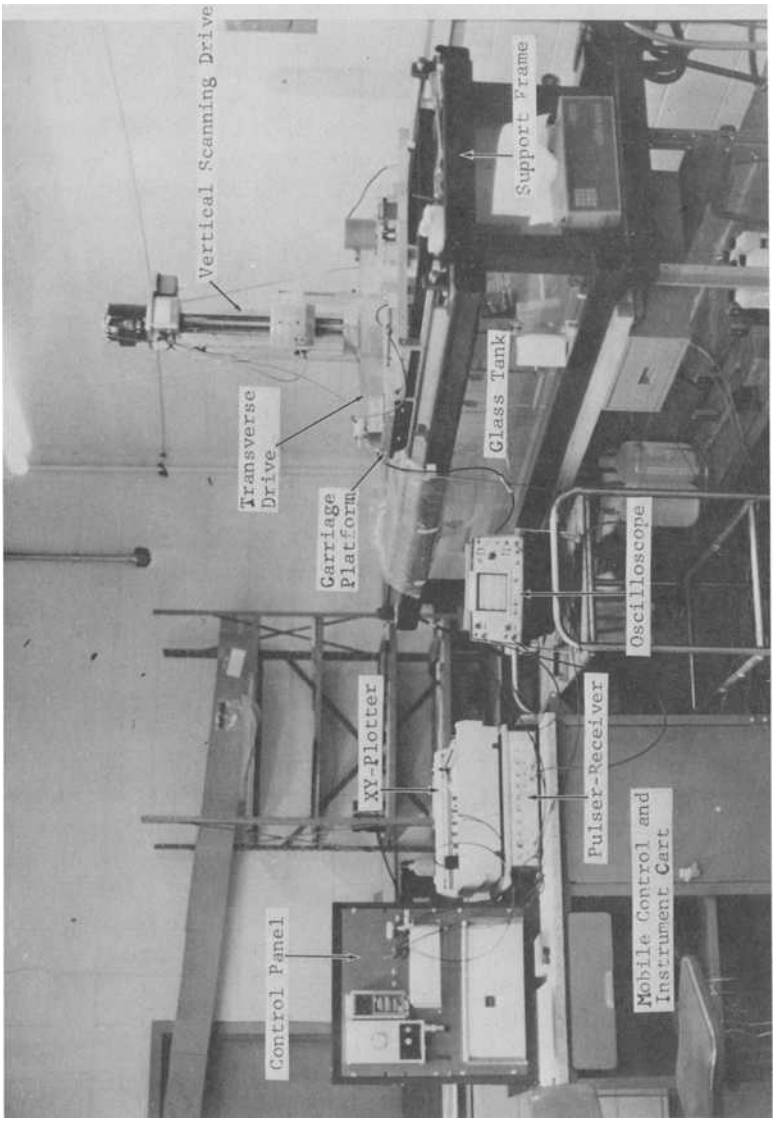

FIG. 1—*Ultrasonic scanning and recording system for nondestructive flaw detection in composite laminates.*

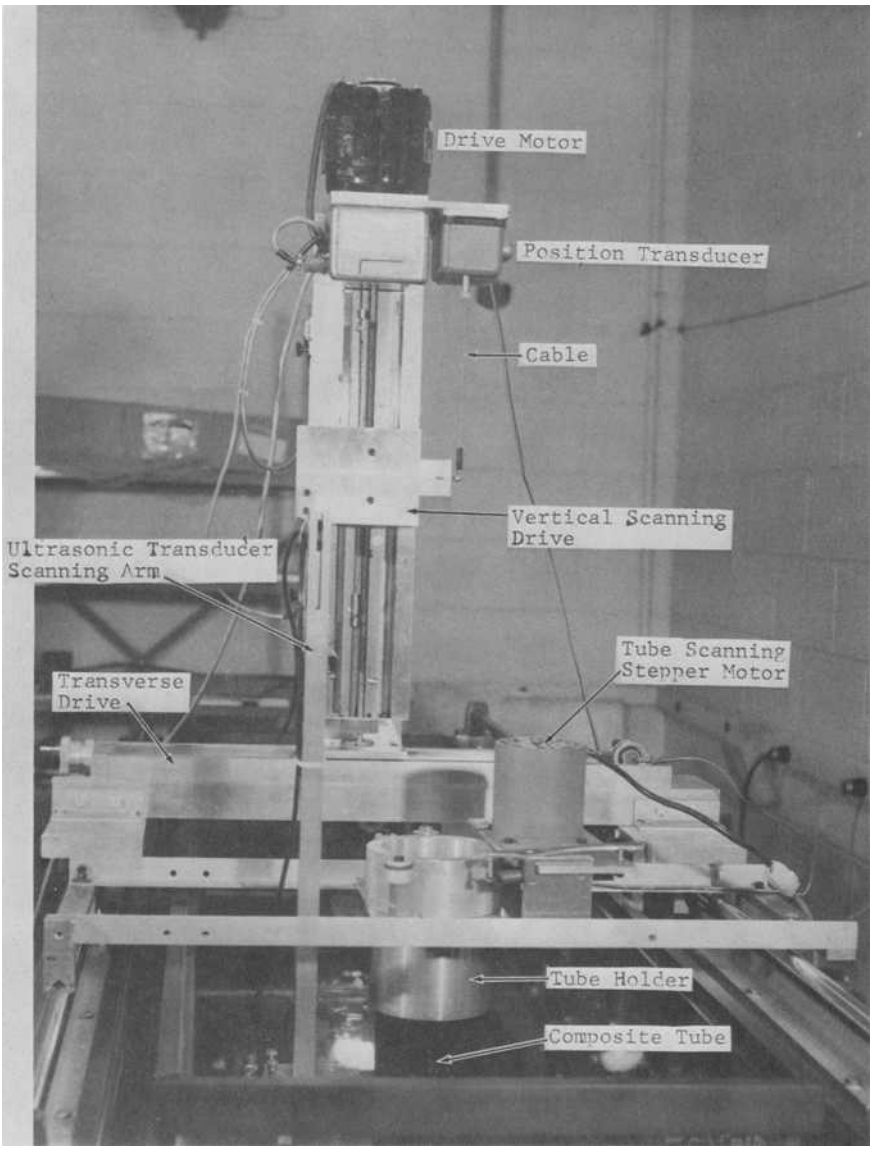

FIG. 2—*Ultrasonic scanning system showing vertical and horizontal drives, vertical position transducer, ultrasonic transducer scanning arm, and auxiliary fixturing for scanning tubular specimens.*

carriage platform and is attached through a Rohlix backlash-free drive nut to a smooth motorized shaft extending through the whole length of the support frame. The shaft and nut comprise the second drive. By means of this drive, the scanning carriage can be located at any position along the tank, permitting the stepper motor drive system to perform accurately monitored longitudinal scans relative to this position. The mechanical scanning system can be operated automatically or manually as desired. Three types of scans can be obtained from flat coupons: A, B and C-scans [*1,10*]. The last type consists of a series of scan lines covering the whole specimen.

Figure 2 shows also auxiliary fixturing built to expand the capacity of the system to scanning composite tubes. The tube is positioned vertically in a ring holder rotated by means of the stepper motor seen alongside the holder. The motor imparts rotary motion to the tube in preselected indexed steps which are multiples of 1.8 deg. The vertical drive of the scanning carriage scans the tube along a vertical line of the longitudinal diametral plane of the tube. In combination with the stepper motor drive, the whole tube can be scanned automatically in the same way as the flat specimen.

Ultrasonic Pulser-Receiver

The electromechanical system, including all the electronic equipment necessary to drive and operate the ultrasonic transducers and recording equipment, is controlled from a central control panel located on a mobile cart. The ultrasonic transducer system is operated by a Model 5052 UA pulser-receiver manufactured by Panametrics, Inc. It is capable of driving the transducers in either the pulse-echo or through-transmission mode [*1, 10*].

The pulser-receiver is a broad-band device which can readily operate transducers in the range of 1 to 20 MHz. It has independent controls for input energy, signal repetition rate, high-pass filter, gain, and attenuation, all of which control the final transducer signal. It provides a time domain output for reviewing the radio frequency (RF) signal on an oscilloscope. It also has a gated peak output detector which can operate one axis of an X-Y recorder pen for plotting the ultrasonic information contained in the variation of the peak output signal.

Transducer Selection and Ultrasonic Procedures

The requirements determining transducer selection were a standoff distance of at least 5.1 cm (2 in.) to clear hardware associated with specimen mounting; high damping and broad bandwidth to provide resolving power for detection of subsurface flaws in the 16-ply graphite/epoxy specimens to be scanned; and a small sound-beam cross section for good definition of flaw boundaries in the plane of the specimen. Broad-band focused

transducers with 15- and 5-MHz central frequencies were selected. The 5-MHz transducer was found to be more suitable for the present application, since its ultrasonic pulse could be more readily interpreted.

This 5-MHz transducer is an immersion-type transducer 2.54 cm (1 in.) in diameter. Its nominal focal length in water is 6.4 cm (2.5 in.). The focal spot size was found to be 1.3 mm (0.050 in.), which makes it possible to outline the boundary of a flaw in the plane of the specimen to within ± 0.64 mm (± 0.025 in.).

Pulse-echo was selected as the ultrasonic scanning mode. In this mode the echo pulse, when analyzed on the oscilloscope display, can be used to locate approximately the position of a detected flaw through the thickness of the specimen.

The procedures for ultrasonic inspection, data acquisition, and recording are as follows. The flat coupon specimens are immersed in the water tank and placed in a holder such that the specimen plane is parallel to the vertical and longitudinal scanning axes of the mechanical scanning system. The activated ultrasonic transducer is focused on the specimen by adjusting the transducer to specimen distance, using the horizontal transverse drive of the scanning carriage. The amplitude-time image of the echo pulse (RF pulse) from the specimen is displayed on an oscilloscope which, together with its camera, is part of the display and recording system. The upper trace of Fig. 3*a* shows a typical RF echo pulse from a specimen location without a flaw. The large "W"-shaped pulse seen on the left represents a reflection from the front face of the specimen.

The reflection from the back face of the specimen is represented by the largest "M"-shaped pulse on the right side of the upper trace of Fig. 3*a*. The lower trace of Fig. 3*a* represents the gated center section of this pulse. The electronic gate in this case is triggered by the front face reflection and blanks out all of the pulse, except the part within the gate. The front-face trigger mode maintains a constant time delay between the front face and the gate, eliminating gate drift which can be caused by imperfect flatness of the specimen. If a flaw of sufficient size is present between the front and back faces of the specimen, such as a delamination or an inclusion, it will produce an impedance mismatch, pulse reflections, attenuation, and dispersion, thereby reducing the peak amplitude of the back-face reflection. An extreme example of this is shown in Fig. 3*b* where the interlaminar inclusion of a single 0.026-mm-thick (1 mil) Kapton film patch in a 16-ply graphite/epoxy coupon completely eliminated the gated back-face reflection.

The gated part of the signal is automatically fed into the peak output detector of the pulser-receiver. The output of the detector is an amplified voltage, proportional to the absolute value of the gated peak. The amplitude of the voltage indicates the presence or absence of a flaw as illustrated in Fig. 3. It is therefore used for the detection and recording of flaws during the automatic scanning of the specimens.

A C-scan flaw indication record is produced for each specimen. To this

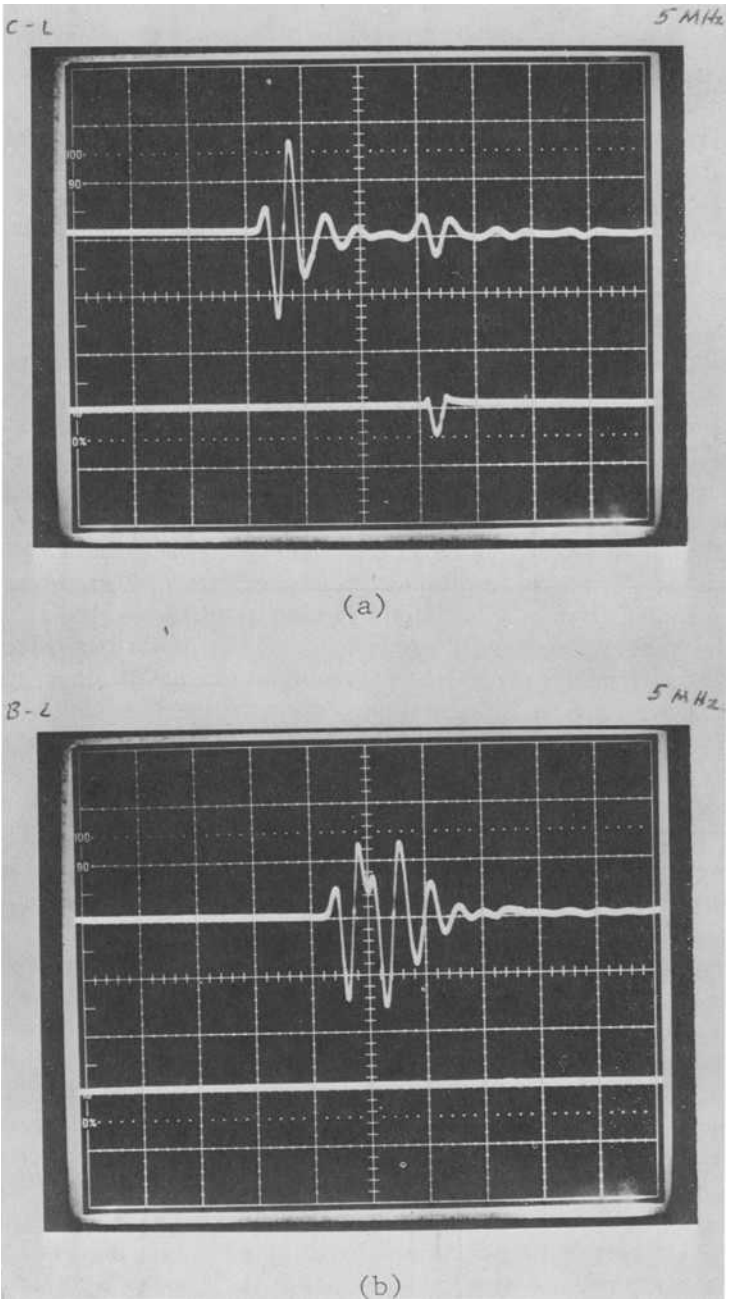

FIG. 3—*Typical oscilloscope records of the reflected ultrasonic pulse through the thickness of a* $[(0/\pm 45/90)_s]_2$ *graphite/epoxy laminate. (Upper traces: full pulse. Lower traces: gated back-face reflection).* (a) *At an unflawed location.* (b) *At a location containing an interply film patch causing total elimination of back-face reflection.*

end, the horizontal and vertical displacement transducers of the scanning drives feed their information into the pen of an X-Y recorder, tracing the motion of the ultrasonic transducer relative to the specimen. Two methods of recording flaw detection are being used, pen-lift and analog. In the pen-lift method the output from the peak detector is channeled through an electronic alarm unit into the pen-lift control of the recorder. The alarm unit is set to trigger the pen-lift whenever the amplitude of the peak detector falls below a prescribed level, indicating a flaw; otherwise the pen stays in contact with the recording paper, tracing a line. Figure 4*a* shows this type of record. It gives detailed flaw locations in the plane of the specimen with definite outlines of the flaw boundaries. The analog method, Fig. 4*b*, supplements this information by giving a continuous record of the amplitude of the gated pulse. It is obtained by scanning the specimen with the alarm unit bypassed. Approximate information of the through-the-thickness location of any flaw observed in the C-scans can be obtained by selectively returning the ultrasonic transducer to the desired location on the specimen, photographing the scope trace of the echo pulse at that location, and analyzing that record later. The selective echo-pulse data acquisition and analysis can be further enhanced by storing the pulse on magnetic tape, or in digitized form in electronic memory devices, for subsequent computer-aided analysis of the data.

Figure 5 shows examples of pen-lift C-scans used for fabrication quality control of composite tubular specimens. They were obtained using the tube scanning system described previously.

Special Problems

The flaw indications in the pen-lift scans depend entirely on the amplitude trigger level set on the alarm unit. This level must therefore be based on known standard flaws. Many types of flaws in laminated composites can produce the amplitude variations of the gated echo pulse used as the alarm trigger. Among those are delaminations, inclusions, ply gaps, resin-rich and resin-starved areas, and surface scratches. Standards for subsurface flaws cannot be readily established, since their determination itself requires a nondestructive method. However, a natural standard for gapless delaminations (unbonded but contacting areas of adjacent plies) is available and was used to set the trigger level in the present application.

The standard was obtained from specimens with drilled holes. It is known that the drilling of a hole in a laminated composite may induce a delamination which extends from the boundary of the hole into the interior. It is a gapless delamination usually undetectable by visual inspection of the hole, but clearly detectable by ultrasonic scanning in both the pulse-echo scope trace and in the analog scan. By setting the trigger level of the alarm unit to the amplitude of the gated pulse of this delamination, a standard trigger level is obtained based on a known flaw.

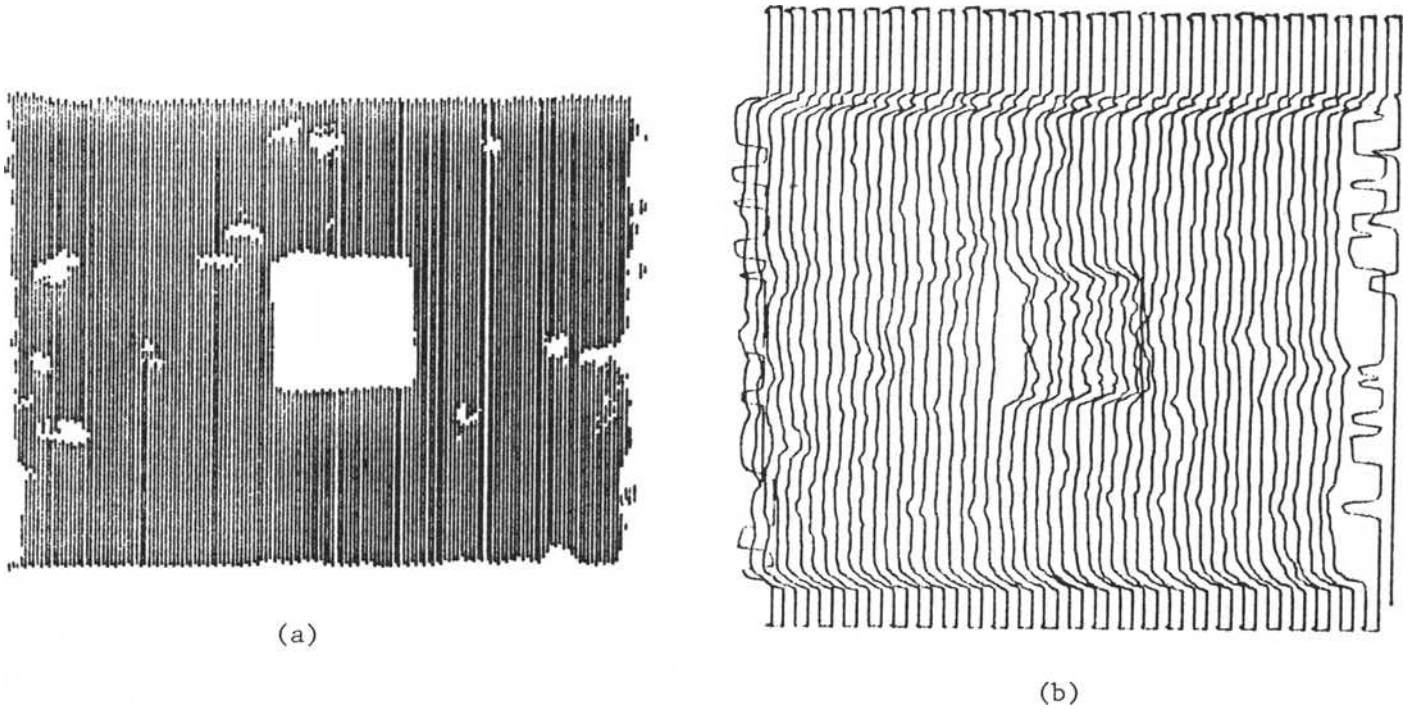

FIG. 4—*Representative ultrasonic C-scans of the same* $[(0/\pm 45/90)_s]_2$ *graphite/epoxy specimen with an initial flaw in the form of an embedded interply square film patch.* (a) *Pen-lift scan.* (b) *Analog scan.*

For delaminations extending to the edge or surface of a specimen, as in the case of holes and surface scratches, it is sometimes observed that in successive scans the flaws "heal" themselves; that is, they diminish in size. This is due to water penetration into the delaminations of the immersed specimen. It causes the specific acoustic impedance to decrease, thereby decreasing the attenuation of the gated pulse. This can easily be remedied by sealing the exposed edges and surface scratches before immersion.

Near-surface flaws, such as first-ply delaminations, may go undetected if they are located near the back face of the specimen. The width of the pulse gate may be large enough to enclose the pulse reflection from such a flaw and consequently the peak detector will show an increase rather than a decrease of the peak amplitude. This situation is recognizable on the scope trace, and can be remedied by providing an amplitude upper-level alarm trigger, in addition to the lower-level trigger. Another approach is to produce separate scans with the ultrasonic transducer facing first one then the other side of the specimen.

The standard used for detecting flaws was based on delaminations. Other flaws may also be included in this trigger level, hence flaw-type discrimination is not simple. It must be supported by knowledge of the material and, possibly, by experience gained by destructive means, such as slicing the specimen through the flaws and analyzing the section under a microscope. Dye penetrants can be used to enhance the delaminations, which can be opened to determine the depth of penetration. Although the nature of a detected flaw in a laminated composite may not be known with certainty from an initial scan, flaw growth observed after subsequent sequences of loading will likely represent delaminations or large cracking originated by these flaws.

Flaw Growth Monitoring

The ultrasonic scanning system and procedures described in the foregoing were designed to perform one of the nondestructive testing and evaluation tasks required by the Composite Serviceability Program [*16,17*] of the Air Force Materials Laboratory. The objective is to monitor the characteristics of flaw growth in initially flawed composite specimens subjected to successive lifetimes of load and environmental fatigue spectra.

All specimens discussed here were 16-ply graphite/epoxy (AS3501-5A) laminates of $[(0/\pm 45/90)_s]_2$ and $[0_2/\pm 45]_{2s}$ layups with four types of initial flaws as shown in Figs. 6 and 7. They are (1) a circular hole, (2) an embedded film patch, (3) an internal ply gap, and (4) surface scratches. They were selected as "worst type" flaws based on their likelihood of occurrence and presumed criticality. The specimen gage section was 5.08 cm (2 in.) long and 3.81 cm (1.5 in.) wide.

The specimens, three of each flaw type and layup, were subjected to fully

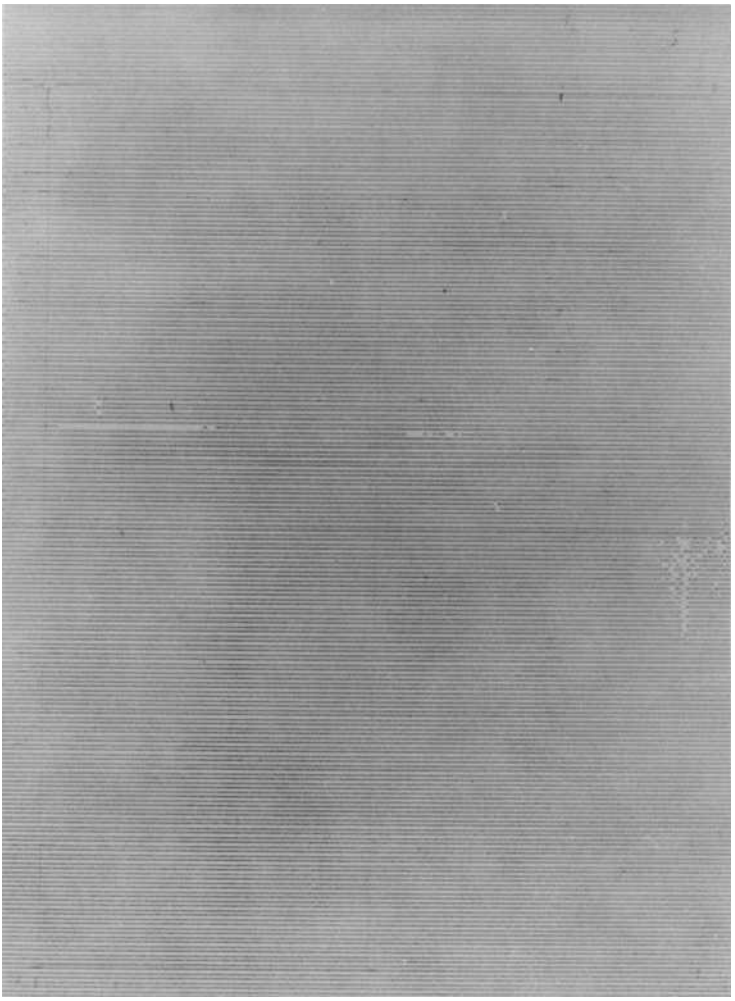

FIG. 5—*Typical ultrasonic C-scans of acceptable and unacceptable* $[0_6]$ *graphite/epoxy (SP286/T300) tubes.*

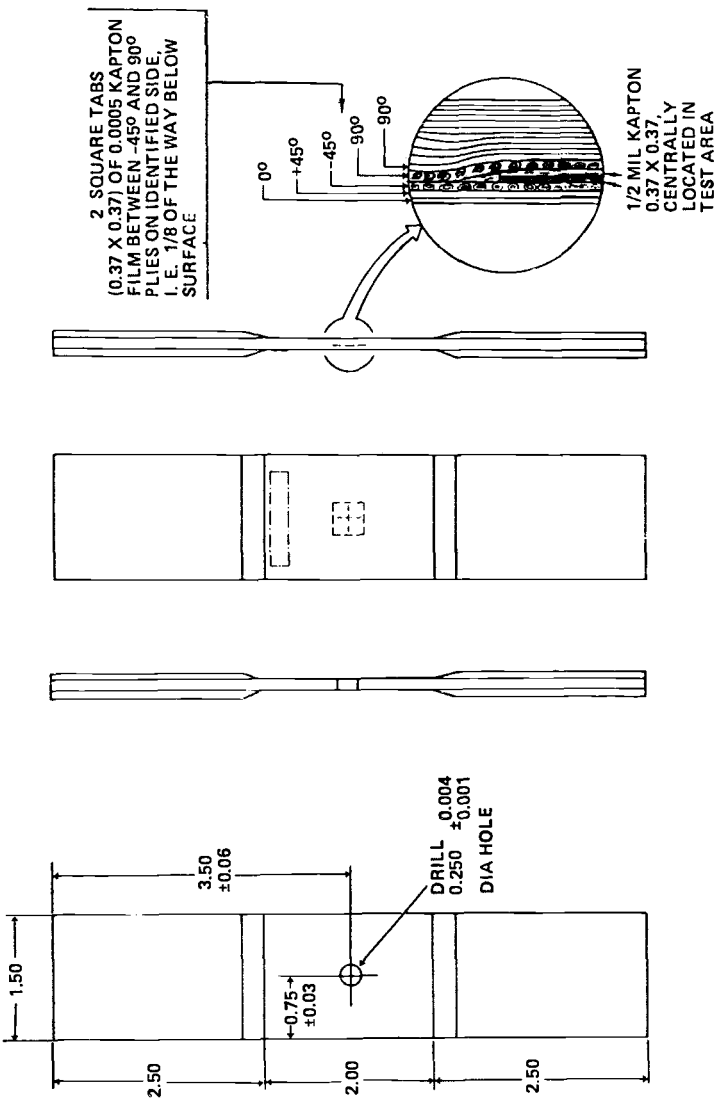

FIG. 6—*Sixteen-ply graphite/epoxy coupons showing two types of initial flaws (a circular hole to produce localized planar sharp stress gradients and an interply embedded film patch to produce localized through-the-thickness stress gradients; all dimensions shown are in inches) (1 in. = 2.54 cm).*

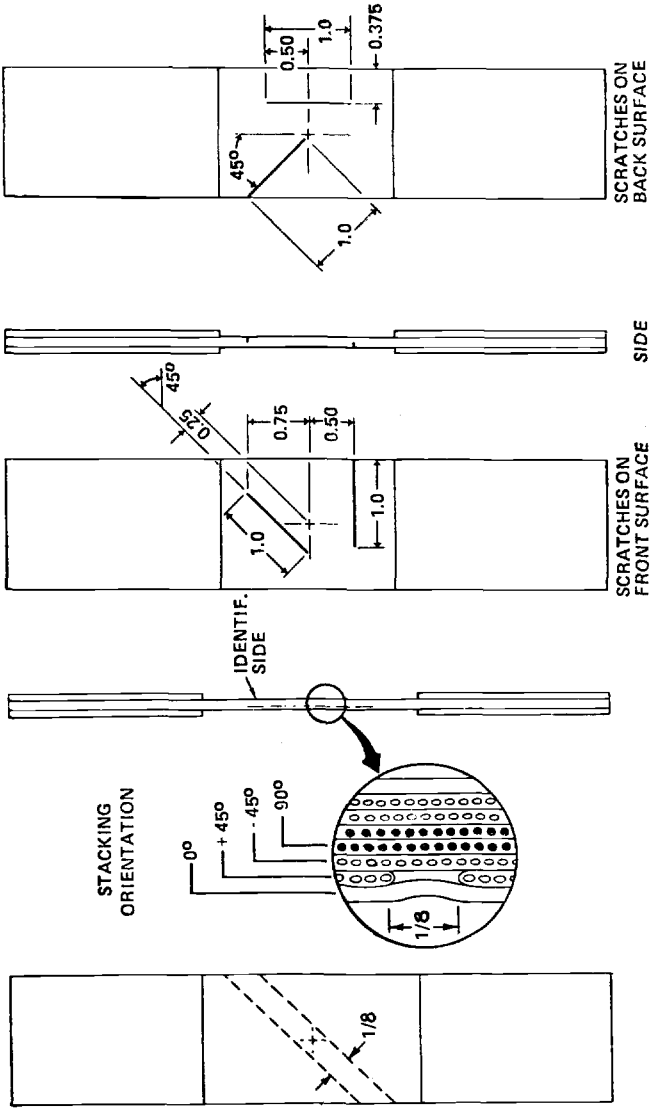

FIG. 7—*Sixteen-ply graphite/epoxy coupons showing two types of initial flaws (a ply gap to produce dispersed stress gradients and surface scratches to produce localized high stress concentrations; all dimensions shown are in inches) (1 in. = 2.54 cm).*

reversed spectrum fatigue loading simulating the load environment experienced by the composite structure. One lifetime of exposure was simulated by 127 500 cycles of tension-compression loading at various levels of peak stress. At a cycling frequency of 3 Hz, this was accomplished in approximately 12 h. The maximum load level for the $[(0/\pm 45/90)_s]_2$ specimens was 160.6 MPa (23.3 ksi), which, depending on the flaw type, represents from 28 to 53 percent of the static tensile strength of corresponding flawed specimens. The maximum load level for the $[0_2/\pm 45]_{2s}$ specimens was 223.4 MPa (32.4 ksi), which, depending on the flaw type, represents from 23 to 53 percent of the static tensile strength of corresponding flawed specimens.

Stress cycling was applied to a chain of five specimens at a time by means of an electrohydraulic closed-loop system. At intervals corresponding to each half lifetime of loading, the specimens were removed from the fatigue machine and inspected ultrasonically. The specimens were tested up to a maximum of four lifetimes. The various C-scans obtained for each specimen were combined into maps illustrating the progressive flaw growth. Following the aforementioned fatigue loading and the ultrasonic monitoring, the specimens were tested statically in tension to failure to determine their residual strength and thus assess the criticality of the various flaws.

Flaw growth contour maps obtained for specimens with the four types of initial flaws discussed herein for the two layups are shown in Figs. 8–11. In general, it can be seen that flaw growth is greater in specimens of $[(0/\pm 45/90)_s]_2$ layup than in those of $[0_2/\pm 45]_{2s}$ layup. In the case of specimens with circular holes (Fig. 8), delaminations grow around the hole boundary in the early stages of load cycling (one to two lifetimes) but no further growth is seen up to four lifetimes. However, additional delamination growth sources develop in the interior, along the edges, and along the edge of the tab. In the case of specimens with embedded patches (Fig. 9), initial delaminations were present throughout. With increasing number of load cycles, these grew and additional ones developed throughout the specimens. In the specimens with internal ply gaps (Fig. 10), some flaw growth followed along this gap but it occurred at other locations as well. In the specimen of $[0_2/\pm 45]_{2s}$ layup, flaw growth was minimal (Fig. 10*b*). Of the two types of specimens with surface scratches, the ones of $[0_2/\pm 45]_{2s}$ layup failed during the first half lifetime of loading. The other specimen (Fig. 11) shows delamination growth, but mostly around the horizontal scratch where the surface 0-deg fibers have been broken.

No significant reduction in residual tensile strength (in general less than 10 percent) was observed for any of these groups of specimens. This may be due to the relatively low fatigue loads resulting mostly in noncritical delamination flaw growth.

Similar flaw growth monitoring has been done on specimens subjected to spectrum fatigue, including temperature and humidity variations.

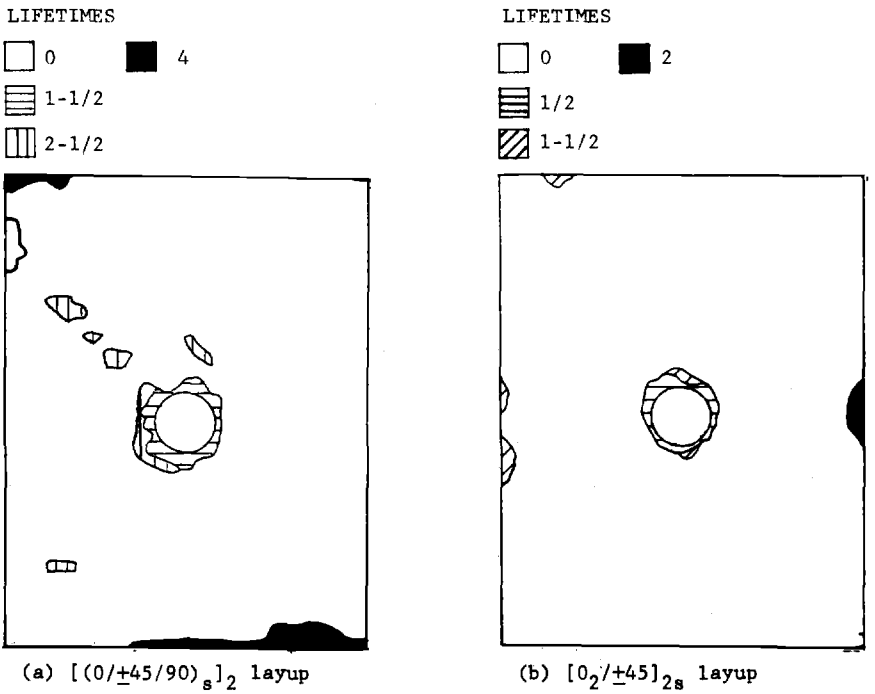

FIG. 8—*Flaw growth under spectrum fatigue loading in graphite/epoxy specimens with 6.4-mm diameter (0.25 in.) hole.*

Summary and Conclusions

An ultrasonic scanning inspection system was constructed and procedures devised to monitor nondestructively the characteristics of flaw growth in initially flawed graphite/epoxy laminate specimens subjected to successive lifetimes of load and environmental fatigue spectra. The method selected was immersion ultrasonics. It was found that a 5-MHz broad-band focused ultrasonic transducer, operated in the pulse-echo mode, was suitable for the application. Its focal length in water of 6.4 cm (2.5 in.) allowed the transducers to clear any fixturing used to hold the specimens. Its focal spot size of 1.3 mm (0.050 in.) made it possible to outline the boundary of a flaw in the plane of the specimen to within ± 0.64 mm (± 0.025 in.). Two types of C-scan recording methods were used to produce hard-copy X-Y plotter records of the ultrasonic flaw data. They were the pen-lift method and analog scans. These were augmented with photographs of scope traces of the ultrasonic echo pulse through the specimen thickness at selected flaw locations.

To detect the presence of a flaw and to identify the flaw type, known

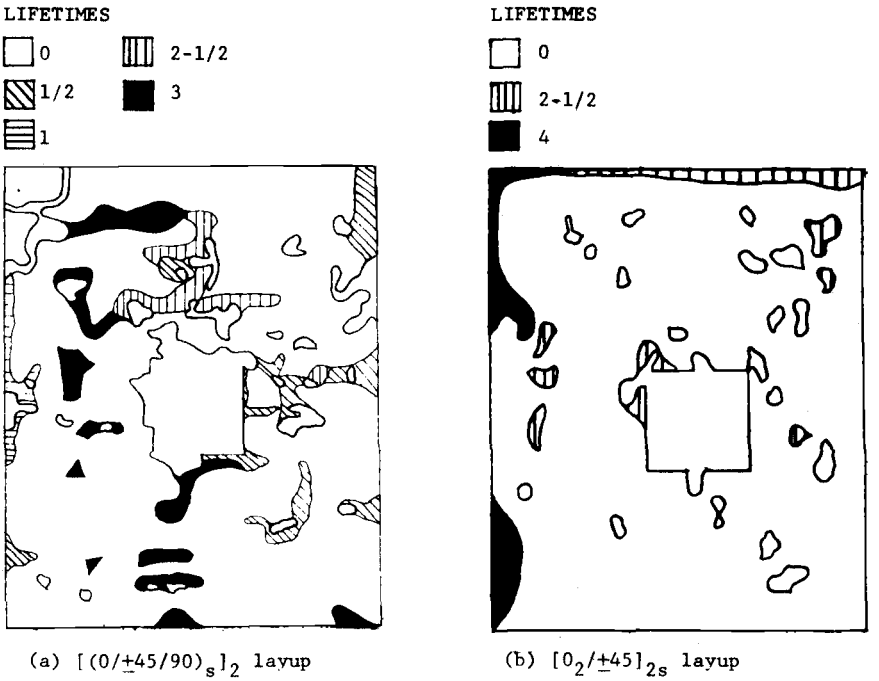

FIG. 9—*Flaw growth under spectrum fatigue loading in graphite/epoxy specimens with 9.4-mm-square (0.37 in.) embedded Kapton patch.*

standard flaws must be used to set the levels of the electronic alarm system. Such prefabricated reliable standards are not available for composite laminates. A "natural" standard was therefore utilized consisting of known gapless delaminations found in the vicinity of a hole drilled into the laminate. Special ultrasonic detection problems, such as "healing" of delamination flaws and nondetection of near-surface flaws, have been observed and explained and remedies for these problems have been found. Flaw type discrimination is not always simple and must be supported by knowledge of the material and possibly by experience gained from destructive testing. It would be especially useful if limited validation of the ultrasonic flaw detection could be performed using various destructive techniques such as specimen slicing and application of dye penetrants. Another approach that needs to be pursued is flaw identification by computer-aided analysis of the information contained in the echo-pulse traces.

Flaw growth monitoring was performed on graphite/epoxy (AS3501-5A) laminate specimens of $[(0/\pm 45/90)_s]_2$ and $[0_2/\pm 45]_{2s}$ layups with four types of initial flaws: (1) a circular hole, (2) an embedded film patch,

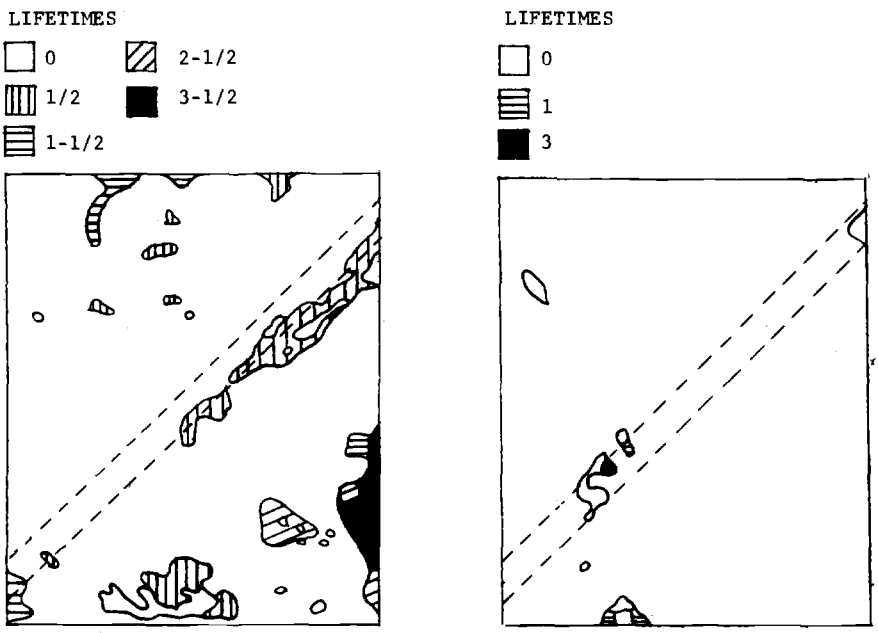

FIG. 10—*Flaw growth under spectrum fatigue loading in graphite/epoxy specimens with 3.2-mm (0.125 in.) gap in outermost 45-deg ply.*

(3) an internal ply gap, and (4) surface scratches. The specimens were subjected to fully reversed spectrum fatigue loading simulating the load environment experienced by the composite structure. One lifetime of exposure was simulated by 127 500 cycles of tension-compression loading at various levels of peak stress. Each specimen was exposed to four lifetimes of spectrum fatigue loading. Stress cycling was applied to a chain of five specimens at a time and at each half lifetime of loading the specimens were removed from the fatigue machine and inspected ultrasonically. The various C-scans for each specimen were combined into maps illustrating the progressive flaw growth. It was found that in general the flaw growth was greater in specimens of $[(0/\pm 45/90)_s]_2$ layup than in those of $[0_2/\pm 45]_{2s}$ layup. Residual strength tests performed on the specimens after four lifetimes of fatigue cycling showed no significant reduction in their tensile strengths (generally less than 10 percent). This may be due to the relatively low maximum fatigue load used during cycling (from 23 to 53 percent of static strength of corresponding initially flawed specimens), resulting mostly in noncritical delamination flaw growth.

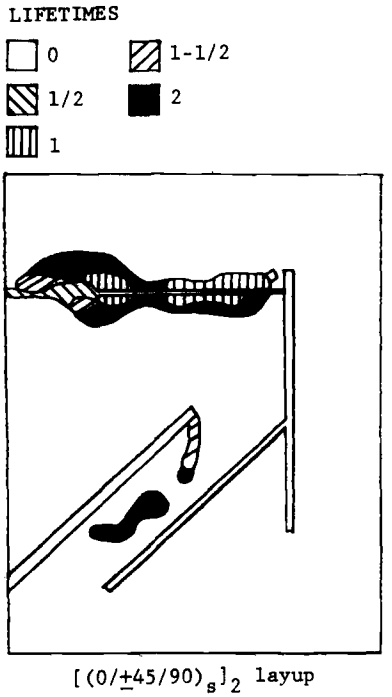

FIG. 11—*Flaw growth under spectrum fatigue loading in graphite/epoxy specimen with 0.25-mm-deep (0.01 in.) surface scratches.*

Acknowledgments

The work described herein was sponsored by the Air Force Materials Laboratory and the Air Force Flight Dynamics Laboratory, Wright-Patterson Air Force Base, Ohio, through a subcontract from Rockwell International Corp., Los Angeles, Calif. The authors would like to thank Mr. P. A. Parmley of the Air Force Flight Dynamics Laboratory for his encouragement and cooperation and Dr. George A. Alers of the Rockwell International Science Center for his invaluable advice on ultrasonic procedures and equipment. The assistance of Messrs. R. LaBedz and W. Hamilton of the IIT Research Institute in assembling and operating the scanning system is gratefully acknowledged.

References

[*1*] *Nondestructive Testing Handbook*, R. C. McMaster, Ed., The Ronald Press, New York, 1963.

[*2*] Mool, D. and Stephenson, R., *Materials Evaluation*, Vol. 29, No. 7, July 1971, pp. 159-164.

[3] Moore, J. F., *Materials Evaluation*, Vol. 25, Feb. 1967, pp. 25-32.
[4] Whiteside, J. B., Daniel, I. M., and Rowlands, R. E., "The Behavior of Advanced Filamentary Composite Plates with Cutouts," Technical Report AFFDL-TR-73-48, Air Force Flight Dynamics Laboratory, Wright-Patterson AFB, Ohio, June 1973.
[5] Rose, J. L., Carson, J. M., and Leidel, D. J. in *Analysis of the Test Methods for High Modulus Fibers and Composites, ASTM STP 521*, 1973, pp. 311-325.
[6] Pettit, D. E., "Residual Strength Degradation for Advanced Composites," Interim Technical Quarterly Report, LR 28360-5, Lockheed-California Co., for Air Force Flight Dynamics Laboratory, 5 Aug. 1978.
[7] Sendeckyj, G. P., Maddux, G. E., and Tracy, N. A. in *Proceedings*, International Conference on Composite Materials, ICCM/2, Toronto, Ont., Canada, 16-20 April 1978, pp. 1037-1056.
[8] Kulkarni, S. V., Pipes, R. B., Ramkumar, R. L., and Scott, W. R. in *Proceedings*, 2nd International Conference on Composite Materials, ICCM/2, Toronto, Ont., Canada, 16-20 April 1978, pp. 1057-1071.
[9] Harrigan, W. C., Jr. in *Proceedings*, 2nd International Conference on Composite Materials, ICCM/2, Toronto, Ont., Canada, 16-20 April 1978, pp. 1123-1140.
[10] Krautkrämer, J. and Krautkrämer, H., *Ultrasonic Testing of Materials*, Springer-Verlag, New York, 1969.
[11] Fredric, J. R., *Ultrasonic Engineering*, Wiley, New York, 1965.
[12] Gericke, O. R. in *Research Techniques in Nondestructive Testing*, R. S. Sharpe, Ed., Academic Press, New York, 1970, pp. 31-61.
[13] Chang, F. H., Kline, R. A., and Bell, J. R., "Ultrasonic Evaluation of Adhesive Bond Strength Using Spectroscopic Techniques," General Dynamics, Fort Worth Division, *Proceedings*, ARPA/AFML Review of Progress in Quantitative NDE, Scripps Institution of Oceanography, La Jolla, Calif., 18-21 July 1978.
[14] "Interdisciplinary Program for Quantitative Flaw Detection," Rockwell International Science Center, Contract No. F33615-74-C-5180, for ARPA/AFML, Sept. 1975.
[15] Mucciardi, A. N. et al, "Adaptive Nonlinear Signal Processing for Characterization of Ultrasonic NDE Waveforms," Task 2, Measurement of Subsurface Fatigue Crack Size, Technical Report AFML-TR-76-44, Air Force Materials Laboratory, Wright-Patterson AFB, Ohio, April 1976.
[16] "Advanced Composite Serviceability Program," IIT Research Institute subcontract to Rockwell International, Air Force Materials and Flight Dynamics Laboratories, Contract No. F33615-76-C-5344 (in progress, 1979).
[17] Parmley, P. A., Konishi, D. Y., and Hofer, K. E. in *Proceedings*, 2nd International Conference on Composite Materials, ICCM/2, Toronto, Ont. Canada, 16-20 April 1978, pp. 1604-1619.

G. E. Maddux[1] *and G. P. Sendeckyj*[1]

Holographic Techniques for Defect Detection in Composite Materials*

REFERENCE: Maddux, G. E. and Sendeckyj, G. P., **"Holographic Techniques for Defect Detection in Composite Materials,"** *Nondestructive Evaluation and Flaw Criticality for Composite Materials, ASTM STP 696,* R. B. Pipes, Ed., American Society for Testing and Materials, 1979, pp. 26-44.

ABSTRACT: The results of an experimental study of holographic interferometry and tetrabromoethane (TBE)-enhanced X-ray photography for damage detection in composite materials are presented. The results show that holographic interferometry using thermal loading can accurately track delamination growth, but cannot find subsurface matrix cracks. It can also provide information on the through-the-thickness distribution of delaminations. TBE-enhanced X-ray photography can find matrix cracks, delaminations, and fiber bundle fractures, but gives no information on the through-the-thickness distribution of the damage.

KEY WORDS: holography, holographic interferometry, tetrabromoethane, X-ray photography, composite materials, graphite/epoxy composites, delaminations, matrix cracks, nondestructive tests

With the increased application of advanced resin-matrix composite materials in aerospace structures, the need for detailed understanding of the failure modes and associated damage accumulation process in composites has become apparent. Since the necessary information can be obtained only through the use of nondestructive evaluation (NDE) methods, a large number of NDE techniques have been tried. Unfortunately, the complexity and small scale of the damage (consisting of matrix cracks, delaminations, and fiber fractures) has taxed the resolution capabilities of conventional NDE methods. Out of the many new techniques being applied in studies of damage growth in composite materials, tetrabromoethane

*This paper is based on in-house work performed at the Air Force Flight Dynamics Laboratory under the Air Force Wright Aeronautical Laboratories Solid Mechanics Project funded by the Mechanics Directorate of the Air Force Office of Scientific Research.

[1] Aerospace engineers, Structural Mechanics Division, Air Force Flight Dynamics Laboratory, Wright-Patterson Air Force Base, Ohio 45433.

(TBE)-enhanced X-ray radiography and holographic interferometry have proved to be most successful [*1,2*].[2]

Herein, we are primarily concerned with the techniques for applying holographic interferometry to damage and flaw detection in composites. Results obtained by using TBE-enhanced X-ray radiography are presented for comparison purposes. From the standpoint of providing detailed information about the nature and extent of the damage, X-ray radiography appears to be the better of the two methods. Unfortunately, it requires that the specimens be treated with TBE, which is a highly toxic fluid and a possible solvent for the resin matrix. A consequence of the toxicity is that either the specimens must be removed from the test frame and soaked under a chemical hood or the test frame must be located inside a chemical hood. In either case, special precautions must be taken. Holographic interferometry can be used with the specimen in the test frame with no special preparation or precautions. It yields information on the depthwise location of the damage and flaw areas. Moreover, it can be used when the damage is totally internal to the specimen, a situation in which TBE-enhanced X-ray radiography could not be used.

The theory of the holographic NDE process will not be presented here, since it is discussed extensively elsewhere [*2-8*]. It suffices to say that holography is a technique by which the image of a three-dimensional object can be stored and retrieved from a two-dimensional photographic emulsion. It is such an accurate recording that if two exposures are made on one emulsion with a slight distortion applied to the body being recorded between the exposures, the reconstructed light waves emanating from each of the recorded states interfere and produce a beat frequency pattern called interferometric fringes. These fringes are like lines of elevation on a contour map in that each fringe represents the locus of points on the surface of the object that have been displaced in the normal direction by a multiple of one-half the wavelength of the light used to record the hologram. For NDE purposes, one is interested in finding anomalies (or abrupt changes) in the fringe pattern.

Experimental Details

Specimen Description

Four out of 50 specimens, with the geometry shown in Fig. 1, were used in the present study. The specimens came from the $[(0/\pm 45/90)_3]_2$ T300/5208 graphite/epoxy panel used in a previous study [*9*]. The composition of the panel, as determined by the nitric acid digestion method, was 64.3 percent fibers by volume, 34.9 percent resin by volume, and 0.8

[2]The italic numbers in brackets refer to the list of references appended to this paper.

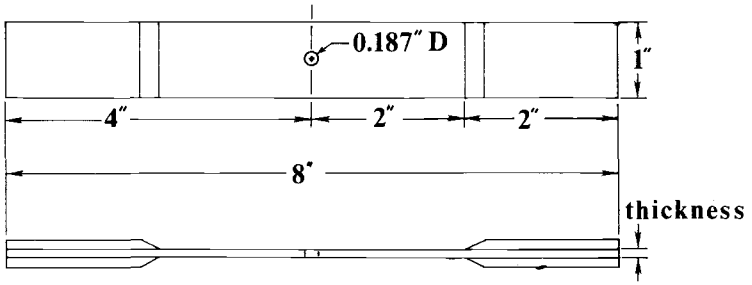

FIG. 1—*Specimen geometry (1 in. = 2.54 cm).*

percent voids. The widths, thicknesses, and hole diameters (as measured with a flat-headed micrometer and go/no-go hole gauges) for the two specimens for which results are presented herein were 25.4 mm (1.000 in.), 2.18 mm (0.086 in.), and 4.75 mm (0.187 in.), respectively.

Test Procedure

First, the initial quality of the specimens was evaluated by using TBE-enhanced X-ray radiography and holographic interferometry. This evaluation defined the fabrication-induced damage and defects initially present in the specimens and served as the baseline for comparison in the damage growth study. Then the specimens were alternately subjected to a loading history and NDE. The loading history consisted of an initial static tensile loading to 13.3 kN (3000 lb) followed by successive blocks of constant-load-amplitude fatigue loading using a sinusoidal waveform. The cyclic loading was performed at 5 Hz. The maximum and minimum cyclic loads were 13.3 kN (3000 lb) and 1.33 kN (300 lb), respectively. Each fatigue loading block contained 50 000 cycles. Note that the maximum cyclic stress used is approximately 86 percent of the static tensile strength of the specimen.

TBE-Enhanced X-Ray Radiography Procedure

Since damage in graphite/epoxy specimens does not provide the necessary X-ray contrast, an X-ray opaque fluid (TBE) was continuously applied to the surfaces of the specimen in the damaged region for 30 min to give it sufficient time to penetrate into all of the matrix cracks and delaminations. After it had fully saturated the damage regions, the excess TBE was removed from the surfaces of the specimens with absorbent towels. The specimens were

then laid directly on top of a Kodak[3] Type R single-coat industrial film pack and X-rayed using a small-focal-spot Norelco 150 unit at a focal film distance of 91.4 cm (36 in.) operating at 25 kV and 5 mA. The film was exposed for 1.5 min. After X-raying, the TBE was withdrawn from the specimen in a vacuum desiccator.

Holographic Setup

The standard off-axis holographic setup, shown in Fig. 2, was used to record the holographic fringe patterns (interferograms) used herein. Two types of recording methods were used. The first one, called "real time" holography, consists of recording a reference image of the specimen in such a way that, when the developed hologram is replaced in a special holder and illuminated with the reference beam used during the recording process, the reconstructed image is located in space precisely where the object is located. If the specimen is then illuminated simultaneously with the hologram, a pair of exactly superimposed images is seen. By applying a slight distortion on the order of a few micrometres normal to the surface of the specimen, the two images form an interference pattern commonly called holographic fringes. These alternating light and dark fringes are similar to lines on a contour map, each dark fringe representing a contour level approximately 0.32 μm (12.5 μin.) above or below the adjacent fringe. For NDE purposes, one is usually not interested in mapping the displacement field but rather in searching for anomalies in the fringe pattern that can be related

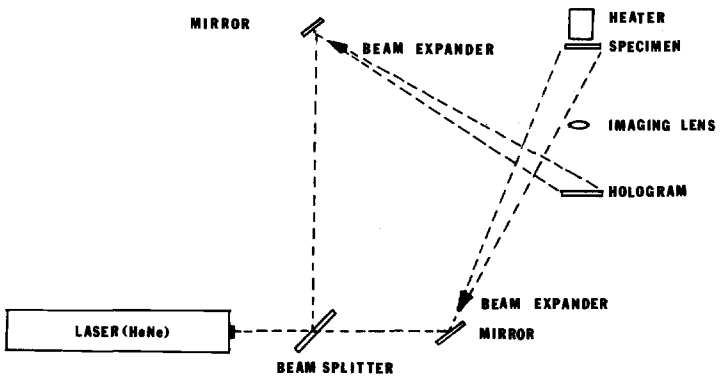

FIG. 2—*Schematic diagram showing standard off-axis holographic setup.*

[3] Reference to a company or product name does not imply approval or recommendation of the product by the Air Force Flight Dynamics Laboratory to the exclusion of others that may be suitable.

to subsurface flaws. The fringe patterns can be either photographed through the hologram or recorded on videotape to observe transient phenomena.

The second recording technique is used when a high-resolution fringe pattern is required for some given time slice of a transient pattern. This is done by first making an exposure of the specimen in the undisturbed condition and, without moving the film plate, applying a transient deformation to the specimen. A second exposure is then made at the chosen time and the holographic plate removed and developed. When illuminated with the reference beam, a fixed fringe pattern results corresponding to the displacement field existing at the selected time slice. The exposure duration must be chosen so that the movement of the specimen is less than 0.16 μm (6 μin.) or a blurred reconstruction and low-contrast fringes will result. This is one of the reasons that the real-time hologram is recorded first when examining a new set of specimens. By observing the transient fringe patterns, one can determine at what time after the initial distortion an optimum recording can be made. Once this time is established for one specimen, it is usually applicable for the rest of the specimens.

A slight variation to the usual holographic setup was used herein. A standard camera lens was placed between the specimen and the film plate to create an image-plane hologram. This arrangement produces a hologram from which the image of the specimen can be reconstructed using noncoherent white light instead of laser light. The resulting image is of much higher quality than the laser light reconstructed image since it does not contain the speckle noise that results from coherent light reconstruction.

In practice, we found that the image-plane recording lens could be left in place when recording and viewing real-time holograms since the fringe patterns could be observed by simply looking around the lens. We used a Schneider Xenotar f/2.8 80-mm flat field lens in the study. Its small outside diameter allows it to be placed close to the specimen without blocking the object illuminating beam. The quality of the lens is not critical since both the reference object image and the distorted object image are seen through the same lens area and, hence, any imperfections that may be present cancel out. We tried to set up an additional optical element to view the aerial image as a real-time hologram. However, the fringe quality was significantly degraded and, hence, this idea was not pursued further.

The image size was selected to cover the area surrounding the hole out to each edge of the specimen and excluding the grip areas since they were of no interest for this study. It should be noted that much greater magnifications are possible if more detail around the damage area is desired. In fact, holography through a microscope is an established technique [*10*] that has not yet been applied to composite NDE.

As mentioned previously, the specimen must be deformed in some manner that will cause anomalies due to the presence of flaws and damage to appear in the fringe pattern. The three most common techniques for deforming

the specimen are mechanical, acoustic, and thermal loading. Mechanical loading consists of applying an out-of-plane force or moment to the specimen, creating a uniform curvature of the specimen surface. This loading technique has been shown to be relatively insensitive to delaminations and matrix cracks in composite materials when using conventional holography. There is a promising approach for use with mechanical loading that has been explored by Dändliker [*11*], but it is not yet in general use. Acoustic loading accomplished with either a loudspeaker driver or by attaching a piezoelectric crystal to the specimen produces a simple harmonic vibration of the test specimen. The real-time holographic fringe pattern is observed as the driving frequency is slowly varied. When the specimen reaches a resonant frequency, a standing wave fringe pattern forms. A flawed specimen usually has distinctly different standing wave patterns than an unflawed one. While more sensitive than the mechanical loading technique, this technique is still not sufficiently sensitive due to the small scale of the damage encountered in the specimens used for this study. Thermal loading has been found to be an excellent method for detecting flaws in honeycomb and laminated metallic structures and, hence, it was selected as the optimum method for applying a small deformation on the specimen. The main purpose of the thermal loading device is to provide a precisely controlled heat flux which can be applied selectively to portions of the test specimen. Various devices (including infrared heat lamps, hot-air blowers, hot and cold fluids, and electrical resistance heaters) have been used in the past. The resistance heater was selected for this study because (1) it can best apply the heat flux necessary to cause a few degrees surface temperature rise without emitting visible light which would fog the photographic plate, and (2) it is easily controlled.

Previous work [*2*] was conducted using a large area heater, which was convenient for searching large panels for defects. For smaller specimens and for local examination of large ones, the more compact heat source shown in Figs. 3 and 4 was developed. Its small size allows it to be easily positioned and also permits localized heating of the specimen. The localized heating minimizes the gross deformation of the specimen, which sometimes causes irreversible changes at the boundary clamp that do not allow the specimen to return to its original position after cool-down and which complicates the interpretation of the fringe patterns during the next heating cycle. Moreover, the presence of a gross deformation tends to mask small fringe anomalies, reducing the accuracy and sensitivity of the loading method.

The thermal output of the heater was controlled in the following manner. As shown schematically in Fig. 3*b*, a Wavetek Model 111 voltage control generator is used to select the desired waveform and frequency. The voltage output from the Wavetek is then fed to a TRIAC 611-1 optical solid-state relay which controls the input voltage to a Variac variable trans-

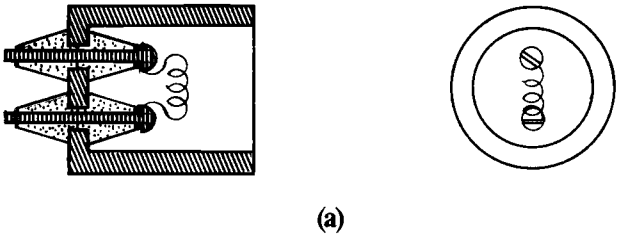

(a)

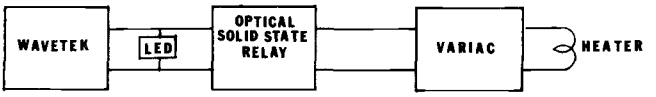

(b)

FIG. 3—(a) *Heater configuration and* (b) *heater control schematic.*

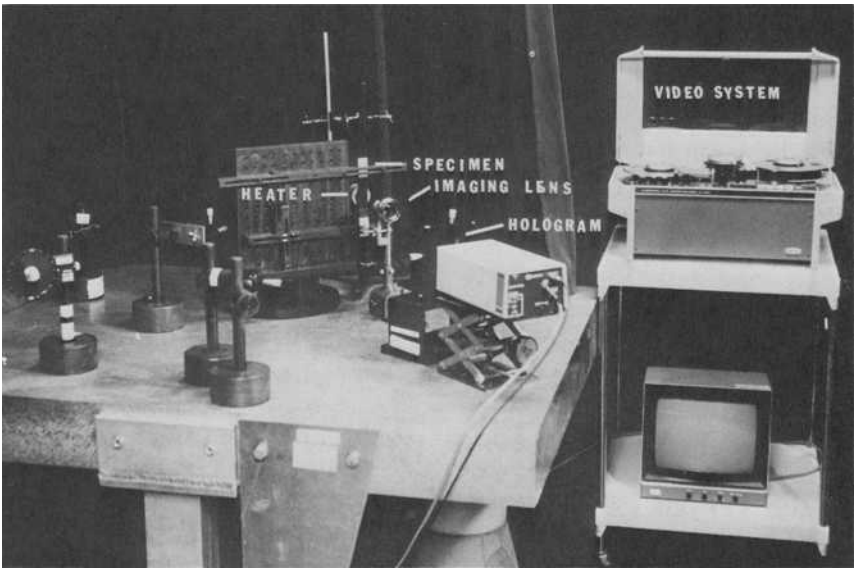

FIG. 4—*Photograph showing the holographic setup: specimen holding fixture, video recording system, and heater.*

former set for a maximum output between 5 and 10 Vac. The Variac controls the thermal output of the heater. This control device allows one to use heating frequencies as low as 0.003 Hz. A light-emitting diode connected across the output of the Wavetek lights up at the beginning of each heating cycle so that the user does not start heating the specimen part way through a voltage-on cycle.

Holography Procedure

The following procedure was used in making the interferograms used in the present paper:

1. The test specimens were stored for a minimum of 4 h in the photomechanics facility to reach temperature equilibrium with the environment.
2. Then the first specimen was mounted with both ends securely clamped in the general-purpose test fixture shown in Fig. 4. The clamped condition provided for a minimum of out-of-plane bending, which tends to obscure the fringe anomalies due to the damage. The fixture and the optical elements were arranged to produce the desired hologram and remained in this position throughout the remaining tests. An angle of 65 deg was set between the object beam and the reference beam where they intersect at the film plate. The film plate was aligned so that its normal coincided with the normal to the test specimen. This differs from the usual procedure of aligning the plate normal to the bisector of the reference-beam/object-beam angle. This was done so that the same holography arrangement could be used for making both the double-exposure image-plane and real-time holograms without any setup changes other than changing the holographic plate holding mechanism. The high beam angle was selected to optimize the image-plane holograms at a small sacrifice to the quality of the real-time ones.
3. A real-time hologram was recorded using an object beam to reference beam intensity ratio of one half.
4. A video recording and playback system using a low-light level camera was then aligned and adjusted to produce a maximum contrast recording.
5. Using the thermal pulsing control device and the real-time holographic fringe patterns, an optimum thermal cycle was determined and recorded on videotape. The optimum time for making the double-exposure image-plane holograms was also determined.
6. The image-plane hologram plate holder and imaging lens were then placed in the holography setup. Using a variable-intensity beam splitter, the beam ratio was reestablished to compensate for the change in the object beam intensity passing through the lens. Experiments were conducted using the image-plane holography setup for real-time holography. However, the fringe contrast was poor and the image intensity was below the light level needed by the video recording system.

7. The specimen was allowed to cool for at least 30 min and then a reference (undisturbed) exposure was made.

8. The optimum thermal cycle determined in Step 5 was then applied, raising the back surface temperature of the specimen approximately 5 to 10 deg C.

9. The second exposure was made at the optimum time determined in Step 5.

10. The exposed plate was then processed for 5 min in Kodak D-19 developer and fixed for 3 min in Kodak Rapid Fix. After a preliminary wash of 1 min, the plate was viewed with a non-coherent white light source such as a small high-intensity lamp or a microscope light. The resulting fringe pattern was evaluated and, if found acceptable, the plate was immediately returned to the wash for 5 min more, soaked for 1 min in Kodak Photo-Flo, had excess water removed, and then was allowed to air dry.

11. The specimen was then reversed and the back side subjected to Steps 7 through 10. It is possible to use a mirror arrangement to simultaneously record the front and back surfaces of the specimen. However, this complicates the design of the thermal loading device and is not necessary when only a few specimens are being examined.

12. When all of the specimens had been holographically recorded, the image-plane hologram holder was removed to a convenient location to hold the holograms during the conventional photographic recording process.

13. For best viewing, the plate was placed with the emulsion side toward the observer and the white light source placed at the same angle with respect to the plate as the recording reference beam in the holography set-up. The distance of the white light source from the plate is not critical. Since the double-exposure image-plane hologram is essentially a complex diffraction grating, the white light is diffracted into the range of colors across the visible spectrum. As one moves his viewing point of the image from side to side, the color of the reconstructed image changes continuously but the fringe pattern does not change. Experience has shown that a yellowish-green image provides excellent fringe contrast for photographic recording of this image with Kodak color or Kodak TRI-X black-and-white negative film. Experience has also shown that viewing projected 35-mm color slides of the holograms is the best technique for examining and interpreting fringe patterns. The photographs for this paper were made with a Nikon F2 camera using a Vivitar Series 1 lens in the macro position.

Discussion of Results

TBE-enhanced X-ray photographs and holographic fringe patterns showing the damage as a function of loading history for the two specimens

are illustrated in Figs. 5-10. Specifically, Figs. 5 and 8 show the holographic fringe patterns (interferograms) on the front (numbered) face of the specimens; Figs. 6 and 9 show the holographic fringe patterns on the back face of the specimens; and Figs. 7 and 10 show the TBE-enhanced X-ray photographs viewing the specimens from the front side. The front and back face interferograms are "mirror images" of each other in that the right-hand sides of the views in Figs. 5 and 8 correspond to the left-hand sides of the views in Figs. 6 and 9. Views *a*, *b*, *c*, and *d* in the figures show the damage present (*a*) initially, (*b*) after a static tensile load of 13.3 kN (3000 lb), (*c*) after 50 000 cycles of fatigue loading with a stress ratio of 0.1 and maximum cyclic load equal to 13.3 kN (3000 lb), and (*d*) after 100 000 cycles of fatigue loading with stress ratio of 0.1 and maximum cyclic load of 13.3 kN (3000 lb), respectively. Note that the maximum cyclic load used is approximately 86 percent of the static tensile strength of the specimens. Hence, the fatigue loading employed in the study

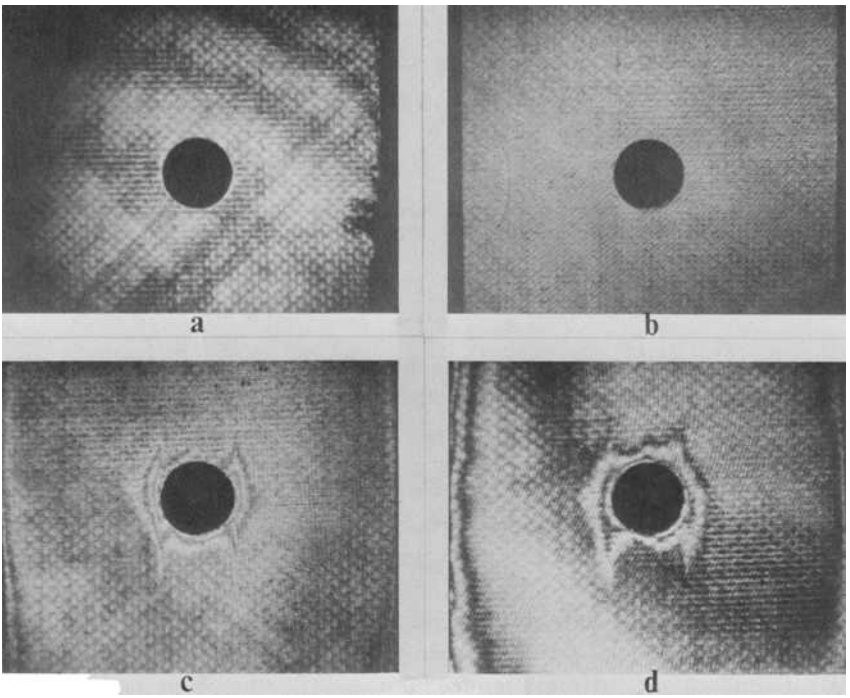

FIG. 5—*Front surface interferograms for Specimen AB-91 showing the damage present* (a) *initially,* (b) *after a static tensile load of 13.3 kN, (3000 lb),* (c) *after 50 000 cycles of fatigue loading with stress ratio of 0.1 and maximum cyclic load of 13.3 kN (3000 lb), and* (d) *after 100 000 cycles of fatigue loading with stress ratio of 0.1 and maximum cyclic load of 13.3 kN (3000 lb).*

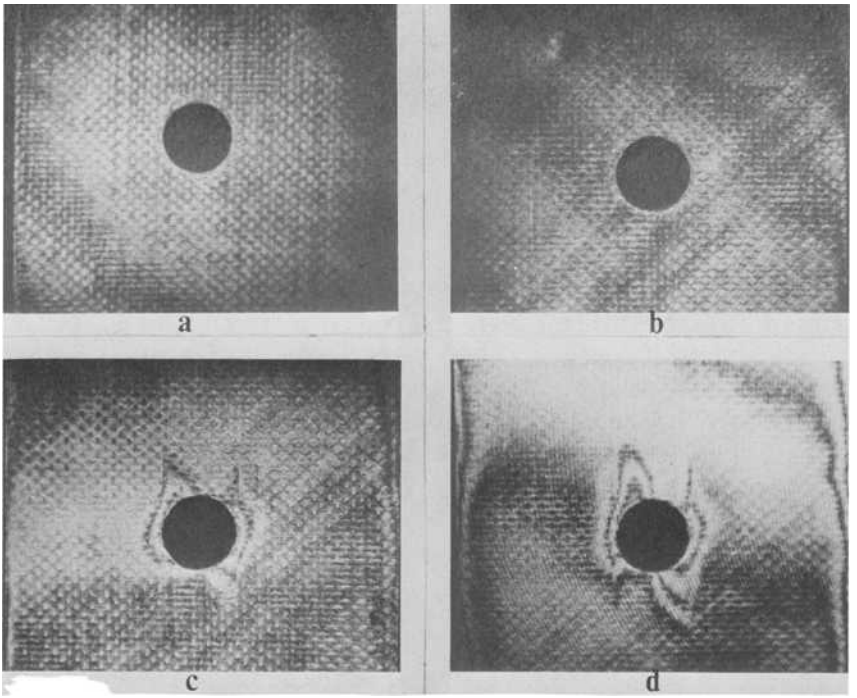

FIG. 6—*Back surface interferograms for Specimen AB-91 showing the damage present* (a) *initially,* (b) *after a static tensile load of 13.3 kN (3000 lb),* (c) *after 50 000 cycles of fatigue loading with stress ratio of 0.1 and maximum cyclic load of 13.3 kN (3000 lb), and* (d) *after 100 000 cycles of fatigue loading with stress ratio of 0.1 and maximum cyclic load of 13.3 kN (3000 lb).*

is extremely severe in comparison with typical fatigue design load levels. The experimental results are interpreted in the following.

Specimen AB-91

Front and back surface interferograms and TBE-enhanced X-ray photographs (viewing the front face) for Specimen AB-91 are shown in Figs. 5–7. The clothlike pattern seen in Figs. 5 and 6 is the impression on the specimen surface left by the release ply used during laminate fabrication. As can be seen from Views *a* in the figures, the specimen contained a small amount of fabrication-induced damage resulting from the hole drilling process. The damage consists of a small delamination region and matrix cracks near the back surface plies of the specimen in the vicinity of the hole. The delamination, which cannot be seen in Fig. 5*a*, appears as barely discernable anomalous fringes near the hole in Fig. 6*a* and as a dark outline near the hole in Fig. 7*a*. The difference in anomalous fringe

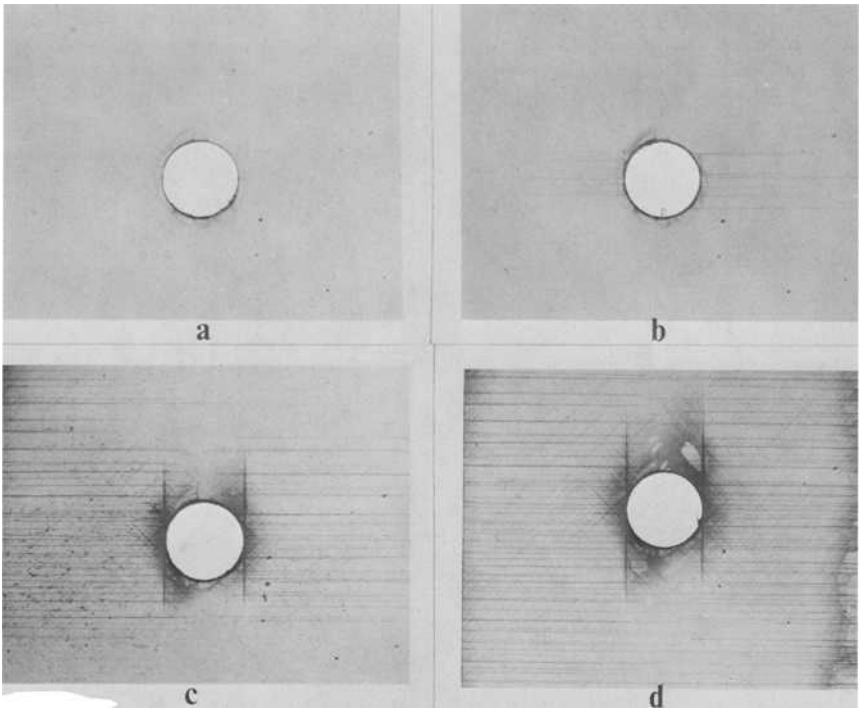

FIG. 7—*TBE-enhanced X-ray photographs (viewing the front face) for Specimen AB-91 showing the damage present* (a) *initially,* (b) *after a static tensile load of 13.3 kN (3000 lb),* (c) *after 50 000 cycles of fatigue loading with stress ratio of 0.1 and maximum cyclic load of 13.3 kN (3000 lb), and* (d) *after 100 000 cycles of fatigue loading with stress ratio of 0.1 and maximum cyclic load of 13.3 kN (3000 lb).*

patterns on both faces of the specimen helps locate the delamination as being near the back face of the specimen. The nonanomalous thermal loading fringes appear as relatively wide, dark bands in the views. The back surface matrix cracks can be seen as dark vertical (0 deg) and diagonal (± 45 deg) lines in Fig. 7*a* and cannot be distinguished at all in Figs. 5*a* and 6*a*. The dark spots that are common to all the views in Fig. 7 are foreign material contamination in the laminate.

The damage resulting from the static tensile load of 13.3 kN (3000 lb) is shown in Views *b* of the figures. As can be seen from a comparison of Views *a* and *b* in Figs. 5 and 6, the holographic damage indications (anomalous fringes near the hole) have not changed, implying that the delaminations have not grown in size. This is confirmed by a comparison of Views *a* and *b* in Fig. 7. As can be seen from this comparison, the fabrication-induced matrix cracks and delaminations have not grown, but damage was done by the load application. This damage consists of matrix

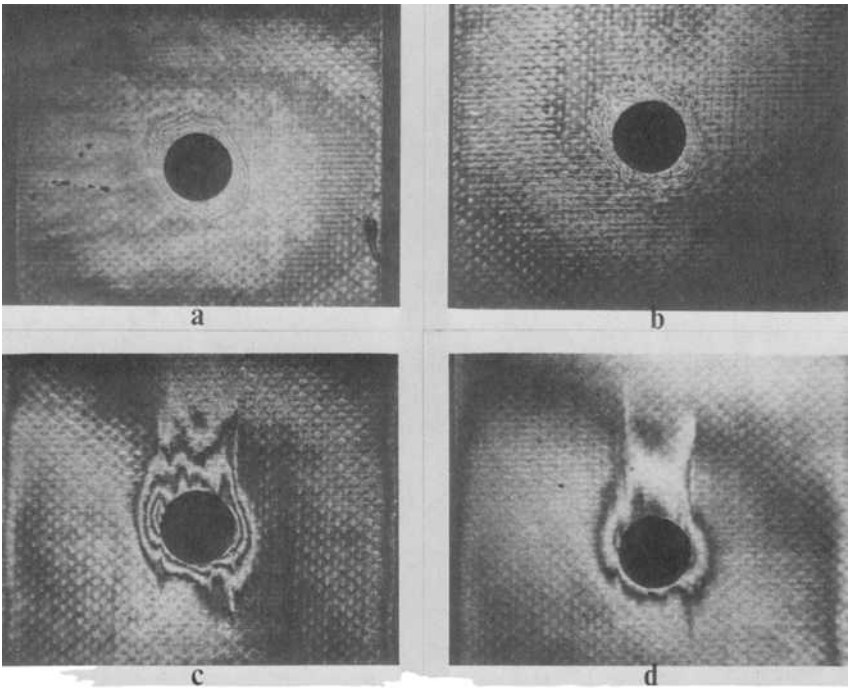

FIG. 8—*Front surface interferograms for Specimen AB-97 showing the damage present* (a) *initially,* (b) *after a static tensile load of 13.3 kN (3000 lb),* (c) *after 50 000 cycles of fatigue loading with stress ratio of 0.1 and maximum cyclic load of 13.3 kN (3000 lb), and* (d) *after 100 000 cycles of fatigue loading with stress ratio of 0.1 and maximum cyclic load of 13.3 kN (3000 lb).*

cracks in the 90-deg plies (dark horizontal lines in Fig. 7*b*), matric cracks in the 0-deg plies (dark vertical lines in Fig. 7*b*), and matrix cracks in the ±45-deg plies (dark diagonal lines in the figure) emanating from the hole. While most of the matrix cracks terminate inside the specimen, some of the 90-deg cracks run to the specimen edges. Note that the matrix cracks seen in Fig. 7*b* cannot be seen in the interferograms in Figs. 5*b* and 6*b*.

The damage resulting from 50 000 cycles of constant-load-amplitude fatigue loading with maximum cyclic load of 13.3 kN (3000 lb) is shown in Views *c* of Figs. 5–7. As can be seen from a comparison of Views *b* and *c* of Figs. 5 and 6, the holographic damage indications have undergone an appreciable change in size and appearance, implying considerable delamination growth due to the fatigue loading. The delamination indications near the hole and specimen edges in Figs. 5 and 6 are distinctly different in appearance. This implies that different delaminations are seen in the front and back face interferograms. The most likely depth location

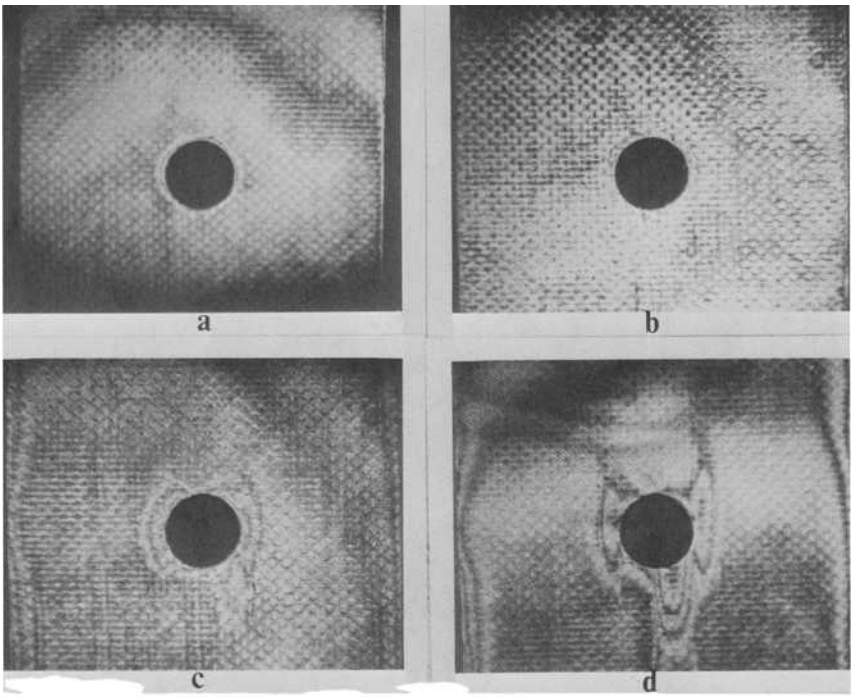

FIG. 9—*Back surface interferograms for Specimen AB-92 showing the damage present* (a) *initially,* (b) *after a static tensile load of 13.3 kN (3000 lb),* (c) *after 50 000 cycles of fatigue loading with stress ratio of 0.1 and maximum cyclic load of 13.3 kN (3000 lb), and* (d) *after 100 000 cycles of fatigue loading with stress ratio 0.1 and maximum cyclic load of 13.3 kN (3000 lb).*

for the delaminations is between the 90-deg and adjacent 45-deg plies. There are also delaminations between the surface 0-deg and subsurface 45-deg plies above and below the hole, but these cannot be separated from the other delaminations in Figs. 5*c* and 6*c*. The vertical cusps and boundaries in the anomalous fringes near the hole suggest the presence of surface ply matrix cracks. By comparison, the TBE-enhanced X-ray photograph shown in Fig. 7*c* clearly indicates the presence of 0-deg ply matrix cracks near the edges of the hole. Moreover, an extensive pattern of matrix cracks in the 90-deg and ±45 deg plies can be seen in Fig. 7c. The matrix cracks in the 90-deg plies run from the edges of the hole to the specimen edges and from the specimen edges toward the center of the specimen above and below the hole. The matrix cracks in the 90-deg plies above and below the hole terminate in the compressive stress regions near the hole. The extensive pattern of dark spots in Fig. 7*c* that cannot be seen in the other views is TBE residue on the specimen surfaces resulting from incomplete cleaning of the specimen surfaces.

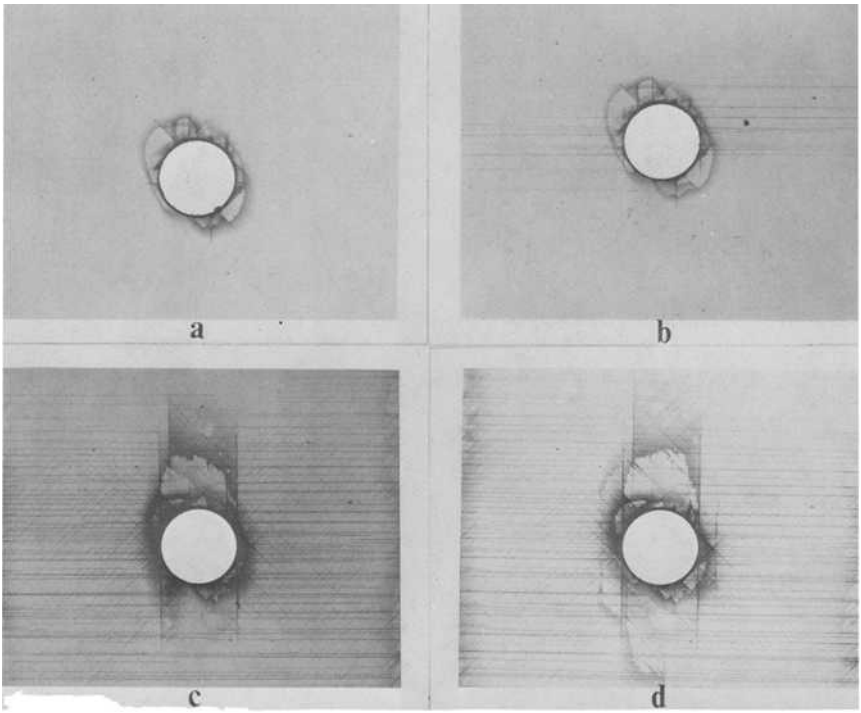

FIG. 10—*TBE-enhanced X-ray photographs (viewing the front face) for Specimen AB-97 showing the damage present* (a) *initially,* (b) *after a static tensile load of 13.3 kN (3000 lb),* (c) *after 50 000 cycles of fatigue loading with stress ration of 0.1 and maximum cyclic load of 13.3 kN (3000 lb), and* (d) *after 100 000 cycles of fatigue loading with stress ratio of 0.1 and maximum cyclic load of 13.3 kN (3000 lb).*

The damage resulting from 100 000 cycles of constant-load-amplitude fatigue loading with maximum cyclic load of 13.3 kN (3000 lb) is shown in Views *d* of Figs. 5–7. As can be seen from a comparison of Views *c* and *d* in Figs. 5 and 6, the holographic damage indications have undergone an appreciable change in size and appearance, implying considerable delamination growth due to the fatigue loading. With the exception of the cusps and vertical boundaries in the anomalous fringe patterns near the hole, there is no evidence of matrix cracking in the interferograms. In contrast, the TBE-enhanced X-ray photograph in Fig. 7*d* shows extensive matrix cracking. The delaminations near the hole and right-hand side of Fig. 7*d* have a splotchy appearance. This is a direct consequence of the extent of the damage present. The TBE, as it penetrates the damage regions, forms a meniscus which results in the dark appearance of the delamination boundaries and the splotchy regions within the delamination boundaries.

Specimen AB-97

Front and back surface interferograms and TBE-enhanced X-ray photographs (viewing the front face) for Specimen AB-97 are shown in Figs. 8–10. As can be seen from View *a* in these figures, the specimen contained a large amount of fabrication-induced damage resulting from the hole drilling. The damage consists of a large delamination region near the front surface of the specimen (anomalous fringes in the vicinity of the hole in Fig. 8*a*) and a small delamination near the back surface (fringe anomalies near the hole in Fig. 9*a*). The cusps seen in the fringes in Fig. 8*a* suggest the presence of front surface matrix cracks. These cracks are clearly seen in the TBE-enhanced X-ray photograph shown in Fig. 10*a*. This figure also shows the presence of matrix cracks in the ±45-deg plies.

The damage resulting from the static tensile load of 13.3 kN (3000 lb) is shown in View *b* of the figures. As can be seen from a comparison of Views *a* and *b* in Figs. 8–10, the delaminations have not grown as a result of the tensile load. As pointed out previously, the tensile load caused matrix cracks in the 0, 90, and ±45-deg plies. These cracks can be seen in Fig. 10.

The damage resulting from 50 000 cycles of constant-amplitude fatigue loading with maximum cyclic load of 13.3 kN (3000 lb) is shown in View *c* of Figs. 8–10. As can be seen from the views, the delaminations grew considerably as a result of the cyclic loading. As was observed previously for Specimen AB-91, the delamination indications in Figs. 8*c* and 9*c* are distinctly different in appearance from each other. This implies that different delaminations are actually seen in the front and back surface interferograms. The vertical cusps in the anomalous fringes near the hole suggest the presence of surface ply matric cracks. This is confirmed in Fig. 10*c*, which shows the TBE-enhanced X-ray photograph. Figure 10*c* also shows an extensive pattern of matrix cracks running in the 90-deg and ±45-deg directions.

The damage resulting from 100 000 cycles of constant-load-amplitude fatigue loading with maximum cyclic load of 13.3 kN (3000 lb) is shown in Views *d* of Figs. 8 through 10. As can be seen by comparing Views *c* and *d* in these figures, the delaminations have grown as a result of the additional fatigue loading. The delaminations have also caused matrix cracks in the 0-deg plies (vertical lines in Fig. 10*d*) away from the hole.

Anomalous Fringe-Causing Mechanism

Once high-quality fringe patterns like the ones in Figs. 8 and 9 have been recorded, they must be related to the damage existing in the specimen. Herein, this was done by comparing the interferograms to TBE-enhanced X-ray photographs showing the same damage. Since it may not be possible

always to do this, the mechanism causing the anomalous fringes corresponding to the damage must be understood. Unlike debonds or core failures in laminated metallic and sandwich structures that are easy to detect and interpret using holography [*3–5*], the damage in composite materials is very complex. It consists of matrix cracks, fiber fractures, and delaminations. Moreover, the nature of the material tends to diffuse the effect of buried damage. In order to produce a surface deformation which results in a fringe anomaly, the effect of the damage has to be transmitted through the layers of intact fibers and matrix. This fact is useful in that by examining the front and back surface fringe patterns one can make a qualitative statement about the depth location of the damage.

After several experiments, the anomalous fringe-producing mechanism is still not clear. The damage consisting of fiber fractures, matrix cracks, and delaminations can affect the displacement behavior of the specimen in three ways. First, it can have an effect on the thermal conductivity and coefficient of thermal expansion of the specimen. Heat flowing from the back face of the specimen encounters a very high resistance across delaminations, creating a nonuniform temperature field within the specimen. Fiber bundle failures and matrix cracks parallel to the fibers reduce the conductivity in the plane of the laminate, also contributing to the nonuniformity of the temperature field. The coefficients of thermal expansion of the plies on opposite sides of the delaminations are expected to be different. This in conjunction with the nonuniform temperature field results in nonuniform mechanical loads in the specimen. The second effect of the damage is on the mechanical properties of the specimen, producing localized changes in stiffness and ability to transmit the thermally induced mechanical loads. The third effect is related to the surface mismatch across delamination interfaces. When a delamination occurs, the mating surfaces are not perfectly smooth, but have a ridged surface following the contours of the fibers [*12*]. The matrix between the fibers is highly hackled (or serrated) [*12*].

When the specimen is heated, the mating surfaces are forced apart. This gives rise to the outer surface displacement and resulting fringe anomaly. The closer the delamination is to the surface, the more pronounced is the fringe anomally. As the specimen cools down, the mating surfaces of the delamination try to return to more or less intimate contact. This is prevented by the local variations in the thermal conductivity and coefficients of thermal expansion, and the presence of the hackles on the delamination surfaces. Hence, the anomalous fringes near the hole persist for a long time after the heat source is turned off. This fact was used by us to eliminate most of the thermal loading fringes without losing information on the delaminations in the interferograms used in the paper.

Conclusions and Recommendations

The experimental results lead to the following conclusions:

1. Holography using thermal loading shows delaminations and cracks in the surface plies. It also provides information on the through-the-thickness distribution of delaminations.

2. The conventional TBE-enhanced X-ray photography used in the paper gives detailed information on the nature and planar distribution of the damage, but does not give any information of the through-the-thickness distribution. It can find fiber fractures, matrix cracks, and delaminations.

3. A single-load application of 13.3 kN (3000 lb) to the specimens used herein causes matrix cracks in the 90-deg plies. These cracks run from the edges of the hole to the edges of the specimen. It also causes matrix cracks in the 0-deg and ± 45-deg plies near the hole. It does not cause growth of the fabrication-induced damage present initially in the specimens.

4. Fatigue loading causes extensive matrix cracking in the 90-deg and ± 45-deg plies. It also causes matrix cracks in the 0-deg plies near the hole. The extensive matrix cracking is believed to cause the delaminations resulting from the fatigue loading. Both the extent of the matrix cracking and size of the delamination zones grow with the number of cycles.

Based on our experience with holographic interferometry and TBE-enhanced X-ray photography, we offer the following recommendations:

1. A procedure for using enhanced X-ray photography for getting information on the through-the-thickness distribution of the damage in composite materials should be developed.

2. Laser speckle photography, a method for obtaining information on the deformation in the plane of the specimen [*13*], should be tried with the specimen in the test frame. It would yield information on the effect of the damage on the strain distribution in the specimen.

Acknowledgments

The authors would like to express their appreciation to E. Porter of Universal Technology Corp. for performing the TBE-enhanced X-ray evaluation of the damage in the specimens and to D. Gochoel of Beta Ind., Inc. for doing an excellent job of printing the interferograms and X-ray photographs.

References

[*1*] Sendeckyj, G. P., Stalnaker, H. D., and Kleismit, R. A. in *Fatigue of Filamentary Composite Materials, ASTM STP 636,* American Society for Testing and Materials, 1977, pp. 123-140.

[*2*] Sendeckyj, G. P., Maddux, G. E. and Tracy, N. A. in *Proceedings, 2nd* International Conference on Composite Materials, B. Noton, R. Signorelli, K. Street, and L. Phillips, Eds., American Institute of Mining, Metallurgical, and Petroleum Engineers, 1978, pp. 1037-1056.

[*3*] Grubinskas, R. C., "State of the Art Survey on Holography and Microwaves in Nondestructive Testing," Technical Report AMMRC MS 72-9, Army Materials and Mechanics Research Center, Watertown, Mass., Sept. 1972.

[*4*] *Holographic Nondestructive Testing,* Erf, R. K., Ed., Academic Press, New York, 1974.

[5] Erf, R. K., Gagosz, R. M., Waters, J. P., Stetson, K. A., and Aas, H. G., "Nondestructive Holographic Techniques for Structural Inspection," Technical Report AFML-TR-74-130, United Aircraft Research Laboratories, East Hartford, Conn., Oct. 1974.

[6] Kurtz, R. L. and Liu, H. K., "Holographic Nondestructive Tests Performed on Composite Samples of Ceramic-Epoxy-Fiberglass Sandwich Structure," NASA Technical Report R-430, National Aeronautics and Space Administration, Washington, D. C., June 1974.

[7] Kinariwala, V. R., Ranson, W. F., and Swinson, W. F., "Flaw Detection in Thin Composite Material Structures with Holographic Techniques," Technical Report ME-AMC 0600, Auburn University, Auburn, Ala., Feb. 1976.

[8] Meyer, M. D. and Katayanagi, T. E., *Journal of Testing and Evaluation,* Vol. 5, Jan 1977, pp. 47–52.

[9] Sendeckyj, G. P. and Stalnaker, H. D. in *Composite Materials: Testing and Design (Fourth Conference), ASTM STP 617,* American Society for Testing and Materials, 1977, pp. 39–52.

[10] van Ligten, R. F., "Holographic Microscopy for the Determination of Failure Mechanisms in Monolithic Circuits," NASA Contractor Report NASA CR-1394, National Aeronautics and Space Administration, Washington, D.C., July 1969.

[11] Dändliker, R., Eliasson, B., Ineichen, B., and Mottier, F. M., "Quantitative Determination of Bending and Torsion through Holographic Interferometry," Brown Boveri Research Report KLR-74-21, Brown Boveri Research Center, Baden, Switzerland, Dec. 1974.

[12] Morri, G. E., this publication, pp. 274–297.

[13] Adams, F. D. and Maddux, G. E., "On Speckle Diffraction Interferometry for Measuring Whole Field Displacements and Strains," Technical Report AFFDL-TR-73-123, Air Force Flight Dynamics Laboratory, Wright-Patterson Air Force Base, Ohio, Dec. 1973.

J. S. Heyman[1] *and J. H. Cantrell, Jr.*[1]

Effects of Material Inhomogeneities on Ultrasonic Measurements: The Problem and a Solution

REFERENCE: Heyman, J. S. and Cantrell, J. H., Jr., **"Effects of Material Inhomogeneities on Ultrasonic Measurements: The Problem and a Solution,"** *Nondestructive Evaluation and Flaw Criticality for Composite Materials, ASTM STP 696*, R. B. Pipes, Ed., American Society for Testing and Materials, 1979, pp. 45-56.

ABSTRACT: Most ultrasonic measurements of materials involve the generation of an acoustic wave and the propagation of that wave from a transducer through a coupling medium to a specimen under test. After interacting with the specimen, the wave propagates through the coupling medium to a receiving transducer and is converted to an electrical signal. The information presented to the observer by the electrical signal depends on each element of the system.

In this paper, we examine the role that the receiving transducer plays in ultrasonic measurements. The phase-sensitive nature of conventional receiving transducers has, for the most part, been neglected in nondestructive evaluations. This is shown to lead to significant data misinterpretation.

A new acoustoelectric transducer (AET) has been developed which is phase insensitive. Comparative data obtained with both conventional and AET transducers are presented and discussed. The AET is shown to produce more accurate measurements for the cases investigated.

KEY WORDS: ultrasonic measurements, phase-insensitive transducer, acoustoelectric transducer, composite materials, material inhomogeneities, flaws, absolute velocity, attenuation, nondestructive tests

In this paper, the complexity of using high-frequency sound for determining material properties is examined. Even a simple "standard" measurement is shown to involve many parameters, some of which may not be sufficiently controlled. Further complexity occurs when conventional phase-sensitive transducers are used as acoustic receivers. These devices may produce measurement artifacts which do not represent the true state of the material being tested. A new power transducer which eliminates phase

[1] Research physicists, NASA Langley Research Center, Hampton, Va. 23665.

artifacts is being applied to materials measurements [*1-5*].[2] The device is based on the work of Weinrich [*6*], Hutson and White [*7*], and Southgate [*8*] in which the acoustoelectric effect was used to achieve phase insensitivity. The device is called an acoustoelectric transducer (AET) and is shown to have desirable characteristics for ultrasonic measurements.

Complexity of Ultrasonic Measurement of Material Properties

The use of sound for measuring material properties is perhaps as old as man himself. No doubt early man thumped wood to determine if it was rotten—just as early railroad engineers tapped metal train wheels to detect fatigue cracks. Acoustic measurements today perform the same function, even though our knowledge of material properties and instrumentation technology permit more sophisticated analysis.

Certain material properties may be determined with acoustics. In particular, measurements can determine sound velocity, c, sound attenuation, α, and material acoustic impedance $Z = \rho c$ (ρ is the material density). These acoustic properties are related to the engineering properties of materials—sometimes directly, sometimes in a rather involved and mixed fashion.

For example, the engineering Young's modulus measured in an isotropic rod is simply $E = \rho C_l^2$ where C_l is the longitudinal sound velocity for a bar (provided that the acoustic wavelength $\lambda \gg d$, the bar diameter). However, the measurement of sound attenuation, which can be used to locate cracks, voids, and disbonds in composite materials, depends not only on the absorbed sound (α_a), but also on the scattered sound (α_s). Furthermore, α_s may include diffraction effects, scattering due to flaws, density variations, residual stress, and the scattering geometry. Thus, even though the concept of measuring the three basic parameters c, α, and Z is seemingly straightforward, in practice it may become quite involved.

The measurement complexity usually increases with the material complexity. Homogeneous, flat, and parallel specimens are the easiest to measure while inhomogeneous, anisotropic specimens of irregular geometry are the most difficult. It is important to recognize the origin of the measurement problem. For the two cases just mentioned, it is clear that difficulty arises when an unfortunate but unavoidable mixture of the three basic parameters exists.

Unfortunately, there are many cases where one is not sure that the intended measurement is in fact isolated (that is, α or c or Z, but not a combination). The analysis of these data is difficult and may lead to misinterpretation.

A typical ultrasonic measurement for nondestructive evaluation (NDE) is

[2]The italic numbers in brackets refer to the list of references appended to this paper.

a C-scan or an ultrasonic image or picture. The data are produced by generating ultrasound (see Fig. 1) at a transducer and coupling the sound to a material under test. The sound propagates through and interacts with the material, and is then converted to an electrical signal by a receiving transducer. In many cases, the generating and receiving transducers are the same, requiring a reflecting boundary at the end of the specimen. The electrical signal is then compared with a set threshold which turns on or off a dot located on a storage cathode ray tube (CRT) screen. As the ultrasonic transducer is scanned across the material, the dot location and density maps out an ultrasonic picture of the material on the CRT. Variations of this method are isometric displays which show the depth (time delay) from which the signal occurs and grey scale in which the intensity of the dot is related to the electrical signal amplitude.

By its very nature, this type of measurement is complicated and related to material attenuation and impedance. For example, the simple "flat-bottomed hole" test block commonly used as an engineering standard provides a signal whose amplitude depends on the size of the hole, the attenuation of the test block and ensuing material, the impedance of the boundary and test block material, the distance of the hole bottom from the transducer, and the ultrasonic frequency—just to mention the obvious variables. And this is assuming normal incidence with initially isotropic tests blocks! In the following sections, specific types of artifacts are discussed.

Transducer Artifacts

A further complication arises from the physics of the receiving transducer. For conventional piezoelectric transducers (such as PZT's), the electrical signal produced from the sound wave is the superposition of all the acoustic wave phase fronts at the transducer. For normal incidence of single-phase wave fronts, the electrical output is simply related to the

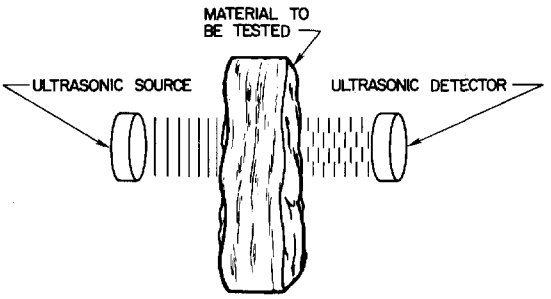

FIG. 1—*Typical ultrasonic transmission measurement.*

acoustic input. As shown in Fig. 2 for two acoustic phase fronts, however, the electrical output is more complex. For out-of-phase or mixed-frequency waves the signal is reduced or modulated as shown in Fig. 2*b* and 2*c* even though the incident acoustic power for each case is the same. If an acoustic power detector is used as a receiver, however, the in-phase, out-of-phase, and mixed-frequency incident acoustic waves produce the same electrical signal as shown in Fig. 2*d*.

A transient acoustic power receiver has been developed and the details of its operation are published elsewhere [*3,5*]. The acoustoelectric transducer (AET) is basically a phonon-charge carrier "drag" device in which the acoustic wave pulls free charge carriers along the propagation direction. The charge carrier transport results in an electrical signal which is insensitive to acoustic phase. Several applications of the AET to materials measurements are presented in the next section.

Impact of Transducer Artifacts on Ultrasonic Measurements

In the following paragraphs, we examine situations where transducer artifacts are likely to lead to significant measurement errors. In all cases the problem can be traced to phase shifts occurring in the specimen.

Misalignment

Even with as simple a structure as a flat plate, alignment of the measurement system can cause problems. First, there is a change in the reflection and transmission coefficients with angle at the boundary of the material and the ensuing medium (usually water). In addition, and of considerable importance, is the directivity of the receiving transducer. The directivity of a receiver is defined as the electrical output as a function of incident wave angle. Directivity measurements as well as other measurements presented in this paper were obtained with the experimental arrangement shown in Fig. 3. A gate width was chosen to prevent standing waves in the water paths (5 cm) yet permit resonance in the graphite/epoxy composite specimen (0.2 cm thick).

An example of the significance of directivity is shown in Fig. 4. These measurements were obtained at 2 MHz with a focused transmitting transducer (10-cm focal length) in through-transmission to the receiving transducer. The receiving transducer angle was changed, which caused a decrease in electrical output signal amplitudes. The data were obtained by measuring the increased electrical signal to the linear transmitter drive amplifier necessary to compensate for the decrease in ultrasonic signal amplitude with increasing angle. The rapid decay in PZT signal results from its inherent phase sensitivity. In contrast, the AET signal is quite flat, as is expected for a phase-insensitive power transducer. Thus, align-

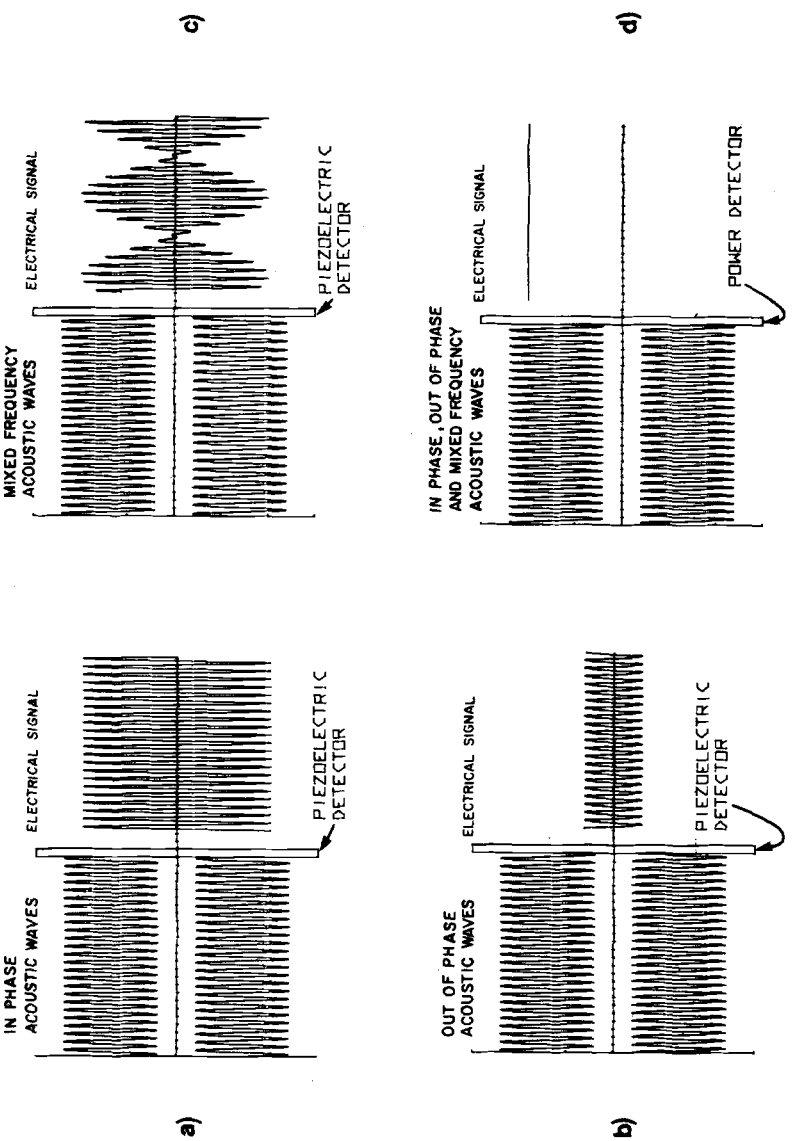

FIG. 2—*Comparison of a phase-sensitive piezoelectric transducer with a phase-insensitive power transducer for several incident waves.*

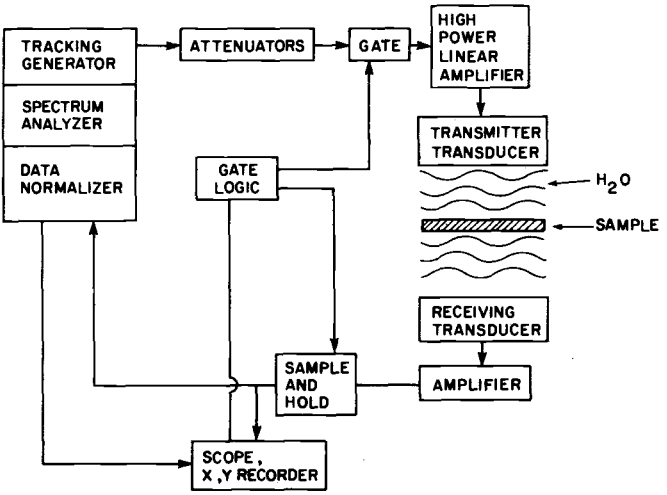

FIG. 3—*Block diagram of experimental measurement system.*

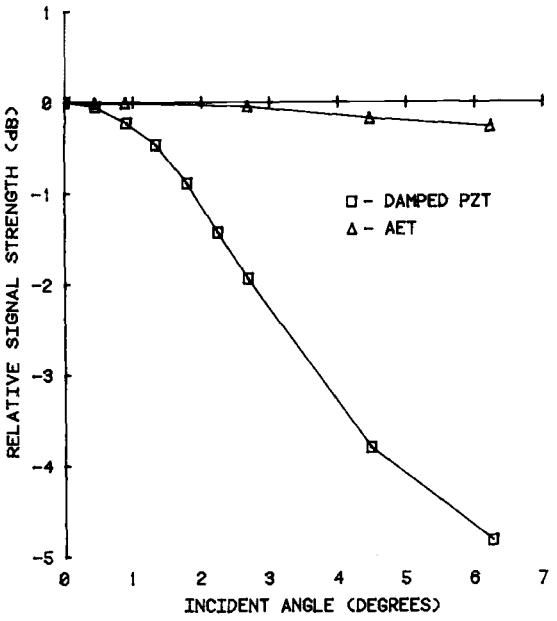

FIG. 4—*Transducer directivity comparison.*

ment-related measurement errors are minimized with the AET, resulting in improved quantitative measurements.

An alignment-related problem occurs for materials that are not flat. Figure 5 illustrates this problem for a composite structure of borsic-aluminum with six built-in flaws. The flaws consist of three squares across the top and three rectangles across the bottom, decreasing in size from left to right. The plate was slightly bent (approximately 5-deg roll) in the upper right-hand corner. Figure 5*a* shows all the major features built into the

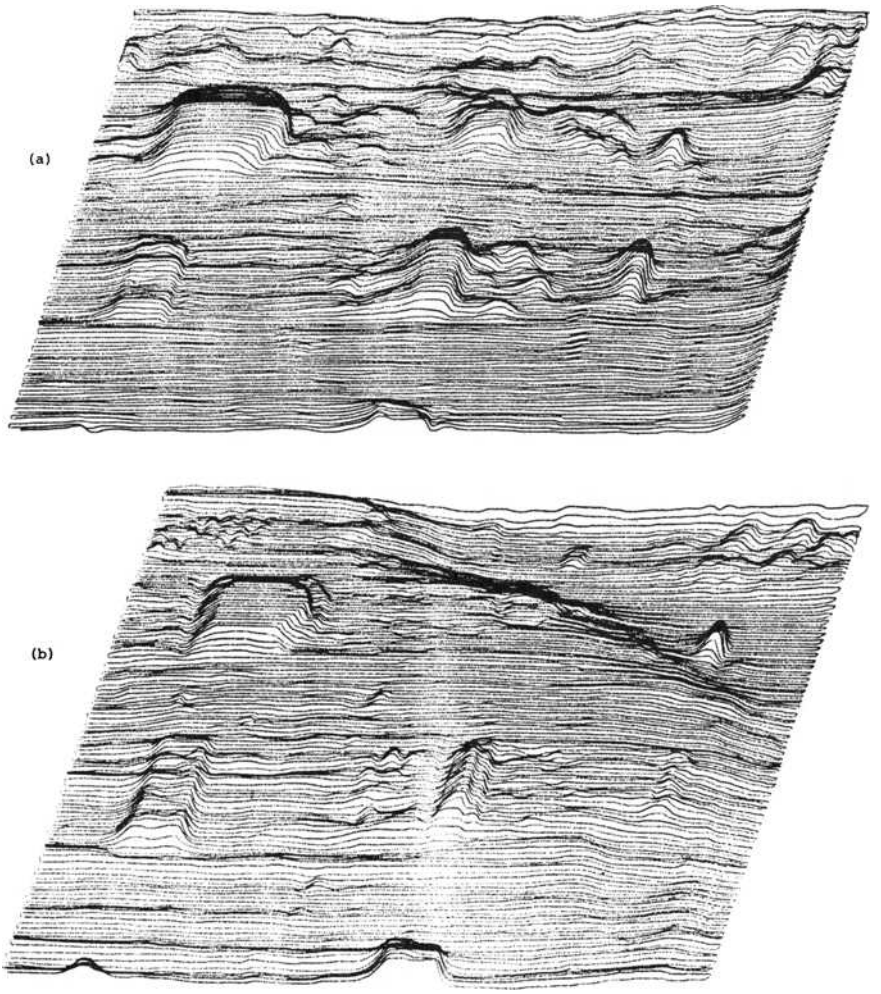

FIG. 5—*Ultrasonic C-scan isometric pictures of a borsic-aluminum composite plate with built-in flaws*: (a) *obtained with an AET transducer*; (b) *obtained with a PZT transducer.*

plate, along with several plate irregularities as seen by the AET. Figure 5*b*, however, obtained with a conventional transducer, shows a line across the plate (due to the slight bend) which obscures the phantom flaw of the middle square.

Abrupt Geometrical Discontinuities

An abrupt change in material thickness or velocity, or a scattering site, may also lead to measurement artifacts. In these cases the primary problem is the change in phase across the acoustic wave front incident on the receiving transducer. As an example, Fig. 6 shows a C-scan picture of the characters "NASA" engraved in an aluminum plate 1.2 cm thick. Each letter was ~0.03 cm deep, ~0.6 cm high, with a line width of ~0.05 cm. Figure 6*a* was obtained with a PZT receiver while Fig. 6*b* was obtained with an AET receiver. Each receiver had a diameter of 1.2 cm. The measurements, made at 10 MHz, show the serious image degradation which occurs with phase-sensitive transducers at abrupt discontinuities.

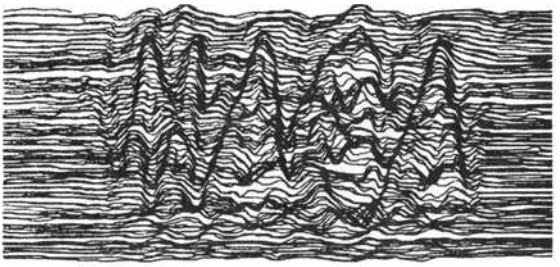

a) PZT

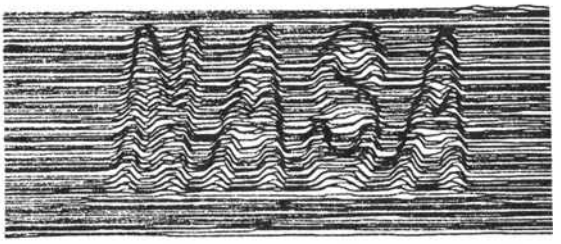

b) AET

FIG. 6—*Ultrasonic C-scan isometric pictures of the engraved letters "NASA":* (a) *obtained with a PZT transducer,* (b) *obtained with an AET transducer.*

Gradients

Inaccurate measurements may also occur in materials which have a gradient in material thickness or sound velocity. An example of a material having a velocity gradient is a nonuniformly stressed rod. Experimentally, a velocity anisotropy is obtained by loading a rod as shown in the top part of Fig. 7.

To illustrate the effect of velocity anisotropy on signal amplitudes, ultrasonic pulses were generated by a PZT transducer which was also used as a receiving transducer for the reflected pulse. The pulse amplitudes were measured by the PZT transducer as well as the AET bonded to the opposite side of the bolt. Figures 7*a*–7*d* show the AET response (top) and the PZT response (bottom) as the bolt load is increased from 0 to 5×10^3 N. Note in Fig. 7*c* that the PZT response has nearly nulled due to phase cancellation effects. The AET output remains virtually unchanged for all load levels.

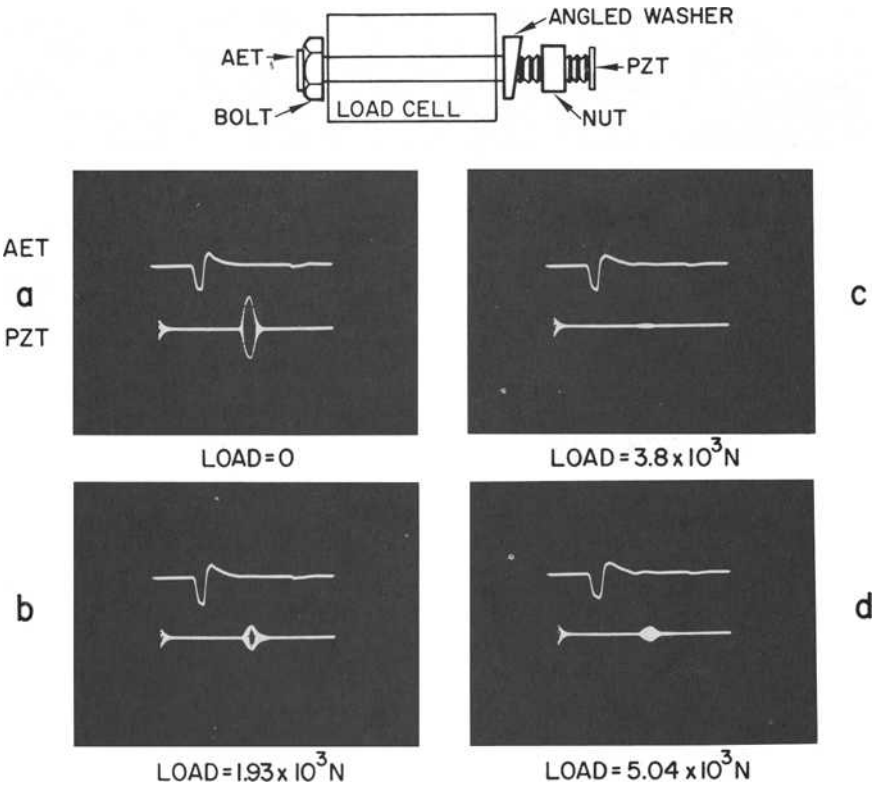

FIG. 7—*Stress gradient test fixture and data comparison for AET and PZT transducers as a function of load.*

Figure 8 shows the data of Fig. 7 plotted as an apparent change in attenuation versus load for the two transducers. The large change in attenuation seen by the PZT transducer is explained only by phase cancellation. The AET signal, however, is shown to be nearly constant. In fact, there is a slight decrease in attenuation with applied load followed by a slight increase. The AET response is entirely consistent with wave propagation in a cylindrical waveguide as calculated in Ref *9*.

Frequency Sweeps

For absolute measurements, phase sensitivity has been shown to lead to amomalous data. In relative measurements, the effect of phase cancellation can also be significant. For example, acoustic continuous waves generated in a homogeneous, flat specimen should produce uniform, periodically spaced resonance peaks as the frequency is swept over a sufficiently large range. The resonances should follow the relationship $F = mc/2a$ where m is the resonance number, c the sound velocity, and a the plate thickness.

An example of using the frequency sweeping technique is shown in Fig. 9 for the somewhat more complicated plate structure consisting of a graphite/epoxy composite with ply sequence (90/±45/0) symmetric. The data were obtained by first measuring the frequency response of the ultrasonic system (transmitter, water path, receiver) without the specimen. The specimen

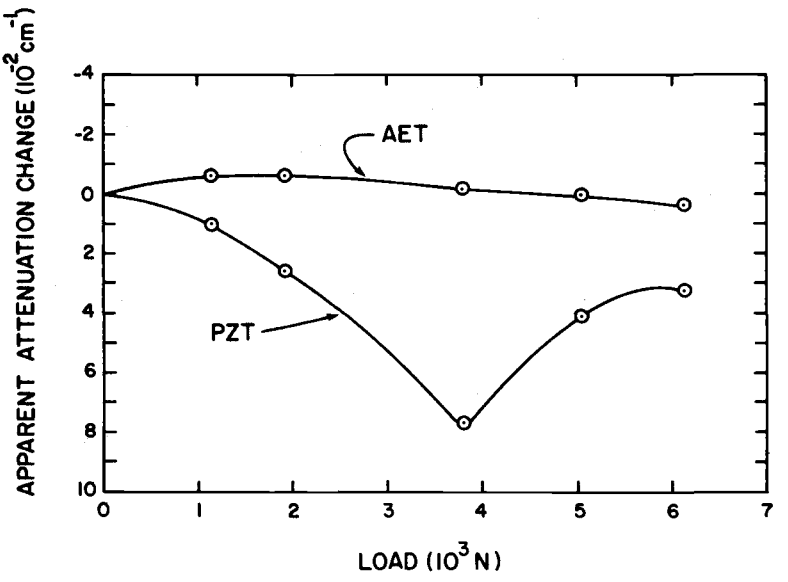

FIG. 8—*Apparent attenuation for nonuniformly stressed rod.*

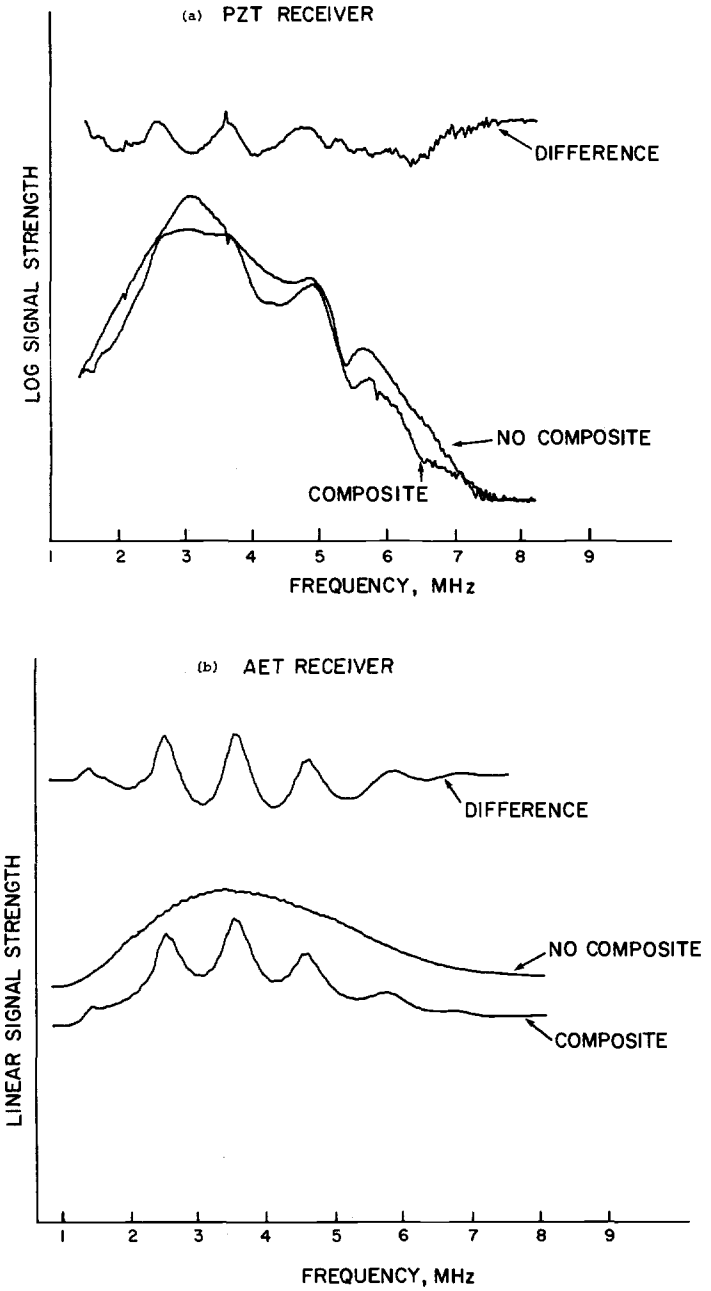

FIG. 9—*Frequency scan of graphite/epoxy composite obtained with* (a) *PZT transducer and* (b) *AET transducer.*

was then inserted and a difference spectra obtained. The PZT data are shown on a logarithmic scale while the AET data are shown on a linear scale. The PZT data shown in Fig. 9*a* are significantly more difficult to read than the data of Fig. 9*b* obtained with an AET transducer. The AET measurements indicate a velocity of 2.4×10^5 cm/s in the 0.12-cm-thick plate. The material attenuation may be determined from the resonance width δF at half power (0.707 V), $\alpha = \pi \delta F / c$. From the data of Fig. 9*b* an attenuation of 4.5 cm^{-1} at 3 MHz is obtained for the composite plate.

Conclusions

Use of conventional ultrasonic transducers can lead to measurement errors. The source of the problem is the phase-sensitive nature of piezoelectric transducers. A new acoustoelectric transducer has been developed which is not subject to phase cancellation errors in measurement of high-frequency acoustic power. Therefore, the new device is capable of more reliable quantitative measurements for a variety of situations encountered in nondestructive evaluation.

References

[1] Miller, J. G., Heyman, J. S., Weiss, A. N., and Yuhas, D. E., "A Power Sensitive Detector for Echocardiography and Other Medical Ultrasonic Applications," presented at the American Institute of Ultrasound in Medicine, Seattle, Wash., 8-10 Oct. 1974.

[2] Heyman, J. S., "Ultrasonic Coupling to Optically Generated Charge Carriers in CdS—Physical Phenomena and Applications," Ph.D. thesis, Washington University, St. Louis, Mo., 1975; also NASA TMX-68732.

[3] Heyman, J. S., *Journal of the Acoustical Society of America*, Vol. 64, 1978, p. 243.

[4] Heyman, J. S. and Cantrell, J. H., Jr. in *Proceedings*, 1977 Ultrasonics Symposium, Institute of Electrical and Electronics Engineers, New York, IEEE Catalog No. 77CH1264-1SU, 1977, pp. 124-128.

[5] Heyman, J. S., Cantrell, J. H., Jr., and Whitcomb, J. D. Abstracts of the 1st International Symposium on Ultrasonic Materials Characterization, National Bureau of Standards, Washington, D.C., 7-9 June 1978, p. 115.

[6] Weinreich, G., *Physical Review*, Vol. 107, 1957, p. 317.

[7] Hutson, A. R. and White, D. L., *Journal of Applied Physics*. Vol. 33, 1962, p. 40.

[8] Southgate, P. D., *Journal of the Acoustical Society of America*, Vol. 39, 1966, p. 480.

[9] Carome, E. F., Witting, J. M., and Fleury, P. A., *Journal of the Acoustical Society of America*, Vol. 33, 1961, p. 1417.

W. E. Dance[1] *and J. B. Middlebrook*[1]

Neutron Radiographic Nondestructive Inspection for Bonded Composite Structures

REFERENCE: Dance, W. E. and Middlebrook, J. B., **"Neutron Radiographic Nondestructive Inspection for Bonded Composite Structures,"** *Nondestructive Evaluation and Flaw Criticality for Composite Materials, ASTM STP 696,* R. B. Pipes, Ed., American Society for Testing and Materials, 1979, pp. 57-71.

ABSTRACT: Neutron radiography was found to be effective as a nondestructive inspection technique for detection of bondline voids/defects in a variety of composite structures. Radiographic data are presented in this paper from typical structures for which the neutron radiographic inspection technique offers advantages over more conventional inspection techniques. Complex composite joints such as box beam members, for example, are difficult to inspect by ultrasonic techniques, and the X-ray attenuation coefficients of the different materials in composite/metal combinations differ in such a manner as to yield very little nondestructive inspection (NDI) information regarding the integrity of the bond. Accurate bondline defect information was achieved in such structures utilizing a transportable californium-252 (^{252}Cf) neutron radiography system containing approximately 2 mg of the ^{252}Cf isotope. Through techniques developed at Vought Corp. Advanced Technology Center, resolution of simulated bondline voids as small as 0.127 mm (0.005 in.) diameter in laminated graphite/epoxy specimens was achieved. It is expected that continuing improvements in imaging techniques, and in mobility of neutron sources for radiography, will spawn wide usage of the neutron technique for nondestructive inspection of complex wing joints, control surfaces, and other airframe structures.

KEY WORDS: neutron radiography, nondestructive tests, composites inspection, adhesive bond evaluation, composite materials

The increasing diversity of materials incorporated into current designs for advanced composite and hybrid composite/metal structures places more stringent requirements than ever before on radiographic and other inspection techniques for structures evaluation. With these designs, significant tech-

[1] Manager, Neutron Radiography, and research scientist, respectively, Vought Corp., Advanced Technology Center, Inc., Dallas, Tex. 75266.

nological gaps have arisen in the ability to achieve full nondestructive testing and evaluation (NDT&E) for areas of these structures. Small voids, cracks, porosity, ply mismatch, resin-rich areas, and flaws in metal shim/composite panels, secondary bondlines, and complex closeout structures are examples of difficult NDT&E areas.

Radiography with thermal neutrons has emerged in recent years as a viable NDT&E technique which provides a powerful complement to ultrasonic and X-ray techniques in the inspection of these structures [*1-6*].[2] In some structures containing metal members adhesively bonded to composite material, neutron radiography appears to be the only technique providing a reliable image of the bondline or of the composite material itself in the presence of the metal.

In the realm of adhesively bonded joints, the common use of adhesive filler (metal oxides, mineral powders, and other extenders) for viscosity control and for thermal expansion or shrinkage control makes difficult the interpretation of conventional X-ray data in many cases. Some adhesives introduce other factors which impact the accuracy of interpretation of X-ray results. Examples of this are multipolymer formulations, precipitated dispersed elastomers, or random or woven mat carriers comprising the adhesive structure. Interpretation of neutron radiographic results is usually more straightforward in these areas since the neutron image is most sensitive to anomalies in the adhesive epoxy itself.

Suitable criteria for establishing minimum defect size and other quality allowables in either bonded composite structures or composite matrix structures are the prime goal in Department of Defense (DoD) and industrial composites programs in quality assurance and structures serviceability. Application of neutron radiography as an additional means of composites inspection will extend the present capabilities for establishing acceptance criteria. Radiographic data are presented in this paper which indicate the value of this method for increasing the ability to generate valid criteria.

Experimental

Radiographic specimens for which data are presented include both laboratory prepared and actual production structural specimens. The two types of specimens were fabricated in the Advanced Technology Center Structures and Materials Laboratories and in the Manufacturing Research and Development Laboratories of Vought, respectively. In the case of specimens prepared with simulated voids, a flat stack design using a polished aluminum mandrel facilitated the orientation of voids within individual plies. The use of the flat-ply design simplified specimen preparation by allowing the use of conventional bagging techniques and a heated platen press. For the

[2] The italic numbers in brackets refer to the list of references appended to this paper.

polyimide structure and certain others, special tools were made for layup, and high-temperature autoclave facilities were used for cure.

Neutron radiography results presented here were achieved with an experimental transportable californium-252 (^{252}Cf) neutron radiography system developed by Vought Advanced Technology Center. This system utilizes approximately 2 mg of the californium isotope, which was supplied on loan from the Louisiana State University Californium-252 Demonstration Center in conjunction with the U.S. Department of Energy Californium-252 Evaluation Program. The thermal neutron flux at the image plane was approximately 4×10^3 neutrons (n)/cm^2 s. A 0.025-mm-thick (0.001-in.) vapor-deposited gadolinium metal film was used as neutron converter to expose Kodak Industrial X-ray film, Type SR-5 (single emulsion). Neutron radiographs were processed and reprinted without photographic enhancement. It should be recalled that considerable contrast and resolution are lost when preparing photographic reproductions and that original negatives should be used for maximum accuracy in visual interpretation of the radiographic data.

The experimental approach described in this paper was designed to yield data which demonstrate the sensitivity of neutron radiographic inspection for detection of composite bondline voids/defects and also its potential for inspection of the composite matrix itself.

Neutron radiography in some cases is capable of distinguishing between different materials having similar densities (that is, close neighbors in the periodic chart) due to the widely varying neutron mass absorption coefficients. (The mass absorption coefficient for thermal neutrons does not depend directly on atomic number as it does for X-rays.) For neutrons, certain elements such as hydrogen, boron, and gadolinium in fact exhibit absorption coefficients which are two to three orders of magnitude greater than the average value for structural metals. The hydrogen content of organic materials such as epoxy adhesives typically ranges from 8 to 12 percent, which is adequate for good radiographic contrast. For a bondline of a specified thickness, variations in the radiographic film density indicate variations in absorber uniformity. Such variations indicate voids, inclusions, or material inhomogeneity. Inclusions, in turn, could be any foreign material such as peel-ply or bits of paper or metal. Voids may be fissures or bubbles extending from adherend to adherend, or they may be localized within a portion of the bondline, such as an unbond at one of the adherend surfaces. An inclusion having a low absorption coefficient will cause the inclusion to appear as a void; inclusions which have high-absorption coefficients are readily recognized as such.

The typical experimental geometry involved mounting the test specimen in the thermal neutron beam directly between the ^{252}Cf source and the imaging assembly, as close as possible to the film plane. Fast neutrons generated by the isotope source are moderated to thermal energies in order

to maximize the neutron absorption contribution from hydrogen. Typical moderators are water, polyethylene, or paraffin materials. The neutron beam is then collimated to achieve spatial resolution, and the ratio of the neutron flux to gamma ray background is maximized for good neutron image contrast. The imaging assembly consists of a light-tight cassette which is held under vacuum in order to maintain intimate contact between the film and the radiation converter inside. The vapor-deposited gadolinium material "converts" the neutrons to electrons for film exposure. After the film is exposed by the products of the reaction between the converter and the neutron beam, it is developed, using standard X-ray film handling procedures. In the interpretation process the basic difference between neutron and X-ray radiographic results lies in the difference in the elemental species which are imaged.

Results and Discussion

The results of radiographic inspection of a bonded metal to fiber glass/epoxy composite structure are shown in Fig. 1. This figure compares an N-ray radiograph with an X-ray radiograph of the same composite structure. The metal attachment plate containing several bolt holes is bonded with an epoxy adhesive to the shoulder of the fiber glass/epoxy structure. As seen in the X-ray image at the left, the metal attachment plate completely absorbs that type of radiation, thus preventing the imaging of the epoxy bondline. On the other hand, the neutron beam, which is partially transmitted through the metal plate, images a number of voids within the bondline joining the metal plate to the fiber glass composite, as seen in the neutron radiograph on the right. Voids appear as light areas in the neutron radiograph (positive print). Note also in this radiograph two sharp lines denoting inclusions in the bondline. Voids and inclusions are all too common on a localized basis in metal-to-composite or composite-to-composite bonding.

In the inspection of the bondlines joining composites in the absence of metal components, the richer hydrogen content of the epoxy adhesive is readily imaged against the lower hydrogen content of the composite matrix. This can be seen in the bonding of different parts of the same composite structure in Fig. 2. These two radiographs image two different bondlines within the same general area of this structure, a square box-beam member with internally bonded reinforcement. In the top figure it is seen that edge-flow of the adhesive is deficient along the narrow portion and completely disappears, leaving gaps as the curvature of the reinforcement sleeve increases. The bottom photograph in Fig. 2 shows an adhesive bondline defect in this structure at a structurally critical point. Precise defect location and defect size determination can be made from these radiographs.

An example of nondestructive inspection of a more complex hybrid

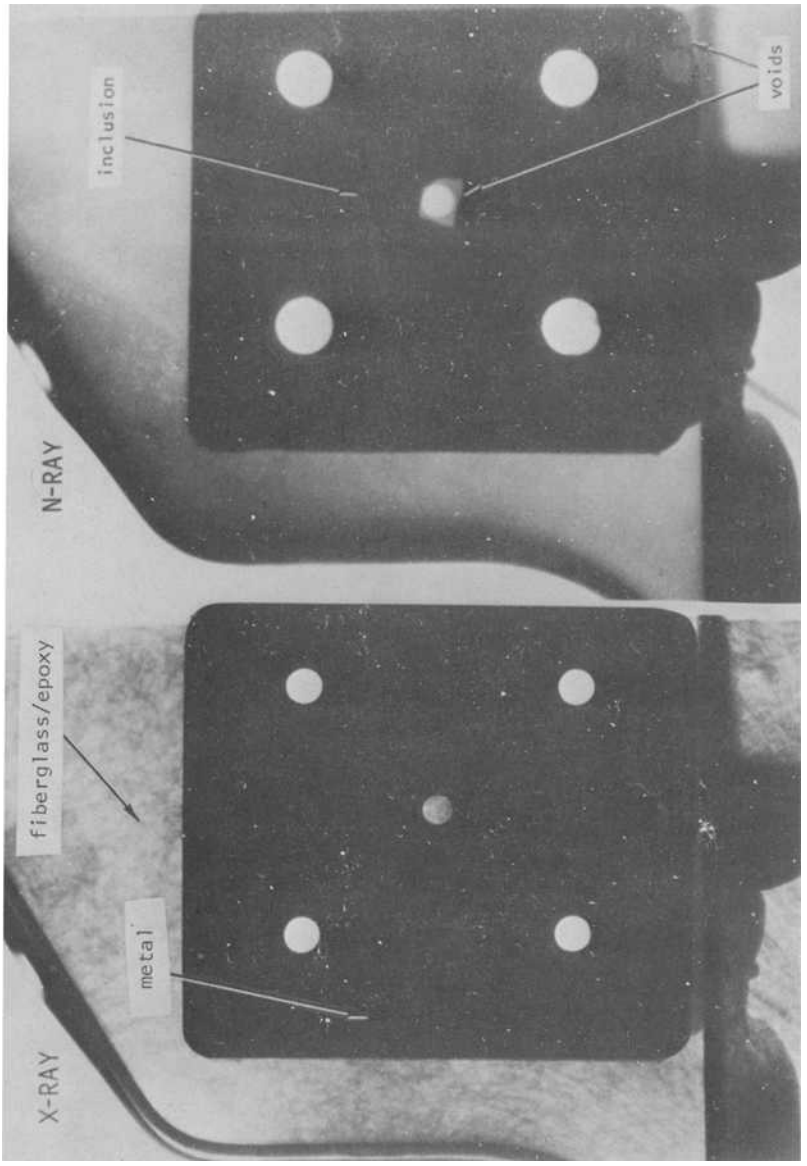

FIG. 1—*Inspection of bonded metal-to-fiber glass/epoxy composite structure.*

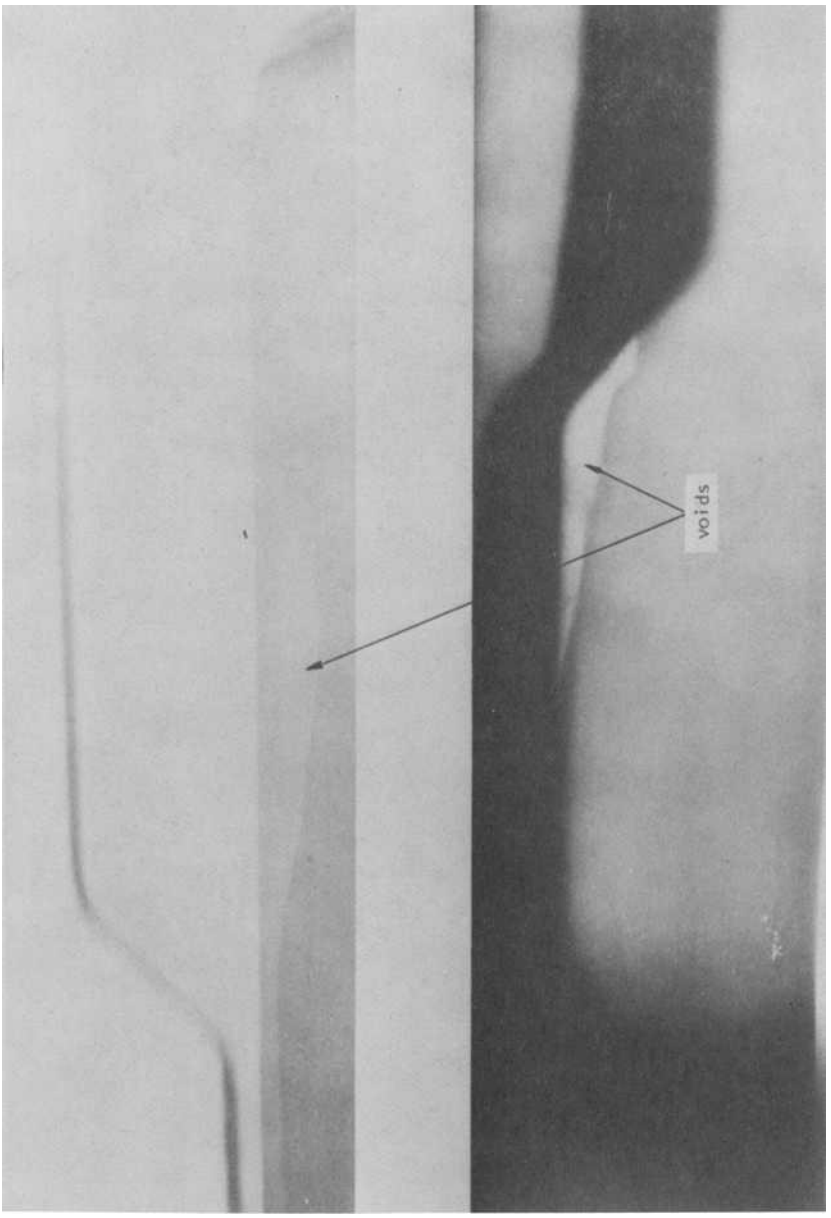

FIG. 2—*Neutron-ray inspection of bonded fiber glass/epoxy composite structure.*

composite/metal structure by means of neutron radiography is shown in Fig. 3. As in Fig. 1, a comparison of neutron and X-ray inspection is made. The specimen was a graphite/epoxy/metal wing skin structure incorporating aluminum honeycomb core, graphite/epoxy face sheets, and titanium shims. As before (Fig. 1), the advantage of neutron inspection is illustrated for imaging bondline flaws which are undetected by X-ray and other techniques, due to the thick titanium shims. Voids in the titanium bondlines are clearly imaged in the neutron radiograph at the left. The X-ray on the right, on the other hand, shows the boundaries of the shims, which are essentially opaque to the X-ray beam in this exposure, and provides no information about the bondline.

Figure 4 is the result of N-ray inspection of an aircraft composite wing spoiler at the trailing-edge closure. This structure involved graphite/epoxy skins bonded to aluminum honeycomb. In addition to the high-contrast imaging of the adhesive pattern at the composite skin-to-core interface [such as at (C) in the figure], the technique also provides an accurate

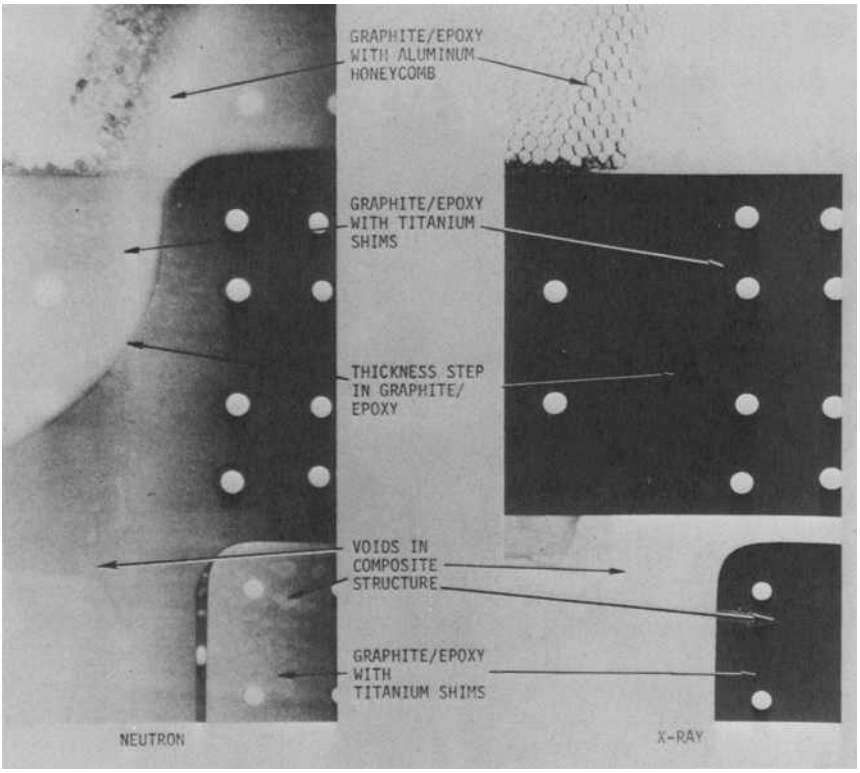

FIG. 3—*Neutron and X-ray inspection of a graphite/epoxy composite structure containing metal components.*

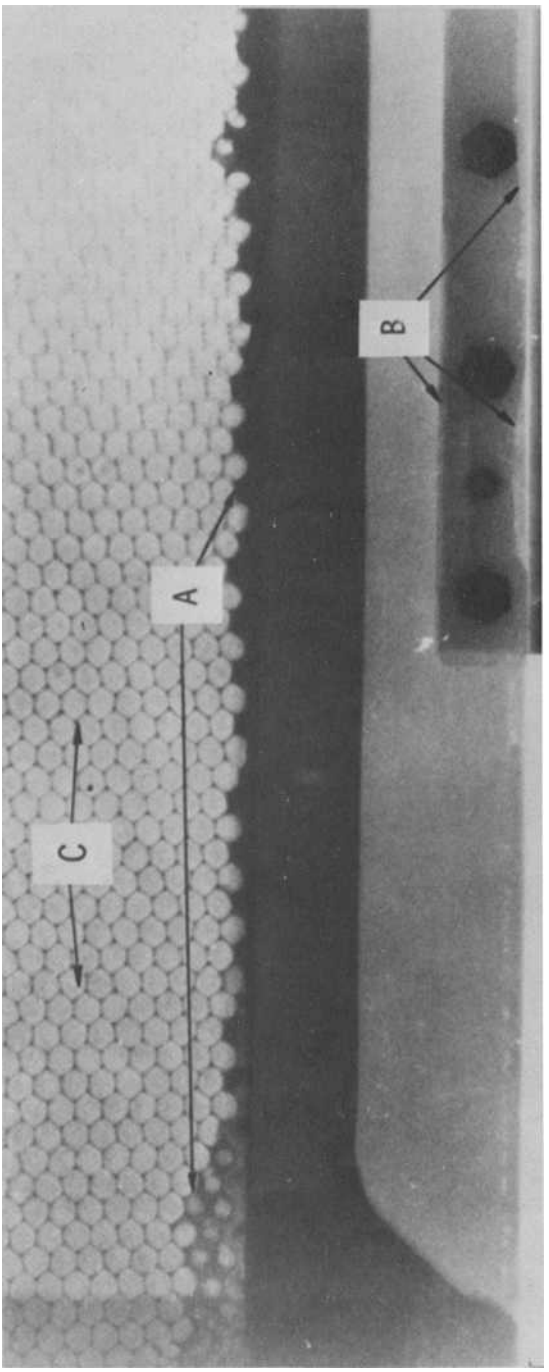

FIG. 4—*Neutron radiograph showing adhesive structure at trailing edge closure in 737 wing spoiler.*

image of the adhesive distribution at the critical core-to-frame interface (A). Voids within a tab-to-frame bondline are indicated at (B).

An example of N-ray inspection of an all-composite component is given by Fig. 5, which is a radiograph of a T-joint structural member composed of graphite/epoxy face sheets over polyimide honeycomb core. This structure simulates configurations based on honeycomb core panels bonded at right angles to honeycomb rib faces. The N-ray radiograph shows the distributions of the adhesive foam which was injected during manufacture for joint reinforcement. In this case, localized "pooling" of the adhesive in a few core cells is apparent.

Figure 6 is a neutron radiograph of adhesively bonded graphite/epoxy specimens containing prepared bondline voids. Specimen A consists of two 2.54-mm (0.1 in.) adherends with a 0.127-mm (0.005 in.) modified-adhesive bondline. Specimen B includes a 1.68-mm (0.066 in.) titanium

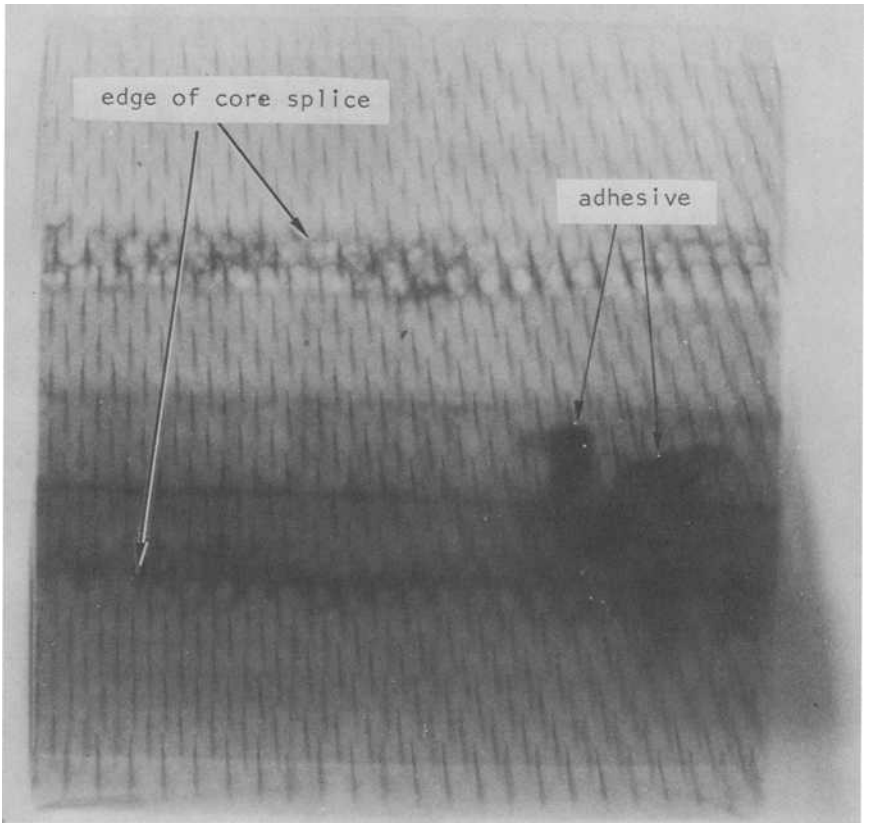

FIG. 5—*Neutron radiograph of graphite/polyimide bonded joint specimen.*

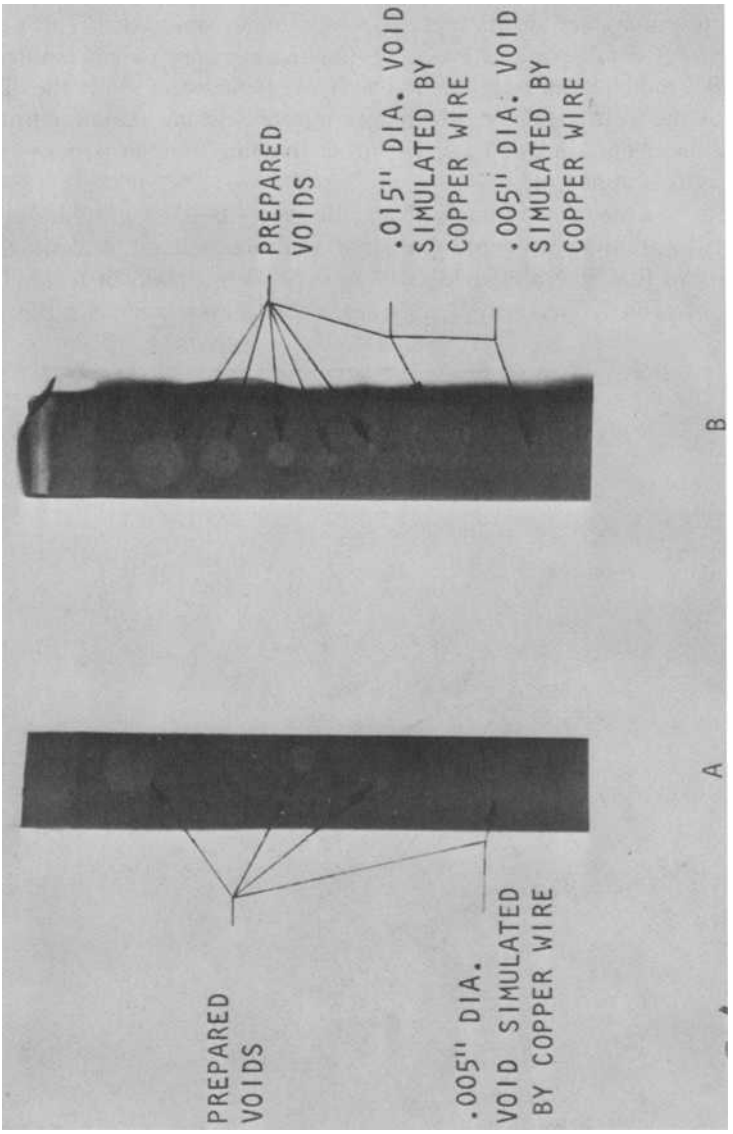

FIG. 6—*Neutron radiograph of bonded composite specimens.*

sheet bonded between 2.54-mm graphite/epoxy adherends. The prepared voids, with diameters as indicated in the figure, were imaged with good resolution. As seen in the radiograph of Specimen B, the insertion of the 1.68-mm titanium plate, with its extra bondline, did not degrade the image of the bondline voids, even down to the smallest, 0.127-mm-diameter (0.005 in.) void.

Anomalous voids, ply mismatch, and areas of excessive resin or fiber content are problems that are common in the manufacture of graphite/epoxy composites. Figure 7 shows neutron radiographs of two different graphite/epoxy laminate specimens which were prepared to demonstrate the effects of bonding pressure and bleeder ply variations during manufacture on the final density of the laminates. The laminate in each case comprised 16 plies of unidirectional 5208/T-300 (Narmco) prepreg tape. The radiograph on the left in Fig. 7 shows a panel with no bleeder application and no autoclave pressure. Vacuum pressure alone [~ 0.103 N/m^2 (~ 15 psi)] was maintained during fabrication of this panel. The gross nonuniformities observed in the N-ray indicate that this composite would

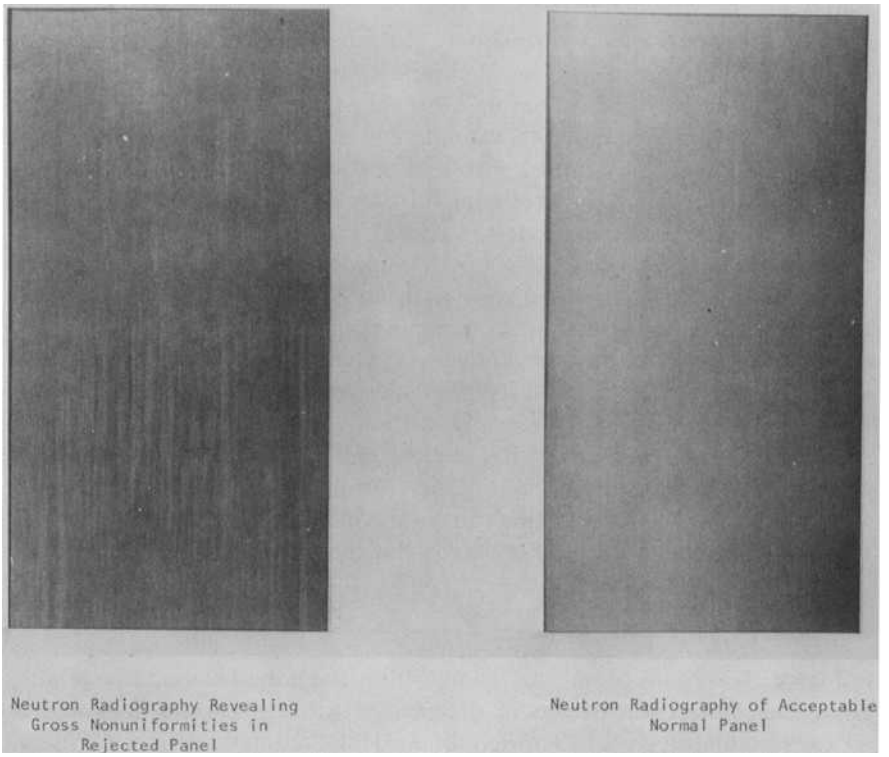

FIG. 7—*Neutron-ray inspection of unidirectional graphite/epoxy composite panels.*

be unacceptable. The radiograph on the right in Fig. 7 images a panel which was fabricated by following the manufacturer's recommended procedure, and indicates a fully dense, acceptable panel. Final evaluation of each panel was based on C-scan nondestructive inspection (NDI) as well as N-ray radiography. Also used for determination of structural integrity were short-beam shear strength tests (room temperature and elevated temperature/humidity), fiber volume/resin content measurements, and photomicroscopy. The specimen on the left in Fig. 7 demonstrates the type and extent of voids that can be induced in a composite when improper layup is made or when loss of pressure in autoclaving occurs.

Foreign-object damage in a composite panel characterized by sublayer through-cracking in the plane perpendicular to the panel was simulated by overlaying a 1.40-mm (0.055 in.) graphite/epoxy specimen containing 0.127-mm (0.005 in.) cracks with an unflawed graphite step wedge, as shown in Fig. 8. The step wedge thicknesses ranged from 0.686 to 2.62 mm (0.027 to 0.103 in.) to indicate the sensitivity for detection of the cracks hidden by outer layers. As seen in the neutron radiograph, the 0.127-mm (0.005 in.) cracks were clearly imaged through the maximum step of 2.62 mm (0.103 in.).

In order to determine the sensitivity of neutron radiography for detection of matrix voids or fiber/resin deficiencies in graphite/epoxy panels, a specimen was prepared containing simulated laminar voids, stepped in thickness by 0.127-mm (0.005-in.) increments, from 0.127 to 2.67 mm (0.005 to 0.105 in.), by cutting disks out of the prepreg tape and replacing the portions cut out with aluminum filler disks. The two plies of tape on each of the outer surfaces contained no holes. This specimen was prepared from 25 plies of Narmco 5208/T-300 prepreg material in a hand-layup, vacuum bag/hydraulic press operation using 76.2-mm-wide (3 in.) prepreg tape and the manufacturer's recommended cure cycle. The tape was laid up to give a symmetrical ± 45-deg ply orientation. The radiograph is shown in Fig. 9. With each successive hole, beginning with the hole designated by an arrow in the upper right of the figure [hole thickness 2.67 mm (0.105 in.)], the thickness of the void or deficiency decreases by one ply thickness, or 0.127 mm (0.005 in.). As seen in the figure, the single-layer hole 0.127 mm (0.005 in.) thick was barely imaged, providing a sensitivity value of 4 percent of the total specimen thickness.

Conclusions

Flaws such as voids and inclusions within the adhesive bondline joining composite panels and defects or deficiencies within the resin-fiber matrix of such composites are accurately imaged and located, nondestructively, using neutron radiography. Significant advantages accrue when the n-ray technique is used along with X-ray radiography and ultrasonic techniques,

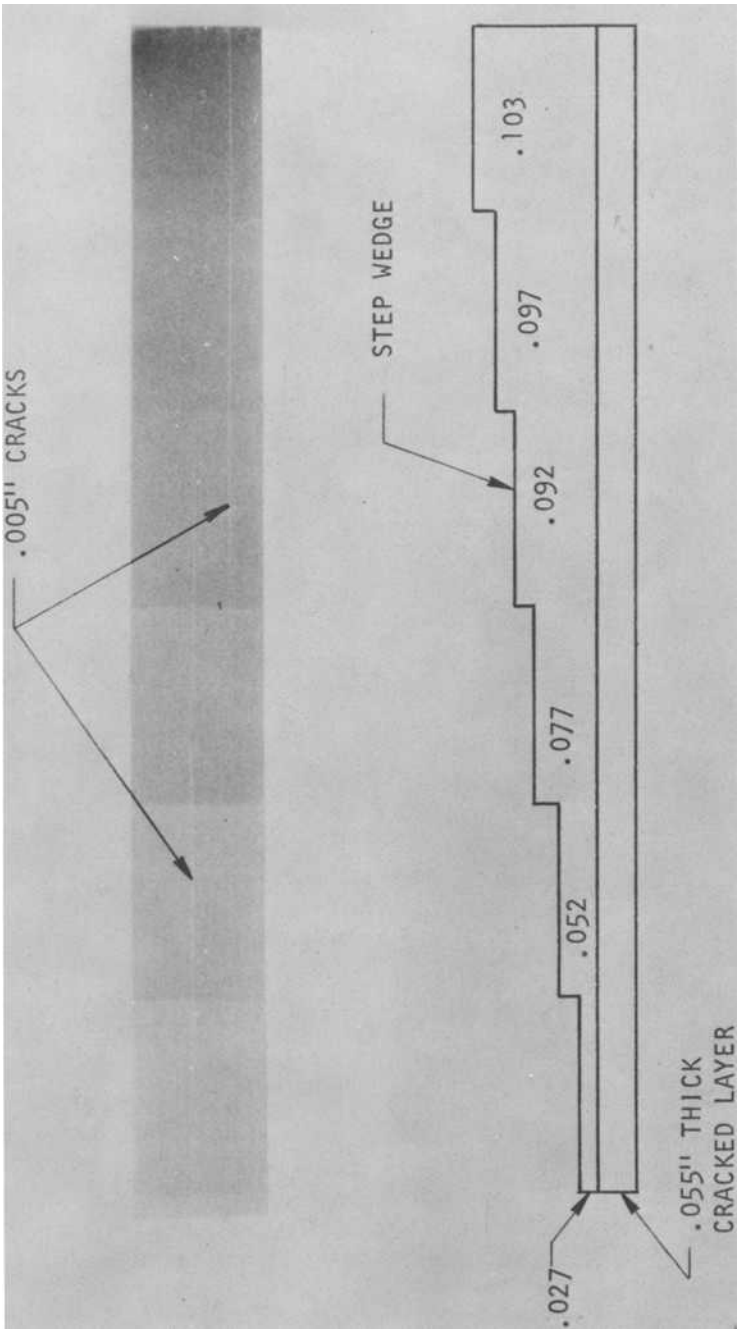

FIG. 8—*Neutron radiographic inspection of graphite/epoxy composite.*

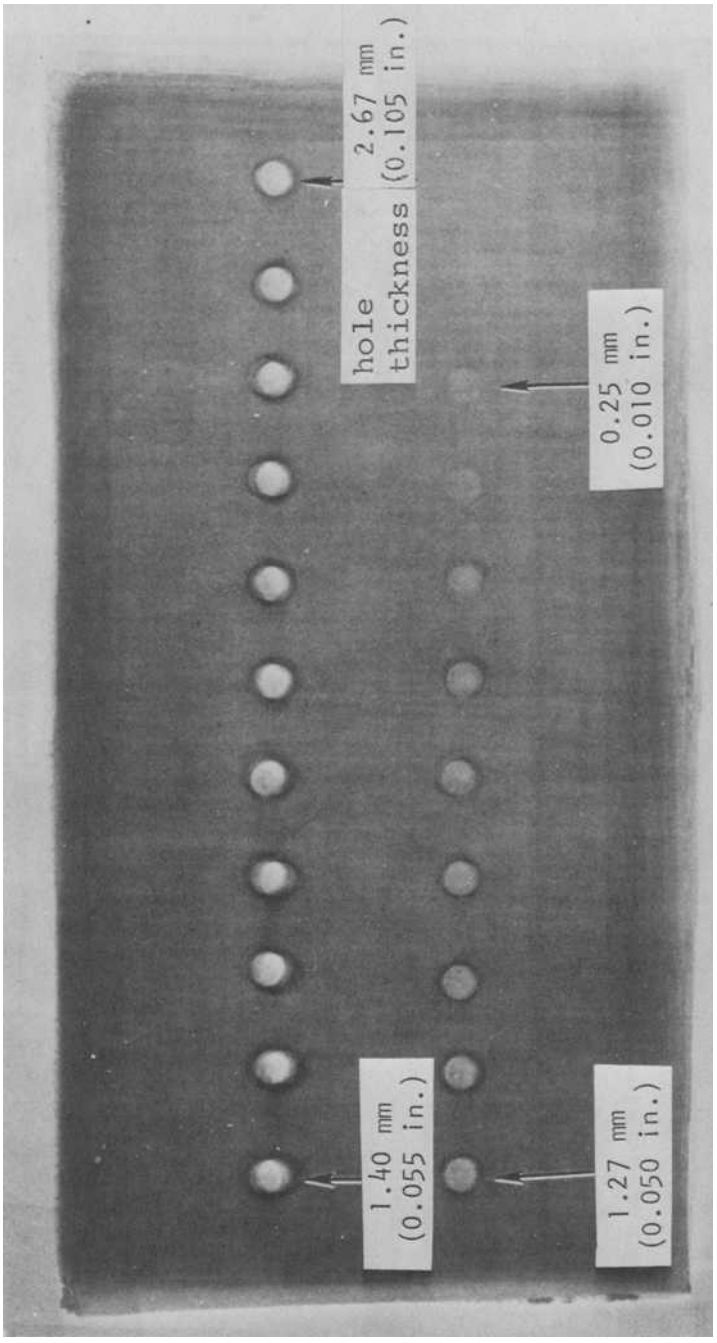

FIG. 9—*Neutron radiograph of graphite/epoxy composite containing a series of reference voids (simulated).*

particularly for many hybrid composite/metal structures. Although each of these NDI methods by itself has definite limitations for complete evaluation of composite structures, quality assessment of total composite structures is enhanced through inclusion of neutron radiographic techniques.

References

[1] Dance, W. E. in *Practical Applications of Neutron Radiography and Gaging, ASTM STP 586,* H. Berger, Ed., American Society for Testing and Materials, 1976, pp. 137-151.

[2] *Practical Applications of Neutron Radiography and Gaging, ASTM STP 586,* H. Berger, Ed., American Society for Testing and Materials, 1976.

[3] Dance, W. E., "Nondestructive Inspection of an Advanced Adhesive Bonded Metallic Primary Wing Structure by Portable Neutron Radiography," Vought Corp. Advanced Technology Center Report No. B-94400/7TR-4, Dallas, Tex., Jan. 1977.

[4] Dance, W. E. and Petersen, D. H., "Verification of the Structural Integrity of Laminated Skin-to-Spar Adhesive Bondlines by Neutron Radiography," Vought Corp. Advanced Technology Center Report, *Proceedings,* Symposium on Durability of Adhesive Bonded Structures, U.S. Army Armament Research and Development Command, 27-29 Oct. 1976.

[5] Dance, W. E., "Evaluation of Mobile ^{252}Cf Neutron Radiography for Field Inspection of Aerospace Structures," U.S. Energy Research and Development Administration Fifth ^{252}Cf Utilization Meeting, 4-6 Nov. 1975; *Californium-252 Progress,* No. 20, Jan. 1976.

[6] Dance, W. E., *Californium-252 Progress,* Nos. 12-22, 1972-1978.

J. A. Charles[1]

Liquid Crystals for Flaw Detection in Composites

REFERENCE: Charles, J. A., **"Liquid Crystals for Flaw Detection in Composites,"** *Nondestructive Evaluation and Flaw Criticality for Composite Materials, ASTM STP 696*, R. B. Pipes, Ed., American Society for Testing and Materials, 1979, pp. 72-82.

ABSTRACT: Liquid crystals have been investigated as an inexpensive nondestructive testing (NDT) technique for composite materials. By imaging the surface temperature distribution on both cyclically loaded and unloaded materials, subsurface flaws are found to be detectable. For specimens under load, likely damage locations and subsequent damage development can be determined. Cut fibers, inclusions, and geometric discontinuities served as flaws. Fiber glass/epoxy and graphite/epoxy composites were tested. It was found that liquid crystals can be used as an alternative to other NDT methods in many cases.

KEY WORDS: composite materials, fiber glass, graphite, nondestructive tests, thermal testing, liquid crystals

Composite materials are currently enjoying a widespread increase in use for structural applications, notably in the automotive and aircraft industries. Expected decreases in the cost of composites will serve to accelerate this growth in the future. Along with the increased use of these materials comes the need for improved methods of testing their structural integrity. Specifically, nondestructive testing (NDT) techniques must be available to ensure the safety of structural composites both before and during service. These NDT methods should be reliable, fast, easy to use, and economical. Several types of nondestructive tests are currently in use or under development, ranging from acoustic emission to holography. All possess some of the desirable qualities mentioned to some degree. An important class of NDT techniques, which exhibits a potential to meet most of the criteria, is based on thermal imaging.

"Thermal imaging" refers to a variety of techniques for visualizing the

[1] Assistant Professor, Department of Mechanical Engineering, The Ohio State University, Columbus, Ohio 43210.

surface temperature distribution on an object of interest. The images can be produced either chemically or electronically. Considerable study has been devoted to the use of electronic thermal imaging in material testing [*1-4*].[2] Electronic imaging usually involves the use of a scanning infrared camera which converts the thermal radiation (infrared) emitted from a body into a visual image displayed on a cathode-ray tube. This technique, popularly called "thermography," can produce very accurate images both spatially and thermally. Furthermore, it has been shown that thermography can be used to test the integrity of composite materials and monitor their condition while in service [*5-7*].

An alternative to electronic thermal imaging is chemical thermal imaging, which can be accomplished using liquid crystals. "Liquid crystals" are a group of chemical compounds which behave mechanically as liquids and optically as crystals. There are a large number of liquid crystal compounds, but only those known as "cholestric" liquid crystals have the characteristics necessary for thermal imaging. Named for their helical structure resembling cholesterol, these liquid crystals display a unique behavior that is temperature-sensitive. When illuminated with white light, cholesteric liquid crystals selectively scatter certain wavelengths of the incident light, producing vivid colors easily visible to the naked eye. The temperature sensitivity results from a change in the pitch of the helical structure as the temperature of the compound changes. Hence, for a given compound, different wavelengths of light are scattered at different temperatures. Thus the image produced changes color according to the surface temperature of the object to which the liquid crystals are applied. This color change usually proceeds from red to yellow, green, and blue as the temperature increases through the temperature-sensitive range of the specific compound. Depending on the chemical composition of the liquid crystal, the range can be as narrow as 3 deg C (5.4 deg F) or as broad as 15 deg C (27 deg F). The first indication of the liquid crystals (red) can be at temperatures as low as —7°C (19.4°F) or above 70°C (158°F). For a given liquid crystal compound, the temperature range will be nearly constant, although the intensity of the colors produced may vary with the previous history of a coating. Other factors which can affect the color response of liquid crystals are chemical environment and mechanical stress. More details on the chemical composition and behavior of liquid crystals can be found in Ref *8*.

This paper presents the results of studies performed to determine the suitability of liquid crystals for testing composite materials. The primary objective of these studies was flaw detection and damage location prediction. Of secondary interest are the results of damage development monitoring.

[2] The italic numbers in brackets refer to the list of references appended to this paper.

Procedure

Equipment

All of the loading for this study was performed using an Instron Model 1350 Servohydraulic Materials Testing System, operating in a stroke-controlled mode. All tests were performed using tension-tension loading, except where noted. No provisions were made for room-temperature control during the tests, which necessitated the use of several different liquid crystal compounds. An artist's airbrush was used to apply the liquid crystals to all specimens. The resulting thermal images were recorded on tungsten-type 35-mm color slide film using a single-lens reflex camera.

Liquid crystals are available in several forms, including encapsulated sheets, premixed liquids and pastes, and user-mixed liquid concentrates. The form used throughout this study was the premixed liquid. These liquid crystals come ready-to-spray and are precalibrated for determining quantitative temperatures from their color indications.

Specimen Preparation

All of the specimens studied were flat, having thicknesses up to 4.85 mm (0.19 in.) and widths up to 73.41 mm (2.89 in.). The specimens were each intended to contain a different flaw or illustrate a different behavior, so no standards were used in their preparation.

The composite materials used in this study were fiber glass/epoxy and graphite/epoxy. Specimens were fabricated in the laboratory to include debonds and cut fibers to simulate internal defects. Both the materials tested were machined using diamond saws and grinders. Some specimens included geometric stress concentrators rather than internal flaws. The individual specimen configurations will be discussed when the results are presented.

A common element in all specimen preparation for liquid crystal studies is the application of an optically-black coating to the surface. Since the color indications from liquid crystals are the result of selective scattering of incident light, it is important that all unscattered light be absorbed at the material surface rather than being reflected. This is easily accomplished with a black paint, although care must be taken that the paint solvent does not contaminate the liquid crystals. Another possibility for blackening is the addition of a carbon-black filler to the liquid crystal. In this study, flat black spray paint was used as the base coat on all specimens. This system was particularly good since the liquid crystals could be washed from the specimen surfaces using petroleum ether without damaging the black base coat.

Procedure

Two types of tests were performed during this study. The majority of the tests were "active" tests. In this case, the material is under cyclic loading and generates heat internally due to hysteresis and other effects. This heat generation is a function of material properties, stress level, loading type, and frequency. However, regions of locally high stress, due to flaws or stress concentrations, produce greater heat generation than surrounding regions, resulting in locally-elevated temperatures. Hence, active tests of composite materials can help one locate flaws and predict eventual damage locations through thermal imaging.

After machining and cleaning, the specimens were given the black base coat discussed previously. A suitable liquid crystal compound was then sprayed on the surface, with care being taken to ensure a uniform coat. The specific compound was selected based on the room temperature at the time of the test. A compound which gave its first indication (red) about 1 deg C above room temperature was found to be best. Then the specimen was cyclically loaded and carefully observed. Photographs of the images on the specimens were taken without stopping the tests. The photo floodlights used to illuminate the specimens during the image recording were left on only long enough to take each photo, since their thermal input to the specimens was enough to cause a color indication in the liquid crystals if left on too long.

The second type of test performed in this study was a "passive" test. In this case, a specimen with suspected flaws is heated by an external source while the surface temperature distributions are observed using liquid crystals. Any flaws in the material disturb the normal flow of heat in the specimen, producing abnormalities in the surface temperature distribution. Visualization of this distribution through thermal imaging can then indicate where major flaws are located in the composite.

The passive tests of this study were performed using infrared heating and contact heating with a heated plate. Infrared heating was found to be superior to contact heating when applied to the large rear surface of the specimen since it provided a uniform heat input to the surface. Images were recorded as they developed during the passive tests.

Results

Several examples of the use of liquid crystals for flaw detection in composites are presented here. The emphasis will be on fiber glass/epoxy laminates, which were fabricated to include various flaws. A few examples of graphite/epoxy tests will also be given.

Active Tests

Most of the active tests were performed on fiber glass/epoxy composites containing debonded areas, broken fibers, and geometric stress concentrations. The specimens were all made of 10 plies of woven glass cloth with [0/90] orientation. The unflawed material displayed an ultimate strength of 208 MN/m^2 (30 220 $lb/in.^2$) after curing at room temperature for 72 h.

Figure 1 shows a black-and-white reproduction of the liquid crystal indication which accompanied the propagation of a fatigue crack in one specimen. The specimen contained two notches of different root diameters. The fatigue crack can be seen as a white line extending to the right from the root of the smaller notch. Associated with the tip of the crack is a region of locally-high energy dissipation, which is the result of plastic deformation, fiber breakage, and matrix cracking. The specimen was being loaded cyclically over a stress range of 15.4 MN/m^2 (2230 $lb/in.^2$) at a frequency of 15 Hz. The stress ratio was 0.70 in this case, so frictional rubbing had a minimal effect on the image.

The liquid crystal image in Fig. 1 has been labeled to indicate the centers of the four color bands present. The particular compound used in this test produced a red color at 30.2°C (86.3°F), yellow at 30.6°C (87°F), green at 31.6°C (89.0°F), and blue at 33.0°C (91.5°F). Room temperature for the test was 29.4°C (85°F). Hence temperature rises of as little as 1 deg C were being indicated by the liquid crystals. A small temperature rise can also be seen adjacent to the larger notch, as some lesser degree of damage or hysteretic heating was occurring there.

Black-and-white reproductions of the liquid crystal images in this study are generally poor representations of the quality of information obtainable from the original color slides. Therefore, subsequent figures will be presented as isochrome maps. Figure 2 is one such illustration, taken from the same slide from which Fig. 1 was made. In Fig. 2, the isochromes may be interpreted as isotherms, although an exact temperature for each may be difficult to assign. Calibration checks on the liquid crystal compounds used showed that the actual temperature of the indication could vary by as much as 1.4 deg C (2.5 deg F) from the manufacturer's specification. The variation appeared to be a function of coating age and previous heating history. Hence, unless a reference system is incorporated into each image record, temperatures can be determined to an accuracy of only about 1.5 deg C. However, this feature of the liquid crystals does not detract from their usefulness as a flaw detection aid, since only relative temperatures and warm regions are of primary importance.

One type of flaw that may be encountered in composite materials is broken or cut fibers. This situation can greatly reduce the load-carrying capability of composites if the broken fibers lie in the direction of loading. Furthermore, such flaws can be impossible to locate visually if the cut

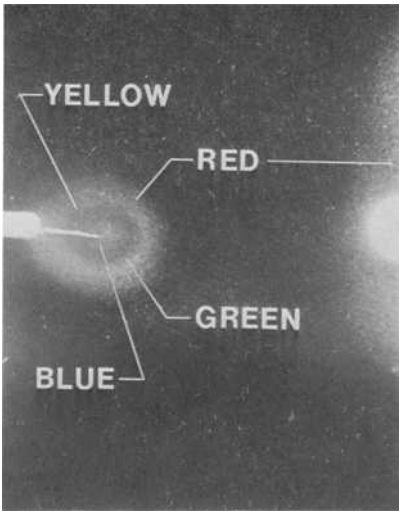

FIG. 1—*Liquid crystal image during crack propagation.*

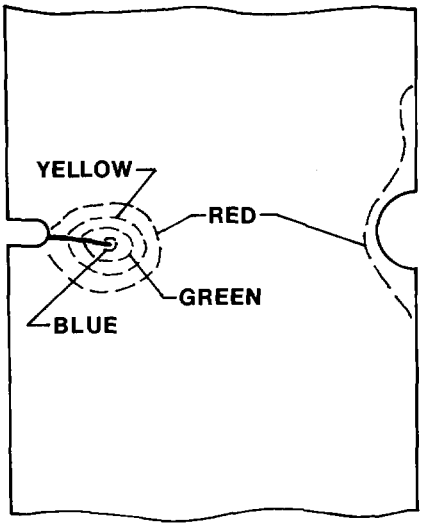

FIG. 2—*Isochrome map of Fig. 1.*

plies are near the center of the laminate. To illustrate how liquid crystals can be used to detect this type of flaw, several fiber glass/epoxy specimens were produced with cut fibers among the intact plies.

Figure 3 presents an isochrome map of one specimen with cut plies. The specimen was of constant cross section, measuring 69.9 mm (2.75 in.) wide and 3.8 mm (0.15 in.) thick, and contained a group of cut fibers within the inside six of the 10 plies. A cut approximately 38 mm (1.5 in.) long was made in each ply before layup, producing a specimen with 60 percent of the fibers cut at one cross section. The specimen was then loaded cyclically at 20 Hz over a stress range of 39.3 MN/m^2 (5690 $lb/in.^2$) with a stress ratio of 0.2. The temperature distribution of the surface of the specimen was visualized with liquid crystals. As seen in Fig. 3, the surface temperature distribution indicates the location of the cut fibers very accurately.

It is likely that fewer than 60 percent of the fibers at one location would be broken in a given specimen. Therefore, another specimen was fabricated with cut fibers in only one interior ply, producing 10 percent broken fibers. This specimen was loaded cyclically under the same conditions as that for the previous specimen. The location and size of the flaw were again readily determinable from the liquid crystal image.

In order to assess the effect of flaw depth and location on the quality of the images, a specimen was produced with multiple locations of cut fibers at different depths. Under loading over a stress range of 63.4 MN/m^2

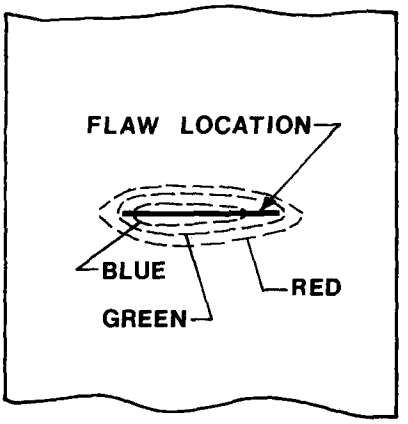

FIG. 3—*Active test of specimen with 60 percent cut fibers.*

(9190 lb/in.^{2}) at a frequency of 15 Hz, each flaw location became clearly visible. One isochrome map of this active test is shown in Fig. 4*a*. The upper flaw contained 30 percent cut fibers at a depth of two plies, the middle flaw was 20 percent cut fibers at the midplane of the specimen, and the lower flaw again contained 30 percent cut fibers but at a depth of eight plies from the surface. The flaws became visible during the test in order of the percentage of cut plies rather than the depth of the flaw.

Figure 4*b* shows the thermal image which accompanied the loading of

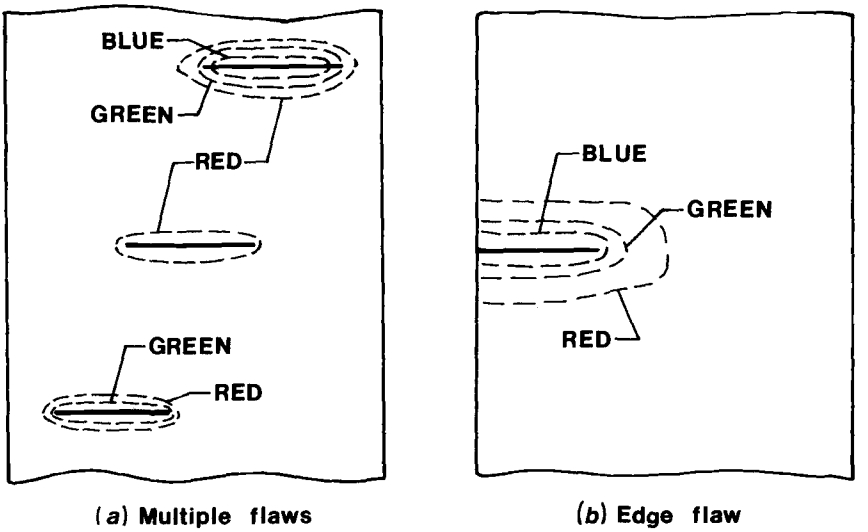

FIG. 4—*Active tests of multi- and edge-flawed specimens.*

a specimen containing 60 percent cut fibers at the left edge of the material. Again, the location and extent of the flaw can easily be determined. The specimen was being loaded at 20 Hz over a stress range of 56 MN/m^2 (8125 lb/in.^{2}). A fatigue crack developed at the flaw location after 25 000 cycles of this loading.

While the crack in the aforementioned specimen propagated, the loading was altered to illustrate the different forms of images which can accompany crack propagation in composites. Two of these forms are shown in Fig. 5. Figure 5*a* shows the liquid crystal image which accompanies a slow-moving crack in tension-tension fatigue. The isochromes are nearly concentric circles about the crack tip, indicating a point source of heat. In Fig. 5*b*, the same specimen is shown under tension-compression loading. In this case, crack rubbing produces a source of heat which slews the isochromes back along the crack surfaces.

A few tests were performed with a graphite/epoxy laminate of ± 45-deg ply orientation. This material was 3.5 mm (0.14 in.) thick, and displayed an ultimate strength of 400 MN/m^2 (58 000 lb/in.^{2}). Specimens were cut which had a reduced section width of 45.7 mm (1.80 in.). One specimen was notched with two 1.0-mm-wide (0.04 in.) notches to a depth of 7.0 mm (0.27 in.) each, while the other was left smooth. Each specimen was loaded at a frequency of 15 Hz over a nominal stress range of 227 MN/m^2 (32 920 lb/in.^{2}) with a stress ratio of zero.

Figure 6 shows a comparison of the early indications obtained on each specimen. The notched specimen in Fig. 6*a* exhibited a symmetrical diamond pattern of temperature rise emanating from the notch roots. This pattern

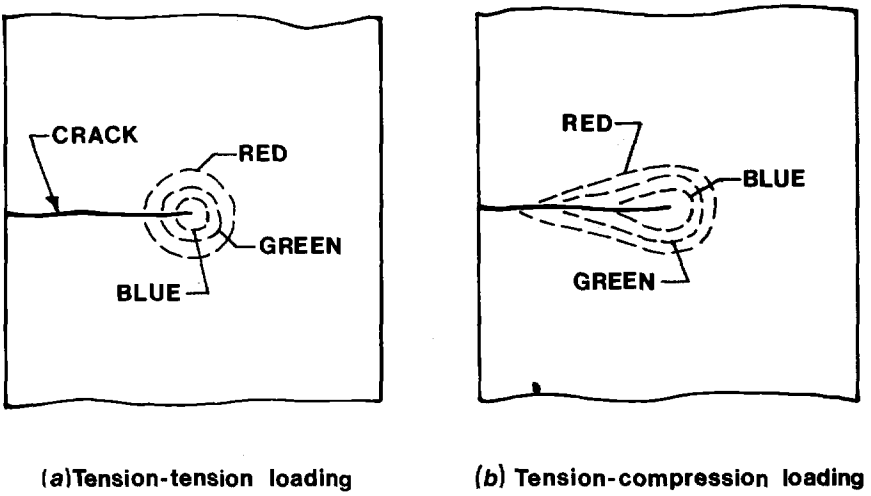

FIG. 5—*Examples of crack propagation images.*

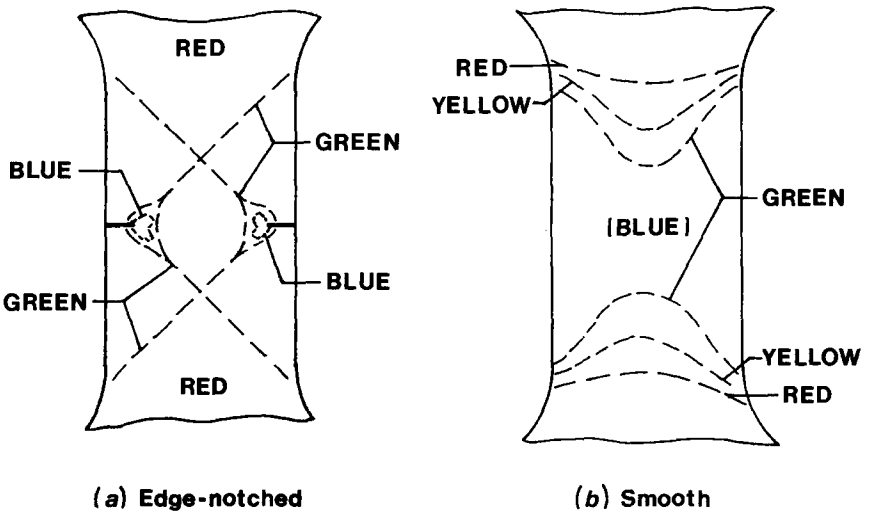

FIG. 6—*Early indications of damage in graphite/epoxy composites.*

is the result of the anisotropic thermal conductivity of the material. The notch roots serve as strong heat-generation locations, but the heat is conducted far more readily along the fiber directions (±45 deg) than in any other direction. Hence, the diamond-shaped pattern is indicative of heat conduction away from the main damage locations rather than an indication of a diamond-shaped damage pattern.

The isochromes shown in Fig. 6*b* for the smooth graphite/epoxy specimen are indicative of a nearly uniform heat generation. In the absense of any geometric stress concentration, this is expected, and the location of the eventual damage site is difficult to determine.

Passive Tests

Passive tests are more difficult to perform than active tests since they are transient in nature and depend upon a uniform transfer of heat from the external source to the specimen. However, several passive tests were performed on composites in this study. It was found that passive tests could be used to locate flaws, inclusions, and crack tips in composites.

As an example of a passive test, a fiber glass/epoxy specimen was prepared with disks of trifluoroethylene resin embedded within the plies. The disks were 9.5 mm (0.38 in.) in diameter, 0.10 mm (0.004 in.) thick, and were located at various depths in the 10-ply laminate. The specimen was heated from behind using an infrared lamp while the temperature distribution on the front surface was monitored using liquid crystals. As

the distribution developed, the internal disks could be "seen" lagging behind the temperature rise of the surrounding areas. This is shown in Fig. 7. Although it is possible to locate the inclusions in this manner, there appears to be no way to accurately ascertain the depth of the flaw. Somewhat better results were obtained testing the same specimen actively under fatigue and vibrational loading.

Discussion and Conclusions

Liquid crystals display a high potential for flaw detection in composites. As has been shown, they may be used to locate flaws, predict damage locations, and monitor damage development. Both active and passive tests can be applied in searching for flaws.

The main advantages liquid crystals have over other NDT techniques for many applications are simplicity and low cost. Liquid crystals do not depend on sophisticated electronics for their imaging, and so can be used easily in remote locations. The color images of liquid crystals are easily interpreted. Although a high-quality coating of liquid crystals yields the best results, it is not at all difficult for a novice to produce an acceptable coat. For the tests performed in this study, each coat of liquid crystals cost only $0.80. In most cases, only one coat was required per test.

There are, of course, some difficulties faced when using liquid crystals for flaw detection in composites. The coatings are susceptible to physical and chemical damage, and have a limited life. The greatest disadvantage of liquid crystals, however, is their fixed temperature range. This necessitates keeping a variety of liquid crystal compounds in stock and knowing the

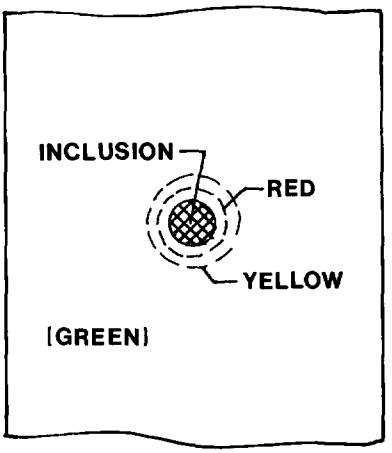

FIG. 7—*Passive detection of included disk in fiber glass/epoxy specimen.*

approximate temperatures to be observed. Often, the correct compound to use is one which gives its first indication just above room temperature. However, the wrong choice of liquid crystal can yield no information where another compound might have worked well.

In the author's opinion, the demonstrated successes and potential benefits of liquid crystals outweigh their disadvantages for flaw detection. With continued development and use, liquid crystals can be a valuable aid for composite material nondestructive testing, complementing other thermal and nonthermal techniques.

Acknowledgments

The author wishes to acknowledge the support of the National Science Foundation, who sponsored this research under Grant No. ENG77-04995. The work was performed while the author was a member of the faculty of the Department of Mechanical Engineering, Montana State University.

References

[1] Attermo, R. and Ostberg, G., *International Journal of Fracture Mechanics*, Vol. 7, No. 1, March 1971, pp. 122-123.

[2] Charles, J. A., Appl, F. J., and Francis, J. E., *Proceedings*, Oklahoma Academy of Science, Vol. 54, 1974, pp. 52-59.

[3] Charles, J. A., Appl, F. J., and Francis, J. E., *Experimental Mechanics*, Vol. 15, No. 4, April 1975, pp. 133-138.

[4] Charles, J. A., Appl, F. J., and Francis, J. E., *Journal of Engineering Materials and Technology*, Vol. 100, No. 2, March 1978, pp. 200-203.

[5] Reifsnider, K. L. and Williams, R. S., *Experimental Mechanics*, Vol. 14, No. 12, Dec. 1974, pp. 479-485.

[6] Marcus, L. A. and Stinchcomb, W. W., *Experimental Mechanics*, Vol. 15, No. 2, Feb. 1975, pp. 55-60.

[7] Charles, J. A., Appl, F. J., and Francis, J. E., *Proceedings*, 12th Annual Meeting of the Society of Engineering Science, Austin, Tex., Oct. 1975, pp. 819-828.

[8] Brown, G. H. and Shaw, W. G., *Chemical Reviews*, Vol. 57, 1957, pp. 1049-1063.

E. G. Henneke, II,[1] *and T. S. Jones*[1]

Detection of Damage in Composite Materials by Vibrothermography

REFERENCE: Henneke, E. G., II, and Jones, T. S., **"Detection of Damage in Composite Materials by Vibrothermography,"** *Nondestructive Evaluation and Flaw Criticality of Composite Materials, ASTM STP 696,* R. B. Pipes, Ed., American Society for Testing and Materials, 1979, pp. 83-95.

ABSTRACT: A new nondestructive inspection method, vibrothermography, has been studied here to determine its degree of application to the investigation of damage in composite materials. Subsurface damaged regions containing delaminations, relatively large matrix cracks, or matrix crazing are easily located by the method. A three-dimensional, anisotropic heat-conduction model, solved by a finite-difference method, has shown that the surface heat patterns monitored by thermography represent accurately the geometry and extent of the subsurface heat source.

KEY WORDS: vibrothermography, thermography, nondestructive tests, composite materials

Because of the laminar, nonhomogeneous, and anisotropic nature of modern fiber-reinforced composite materials, many of the existing nondestructive inspection (NDI) techniques are not immediately applicable for the detection of damage or the assessment of quality of these materials. Usually, major modifications must be made in order to apply these techniques and to interpret the resulting data. Indeed, it has often been found necessary to develop new NDI methods to study the new types of damage mechanisms occurring in composites as compared with the older, standard materials. A new technique, vibrothermography, was so developed and proposed for application to composites as well as to the more usual engineering materials [*1*].[2] Vibrothermography utilizes low-amplitude mechanical vibrations to induce localized heating in a material and real-time

[1] Professor and graduate student, respectively, Department of Engineering Science and Mechanics, Virginia Polytechnic Institute and State University, Blacksburg, Va. 24061. Co-author Jones is presently with McDonnell Aircraft Co., St. Louis, Mo.

[2] The italic numbers in brackets refer to the list of references appended to this paper.

thermography to record the resulting heat patterns. It was observed [*1*] that the localized heating was preferentially located around damaged regions in the material. For both composite and homogeneous materials, vibrothermography appeared to offer a viable method for the detection of certain types of damage and one that could be developed into a field technique.

The purpose of the present work was to further study the vibrothermography method to determine (1) what types of damage in composite materials, resulting from both load histories and manufactured defects, could be delineated by vibrothermography, (2) the degree of sensitivity of the method to such parameters as frequency of vibration, and (3) how representative of subsurface defects was the observed surface heat pattern. The first two items were studied by controlled experiments while the last item required numerical solution of the three-dimensional heat-conduction equation in an orthotropic material.

The first section of this paper outlines the finite-difference solution scheme used to solve the heat-conduction problem in a laminate. The experimental technique is described in the second section and the results are compared with the heat-conduction model in the last section.

Heat Conduction Model

The analytical model used here is similar to one reported earlier by Trezak and Balk [*2*]. These investigators considered the use of thermal imaging techniques for the nondestructive testing of metals. In their case, provocative techniques were used to obtain thermal radiation patterns for various materials and flaws. Stressing the importance of the use of an analytical model to aid in the interpretation of these patterns, the authors used a three-dimensional finite-difference heat-conduction analysis. They were able to input various flaw types to obtain a first-order approximation of the expected thermal pattern that could then be compared with experiment.

The literature also contains several schemes for defining the diffusion of heat through a composite material. Maewal, Bache, and Hegemier [*3*] showed good results using a continuum model for this process. An approximation was obtained by using a truncated power-series solution. In general, the zeroth or the first-order solution is sufficient for most problems. Estes and Mulholland [*4*] have developed a rather complex mathematical method for describing the diffusion of heat through a multilayered composite material. The scheme developed in their paper does not allow for internal heat generation. It does, however, allow for rather complex boundary conditions.

The model used in the present work begins with the partial differential

heat-conduction equation for an anisotropic material written as (see any standard text such as Ref 5)

$$\rho c_p \frac{\partial t}{\partial \tau} = K_{ij} \frac{\partial^2 t}{\partial x_i \partial x_j}$$

where

ρ = mass density,
c_p = specific heat at constant pressure,
t = temperature, and
τ = time.

Any material that has orthotropic symmetry will possess only three independent thermal conductivities, K_{11}, K_{22}, and K_{33}, when the x, y, z-coordinate axes are taken to be parallel to the principal axes of the material. For a composite laminate composed of several layers of material oriented in different directions, it is more convenient to choose one fixed set of coordinate axes. When one considers rotations only in the 1,2-plane, the thermal conductivity tensor becomes, with respect to the general x,y-coordinate system

$$K_{ik}' = \begin{bmatrix} K_{xx} & K_{xy} & 0 \\ K_{xy} & K_{yy} & 0 \\ 0 & 0 & K_{zz} \end{bmatrix} \tag{1}$$

where

$$\begin{aligned} K_{xx} &= \cos^2\theta\, K_{11} + \sin^2\theta\, K_{22} \\ K_{xy} &= \cos\theta \sin\theta\, K_{11} - \cos\theta \sin\theta\, K_{22} \\ K_{yx} &= K_{xy} \\ K_{yy} &= \sin^2\theta\, K_{11} + \cos^2\theta\, K_{22} \\ K_{zz} &= K_{33} \\ K_{xz} &= K_{zx} = K_{yz} = K_{zy} = 0 \end{aligned} \tag{2}$$

The heat-conduction equation for each lamina can now be written as

$$\rho c_p \frac{\partial t}{\partial \tau} = K_{xx} \frac{\partial^2 t}{\partial x^2} + K_{yy} \frac{\partial^2 t}{\partial y^2} + K_{zz} \frac{\partial^2 t}{\partial z^2} + 2K_{xy} \frac{\partial^2 t}{\partial x \partial y} \tag{3}$$

To solve Eq 3, a finite-difference method demonstrated by Chapman [6] is used. The spatial and time derivatives in Eq 3 are replaced by finite-

difference approximations based upon Taylor expansions. A change in the system of notation as shown in Fig. 1 is employed so that the updated temperature at an arbitrary node, t_a', can be written from Eq 3 as

$$t_a' = t_a \left[1 - \frac{\Delta\tau}{\rho c_p \Delta V} \left[\frac{2}{R_{xx}} + \frac{2}{R_{yy}} + \frac{2}{R_{zz}} \right] \right] + \frac{\Delta\tau}{\rho c_p \Delta V} \left[\frac{t_d + t_e}{R_{xx}} + \frac{t_b + t_c}{R_{yy}} + \frac{t_f + t_g}{R_{zz}} + \frac{t_{ce} + t_{bd} - t_{cd} - t_{be}}{R_{xy}} \right] \tag{4}$$

where

$$R_{xx} = \frac{\Delta x}{K_{xx} \Delta y \Delta z}, \qquad R_{yy} = \frac{\Delta y}{K_{yy} \Delta x \Delta z}$$

$$R_{zz} = \frac{\Delta z}{K_{zz} \Delta x \Delta y}, \qquad R_{xy} = \frac{2}{K_{xy} \Delta z}$$

The boundary conditions which must be satisfied for the outer nodes of each lamina alter the essential form of Eq 4. In fact, for any arbitrary layer it is necessary to write nine distinct equations, one equation for each corner node of the layer, one equation for the nodes along each of the four edges, and one equation for the interior nodes. The boundary conditions used are (1) an adiabatic midplane due to the symmetry conditions; (2) adiabatic surfaces along the short edges, that is, along the edges in the y-z plane; and (3) convective surfaces along the top surface and long edges, that is, the free edges in the x-z plane. Also, it is necessary to separate R_{zz} into R_u for conduction or convection from above and R_d for conduction from below. In addition, R_c is defined as the convective resistance

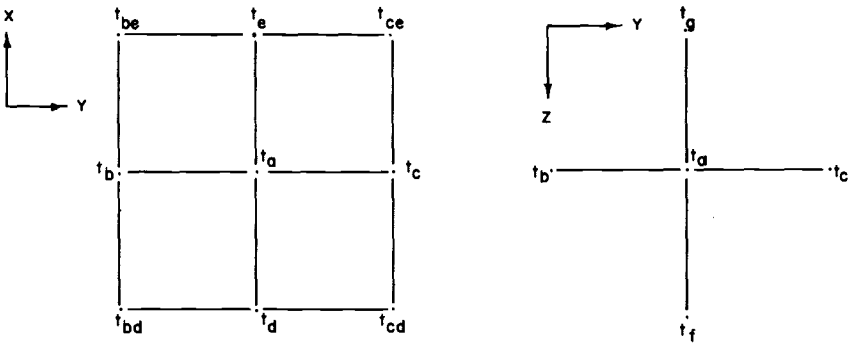

FIG. 1—*Coordinate axes and notation system used to denote temperatures of an arbitrary nodal element and its nearest neighbors.*

$$R_c = \frac{1}{h\Delta x \Delta z}$$

and, for the surface ply only

$$R_u = \frac{1}{h\Delta x \Delta y}$$

where h is the film coefficient.

Examination of Eq 4 indicates that there is a stability requirement on the value of $\Delta\tau$. If $\Delta\tau$ is chosen large enough, the coefficient of t_a becomes negative. If this is allowed to happen, it would imply that the hotter the temperature t_a at time τ, the cooler the temperature t_a' at time $\tau + \Delta\tau$. Since this is obviously physically impossible, it is necessary to choose $\Delta\tau$ so that the coefficient of t_a remains positive. The requirement on $\Delta\tau$ can be written as

$$\Delta\tau < \frac{\rho c_p \Delta V}{2} \left\{ \frac{1}{R_c} + \frac{1}{R_{xx}} + \frac{1}{R_{yy}} + \frac{1}{2R_u} + \frac{1}{2R_d} \right\}^{-1} \quad (5)$$

where R_{zz} has been separated into R_u, R_d, and R_c as noted in the preceding.

Heat sources in the laminate were modeled as having a linear temperature increase with time. For the present work an increasing temperature source was chosen instead of a steady-state one to better model the vibrothermography experiment. Thus when the mechanical shaker is turned on at initial time, every point in the laminate is at room temperature. As the specimen begins to vibrate, those regions that serve as local hot spots begin to have a temperature rise. Because the numerical iteration procedure is halted after approximately two seconds of conduction time, one need not worry about the unrealistic ever-increasing temperature of the source.

Experimental Technique

Composite laminate specimens of graphite/epoxy were attached to a low-amplitude mechanical shaker and vibrated in a longitudinal mode. To initiate damage in them, the specimens had been either previously loaded quasi-statically or in fatigue or manufactured with intentional flaws. The mechanical shaker vibrated at a nominal frequency of 18 kHz and a maximum strain amplitude of less than 1 μm/m. The specimens were attached to the shaker at one end only and hence were inertia loaded. Because of this and the very low amplitude of motion, no additional damage was imparted to the specimens during their vibration.

A standard, commercially available, thermographic camera was used to monitor the temperature patterns established in the laminates by the

vibration. Both black-and-white and color television monitors were used to observe the steady-state patterns. A 35-mm camera was used to make a permanent record of the temperature pattern directly from the monitor.

Results and Discussion

Software was written, based upon the previously discussed three-dimensional heat-conduction model, to calculate the temperature patterns resulting on the surface of a laminate due to some subsurface heat source. Figure 2 shows the nodal pattern of 100 nodes used for each lamina. The heat source geometries were chosen by making reasonable estimations as to the shape and size of real damaged regions observed in composite laminates. In several cases, the geometry of the heat source was chosen to match the geometry of known flaws manufactured in the laminates during the fabrication process. The material properties used in the numerical analysis are given in Table 1. The resulting temperature pattern at the specimen surface was calculated at the end of a specified number of iterations corresponding to approximately 1.5 s of real time. It was found from

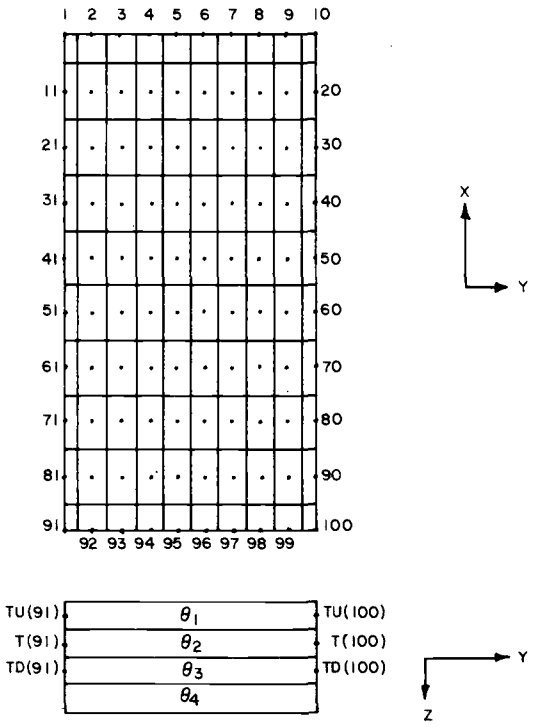

FIG. 2—*Numbering system used to denote nodal elements across width of specimen.*

TABLE 1—*Material properties.*

Property	Graphite/Epoxy	Boron/Epoxy
Conductivity 1-direction (cal/°C-cm-s)	0.01033 [7]	0.00551 [8]
Conductivity 2-direction (cal/°C-cm-s)	0.00155 [7]	0.00248 [8]
Conductivity 3-direction (cal/°C-cm-s)	0.00125 [a]	0.00200 [a]
Film coefficient (cal/°C-cm^2-s)	0.0007 [a] [6]	0.0007 [a]
Density (g/cm^3)	1.61 [7]	1.61 [a]
Specific heat (cal/°C-g)	0.22 [9]	0.28 [9]

[a] Estimated value based on best information in Ref's 6-9.

calculations using a steady heat source that the subsurface heat pattern is conducted very rapidly to the surface. Hence the time interval chosen to end the iteration process for the linear increasing temperature source was more than sufficient to obtain a good surface heat pattern due to the internal heat source. Increasing the final time would have served only to increase the surface temperatures, and not their distribution. The results of the numerical calculations are presented here in the form of isothermal plots. A temperature of 20°C was used as ambient and two isotherms were drawn in each figure presented herein, one for 20.3°C (fine line) and one for 22.0°C (thick line).

In order to form the shape patterns required to simulate the damage in specimens, a certain number of elements must be declared as damaged elements. Since the number of elements is limited to 100 per ply, a size distortion occurs in some of the computer-generated temperature patterns. In order to reduce this distortion, in some cases the dimensions of the interior elements were changed from rectangular, which naturally fitted the specimen's overall geometry, to square. For these cases, the area actually analyzed is represented in the figures as being that between the dashed lines.

Many different specimens have been studied both analytically and experimentally. Experimentally, it was found that the heat patterns developed very quickly after the mechanical shaker was turned on with a steady state obtained within a few seconds. The type of damage that was most readily observed was delamination or relatively large cracks or crazing in the matrix. The heat patterns were quite sensitive to the frequency of vibration but had no apparent direct connection to the natural vibration modes of the specimen. For example, a vibrothermograph of a virgin specimen showed a uniform temperature pattern while after 10 000 cycles in fatigue a very intense heat pattern developed around an edge delamination that had been induced by the loading. Other specimens were changed around in the shaker to vary the possible nodal positions of the natural modes, but the heat patterns always developed around the same damaged locations. Due to space limitations here, only a few typical results are presented.

To begin, Fig. 3 presents a vibrothermographic picture of a damaged region in a graphite/epoxy $[0/\pm 45/90]_s$ laminate that had been previously quasi-statically loaded to 12 kN (2700 lb). Edge delaminations and transverse cracks in the 90-deg and adjacent −45-deg plies were both present in this specimen. In this thermograph, a temperature range of 2 deg C was used. The grey shadings shown across the bottom of the photograph indicate a difference of 0.2 deg C between each shade, with black being the coolest and white the hottest. It can be seen that at this frequency of vibration there is an obvious heat source along only one edge of the specimen, the extent and depth of which closely correspond to the edge delamination. Thus, again referring to Fig. 2, Elements 30, 40, 50, 70, and 80 in the innermost layer of the laminate were chosen for the heat source since these most closely corresponded to the size of the heat source. The resulting calculated thermograph is shown in Fig. 4. As can be seen, the patterns in Figs. 3 and 4 are very similar. In the computer-generated temperature pattern, the indentation between the two generating areas is larger than the actual thermograph. This discrepancy could perhaps be remedied if more elements per ply were used, which would allow the size of each node to be smaller. Given smaller nodes, the gap between the two generating patterns could be reduced and the indentation seen in the computer-generated temperature pattern would also be reduced. Also, it is possible that the region between the two intense areas on the thermograph is generating at a lower rate than the two intense areas. The computer program, as written, does not allow for varying degrees of heat generation. The computer program did, however, reproduce reasonably well the experimental temperature pattern with the given input data.

When the frequency of the shaker to which the specimen was attached was slightly changed (by less than 10 percent), a second heat source on the other edge appeared, Fig. 5, again corresponding to an edge delamination there. Figures 3 and 5 are interesting evidence of the strong dependence of the heat patterns on vibration frequency. The heat generators input into the computer program to model the damage responsible for the thermograph in Fig. 5 were Elements 30, 32, 40, 50, 69, 70, 79, and 80 in the innermost layer. The thermograph resulting from the computer-generated temperature pattern for this input data is seen in Fig. 6. The pattern on the right is a reasonable match for the experimental thermograph. The restriction of the size and shape of the elements causes some discrepancy again in the gap between the two intense sources on the right. The computer-generated pattern on the left is not an especially good match with regard to the lower-temperature isotherm. This is due obviously to the failure to put in the lower heat source on the left-hand edge and also to the inadequacies of the program due to the large element sizes.

Detailed examination of the edge of the graphite/epoxy specimen appearing in Figs. 3 and 5 showed extensive edge delaminations in the inner

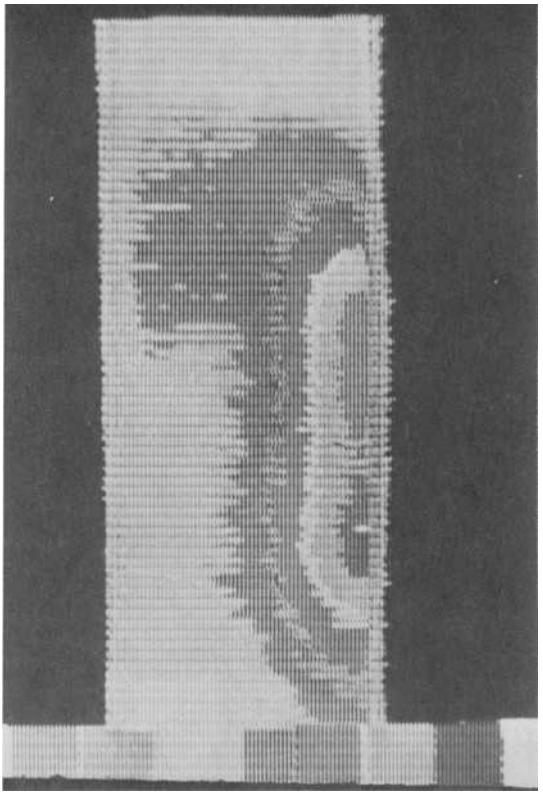

FIG. 3—*Thermograph of graphite/epoxy specimen after quasi-static tensile loading to 12 kN (2700 lb).*

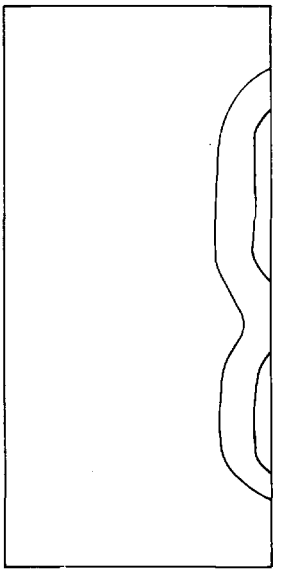

FIG. 4—*Computer-generated thermograph modeling edge delamination in Type I specimen shown in Fig. 3.*

90-deg plies along the entire length of both edges. In addition, transverse cracks existed in both the 90-deg plies and the adjacent −45-deg plies. Examination of other similar specimens has shown that the extent to which the edge delaminations grow across the width of the specimen may vary along the length. It is believed that this is the reason for the particular heat patterns observed in Figs. 3 and 5. That is, the depth of the delamination is probably greater in those regions indicated by the higher temperatures. However, this particular specimen was not sectioned to verify this point.

A graphite/epoxy laminate $[(0/90)_2]_s$, 7.62 by 20.32 cm, was manufactured with several intentionally included flaws. As shown in the schematic, Fig. 7, two pieces of waxed paper were included at the midplane of the specimen. A 2.54-cm (1 in.) square of the paper was placed near one end of the plate and a 2.54-cm (1 in.) "T" was placed near the other end. One layer away from the midplane and in the center of the specimen, a diamond-

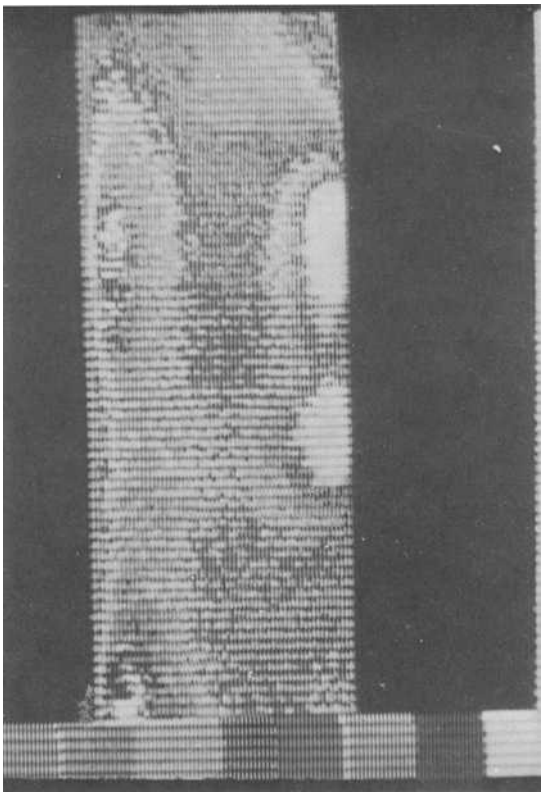

FIG. 5—*Thermograph of specimen shown in Fig. 3 after changing vibration frequency by less than 10 percent.*

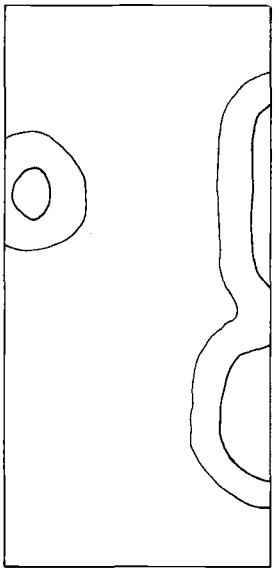

FIG. 6—*Computer-generated thermograph of graphite/epoxy specimen with edge delaminations modeled along both edges.*

shaped piece of plastic sheet was inserted. Two layers away from the midplane and near the base of the T, two small, thin smears of graphite grease were included. These inclusions were intended to represent delamination-like flaws in the cured specimen. With the use of vibrothermography, each of the synthetic flaws, with the exception of the graphite grease smears, was successfully located. Figure 8 shows, for example, the vibrothermograph produced by the plastic, diamond-shaped inclusion. In the color photograph of this figure, the T-shaped inclusion could also be seen. Since it was a lower-intensity heat source, the shades of grey in the black and white photograph make it difficult to distinguish here. Failure to locate the grease smears may have been due either to the small amount of grease used and the proximity to the edge of the specimen, allowing enough of the grease to be removed from the specimen during curing to allow an adequate bond to form in this area, or to the fact that the grease served to lubricate the material, reducing coulomb effects.

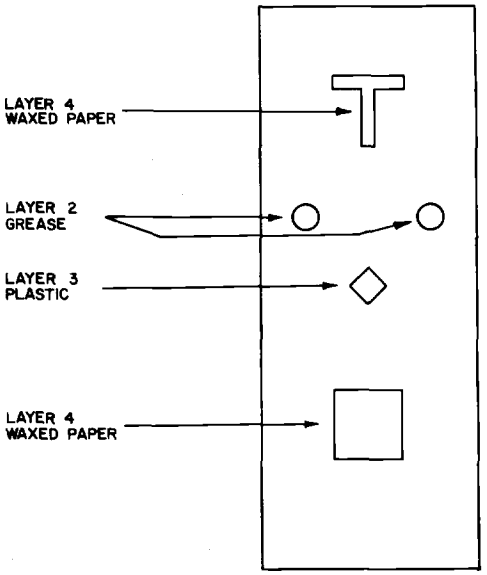

FIG. 7—*Schematic diagram of intentionally manufactured flaws in graphite/epoxy specimen.*

Since the damage in this specimen was intentionally included during fabrication, the approximate damage shape was known. For example, the diamond-shaped inclusion was located at Nodes 35, 44, 45, 46, and 55 in the third lamina below the surface. The resulting calculated thermograph is shown in Fig. 9. The comparison between the experimental and theoretical temperature patterns is very good for this case. The diamond-shaped pattern is more distinctive in Fig. 9 than in Fig. 8, but the angular sides of the experimental pattern are clearly distinguishable in Fig. 8.

Conclusions

Vibrothermography is a new nondestructive inspection method that has a large potential for use in study of composite materials. With additional development, the technique will become valuable both for laboratory study of damage mechanisms and for field monitoring of in-service structures. Present work indicates that delaminations, large matrix cracks, and matrix crazing are the types of damage most susceptible to detection by vibrothermography. A very limited vibration frequency regime has been studied, however, and the technique might prove itself useful for the detection of smaller cracks at higher frequency levels. As has been shown here, the developed heat pattern is very sensitive to the vibration frequency. With further study,

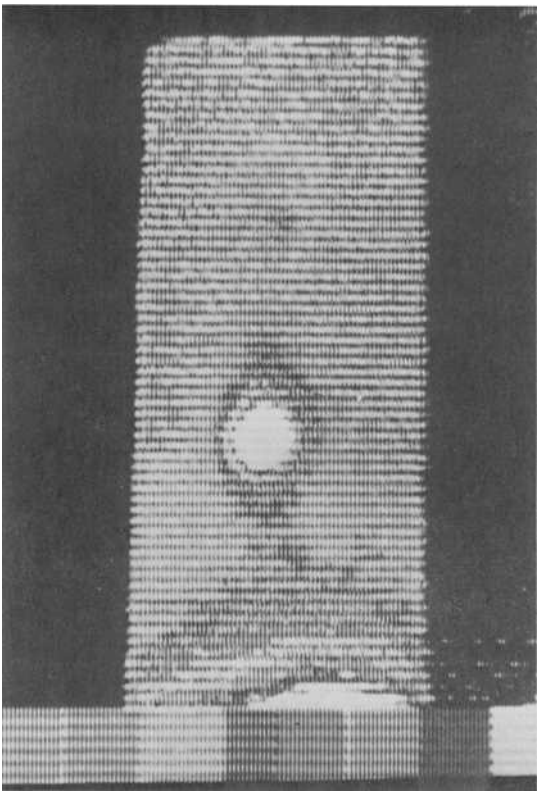

FIG. 8—*Thermograph showing heat pattern developed by plastic diamond inclusion.*

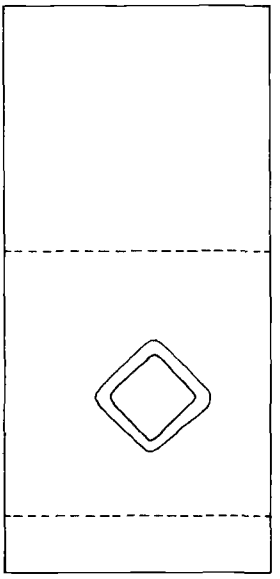

FIG. 9—*Computer-generated thermograph for the diamond inclusion in the specimen shown in Fig. 8.*

it is hoped that one will be able to show a correlation between frequency of vibration and the size or extent of the damage.

As part of the present effort, a three-dimensional heat-conduction model has been developed to describe heat flow in an orthotropic composite laminate. The solution obtained from this model indicates that the surface heat pattern resulting from a subsurface heat source quite accurately describes the geometry and extent of the heat source, at least for the eight-ply laminates studied here. Comparison of experimental and theoretical results have shown this conclusion to be valid.

Acknowledgment

This work was supported by the Air Force Materials Laboratory, Wright-Patterson Air Force Base, under Contract No. F 33615-75-C-5119.

References

[1] Reifsnider, K. L., Henneke, E. G., II, and Stinchcomb, W. W., "Defect-Property Relationships in Composite Materials," Technical Report AFML-TR-76-81, Air Force Materials Laboratory, Wright-Patterson Air Force Base, Ohio, April 1976.

[2] Trezek, G. J. and Balk, S., *Materials Evaluation,* Vol. 34, Aug. 1976, pp. 172-176.

[3] Maewal, A., Bache, T. C., and Hegemier, G. A., *Journal of Heat Transfer,* Vol. 98, Feb. 1976, pp. 133-138.

[4] Estes, R. C. and Mulholland, G. P., *Fibre Science and Technology,* Vol. 7, Oct. 1974, pp. 257-279.

[5] Carslaw, H. S. and Jaeger, J. C., *Conduction of Heat in Solids,* Oxford University Press, London, U.K., 1947.

[6] Chapman, A. J., *Heat Transfer,* MacMillan, New York, 1974.

[7] Hofer, K. E., Larsen, D., and Humphreys, V. E., "Development of Engineering Data on the Mechanical and Physical Properties of Advanced Composite Materials," Technical Report AFML-TR-74-266, Air Force Materials Laboratory, Wright-Patterson Air Force Base, Ohio, Feb. 1975.

[8] Hofer, K. E., Rao, N., and Larsen, D., "Development of Engineering Data on the Mechanical and Physical Properties of Advanced Composite Materials," Technical Report AFML-TR-72-205, Part II, Air Force Materials Laboratory, Wright-Patterson Air Force Base, Ohio, Feb. 1974.

[9] Kasen, M. B., *Cryogenics,* Vol. 15, Dec. 1975, pp. 701-722.

Summary

In dealing with nondestructive evaluation and flaw criticality in composite materials the nondestructive inspection (NDI) specialist is confronted with difficult questions about what flaws should be investigated and what flaw parameters should be measured. Detailed answers to such questions are, more often than not, unavailable and can come only through interactions among mechanics, materials, and NDI communities.

Because progress in such interdisciplinary efforts proceeds through interactive contributions, it is important that each specialist be alert to progress in other fields in order to apply techniques and expertise where and when they are needed.

Present trends in NDI research have been strongly influenced by the need to define and cope with those properties and defects which are unique to composites. Among the well-developed NDI techniques, penetrants, eddy current, radiography, and ultrasonics have all received attention for composites.

In radiography, it has been found that low-density inhomogeneous composite materials exhibit poor flaw contrast with conventional X-ray procedures, driving the development of radio-opaque penetrants, low-kilovolt X-ray radiography, and neutron radiography, the latter providing high contrast for organic materials even in the presence of metallic structure.

Since radiographic interpretation is largely a visual procedure, future advances must involve some refinement of the techniques and development of radiographic standards needed for particular defects.

A large number of advances in image processing, pattern recognition, and real-time radiography, imminent in medical and industrial applications, may also be useful here; at present, however, these appear to provide no unique advantages for composites and should not be looked to for solving fundamental problems in the area.

In ultrasonic inspection, material inhomogeneity and anisotropy severely limit the capability for characterizing discrete defects. As a result, necessary size, shape, and position information on defects is obtained with much less accuracy than in homogeneous materials and particular types of defects are classified with much less certainty. Since interpretation of acoustic interaction in monolithic materials is far from routine, understanding the interactions of ultrasonic waves with defects in composites will remain a research challenge for some time to come.

Eddy current techniques have received limited attention in connection with metal matrix composites; recently, however, there has been interest in using

them to investigate conduction patterns in graphite fiber-reinforced plastics. Few if any results have been published in this latter area; consequently applications to composite inspection are, perhaps, still to be discovered.

A number of techniques less widely used than those discussed in the foregoing, including holography, acoustic emission (AE), positron annihilation, exoelectron emission, and thermography, may also prove useful for composite NDI.

In these cases the techniques themselves are evolving rapidly and their capabilities will require periodic assessment to determine when they are ready for exploitation.

In acoustic emission, some promising investigations with unidirectional material and low-fiber-density specimens have indicated that unique acoustic signatures are associated with certain damage and deformation mechanisms in composites. But unfortunately, even if complete data on all such intrinsic signatures are available, the capability to recognize these in a multidirectional laminate would still require extensive theoretical and experimental work of the type possible in only few laboratories. In the absence of such a unified approach, advances will most likely occur through cumulative cataloging of AE signatures in specific applications for which a limited number of potential defects and failure modes are present.

Thermography, a nondestructive testing technique which indicates defects by imaging nonuniform temperature distribution, holds promise as a large-area inspection tool for all types of materials. Although this large-area capability is generally implemented through a rather expensive thermal imaging capability, low-cost liquid-crystal techniques are also available and suitable for many research applications. Anisotropic heat conduction is, of course, a unique aspect of composite thermography, but probably it does not present the difficulties associated with techniques such as vibrothermography, in which anomalous heat patterns are generated around defect sites by fatigue or vibration loading.

An analysis of the latter testing technique could easily involve studies of vibration analysis, viscoelastic theory, heat conduction, and fracture mechanics.

Clearly, research of this type may present opportunities for some of the most challenging and potentially fruitful interdisciplinary studies in the field of composite materials.

Holography is another technique with high potential, which, although it may have no unique capability for composites, will find increasing application in all areas of NDI. Much of its use, however, will depend on bringing it out of the laboratory, packaging the capability, and, most of all, learning to interpret the results which it provides. Advancements in laser technology for producing bright, highly coherent pulsed devices and the development of speckle-shearing interferometry will probably contribute strongly to bringing this technique into wider use.

For techniques such as exoelectron emission and positron annihilation,

which are carried out in a limited number of laboratories, one can probably only await the availability of more practical instrumentation before assessing their full potential.

As composites come into increasing use and the nature of their defects becomes better understood, the NDI specialist will be required to make increasingly more sophisticated measurements on these materials. A knowledge of how all of the various NDI techniques are applied to composites and of the information which they can provide will be a valuable resource in the evaluation of these materials.

W. R. Scott

Naval Air Development Center, Johnsville, Pa.; coeditor.

Flaw Criticality of Composite Materials

D. E. Pettit[1]

Characterization of Impact Damage in Composite Laminates

REFERENCE: Pettit, D. E., **"Characterization of Impact Damage in Composite Laminates,"** *Nondestructive Evaluation and Flaw Criticality for Composite Materials, ASTM STP 696,* R. B. Pipes, Ed., American Society for Testing and Materials, 1979, pp. 101-124.

ABSTRACT: The potential application of the Holscan 400 as a laboratory tool to monitor and characterize impact damage in graphite/epoxy composite material was evaluated. Impact damage in 16- to 32-ply-thick material was examined. A number of modifications were made to the basic Holscan system and the unit evaluated in terms of impact damage characterization ability and ease of operation in a laboratory environment. The results showed several of the modifications to be needed to provide a system with the desired capability and ease of operation.

KEY WORDS: nondestructive tests, composite materials, impact damage, ultrasonics

The introduction of advanced composite materials into aircraft structural applications in recent years has necessitated the development of analytical methodologies to assure the same level of structural reliability found in comparable metal structures. Composite materials, however, are not well suited to a simple extrapolation of analysis methods used in metals. This is a result of the differences between the basic characteristics of composites and metals. For example, composites are strongly anisotropic by nature and contain major microscopic inhomogeneities consisting of the matrix/interface fiber nature of the material. As a result, the initial damage in composites may take many different forms which, unlike metals where most types of defects could conservatively be considered as cracks, may have entirely different characteristics and possibly propagate in a non-selfsame manner. A common type of damage which is unique to composites is that due to low-velocity impact.

Associated with the difficulties in defining the exact nature of damage

[1] Research scientist, Lockheed-California Co., Burbank, Calif. 91520.

and its effect on service life are the problems of developing adequate nondestructive inspection (NDI) methods to detect the damage and analysis methods to define its severity. To permit the development of adequate durability and damage tolerance design methodology, it is highly desirable to develop NDI methods which can be used to characterize the damage in a laboratory setting. This is required to develop the needed data base.

At the present state of the art, most NDI methods which provide some damage detail cannot be used continuously without introducing the adverse conditions of (1) inserting a foreign substance and an accompanying unknown effect (that is, penetrants, X-ray enhancing liquids, etc.), (2) a water bath environment (ultrasonics and acoustic imaging), or (3) temperature excursions (thermography). In this program the major criterion for the selection of an NDI method was twofold: (1) to select a method which provides the most detailed information as to the size, shape, and the type of damage which is present, and (2) to provide a readily usable system for damage detection and monitoring in the laboratory environment with minimum impact on the material under test. For this study the type of potentially significant damage selected for use was damage due to low-velocity impact such as that due to tool drop, etc.

Nondestructive Inspection System

The system selected for evaluation was a basic Holosonic System 400 (Fig. 1) with the following modifications:

1. The "flex-arm" transducer mount was replaced with a digital mechanical scanner interfaced with the System 400 electronics as shown labeled "A" in Fig. 1.

2. A digital memory, "B" in Fig. 1, with a real-time image display electronic processor and dual-mode scope was interfaced with the System 400 electronics to provide a digital memory storage unit to retain and provide subsequent display of the data in C-scan and associated B-scan format as well as a 3-D isometric format.

3. The flex-arm transducer mount shown in Fig. 2 was retained for "quick look" capability.

4. A vertical mounting and water column coupling system containing its own water pump, marked "C" in Fig. 1, was attached to the transducer/digital scanner. Inclusion of this unit (available only with the digital scanner discussed in Item 1) provides a system which can be used on test specimens mounted in the test frame, thus eliminating the necessity of removing and reinstalling specimens each time they are to be examined. Figure 3 shows the digital mechanical scanner mounted in place and ready for use.

FIG. 1—*Photograph shows the modified Holosonic System 400 electronics* (A), *the digital mechanical scanner* (B), *vertical mounting system pump* (C), *and digital memory* (D).

Specimen Preparation

Two impact study panels 50.8 by 60.9 cm (20 by 24 in.) were fabricated of T300/5208.[2] The first was a 32-ply quasi-isotropic laminate (Panel A) with a $(0/+45/90/-45_2/90/+45/0)_{2s}$ layup; the second panel was a 24-ply 67 percent, 0-deg fiber laminate (Panel B) with a $(0/+45/0_2/-45/0_2/+45/0_2/-45/0)_s$ layup. In addition, one 16-ply T300/5209 panel (Panel C)[3] was used which had a $(0/\pm 45/0)_4$ layup. For these tests, a drop tower with a trifluoroethylene guide tube mounted in a support frame was used to induce damage. The impactors consisted of a 2.54-cm-diameter (1 in.) adjustable-weight steel cylinder with interchangeable impact heads, one a 2.54-cm-diameter (1 in.) hemispherical head, and one a No. 2 standard Phillips Head screwdriver point. Drop heights were preset by use of loca-

[2]Pettit, D. E., "Residual Strength Degradation for Advanced Composites," Lockheed-California Co. Interim Technical Quarterly Report, LR 28360-4, Burbank, Calif., 5 May 1978.
[3]Pettit, D. E., "Experimental Techniques, Impact Damage of Composite Materials," Lockheed-California Co. Report, LR 28001, to be published.

FIG. 2—*Flex-arm transducer mount in use.*

tion pins which extended through the trifluoroethylene guide tube. Impactor velocity at impact, the deflection dynamics of the specimen and impactor, and the rebound velocity of the impactor were monitored by a high-speed motion picture camera. Triplicate drops were made for each of four mass/heights with each of the two impactor head configurations at locations defined by a 7.62-cm-square (3 in.) grid on the panel. The test panels were supported during impact by a 0.95-cm-thick (3/8 in.) section of HRH10-3/16-3.5 honeycomb core material. This support method was selected since tests have indicated (see footnote 3) that this provides a reproducible damage size for low-velocity impact testing. A summary of the impact conditions and approximate apparent width, X, and height, Y (parallel to the 0-deg fiber direction) of the individual damage sites from

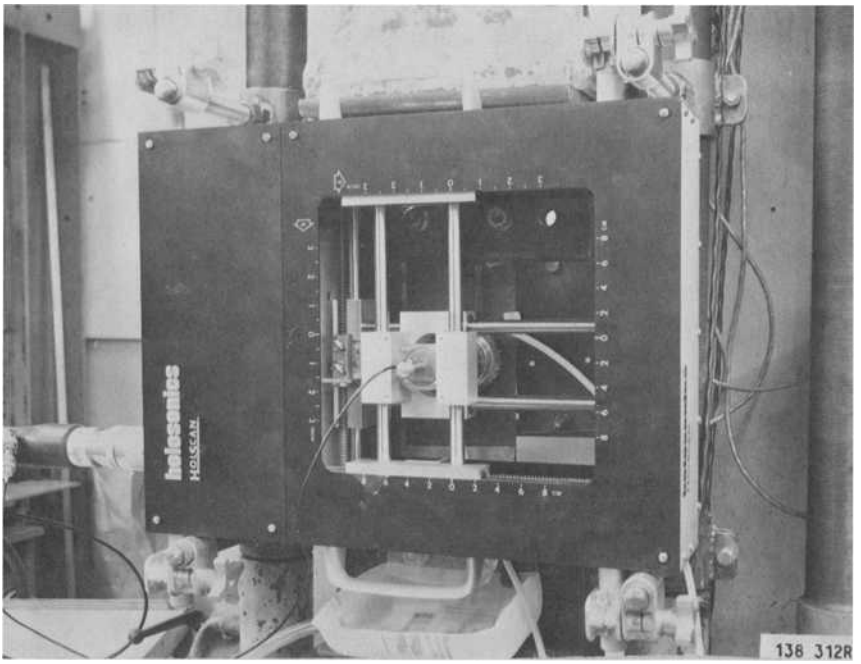

FIG. 3—*Digital mechanical scanner with vertical mounting in place for panel examination.*

C-scan examination is presented in Tables 1 and 2 for the 32-ply and 24-ply T300/5208 materials, respectively.

Following impact, panels were ultrasonically C-scanned to determine the basic plan area view size of the resulting damage at each site. Detailed examination of the impact damage was then conducted using the Holscan ultrasonic unit.

Results

Initial Evaluation of Panel C

Initial tests were conducted on the 16-ply T300/5209 Panel C using the equipment as previously described with the exception of the use of an analog rather than a digital memory unit. Two impact damage areas were selected for the evaluation. The first, referred to as Site 2, was formed by impact of a 1.21-kg (2.68 lb) mass with a 2.54-cm-diameter hemispherical end dropped from a height of 43.18 cm (17 in.). The second damage site, No. 7, was formed by impact of a 0.61-kg (1.36 lb) impactor with a No. 2 Phillips Head screwdriver tip which was dropped from a height of

TABLE 1—*Preliminary impact damage evaluation results on Panel A: 32-ply quasi-isotropic laminate.*

Condition	Locations	Test Run No.	Drop Height, m	Drop Height, (in.)	Impact Head Type [a]	Impact Mass, kg	Impact Mass, (slug)	Impact Velocity, m/s	Impact Velocity, (ft/s)	Kinetic Energy, E_K J	Kinetic Energy, (ft/lb)	Apparent Damage Size, X by Y mm	Apparent Damage Size, (in.)
1	1	37	1.24	(48.8)	1	0.240	(0.016)	4.02	(13.2)	1.94	(1.43)	0	0
	2	38	1.24	(48.8)	1	0.240	(0.016)	3.96	(13.0)	1.87	(1.38)	0	0
	3	39	1.24	(48.8)	1	0.240	(0.016)	4.11	(13.5)	2.02	(1.49)	0	0
2	4	40	0.48	(18.8)	1	0.590	(1.040)	2.44	(8.0)	1.75	(1.29)	17.8 × 19.0	(0.70 × 0.75)
	5	41	0.48	(18.8)	1	0.590	(1.040)	2.50	(8.2)	1.84	(1.36)	17.5 × 17.3	(0.69 × 0.68)
	6	42	0.48	(18.8)	1	0.590	(1.040)	...	...	...	...	18.3 × 18.3	(0.72 × 0.72)
3	7	43	0.73	(28.8)	1	0.590	(1.040)	3.29	(10.8)	3.20	(2.36)	20.8 × 23.1	(0.82 × 0.91)
	8	44	0.73	(28.8)	1	0.590	(1.040)	3.23	(10.6)	3.08	(2.27)	21.6 × 22.4	(0.85 × 0.88)
	9	45	0.73	(28.8)	1	0.590	(1.040)	3.35	(11.0)	3.31	(2.44)	20.3 × 22.6	(0.80 × 0.89)
4	10	46	0.73	(28.8)	1	0.240	(0.016)	3.23	(10.6)	1.25	(0.92)	0	0
	11	47	0.73	(28.8)	1	0.240	(0.016)	3.47	(11.4)	1.44	(1.06)	0	0
	12	48	0.73	(28.8)	1	0.240	(0.016)	3.35	(11.0)	1.34	(0.99)	0	0
5	13	49	1.24	(48.8)	2	0.248	(0.017)	4.14	(13.6)	2.13	(1.57)	13.7 × 13.2	(0.54 × 0.52)
	14	50	1.24	(48.8)	2	0.248	(0.017)	4.14	(13.6)	2.13	(1.57)	10.4 × 11.4	(0.41 × 0.45)
	15	51	1.24	(48.8)	2	0.248	(0.017)	4.24	(13.9)	2.22	(1.64)	12.4 × 12.7	(0.49 × 0.50)
6	16	52	0.73	(28.8)	2	0.248	(0.017)	3.17	(10.4)	1.25	(0.92)	2.5 × 1.2	(0.10 × 0.05)
	17	53	0.73	(28.8)	2	0.248	(0.017)	3.35	(11.0)	1.40	(1.03)	3.0 × 5.3	(0.12 × 0.21)
	18	54	0.73	(28.8)	2	0.248	(0.017)	3.26	(10.7)	1.32	(0.97)	10.2 × 8.9	(0.40 × 0.35)
7	19	55	0.73	(28.8)	2	0.598	(1.041)	3.23	(10.6)	3.01	(2.27)	16.5 × 16.5	(0.65 × 0.65)
	20	56	0.73	(28.8)	2	0.598	(1.041)	...	...	...	...	17.3 × 16.8	(0.68 × 0.66)
	21	57	0.73	(28.8)	2	0.598	(1.041)	3.54	(11.6)	3.69	(2.72)	19.8 × 20.0	(0.78 × 0.79)
8	22	58	0.48	(18.8)	2	0.598	(1.041)	2.96	(9.7)	2.58	(1.90)	14.7 × 14.5	(0.58 × 0.57)
	23	59	0.48	(18.8)	2	0.598	(1.041)	2.59	(8.5)	1.98	(1.46)	15.2 × 15.2	(0.60 × 0.60)
	24	60	0.48	(18.8)	2	0.598	(1.041)	2.47	(8.1)	1.80	(1.33)	14.0 × 14.7	(0.55 × 0.58)

[a] 1 = 2.54-cm-diameter (1 in.) round head; 2 = No. 2 Phillips Head screwdriver point.

TABLE 2—*Preliminary impact damage evaluation results on Panel B: 24-ply, 67 percent 0-deg fibers.*

Condition	Locations	Test Run No.	Drop Height, m	Drop Height, (in.)	Impact Head Type[a]	Impact Mass, kg	Impact Mass, (slug)	Impact Velocity, m/s	Impact Velocity, (ft/s)	Kinetic Energy, E_K J	Kinetic Energy, (ft/lb)	Apparent Damage Size, X by Y mm	Apparent Damage Size, (in.)
	1	31	0.477	(18.8)	1	0.240	(0.016)	2.65	(8.7)	0.84	(0.62)	8.9 × 10.7	(0.35 × 0.42)
1	2	32	0.477	(18.8)	1	0.240	(0.016)	2.65	(8.7)	0.84	(0.62)	0	0
	3	33	0.477	(18.8)	1	0.240	(0.016)	2.74	(9.0)	0.89	(0.66)	0	0
	4	34	0.732	(28.8)	1	0.164	(0.011)	3.26	(10.7)	0.87	(0.64)	8.1 × 13.2	(0.32 × 0.52)
2	5	35	0.732	(28.8)	1	0.164	(0.011)	3.32	(10.9)	0.91	(0.67)	10.2 × 14.2	(0.40 × 0.56)
	6	36	0.732	(28.8)	1	0.164	(0.011)	3.26	(10.7)	0.87	(0.64)	10.7 × 15.2	(0.42 × 0.60)
	7	61	0.477	(18.8)	1	0.164	(0.011)	2.68	(8.8)	0.59	(0.435)	0	0
3	8	62	0.477	(18.8)	1	0.164	(0.011)	2.53	(8.3)	0.53	(0.39)	0	0
	9	63	0.477	(18.8)	1	0.164	(0.011)	2.56	(8.4)	0.54	(0.40)	5.6 × 6.4	(0.22 × 0.25)
	10	64	0.477	(18.8)	1	0.240	(0.016)	2.53	(8.3)	0.77	(0.565)	0	0
4	11	65	0.477	(18.8)	1	0.240	(0.016)	2.50	(8.2)	0.75	(0.55)	7.6 × 14.2	(0.30 × 0.56)
	12	66	0.477	(18.8)	1	0.240	(0.016)	2.53	(8.3)	0.77	(0.565)	7.9 × 12.2	(0.31 × 0.49)
	13	67	0.477	(18.8)	2	0.248	(0.017)	2.65	(8.7)	0.87	(0.64)	7.4 × 12.2	(0.29 × 0.49)
5	14	68	0.477	(18.8)	2	0.248	(0.017)	2.59	(8.5)	0.83	(0.61)	7.4 × 10.2	(0.29 × 0.40)
	15	69	0.477	(18.8)	2	0.248	(0.017)	2.65	(8.7)	0.87	(0.64)	7.1 × 13.0	(0.28 × 0.51)
	16	70	0.732	(28.8)	2	0.172	(0.012)	3.17	(10.4)	0.87	(0.64)	7.6 × 10.2	(0.30 × 0.40)
6	17	71	0.732	(28.8)	2	0.172	(0.012)	3.23	(10.6)	0.89	(0.66)	7.9 × 11.4	(0.31 × 0.45)
	18	72	0.732	(28.8)	2	0.172	(0.012)	3.29	(10.8)	0.94	(0.69)	7.1 × 14.7	(0.28 × 0.58)
	19	73	0.477	(18.8)	2	0.172	(0.012)	2.53	(8.3)	0.56	(0.41)	6.6 × 10.2	(0.26 × 0.40)
7	20	74	0.477	(18.8)	2	0.172	(0.012)	2.65	(8.7)	0.60	(0.445)	5.8 × 10.2	(0.23 × 0.40)
	21	75	0.477	(18.8)	2	0.172	(0.012)	2.59	(8.5)	0.58	(0.425)	5.3 × 9.6	(0.21 × 0.38)
	22	76	0.477	(18.8)	1	0.590	(1.040)	2.53	(8.3)	1.88	(1.39)	15.7 × 21.3	(0.62 × 0.84)
8	23	77	0.477	(18.8)	1	0.590	(1.040)	2.53	(8.3)	1.88	(1.39)	13.0 × 18.5	(0.51 × 0.73)
	24	78	0.477	(18.8)	1	0.590	(1.040)	2.65	(8.7)	2.07	(1.53)	14.0 × 20.6	(0.55 × 0.81)

[a] 1 = 2.54-cm-diameter (1 in.) round head; 2 = No. 2 Phillips Head screwdriver point.

119.38 cm (47 in.). The general procedure used was to do a complete C-scan of the damage site, store the image on a memory oscilloscope, and then preselect regions on the C-scan to call up from memory in a B-scan presentation.

Figure 4 shows the results of this procedure for Damage Site 7.[4] The results show the damage to consist of two primary regions, the main damage beginning about four plies below the impacted surface and being roughly circular. Secondary damage occurred by delamination of the back ply along a 45-deg line which extended beyond the main damage area. Two alternative methods of combining the display into isometric modes are shown in Fig. 5.

A second procedure, consisting of combining the C-scan and subsequently located B-scans from both the front and back surfaces, was used on Damage Site 2. The intent of this was to minimize the region "shadowed" by the first layer of damage that the ultrasonic signal encounters. A sample of the combination of two of the B-scans taken at a common location but from opposite sides of the panel is shown in Fig. 6. Figure 7 presents a buildup of a series of the combined B-scans across the C-scan indication. The results indicate major delaminations at the 4/5-ply and the 11/12-ply regions with additional less extensive damage occuring throughout the internal regions between these two locations.

Evaluation of the results obtained by this method was found generally to be acceptable, with one exception. The equipment, as evaluated, had an analog memory which divided the return time of the reflected waves into nine parts. This was marginally adequate for the 16-ply trial panel, but would not be adequate to define the ply level of damage accurately in 24- and 32-ply material. As a result, the analog memory was replaced with a digital memory which divided the return time into over 250 increments to overcome this limitation.

Evaluation of Impact Damage Conditions in the 32-Ply Quasi-Isotropic Material (Panel A)

First, the ultrasonic C-scan results shown in Fig. 8 for the 32-ply Panel A were examined. Impact Conditions 1 and 4 (Impact Locations 1-3 and 10-12) were found to be below the damage-producing threshold for these impact conditions and material. Impact Condition 6 (Location 16-18) was also eliminated from consideration due to the generally small and highly variable damage size observed. Of the remaining five impact conditions, Condition 3 (Location 7-9) resulted in damage areas with the dimension X in the specimen width direction greater than 20 mm (0.80 in.). These

[4]Pettit, D. E., "Residual Strength Degradation for Advanced Composites," Lockheed-California Co. Interim Technical Quarterly Report, LR 28360-2, Burbank, Calif., 10 Feb. 1978.

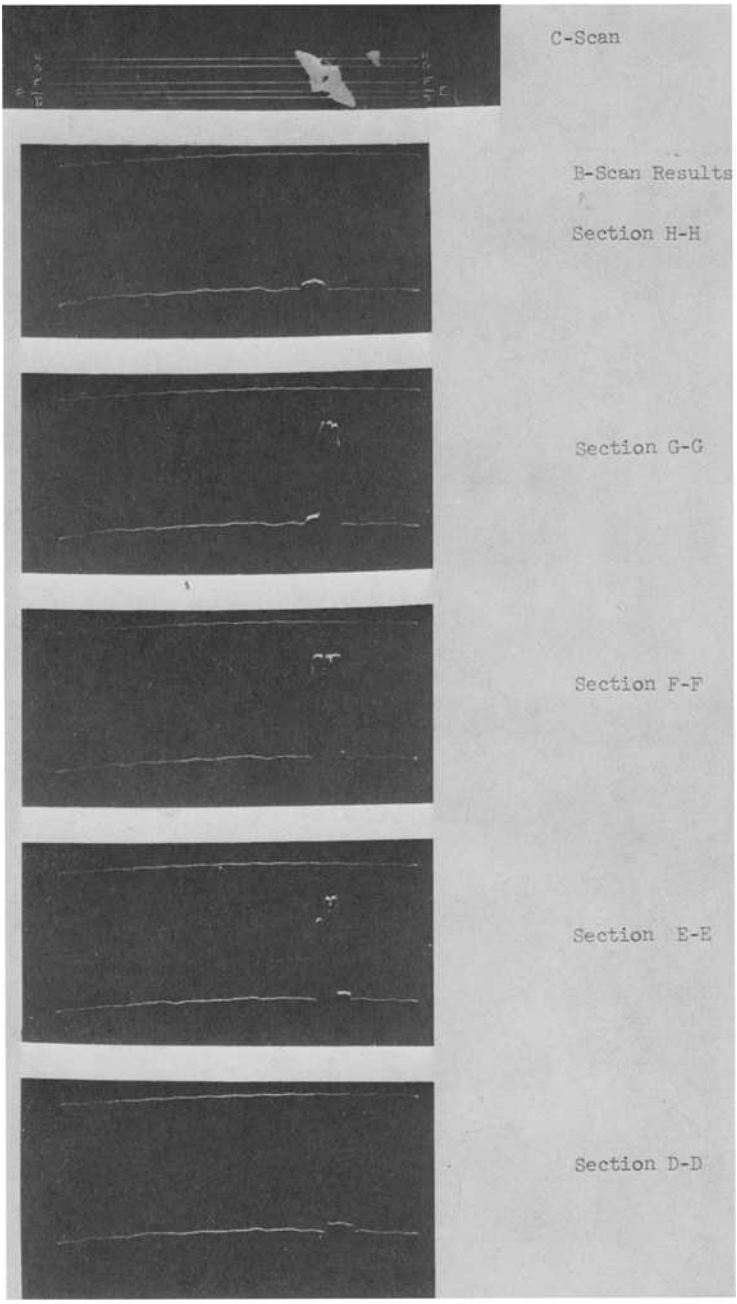

FIG. 4—*Ultrasonic inspection results for Damage Site 7, Panel C.*

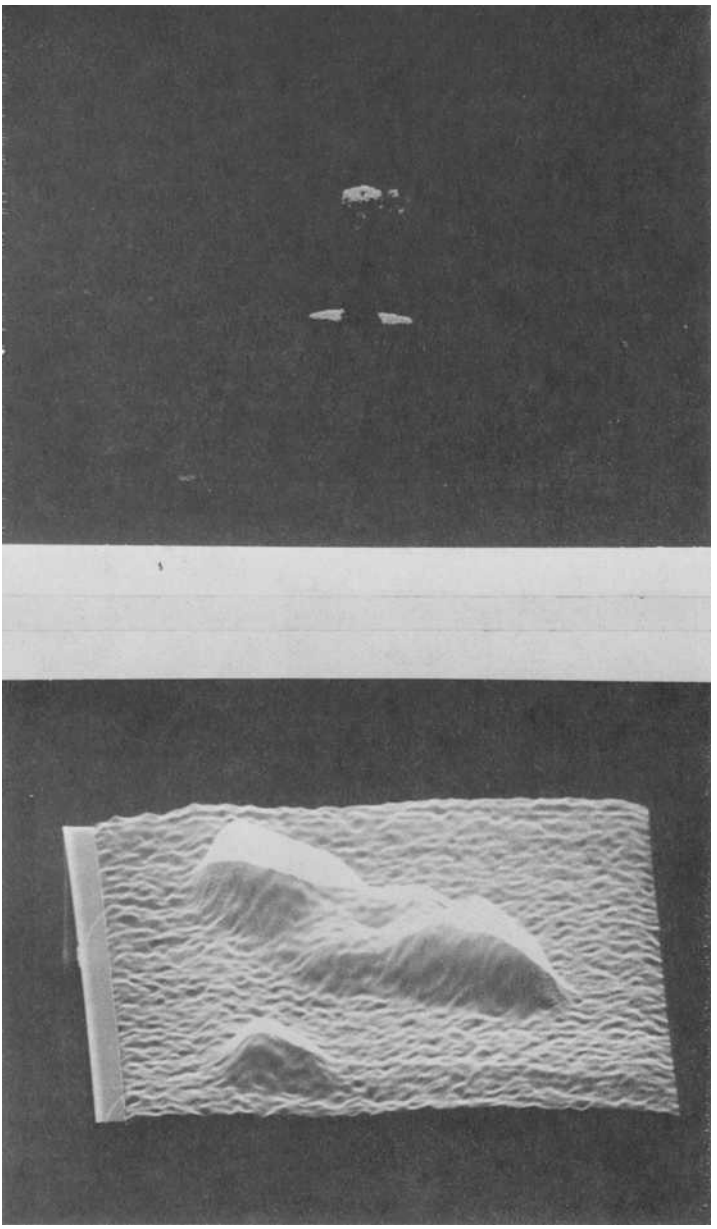

FIG. 5—*Alternative formats for isometric presentation of damaged region—Panel C, Site 7.*

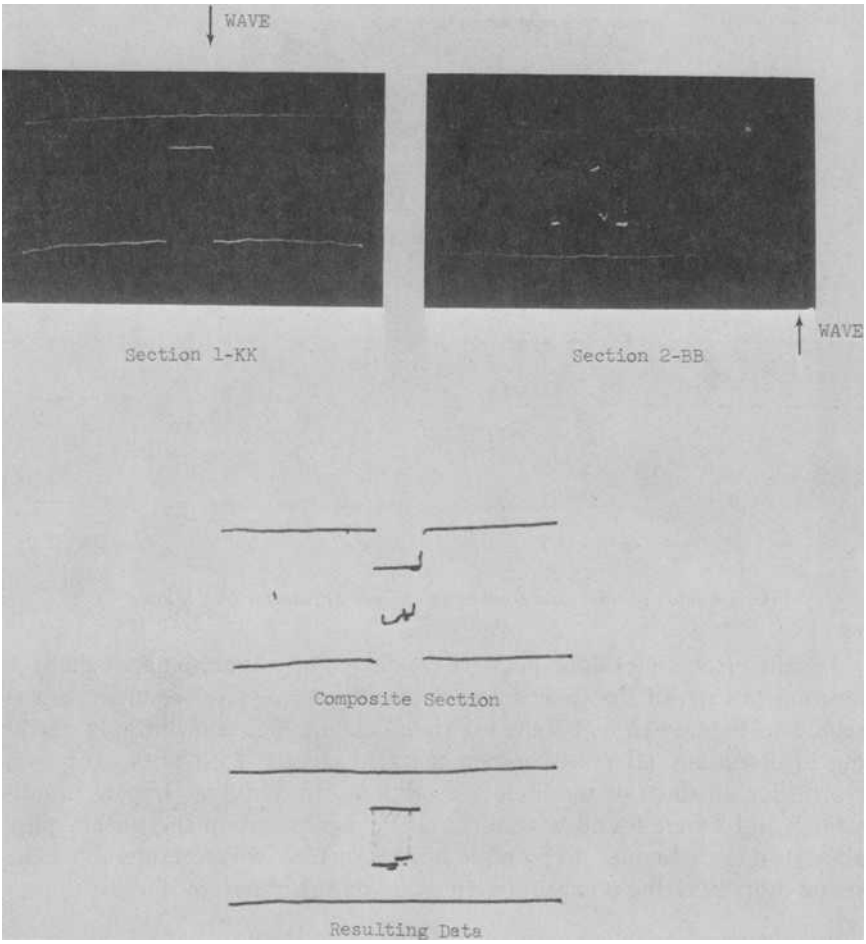

FIG. 6—*Typical ultrasonic B-scan data combination procedure—Panel C, Site 2.*

initial damage sizes are considered too large for laboratory studies of impact damage since they would allow insufficient room for damage growth measurement during tests of small-size specimens. Since Conditions 7 and 8 (Locations 19-21 and 22-24, respectively) were generated under similar conditions and the resulting damage areas were only slightly different, Condition 8 was retained and Condition 7 eliminated. The remaining three impact conditions—2, 5, and 8 (Locations 4-6, 13-15, and 22-24, respectively)—were thus selected for further examination using the Holscan system to characterize the damage present. These three damage conditions represent one due to a blunt impactor (Condition 2) and two using a Phillips Head screwdriver point (Conditions 5 and 8).

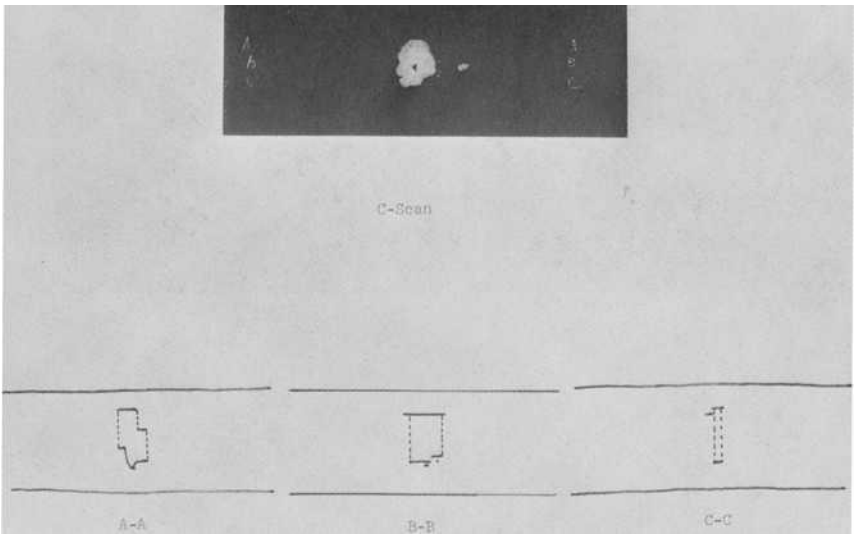

FIG. 7—*Series of composite B-scans and C-scan of Damage Site 2, Panel C.*

Detailed Holscan evaluations were conducted on a representative damage location of each of the three selected conditions.[5] Typical results are presented in Figs. 9–12 and show multiple delamination and intraply cracking in essentially all plies between the 4th and the 28th plies. This was typical for all three of the impact conditions. In addition, Impact Conditions 5 and 8 were found to result in a slight puncture of the surface plies about two to three plies deep on the impact surface, which resulted in some signal dropout at the point of the puncture on the impact surface.

Evaluation of Impact Damage in the 24-Ply Material (Panel B)

Preliminary analysis based on ultrasonic C-scan results shown in Fig. 13 shows impact Conditions 1, 3, and 4 (a verification of Condition 1) to be unsuitable due to lack of consistent damage development. This indicates that these conditions represent a threshold level for damage development under the test conditions examined. Of the remaining five conditions, Condition 7 was eliminated because the resulting damage was considered too small, the dimension X in the specimen width being less than 6 mm ($\sim$¼ in.). The four remaining damage conditions produced reasonably consistent damage size X in the range of 7 to 15 mm (0.28 to 0.6 in.). A representative damage site for each of these four conditions was selected

[5]Pettit, D. E., "Residual Strength Degradation for Advanced Composites," Lockheed-California Co. Interim Technical Quarterly Report, LR 28360-5, Burbank, Calif. 5 Aug. 1978.

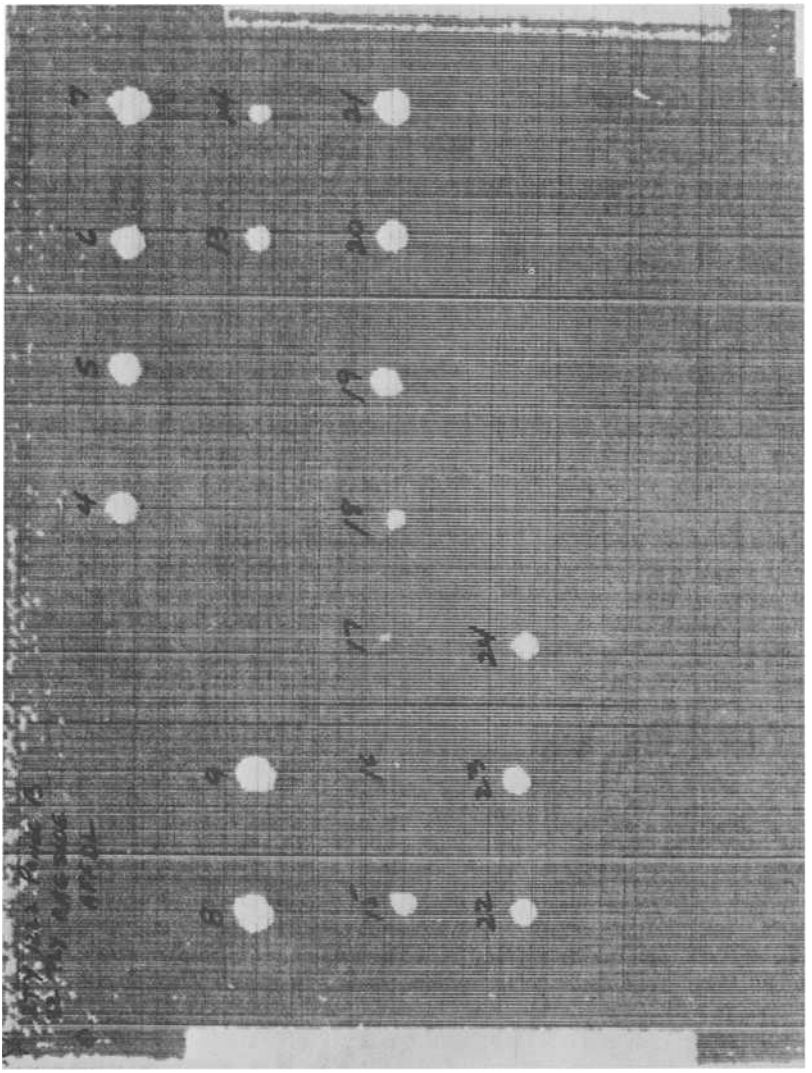

FIG. 8—*Standard ultrasonic C-scan results for 32-ply T300/5208, Panel B.*

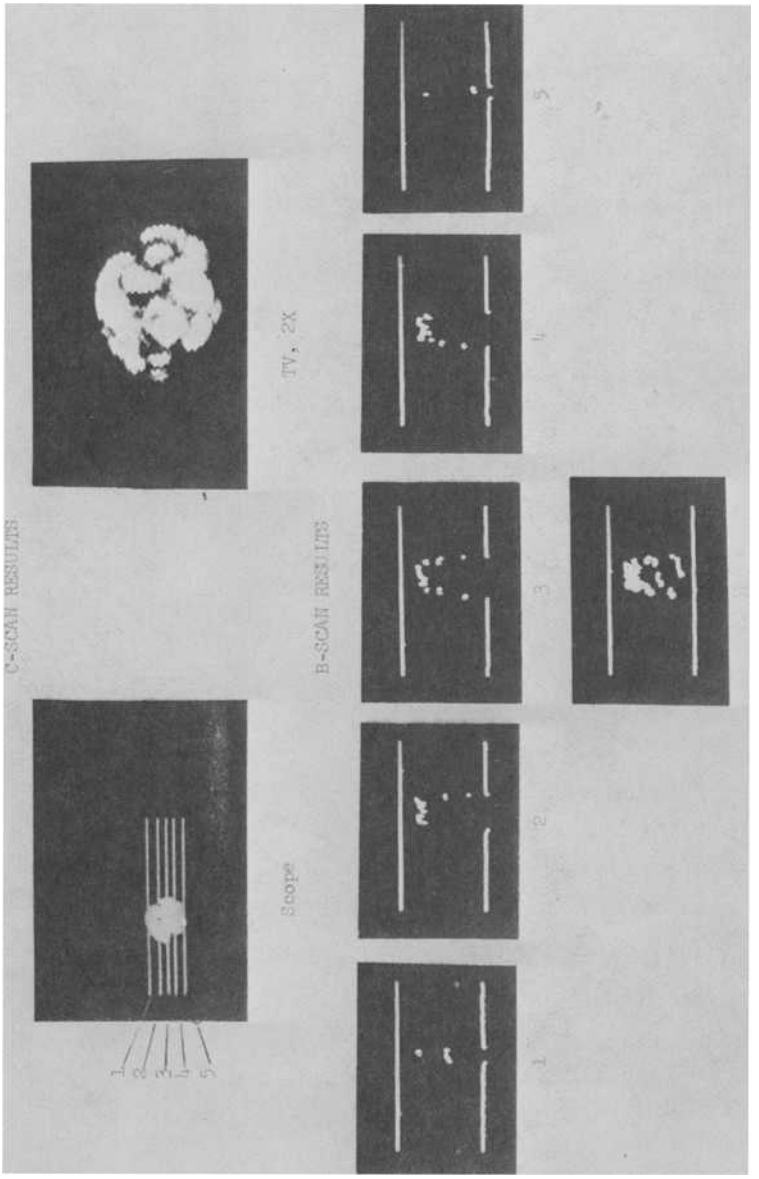

FIG. 9—*Panel No. 2TY-1222, 32-ply Site 4, viewed from impact side, 0-deg fiber orientation —.*

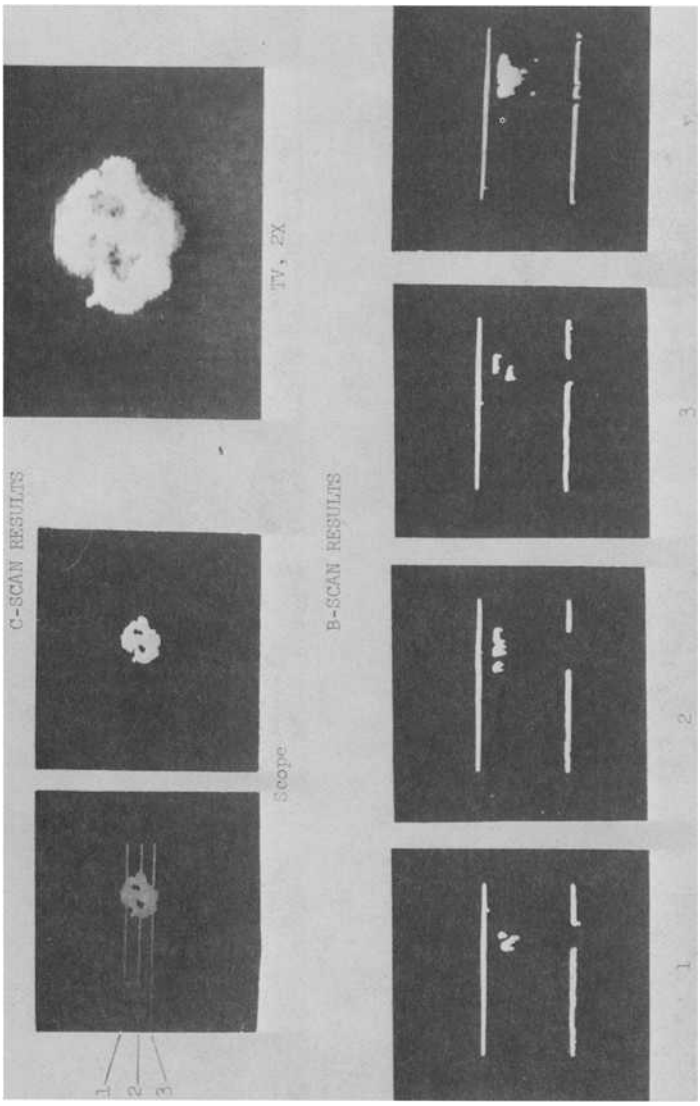

FIG. 10—*Panel No. 2TY-1222. 32-ply Site 4, viewed from back side, 0-deg fiber orientation →.*

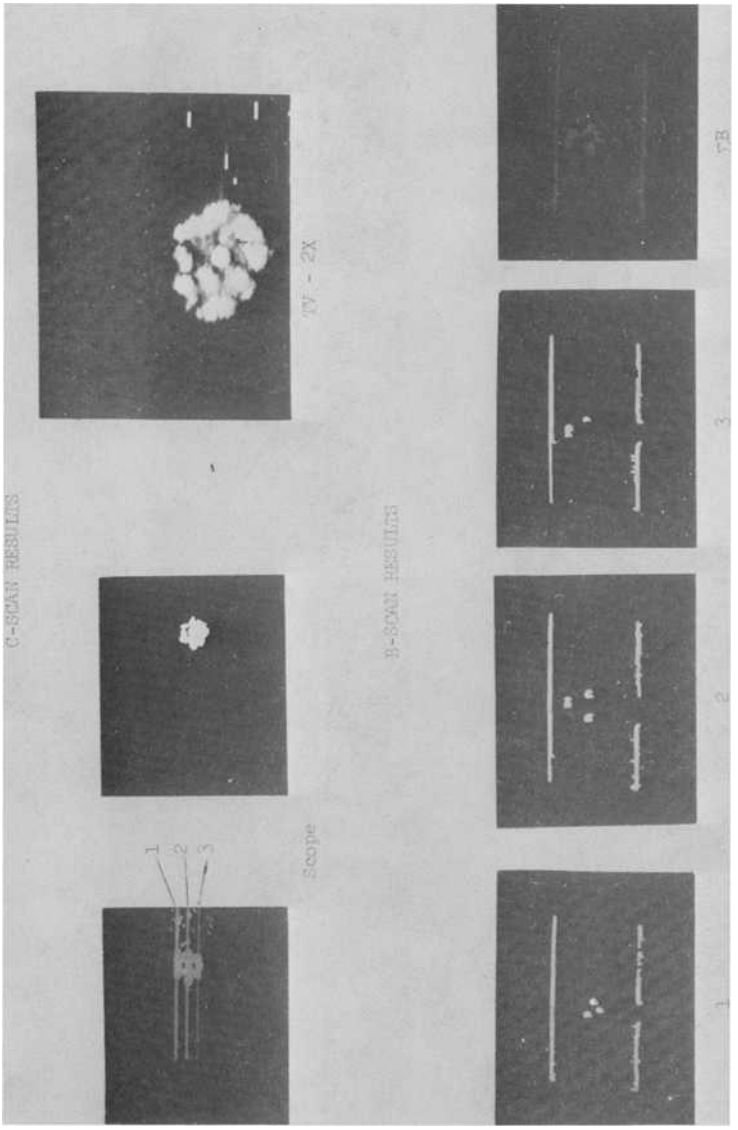

FIG. 11—*Panel No. 2TY-1222, 32-ply Site 15, viewed from back side, 0-deg fiber orientation →.*

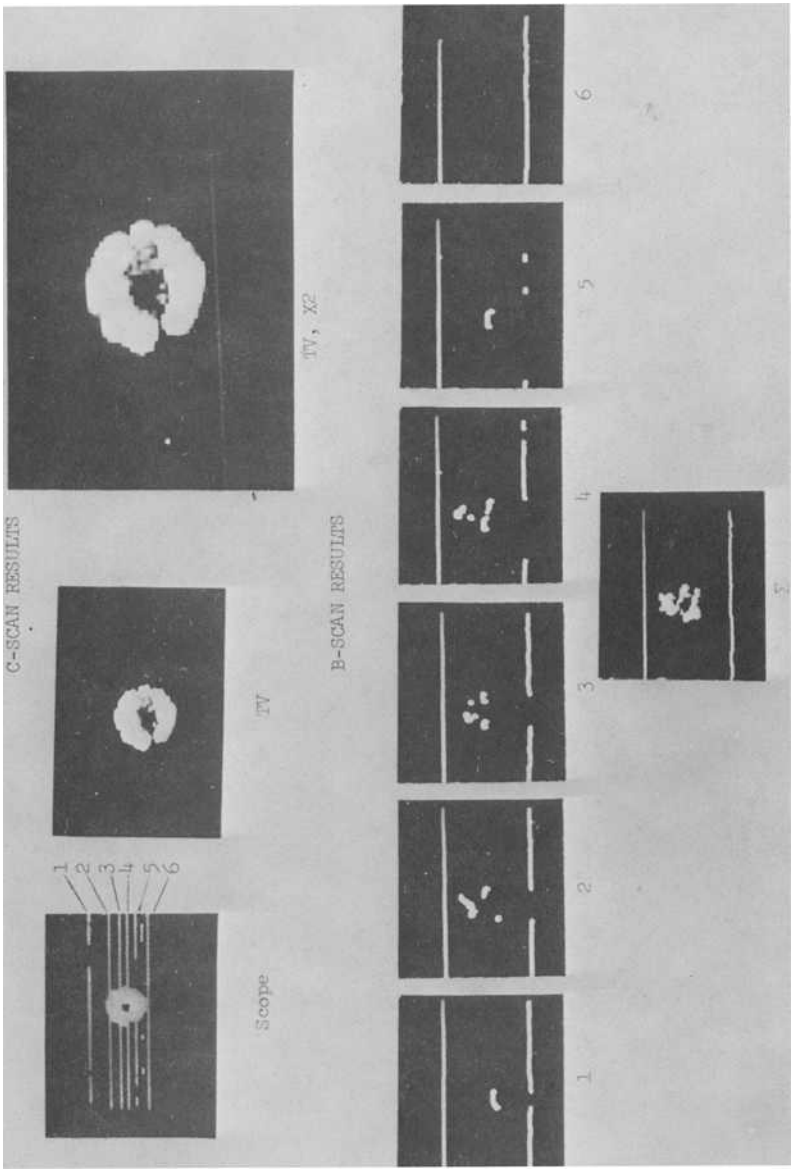

FIG. 12—*Panel No. 2TY-1222, 32-ply Site 15, viewed from impact side, 0-deg fiber orientation →.*

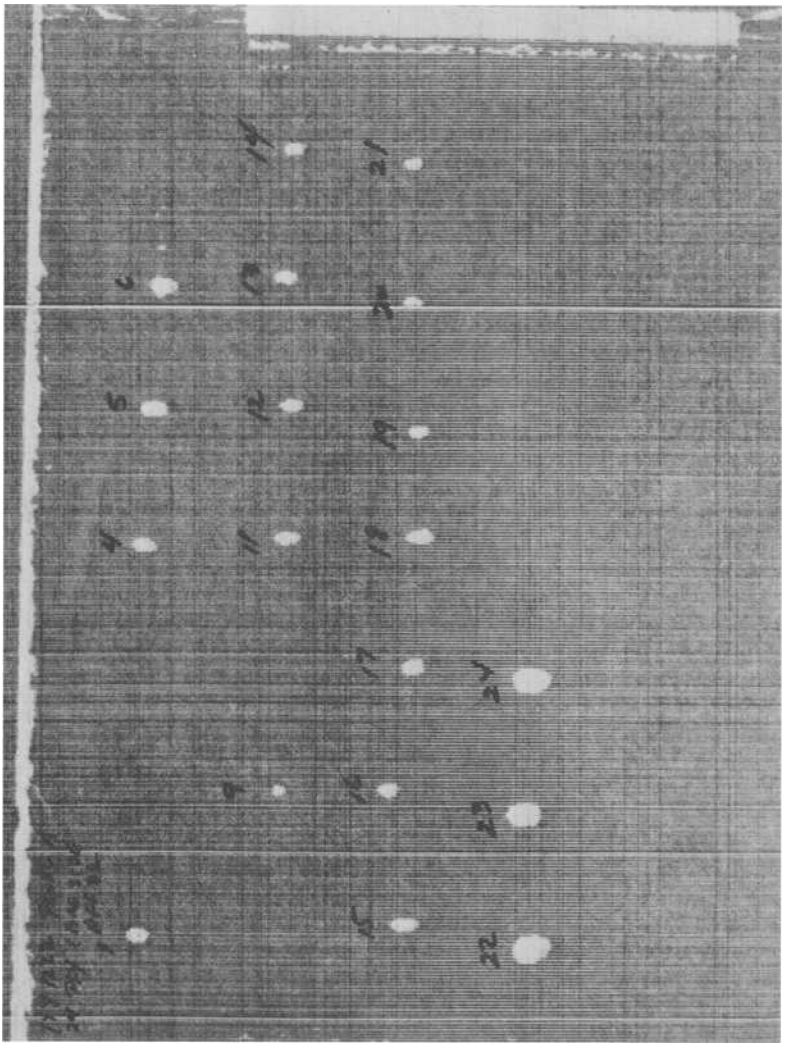

FIG. 13—*Standard ultrasonic C-scan results for 24-ply T300/5208, Panel A.*

and subjected to a detailed Holscan analysis (footnote 5). This selection represents two conditions (2 and 8) with the 2.54-cm-diameter (1 in.) hemisherical impact head and two conditions (5 and 6) with the No. 2 Phillips Head screwdriver point impact head.

Typical detailed Holscan examinations shown in Figs. 14–17 revealed multiple delaminations and intraply cracking located primarily in Plies 4 through 20, very similar to that which was observed in the 32-ply material. However, no surface puncture marks were observed for locations which were impacted with the No. 2 Phillips Head screwdriver.

Summary

Evaluation of the applicability of the Holscan 400 system as a laboratory tool for monitoring and characterizing damage in composite materials has led to the following observations.

1. The basic flex-arm transducer mount is useful for "quick-look-type" applications. For detailed evaluation, however, the hand scanning is not by nature very reproducible. In addition, the data readout is limited to real-time C-scan and either cumulative B-scan or isometric presentation.

2. Replacement of the flex-arm transducer mount by a digital scanner mount with digital mechanical scanner control interfaced with the System 400 electronics overcomes the System 400 limitations of requiring manual hand scanning and the lack of ability to add any storage or recall memory capability. In addition, this mounting system permits a larger selection of transducers.

3. A digital memory real-time image display electronic processor and dual-mode scope interfaced with the System 400 electronics provides a digital memory storage unit to retain and provide subsequent display of the data in a C-scan and associated B-scan format as well as in a 3-D isometric format which can be rotated on the scope. This provides a major tool to assess composite damage characteristics in that the ply level at which damage occurs can be estimated.

4. The vertical mounting and coupling system attached to the transducer digital scanner provides a system which can be used on test specimens mounted in the test frame, thus eliminating the necessity of removing and reinstalling specimens each time they are to be examined. This is a significant improvement also in that the specimen is not immersed in water for extended periods such as occur during normal C-scan, the water contact being limited to the water column directly in front of the scanning transducer.

5. The full potential of the unit could be better exploited if more flexibility in the data withdrawal methods were available, such as a minicomputer interface.

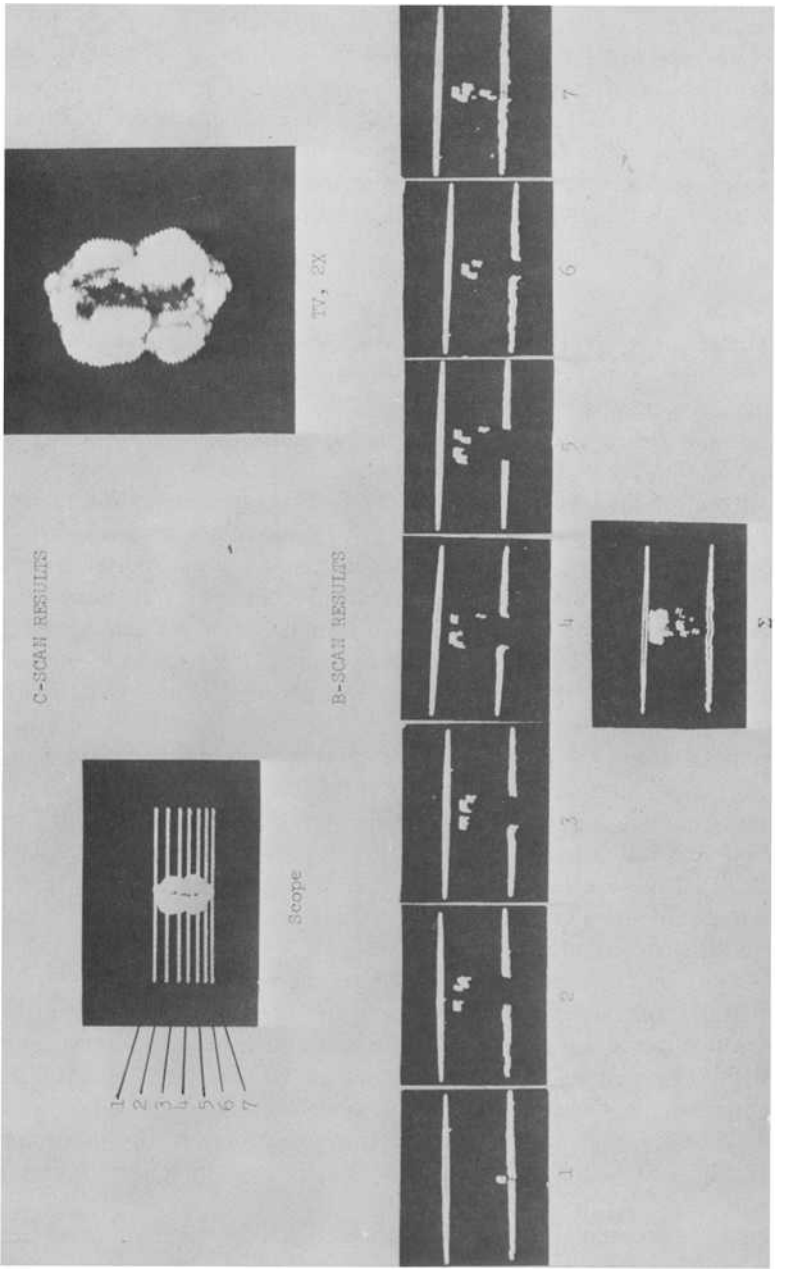

FIG. 14—*Panel No. 1TY-1222, 24-ply Site 24, viewed from impact side, 0-deg fiber orientation* ↑.

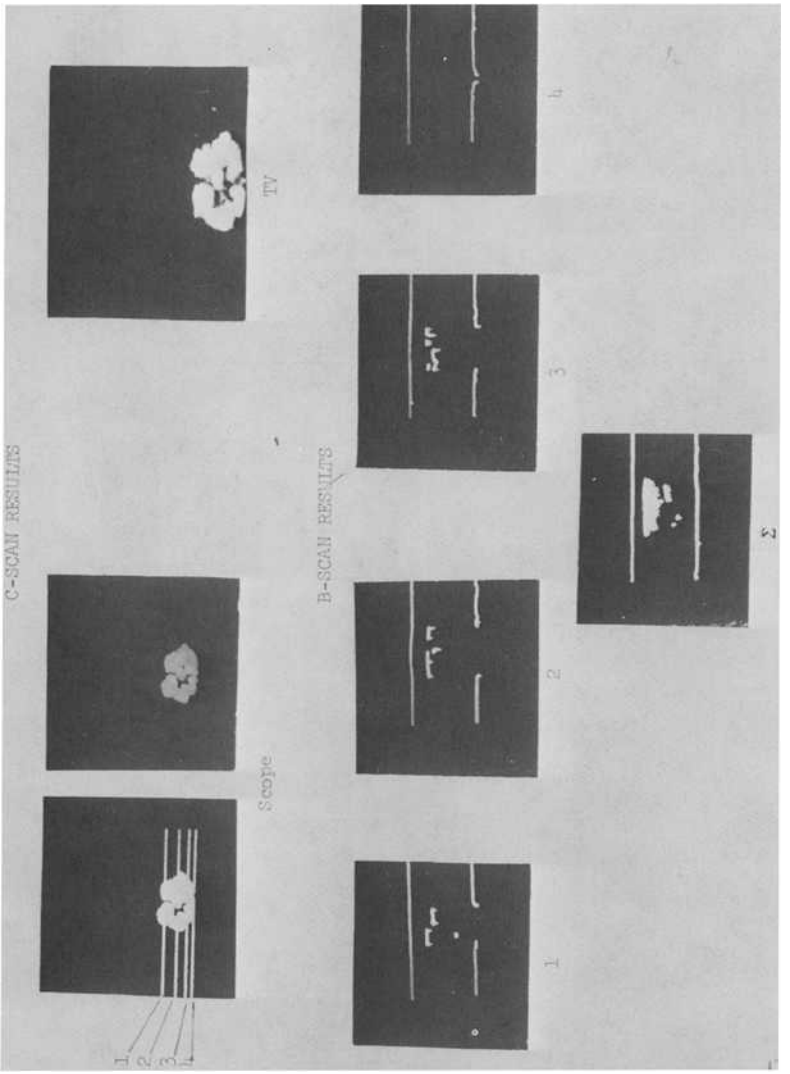

FIG. 15—*Panel No. 1TY-1222, 24-ply Site 24, viewed from back side, 0-deg fiber orientation →.*

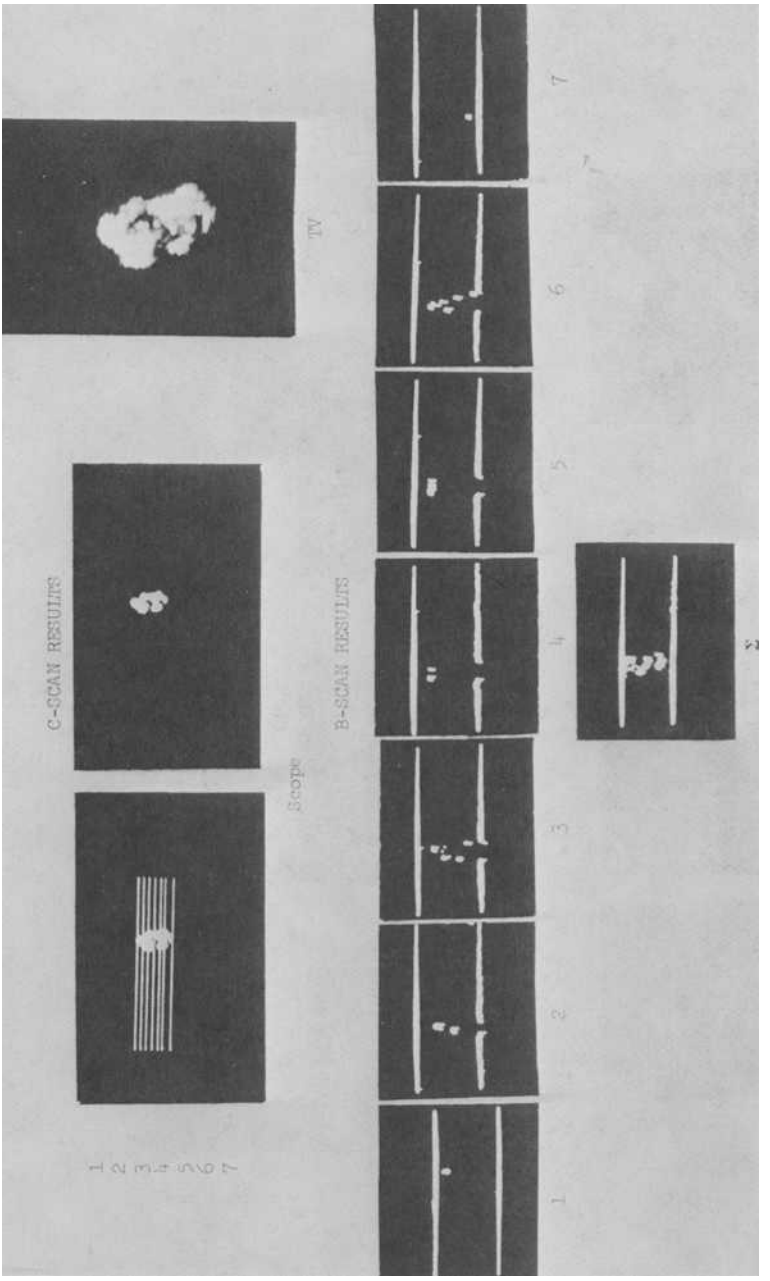

FIG. 16—*Panel No. 1TY-1222, 24-ply Site 17, viewed from impact side, 0-deg fiber orientation* ↑.

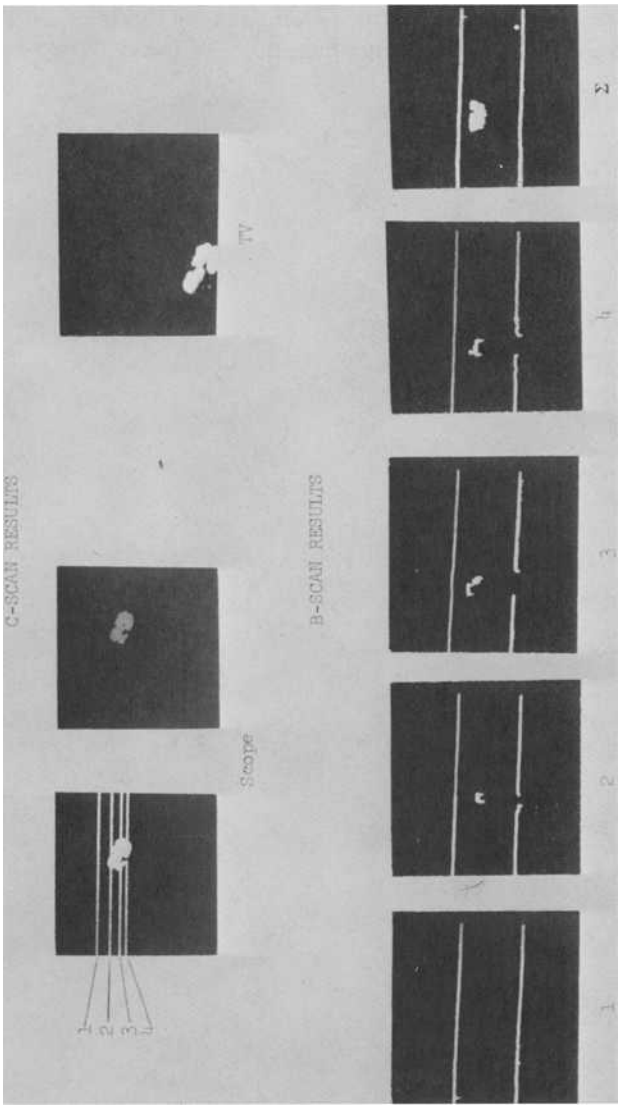

FIG. 17—*Panel No. 1TY-1222, 24-ply Site 17, viewed from back side, 0-deg fiber orientation →.*

Acknowledgments

This work was sponsored in large part by the Air Force Flight Dynamics Laboratory, Contract F33615-77-C-3084, "Residual Strength Degradation Modeling in Advanced Composites," Dr. George Sendeckyj, technical monitor. The author offers a special thanks to the staff at Holosonics, San Rafael, Calif., for their cooperation in this effort.

D. Y. Konishi[1] *and K. H. Lo*[2]

Flaw Criticality of Graphite/Epoxy Structures

REFERENCE: Konishi, D. Y. and Lo, K. H., **"Flaw Criticality of Graphite/Epoxy Structures,"** *Nondestructive Evaluation and Flaw Criticality for Composite Materials, ASTM STP 696*, R. B. Pipes, Ed., American Society for Testing and Materials, 1979, pp. 125-144.

ABSTRACT: The orderly assessment of the serviceability of graphite/epoxy structures requires a knowledge of their flaw criticality. In the Serviceability Program, industry-wide flaw likelihood/criticality surveys have been conducted and the results have been qualitatively assessed. These results were used to set nondestructive evaluation (NDE), analytic study, and experimental verification goals. The progress of this program is reported herein.

Flaws, which can result from the fabrication process, normal service utilization, and battle damage have been categorized into five types, depending on their associated stress field disturbance. Flaw detectability studies have been conducted to determine the optimal NDE process to detect these flaws. Analytic studies have been conducted to determine the disturbance to the stress field in the vicinity of the flaws and to assess their criticality, that is, their structural integrity.

These results were used to define coupons and elements where the elements represent structures that are in a realistic stress state. Accelerated "worst expected" case environmental fatigue testing has been conducted. The preliminary results show, as expected, that advanced composites are relatively damage-tolerant. Since further testing is being conducted, an up-to-date status of the program is given.

Three types of coupons are being tested. The tension coupons contain flaws such as holes, delaminations, ply separations, and scratches. The compression coupons contain delaminations, in untapered and tapered regions, and ply separations. The bolted-joint coupons contain notches at bolt holes, oversized holes, and delaminations. Static tests, both room-temperature dry and 82°C (180°F) temperature wet, are being conducted. Spectrum fatigue tests followed by residual strength tests are also being conducted. Both room-temperature dry and realistic temperature/moisture environments are used. Flaw growth specimens are also being tested. The results for the tension flaw screening specimens are presented and assessed.

KEY WORDS: advanced composites, graphite/epoxy, flaw screening, flaw criticality, static strength, strength degradation, moisture, temperature, spectrum loadings, nondestructive tests, composite materials

[1] Member of technical staff, Rockwell International, North American Aircraft Division, Los Angeles, Calif. 90009.

[2] Assistant professor, Department of Mechanical Engineering, Washington University, St. Louis, Mo.

This paper assesses the state of the art of the serviceability of graphite/epoxy structures. To accomplish this, a systematic study is being conducted to determine (1) what flaws are likely to occur during the fabrication process; (2) which flaws are critical from a residual strength retention standpoint after spectrum (loading/temperature/moisture) loading; (3) the accuracy (threshold/sensitivity) of existing nondestructive evaluation (NDE) methods to determine the extent of these flaws; (4) analytically, the stress field in the neighborhood of the flaw in order to hypothesize the wearout model; and (5) experimentally, the wearout (loss of residual strength after exposure to spectrum loading) of simple coupons.

This work is part of the Advanced Composites Serviceability Program. Contract F33615-76-C-5344 is monitored by the U. S. Air Force Materials Laboratory and jointly sponsored with the U. S. Air Force Flight Dynamics Laboratory. Rockwell International, North American Aircraft Division, is the prime contractor and its Science Center is a subcontractor. IIT Research Institute is a subcontractor engaged to perform all the coupon testing, and Washington University, St. Louis, Mo., is a subcontractor engaged to develop analytic techniques.

Flaw Occurrence During Fabrication

An industry-wide survey was conducted in two rounds of questionnaires to characterize the likelihood and occurrence of flaws during the fabrication process. The results were presented in an earlier paper [*1*].[3] Table 1 summarizes the likelihood of occurrence of flaws and classifies them into categories which describe the stress gradients caused by a flaw embodied in a laminate undergoing a far-field uniform stress field.

Flaw Criticality

Table 2, taken from Ref *1*, gives an index of effects. This index is a measure of the likelihood/criticality of a flaw occurrence. The flaws with high indices of effects are being used for further studies, such as for NDE threshold/sensitivity studies, coupon testing, and analytic techniques.

NDE Threshold Sensitivity

The NDE threshold/sensitivity studies will be concluded during the next fiscal year. At the present time, candidate methods have been selected and a limited number of experiments have been conducted and reported. The major emphasis, however, has been to conduct NDE on the coupon speci-

[3] The italic numbers in brackets refer to the list of references appended to this paper.

mens in order to measure flaw growth as a function of initial flaw size and loading spectrum life.

A pulse echo ultrasonic analysis with a focused transducer is being used to locate the edges of a delamination in the coupons being tested. Experiments conducted on known flaws in the 16-ply coupons have shown that it is possible to locate the edge of delamination to within 0.6 mm (0.025 in.). Thus the threshold flaw is 1.2 mm (0.050 in.) and the sensitivity is 0.6 mm (0.025 in.). This should hold through thicknesses up to 50 plies. Thicker specimens would have lower sensitivities and larger threshold flaw sizes.

Analytical Developments

The objective of the analytic effort is to predict the strength degradation of laminates weakened by flaws, such as holes or scratches, and subjected to uniaxial and biaxial loading conditions. An analytical/empirical method has been developed [*2*] to achieve this objective for localized planar through-the-thickness flaws such as holes or cracks. This method, together with a progressive stiffness degradation model, has the ability to predict the sequential failure of laminates with localized planar through-the-thickness flaws from the first ply failure to the ultimate failure of the laminate. In addition, an estimate of the damage propagation trajectory is also obtained. Numerical simulations show that the method correlates well with experimental data.

This approach uses the properties of a single lamina to obtain the progressive strength degradation of a laminate with a through-the-thickness flaw, which herein will be considered to be a crack. Hence, it can be applied to any lamination geometry, loading condition, and crack size. Furthermore, variation of material properties through the thickness of the laminate, as in hybrid composites, can be considered.

The properties of the single lamina used in the present approach are

1. ultimate strength and strain,
2. stiffness, and
3. characteristic limiting dimension r_c in front of the crack tip.

The dimension r_c has been hypothesized by Wu [*3*]; a value of r_c equal to 0.203 cm (0.08 in.) has been used in the present study. Failure of the lamina is said to occur if the state of stress/strain at a distance r_c from the crack tip and at a critical angle θ falls on the failure envelope of the lamina (Fig. 1). It has been assumed that r_c is a property of the lamina and is independent of lamination geometry.

The failure criterion, lamination geometry, loading condition, and crack geometry are input parameters in this approach. Three different failure criteria have been used in this study: maximum stress, maximum strain, and the tensor polynominal. The stress field in the neighborhood of the crack is obtained through finite-element modeling. Elasticity theory can be

TABLE 1—*Characterization of flaws in graphite/epoxy by stress field and probability of occurrence for the purpose of serviceability evaluation.*

Flaw Type No.	Flaw Type Description	Flaws	Measure of Occurrence
1	localized, planar, and sharp	oversized hole	2-3% drilled holes
		mislocated hole-resin refilled, redrilled	0.00006-0.001% drilled holes
		out-of-round hole	1.5% drilled holes
		Fig. 8 hole	0.3-1.2% drilled holes
		edge notch or through crack	
		mislocated hole—not required	0.3-2% drilled holes
2	localized, through-the-thickness stress gradients	tearout or pull-through in countersink	0.13-2% countersinks
		edge delamination, splintering	3.5% edge length
		improper fastener seating	3.0% fasteners
		countersink on wrong side of laminate	0.0005% countersinks
		internal delamination, blister	0.0001-0.0003% internal ply area
		nonuniform agglomerations of hardner agents over small volume	0-0.001% volume
		nonuniform bond joint thickness	2-9% bond area
		small external delamination, loose fiber, or disbond area	0.0005% external area
		foreign particle, contamination, inclusion	1-2% particles/ft^2/ply
		dent, no fiber breakage, damage done in handling	0.0001-0.0004% external area
		pills and fuzz balls	0.12-1.3% ply area
		misfitting parts cutting fibers in fillets corner notch or crack (thin specimen)	0.9-6% per 100 corners
		ply underlap, gap	0.001-0.005% ply area
		ply overlap	less than 1.0% ply area
		pool impressions	0.005% surface area
		resin-rich or fiber-starved condition over small volume	3.5% ply surface area
		overtorqued fasteners	

3	defects yielding dispersed stress gradients	hole exit side broken fibers, breakout	less than 30% drilled holes
		tearout or pull-through in countersinks	0.13–2% countersinks
		reworked areas	3.5% visible surface areas
		marcelled fibers	
		wrinkles, waviness, miscollimation	
		external delamination, loose fibers, disbonding	0.0005% external area
		mislocated cocured assemblies in same tool	2.0% cocured elements
		viable cure, temperature inhomogeneities in oven	0.5% resin volume
		grossly nonuniform agglomerations of hardener agents	0.001% volume
		excessive porosity, voids	0.003% volume
		ply underlap, gap	0.005% ply area
		ply overlap	less than 1.0% ply area
		resin-rich or fiber-starved areas	3.5% ply surface area
4	surface-localized, high stress concentration	hole exit side broken fibers, breakout	less than 30% drilled holes
		improper fastener seating	3.0% fasteners
		external delamination, loose fibers, disbonding	0.0005% external area
		dent, no fiber breakage, damage done in handling	0.0001–0.0004% external area
		pills and fuzz balls	0.12–1.3% ply area
		misfitting parts cutting fibers in fillets, poor seating	
		corner notch or crack	0.3–6.0 per 100 corners
		tool impressions	0.005% surface area
		outer ply separation	0.006% outer ply area
		scratch, fiber breakage, damage done in handling	
5	lower stiffness, asymmetry	prepreg variabilities exceeding preset levels	7.5% prepreg volume
		marcelled fibers	
		wrinkles, waviness, miscollimation	
		external delaminations, loose fibers, disbonding	0.0005% external area
		misoriented ply	0.05–8% designated plies
		variable cure, temperature inhomogeneities in oven	0.05% resin volume
		missing ply or plies	0.08–0.6% designated plies
		excessive porosity, voids	0.003% volume
		ply overlap	less than 1.0% ply area
		resin-rich or fiber-starved areas	3.5% ply surface area
		outer ply separation	0.006% outer ply area

TABLE 2—*Scores of flaws in graphite/epoxy in response to Questionnaire 1.*

Flaw Type	Indices		
	Criticality	Likelihood	Effects
External delamination, loose fibers, disbonding	1.5	2.5	25
Internal delamination, blister	1.5	2.5	25
Oversized hole	3.0	3.5	66
Hole exit side broken fibers, breakout	1.5	4.0	38
Tearout or pull-through in countersinks	2.5	2.0	32
Prepreg variabilities exceeding preset levels	2.5	4.0	62
Edge delamination, splintering	1.25	4.0	31
Mislocated hole—resin refilled, redrilled	1.5	3.0	28
Wrinkles, waviness, miscollimation	1.25	3.5	27
Marcelled fibers	1.25	3.5	28
Reworked areas	1.25	3.5	29
Out-of-round hole	1.0	4.0	25
Improper fastener seating	1.25	3.5	27
Nonuniform bond joint thickness	2.0	2.0	25
Countersink on wrong side of laminate	1.5	2.5	25
Mislocated cocured assemblies in same tool	1.5	2.5	25
Grossly nonuniform agglomerations of hardener agents	2.0	2.0	25

Index of Effects = (likelihood scores) × (criticality scores) on a scale of 0 to 100 as follows:

100 = (very frequent flaw) × (most crucial effects) = $2.5^2 \times 4 \times 4$
56 = (fairly common experience) × (critical flaw) = $2.5 \times 2.5 \times 3 \times 3$
25 = (occasional occurrence) × (possibly critical flaw) = $2.5 \times 2.5 \times 2^2$
6 = (rare, low likelihood) × (minor effects) = $6.25 \times 1 \times 1$

Dropped or eliminated when index scores less than 25 or flaw is a design error.

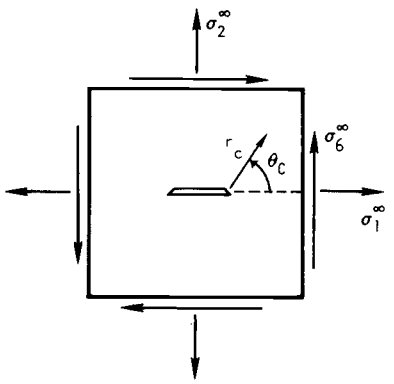

FIG. 1—*Generalized failure model.*

used to obtain the stress state but would prove cumbersome when localized progressive damage is considered.

Consider a laminate with a through crack (Fig. 1) which has been stressed to the point where one of its laminae has failed. When the lamina fails, the laminate experiences a stiffness degradation around the crack tip due to first-ply failure of the transverse plies. The new stiffness in this damaged region can be recalculated approximately by removing the stiffness of the matrix material in the lamina that has failed and keeping only the stiffness component of that lamina in the fiber direction, namely, Q_{11}.

The shaded area in Fig. 2 represents the localized damage zone due to the failure of a lamina in the laminate at a location characterized by r_c and θ_c. A good estimate of the damaged zone size can be obtained by a detailed consideration of the stress vector and strength vector contours. Typical plots of such contours can be found in Ref *3*. For simplicity, a shaded sector including an angle of 10 to 20 deg on either side of θ_c is sufficient. Because of the small localized character of this damaged area, stress redistributions only through the thickness of the laminate and only in the damaged region are assumed to occur. Such an assumption satisfies the overall equilibrium consideration of the laminate. However, it is realized that local equilibrium and compatibility at the lamina level may be violated at the boundary of the damaged zone.

Figures 3 and 4 give the numerical predictions of the notched strength of a $[0/\pm 45/90]_s$ laminate as a function of the initial crack length. Both figures demonstrate that good correlation with the experimental data [*4*] is obtained.

To demonstrate that the model can give equally good predictions for other materials and lamination geometries, Fig. 5 shows the notched

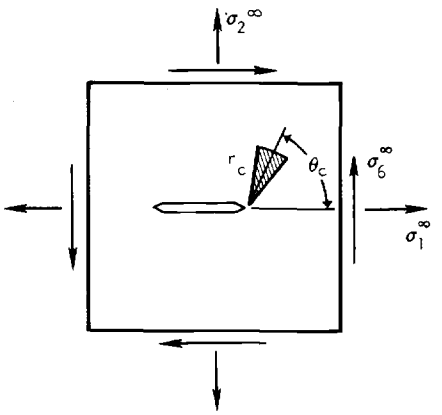

FIG. 2—*Local degradation model.*

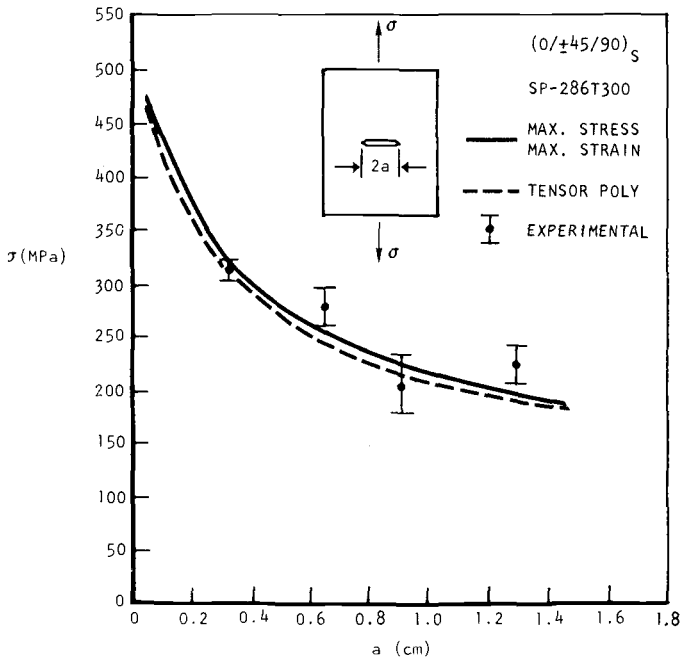

FIG. 3—*Uniaxial laminate.*

strength of a $[0/\pm 45]_s$ laminate. The material is T300/5208. Again, a reasonably good correlation with the experimental data extracted from Ref 5 is obtained. Numerical predictions of the three different failure criteria used in this study are close to each other. Hence, they are represented by a single curve in Fig. 5.

It has been observed experimentally that for a laminate with an inclined crack under uniaxial loading the notched strength of the laminate when plotted against its projected crack length can be represented by a single curve. The same behavior has been predicted numerically by the models used in the present study [2]. Different curves were obtained for the three different crack inclination angles studied. However, they were so close together that they can be represented by a single curve. The numerical results obtained in this study indicate that the method used can be applied to determine the notched strength of laminates with through cracks under any in-plane membrane loading conditions.

Status of Experimental Wearout Due to Spectrum Loading

The test program shown in Table 3 is being conducted. Test series T_1, C_1,B_1 ... T_4,C_4,B_4 represent a screening program whose objective is to determine the critical flaws for laminates undergoing an accelerated test

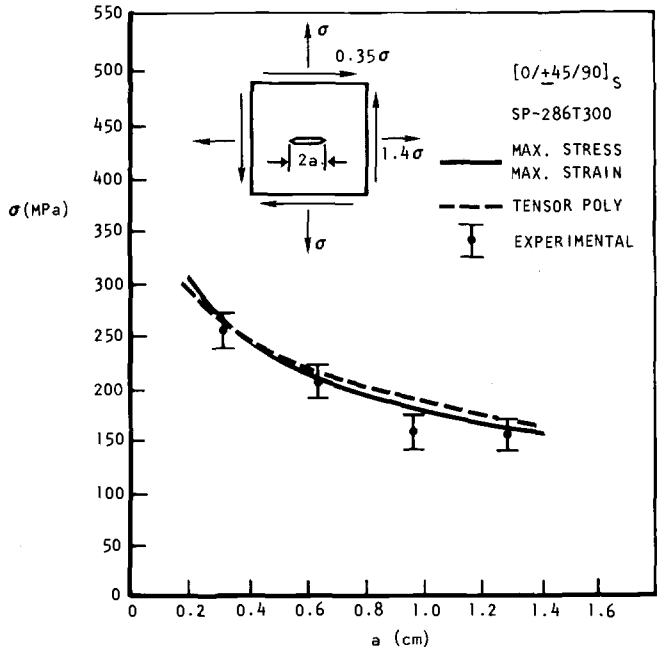

FIG. 4—*Biaxial laminate.*

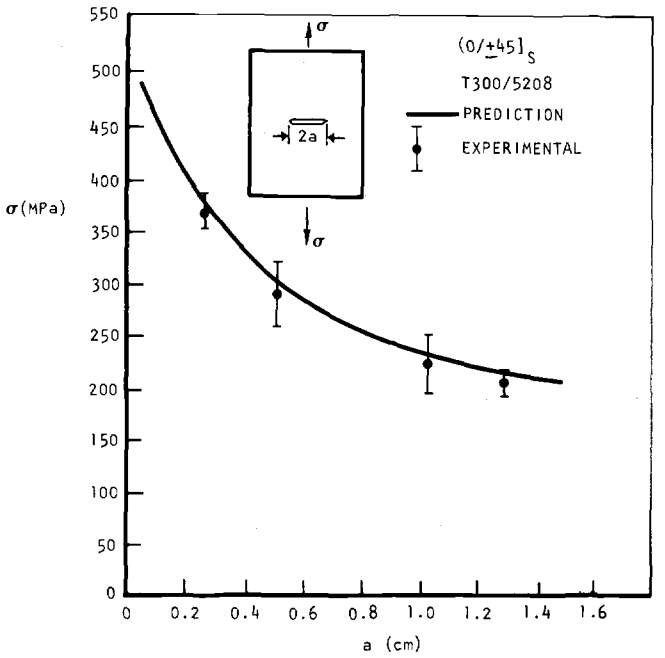

FIG. 5—*Notched strength of a* $[0/\pm 45]_s$ *laminate.*

TABLE 3—*Coupon test matrix.*

Test Series	Material	Laminate	Flaw Type	Flaw Size	Test Condition			Life Times				Total Specimens	Notes
					Moisture	Fatigue Temperature	Residual Temperature	0	1	2	4[1]		
T_1/C_1	A	1,2	0,1,2,3,4	A	dry	RT	RT	3		3[2]		60 + 60	
T_2/C_2		1,2	0,1,2,3,4	A	wet	real	hot	3		3[2]		60 + 60	
T_3/C_3		1,2	C_1 and C_2	B	dry	RT	RT	3		3		24 + 24	
T_4/C_4		1,2	C_1 and C_2	B	wet	real	hot	3		3		24 + 24	
T_5/C_5		1	0		dry		−65	3		0		3 + 3	
			C_1 and C_2	critical	dry	real	−65	3		3		12 + 12	
T_6/C_6			0		wet		−65	3		0		3 + 3	
			C_1 and C_2	critical	wet	real	−65	3		3		12 + 12	
T_7/C_7			critical	A	dry	RT	RT	2	0	0	5	7 + 7	
				B				2	0	0	5	7 + 7	
				C				5	5	5	0	15 + 15	
T_8/C_8				critical	dry	real	hot	3	0	5	0	8 + 8	
T_9/C_9				critical	wet		RT	3	0	0	0	3 + 3	
T_{10}/C_{10}				A	wet	real	hot	2	0	2	5	9 + 9	
				B				2	5	2	5	14 + 14	
				C				5	10	10	0	25 + 25	
T_{11}/C_{11}	B	1	critical	critical	wet	real	hot	5	0	5	0	10 + 10	
T_{12}/C_{12}	A	1	critical	critical	wet	real	hot	3	3	5	0	11 + 11	2nd stacking sequence
$T_{13}{}^a/C_{13}{}^a$	A	1	critical	critical	wet	real	hot	3	0	3	0	6 + 6	increase width to 6 in.
T_{14}/C_{14}	A	1	0	0	wet	RT	RT	3	0	3	0	6 + 6	control for element tests
T_{15}/C_{15}	A	1	0	0	dry		hot	3	0	0	0	3 + 3	control for element tests

B_1	A	1	0,1,2,3	A	dry	RT	RT	3		$3^{(2)}$		24	
B_2		1	0,1,2,3	A	wet	real	hot	3		$3^{(2)}$		24	
B_3		1	C_1 and C_2	B	dry	RT	RT	3		3		12	
B_4		1	C_1 and C_2	B	wet	real	hot	3		3		12	
B_5		1	critical	A	dry	RT	RT	2	0	0	5	7	
				B				2	0	0	5	7	
				C				5	5	5	0	15	
B_6				critical	dry	real	hot	3	0	5	5	13	
B_7				critical	wet		RT	3	0	0	0	3	
B_8				A	wet	real	hot	2	0	2	5	9	
				B				2	5	2	5	14	
				C				5	10	10	0	25	
B_{10}		1	critical	critical	wet	real	hot	3	3	5	0	11	2nd stacking sequence
B_{11}[a]		1	critical	critical	wet	real	hot	3	0	3		6	increase thickness
B_{12}		1	0	0	wet	RT	RT	3	0	3	0	6	control for element tests

[a] Test conducted by Rockwell

(1) or until critical damage size is reached.

(2) or until damage growth is discernible but not greater than four lifetimes.

Material:

A = AS3501-5A graphite/epoxy.

B = T300/5208 graphite/epoxy.

C_1 and C_2 are the two most critical flaws from screening tests.

Orientation:

1 = $[(0/\pm 45/90)_s]_2$

2 = $[(0/\pm 45/0)_s]_2$

spectrum [*6*]. Tension, compression, and bolted-joint specimens (Figs. 6–8) are tested. The critical size flaw is that which causes the specimen to fail in fatigue after two lifetimes of spectrum loading. Two types of spectra are applied. The room-temperature dry spectrum considers only the effects of the $R = -1$ spectrum (fully reversed) loading, while the real-temperature wet spectrum considers the coupled effects of loading/temperature/moisture. The temperature varies from −54°C (−65°F) to 132°C (270°F), and the moisture content is up to 1.29 percent. In the former case the residual strength is taken at room temperature, while in the latter it is taken at the expected failure temperature, which for tension specimens is 82°C (180°F).

The tension Flaw Size A screening tests, series T_1 and T_2 in Table 3, have been completed except for the unflawed two-lifetime, Orientation 2 $[0_2/\pm 45]_{2s}$ real-temperature wet spectrum tests, which have not been conducted yet, and for the Orientation 2, Type 4 flaw (scratch) room-

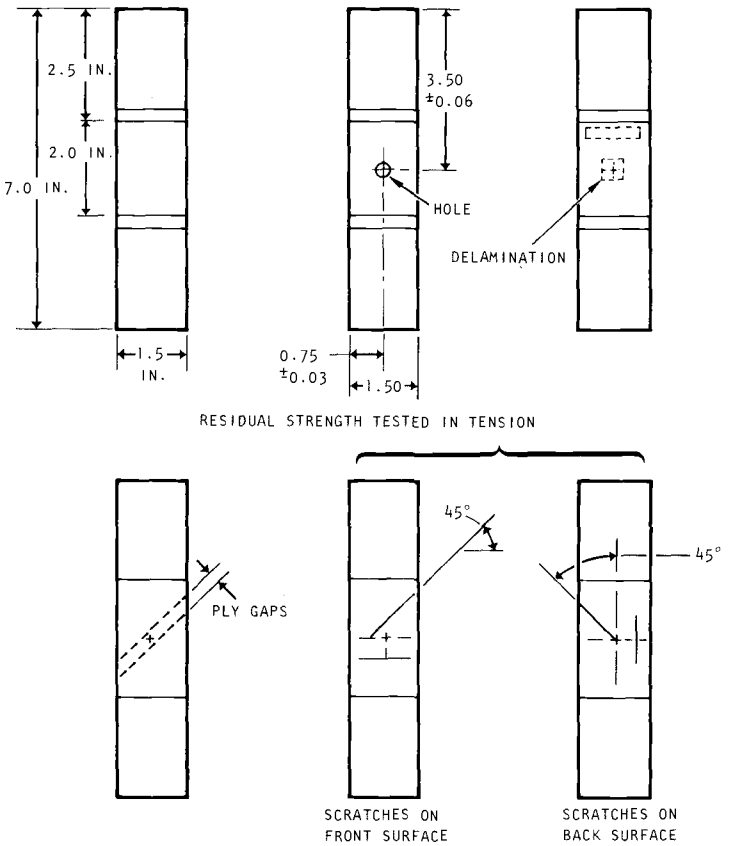

FIG. 6—*Tension coupon configurations.*

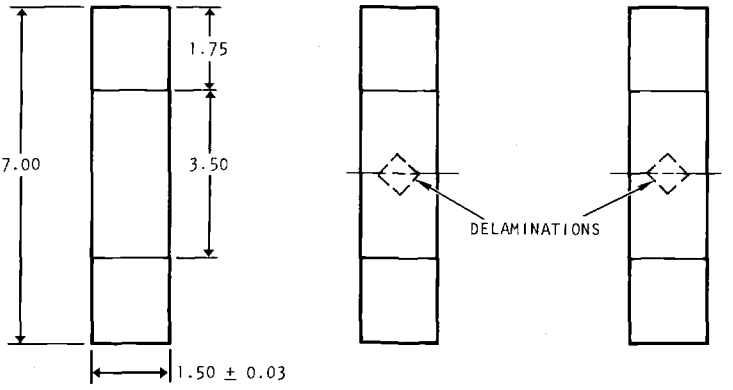

FIG. 7—*Compression coupon configurations.*

temperature dry spectrum tests, which are being rerun because of premature failures of two of the three specimens. Figures 9 through 18 show the results. Since this is only a screening program, only three replicates were tested. Therefore, no statistical inference is made from the results and only the trends are discussed. The lines shown on the figures are straight lines going through the (1) maximum points, (2) arithmetic mean, and (3) minimum. All the wearout tests were scheduled for two lifetimes of spectrum loading. Since this was still in the screening program, however, if the flaw growth was such that the boundaries were in danger of being violated the tests were stopped at less than two lives, and when there was no flaw growth the test was either continued to four lives or terminated when the flaw extent began to violate the boundaries.

As expected, there appears to be very little strength degradation due to application of spectrum loading or due to the residual strength test being

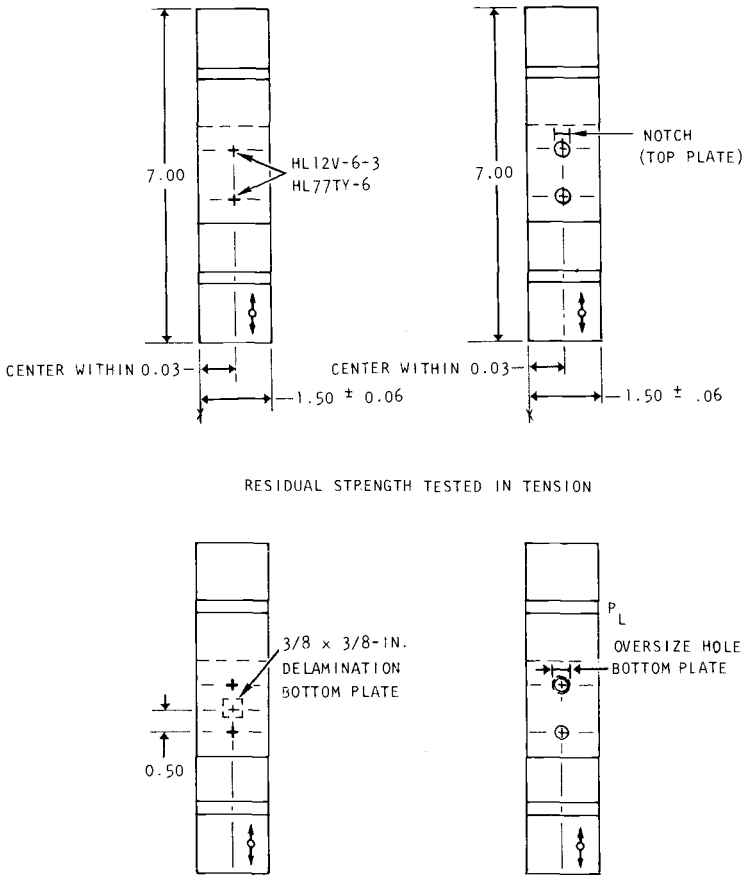

FIG. 8—*Two-bolt joint coupon configurations.*

conducted at 180°F [7]. There does appear to be a reinforcement of the trend for larger scatter, however. The main reduction in residual strength is due to cutting the longitudinal fibers in the "hole" and "scratch" tests causing eccentric (bending) loads in the "scratch" specimens. Since little or no fiber breakage is caused by the spectrum loading, the "wearout" consists of a larger scatter in the residual strength due to irregular growth of the flaw region.

The critical flaw candidates are, as expected, those that involve longitudinal fiber termination, namely, Flaw Type 1 [6.35-mm (0.25 in.)] hole and Flaw Type 4 (scratches). Further experimentation is being conducted to determine their critical sizes. Once the critical flaw and size are found, a statistical "wearout" curve will be defined and studies will be conducted to determine its relationship to the flaw extent as ascertained from NDE.

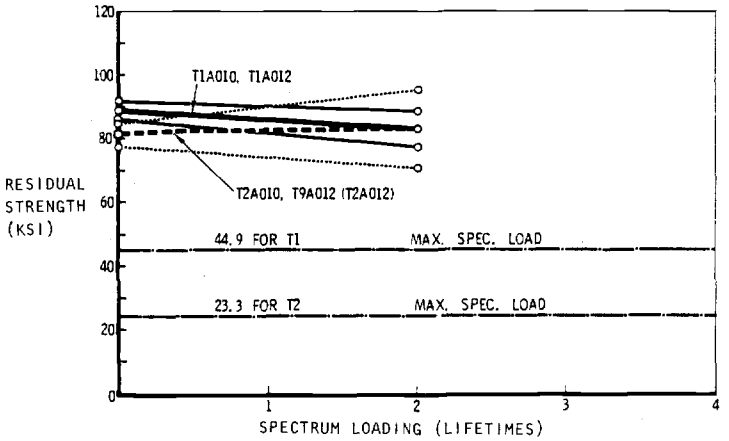

FIG. 9—*Orientation 1, Flaw Type 0 (no flaws).*

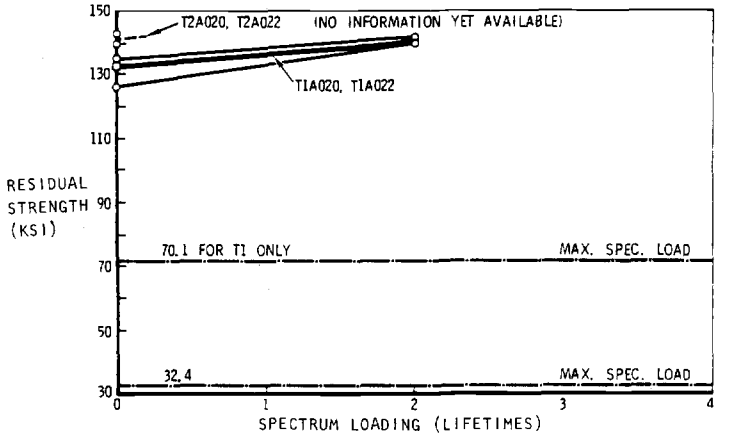

FIG. 10—*Orientation 2, Flaw Type 0 (no flaws).*

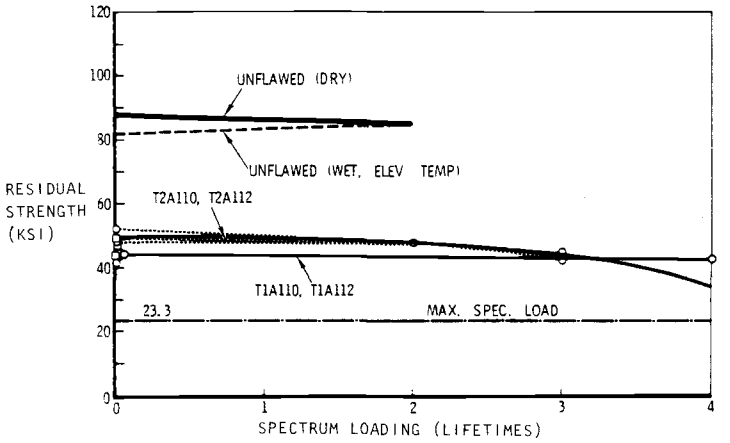

FIG. 11—*Orientation 1. Flaw Type 1 [6.35-mm (¼ in.) ϕ hole].*

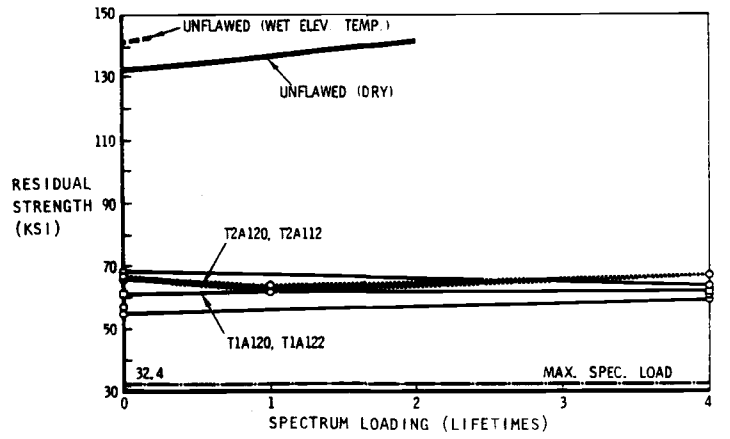

FIG. 12—*Orientation 2. Flaw Type 1 [6.35-mm (¼ in.) ϕ hole].*

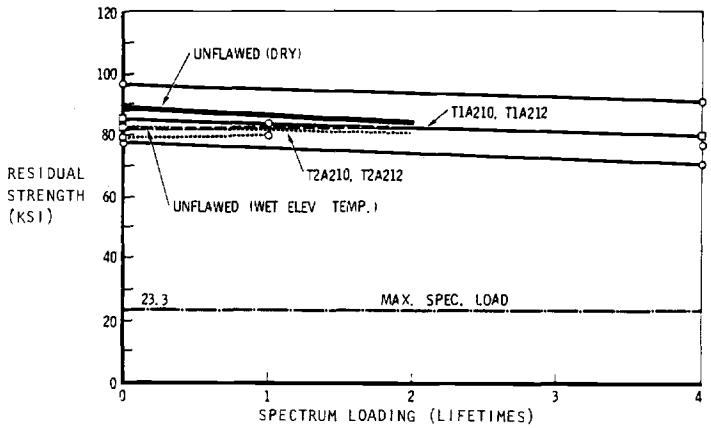

FIG. 13—*Orientation 1. Flaw Type 2 (insert).*

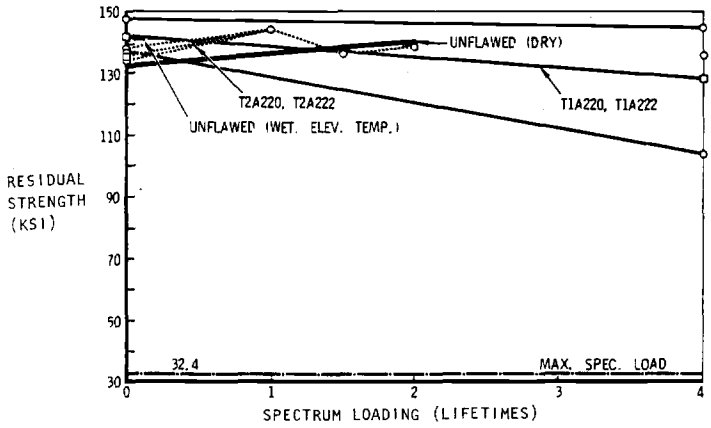

FIG. 14—*Orientation 2. Flaw Type 2 (insert).*

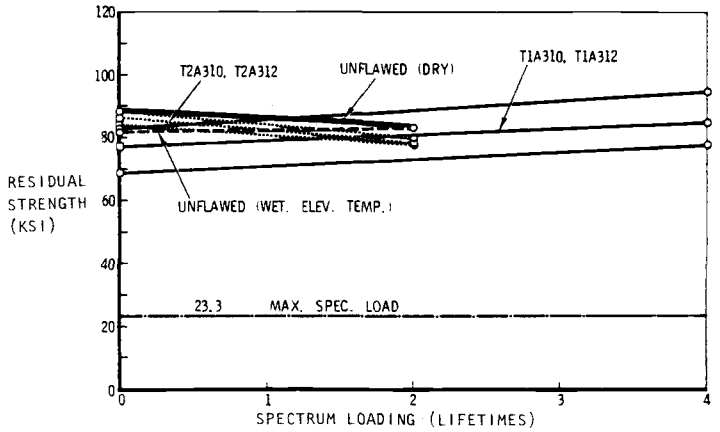

FIG. 15—*Orientation 1, Flaw Type 3 [6.35-mm (¼ in.) gap].*

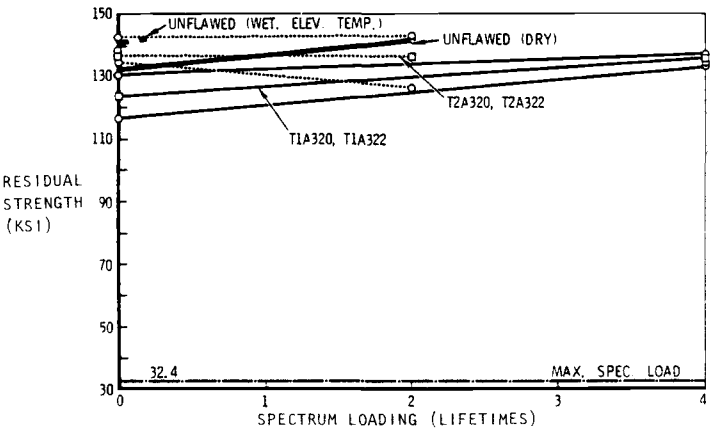

FIG. 16—*Orientation 2, Flaw Type 3 [6.35-mm (¼ in.) gap].*

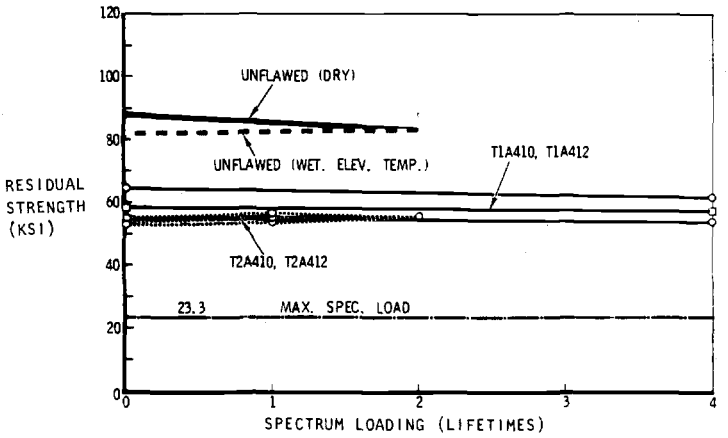

FIG. 17—*Orientation 1, Flaw Type 4 (scratch).*

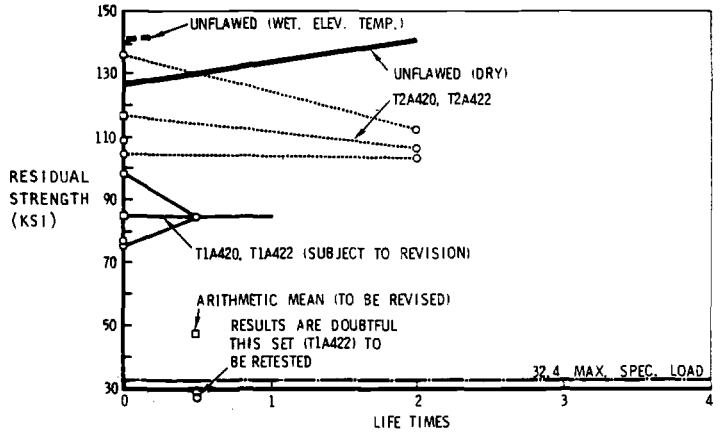

FIG. 18—*Orientation 2, Flaw Type 4 (scratch).*

References

[1] *Case Studies in Fracture Mechanics*, T. P. Rich and D. J. Cartwright, Eds., AMMRC MS 77-5, Watertown, Mass., June 1977.

[2] Burroughs, B. et al, "Advanced Composites Serviceability Quarterly Progress Report, 1 October 1977 to 30 December 1977," Rockwell International Los Angeles Division Report NA-76-783-5, Jan. 1978.

[3] Wu, E. M. in *Composite Materials*, L. J. Broutman, Ed., Academic Press, New York, Vol. 5, 1974.

[4] Daniel, I. M. "Biaxial Testing of Graphite/Epoxy Composites Containing Stress Concentration, Part I," Air Force Technical Report AFML-TR-76-244, Air Force Materials Laboratory, Wright-Patterson Air Force Base, Ohio, Dec. 1976.

[5] Konish, H. J., Jr., and Cruse, T. A. in *Composite Reliability. ASTM STP 580.* American Society for Testing and Materials, 1974, pp. 490–503.
[6] Parmley, P. A. et al in *Proceedings.* 1978 International Conference on Composite Materials, The Metallurgical Society of AIME, April 1978, pp. 1604–1619.
[7] Konishi, D. Y. in *Proceedings.* Fourth Conference on Fibrous Composites in Structural Design, San Diego, Calif., Nov. 1978 (to be published as AMMRC-MS-78-X).

J. H. Starnes, Jr.,[1] *M. D. Rhodes,*[1] *and J. G. Williams*[1]

Effect of Impact Damage and Holes on the Compressive Strength of a Graphite/Epoxy Laminate

REFERENCE: Starnes, J. H., Jr., Rhodes, M. D., and Williams, J. G., **"Effect of Impact Damage and Holes on the Compressive Strength of a Graphite/Epoxy Laminate,"** *Nondestructive Evaluation and Flaw Criticality for Composite Materials, ASTM STP 696*, R. B. Pipes, Ed., American Society for Testing and Materials, 1979, pp. 145-171.

ABSTRACT: The effect of low-velocity impact damage and circular holes on the compressive strength of a 48-ply orthotropic graphite/epoxy laminate has been studied experimentally. Unidirectional tapes made of Thornel 300 graphite fibers preimpregnated with Narmco 5208 epoxy resin were used to fabricate the $[\pm 45/0_2/\pm 45/0_2/\pm 45/0/90]_{2s}$ laminate. Aluminum spheres 1.27 cm in diameter were used as projectiles and propelled at speeds between 52 and 101 m/s. The extent of interior laminate damage caused by impact was determined by ultrasonic inspection and, in some cases, by cross-sectioning specimens for visual inspection. Some specimens were impacted and then loaded to failure in compression to determine their residual strength. Other specimens were loaded to a prescribed compressive strain and impacted at that applied load. Some of these loaded specimens failed catastrophically on impact. Specimens that did not fail catastrophically were subsequently loaded to failure in compression to determine their residual static strength. It was found that low-velocity impact damage can seriously degrade the laminate static compressive strength. Several impact-damaged specimens were subjected to low-strain compression-compression cyclic loading, which was found to degrade further the laminate compressive strength. Specimens with circular holes with diameters up to a third of the specimen width were loaded in static compression to failure, and it was found that holes can also degrade the compressive strength of the laminate. Impact at the higher speeds reduced the compressive strength of the laminate more than the largest holes studied.

KEY WORDS: composite materials, graphite composites, epoxy resins, impact damage, circular holes, compressive strength, compressive cyclic loads, nondestructive tests

Advanced composite materials offer an attractive potential for reducing the mass of modern aerospace-vehicle structural components. To achieve this potential, minimum-mass structural designs must be provided that reliably

[1] Aerospace engineers, Structural Mechanics Branch, Structures and Dynamics Division, NASA Langley Research Center, Hampton, Va. 23665.

satisfy required design constraints and carry design loads. Reliable designs can be provided only when all failure mechanisms and operational hazards that affect the intergrity of a structural component are identified and understood. One operational hazard that can affect the structural integrity of composite compression components is low-velocity impact damage that can occur in service or during maintenance.

Test results from preliminary studies [*1,2*][2] indicate that the failure strain of minimum-mass hat-stiffened graphite/epoxy compression panels designed for high strains can be degraded seriously by low-velocity impact damage. Other test results from these studies [*1*] indicate that the presence of a small circular hole can also reduce the compresssive failure strain of these hat-stiffened panels. The geometric complexity of stiffened panels makes it difficult to isolate and identify the fundamental mechanisms that contribute to the reduction in panel compressive strength. Studies of the effects of low-velocity impact damage on the compressive strength of composite components can be simplified by studying geometrically simpler flat laminates.

This paper presents the results of an exploratory test program to determine the effect of low-velocity impact damage on the compressive strength of a 48-ply orthotropic graphite/epoxy flat laminate. The projectile mass and speeds simulate momenta typical of low-velocity impact hazards that can occur in commercial aircraft service. The laminate selected is typical of designs being proposed for future heavily loaded aircraft wing skins and has extensional and shear stiffness properties similar to existing transport aircraft wing skins designed for an ultimate compressive loading of 2.63 MN/m. Results from tests performed to determine the effect of circular holes on the compressive strength of the same laminate are also presented for comparison with the impact-damage results. The character of the laminate local impact damage is described, the effects of impact damage and circular holes on the static compressive strength of the laminate are discussed, and the effect of cyclic compressive loading on impact-damaged specimens is described.

Test Specimens

The specimens tested in this investigation were fabricated from commercially available 450 K cure graphite/epoxy preimpregnated tapes. The tapes were made of unidirectional Thornel 300 graphite fibers preimpregnated with Narmco 5208 epoxy resin and were laid up to form a $[\pm 45/0_2/\pm 45/0_2/\pm 45/0/90]_{2s}$ laminate with 48 plies. These laminates were cured in an autoclave using the manufacturer's recommended procedures. Following cure, the laminates were ultrasonically inspected to establish specimen quality, cut into test specimens, and the ends of the specimens were ground flat and parallel to permit uniform compressive loading. Most

[2]The italic numbers in brackets refer to the list of references appended to this paper.

specimens were 11.4 cm wide by 24.8 cm long, but a small number were 12.7 cm wide by 25.4 cm long. Circular holes were machined in the center of some of the specimens with diamond-impregnated core bits. One side of the specimens was painted white to reflect light so a moire-fringe technique could be used to monitor out-of-plane deformations. The other side of the impact specimens was coated with a brittle lacquer to provide a qualitative measure of impact damage.

The length and width of the specimens were chosen so the fundamental mechanisms that affect compressive strength could be identified and studied without the use of any interior lateral restraints away from the specimen edges. The width of the specimens was selected so that the local region influenced by the initial impact damage or holes would be removed from specimen edge effects. Also, the width and length were sized so that a strength failure would be more likely to occur than a buckling failure. The buckling load of the 11.4 by 24.8 cm specimens without impact damage or holes was determined, using the BUCLASP 2 computer code [*3*], to be 4.40 MN/m at a longitudinal strain of 0.0093. The lamina properties used for the analysis are given in Table 1.

Apparatus

Test specimens were loaded in axial compression using a 1.33-MN-capacity controlled-displacement hydraulic testing machine for the static load tests and a 0.51-MN-capacity controlled-load hydraulic testing machine for the cyclic load tests. The loaded ends of the specimens were clamped by fixtures during testing and the edges were simply supported by knife-edge restraints to prevent the specimen from buckling as a wide column. A typical specimen in the support fixture is shown in Fig. 1.

Electrical resistance strain gages were used to monitor strains, and d-c differential transformers were used to monitor axial displacement and displacements normal to the specimen surface. All electrical signals and the corresponding applied loads were recorded on magnetic tape at regular time intervals during the tests. Deflections normal to the specimen surface were also monitored by the moire-fringe technique.

The equipment used to propel the 1.27-cm-diameter aluminum spheres used as impact projectiles is shown schematically in Fig. 2. Air pressure

TABLE 1—*Lamina properties used in buckling analysis.*

Cured ply thickness, mm	0.14
Longitudinal modulus, GPa	131.0
Transverse modulus, GPa	13.0
Shear modulus, GPa	6.4
Major Poisson's ratio	0.38

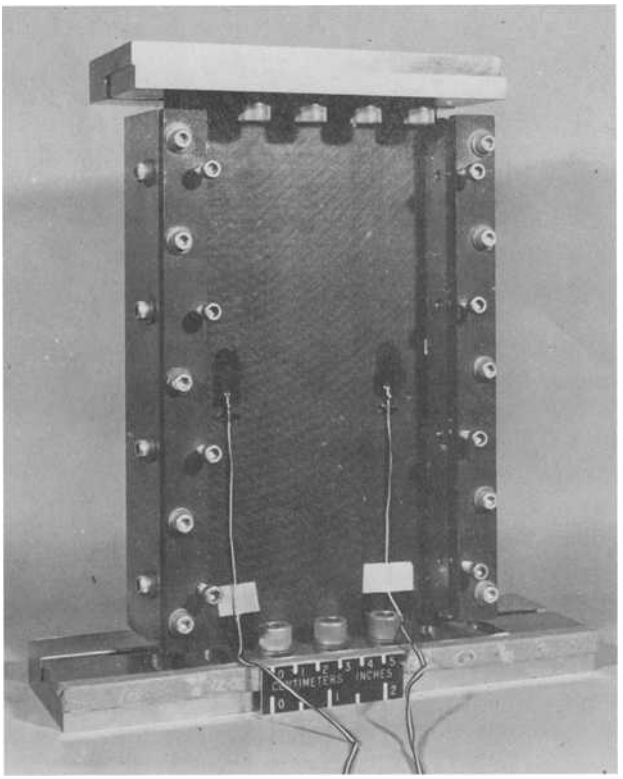

FIG. 1—*48-ply graphite/epoxy specimen in test fixture.*

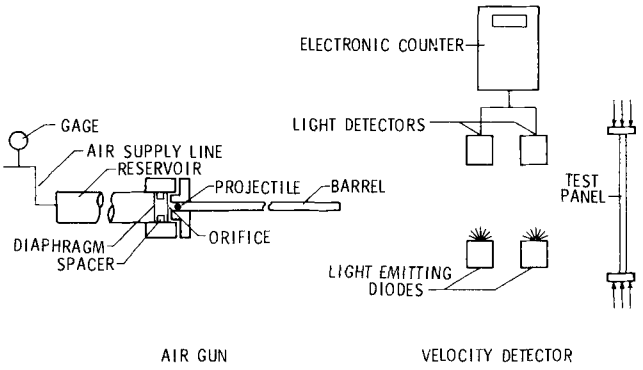

FIG. 2—*Schematic drawing of air gun and velocity detector.*

developed in the reservoir ruptures the diaphragm and allows the compressed air in the reservoir to pass through an orifice and force the projectile down the barrel. An electronic detector at the end of the barrel measures the projectile speed.

An ultrasonic C-scan flaw detector was used to measure the extent of impact damage. This detector is a high-resolution commercial instrument that uses a focused pulse-echo-type 15-MHz piezoelectric transducer. Both the transducer and the specimens were immersed in a tank of water, and the transducer was mounted to a traversing mechanism to scan the region of interest. This equipment and procedure are described further in Ref. *4*.

Tests

The three types of tests conducted during this investigation are: (1) damage characterization tests on specimens to determine the nature of local impact damage; (2) static compressive load tests on control specimens without any impact damage or holes, on specimens subjected to impact damage, and on specimens with circular holes to determine their compressive strength; and (3) cyclic compression-compression tests on impact-damaged and undamaged specimens to determine the effect of low-strain cyclic loading on compressive strength.

Damage Characterization Tests

Unloaded specimens were supported in the test fixture and subjected to impact damage. The impacted specimens were then inspected both visually and by the ultrasonic C-scan procedure. Some of these specimens were cross-sectioned through the damaged region and examined microscopically.

Static Load Tests

Control Specimens—Five control specimens without impact damage or holes were tested in compression to determine their critical compressive loads and strains. Buckling was defined by the load-strain response and strain-reversal techniques. The strain measurements were complemented by the moire-fringe method, which provided visual definition of out-of-plane deformations.

Impact-Damage Specimens—Four specimens were impacted without any applied compressive load and then loaded in axial compression to determine their residual strength. Eighteen specimens were loaded to prescribed axial compressive strains and impacted while loaded. Specimens that did not fail catastrophically on impact were subsequently loaded to failure to determine their residual strength. During the residual strength tests of these specimens a moire-fringe method was used to observe the out-of-plane deformations. In

all impact tests, the projectiles were directed normal to the specimen surface at speeds that ranged from 52 to 101 m/s.

Circular-Hole Specimens—Ten specimens, each with a single circular hole in the center, were loaded in compression to failure. The specimens had hole diameters ranging from 0.16 to 3.81 cm (diameter-to-width ratios ranging from 0.014 to 0.333). Small strain gages were used to monitor the strains in the hole region. Gages 1.3 mm wide by 0.8 mm long were used to measure interlaminar normal strains on the surface of the hole and gages 0.3 mm wide by 1.8 mm long were used to measure the in-plane axial strains near the hole boundary. Gages 3.2 mm wide by 6.4 mm long were used to measure the in-plane axial strains far from the hole. The strain measurements were complemented by the moire-fringe method for out-of-plane deformations.

Cyclic Load Tests

Three undamaged and four impact-damaged specimens were subjected to low-strain cyclic compression-compression loading to determine its effect on compression strength. To minimize thermal effects, these specimens were cycled at a constant-amplitude sine wave loading at a rate of 5 Hz. The growth of the damaged region was observed visually.

Results And Discussion

Damage Characterization Tests

Unloaded specimens were subjected to impact to determine the character of local impact damage. Photographs of the back surfaces of two specimens impacted at 58 and 95 m/s are shown in Fig. 3. The light-colored regions shown in the figure are regions where the brittle lacquer spalled behind the impact location. Radial cracks in the brittle lacquer near the spalled region are also visible. Both the radial cracks and the spalled region indicate that significant deformations have occurred locally due to impact. There is no visible damage to the graphite/epoxy on the back surface of the specimen impacted at 58 m/s, but some local surface cracks in the graphite/epoxy are visible on the back surface of the specimen impacted at 95 m/s. There is no visible front-surface damage at the impact location of either specimen. Photographs of ultrasonic C-scans of the damaged regions of these specimens are shown in Fig. 4 with the same scale as used in Fig. 3. Each pass of the transducer is represented by a light-colored line in the figure. The size of the dark regions indicates the extent of damage in both specimens as a result of impact. The damaged region of the specimen impacted at 58 m/s is smaller and more elongated in the 0-deg direction than the specimen impacted at 95 m/s. Ultrasonic inspection also indicates that the spalled brittle lacquer provides a qualitative approximation to the size of the damaged region.

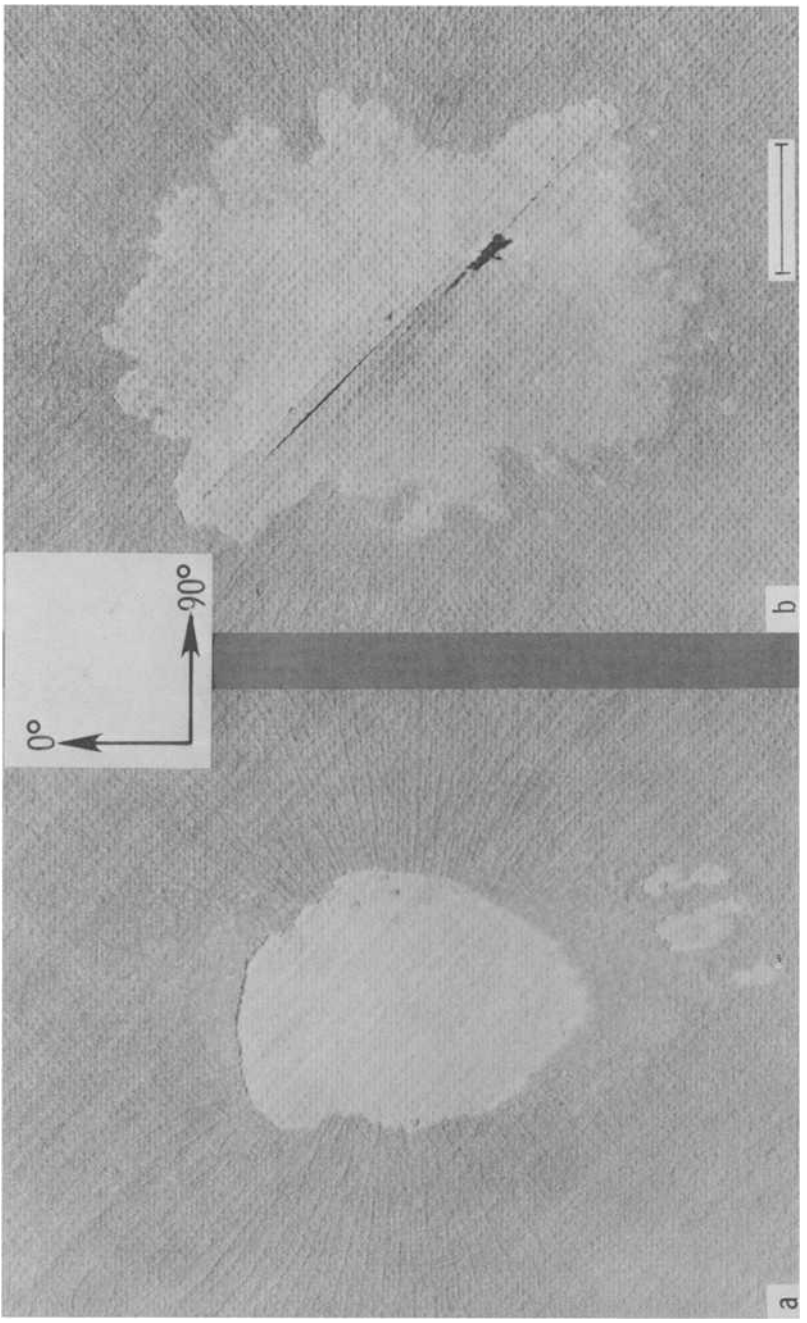

FIG. 3—*Brittle-lacquer spalling pattern on impact-specimen back surface:* (a) *58 m/s projectile impact speed;* (b) *95 m/s projectile impact speed. Scale mark indicates 10 mm.*

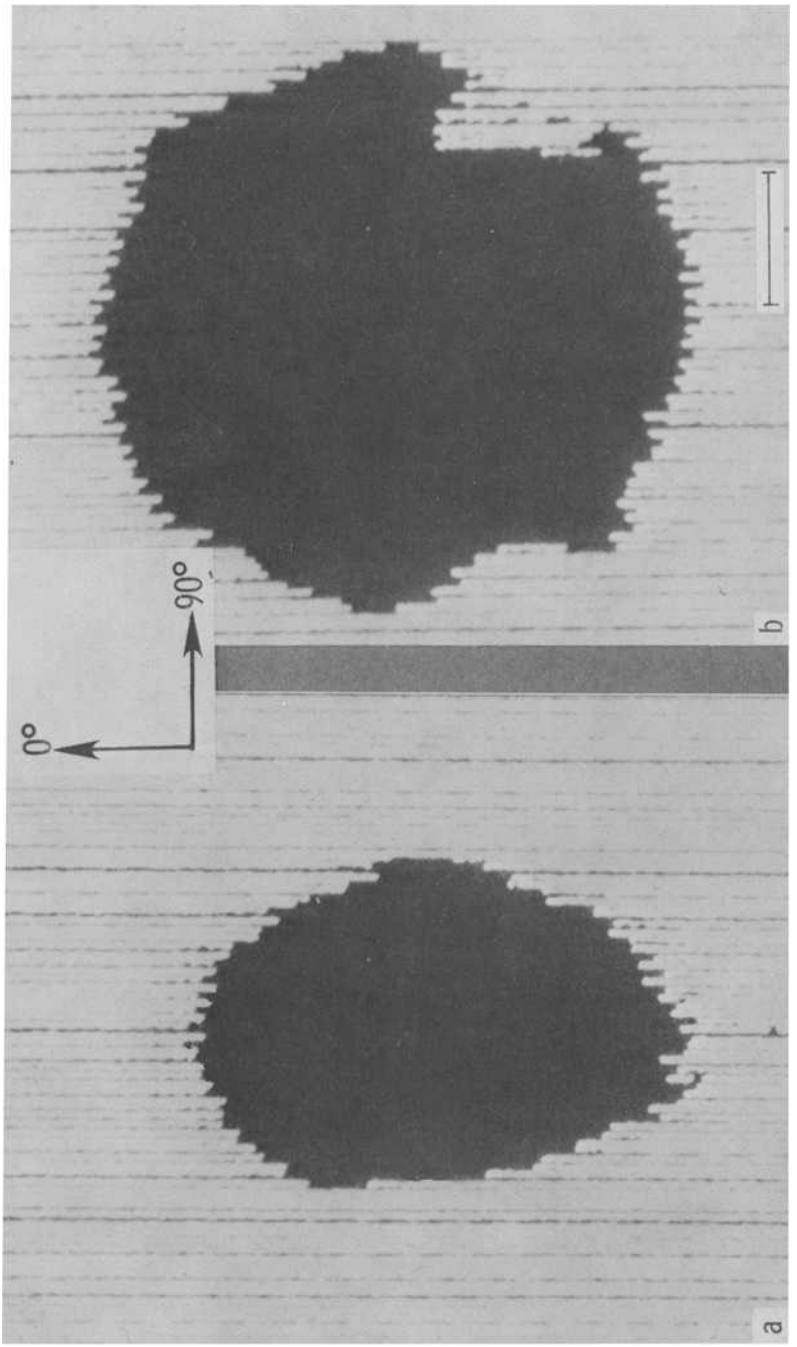

FIG. 4—*Ultrasonic C-scan of impact site:* (a) *58 m/s projectile impact speed;* (b) *95 m/s projectile impact speed. Scale mark indicates 10 mm.*

Photomicrographs of a cross section normal to the 0-deg fibers through the damaged region of the specimens are shown in Fig. 5. The photomicrograph of the specimen impacted at 58 m/s shows only a small amount of intraply cracking and delamination in the impact region. The photomicrograph of the specimen impacted at 95 m/s shows extensive intraply matrix cracking and delamination in the impact region. This cracking and delamination extends 3.4 cm across the width of the specimen. This extensive region of delamination has changed the 48-ply orthotropic laminate into a number of thinner sublaminates in the damaged region that are likely to be anisotropic, thus reducing local stiffnesses and causing local anisotropic coupling. The ultrasonic C-scans in Fig. 4 and the photomicrographs in Fig. 5 indicate that the projectile used in this study causes substantial internal damage to the laminate with no visible external damage at the impact site for speeds up to approximately 100 m/s.

Static Load Tests

Control Specimens—The results of the control-specimen tests are presented in Table 2. Moire-fringe patterns indicated that Specimens N1, N3, N4, and F1 buckled into two axial half-waves and one transverse half-wave. Specimen N2 failed near an end fixture after back-to-back strain gages indicated the onset of bending. Specimens N1 and F1 failed near an end fixture just after buckling was indicated by the moire-fringe patterns. The loading of Specimens N3 and N4 was stopped before failure, but after the moire-fringe patterns indicated buckling. These specimens (N3 and N4) were subsequently used for impact-damage tests. The differences in the control-test results were caused by local stress concentrations that developed in small gaps between the end fixtures and edge supports when out-of-plane deformations occurred. When out-of-plane deformations occurred, the end fixtures and edge supports moved relative to one another, causing the specimens to fail in one of these gaps. Also, small surface irregularities could affect the tightness of fit of the edge supports and introduce different degrees of edge-support flexibility. Even though there is scatter in the results presented in Table 2, these results confirm that the specimens buckle at strains high enough to assure that strength-controlled failures are likely to occur when there is impact damage or a hole in a specimen.

Impact-Damage Specimens—The results of the impact-damage tests are presented in Table 3, and the effect of projectile speed on specimens impacted while loaded to a prescribed axial strain is shown in Fig. 6. The applied axial strains of the loaded specimens that failed catastrophically on impact are represented by the filled circles in Fig. 6 and the applied strains of the specimens that did not fail catastrophically on impact are represented by

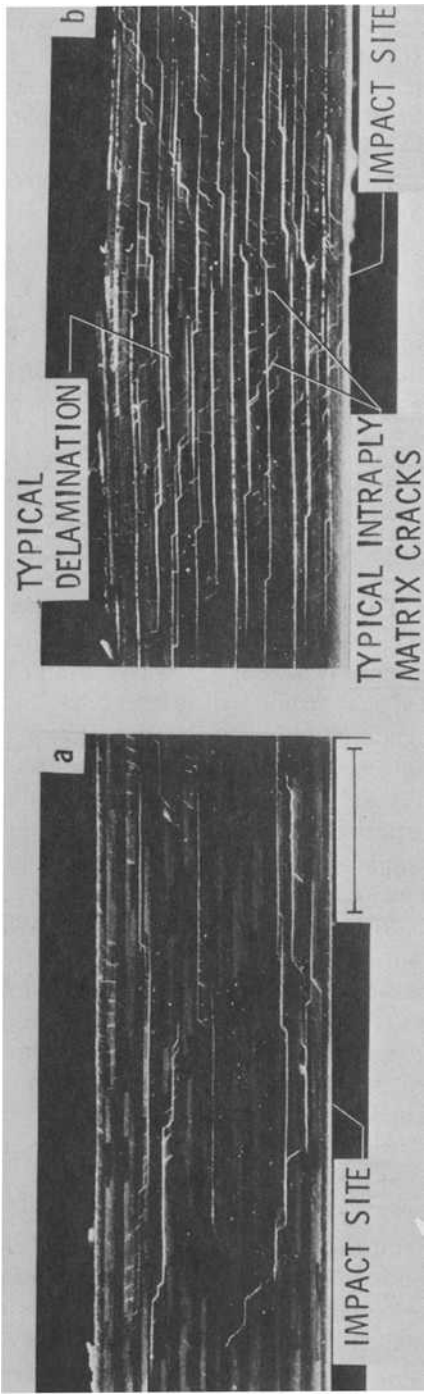

FIG. 5—*Photomicrographs of cross sections through the impact site normal to the 0-deg fibers:* (a) *58 m/s projectile impact speed. Scale mark indicates 5 mm.* (b) *95 m/s projectile impact speed.*

TABLE 2—*Results of control specimen tests.*

Specimen[a]	Thickness, cm	Load, kN	Maximum Applied Strain
N1	0.70	427	0.0089
N2	0.70	403	0.0082
N3	0.70	495	0.0105
N4	0.70	448	0.0095
F1	0.68	467	0.0083

[a]Specimen dimension code: N = 11.4 by 24.8 cm; F = 12.7 by 25.4 cm.

open circles. For comparison, the results from Table 2 for the undamaged control specimens are shown on the ordinate as open circles, and the projectile kinetic energy is also shown on the abscissa for reference. The dashed curve in Fig. 6 represents a lower-bound or catastrophic failure threshold separating results of specimens that failed on impact from those that did not. The trend of this catastrophic failure threshold indicates that the compressive strength of these loaded impact specimens is seriously degraded with increasing projectile speed, with most of the degradation having occurred by about 80 m/s. A typical failed specimen is shown in Fig. 7.

The effect of projectile speed on the residual strength of all specimens that did not fail catastrophically on impact is shown in Fig. 8. The open circles in Fig. 8 indicate the axial strain the specimens were carrying at the moment of impact, and the filled circles represent the strain at failure measured during residual strength tests. Each open circle in Fig. 8 has a corresponding filled circle directly above it, and the difference in strain between two corresponding circles represents the additional applied axial strain carried by a damaged specimen. For comparison, results from Table 2 for the control tests are shown on the ordinate of Fig. 8 as filled circles, and the projectile kinetic energy is shown on the abscissa for reference. Also for comparison, the catastrophic failure threshold curve from Fig. 6 is shown in Fig. 8 as a dashed curve. Specimens impacted in the 50 to 60-m/s range that did not fail catastrophically on impact have residual strengths between 0.0104 and 0.0087 axial strain, which is on the same order as the undamaged control specimens. Three of the four specimens impacted in this speed range failed near an end fixture and the fourth failed through the impact site. Specimens impacted in the 80 to 100-m/s range have residual strengths that are between only 0.0044 and 0.0034 axial strain. Specimens impacted in this speed range with no applied load fail at higher values of applied axial strain than those impacted while loaded axially and, consequently, have higher residual strengths. Furthermore, a comparison of the residual strength results of Fig. 8 with the catastrophic failure threshold from Fig. 6 indicates that catastrophic failure of specimens impacted while loaded axially occurs at ap-

TABLE 3—*Test results for impact-damaged specimens.*

Specimen[a]	Thickness, cm	Load Conditions at Impact: Applied Strain	Load Conditions at Impact: Load, kN	Impact Data: Projectile Speed, m/s	Impact Data: Interior Damage Size, cm	Residual Strength: Applied Strain	Residual Strength: Load, kN
N5	0.67	0	0	60	data not available	0.0087	428
N6	0.70	0	0	79	3.6 wide by 4.6 long	0.0044	226
N7	0.70	0	0	91	3.6 wide by 4.3 long	0.0039	189
N8	0.67	0	0	93	4.6 wide by 5.8 long	0.0039	191
N9	0.67	0.0071	363	52	failed on impact	...	...
N3	0.70	0.0042	220	53	1.8 diameter circle	0.0104	495
N4	0.70	0.0054	274	58	2.3 diameter circle	0.0095	449
N10	0.70	0.0062	310	56	2.5 diameter circle	0.0102	479
N11	0.70	0.0069	346	60	failed on impact	...	...
N12	0.70	0.0041	209	84	failed on impact	...	...
N13	0.70	0.0047	241	95	failed on impact	...	...
N14	0.70	0.0061	308	99	failed on impact	...	...
N15	0.67	0.0027	144	100	data not available	0.0034	155
N16	0.67	0.0030	161	99	failed on impact	...	...
N17	0.67	0.0033	174	98	failed on impact	...	...
N18	0.67	0.0036	191	98	failed on impact	...	...
N19	0.67	0.0039	206	100	failed on impact	...	...
N20	0.67	0.0027	143	100	5.1 wide by 3.8 long	residual strength not determined	
F2	0.68	0.0036	205	76	failed on impact	...	...
F3	0.69	0.0032	179	80	data not available	0.0035	194
F4	0.67	0.0031	178	89	failed on impact	...	...
F5	0.67	0.0027	156	88	data not available	0.0031	173

[a]Specimen dimension code: N = 11.4 by 24.8 cm; F = 12.7 by 25.4 cm.

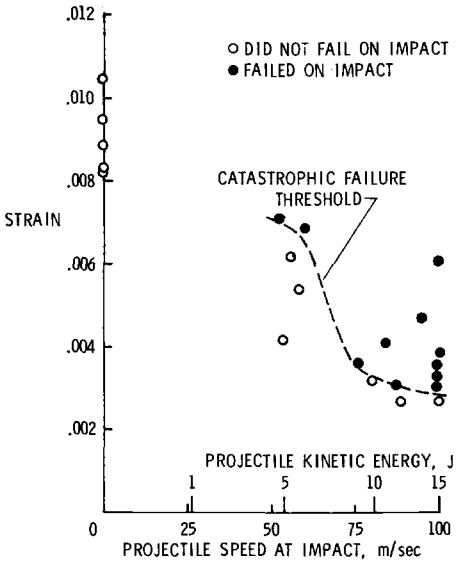

FIG. 6—*Effect of projectile speed on catastrophic failure strain.*

plied strains that are slightly below the residual strength results of specimens impacted without applied axial load in the 80 to 100-m/s projectile speed range. In the 50 to 60-m/s projectile speed range, however, the catastrophic failure threshold strains for specimens impacted while loaded axially is on the order of 0.002 to 0.003 less strain than the residual strength results for specimens impacted without applied axial load. This difference in loaded and unloaded impact test results indicates that there is an interaction or coupling between the applied in-plane load and the local deformations associated with impact. The existence of this coupling is also supported by ultrasonic C-scan and cross-sectional photomicrograph data. Ultrasonic C-scans made before the residual strength tests indicate that damage due to impact for the specimens impacted between 50 and 60 m/s is local and approximately circular with diameters 1.8 to 2.5 cm. These specimens had no visible front- or back-surface damage. Visual inspection of the specimens impacted between 80 and 100 m/s indicated that some local 45-deg cracks existed on the back surfaces but no front-surface damage was evident. Ultrasonic C-scans of these specimens indicate that the local damage due to impact is elliptical. For the specimens impacted without any applied axial strain, the size of the ellipse ranges from 3.6 cm wide by 4.3 cm long to 4.6 cm wide by 5.8 cm long with semimajor axes oriented in the axial direction. For Specimen N20, which was impacted at 100 m/s while loaded by an applied axial strain of 0.0027, the ellipse is 5.1 cm wide by 3.8 cm long with its semimajor axis oriented in the transverse direction, which is a change in orientation of

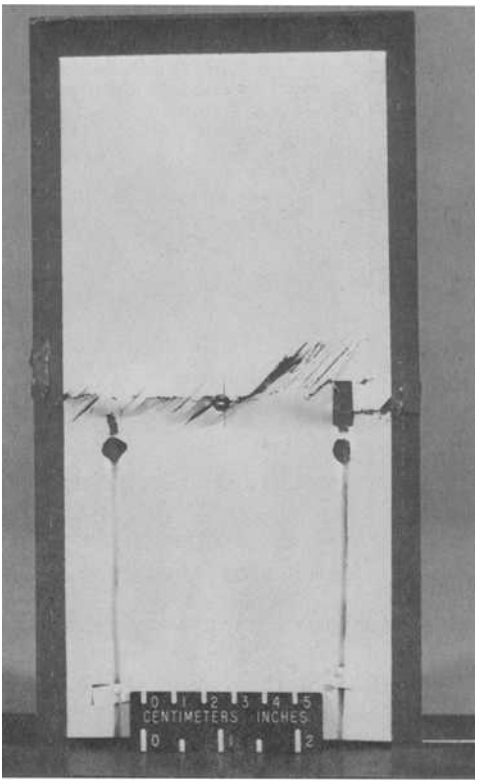

FIG. 7—*Typical failed impact-damaged specimen.*

90-deg from the specimens impacted without applied axial strain. Instead of determining its residual strength, Specimen N20 was cross-sectioned through the local impact-damaged region to determine the character of the damage. Photomicrographs of the damaged region show extensive local delamination and intraply matrix cracking that extends 4.6 cm across the width of the specimen and is similar to that shown in Fig. 5*b*. This 1.2-cm increase in delamination width over the 3.4-cm delamination width of the unloaded damage characterization specimen impacted at 95 m/s indicates that there is coupling between the applied axial load and local deformation due to impact. This coupling may account for the lower residual strength of the specimens impacted while loaded axially.

Photographs of successive moire-fringe patterns from the residual strength test of Specimen N7 are shown in Fig. 9. Specimen N7 was impacted at 91 m/s with no applied axial load. The photograph in Fig. 9*a* shows the moire-fringe pattern of the damaged region at 48 percent of the specimen residual strength. The small light-colored circular region in the center of the

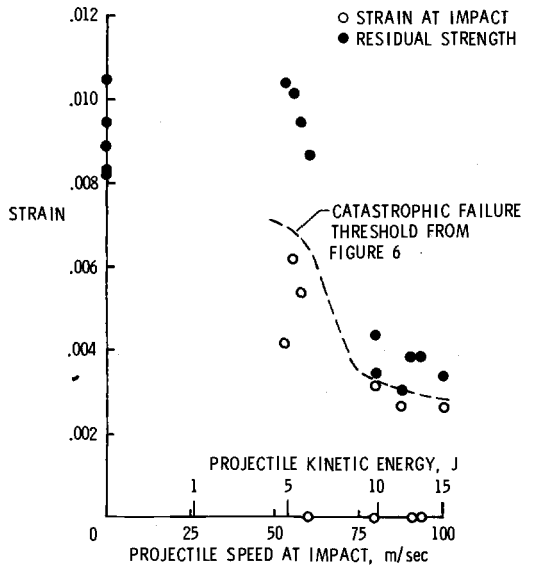

FIG. 8—*Effect of projectile speed on residual strength.*

specimen is the impact site which is beginning to deform out of plane. This deformation is the first observable response of the damaged region to the applied axial load. Subsequent moire-fringe patterns (Figs. 9*b* and 9*c*) represent local buckling of the impact-damaged region that grows laterally as the applied load is increased. The photograph in Fig. 9*d* shows the failed specimen with the damage propagated laterally across the specimen in the same manner as the example shown in Fig. 7. Examination of the failed specimen removed from the test fixture confirmed that the damage propagated laterally and was confined axially to the region indicated in Fig. 9*d*.

Circular-Hole Specimens—Axial strains ϵ_x measured in the vicinity of four different-diameter holes are shown in Fig. 10 normalized by the applied axial strain ϵ_a of 0.0026. The seven strain gages used to measure these strains were distributed along a line indicated by the y-axis in the sketch in Fig. 10. One of these gages was located on the surface of the hole edge and the other six were located at 0.16, 0.32, 0.64, 1.27, 1.91, and 2.54 cm from the hole edge. The gage locations y in Fig. 10 are normalized by the hole diameter D. The ratio of measured strain to applied strain for the four holes is slightly higher than the calculated value of 3.31 for the ratio of maximum strain to applied strain for an infinitely wide orthotropic plate determined from Ref. 5. Even though the results indicate some finite-width effects for these 11.4-cm-wide specimens, the strains near the hole decrease rapidly to the value of the applied strain as the distance from the holes increases. In addition to the local

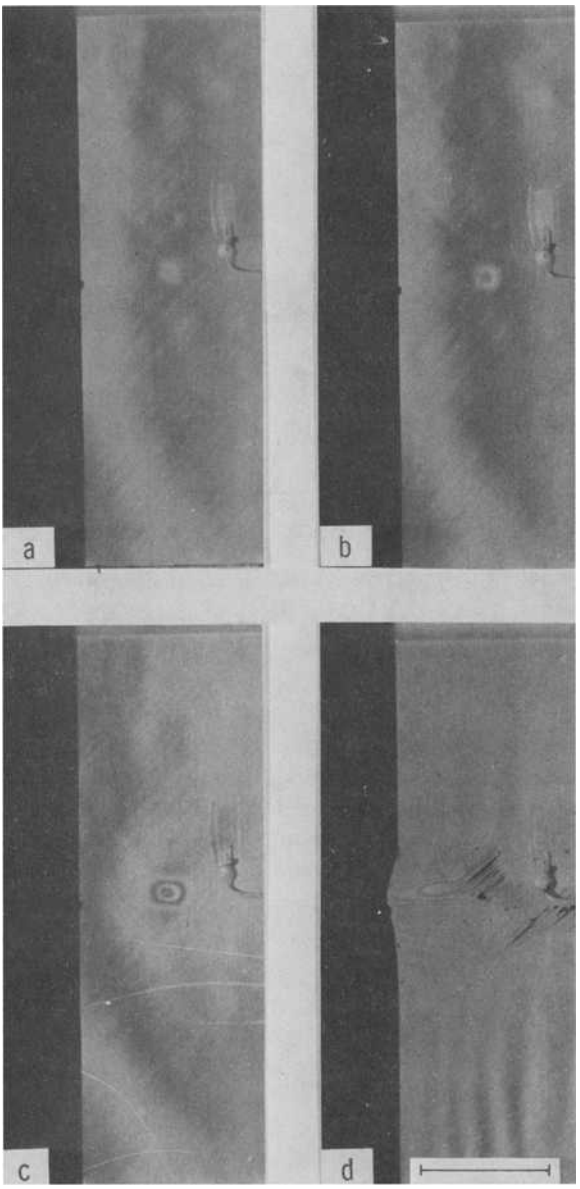

FIG. 9—*Moire-fringe patterns during residual-strength test of an impact-damaged specimen:* (a) *48 percent of residual strength;* (b) *61 percent of residual strength;* (c) *98 percent of residual strength;* (d) *failed specimen. Scale mark indicates 5 cm.*

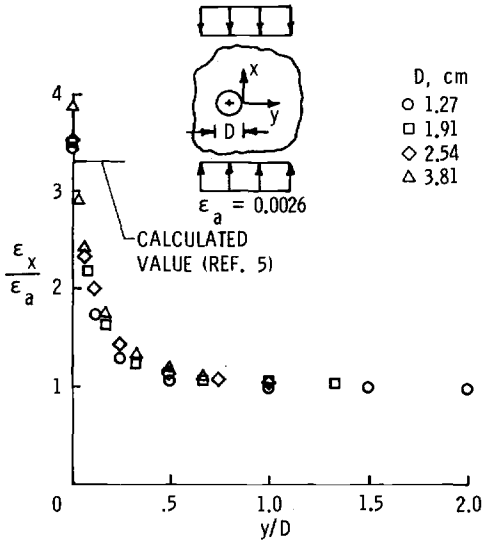

FIG. 10—*Strain concentration in hole region.*

in-plane axial strains, through-the-thickness or interlaminar normal strains were measured at points on the free edge of the larger holes with strain gages oriented parallel to the hole axis. Typical data measured by three of these gages for a 1.91-cm-diameter hole are shown in Fig. 11 as a function of applied load. The applied axial strain is also shown for comparison. The location of these three gages is represented by the small filled circles in the sketch in Fig. 11 and the gages are labeled 1, 2, and 3. Gage 1 indicates a tensile strain between 20 and 30 percent of the applied axial strain. Gage 3 indicates a compressive strain of about 38 percent of the applied strain. Gage 2 indicates a small compressive strain of about 8 percent of the applied axial. Near failure, Gages 1 and 2 become very erratic. The combination of the high in-plane compressive strain and the high interlaminar tensile strain near the hole causes local delamination to occur and propagate across the specimen as the applied load is increased. The erratic behavior of Gages 1 and 2 near failure is probably due to local delamination in the hole region.

A series of photographs of the propagating moire-fringe patterns for a specimen with a 1.91-cm-diameter hole is shown in Fig. 12 for increasing values of applied load. Figure 12*a* shows a photograph of the specimen loaded to 92.8 percent of the ultimate failure load and the absence of moire fringes indicates there are no out-of-plane deformations evident. At a slightly higher load (Fig. 12*b*) a small out-of-plane deformation region developed at the left edge of the hole. These results, along with the strain-gage results in the hole region and direct visual observations, indicate that a local delamina-

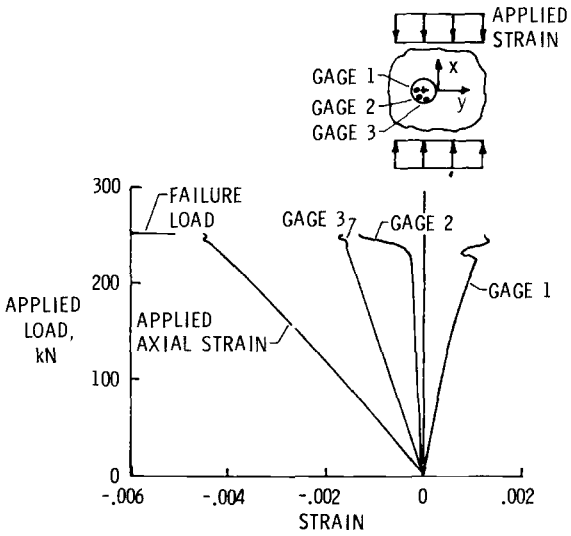

FIG. 11—*Interlaminar normal strains at the hole edge for a 1.91-cm-diameter hole.*

tion has developed near the hole. A second local delamination developed at the right edge of the hole (Fig. 12*c*) after another slight increase in applied load. These delaminated regions continued to propagate, first in short discrete increments (Fig. 12*d*), and then rapidly at the failure load (Fig. 12*e*). The failed specimen shown in Fig. 12*e* was cut along an axial line passing through the center of the hole. A photograph of the cross section of the specimen in Fig. 13 shows many local delaminations through the thickness of the laminate. These delaminations extend completely across the specimen width but extend only a short distance in the axial direction.

The test results for the hole specimens are presented in Table 4, and the effect of hole diameter on failure strain is shown in Fig. 14. Results from Table 2 for the control tests are also shown for comparison on the ordinate of Fig. 14. Specimen H1 with the 0.16-cm-diameter hole failed near an end support fixture like the control specimens and at about the same strain. Thus, local effects associated with the test fixture were more critical than those of the hole for this specimen. All other specimens failed in the hole region at applied strains that decrease as the hole diameter increases. The catastrophic failure threshold from Fig. 6 for specimens impacted at 100 m/s is also shown in Fig. 14 as a dashed line for comparison with the hole results.

A comparison of the hole results with the impact-damage results indicates that, for the projectile used in this investigation, impact speeds of about 100 m/s degrade the laminate compressive failure strain about 0.001 more than the largest hole studied. Impact speeds of about 50 to 60 m/s have little effect on the compressive failure strain even though ultrasonic C-scan inspection

indicates interior damage (Fig. 4*a*). However, a specimen loaded axially during impact at a speed of 50 to 60 m/s will fail at about the same strain as a specimen with a 0.64-cm-diameter hole. As indicated by a comparison of Figs. 9*a* and 12*b*, the load at which delamination occurs in specimens with holes and impact damage usually differs. Delamination can occur due to impact regardless of the applied load, and the delamination may not be evident from a visual inspection of the impacted surface. Sublaminates formed by impact-induced delamination can buckle locally, causing the delamination to propagate when the specimen is loaded. For a specimen with a hole, delamination is not initiated until the applied axial load is high enough to cause a local failure at the hole boundary. Thus, the loads necessary to propagate delaminations could be different for specimens with impact damage or holes, and the use of hole-strength data to predict impact-damage strength may be questionable.

Cyclic Load Tests

The test parameters and results for the cyclic-load specimens are presented in Table 5. Three specimens without impact damage were subjected to at least one million cycles with maximum applied axial strains of 0.003, 0.004, and 0.005, respectively. These specimens showed no evidence of any change in stiffness due to the cyclic loading and there was no evidence of interior damage from ultrasonic C-scan inspection due to cyclic loading.

Four unloaded specimens were impacted by projectiles at speeds of about 100 m/s and then loaded cyclically with various maximum applied strain levels. The initial impact damage was similar to that of the other specimens impacted at this speed and reported in the previous section. Three of the four impact-damaged specimens failed at or less than 173 000 cycles; the specimen with the lowest maximum applied strain did not fail before the test was terminated at a million cycles. The maximum cyclic strains and the static failure strains for specimens impacted without any applied axial load are shown in Fig. 15. The open circles on the abscissa represent the impact speeds for the unloaded impact specimens and the filled circles represent their residual failure strain. The results from Table 2 for the control specimens are shown for comparison as filled circles on the ordinate. The open square in Fig. 15 represents a test where the load was cycled a million times without failure. The filled squares represent tests where failure occurred within a million cycles. The maximum cyclic strains that failed these specimens are below the residual strength of the corresponding statically loaded specimens. During cyclic loading the impact-induced delaminated region buckled cyclically out of plane. Specimen C6 failed by progressive delamination that started to grow after about 140 000 cycles. The growth of the delaminated region was monitored by observing the changes in the spalled region of the brittle lacquer on the specimen as shown by the photo-

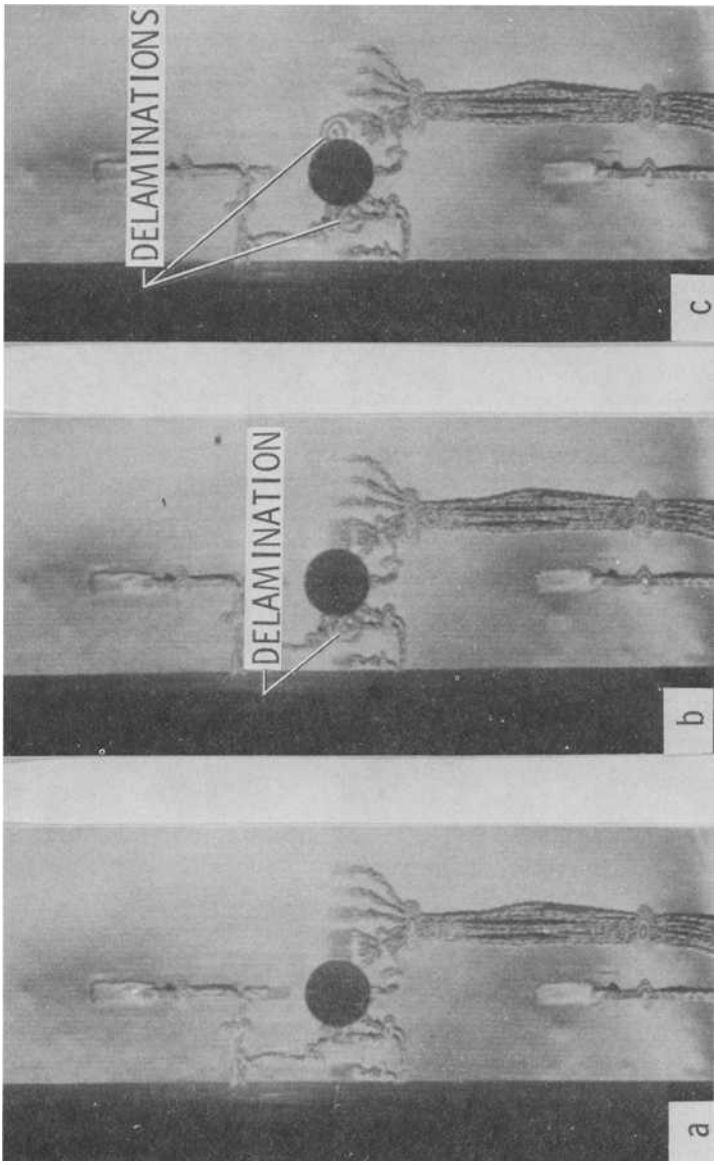
DELAMINATIONS
DELAMINATION
a
b
c

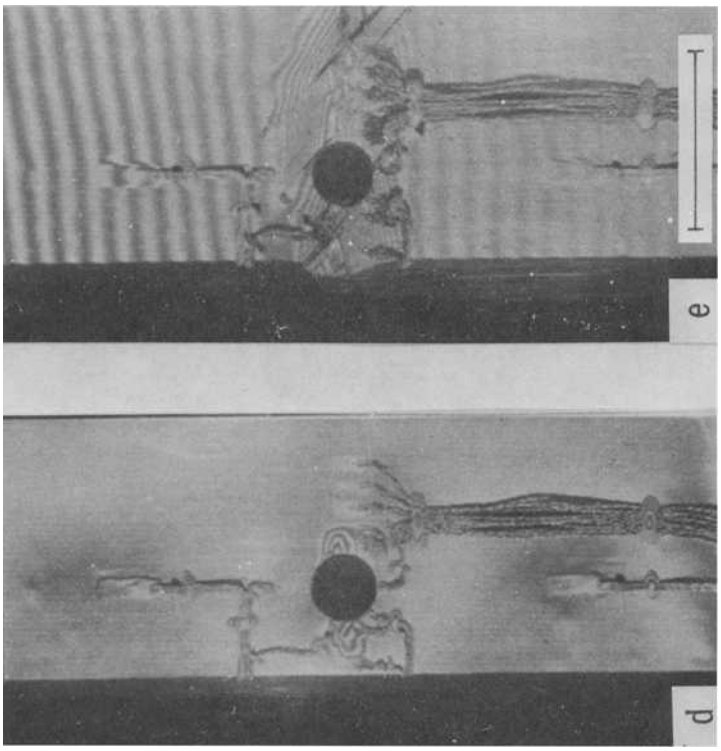

FIG. 12—*Local delamination in hole region and propagation to failure for 1.91-cm-diameter hole:* (a) *92.8 percent of ultimate load, no delamination;* (b)*95.4 percent of ultimate load, delamination to left of hole;* (c) *95.9 percent of ultimate load, additional delamination to right of hole;* (d) *98.1 percent of ultimate load, delamination growth;* (e) *failed specimen. Scale mark indicates 5 cm.*

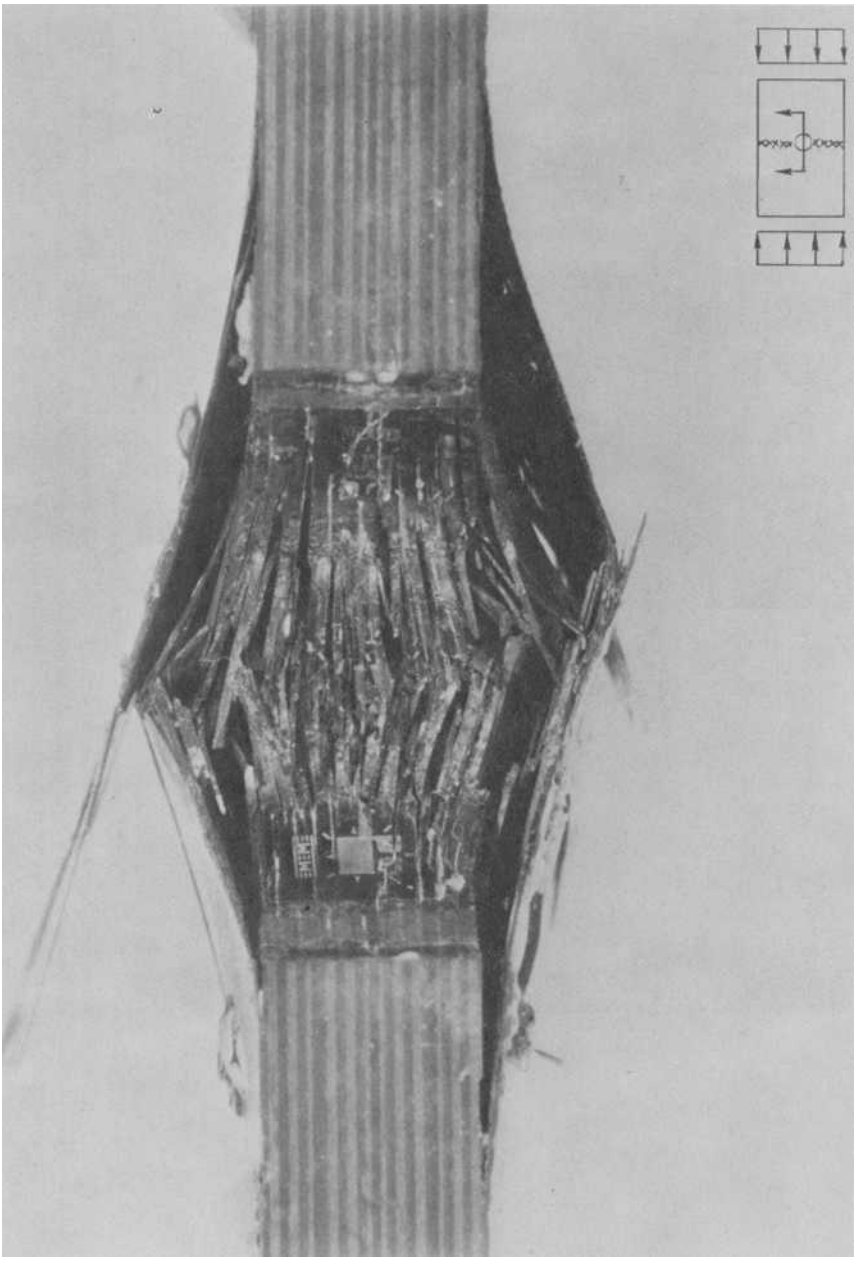

FIG. 13—*Cross section of a failed specimen with a 1.91-cm-diameter hole.*

TABLE 4—*Test results for circular hole specimens.*

Specimen	Thickness, cm	Hole Diameter, cm	Failure Strain	Failure Load, kN
H1	0.65	0.16	0.0088	471
H2	0.70	0.64	0.0070	343
H3	0.69	1.27	0.0057	297
H4	0.69	1.91	0.0045	252
H5	0.70	1.91	0.0045	250
H6	0.69	2.54	0.0045	265
H7	0.70	2.54	0.0044	228
H8	0.69	3.18	0.0040	201
H9	0.69	3.81	0.0039	190
H10	0.69	3.81	0.0039	190

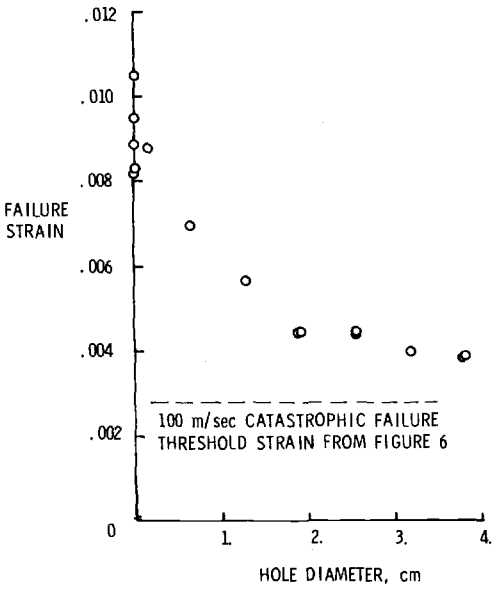

FIG. 14—*Effect of hole diameter on laminate compressive strength.*

graphs in Fig. 16. Changes in the spallation pattern of the brittle lacquer provided a direct way to monitor visually the growth of subsurface damage. At the conclusion of this test the specimen was inspected ultrasonically, and the results indicated that the failure was confined to the spalled region shown in Fig. 16*c*.

The impact damage in Specimen C4 did not grow after a million cycles and the specimen was statically loaded to failure to determine its residual strength. The specimen failed through the impact-damaged region at an applied strain of 0.0034, which is on the same order as the statically loaded im-

TABLE 5—*Test results for cyclic compression-compression loaded specimens.*

	Test Conditions			Results	
Specimen	Projectile Impact Speed, m/s	Maximum Applied Strain	R^a	Number of Cycles in Millions	Response
C1	0	0.0030	35.9	1.73	no damage, test terminated
C2	0	0.0040	45.8	1.0	no damage, test terminated
C3	0	0.0050	58.3	1.0	no damage, test terminated
C4	100	0.0020	24.0	1.0	no damage growth, test terminated
C5	101	0.0022	26.0	0.042	failed during test
C6	96	0.0025	28.8	0.173	slow delamination growth to failure
C7	96	0.0026	31.3	0.016	failed during test

[a] R is the ratio of minimum to maximum applied loads.

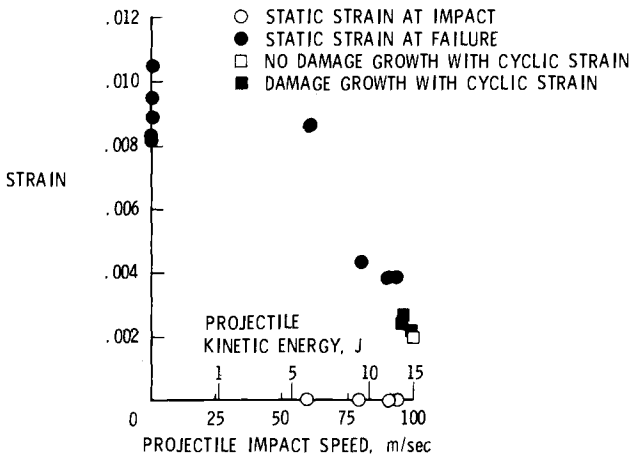

FIG. 15—*Effect of cyclic compression-compression loading on the residual strength of impact-damaged specimens.*

pact specimens. These preliminary data suggest that cyclic compression loading of an impact-damaged laminate may further degrade the residual strength.

Concluding Remarks

An experimental investigation was conducted to determine the effect of low-velocity impact damage and unloaded circular holes on the compressive strength of a 48-ply orthotropic laminate made of unidirectional Thornel 300

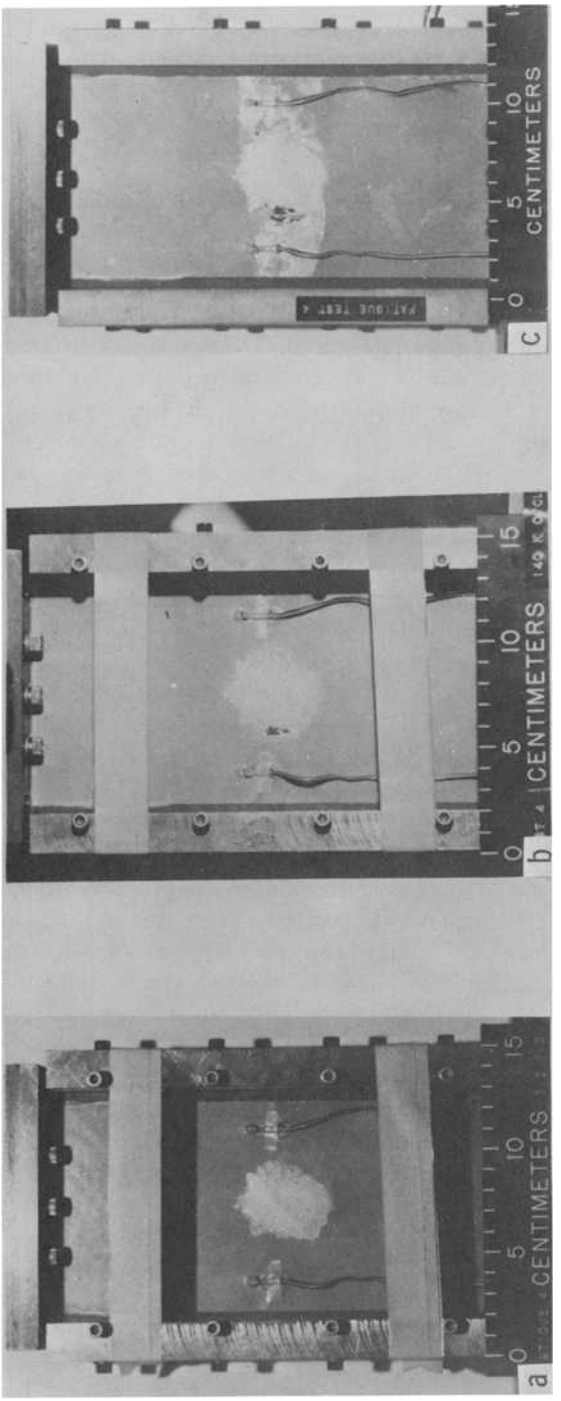

FIG. 16—*Effect of cyclic compression-compression loading on a laminate with impact damage. Brittle lacquer spalling reflects damage growth. Maximum applied axial strain is equal to 0.0025:* (a) *specimen with initial impact damage;* (b) *specimen after 140 000 cycles;* (c) *specimen after failure at 173 000 cycles.*

graphite fibers preimpregnated with Narmco 5208 epoxy resin. Forty-two specimens were fabricated from unidirectional tapes laid up to form a $[\pm 45/0_2/\pm 45/0_2/\pm 45/0/90]_{2s}$ laminate and were tested by either static or cyclic compression.

Specimens were impacted by a 1.27-cm-diameter aluminum sphere with speeds ranging from 52 to 101 m/s. Some specimens were impacted without any applied compressive load and then loaded to failure to determine their residual strength. Other specimens were loaded to a prescribed axial compressive strain and impacted while at that applied load. Loaded specimens that did not fail catastrophically on impact were inspected for damage and subsequently loaded to failure to determine their residual strength. For the range of projectile speeds considered, low-velocity impact damage caused extensive local interior damage in the laminate in the form of matrix cracking and delamination without causing any visible external damage at the impact site. Low-velocity impact damage can seriously degrade the static compressive strength of the laminate. Specimens that fail at axial strains above 0.008 in the undamaged condition can fail at strains as low as 0.0031 when impacted at 100 m/s. The compressive strength of specimens impacted while loaded axially is lower than that of specimens impacted without any applied axial load. This difference indicates there is a coupling between the local deformation due to impact and the applied compressive strain. Once local interior damage occurs, it can propagate across the specimen as the applied load is increased and can fail the specimen.

Cyclic compression-compression loading can further degrade the compression strength of impact-damaged specimens. Specimens impacted at 100 m/s failed after less than a million cycles for maximum applied axial cyclic strains below the static residual strength values.

Circular holes can also reduce the static compressive strength of the laminate. The failure strain of the specimens decreased as the hole diameter was increased. Specimens impacted at speeds of 100 m/s failed at lower applied axial strains than the specimen with the largest hole diameter tested. A distinction between the effects of holes and impact damage is the load at which delamination occurs. Impact-induced delamination occurs on impact for sufficiently high impact speeds regardless of the applied strain level. For holes, delamination occurs near the hole boundary when the applied strain is sufficiently high to cause local failure due to local strain concentrations. Because of this difference between holes and impact damage, the use of hole-strength data to predict impact-damage strength may be questionable when high compressive strains must be carried.

References

[1] Rhodes, M. D., Williams, J. G., and Starnes, J. H., Jr., "Effect of Low-Velocity Impact Damage on the Compressive Strength of Graphite-Epoxy Hat-Stiffened Panels," NASA

Report TN D-8411, National Aeronautics and Space Administration, Washington, D. C., April 1977.

[2] Rhodes, M. D., Williams, J. G., and Starnes, J. H., Jr., *The Society of Advanced Materials and Process Engineering Series*, Vol. 23, May 1978, pp.300–319.

[3] Viswanathan, A. V. and Tamekuni, M., "Elastic Buckling Analysis for Composite Stiffened Panels and Other Structures Subject to Biaxial Inplane Loads," NASA Report CR-2216, National Aeronautics and Space Administration, Washington, D. C., March 1973.

[4] Platt, R. J., Jr., and Thurston, L. B., Jr., "Holographic and Ultrasonic Detection of Bond Flaws in Aluminum Panels Reinforced with Boron-Epoxy," NASA Report TN D-7632, National Aeronautics and Space Administration, Washington, D. C., July 1974.

[5] Lekhnitskii, S. G., *Theory of Elasticity of an Anisotropic Elastic Body*, Holden-Day, San Francisco, Calif., 1963.

J. D. Labor[1]

Impact Damage Effects on the Strength of Advanced Composites

REFERENCE: Labor, J. D., **"Impact Damage Effects on the Strength of Advanced Composites,"** *Nondestructive Evaluation and Flaw Criticality for Composite Materials, ASTM STP 696.* R. B. Pipes, Ed., American Society for Testing and Materials, 1979, pp. 172-184.

ABSTRACT: This paper discusses the effect of flaws created by impact damage on the strength of graphite/epoxy panels that were tested as sandwich beams and as skin panels on box beams. A majority of the panels were exposed to random spectrum fatigue loads prior to failing them under static loading conditions. The maximum loads in the fatigue spectrum were scaled to provide a strain equal to the B-basis matrix failure strain for the resin system used. Box beam skin panels were designed to fail by compressive panel buckling in order to evaluate the effect of the impact damage on the buckling strength of the panels. All testing was conducted at room temperature on panels with no moisture conditioning.

Marginally visible damage was found to cause a strength loss up to 35 percent in compression but less in tension. Acoustic C-scan inspections showed that none of the impact damage sizes grew during spectrum loading. Panel stability was unaffected by localized impact damage. The most severe impact damage caused strength losses comparable to drilled fastener holes.

KEY WORDS: graphite/epoxy, composite materials, impact damage, strength testing, nondestructive tests

There is an increasing awareness by designers that impact damage can occur in certain advanced composite structural applications and that its effects must be considered. Various investigators [*1-7*][2] have shown that because resin matrix composites are basically brittle materials, they are readily damaged to some degree by impacts. It has been shown [*7-8*] that low-velocity impacts which leave no visible damage on the surface can cause matrix cracking, delaminations, and sometimes even broken fibers internally or on the back face. Although limited information is available on service

[1] Senior technical specialist, Northrop Corp., Aircraft Group, Hawthorne, Calif. 90250.
[2] The italic numbers in brackets refer to the list of references appended to this paper.

experience with advanced composite components, there have been some instances of damage [*9,10*], and methods for repairing such damage have been developed [*11,12*].

The effects of damage caused by impacts are of concern for two reasons. First, if damage causes a significant strength loss, safety of flight can be jeopardized. Many composite components are not strength critical, however, being governed by stiffness, minimum gage, or other requirements. For these parts, damage due to impact represents a cost consideration in terms of time out of service in addition to the direct cost of the necessary inspection and repair.

It is desirable, therefore, to provide as much impact resistance as possible in areas subject to impact damage, to the extent that additional weight or additional fabrication costs will permit. Ideally, materials would be used for which increased impact resistance could be obtained for little or no cost or weight penalty.

Toward this end, a study was made of several materials and configurations to identify their relative impact resistance [*8*]. By accurately measuring the energy absorbed during impacts at various levels of severity, certain trends were established. Briefly, laminates made with woven fabric prepreg were shown to require more energy for a specific measure of damage than laminates made with unidirectional tape. Similarly, it was shown that impact energy was increased by the addition of one or more plies of various high-strain-to-failure materials (S-glass, Kevlar, nylon, etc.).

Since these materials had shown some promise for increased resistance to impact, their structural behavior with damage present became of interest. A test program was planned to evaluate their strength properties, including the effects of random spectrum loading on potential damage growth. Two types of specimens were used. Full-depth honeycomb sandwich beams with a composite face sheet were tested to evaluate the basic strength of the materials in both tension and compression with and without impact damage. A separate series of tests used a box beam configuration in which the effect of the impact damage on the stability of the composite skin in compression was evaluated.

Experimental Procedures

Two basic materials were used for the test specimens. One was woven prepreg designated HMF133. This is an 8-harness satin weave with T300 graphite fibers in a 3501-6 epoxy matrix. For several specimens a surface ply of 181-style S-glass cloth prepregged with 3501-6 epoxy resin was added. Nominal ply thicknesses for these materials were 0.33 mm (0.013 in.) for the woven graphite and 0.25 mm (0.010 in.) for the S-glass.

The basic properties of these materials were not characterized in the current program. Limited strength data are available which indicate that

the strengths of the woven materials are less than for corresponding amounts of unidirectional tape material.

The configuration of the sandwich beam specimen is shown in Figure 1. The composite face sheets were four plies of woven material $[45/0]_s$. The glass surface ply used on some specimens was oriented at 45 deg. A titanium sheet 2.29 mm (0.090 in.) thick was used for the skin opposite the composite face. Both faces were cocured at 690 kPa (100 psi) and 177°C (350°F) with FM300 film adhesive to aluminum honeycomb core. The core in the test section was 130 kg/m^3 (8.1 lb/ft^3) with 3.175 mm (0.125 in.) cells, and was 38.1 mm (1.5 in.) thick. Overall specimen length was 55.9 cm (22 in.), and width 18.1 cm (7.12 in.). The core, adhesive, and titanium face sheet were all sized so that failure would occur in the composite face sheet.

The configuration of a box beam specimen is shown in Fig. 2. Four specimens had a monolithic test skin made of 12 plies of woven graphite/epoxy with one cocured surface ply of S-glass. The orientation was $[45_{GL}] + [(45_{GR}/0_{GR})_3]_s$. Two specimens had a sandwich skin consisting of an outer skin of four plies of woven graphite $[45/0]_s$ with a 45-deg surface layer of S-glass, a 4.75-mm-thick (0.187 in.), 50 kg/m^3 (3.1 lb/ft^3) aluminum honeycomb core, and an inner skin of one 45-deg ply of woven graphite/epoxy.

The test skins were attached to channel-shaped spars of 7075-T6 aluminum with steel bolts and the opposite skin was also 7075-T6 aluminum 4.83 mm (0.190 in.) thick. All specimens were 106 cm (42 in.) long. Specimens with monolithic test skins were 17.8 cm (7 in.) wide and those with sandwich skins were 29.2 cm (11.5 in.) wide.

One purpose of the box beams was to test the more damage-resistant material in a configuration which realistically represented an aircraft part with mechanical attachments to substructure. In addition, a specific purpose of the box beams was to evaluate the effects of impact damage on overall panel stability or, conversely, the effect of initial panel buckling on the possible propagation of impact damage during the spectrum loading. To correspond to a real design condition, the composite test panels were sized so that initial buckling would occur above a design limit load, but at less than design ultimate load. To obtain a severe loading condition, design limit load was defined to cause a strain of 4330 μm/m. For prediction of initial buckling, edge conditions between fixed and simply supported were assumed.

The test arrangement for the sandwich beams is shown in Fig. 3. A four-point loading was used to provide a constant moment in the center test section. A similar fixture was used for the box beam loading.

Most of the sandwich beams and all of the box beams were exposed to random spectrum fatigue loading. The spectrum selected was based on wing root bending of the F-5E aircraft. This spectrum is more severe in terms of the relative number of high loads versus low loads than most

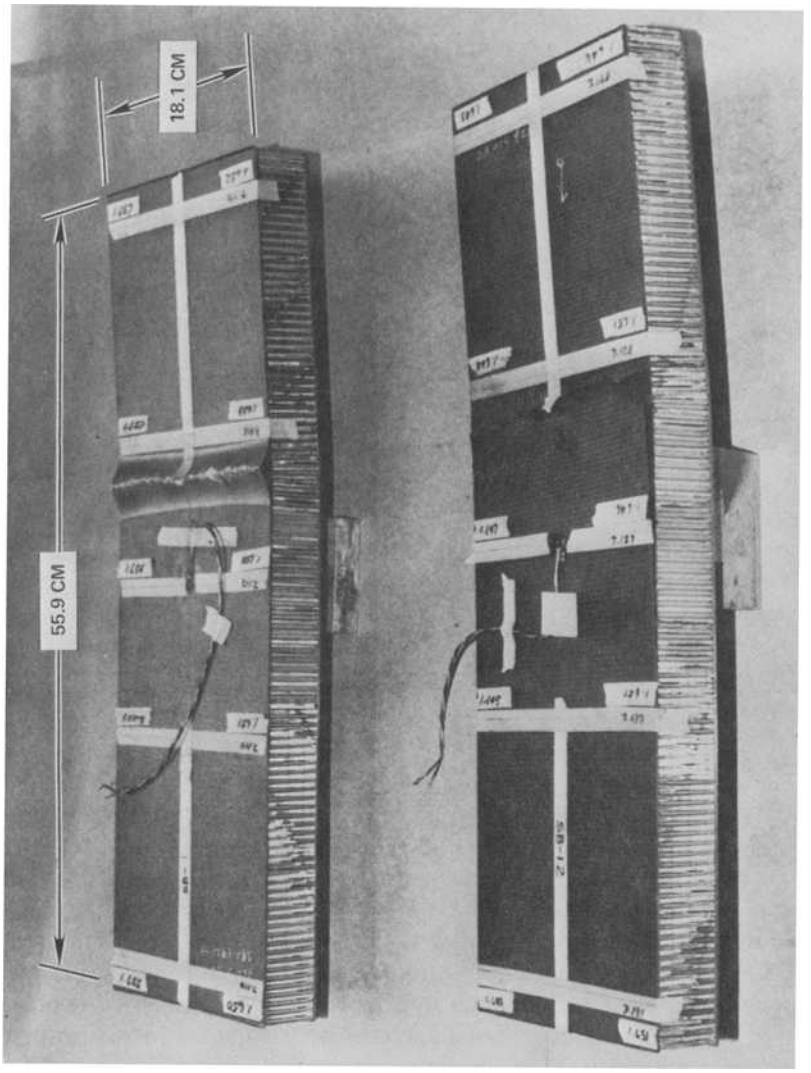

FIG. 1—*Sandwich beam specimens.*

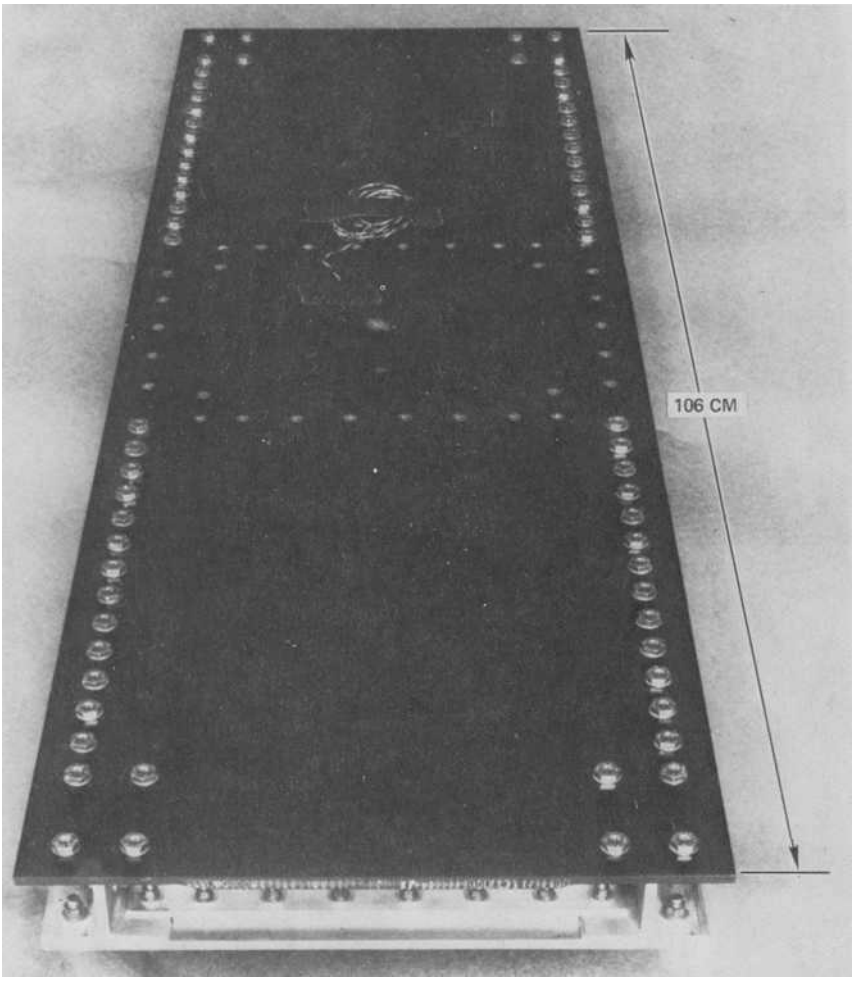

FIG. 2—*Box beam specimen.*

spectra used for other aircraft parts, such as tail surfaces. The spectrum used did not include load reversal. Approximately one-half million loading conditions are applied per lifetime, and typically two lifetimes of loading were used for each specimen. Loading rates were adjusted to ensure that specimen response did not effect the correct magnitude of loading.

The maximum load in the spectrum was established as the load at which the spanwise strain was 4550 μm/m. This strain level is the B-basis room-temperature dry matrix tensile failure strain for the 3501-6 resin system as determined for AS/3501-6 unidirectional tape, and has been considered to apply also for matrix failure criteria for the woven material with the same resin system. The same maximum strain was used for compression

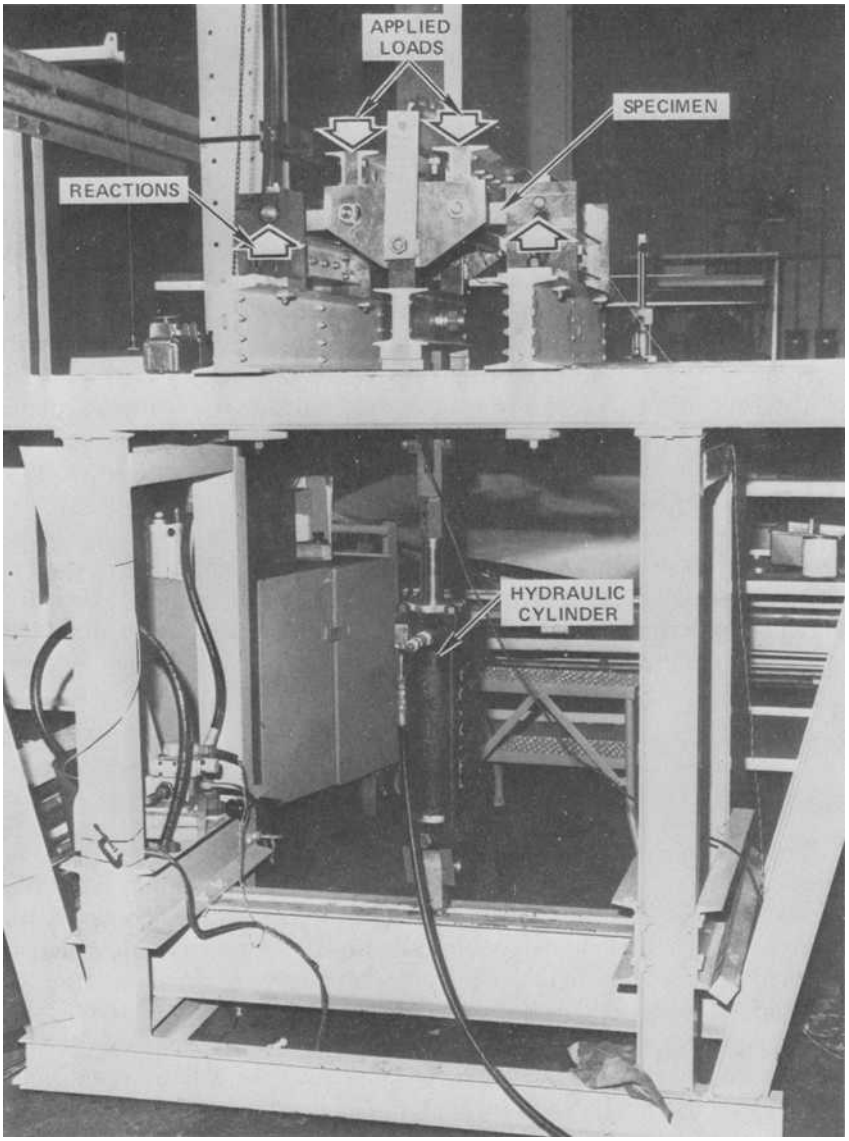

FIG. 3—*Sandwich beam test arrangement.*

spectrum loading, and is considered severe based on typical design allowables for laminates with fastener holes.

All specimens had strain gages applied remote from the damage. Strains were checked prior to spectrum loading and the predicted loading was adjusted slightly when necessary so that spectrum loading did cause the desired maximum strain levels. Strains were also monitored periodically

during spectrum load exposure, and recorded during static loading to failure for each specimen.

Except for undamaged control specimens, each beam had some form of initial damage. A 15.9-mm-(0.625 in.) diameter hole was drilled in the specimens as the limiting case of impact damage that was made using a 15.9-mm (0.625 in.) spherical steel impactor. Impacts referred to as "visible" typically caused a slight surface indentation but little or no fiber breakage on the impacted surface. Specimens with a surface ply of glass cloth showed less indentation because of the ductility of the glass, although a small area of lighter color was noticeable due to localized delamination of the glass ply. Impact referred to as "severe" caused significant broken fibers with the impactor penetrating approximately 7.6 mm (0.3 in.) through the face sheet. "Visible heel" damage was caused by impact with a wedge-shaped rubber impactor and typically caused a depression with a maximum depth of 1.93 mm (0.076 in.), a width of 38 mm (1.5 in.) in the spanwise direction, and a length of 63 mm (2.5 in.) across the specimen, with no surface fiber breakage.

Each specimen containing impact damage was acoustically inspected and C-scan records made both before and after spectrum load exposure. Through-transmission acoustic equipment was used with waterjets for a coupling medium. Appropriate frequencies and gain settings were used to indicate the maximum size of damage.

Experimental Results

Sandwich Beams

Table 1 summarizes the sandwich beam test results and also lists the type of spectrum load exposure for each specimen. For those that failed during spectrum loading, the strain caused by the load which caused the failure is shown. Residual strength is shown for specimens which survived two lifetimes of spectrum loading. Values for stress are computed from the applied load using the nominal skin thickness, which includes the thickness of the glass plies used.

Several observations can be made by comparing the data from individual specimens. First, it is significant that several specimens with either drilled holes or severe impact damage failed before completing two lifetimes of spectrum loading. This indicates that the spectrum, with a maximum load that caused a strain of 4550 μm/m, is a severe loading condition, probably more severe than typical composite parts would ever experience in actual service.

By comparison of the strains which caused failure during spectrum loading, it is apparent that the strength loss due to a severe impact which penetrates the laminate is approximately the same as that caused by a

TABLE 1—*Sandwich beam test results.*

Specimen No.	Glass Surface Ply	Initial Damage	Initial Damage Size, mm	Spectrum Loading		Final Damage Size, mm	Residual Strength		
				Type[a]	Strain at Failure, $\mu m/m$[b]		Stress MPa[c]	Strain $\mu m/m$	Type[a]
SB-1	yes	none	...	none	...	...	351.4	6850	C
-2		none	...	none	...	...	464.3	8682	T
-3		15.9-mm-diameter hole	...	T	...	...	336.1	6000	T
-4		15.9-mm-diameter hole	...	C	4200	...	...	...	...
-5		visible impact	16.5 diameter	T	...	16.5 diameter	386.7	7300	T
-6		visible impact	16.5 diameter	C	...	16.5 diameter	237.5	4650	C
-7		visible impact	15.2 diameter	none	...	...	[d]	[d]	C
-9		visible heel	31.7 × 63.5	T	...	31.7 × 63.5	444.4	8150	T
-10		visible heel	31.7 × 63.5	C	...	20.3 × 71.1	204.4	3500	C
-11		severe impact	21.6 diameter	C	4100	...	...	...	...
-12	no	none	...	none	...	...	397.3	7640	C
-13		15.9-mm-diameter hole	...	C	4550	...	...	...	...
-14		visible impact	16.5 diameter	none	...	...	265.9	4980	C
-15		visible impact	16.5 diameter	C	4100	...	...	...	...
-16		visible impact	12.7 diameter	C	...	15.2 × 20.3	262.1	4930	C
-17		severe impact	21.6 diameter	C	4170	...	...	...	...

[a] T = tension; C = compression.
[b] Values listed only for specimens which failed during spectrum loading.
[c] 100 MPa = 14.50 ksi.
[d] Failed by disbond of titanium skin at 177.5 MPa and 3480 $\mu m/m$.

drilled hole of similar size, that is, a reduction of 40 to 45 percent. The strains at failure for the impact are slightly lower than for the drilled hole, probably because of the localized delamination surrounding the impact, which tends to initiate a compressive failure by local buckling of individual plies. The less-severe visible impact damage causes a strength loss which is less than the loss for a drilled hole. In compression, the visible impact causes strains at failure which are approximately 35 percent less than for an undamage specimen, and in tension a 15 percent reduction was found.

The effect of compressive spectrum loading on a specimen with marginally visible impact damage is shown to be negligible by comparison of SB-16 with SB-14. For these specimens, residual strengths and strains to failure are nearly identical. Both were impacted with nearly the same severity, that is, 5.0 J (3.67 ft·lbf) absorbed for SB-14 and 4.5 J (3.28 ft·lbf) for SB-16. The conclusion to be drawn from these data is that essentially all the strength loss of these specimens (as compared with undamaged Specimen SB-12) is due to the impact damage, and that spectrum load exposure did not further degrade the strength. The apparent growth of the damage size for SB-16 as shown by C-scan measurements is felt to be caused primarily by a lack of exact repeatability in the C-scan images made at different times. For all other specimens, C-scan measurements indicated no growth of the damage, even with the severe spectrum used.

Previously reported data [*13*] have shown progressive delamination at fastener holes during cyclic loading. The lack of such progressive delamination for impact damage suggests that it may be caused, at least partially, by interlaminar tension at the free edge of the hole, since no such free edge exists for the visible impact damaged laminates.

Since all of the compressive failures involved face sheet instability, it was of interest to determine the full compressive strength of the face sheets. Compression coupons 51 mm (2 in.) wide by 76 mm (3 in.) long were cut from an undamaged area of the face sheets of Specimens SB-1 and SB-12 and the core was carefully removed to leave only the face sheet as the test coupon. These were tested in a fixture which fully contains the specimen and prevents local buckling of fibers in surface plies so that essentially the full-block compressive strength is measured. Both coupons failed at nearly identical strains of approximately 7800 μm/m, indicating that the sandwich beams which failed at 6850 and 7640 μm/m were approaching their full strength capability when face sheet instability occurred. Previous test data for the same woven graphite/epoxy material have shown similar strain levels at failure; that is, $\epsilon_1^c = 7307$ μm/m was 80 percent of the average test results and was used as a design allowable [*14*].

Specimens tested both with and without the glass surface ply provide approximately the same trends. However, failure modes frequently involved more delamination of the glass ply than of the graphite plies. In addition,

for corresponding specimens, those with the glass plies failed consistently at strain levels about 7 percent less than those without the glass plies.

Box Beams

Test results for box beams are summarized in Table 2. In addition to the visible and severe types of impact damage as previously described, one of the box beam skins was subjected to multiple impacts. Two impacts comparable to the visible impacts described were located 19 mm (0.75 in.) apart on a transverse line at midspan. Since damage size on the C-scans was larger than anticipated, the initial damage from the two adjacent impacts merged into one elongated damage area.

All six box beams survived spectrum loading and C-scans showed no significant change in the sizes of the damaged areas. Since maximum spectrum loads were near the theoretical buckling loads, it is significant that no further damage propagation occurred under such a potentially severe condition.

Back-to-back axial strain gages aligned in the spanwise direction were monitored during residual strength testing. A divergence of the two gage readings, which indicates out-of-plane bending caused by buckling, was noted for the undamaged monolithic panel, BB-1, starting at approximately 6500 μm/m, and the maximum strain at failure was 7700 μm/m. None of the other monolithic panels showed any overall panel buckling prior to failure, although local buckling of the plies on the inner face at the impact-damaged location appears to have precipitated the failure. There is no indication that the impact damage lowered the load required for overall panel buckling.

Back-to-back gage readings for both sandwich panels, BB-5 and BB-6, indicated initial panel buckling starting at approximately 2000 μm/m for both, which also indicates that the buckling load was not lowered by the impact damage on Panel BB-6. Because there was no local failure through the impact damage on Panel BB-6, and because both the damaged and undamaged panels failed by overall panel buckling at nearly the same strains, it appears that the effect of the damage was minor.

Discussion and Conclusions

Tests have shown that marginally visible impact damage which might go undetected on composite panels can reduce their strength to approximately 65 percent of the unflawed laminate strength for compressive loading and to approximately 85 percent for tensile loading. The remaining strength and strains to failure are still well above the ultimate allowables commonly used for design purposes as limited by matrix failure criteria or based on

TABLE 2—*Box beam test results.*

Specimen No.	Test Skin Configuration	Initial Damage	Initial Damage Size, mm	Final Damage Size, mm	Residual Strength	
					Stress MPa	Strain $\mu m/m^a$
BB-1	12-ply woven graphite/ epoxy + 1 ply of S-glass	none	...	...	414.1	7700
BB-2	↓	visible impact	22.9 × 25.4	25.4 diameter	268.9	5200
BB-3	↓	severe impact	27.9 diameter	27.9 diameter	245.3	4900
BB-4	↓	multiple impacts	22.9 × 43.2	25.4 × 43.2	231.2	4400
BB-5	4-ply woven graphite/ epoxy + 1 ply of S-glass on 50-kg/m^3 (3.1 lb/ft^3) aluminum core	none	...	...	243.3	4950
BB-6	↓	visible impact	25.4 diameter	25.4 diameter	220.7	4350

[a] Strain gage on outer face.

fastener attachment holes. Acoustic C-scans have also shown that the damages due to impacts have not grown during severe spectrum loading, even for panels loaded in compression near their buckling strength.

These observations indicate that minor undetected impact damage on composite parts would not jeopardize safety of flight. Furthermore, impact damage which is more severe, causing obvious broken fibers on the surface, is approximately as damaging as drilled holes, with the remaining strength still above design ultimate allowables. The obvious damage would undoubtedly be repaired.

Although the observations which have been made are reassuring, it is necessary to note the limitations of the data. All testing was done at room temperature on specimens which had no moisture conditioning. Both elevated temperature and moisture are known to degrade the properties of the matrix. The damage from impacts causes considerable delamination and matrix cracking prior to any visible fiber failure, and under adverse environmental conditions it is possible that damage could grow during fatigue loading and cause larger reductions in strength than were found for dry materials. In addition, all testing was done on [±45/0/90] laminates and variations in the results might occur for more highly orthotropic laminates, for thicker laminates, or for larger damaged areas.

In spite of the observed limitations, the results reported here tend to indicate that, while the brittle nature of composite material makes it susceptible to impact damage, it generally retains sufficient strength to provide for safety of flight with impact damage present because of the relatively low design allowables that are commonly used.

Acknowledgment

This work was accomplished as a part of Air Force Flight Dynamics Laboratory Contract No. F33615-76-C-3142, "Service/Maintainability of Advanced Composite Structures."

References

[1] Greszczuk, L. B. and Chao, H. in *Composite Materials: Testing and Design (Fourth Conference)*, *ASTM STP 617*. American Society for Testing and Materials, 1977, pp. 389-408.

[2] Adsit, N. R. and Waszczak, J. P., "Investigation of Damage Tolerance of Graphite/Epoxy Structures and Related Design Implications," NADC-76387-30, Naval Air Development Center, Dec. 1976.

[3] McQuillen, E. J., Gause, L. W., and Llorens, R. E., "Low Velocity Transverse Normal Impact of Gr/Ep Composite Laminates," *Journal of Composite Materials*. Vol. 10, 1976, pp. 79-91.

[4] Rhodes, M. D., Williams, J. G., and Starnes, J. H., Jr., "Effect of Low Velocity Impact Damage on the Compressive Strength of Graphite/Epoxy Hat-Stiffened Panels," NASA TMX-73988, National Aeronautics and Space Administration, Washington, D.C., Dec. 1976.

[5] Oplinger, D. W. and Slepetz, J. M. in *Foreign Object Impact Damage to Composites. ASTM STP 568.* American Society for Testing and Materials, 1975, pp. 30–48.

[6] Husman, G. E., Whitney, J. M., and Halpin, J. C. in *Foreign Object Impact Damage to Composites. ASTM STP 568.* American Society for Testing and Materials, 1975, pp. 92–113.

[7] Bhatia, N. M., "Impact Damage Tolerance of Graphite/Epoxy Laminates," Army Symposium on Solid Mechanics, Army Materials and Mechanics Research Center, Oct. 1978.

[8] Labor, J. D., "Service/Maintainability of Advanced Composite Structures," AFFDL Contract No. F33615-76-C-3142, Quarterly Progress Report No. 3, Air Force Flight Dynamics Laboratory, Wright-Patterson AFB, Ohio, Aug. 1977.

[9] Stoecklin, R. L., "737 Graphite Composite Flight Spoiler Flight Service Evaluation," NASA Contract NAS1-11668, NASA CR 145207, National Aeronautics and Space Administration, Washington, D.C., Aug. 1977.

[10] Bennett, T., "Impact Damage Service Experience on C5 Slat and F4 Rudder," Department of Defense/National Aeronautics and Space Administration Mini-Symposium on Effect of Impact Damage on the Behavior of Composite Materials, Bergamo Conference Center, Dayton, Ohio, Nov. 1977.

[11] Studer, V. J. and LaSalle, R. M., "Repair Procedures for Advanced Composite Structures," AFFDL-TR-76-57, Air Force Flight Dynamics Laboratory, Wright-Patterson AFB, Ohio, Dec. 1976.

[12] Kiger, R. W. and Myhre, S. H., "Large Area Composite Structure Repair," AFFDL-TR-78-83, Air Force Flight Dynamics Laboratory, Wright-Patterson AFB, Ohio, 1978.

[13] Rosenfeld, M. S. and Huang, S. L., "Fatigue Characteristics of Graphite/Epoxy Laminates Under Compression Loading," *Journal of Aircraft*, Vol. 15, No. 5, May 1978, pp. 264–268.

[14] Noyes, J. V., "Wing/Fuselage Critical Component Development Program," Contract No. F33615-77-C-5078, Interim Report, Air Force Flight Dynamics Laboratory, Wright-Patterson AFB, Ohio, Feb. 1978.

W. I. Griffith,[1] *M. F. Kanninen,*[2] *and E. F. Rybicki*[2]

A Fracture Mechanics Approach to the Analysis of Graphite/Epoxy Laminated Precracked Tension Panels

REFERENCE: Griffith, W. I., Kanninen, M. F., and Rybicki, E. F., "**A Fracture Mechanics Approach to the Analysis of Graphite/Epoxy Laminated Precracked Tension Panels,**" *Nondestructive Evaluation and Flaw Criticality for Composite Materials, ASTM STP 696*, R. B. Pipes, Ed., American Society for Testing and Materials, 1979, pp. 185-201.

ABSTRACT: A methodology for the prediction of fracture in fiber composite laminates under monotonically increasing load is presented. In the model, laminate behavior is based on damage growth in individual plies with a fracture mechanics approach being used to continually assess the damage in each ply. Within each ply, damage may occur by crack extension parallel to or perpendicular to the fiber orientation in the ply. Critical values of strain energy release rate for both modes of damage are inferred from experimental data on center-cracked, zero-degree unidirectional laminates. At present, interply interactions are neglected. Despite this severe oversimplification, a comparison of strength predictions from the laminate model shows reasonable agreement with experimental results, both quantitatively and qualitatively, for $[0/90]_{4s}$, $[\pm 45]_{4s}$, and $[0/\pm 45/0]_{2s}$ graphite/epoxy laminates. The features of the laminate model are contrasted with the models of a number of other researchers.

KEY WORDS: fracture properties, composite materials, graphite/epoxy, crack propagation, nondestructive tests

The failure of a structural component can generally be connected with a crack-like defect in the material. For fiber composite laminates, flaws can be introduced by the cutting and bonding processes necessary to fabricate a serviceable structure. Damage by mishandling and other accidents can also occur during installation and service. Even if these can be avoided, com-

[1]Research associate, Department of Engineering Science and Mechanics, Virginia Polytechnic Institute and State University, Blacksburg, Va. 24061.
[2]Senior research scientists, Battelle's Columbus Laboratories, Columbus, Ohio 43201.

posites always contain inherent defects that can trigger the failure process. Hence, it is logical to focus upon the initiation and growth of crack-like defects in devising a prediction of the strength of fiber-reinforced composite laminates.

Fracture mechanics is an analysis procedure that encompasses all material failure processes emanating from a crack-like defect. Yet, most applications of fracture mechanics to fiber composites have not met with nearly the degree of success that has been achieved for metals and other engineering materials. The reason is that, in most instances, techniques successful for metals have been applied to composites without regard for the special character of crack growth in these materials. In particular, direct applications of the stress intensity factor have been made using linear elastic fracture mechanics (LEFM)—a specialization applicable to homogeneous, isotropic materials where crack growth occurs in a self-similar manner. These assumptions are not usually appropriate for composites. Consequently, a fracture mechanics approach which does not require these debilitating assumptions will provide a more realistic approach for fiber composite materials.

The research described in this paper is aimed at the development of a mathematical model for laminate behavior based on damage growth in individual plies. The basis of the laminate model is the fracture mechanics treatment of crack growth in individual plies. This treatment uses the energy release rate as the driving force for crack growth. Specifically, the crack is allowed to grow in each ply in the direction in which an equality between the crack driving force and the fracture resistance corresponding to growth in that direction is first satisfied.

At the present stage of this work, crack driving forces for crack growth normal to and parallel to the fiber direction are computed for the individual plies in a laminate. As an expedient, the laminate calculations presently ignore any interaction between the plies. Crack propagation in each ply takes place in accord with the load carried by that ply, this being a function of the compliance of the ply relative to that of the laminate as a whole. As the load point displacement increases, localized crack growth occurs. The load is then redistributed among the plies as dictated by the compliance changes due to crack growth. The computation continues until every ply has been fractured.

Comparisons with experimental results on center-cracked graphite/epoxy panels obtained by Brinson and Yeow [*1,2*][3] and others [*3,4*], have been made. The results for final failure show that the maximum loads computed with the model are reasonable, particularly in view of the uncertainties in material properties that now exist. Other local failure events preceding final failure are identifiable and can qualitatively be correlated with events noted in the experiments of other investigators.

[3]The italic numbers in brackets refer to the list of references appended to this paper.

It is apparent that a great deal of interest exists in using acoustic emission (AE) techniques for fiber composites. Undoubtedly, AE can be a highly useful technique. Good success has already been achieved by many investigators in correlating peaks and valleys in the count rates with the imminence of failure in various systems. Neverthless, it seems clear that AE could be made much more effective if used concurrently with a failure analysis procedure.

The AE output must be due to micromechanical damage processes occurring in the material. The kind and severity of these processes will certainly depend upon the type of composite system and layup together with the applied loads and geometry (including stress raisers) of the component being tested. Clearly, therefore, calibrating the AE response with the integrity of the material in one set of conditions gives limited information about any other set of conditions. A great deal of testing must therefore be required to determine the effect of various parameters. Much of this could be avoided (and considerable confidence gained) if AE studies were accompanied by analyses in which the damage mechanisms giving rise to the AE counts were explicitly taken into account. This could be accomplished with the kind of analysis described in this paper. Other nondestructive testing (NDT) methods such as acoustic attenuation or low-level X-ray could similarly benefit.

The ultimate objective of the present work is to integrate a previously developed micromechanical failure analysis model [*5,6*] into the laminate model described here. Such an integration has not been attempted thus far.

The Laminate Failure Model

Basis of the Approach

A fracture mechanics approach generally takes the point of view that there is a dominant flaw that can be considered to the exclusion of all others. Thus, it is consistent with the general aim of the research to consider the type of experiment performed by Brinson and Yeow [*1,2*], Yeow et al [*3*], Yeow and Brinson [*4*], and others; that is, long through-thickness cracks in laminated tension panels. More specifically, a fracture mechanics treatment, generalized to treat crack growth in a fiber composite material, is used here to obtain the extent of damage and consequent stiffness reductions in each individual ply in a laminate. The basic idealization used in accomplishing this is to treat a lamina as a two-dimensional elastic body (plane stress) with directionally dependent properties. As shown in Fig. 1, crack growth emanating from a preexisting crack or conventional stress riser is considered to occur either across or along the fibers. The linear elastic strain energy release rate corresponding to crack growth in a given direction is then taken as the parameter governing crack growth.

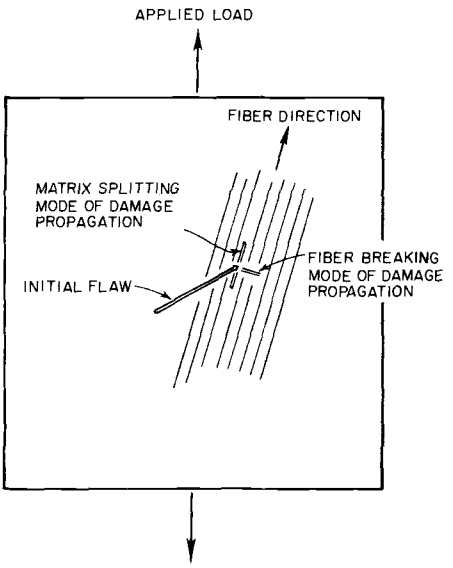

FIG. 1—*Unidirectional (single ply) panel containing a flaw showing conceptually the two possible in-plane damage propagation modes permitted in the analysis.*

Consistent with a suggestion made by Jones [*7*], a treatment modifying laminated plate theory to take account of the degradation and failure of individual plies via a "parallel-spring" model has been adopted. This procedure for integrating lamina behavior into the laminate is illustrated in Fig. 2. As is appropriate for an initial attempt, the current computations are kept as simple as possible by assuming that no interaction occurs between the individual plies. It is also assumed that, once a crack has propagated completely across a ply, its residual strength can be neglected. A further idealization is that the problem is two-dimensional; that is, the flaw can be considered to penetrate completely through the ply thickness.

We emphasize that these are *not* necessary assumptions for the success of the present model. They are instead only simplifications adopted temporarily for expediency in testing the model. More realistic ply interaction conditions together with interply delamination can and will be included at a later stage of the model development.

Computational Procedure

The energy release rate is calculated from the elastic crack closure energy for an increment of growth from a stress riser taken as a crack-like flaw. Crack growth is permitted as either fiber breakage or as matrix splitting. Which event will actually occur depends upon which of the two conditions

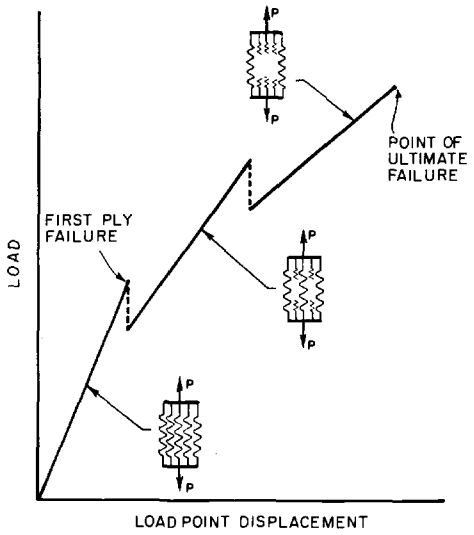

FIG. 2—*Conceptual illustration of the parallel spring model for the failure of a laminate.*

$$G_{FB} = R_{FB} \text{ and } G_{MS} < R_{MS}$$

or (1)

$$G_{MS} = R_{MS} \text{ and } G_{FB} < R_{FB}$$

is satisfied at the lower applied stress. Here, G denotes the strain energy release rate while R denotes the fracture resistance. The subscripts FB and MS denote crack advance involving fiber breakage and matrix splitting, respectively.

By comparing the energy release rate for a given load level and crack length to the critical value for growth in that direction, the progress of crack growth within a ply can be completely characterized. These results then serve as the elements of the parallel-spring model shown in Fig. 2. But, before the model can be used to make failure predictions, a number of preliminary calculations must be made. The first of these calculations is to establish critical values for R_{MS} and R_{FB}. This requires the use of both experimental data and finite-element calculations.

Experimental load-crosshead deflection charts from center-cracked T300/934 graphite/epoxy unidirectional laminates were supplied by Prof. H. F. Brinson and his associates at Virginia Polytechnic Institute and State University. When loading is parallel to the fibers, these laminates first split axially at both crack tips, as illustrated conceptually in Fig. 3. Only after the cracks have advanced to leave two remaining ligaments does significant fiber

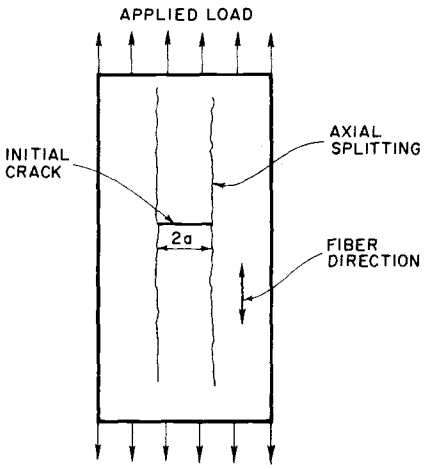

FIG. 3—*Axial splitting in a unidirectional fiber composite center-cracked panel with the load in the fiber direction.*

breakage occur. The onset of axial splitting is accompanied by momentary drops of load, increased acoustic emission, and visible damage growth. Thus, it was possible to estimate critical load levels for the onset of axial splitting in these experiments. The average load at which splitting began for three different 16-ply, 0.223-cm-thick laminates with a crack length to panel width ratio, a/W, of 0.25 was 315.8 mPa. Finite-element calculations were employed to convert this load level to a critical strain energy release rate for matrix splitting, as described in the following.

Finite-Element Computations

The finite-element models utilized plane-stress linear elastic constant-strain triangles or quadrilateral elements assembled from four triangles. Orthotropic properties, obtained experimentally from the same laminate, were used. These were

$$E_{11} = 124.1 \text{ GPa}$$
$$E_{22} = 13.8 \text{ GPa}$$
$$\nu_{12} = 0.3$$
$$G_{12} = 6.9 \text{ GPa}$$

The actual specimens were 2.54 cm wide and 12.7 cm long. To reduce the size of the finite-element models, however, a 5.08-cm gage length was used.

Crack extension in the axial direction was facilitated by using a double

set of nodes along the axial splitting path. These nodes were coupled by orthogonal linear springs in both in-plane degrees of freedom. The crack was mathematically allowed to advance by uncoupling the springs at adjacent nodes. Thus, a series of calculations was made representing various lengths of axial splitting. After the equilibrium nodal positions were calculated, the springs were again used to calculate the energy release rate using the method of crack closure devised by Rybicki and Kanninen [*8*].

In the crack closure method of Ref *8*, the forces between adjacent nodes at the crack tip are evaluated using the spring constant and the calculated relative displacements. The forces are determined with respect to a coordinate system parallel to the direction of crack advance. A relatively large spring constant is used so that compatibility at the crack tip is ensured to at least six significant figures.[4] The relative displacements of the adjacent nodes are calculated with respect to the same coordinate system. If the mesh density is uniform and the amount of crack advance is sufficiently small, the imposition of the forces calculated at the crack tip removes the relative displacements at the adjacent nodes. From the preceding argument it then follows that the strain energy release rate can be calculated from

$$G = \frac{1}{2t\Delta a}\left\{F_{xi}\delta_{xi} + F_{yi}\delta_{yi}\right\} \tag{2}$$

where t is the ply thickness. Notice that this takes the linear sum of the contributions from the "opening" mode and "sliding" mode of crack advance. In Eq 2 Δa is the (hypothetical) increment of crack advance (equal in this paper to the width of a finite element) while F and δ denote nodal forces and crack opening displacements (COD's), respectively. A more complete description of the basis for this calculation can be found in Ref *8*.

The results of a series of calculations for the zero degree, $a/W = 0.25$, graphite/epoxy laminate are shown in Fig. 4. These show G as a function of c where c is the distance that axial splitting has progressed. The ends of the model were constrained to move with constant displacement as is approximately the case in a testing machine. Three different grids were used for the zero-degree case. Each mesh contained detail in a different area of crack advance, c. All of the results from the analyses indicated reasonably uniform convergence.

A degree of arbitrariness exists at the present time with regard to the values of R_{MS} and R_{FB}. Values suitable for this analysis have not been directly determined. Hence, as an expedient, the test results on the zero-degree unidirectional graphite/epoxy specimens tested by Brinson and Yeow [*1,2*] were used to infer these values. To do this, some initial axial flaw length must

[4]The spring may not be made arbitrarily large since inadequate significant digits may be left to calculate coupled nodal forces, or the system of equations may become ill-conditioned, or both.

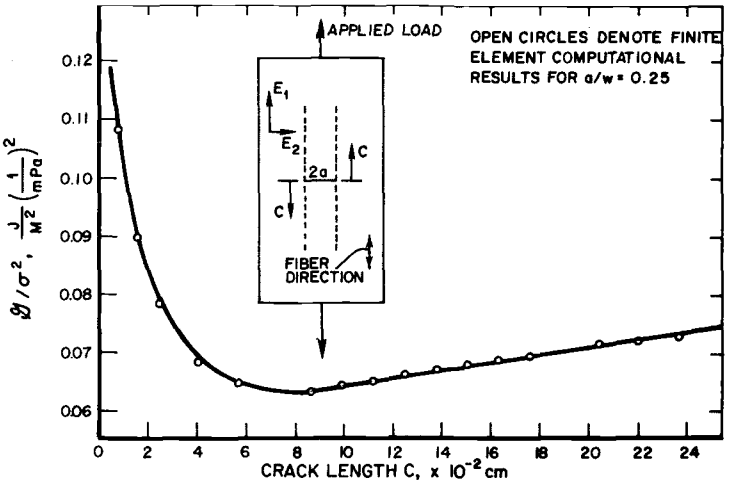

FIG. 4—*Calculated values of crack-driving force for a graphite/epoxy center-cracked ply as a function of crack propagation distance in the direction normal to the initial crack. Load applied in the fiber direction; initial crack normal to fiber direction.*

be specified; NB, the value for zero crack growth is unrealistic, as shown in Fig. 4. Following the suggestion implicit in the Brinson and Yeow results, a flaw length of one ply thickness, or 0.014 cm, was chosen. When the necessary corrections for model thickness are made, R_{MS}, the critical strain energy release rate for matrix splitting, is found to be 2440 J/M^2.

A similar calculation was performed for the ligaments that remain after axial splitting has occurred. In this instance crack growth is selfsimilar and aligned with the principal axes of the material. The assumed flaw length was again taken as one ply thicknesses, 0.014 cm. Then, R_{FB}, the critical strain energy for fiber breakage, was calculated to be 20 800 J/M^2. This is roughly an order of magnitude greater than that calculated for matrix failure. These values of critical energy release rate were used for all the subsequent analyses.

Calculations were also performed for 30, 45, 60, and 90-deg plies. In each of these cases, a G versus c relationship was determined for the same ply width ratio and properties described earlier. The G versus c curves for 0, 30, 45, and 60-deg plies are shown in Fig. 5. Conceptually, matrix splitting as well as fiber breakage can be allowed in each ply. Thus, the 60-deg model for matrix splitting could be used as the 30-deg case for fiber breakage after the appropriate material property rotation. Calculations were performed only for an a/W of 0.25 since each new a/W value requires a new family of finite-element models.

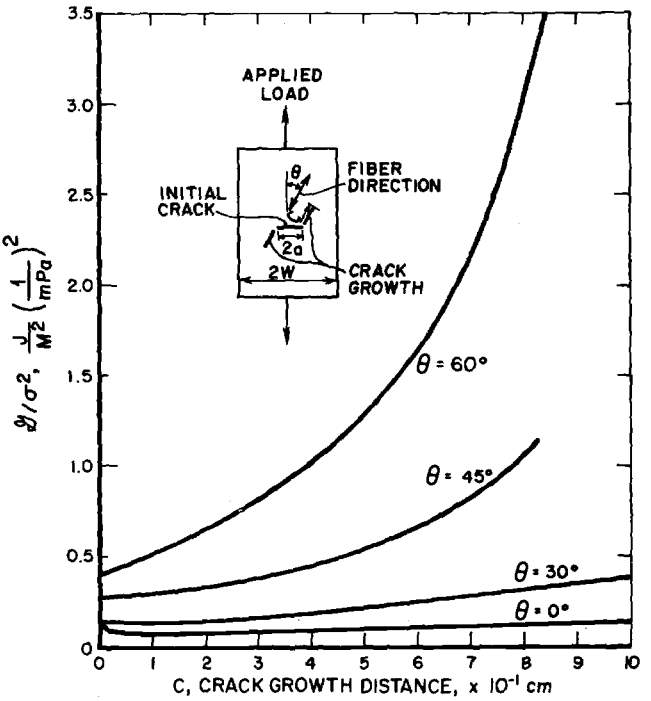

FIG. 5—*Calculated values of crack-driving force to center-cracked graphite/epoxy plies as a function of crack propagation distance in the fiber direction.* (a/W = 0.25).

Comparison with Experimental Results on Graphite/Epoxy Panels

A large body of experimental results obtained by Brinson and Yeow and others [*1-4*] on graphite/epoxy laminates is available for comparison with the computational results. These data were obtained in uniaxial tension tests performed on 2.54-cm-wide (1-in.) specimens containing edge and center cracks together with central holes and square cutouts. Both unidirectional and multiply laminates were tested. Brinson and Yeow observed that, for all tests on unidirectional laminates, crack growth was in the matrix with the fracture planes parallel to the fiber direction. With the exception of the $[0/\pm 30/0]_{2s}$ tests, the fracture planes for the pre-cracked multidirectional laminates were also generally parallel to the direction of the principal fibers.

Observations on the jagged appearance of the fracture surface in their tests led Brinson and Yeow to conclude that crack growth occurred in inner and outer plies at different times and directions. They also noticed

that audible noise accompanied the instantaneous load reductions that occurred several times prior to complete fracture. For the outer plies, these could be visually connected with stable crack growth occurring in an outer ply. It therefore seems likely that the load reductions observed in the test are always due to crack growth somewhere in the laminate.

Other observations made by Brinson and Yeow relevant to the model predictions involve the inherent flaws found in the material. Typical flaws identified with scanning electron microscopy (SEM) techniques include cylindrical voids and crack-like defects with lengths on the order of a ply thickness [*4*]. It is of considerable interest to notice that, in some tests using very small initial cracks and holes, fracture actually occurred on other sections. In those instances Brinson and Yeow conjectured that an inherent flaw at the actual fracture site was more critical than the cut-in artificial flaw. Their results appear to be roughly consistent with an inherent flaw length equal to one ply thickness. As stated in the foregoing, this observation has led to the adoption of this "inherent" crack length for the determination of the characteristic fracture resistance values for the laminate calculations.

Computations with the parallel-spring laminate model of Fig. 2 can be made for comparison with the experimental results of Brinson and Yeow and others using the calculated G-values shown in Fig. 5 together with the R values deduced earlier. Using such results, the crack is allowed to grow in each ply in accord with Eq 1. In this way, the "spring constant" for each ply as a function of crack growth is determined.

For a given layup, the "springs" corresponding to the plies comprising the laminate are assembled. Crack propagation in each ply is then monitored as the load point displacement is increased monotonically. As the load increases, localized crack growth occurs. The load is then redistributed among the plies as dictated by compliance changes due to crack growth. The computation continues until every ply has been fractured.

Comparisons of the failure loads for four different graphite/epoxy center-cracked laminates, all with $a/W = 0.25$ initially, are shown in Figs. 6–9. It can be seen that the predictions are reasonable although, to be sure, substantial room for improvement exists. Of perhaps more significance, local failure events preceding final failure are identifiable and presumably can be correlated with experimental observations. This has not yet been accomplished.

Discussion

Limitations of the Current Model

While the laminate failure model described in this paper offers something beyond the usual assumption of homogeneous orthotropy, it is clearly

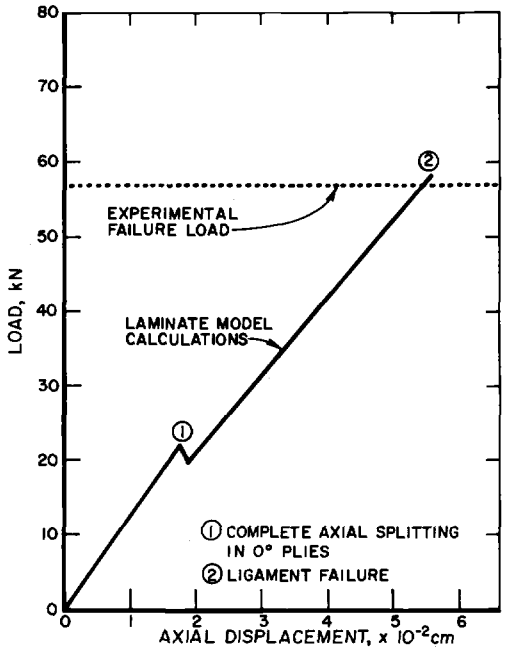

FIG. 6—*Calculated load-deflection for a center-cracked graphite/epoxy panel* $[0]_{8s}$ *laminate.*

not without limitations. One particularly sensitive aspect is the establishment of the critical strain energy release rate for matrix failure. In the calculation, both the flaw size and load at incipient growth had to be estimated. Obviously, an error in either of these parameters would lead to an error in R_{MS}. This error would then be reflected in all subsequent calculations involving nonzero-degree plies. In the absence of a direct determination, an improvement in the estimate might be obtained using experimental data from off-angle unidirectional laminates as well as zero-degree laminates, or by using zero-degree laminates of several different a/W 's. If the values of R_{MS} determined in this fashion varied significantly, other considerations for flaw length and load at first failure would have to be made.

One factor tending to make the laminate model overestimate the strength of flawed laminates consisting of zero-degree and off-axis plies is that the strength of the zero-degree plies dominates. However, a detailed examination of the experimental data of Brinson and Yeow and others indicates that, in flawed composites, the strength of the zero-degree plies is significantly less than the same plies in a unidirectional zero-degree laminate. Thus, some form of ply interaction and damage transmittance is obviously

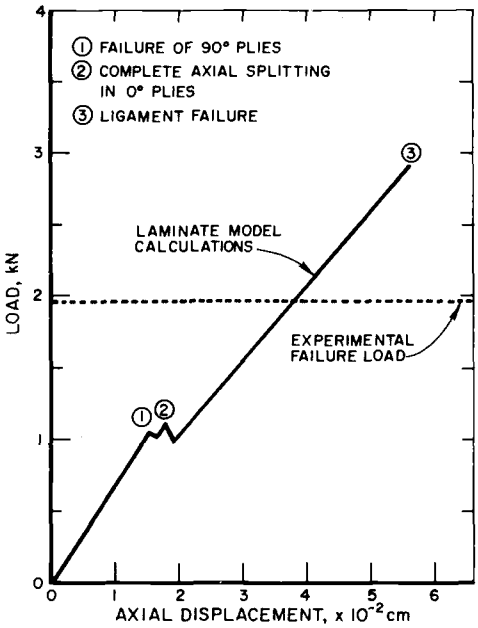

FIG. 7—*Calculated load-deflection for a center-cracked graphite/epoxy panel* $[0/90]_{4s}$ *laminate.*

present. At the same time, neglect of interply delamination will cause the model to underestimate the true strength. Consequently, as the comparisons of Figs. 6–9 show, the model is neither an over nor an under-estimate of the strength of angle-ply laminates.

As a further example of the limitations of the current model, consider a laminate with some 90-deg plies. In an uncoupled model, these 90-deg plies will fail at a very low load and will be left out of the subsequent simulation. In reality, however, these plies will continue to restrain the laminate in the transverse direction. This transverse restraint would likely contribute to the stiffness of off-axis plies and possibly help restrain damage in such plies. This brings to mind several possibilities for including some interlaminar effects while maintaining an uncoupled model. For example, the boundary conditions on transverse material properties could easily be modified to account for adjacent 90-deg plies. The introduction of such effects will be considered in subsequent work.

Qualitative Comparison with Experimental Results

Strain distributions around crack tips in quasi-isotropic graphite/epoxy specimens were determined by Daniel [*9*] from isochromatic fringe patterns

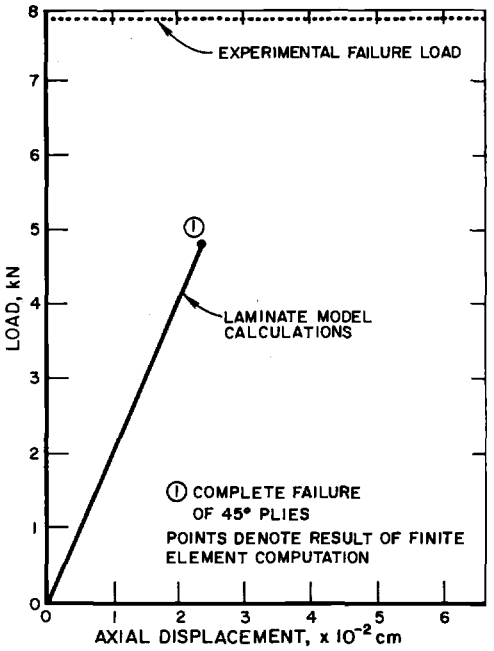

FIG. 8—*Calculated load-deflection for a center-cracked graphite/epoxy panel* $[\pm 45]_{4s}$ *laminate.*

in photoelastic coatings. In general agreement with the observations of Mandell et al [*10*], these revealed a damage zone consisting of subcracks along the fibers of individual plies together with local delamination and fiber breakage. Daniel noted that the size of the damage zone increases with applied stress up to some critical size at which the specimen fails catastrophically. For a $[0/\pm 45/90]_{2s}$ graphite/epoxy specimen with a 2.54-cm crack, the mean diameter of the damage zone just prior to failure was approximately 0.5 cm. Daniel also reported that deviations from nonlinearity (for example, in strains measured ahead of the crack tip with increasing load) accompanied by audible cracking noises occurred at about the point of crack growth initiation predicted by LEFM. These findings are clearly consistent with the approach described in the preceding.

A qualitative comparison with the results obtained by Morris and Hahn [*11*] can also be made. They conducted a series of experiments on center-cracked graphite/epoxy tension specimens to obtain crack growth resistance curves. Their results typically show a series of rapid COD changes followed by linear behavior, in essential agreement with the model results shown in Figs. 6-9. It is of interest to note that Morris and Hahn reported that the rapid changes in COD were accompanied by audible levels of acoustic

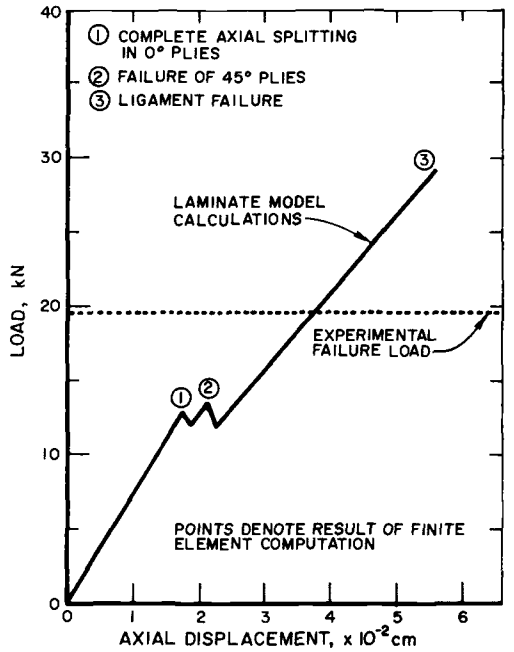

FIG. 9—*Calculated load-deflection for a center-cracked graphite/epoxy panel* $[0/\pm 45/0]_{2s}$ *laminate.*

emission. But, no visible self-similar crack growth was observed. This is also completely consistent with the predictions of the model described in this paper.

Other Laminate Failure Analyses

Approaches to determine the strength of laminates are well summarized by Jones [*7*]. It is clear from this and other more recent accounts appearing in the literature—for example, Pagano [*12*] and Rowlands [*13*]—that existing laminate failure theories are mainly based on either

1. a phenomenological failure surface and a characteristic volume for the laminate, or
2. a ply failure criterion used in conjunction with a classical laminated plate theory.

The disadvantage of a phenomenological approach, for example, such as that of Wu [*14,15*] is that new tests must be conducted to define the failure surface for each new laminate configuration. Wu has demonstrated, however, that the surface can be evaluated with a minimum number of

tests. This approach does not have a basic predictive capability, but it is of definite use when designing with a given group of laminate configurations.

The ply failure-laminated plate theory approaches are of two types, those predicting first-ply failure and those allowing for sequential failure in individual laminae. In some instances the first-ply failure models, such as that of Rotem and Hashin [*16*], also predict laminate failure for symmetric angle-ply laminates. More often, however, the first-ply failure models greatly underestimate laminate strength. Simplified approaches have been given by Tsai and Azzi [*17*], by Petit and Waddoups [*18*], and by Chiu [*19*]. Typically, these treatments assume a stepwise degradation in laminate properties to account for sequential failure of individual laminae. The work of Rosen et al [*20*], McLaughlin et al [*21,22*], and Kulkarni et al [*23*] has primarily concerned itself with the failure mechanisms associated with fatigue. Damage was assumed to occur parallel to or transverse to the fiber direction on a ply-by-ply basis. These approaches [*17-23*] have recognized that, not only does progressive damage in the individual plies generally precede the ultimate failure of the laminate, but the quantitative determination of the damage is a necessary prerequisite to determining the final failure state.

Nuismer and Brown [*24*] consider that, as partial or total failure of a ply takes place, corresponding stiffness changes can be made in the laminate via laminated plate theory. They use an ultimate-strain criterion as the ply failure criterion. Specifically, failure is assumed to occur in the fiber direction when the strain in that direction reaches a critical value, while matrix failure occurs when either the transverse or shear strains reach critical values. These critical values are determined from an experiment. A finite-element computation is then used to trace the damage and, hence, to determine the appropriate ply stiffness.

Nuismer and Brown further take account of the fact that, if a ply fails in the fiber direction, it retains its stiffness in the transverse direction. Similarly, if a ply sustains a matrix failure, it loses its transverse and shear stiffnesses, but not its stiffness in the fiber direction. The stiffness of the laminate at any stage of the loading is determined using the appropriate ply stiffnesses (that is, either the stiffness of the ply or the reduced stiffness corresponding to either matrix or fiber failure) in conjunction with laminated plate theory. As Nuismer and Brown point out, laminated plate theory is justifiable provided extensive delamination does not precede ultimate failure.

Clearly, the laminate failure analysis described in this paper has much in common with that of Nuismer and Brown. The major difference is in the local ply damage criteria that are used. In our work, local damage is computed as directional crack growth, as suggested by Harrison [*25*]. In the Nuismer-Brown approach the exact form of the damage is ignored.

Crack growth as a local failure mechanism is well supported by ex-

perimental observations [*1-4,9,10*]. Thus, ours would seem to be a fundamentally correct approach. In addition, our point of view provides a way of relating ply failure to micromechanical damage mechanisms (that is, through establishing critical values of G with the micromechanical model) that perhaps cannot be done in any more suitable manner.

For a more thorough treatment of the limitations of current applications of fracture mechanics to composite materials, the reader is referred to the work of Smith [*26*], Kanninen et al [*27*], and Dharan [*28*].

Acknowledgments

The authors would like to thank D. P. Williams of National Aeronautics and Space Administration (NASA) headquarters, Washington, D.C., and H. G. Nelson of the Materials and Physical Sciences Branch, NASA-Ames Research Center, Moffet Field, Calif., for their continued support of this work. In addition, the authors would like to thank H. F. Brinson of Virginia Polytechnic Institute and State University, Blacksburg, Va., and Y. T. Yeow of Allied Chemical, Morristown, N.J., for supplying additional data not found in their papers.

References

[*1*] Brinson, H. F. and Yeow, Y. T., "An Investigation of the Failure and Fracture Behavior of Graphite/Epoxy Laminates," VPISU Report to NASA-Ames Research Center, No. VPI-E-75-23, Virginia Polytechnic Institute and State University, Blacksburg, Va., 1975.

[*2*] Brinson, H. F. and Yeow, Y. T. in *Composite Materials: Testing and Design (Fourth Conference)*, *ASTM STP 617*, American Society for Testing and Materials, 1977, pp. 18-38.

[*3*] Yeow, Y. T., Morris, D. H., and Brinson, H. F., "A Correlative Study Between Analysis and Experiment on the Fracture Behavior of Graphite/Epoxy Laminates," VPISU Report to NASA-Ames Research Center, No. VPI-E-77-20, Virginia Polytechnic Institute and State University, Blacksburg, Va., 1977.

[*4*] Yeow, Y. T. and Brinson, H. F., "A Study of Damage Zones or Characteristic Lengths as Related to the Fracture Behavior of Graphite/Epoxy Laminates," VPISU Report to NASA-Ames Research Center VPI-3-77-15, Virginia Polytechnic Institute and State University, Blacksburg, Va., 1977.

[*5*] Kanninen, M. F., Rybicki, E. F., Griffith, W. I., and Broek, D., "Fundamental Analysis of the Failure of Polymer-Based Fiber Reinforced Composites," NASA CR-2689, National Aeronautics and Space Administration, Washington, D.C., 1976.

[*6*] Kanninen, M. F., Rybicki, E. F., and Griffith, W. I. in *Composite Materials: Testing and Design (Fourth Conference)*, *ASTM STP 617*, American Society for Testing and Materials, 1977, pp. 53-69.

[*7*] Jones, R. M., *Mechanics of Composite Materials*, Scripta Book Co., Washington, D.C., 1975, pp. 188-210.

[*8*] Rybicki, E. F. and Kanninen, M. F., *Engineering Fracture Mechanics*, Vol. 9, 1977, p. 931.

[*9*] Daniel, I. M., *Experimental Mechanics*, Vol. 18, 1978, p. 246.

[*10*] Mandell, J. F., Wang, S., and McGarry, F. J., *Journal of Composite Materials*, Vol. 9, 1976, p. 266.

[*11*] Morris, D. H. and Hahn, H. T. in *Composite Materials: Testing and Design (Fourth*

Conference). ASTM STP 617, American Society for Testing and Materials, 1977, pp. 5–17.

[12] Pagano, N. J., *International Journal of Solids and Structures*, Vol. 14, 1978, p. 385.

[13] Rowlands, R. E., *Experimental Mechanics*, Vol. 18, 1978, p. 253.

[14] Wu, E. M. in *Composite Materials. Vol. 5, Fracture and Fatigue.* L. J. Broutman and R. H. Krock, Eds., Academic Press, New York, 1974, p. 191.

[15] Wu, E. M. in *Proceedings*, U.S.-U.S.S.R. Seminar on Fracture of Composite Materials, Riga, Latvia, U.S.S.R., 4–7 Sept. 1978.

[16] Rotem, A. and Hashin, Z., *Journal of Composite Materials*, Vol. 9, 1975, p. 191.

[17] Tsai, S. W. and Azzi, V. D., *Journal*, American Institute of Aeronautics and Astronautics, Vol. 4, 1966, p. 296.

[18] Petit, P. H. and Waddoups, M. E., *Journal of Composite Materials*, Vol. 3, 1969, p. 2.

[19] Chiu, K. D., *Journal of Composite Materials*, Vol. 3, 1969, p. 578.

[20] Rosen, B. W., Kulkarni, S. V., and McLaughlin, P. V., Jr. in *Inelastic Behavior of Composite Materials*, C. T. Herakovich, Ed., American Society of Mechanical Engineers AMD, Vol. 13, 1975.

[21] McLaughlin, P. V., Jr., Kulkarni, S. V., Huang, S. W., and Rosen, B. W. in *Proceedings*, National Aeronautics and Space Administration/U.S. Air Force Third Conference on Fibrous Composites in Flight Vehicle Design, Williamsburg, Va., Nov. 1075; also NASA CR-132747, 1975.

[22] McLaughlin, P. V., Jr., Huang, S. V., and Rosen, B. W., "Investigation of Failure Mechanisms in Fiber Composite Laminates," TFR 7508, Materials Sciences Corp., Final Report, Contract No. N62269-74-0662, NADA, Warminster, Pa., June 1975.

[23] Kulkarni, S. V., McLaughlin, P. V., Jr., Pipes, R. B., and Rosen, B. W. in *Composite Materials: Testing and Design (Fourth Conference), ASTM STP 617*, American Society for Testing and Materials, 1977, pp. 70–92.

[24] Nuismer, R. J., and Brown, G. E. in *Proceedings*, 13th Annual Meeting of the Society of Engineering Science, 1–3 Nov. 1976.

[25] Harrison, N. L., *Fibre Science and Technology*, Vol. 6, 1973, p. 25.

[26] Smith, C. W., *Inelastic Behavior of Composite Materials*, American Society of Mechanical Engineers, AMD 13, C. T. Herakovich, Ed., 1975, p. 517.

[27] Kanninen, M. F., Rybicki, E. F., and Brinson, H. F., *Composites*, Vol. 7, 1977, pp. 17–22.

[28] Dharan, C. K. H., *Journal of Engineering Materials and Technology*, Vol. 100, 1978, pp. 233–247.

Summary

The detection of flaws in materials and structures has long been the task of the nondestructive evaluation (NDE) analyst. In evaluating the integrity of metallic structural elements, nondestructive inspection has focused upon detection of both surface and subsurface flaws and determination of an effective flaw size. Given the flaw size, classical fracture mechanics technology has been employed to predict its rate of growth and the critical length which corresponds to failure of the element. Inherent in this approach is the assumption that microscopic flaws and imperfections grow into macroscopic cracks when the structural element containing the flaw is subjected to a fatigue loading or an adverse environment or to both. In addition, the macroscopic isotropy of metallic materials meant that generally Mode I fracture dominated the material response. Hence, for contemporary materials and structures, technology sufficient to detect and assess the criticality of flaws upon component life has been developed. Of course, there continues to be a need to refine NDE techniques and crack growth models.

Fiber-reinforced composite materials are more complex at the macroscopic level than contemporary metallic materials. These materials therefore present the nondestructive evaluation analyst with new problems and challenges both in flaw detection and in assessing the influence of flaw characteristics upon strength. Also, determination of the influence of a given flaw geometry upon strength and stiffness is considerably more complex than the classical fracture mechanics approach due to the anisotropy of the fiber-reinforced composite materials.

Until recently, there was no formal quantitative criterion for inspection of advanced composite materials. With the introduction of the Aircraft Structural Integrity Program (MIL-STD-1503A) and the Federal Aviation Administration certification requirements for civil composite commercial airframe structures (FAR, Part 25), a quantitative approach to inspection and damage tolerance has been evolved. Allowable flaw limits and damage growth rates must be determined to establish inspection intervals and the flaw characteristics which make repair mandatory. Thus, a technology to assess the effects of defects must be developed.

In order to develop the nondestructive inspection technology for fiber-reinforced composite materials, it is necessary that the development of detection capabilities be coupled with development of the technology that

is capable of assessing the influence of flaw geometry upon strength and stiffness. By coupling the development of these two capabilities, it will be possible to define critical flaw geometries and thereby focus development of detection techniques for these geometries. To that end, this publication addresses the problem of (1) the definition of strength and service life limiting flaws in graphite fiber-reinforced epoxy matrix composites, (2) identification of flaw parameters for use in quantifying the severity of such flaws, and (3) nondestructive testing for identifying these flaws and measuring flaw parameters.

Defects in fiber-reinforced composite laminated structural components originate during fabrication and during service. Fabrication or "birth defects" may occur during the preparation of the prepreg, laminate layup and cure, or structural component assembly. Service damage will occur due to a fatigue load spectrum, impact or foreign object damage (FOD), or environment. Various types of flaws may originate and propagate during the service phase (life) of a structural component. These flaws may be present as an isolated defect; they may originate from other built-in imperfections such as cutouts and bolted joints; or, finally, flaws may accumulate in a random fashion resulting in an interaction among them. Also, the initiation and growth of flaws are a function of the superimposed loads and the laminate construction.

It is important to realize what the objectives of the critical flaw identification problem should be. Of primary interest is the development of the methodology to determine whether the structure is fail-safe or damge-tolerant. That is, catastrophic crack growth must be avoided. In order to understand this, the flaw or damage growth rate and the time of its unstable propagation must be known. Also, such information is essential to determine periodic intervals for the inspection of in-service structural components. Another objective of any investigation concerning failure should be the ability to define failure appropriately. Should fracture as defined by a certain crack length be defined as failure, or should there be an alternative definition of degradation? An important reason for the use of composites is their high stiffness, and any reduction in stiffness will reflect adversely on some design parameters like the buckling load or the flutter speed. Thus, excessive stiffness degradation can also be termed as failure.

In order to arrive at a definition of a critical flaw, it is necessary to formulate analytical models, which are capable of predicting the direction and rate of growth and critical size (at failure). Due to the complexity of the problem of failure in composite laminates, it is impossible for a single analytical model to encompass the whole spectrum of fracture and fatigue.

In summary, the problem of "critical flaw evaluation" consists of essentially of three tasks:

1. Determining *what* (type of flaw), *where* (location of the flaw), *when*

(inspection interval), and *how* (type of nondestructive inspection [NDI] technique) to look for flaws? This aspect of the problem lies within the realm of the nondestructive testing and evaluation (NDT&E) specialist.

2. Formulation of analytical models for different predictions of critical flaw sizes, mode of failure, lifetime, and residual strength.

3. Experimental confirmation of analysis predictions and establishing a one-to-one correspondence between "real-world" composite structures and environment and laboratory coupon tests.

The various papers in this session address one or more of the aforementioned tasks.

In the paper by Konishi and Lo, the results of an industry-wide flaw likelihood criticality survey have been qualitatively assessed. Flaws have been categorized on the basis of their associated stress field disturbance and studies have been conducted to determine the optimal NDE process to detect these flaws. Analytic studies have been performed to determine the disturbance to the stress field in the vicinity of the flaws and to assess their criticality, that is, their structural integrity. These results were used to define coupons and elements where the elements represent structures that are in a realistic stress state. Preliminary results of the accelerated "worst expected" case environmental fatigue testing show, as expected, that advanced composites are relatively damage-tolerant.

The effect of low-velocity impact damage and circular holes on the compressive strength of a thick orthotropic graphite/epoxy laminate has been studied experimentally by Starnes, Rhodes, and Williams. Some specimens were impacted and then loaded to failure in compression to determine their residual strength. Other specimens were loaded to a prescribed compressive strain and impacted at that applied load. Some of these loaded specimens failed catastrophically on impact. Specimens that did not fail catastrophically were subsequently loaded to failure in compression to determine their residual static strength. It was found that low-velocity impact damage can seriously degrade the laminate static compressive strength. Several impact-damaged specimens were subjected to low-strain compression-compression cyclic loading, which was found to degrade further the laminate compressive strength. Specimens with circular holes were loaded in static compression to failure and it was found that holes can also degrade the compressive strength of the laminate.

Labor discusses the effect of flaws created by impact damage on the strength of graphite/epoxy panels that were tested as sandwich beams and as skin panels on box beams. A majority of the panels were exposed to random spectrum fatigue loads prior to failing them under static loading conditions. The maximum loads in the fatigue spectrum were scaled to provide a strain equal to the B-basis matrix failure strain for the resin system used. Box beam skin panels were designed to fail by compressive

panel buckling in order to evaluate the effect of the impact damage on the buckling strength of the panels. All testing was conducted at room temperature on panels with no moisture conditioning. Marginally visible damage was found to cause a strength loss up to 35 percent in compression but less in tension. Acoustic C-scan inspections showed that none of the impact damage sizes grew during spectrum loading. Panel stability was unaffected by localized impact damage. The most severe impact damage caused strength losses comparable to drilled fastener holes.

The potential application of the Holscan 400 as a laboratory tool to monitor and characterize impact damage in graphite/epoxy composite material has been evaluated by Pettit. Impact damage in 16- to 32-ply-thick material was examined using a number of modifications in the basic system and the results evaluated in terms of impact damage characterization ability and ease of operation in a laboratory environment. The results showed several of the modifications to be needed to provide a system with the desired capability and ease of operation.

A methodology for the prediction of fracture in fiber composite laminates is presented in the paper by Griffith, Kanninen, and Rybicki. The laminate behavior is based on damage growth in individual plies. A fracture mechanics approach is used to continually assess the damage in each ply under monitonically increasing load. Within each ply, damage may occur by crack extension parallel to or perpendicular to the fiber orientation in the ply. Critical values of strain energy release rate for both modes of damage are inferred from experimental data on center-cracked zero-degree unidirectional laminates. At present, the laminate model assumes the plies to act in an independent manner. A comparison of experimental results and strength predictions from the laminate model is made. Reasonable agreement is shown both quantitatively and qualitatively. The features of the laminate model are contrasted with the models of a number of other researchers.

S. V. Kulkarni

Lawrence Livermore Laboratories, Livermore, Calif. 94550; coeditor.

Flaw Characterization in Composite Materials

C. D. Shirrell,[1] *W. H. Leisler,*[2] *and F. A. Sandow*[2]

Moisture-Induced Surface Damage in T300/5208 Graphite/Epoxy Laminates

REFERENCE: Shirrell, C. D., Leisler, W. H., and Sandow, F. A., **"Moisture-Induced Surface Damage in T300/5208 Graphite/Epoxy Laminates,"** *Nondestructive Evaluation and Flaw Criticality for Composite Materials, ASTM STP 696,* R. B. Pipes, Ed., American Society for Testing and Materials, 1979, pp. 209-222.

ABSTRACT: A microscopic examination of hygrothermally exposed T300/5208 cross-ply laminates is described. Moisture-induced surface and edge microcracks were observed in specimens exposed at 82° and 9, 20, 37, 74, and 91 percent relative humidity or water immersion. Specimens exposed at similar relative humidities but at lower temperatures (21, 43, and 63°C) generally did not form microcracks.

The severity and frequency of the microcracking at 82°C increased with relative humidity. The majority of the microcracks were observed to be oriented parallel to the graphite fibers in the surface laminae. Specimens with extensive microcracks were also observed to exhibit non-Fickian diffusion phenomena during their hygrothermal exposure.

KEY WORDS: composite materials, moisture, swelling, surface cracks, non-Fickian diffusion, nondestructive tests

Water is a universally present compound capable of being absorbed and diffused into many polymers. In many cases this absorbed moisture can have significant deleterious effects upon the physical properties of the polymeric material. As a result, the utilization of polymers in structural applications is strongly dependent upon their long-term stability under the environmental conditions encountered during actual use.

The epoxy resins currently used as matrix material in advanced composites tend to be slightly hygroscopic and they can absorb as much as 6 to 10 percent moisture by weight. A direct consequence of this absorbed moisture in an epoxy composite laminate is a hydrostatic dilitation of the resin matrix.

[1]Formerly with the Air Force Flight Dynamics Laboratory, Wright-Patterson Air Force Base, Ohio 45433; presently, senior research engineer, Polymers Department, General Motors Research Laboratories, General Motors Technical Center, Warren, Mich. 48090.

[2]Engineering technician and aerospace engineer, respectively, Structural Mechanics Division, Air Force Flight Dynamics Laboratory, Wright-Patterson Air Force Base, Ohio 45433.

This induced dilitation coupled with transient conditions can produce nonuniform swelling through the thickness of a laminate. The swelling stresses thus induced may lead to the formation of microcracks and potentially degrade the mechanical properties of the composite.

As part of a study [*1,2*][3] to determine the equilibrium solubility, diffusivity, and diffusion mode of moisture in Narmco's T300/5208[4] graphite/epoxy material system, hygrothermally exposed specimens were examined by a scanning electron microscope (SEM) for the presence of moisture-induced microcracks. The nature and extent of this moisture-induced damage are presented in this paper.

Experimental

The materials and the hygrothermal exposure techniques used in this study have been described previously [*1,3*]. Briefly, specimens from a symmetrical [0/90] seven-ply T300/5208 panel were exposed to a total of 33 different hygrothermal environments. These conditions were made from combinations of four temperatures (21, 43, 63, or 82°C) with 12 humidities (0 through 98 percent relative humidity) or water immersion. Periodically the specimens were removed from their hygrothermal environments, placed in chambers of approximately the same relative humidity at room temperature, allowed to cool, and then weighed. After some length of time the specimens were observed to come to an equilibrium moisture content.

After the specimens had maintained this moisture content for several months, one specimen was randomly chosen from the replicate exposure set for microscopic examination. Due to size limitations of the SEM specimen chamber, it was necessary to section the large hygrothermally exposed specimens into smaller specimens with the approximate dimensions of 1.0 by 1.0 cm. The hygrothermally exposed edges of the small specimens were clearly marked to eliminate confusion with the unexposed edges during the microscopic examination.

Since it is possible only to view electrically conducting surfaces with the SEM, it was necessary to coat the small specimens with a conductive film before examination. This coating was applied by depositing carbon upon the specimens using vacuum evaporation techniques. The thickness of this deposited layer was approximately 20 to 30 nm.

Specimens prepared in this manner were then examined on an Advanced Metals Research Model 1000 SEM that was operating in the secondary electron mode. The electron accelerating potential was 20 kV.

[3]The italic numbers in brackets refer to the list of references appended to this paper.

[4]The discussion of materials by brand names in this paper is in no way to be taken as an endorsement or criticism by the U.S. Government. They were selected as representative of certain classes of materials and their names are a convenient way of handling and discussing them.

Results and Discussion

The specimens exposed to the hygrothermal conditions given in Table 1 were examined with the SEM for the presence of moisture-induced microcracks on exposed surfaces. Not all hygrothermal conditions given in this table resulted in the formation of moisture-induced damage. Table 2 gives a qualitative evaluation of the occurrence and severity of the observed hygrothermally induced microcracks.

Examination of postcured specimens, maintained at 21°C/0 percent relative humidity for the duration of the hygrothermal exposures used in this study, revealed the presence of extremely small and infrequent microcracks in their edges (see Fig. 1 for definition of the cracking modes). These

TABLE 1—*Hygrothermal exposure conditions.*

Temperature, °C	Relative Humidity, %
21	0, 13, 33, 52, 75, 98, and water immersion
43	0, 14, 34, 48, 76, 93, and water immersion
63	0, 12, 30, 41, 74, 94, and water immersion
82	0, 9, 20, 37, 74, 91, and water immersion

TABLE 2—*Observed hygrothermally induced damage.*

		Damage[a]	
Temperature, °C	Relative Humidity, %	Surface	Edge
	NONPOSTCURED		
82	37	vs	s
	74	e	e
	91	e	e
	water immersion	s	s
	POSTCURED		
21	water immersion	...	vs
43	water immersion	vs	...
63	water immersion	vs	vs
82	9	...	vs
	20	vs	vs
	37	s	s
	74	e	e
	91	ve	e
	water immersion	e	e

[a]The following symbols are used in this table: vs = very slight, small cracks visible at ×1000 (These microcracks were larger and more frequent than those caused by the postcuring process); s = slight, frequent cracks visible at ×500; e = extensive, frequent microcracks visible at ×200; and ve = very extensive, very frequent microcracks visible at ×100.

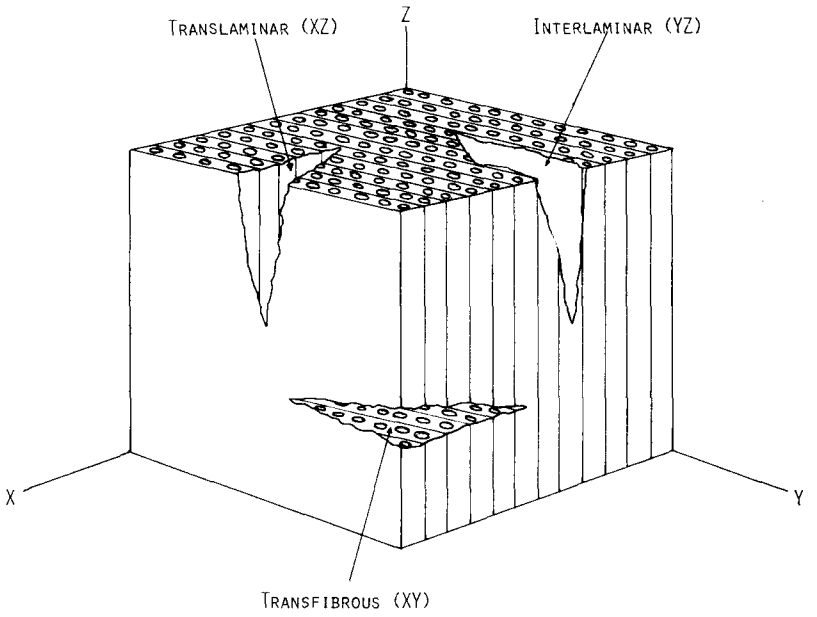

FIG. 1—*Definition of cracks (from Ref 4).*

microcracks were visible at magnifications of $\times 1000$ or higher. Presumably, this microcracking was caused by the thermal stresses generated during the postcuring process. Nonpostcured specimens exposed to identical hygrothermal conditions did not have any microcracks. The presence of the microcracks in the postcured specimens was unexpected since a slow heatup and cooldown rate (1 °C/min) was used during the postcuring process. During the subsequent examination of the hygrothermally exposed postcured specimens, the presence of any extremely small and infrequent microcracks in their edges was interpreted as being caused by the postcuring procedure—not by the hygrothermal exposure.

The faces of the graphite/epoxy specimens were composed of an outer layer of pure resin which was deeply textured by the impression of the woven separator cloth used in the fabrication of the panels (Fig. 2). The mark-off from this separator cloth resulted in the formation of alternating depressions and "hills" across the faces of the specimen in a checkerboard pattern. Examination of these surfaces at a higher magnification, Fig. 3, and cross-sectional analysis of the specimens revealed that these "hills" consisted of pure resin with the approximate thickness of 0.1 mm and that the depressions were resin-lean regions in which the graphite fibers were covered with only a thin film of resin.

The microcracks in Figs. 3 and 4 are representative of the majority of those

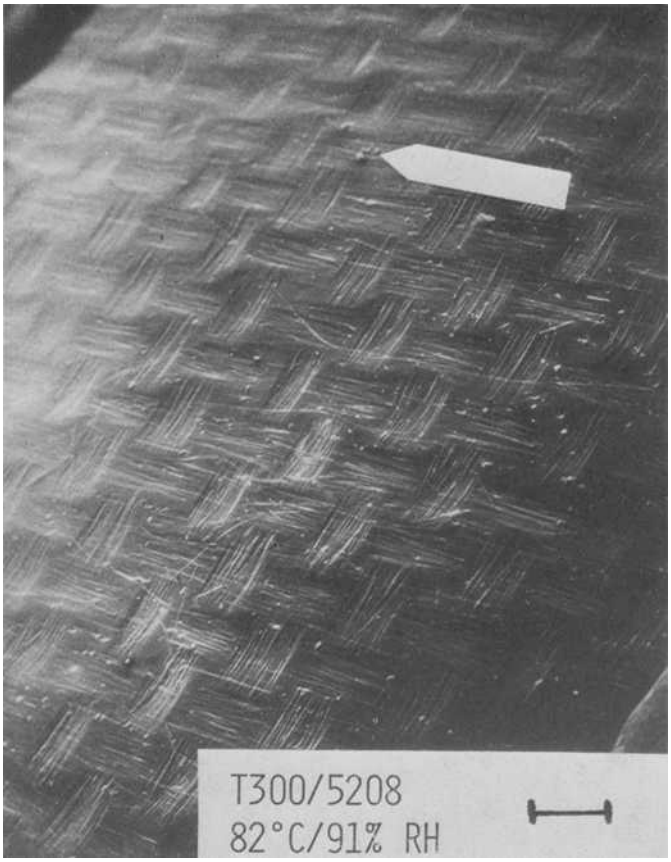

FIG. 2—*Nonpostcured specimen exposed at 82°C/91 percent relative humidity. Arrow indicates the surface ply orientation. (Scale mark indicates 5000 μm.)*

observed in the faces of the specimens exposed to the hygrothermal conditions given in Table 2. The microcracks, which penetrated through the resin-rich surface and into the graphite fibers of the surface ply, were observed to be oriented parallel to the graphite fibers. Smaller and less-frequent microcracks were observed in the resin-rich regions of the faces. These microcracks were oriented in an apparent random manner. They did not appear to penetrate into the graphite fiber layer of the surface ply. At high magnifications the translaminar microcracks could clearly be seen to have very sharp, straight-sided walls with very few side branches (Fig. 5).

Cracks in polymeric surfaces are generally believed to initiate from crazes which develop at stress concentrations around the defects in the polymer surface. A crack will propagate through a craze when a cavity formed at a defect

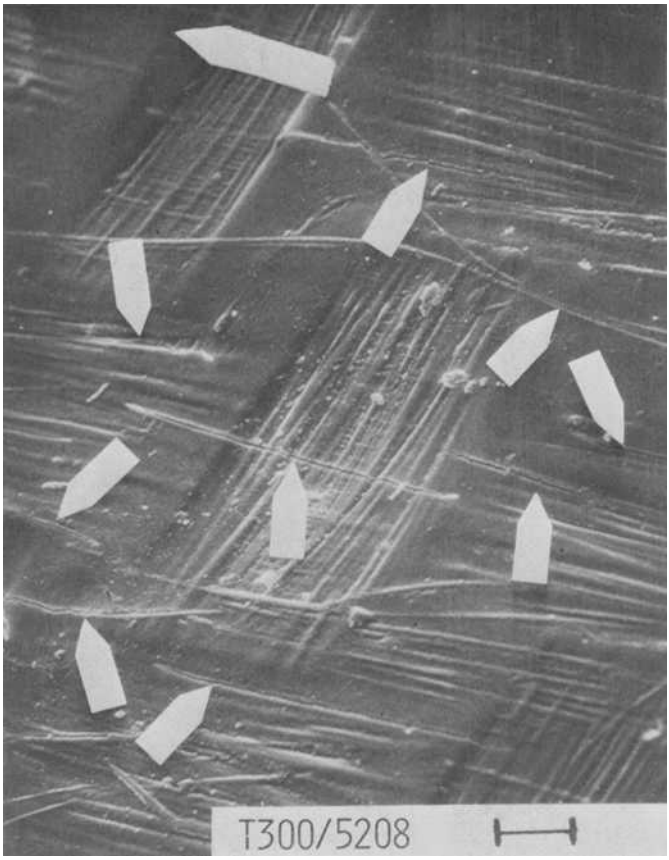

FIG. 3—*Nonpostcured specimen exposed at 82°C/91 percent relative humidity. Arrows indicate hygrothermally induced microcracks. Large arrow indicates surface ply orientation. (Scale mark indicates 1000 μm.)*

attains a critical size and begins to propagate perpendicularly to the tensile stress through the craze [5]. Low-molecular-weight diluents are known to significantly influence the crazing process in glassy polymers. Numerous studies have indicated that this phenomenon can be extremely complex and it is generally not well understood on the molecular level [5, 6].

The defect sites that lead to the formation of crazes may possibly be of several types. It has been shown that many thermosetting polymers consist of highly cross-linked and microscopic micelles surrounded by lower cross-linked density regions [6, 7]. Some authors [8] have proposed that these low cross-linked density regions act as collection sites where diluents are likely to accumulate and cause localized swelling stresses. Other authors [5] believe that microvoids (formed either by moisture-induced cavitation, ejection of

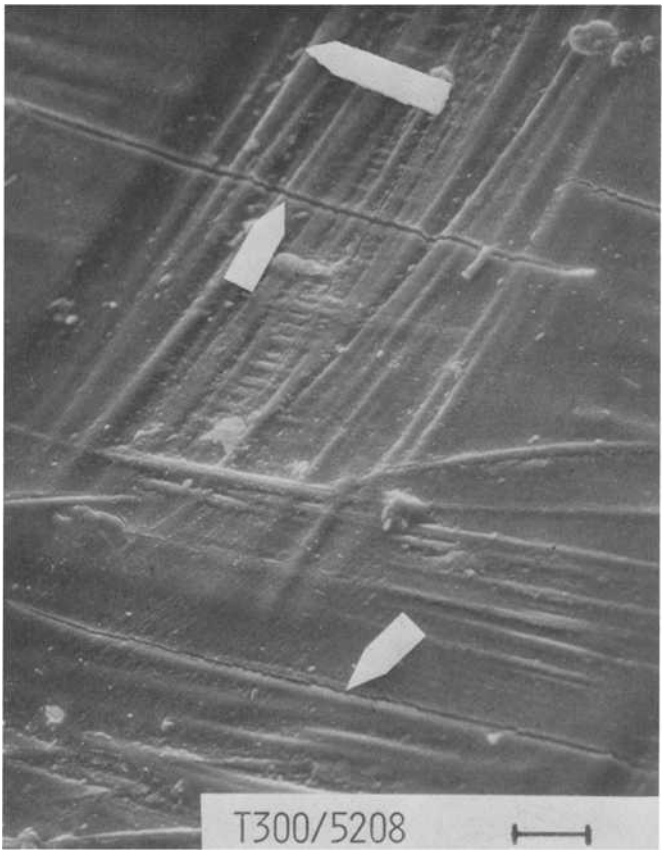

FIG. 4—*Nonpostcured specimen exposed at 82°C/91 percent relative humidity. Arrows indicate hygrothermally induced microcracks. Large arrow indicates surface ply orientation. (Scale mark indicates 500 μm.)*

low-molecular-weight material during cure, or possibly leaching of any unreacted material by sorption and desorption of the diluent) act as the craze initiation sites.

It has been reported [*5*] that both low cross-linked density regions and microvoids are present in an epoxy resin matrix system similar to that used in this study. Additional studies of this material [*9,10*] have also indicated that it fails by a crazing process.

The experimental procedures used to monitor the absorption weight gains of the hygrothermally exposed specimens influenced—if not initiated—the formation of the severe microcracks observed in the specimens exposed at elevated temperatures. The process of removing the specimens from their elevated-temperature humidity chambers and then allowing them to cool at

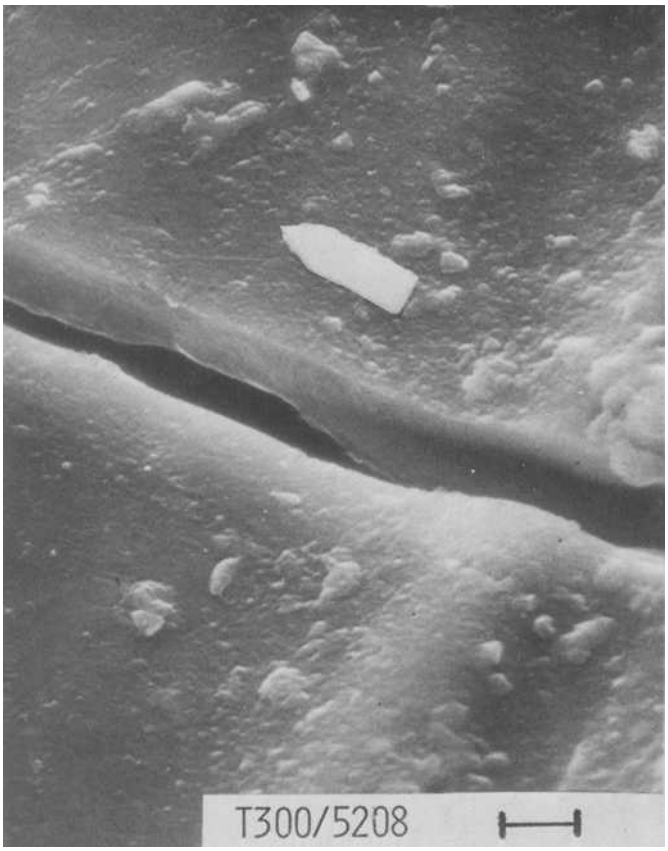

FIG. 5—*Nonpostcured specimen exposed at 82°C/91 percent relative humidity (scale mark indicates 50 μm). Arrow indicates surface ply orientation.*

room temperature (prior to weighing) exposed the specimens to a mild thermal shock. McKague [*11*], Browning [*12*], and Hedrick [*13*] have found that epoxy laminates are damaged after thermal spike exposure as indicated by abnormally large increases in subsequently absorbed moisture. Similar increases of absorbed moisture were observed during the hygrothermal exposure of the specimens used in this study [*1*].

It is generally assumed that this thermally induced damage occurs during the rapid cooldown portion of the thermal spike. (In this study the "thermal spike" is actually an inverted thermal spike since the elevated exposure temperatures are above that of the specimen weighing temperatures.) In the vicinity of the surfaces of a cooling specimen, the relative humidity of the surrounding air is reduced by the heat absorbed from the specimen. As a result,

moisture could be desorbed from the surfaces of a cooling specimen, particularly if it had previously been exposed to a high-humidity environment. This would lead to a severe moisture gradient through the specimen since the moisture in its interior could not diffuse rapidly enough to be desorbed from its surfaces during the cooldown portion of the thermal spike. The accompanied nonuniform swelling would result in the formation of a surface tensile stress. In addition, the rapid cooldown rate of the specimen causes the exterior to be cooler than the interior, resulting in a thermally induced surface tensile stress. Together, these surface tensile stresses are sufficiently large to cause permanent damage in the surfaces of the laminate by the crazing mechanism mentioned earlier. Periodic weighings of the specimens would subject them to oscillatory surface swelling stresses caused by moisture absorption during the hygrothermal exposures and moisture desorption in the subsequent cooldown portion of the inverted thermal spikes. Examination of Table 2 indicates that the most extensive microcracking occurred for the specimens which had been exposed at 82°C/91 percent relative humidity (Fig. 6).

Specimens immersed in water at 82°C were observed to have both less frequent and less severe microcracks than those exposed at 82°C/91 percent

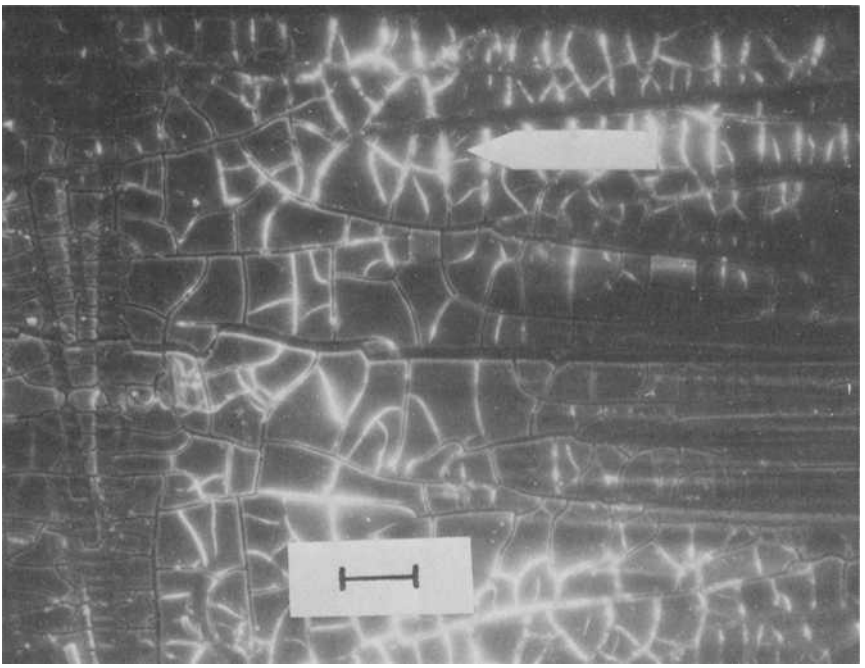

FIG. 6—*Postcured specimen exposed at 82°C/91 percent relative humidity (scale mark indicates 500 μm). Arrow indicates surface ply orientation.*

relative humidity. The surfaces of the elevated-temperature water immersion specimens did not desorb a significant amount of moisture during the weighing process since the specimens were allowed to cool in water maintained at room temperature prior to weighing. As a consequence the severe moisture gradients and the resulting surface tensile stresses (which had developed in the atmospherically exposed specimens) did not occur in the water-immersion specimens. Thus, less microcracking should occur in the water-immersion specimens.

As indicated in Table 2, however, microcracks were observed in the postcured water-immersion specimens exposed as low as 21 °C. Presumably, the large swelling of the water-immersion postcured specimens and possibly the leaching effects of the water would enhance crack formation even at this temperature.

As a comparison of Figs. 4 and 6 illustrates, the microcracks in the postcured specimens were both more frequent and more severe than those observed in identically exposed nonpostcured specimens. Both translaminar and transfibrous microcracks were observed in the surfaces of the postcured specimens. The translaminar microcracks appeared to be very similar to those observed in the postcured specimens. The transfibrous microcracks generally occurred in the resin-rich surface regions as in the nonpostcured specimens. However, the nonpostcured specimens at 82°C/91 percent relative humidity (Fig. 6) have transfibrous microcracks that penetrate into the graphite fiber layer of the surface ply, breaking some of the graphite fibers in the process. The postcuring treatment could enhance the possibility of microcracking in several ways: (1) it would result in embrittlement of the resin; (2) residual thermal stresses are formed in the laminate; and (3) thermally induced microvoids and microcracks result in increased defect sites on the polymer surface.

Both translaminar and interlaminar microcracks were observed in the edges of the specimens for the hygrothermal conditions given in Table 2. As can be observed in Fig. 7, the translaminar microcracks usually terminated at the boundary between the orthogonally oriented plies on either side of the cracked lamina. Occasionally these microcracks would break one or two of the graphite fibers in the adjacent plies. In several cases anisotropic swelling stresses between adjacent orthogonal laminae apparently resulted in the formation of translaminar microcracks along the interface between the plies (Fig. 8). Occasionally, small sections ($\sim$5 mm) of adjacent plies were observed to be delaminated.

The microcracks in the edges of the specimens propagated along the graphite fiber/epoxy resin interface and through resin-rich regions between adjoining fibers. Highly polished cross-sectional pieces, taken from along the edges of specimens which had been exposed at 82°C/91 percent relative humidity, showed good adhesion between the epoxy resin and the graphite fibers.

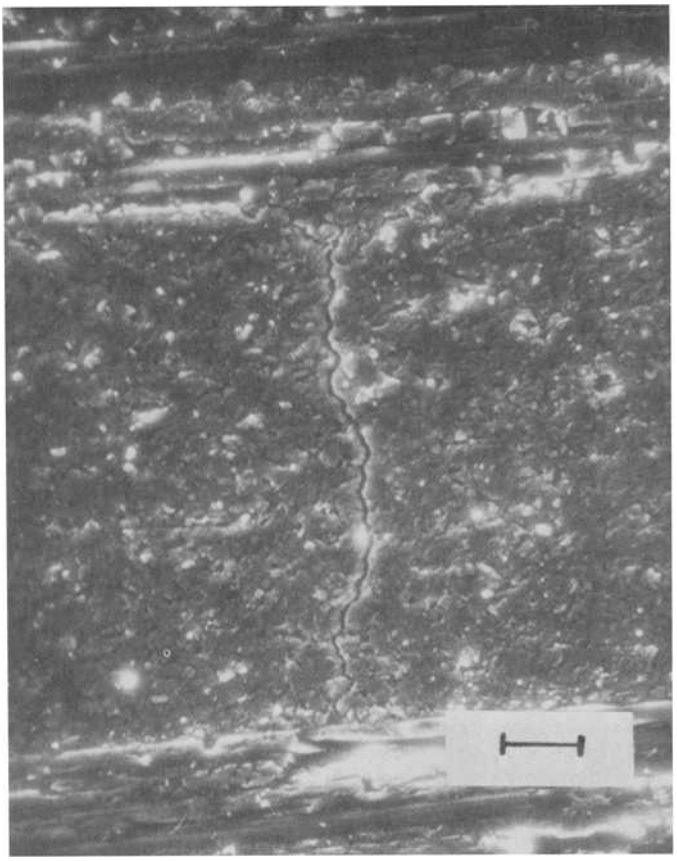

FIG. 7—*Nonpostcured specimen exposed at 82°C/74 percent relative humidity (scale mark indicates 200 μm). Surface texture of specimen edge was a result of machining by a diamond saw.*

Long-term moisture desorption increased the occurrence of small microcracks in the resin-rich regions of the faces of specimens which previously had been exposed to the conditions given in Table 2 (see Figs. 4 and 9). The large microcracks found in both the edges and faces of these specimens were apparently unaffected. Specimens (exposed at 75 percent relative humidity) which had not formed microcracks upon moisture absorption did not form microcracks upon desorption.

Conclusions

Postcured and nonpostcured T300/5208 crossply laminates developed microcracks in the faces and the edges of specimens which had been exposed

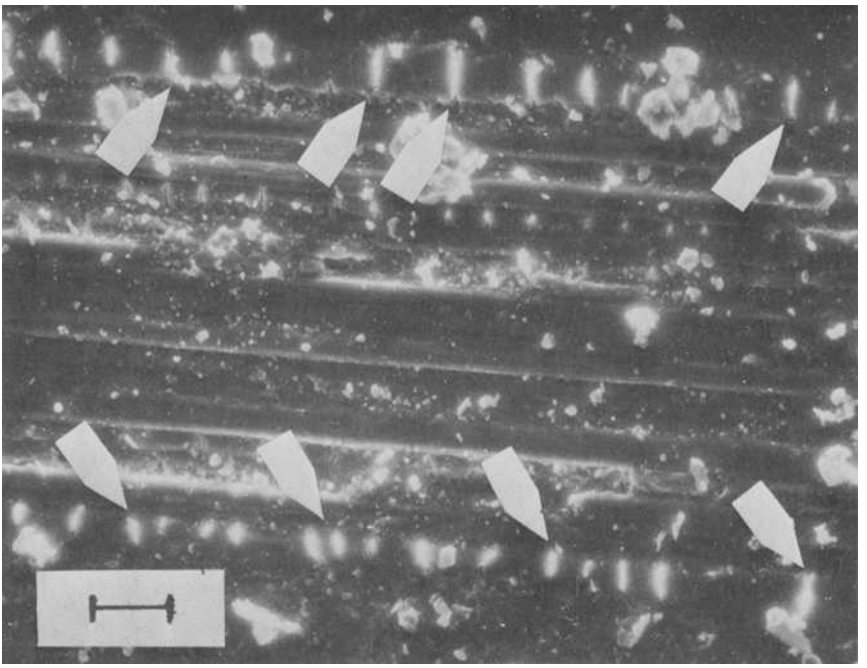

FIG. 8—*Postcured specimen exposed at 21°C/water immersion (scale mark indicates 250 μm). Arrows terminate at ply boundaries and also indicate the hygrothermally induced microcracks. Surface texture of specimens was a result of machining by a diamond saw.*

to various hygrothermal conditions. The most severe microcracks were observed for the specimens exposed at 82°C. The severity and frequency of these microcracks increased with relative humidity. Postcured specimens generally formed more severe microcracks than identically exposed non-postcured specimens.

The formation of these microcracks cannot be attributed solely to the effects of absorbed moisture. Rather, the experimental techniques used to monitor the specimen weight gains during their hygrothermal exposure would subject the specimens to an inverted thermal spike which might initiate the microcracking. Specimens with extensive microcracks also exhibited non-Fickian diffusion anomalies during their hygrothermal exposure [*1*]. However, further work is needed in this area to clarify the relationship between anomalous diffusion and surface microcracking.

Translaminar microcracks on the faces of the specimens were both more frequent and more severe than transfibrous microcracks. Resin rich regions on the specimen faces contained very small randomly oriented transfibrous microcracks.

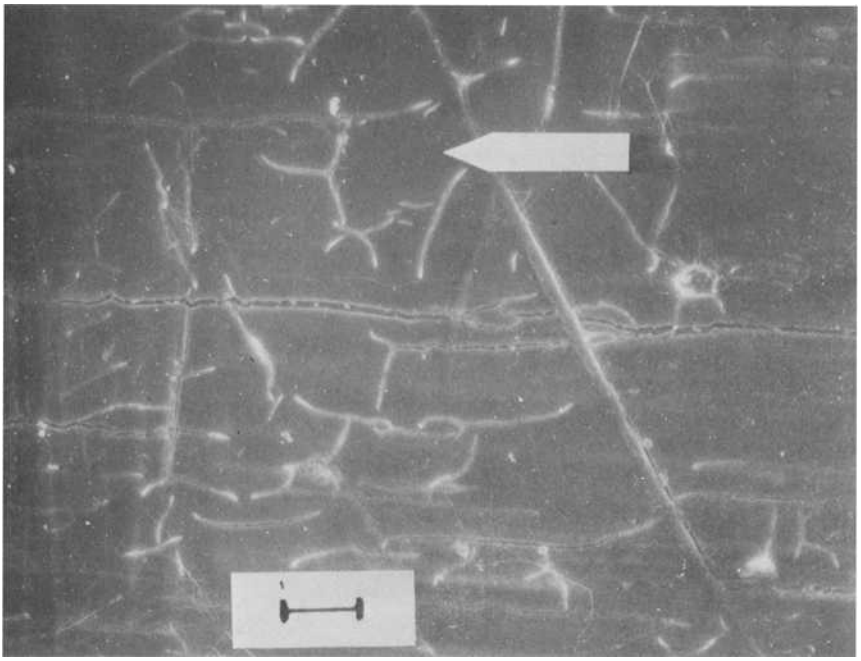

FIG. 9—*Nonpostcured specimen exposed at 82°C/91 percent relative humidity and subsequently dried at 82°C/0 percent relative humidity (scale mark indicates 500μm). Arrow indicates surface ply orientation.*

Interlaminar and translaminar microcracks occurred in the edges of the specimens. Adhesion of the epoxy resin to the graphite fibers did not appear to be deleteriously affected by the hygrothermal conditions used in this study. The presence of anisotropic swelling stresses between adjacent orthogonally oriented laminae was indicated by microcrack formation along the interface of the laminae. Hygrothermally induced delaminations also occurred between adjacent laminae.

Acknowledgments

The authors wish to express their appreciation to Mr. Joseph Henry of the Metals and Ceramics Division, Air Force Materials Laboratory, for allowing us access to the SEM used in this work. This study is part of an in-house work unit sponsored by the Structures and Dynamics Division, Air Force Flight Dynamics Laboratory, Wright-Patterson Air Force Base, Ohio. The U.S. Government is authorized to reproduce and distribute reprints for governmental purposes notwithstanding any copyright notation hereon.

References

[1] Shirrell, C. D. in *Advanced Composite Materials—Environmental Effects, ASTM STP 658*, American Society for Testing and Materials, 1977, pp. 21-42.

[2] Shirrell, C. D. in *Selective Application of Materials for Products and Energy*, Society for the Advancement of Material and Process Engineering, 1978, pp. 175-191.

[3] (*a*) Shirrell, C. D., "Moisture Absorption by T300/5208 Graphite-Epoxy Composite Laminates," AFFDL-TM-78-75-FBS, Air Force Flight Dynamics Laboratory, Wright-Patterson AFB, Ohio, in press; (*b*) Shirrell, C. D., "Moisture Sorption by T300/5208 Graphite-Epoxy Composite Laminates," AFFDL Technical Memorandum, Air Force Flight Dynamics Laboratory, Wright-Patterson AFB, Ohio, in preparation; (*c*) Shirrell, C. D., "Kinetics of Moisture Diffusion in T300/5208 Graphite-Epoxy Composite Laminates," AFFDL Technical Report, Air Force Flight Dynamics Laboratory, Wright-Patterson AFB, Ohio, in preparation.

[4] Cook, W. G. and Downhill, A. G. in *Carbon Fibers in Engineering*, M. Langley, Ed., McGraw-Hill, New York, 1973, Chapter 7.

[5] Morgan, R. J. and O'Neal, J. E., *Polymer-Plastic Technology and Engineering*, Vol. 10, No. 1, 1978, pp. 49-116.

[6] Rebenfeld, L., Makarewicz, P. J., Weigmann, H. D., and Wilkes, G. L., *Journal of Macromolecular Science—Reviews in Macromolecular Chemistry*, Vol. C15, No. 12, 1976, pp. 279-393.

[7] Erath, E. H. and Spurr, R. A., *Journal of Polymer Science*, Vol. 35, 1959, pp. 391-399.

[8] Eakins, W. J. in *Interfaces in Composites, ASTM STP 452*, American Society for Testing and Materials, 1969, pp. 137-148.

[9] Morgan, R. J. and O'Neal, J. E., *Journal of Materials Science*, Vol. 12, 1977, pp. 1966-1980.

[10] Morgan, R. J. and O'Neal, J. E., *American Chemical Society, Division of Organic Coatings and Plastics Chemistry Preprints*, Vol. 36, No. 2, 1976, pp. 289-301.

[11] McKague, E. L., "Life Assurance of Composite Structures," Technical Report AFML-TR-75-51, Air Force Materials Laboratory, Wright-Patterson AFB, Ohio, 1975.

[12] Browning, C. E., "The Mechanism of Elevated Temperature Property Losses in High Performance Structural Epoxy Resin Matrix Materials After Exposure to High Humidity Environments," Ph.D. dissertation, University of Dayton, Dayton, Ohio, Aug. 1976.

[13] Hedrick, I. G. and Whiteside, J. B., "Effects of Environment on Advanced Composite Structures," American Institute of Aeronautics and Astronautics Conference on Aircraft Composites: The Emerging Methodology for Structural Assurance, Paper No. 77-473, San Diego, Calif., 24-25, March 1977.

A. G. Miller[1] *and A. L. Wingert*[1]

Fracture Surface Characterization of Commercial Graphite/Epoxy Systems

REFERENCE: Miller, A. G. and Wingert, A. L., **"Fracture Surface Characterization of Commercial Graphite/Epoxy Systems,"** *Nondestructive Evaluation and Flaw Criticality for Composite Materials, ASTM STP 696,* R. B. Pipes, Ed., American Society for Testing and Materials, 1979, pp. 223-273.

ABSTRACT: The fracture surface morphologies of graphite/epoxy composite materials have been studied to determine the influences of load history, material configuration, temperature, moisture, and matrix system type. Three commercially available systems with unidirectional tapes loaded in tension and fabrics tested in shear were chosen for analysis. Elevated temperature, moisture exposure, or both increased the amount of fiber pullout in the unidirectional tapes. Only in one case was the pullout fracture mode changed from a cohesive to an adhesive type of fracture process. The shear-loaded fabrics displayed either a tensile flexure fracture or an apparent shear fracture mode. The latter mode was believed to be actually a tensile rupture mode due to a resolution of shear stresses into tensile stresses. A transition temperature was defined to denote the temperature at which the fracture mode changed from tensile flexure to apparent shear. Significant differences in fracture surface morphology were observed among the three commercial graphite/epoxy systems.

KEY WORDS: fractography, composite materials, graphite/epoxy, fracture (materials), crack propagation, nondestructive tests

Fracture processes in graphite/epoxy composite materials are complex and poorly understood. Analysis of the fracture surfaces of these materials is important in order to determine what factors influence the fracture process. Microstructural features that may offer an easy mode of fracture may be identified so that they can be removed to increase the strength of the material. When flaws control the fracture process, fracture surface characterization may be able to identify the flaw type and thereby suggest a means for removing them. The ability to analyze a given fracture surface

[1] Specialist engineer and manager, Analytical Group, respectively, Boeing Materials Technology, Boeing Commercial Airplane Company, Seattle, Wash. 98124.

and determine the origin and mode of fracture is essential in order to identify the cause and either remove it from future components or design with the flaw present. Thus, fracture surface characterization is an essential component in understanding graphite/epoxy systems so that better utilization of their excellent mechanical properties can be achieved.

The specific objectives of this study were to (1) develop a classification framework to characterize and compare fracture surfaces; (2) examine the influence on fracture surfaces of loading history, material configuration, temperature, moisture exposure, and matrix system type; and (3) identify crack initiation sites and crack propagation modes.

This report includes some of the results obtained from an ongoing research program within the Boeing Commercial Airplane Co. In order to contrast sharply the types of problems encountered in these studies, attention is focused herein on two of the extremes encountered, that is, unidirectional tapes loaded in tension and shear loading of fabrics. These two cases offer a good sampling of the types of fracture surfaces one might expect to see from an arbitrary section of material that has fractured. The view taken throughout this report is phenomenological in concept and is based upon microstructural examination by scanning electron microscopy and optical microscopy.

Three commercially available graphite/epoxy systems are investigated to determine the influences of temperature from −54 to 132°C and of moisture on the fracture surface morphology. Mechanical testing was performed by loading the unidirectional tapes in tension and the fabrics in shear.

Materials and Methods

Table 1 gives the composition of the three commercial graphite/epoxy systems studied. All systems use the same major resin and hardener, although different levels of hardener are employed. All systems are hypostoichiometric and cured at 177°C. Systems A and C contain a second

TABLE 1—*Constituents of the three commercial graphite/epoxy systems studied.*

System	Major Resin	Minor Resin	Hardener	Catalyst	Sizing	Fibers
A	MY 720	yes[a]	DDS (low)	no	yes[c]	Type A
B	MY 720	no	DDS (high)	yes[b]	unknown	Type B
C	MY 720	yes[a]	DDS (intermediate)	yes[b]	yes[c]	Type A

[a]The minor resins are epoxy-based, although System A uses a different minor resin than does System C.

[b]All catalysts used are BF_3-amine types.

[c]The composition of the sizing agents is not known.

resin, while System B does not. Systems B and C contain a BF_3-amine catalyst. Systems A and C use a sizing on the fibers although the exact composition of the sizing is unknown. System B uses what will be termed Type B fibers, while Systems A and C use the same Type A fibers. All the fibers are high-modulus type.

Tension tests were performed on eight-ply unidirectional tapes. All tapes were 0-deg tapes, that is, the load axis was coincident with the fiber axis. Short beam shear (SBS) tests were conducted on fabric specimens. This is a three-point loading test with a span-to-width relationship of 4:1. All tests were performed on an Instron testing unit. All specimens denoted by the dry condition were tested in the as-cured condition. All specimens tested in the wet condition were exposed to 100 percent relative humidity at 71° for two weeks. These specimens were kept moist until tested in an environmental chamber at the specified temperature.

Scanning electron micrographs (SEM's) were taken on the gold-coated specimens in AMR 1400 and ISI MSM-5 scanning electron microscopes. Optical microscopy was performed on polished specimen surfaces by standard methods.

Results

Mechanical Tests

Fibers that are parallel to the tensile loading axis are defined as 0-deg fibers, while those perpendicular to the fiber axis are denoted as 90-deg fibers. Table 2 gives the ultimate stress data for the unidirectional 0-deg tapes loaded in tension. Figure 1 shows these data when the results of each group have been normalized to their own 21°C/dry condition. A lower relative stress is obtained at −54°C (0.84) than at 21 and 132°C (1.03) for the dry condition. The 21°C/wet condition was the same as the 21°C/dry condition (1.01 versus 1.00). Systems B and C showed a

TABLE 2—*Ultimate stress values of 0-deg tapes loaded in tension.*

System	Test Condition				
	−54°C/dry	21°C/dry	21°C/wet	132°C/dry	132°C/wet
A	979[a] ± 100	1171 ± 81	1200 ± 79	1258 ± 64	1248 ± 30
B	1442 ± 97	1613 ± 95	1629 ± 106	1658 ± 85	1366 ± 99
C	1086 ± 208	1354 ± 87	1363 ± 53	1358 ± 92	1156 ± 75

[a] All values are mean ± one standard deviation in MPa.

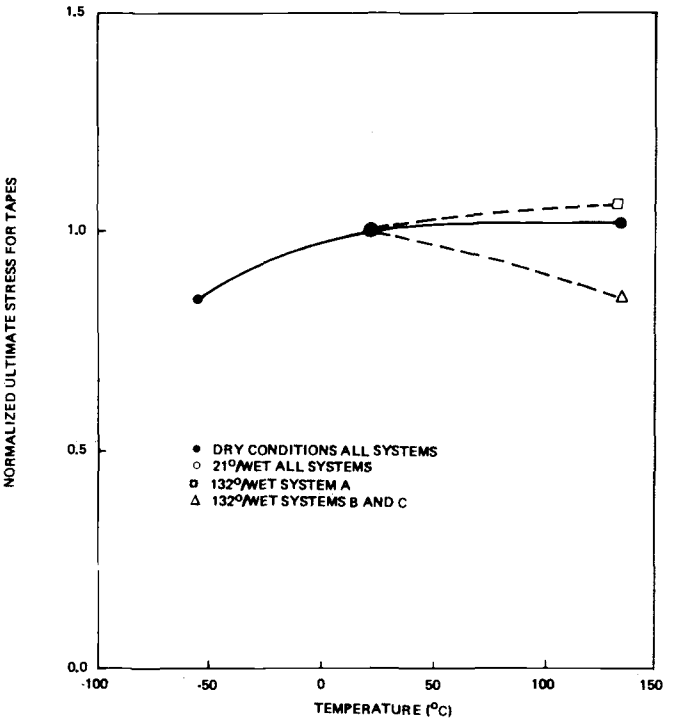

FIG. 1—*Influence of temperature and moisture on relative ultimate stress of unidirectional tapes loaded in tension.*

decrease in relative stress for the 132°C/wet condition (0.85), but System A showed no decline (1.06).

Low temperature (−54°C) caused an apparent decrease in relative stress. This could arise from two sources. First, although tests were performed in a nitrogen atmosphere, water condensation and freezing could have caused grip slippage and perhaps lower apparent ultimate stresses. However, operator observations did not corroborate this effect. A second concept would be that the flaw sensitivity of the specimens, that is, the matrix phase, may have been increased and thereby reduced the observed ultimate stress. Which of these views is correct is not known at this time.

Exposure to water did not decrease the ultimate stress at 21°C (1.01 versus 1.00). System A showed no decline in ultimate stress at 132°C/wet (1.06 versus 1.03), while Systems B and C showed a sharp decline (0.85 versus 1.03). As discussed in the preceding section, Systems A and C use the same reinforcing fibers; therefore, differences between them should be related to variations in their matrix composition or fiber-matrix bond strengths. The cause of this difference between the systems in relative

ultimate stress due to combined moisture and temperature exposure is not yet clear in that the role of specific matrix components on mechanical properties is not well understood.

The mechanical tests of the 0-deg tapes showed that low temperatures decrease the apparent ultimate stress, while high temperatures do not affect the ultimate stresses relative to ambient temperatures. The low-temperature effect is not understood, as it could be due to testing techniques or due to matrix flaw sensitivity effects. Because the fibers dominate the mechanical properties of these specimens, the high-temperature results are not entirely unanticipated, since the fibers themselves would not be expected to be temperature-sensitive in these ranges of temperatures. Moisture did not affect the 21°C case data, although it decreased the ultimate stresses observed for the 132°C/wet case for Systems B and C. System A specimens did not show the influences of 132°C/wet for the ultimate stresses. The cause of this effect may be matrix-controlled, although the precise origin is unclear.

Table 3 gives the ultimate stress data for the SBS specimens. Figure 2 plots these data when the results of each group have been normalized to their own 21°C/dry condition. No change in relative ultimate stress is observed between −54 and 21°C. A small decline in relative ultimate stress is observed for the 71°C case (0.91) and a larger decline for the 132°C case (0.28). The SBS test is designed to test primarily matrix properties. The effect of increasing temperature above 21°C was to reduce the ultimate stress. No drop in ultimate stress was observed at −54°C as for the 0-deg tapes, which may support the view that testing methodology may have played a role in the 0-deg tape data.

In summary, increasing temperature did not degrade the 0-deg tape ultimate stresses, although the SBS specimens did show a decline. Water exposure did not affect the room-temperature strengths for the 0-deg tapes, but did decrease the ultimate stresses at 132°C for Systems B and C. System

TABLE 3—*Mechanical properties of fabrics tested as short beam shear specimens.*

System	Test Temperature			
	−54°C	21°C	71°C	132°C
A	61[a] ± 3	61 ± 5	59 ± 1	51 ± 3
B	73 ± 8	77 ± 5	69 ± 3	44 ± 5
C	63 ± 3	66 ± 6	58 ± 5	45 ± 2

[a] All values are mean ± one standard deviation in MPa.

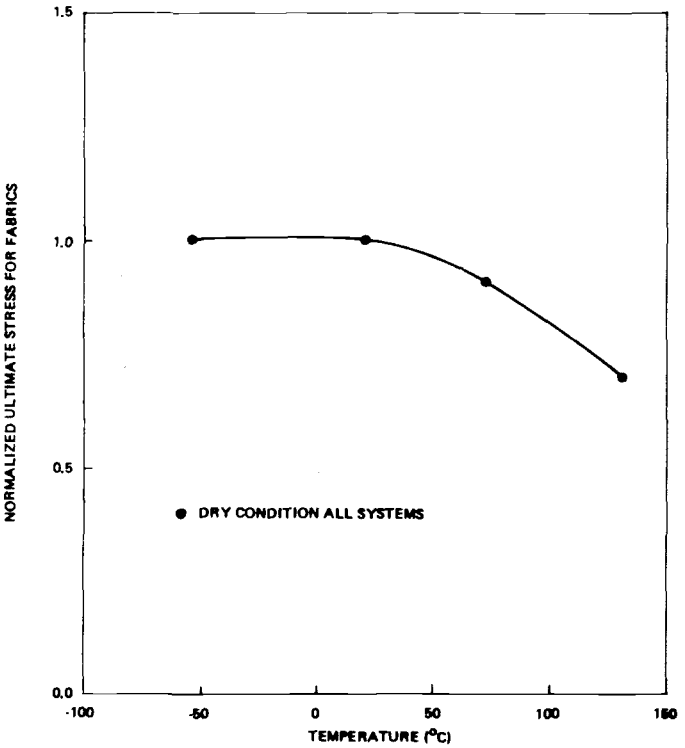

FIG. 2—*Influence of temperature on relative ultimate stress of fabrics loaded in shear.*

A did not display lowered strengths due to 132°C/wet conditions. The origins of the effect are believed to be matrix-related.

Fracture Studies

The following sections describe the fracture surface morphologies observed for the commercial graphite/epoxy systems investigated. The first section shows the microstructures found for the 0-deg tapes loaded in tension. The second section describes the microstructures of the fabrics tested in a shear mode by use of the short beam shear (SBS) test as described in the section on methods.

0-deg Tapes

System A—Figures 3-6 show SEM's of the fracture surface morphology of System A 0-deg tapes loaded in tension. Figure 3 shows a typical fracture surface from the −54°C/dry and 21°C/dry environments. The overall

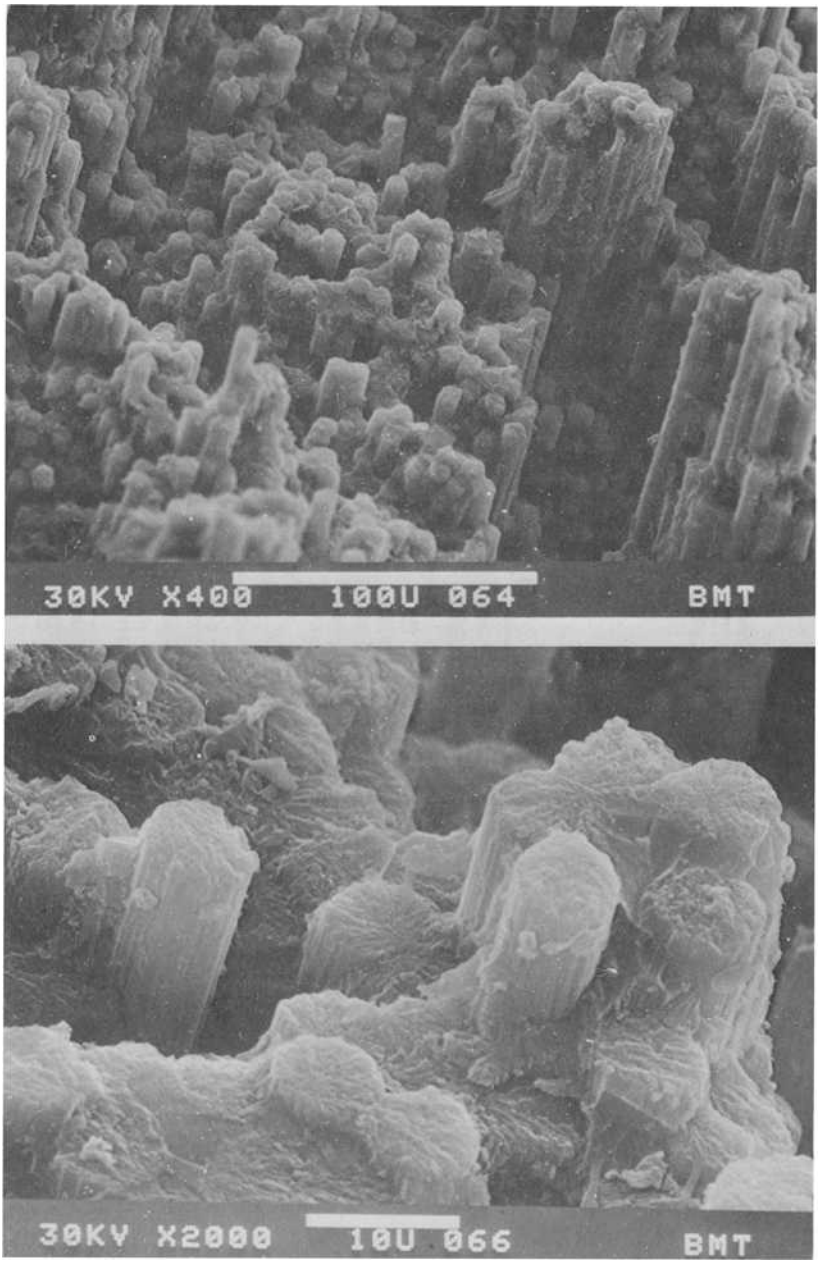

FIG. 3—*Typical microstructures observed for System A specimens at −54 and 21°C/dry. (Editor's note: Figures 3–46 at 70 percent of original size. Allow for this reduction on magnifications shown.)*

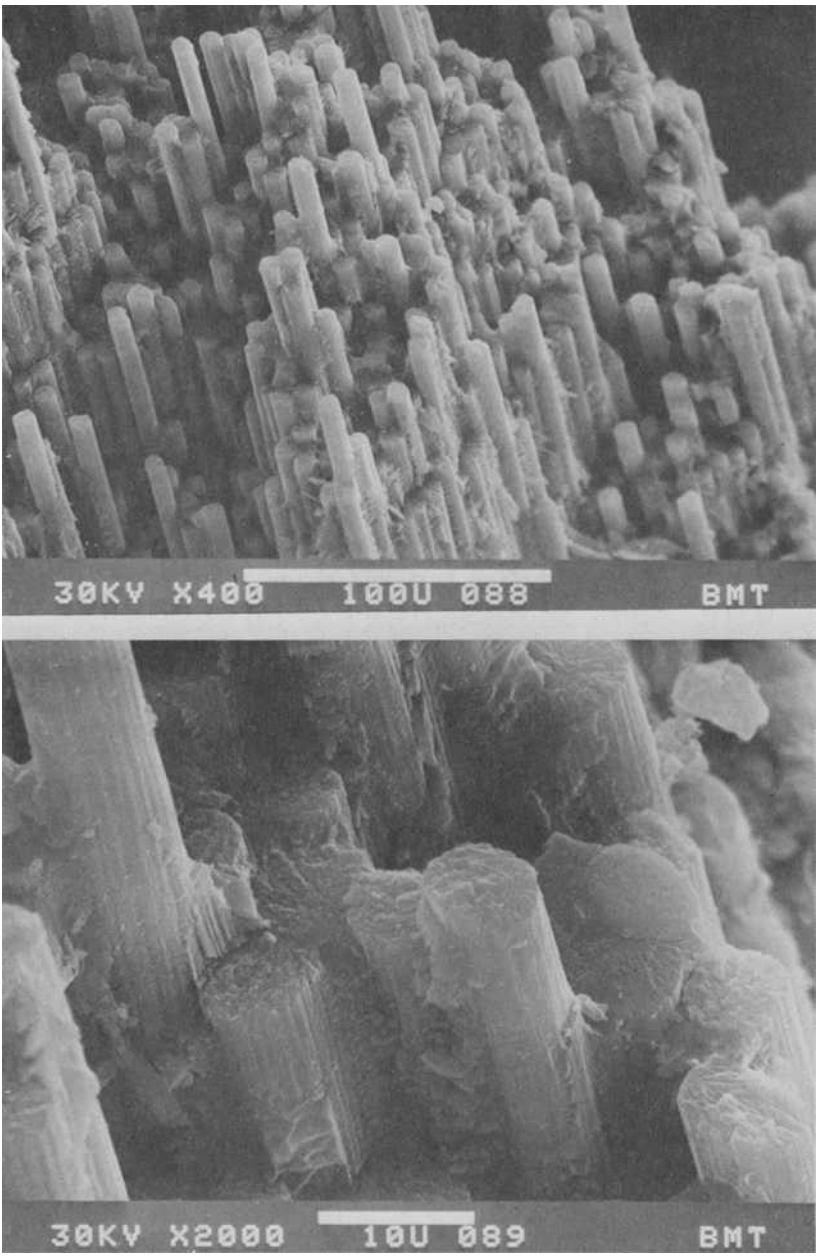

FIG. 4—*Typical microstructures observed for System A specimens at 132°C/dry.*

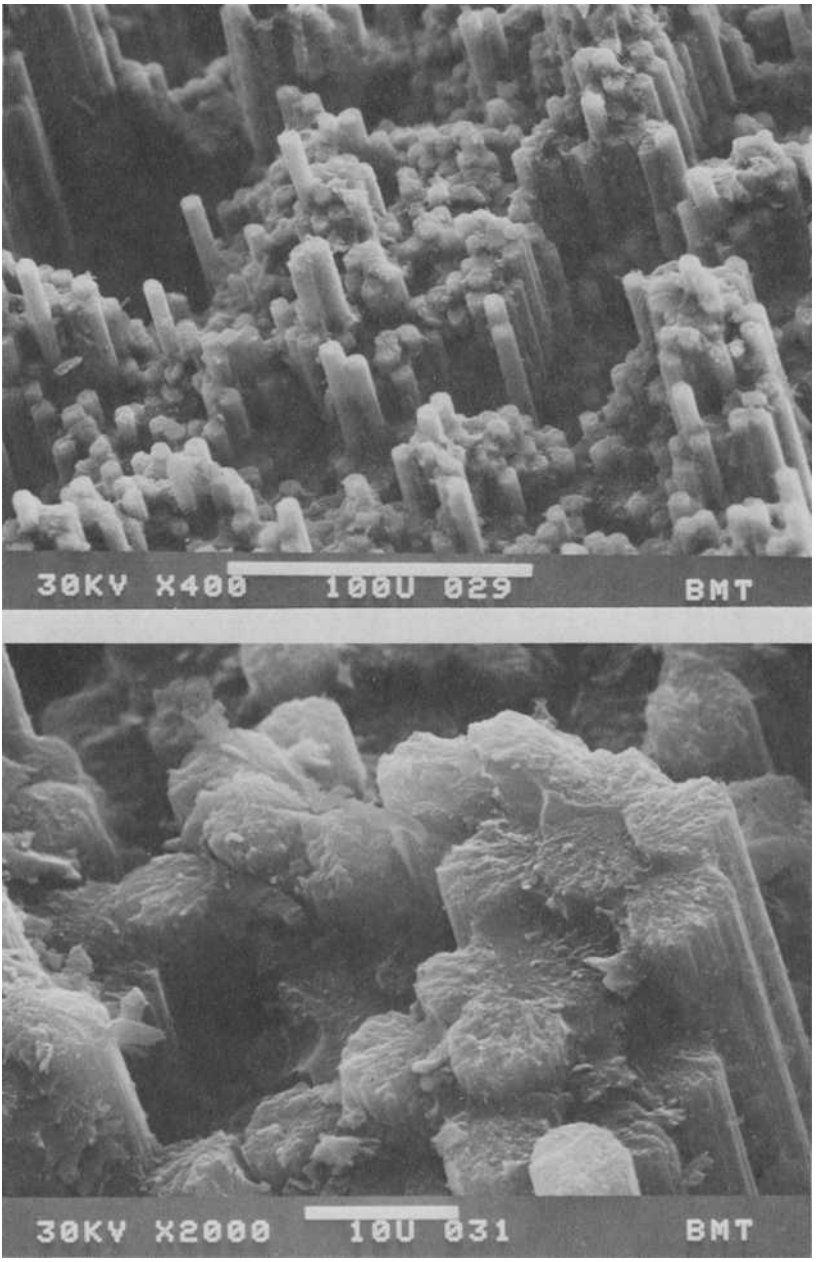

FIG. 5—*Typical microstructures observed for System A specimens at 21°C/wet.*

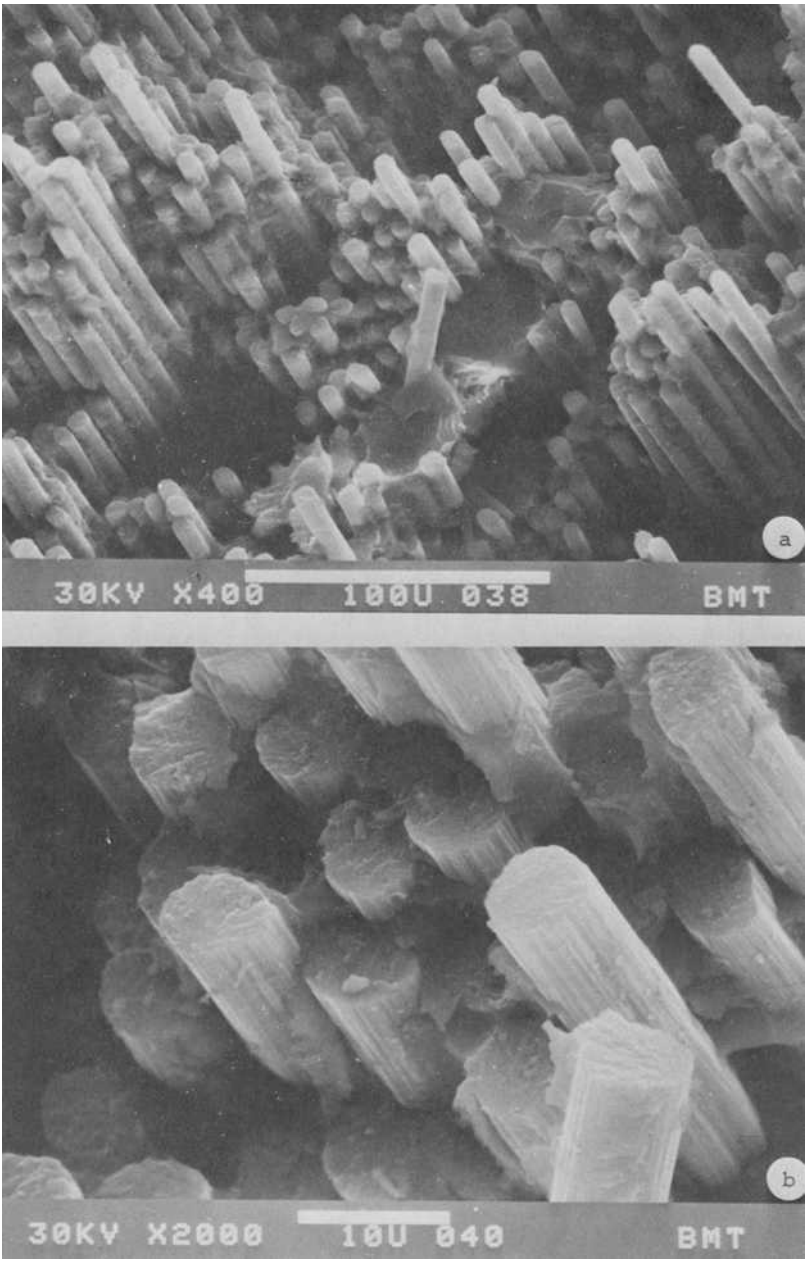

FIG. 6—*Typical microstructures observed for System A specimens 132°C/wet.*

fracture surface is tiered with each tiered area having a relatively flat structure, similar to that observed by Sinclair and Chamis.[2] This microscale flat morphology suggests that local crack propagation occurred in a cooperative manner between fibers. This general phenomenon will be described hereafter as cooperative fiber fracture, to indicate the apparent local planar crack propagation path. The tiered structure could be due to microheterogeneities in the chemistry of the matrix, for example, to variations in hardener concentration,[3] or to a changing stress state during fracture, or to both. Available experimental data do not distinguish between these alternatives. The overall fracture surface also shows the presence of some short fiber pullout, although this is only of limited extent.

In Fig. 4 the microstructure is shown for the testing at the 132°C/dry case. While there is similarity to the previous figure, the amount of fiber pullout has increased. At low magnifications, the ends of the pulled-out fibers appear relatively clean of adhering matrix, although close examination of these fiber surfaces indicates some residual matrix adhering to the fibers as a very thin layer. The increased temperature, which softens the matrix, may permit easier fiber pullout. Because the local fiber-matrix interactions are similar to adhesive-bonded joints, fracture between the fiber and the adjacent matrix will be termed "adhesive" fracture, while fracture that occurs in the matrix adjacent to the fiber will be designated as "cohesive." Thus, clean pulled-out fibers would indicate an adhesive fracture process for pullout. However, the thin adhering matrix suggests a partially cohesive fracture component.

Figure 5 shows the microstructure found in the 21°C/wet case. The overall microstructure is similar to that observed for the 21°C/dry case, Fig. 3. Some additional number of individual fiber pullouts are observed. Similar to the microstructure observed in Fig. 4, the fiber pullout process appears largely to be cohesive in nature, due to the thin adhering matrix layers on the fiber surfaces.

Figure 6 shows the microstructure found in the 132°C/wet condition. Significant amounts of fiber pullout are observed with a decreased amount of cooperative fiber fractures. The overall microstructure is similar to that observed for the 132°C/dry case, Fig. 4, because of the large amount of fiber pullout. At this temperature, moisture did not cause a dramatic change in microstructure. A close examination of the pulled-out fiber surfaces showed some very thin layers of matrix still adhering to many of the fibers, as can be seen in Fig. 6*b*. Thus, an adhesive fracture component was again present in the pullout process. On the right-hand side of Fig. 6,

[2] Sinclair, J. H. and Chamis, C. C., "Fracture Surface Characteristics of Off-Axis Composites," NASA TM-73700, presented at 14th Annual Meeting of the Society of Engineering Sciences, Inc., Bethlehem, Pa., 14-16 Nov. 1977.

[3] Morgan, R. J. and O'Neal, J. E. in *Epoxies as Composite Matrices*, American Chemical Society Organic Coatings and Plastic Chemistry Preprints, 1978, pp. 485-490.

a resin-rich zone is observed. This area is thought to be a ply boundary where two tapes were joined. Fracture of this area appeared to be by cleavage.

System A specimens showed modest effects due to moisture and more dramatic effects due to temperature. High temperature increased the amount of fiber pullout. Moisture similarly increased the extent of pullout, but did so in a less pronounced manner. System A specimens, therefore, showed a low sensitivity to moisture. Thin layers of adhering matrix were commonly observed on the pulled-out fiber surfaces, indicating a cohesive pullout fracture process.

System B—Figures 7–13 show the microstructures observed for System B 0-deg tapes loaded in tension. Figure 7 shows a typical fracture surface found in the −54°C/dry and the 21°C/dry conditions. A tiered structure with the cooperative fiber fracture surfaces described in the preceding is seen with little evidence of pullout. The few pulled-out fibers observed demonstrate an apparently strong fiber-matrix bond as shown by Fig. 8, where the adhering matrix is observed.

The effect of elevated temperature, 132°C, is shown in the micrographs of Fig. 9. While some cooperative fiber fracture areas are seen, an increased amount of fiber pullout is observed. Unlike previous situations, significant amounts of matrix are seen adhering to the pulled-out fiber surfaces even at low magnification. The increased temperature enhanced fiber pullout but apparently did not seriously degrade the fiber-matrix bond in this system. In this case, the pullout fracture mode was more obviously cohesive in nature. The thermal softening of the matrix was the apparent primary cause for the increased fiber pullout.

Figure 10 shows the microstructure observed for the 21°C/wet specimens. While some cooperative fiber fracture areas are seen, an increased amount of fiber pullout is present when the micrograph is compared with Fig. 8. Close examination of the pulled-out fiber surfaces and of a typical matrix hole from which a fiber was pulled out, Fig. 11, shows adhering matrix on the fiber surface. The pullout process would be expected to cause shear stresses at the fiber-matrix interface. These shear stresses could be resolved into tensile stresses and thereby cause the formation of matrix lacerations as observed on the fiber surfaces, Fig. 11*a*. Similar lacerations are observed in the matrix area shown in Fig. 11*b*. Thus, as just noted, the pullout process appears to be largely cohesive in nature. Moisture at this temperature did not appear to degrade the fiber-matrix bond.

Figure 12 shows the microstructure of the 132°C/wet condition. Few cooperative fiber fracture events are seen, while fiber pullout dominates the microstructure. Some matrix is adhering to adjacent fibers and acts as an interfiber connection. Examination of the pulled-out fiber surfaces shows no adhering matrix, Fig. 13*a*. Matrix areas where fibers have been

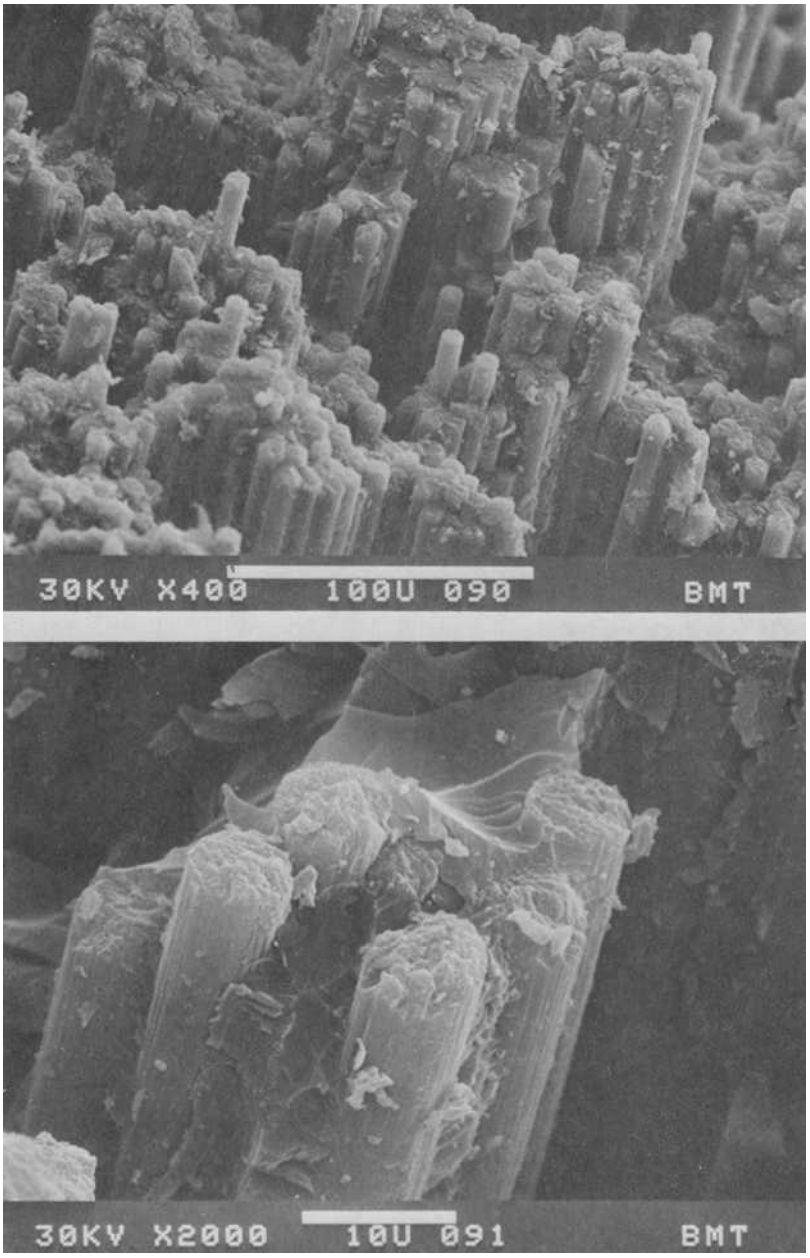

FIG. 7—*Typical microstructures observed for System B specimens at −54 and 21°C/dry.*

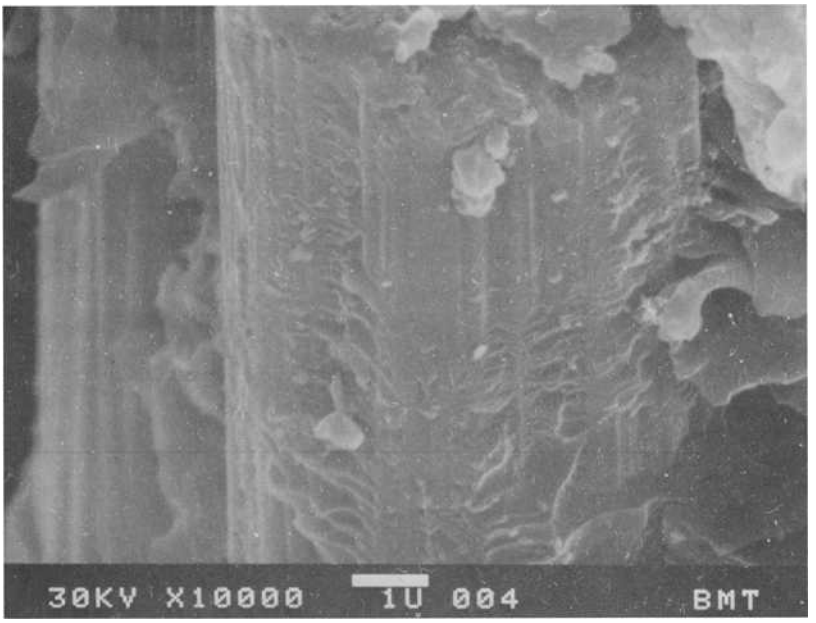

FIG. 8—*Pulled-out fiber surface from System B specimens at 21°C/dry.*

pulled out show little deformation, Fig. 13*b*. System B specimens at 132°C/wet undergo fiber pullout by an adhesive fracture process. The effect of the elevated temperature was seen in Fig. 9 to increase fiber pullout by a cohesive fracture process. In this case of 132°C/wet, the presence of moisture increased the amount of fiber pullout and changed the pullout fracture mode from cohesive to adhesive. While temperature can decrease the modulus of the matrix, moisture can act similarly by playing the role of a plasticizer. Water can also potentially degrade the fiber-matrix bond by diffusing along the fiber-matrix interface. The contrast in pullout mode between Figs. 9 and 12 suggests that in System B the fiber-matrix interface was degraded by the moisture at high temperatures.

While System A showed only modest effects of moisture, System B shows a pronounced moisture sensitivity. Because the fiber-matrix bond did not appear degraded in the 21°C/wet case, Fig. 10, the increased fiber pullout is suggested to be due to moisture softening of the matrix at 21°C. At high temperatures, the pullout fracture mode changed to a nearly perfect adhesive process, suggesting that at high temperatures with moisture present the fiber-matrix bond is degraded. Similarly to System A, high temperature alone increased fiber pullout. However, the large amounts of adhering matrix imply that the enhanced fiber pullout was due to thermal softening of the matrix.

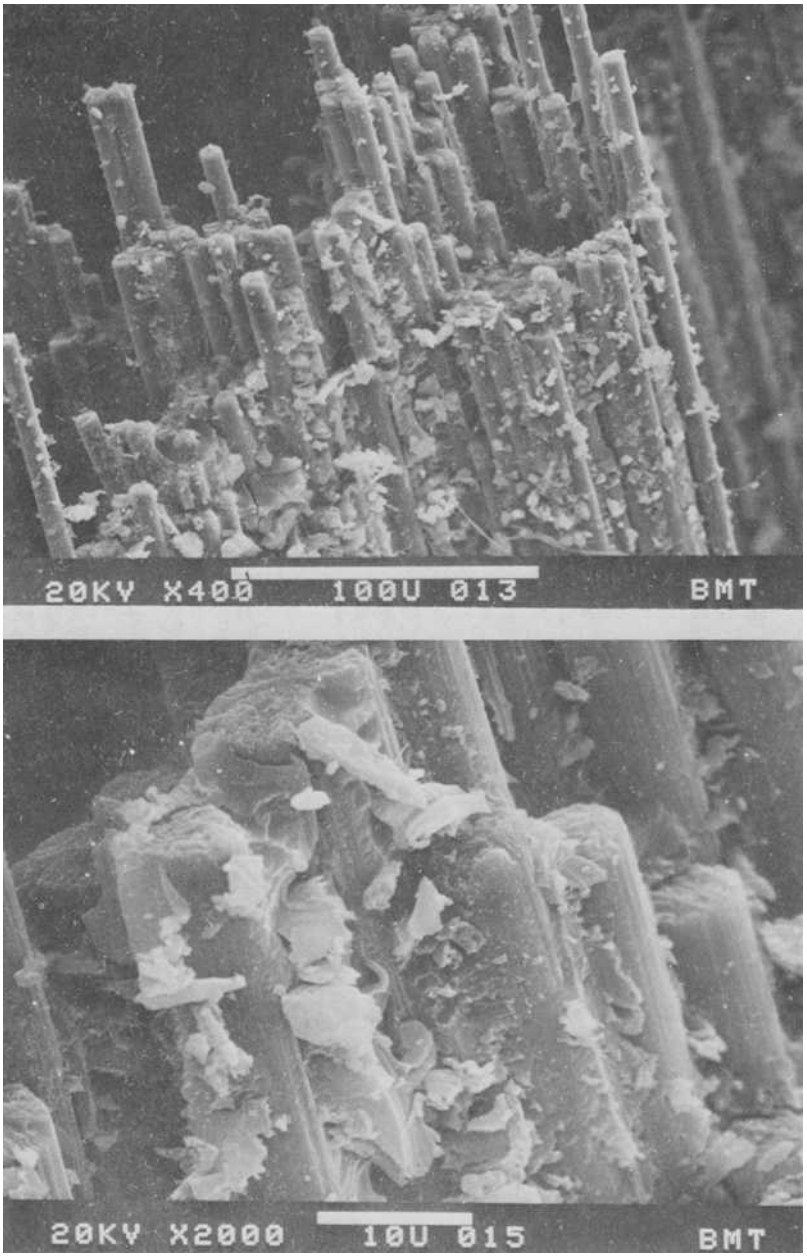

FIG. 9—*Typical microstructures observed for System B specimens at 132°C/dry.*

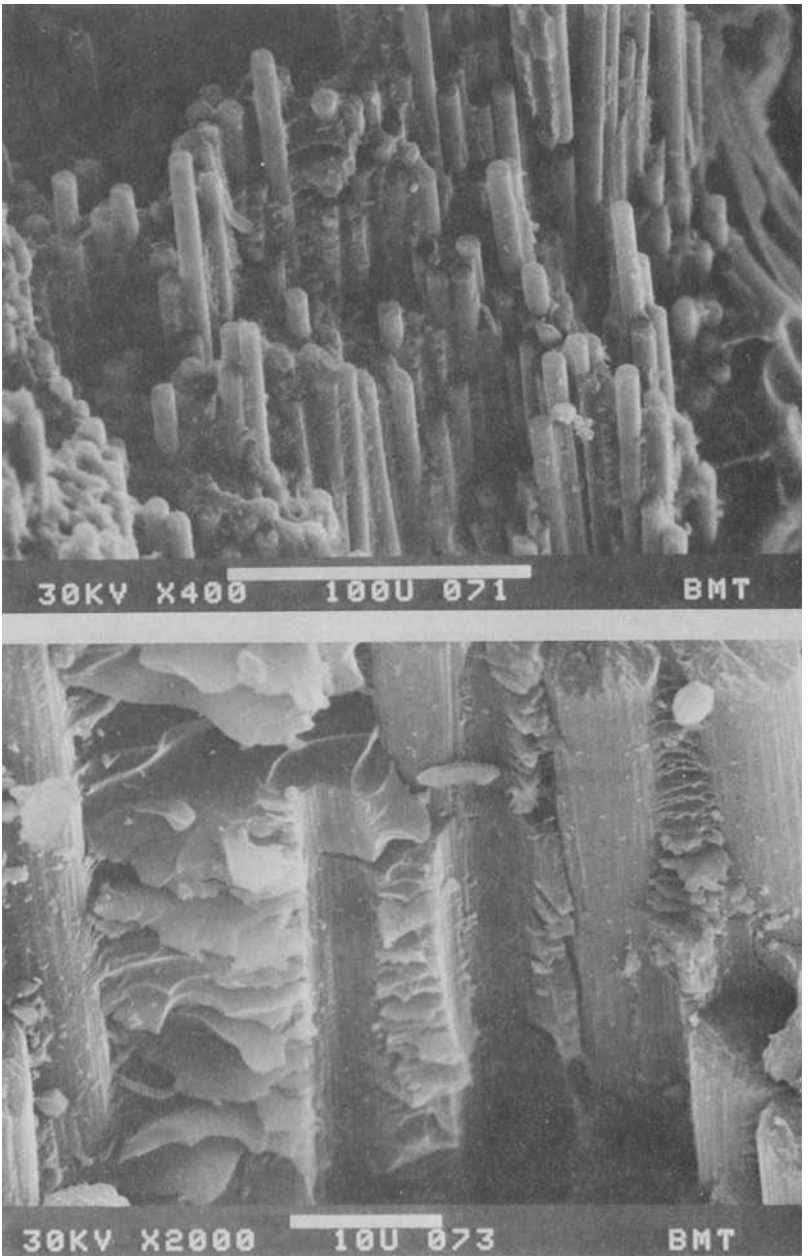

FIG. 10—*Typical microstructures observed for System B specimens at 21°C/wet.*

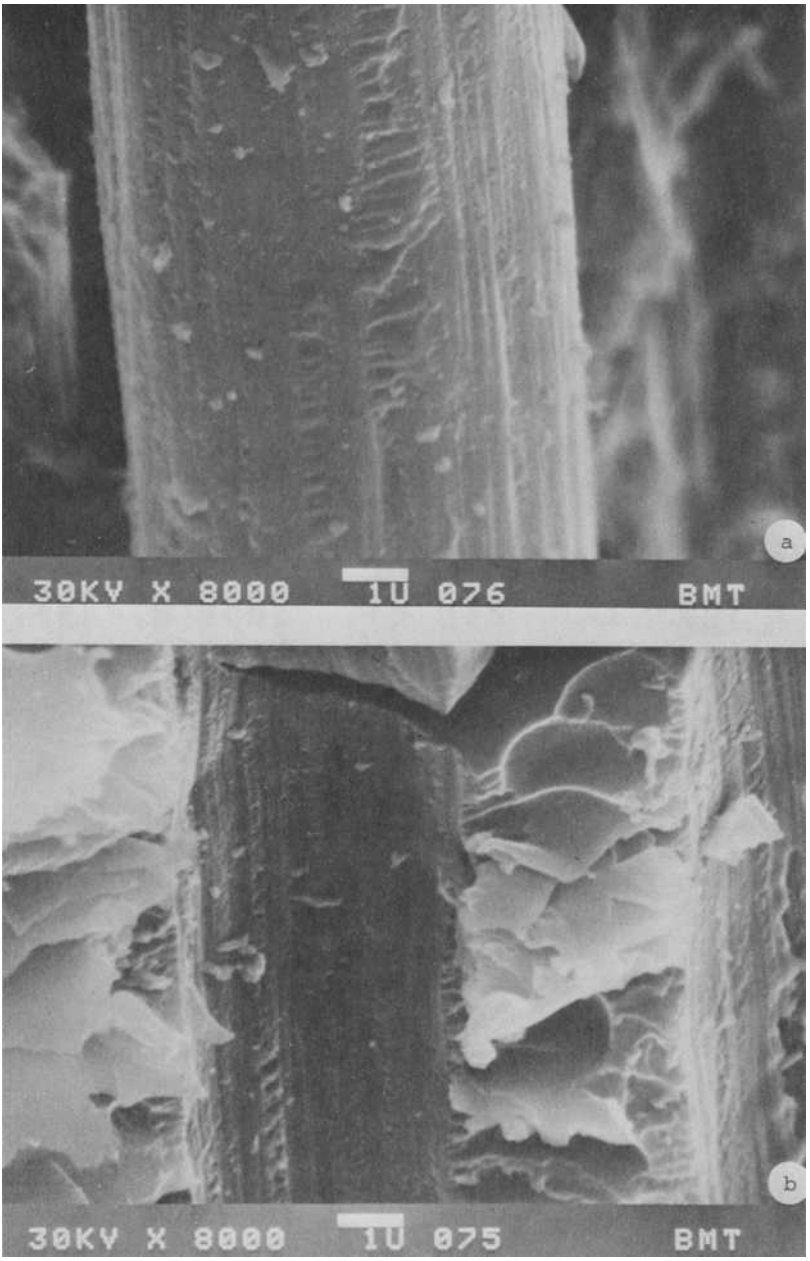

FIG. 11—*A pulled-out fiber surface and a matrix hole from which a fiber was pulled for a System B specimen at 21°C/wet.*

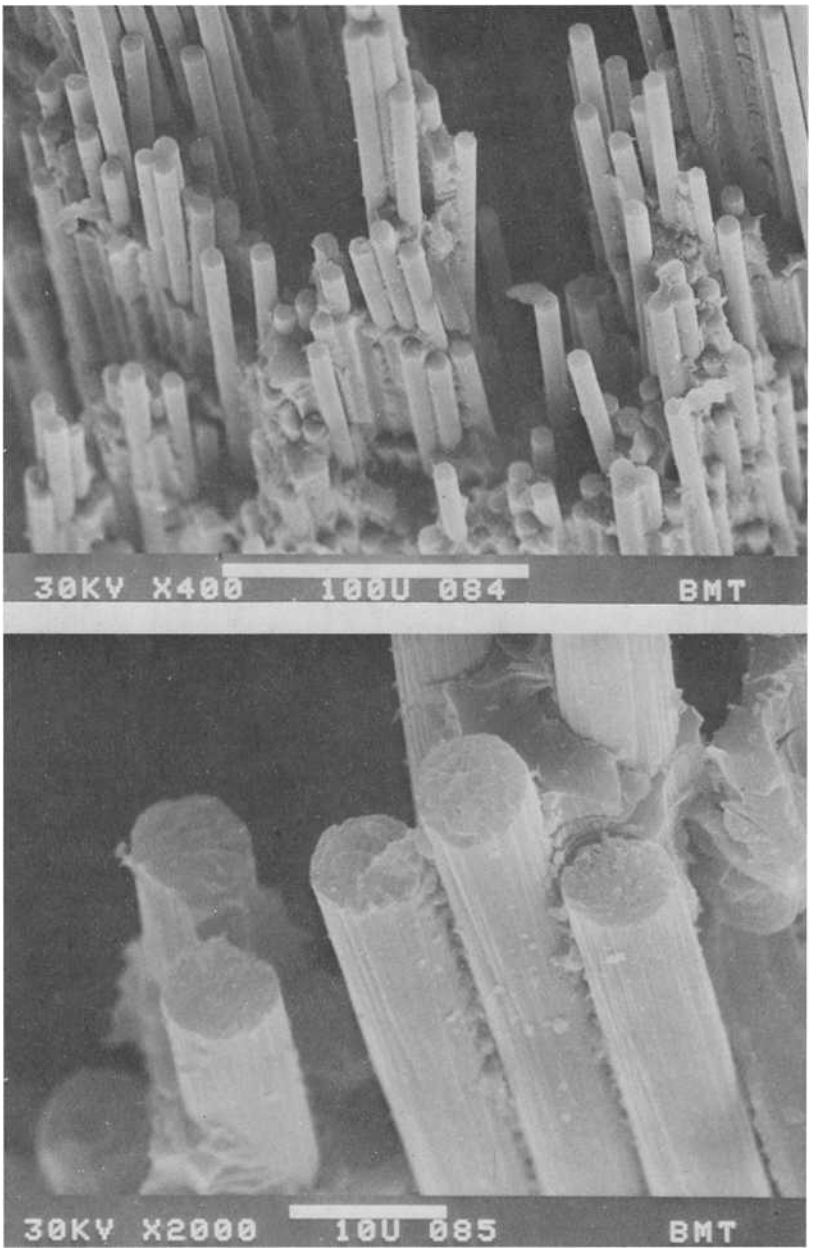

FIG. 12—*Typical microstructures observed for System B specimens at 132°C/wet.*

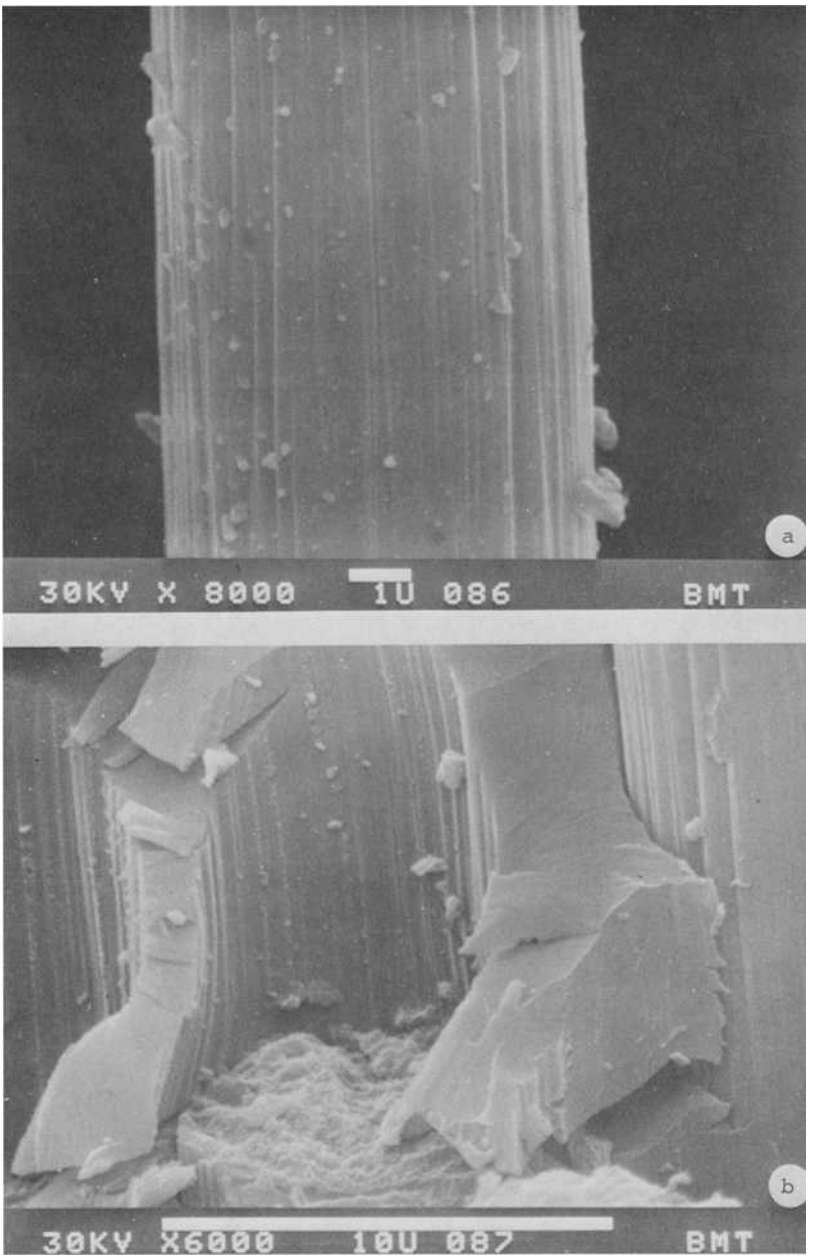

FIG. 13—*A pulled-out fiber and a matrix hole from which a fiber was pulled for a System B specimen at 132°C/wet.*

System C—Figures 14-17 show the fracture surface morphologies of System C 0-deg tapes loaded in tension. Figure 14 shows the typical microstructure observed for the −54°C/dry and 21°C/dry cases. Some areas can be seen in which cooperative fiber fracture events have occurred; however, the overall fracture surface is noted to have many pulled-out fibers. Inspection of the pulled-out fiber surfaces indicate some thin layers of adhering matrix. Thus, the pullout events occurred by a cohesive fracture process.

Figure 15 shows the microstructure for the 132°C/dry case. Greatly increased amounts of fiber pullout are observed. System C does not show a strong influence of temperature on fracture mode between −54 and 21°C, but does so at 132°C. Adhering matrix is observed at 132°C, although not to the extent observed for System B specimens.

Figure 16 shows the microstructure observed for the 21°C/wet case. The number of fiber pullouts did not increase dramatically over the number observed for the −54, 21°C/dry cases, Fig. 14. However, the average length of each pullout has increased due to the moisture exposure.

Figure 17 shows the microstructure observed for the 132°C/wet case. Very long fiber pullouts are seen with some adhering matrix on the fiber surfaces. Thus, pullout occurred in at least a partially cohesive manner.

System C specimens display more fiber pullout at low temperatures than do the System A and B specimens, as shown by a comparison of Figs. 3, 7, and 14. Increased temperature enhances the amount and length of pulled-out fibers. Moisture at 21°C increased the length of the pulled-out fibers, while at 132°C moisture caused very long individual fiber pullouts.

Fracture Process—The fracture events occurring in the 0-deg tapes loaded in tension are extremely complex. As discussed in the preceding, increasing temperature affects the fracture mode by increasing fiber pullout. Moisture modestly increases fiber pullout at 21°C and dramatically increases it at 132°C. The individual events leading to these microstructures are complex, for example, a change in fiber pullout caused by an adhesive versus a cohesive fracture process. Crack propagation does not progress by development and motion of a well-defined crack front. Local fracture events appear to be due to flaw-initiated cracks and possibly to rapid stress wave propagation. As an example of an internal fiber flaw, Fig. 18 is typical. Note the origin in the leftmost fiber fracture surface. Such microstructures are common. Surface flaws due perhaps to fiber processing can be active, as shown in Fig. 19, where a deep surface groove apparently initiated local fracture. The area between two adjacent fibers may contain a flaw, as shown in Fig. 20. In this case, the crack appears to have propagated nearly simultaneously in opposite directions into two adjacent fibers. A fiber fracture event may itself cause fracture in an adjacent fiber via rapid stress wave propagation, Fig. 21. Note that the crack lines which point to an origin in the leftmost fiber also extend without break into the right-

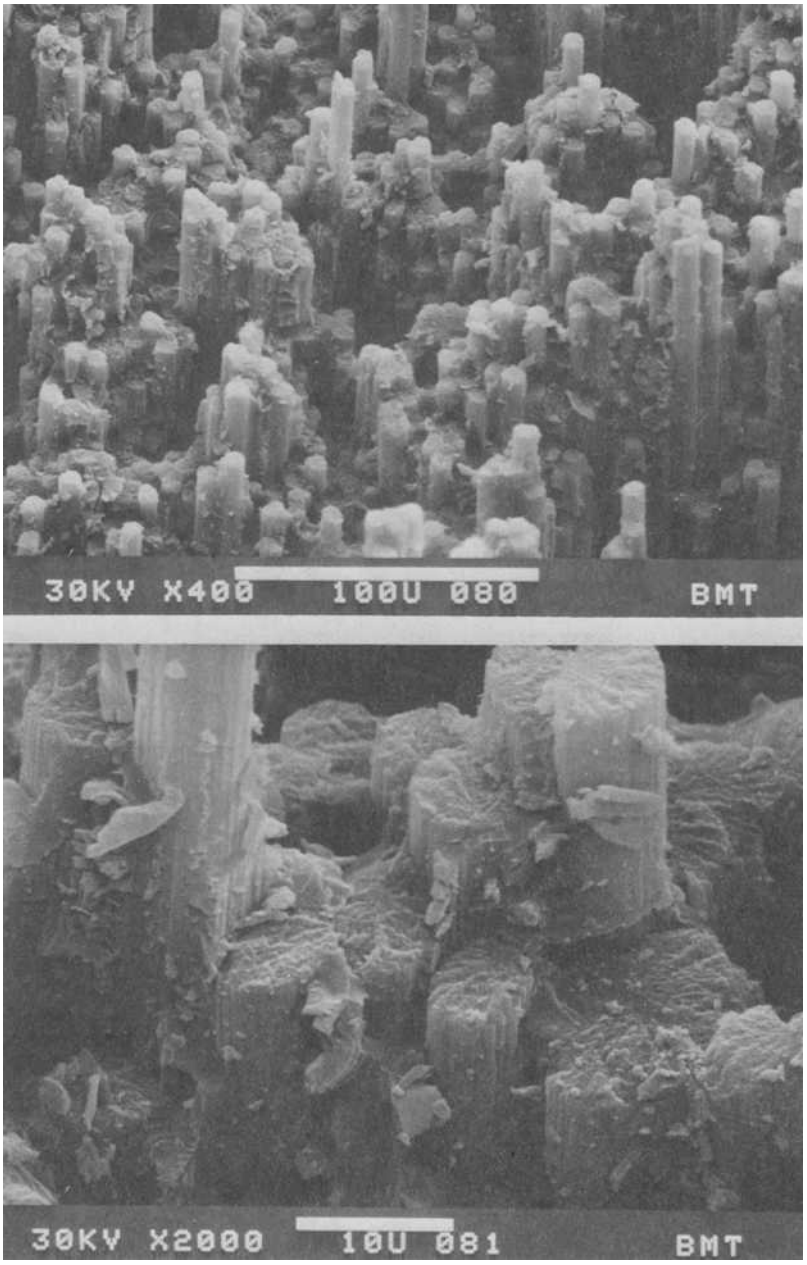

FIG. 14—*Typical microstructures observed for System C specimens at −54 and 21°C/dry.*

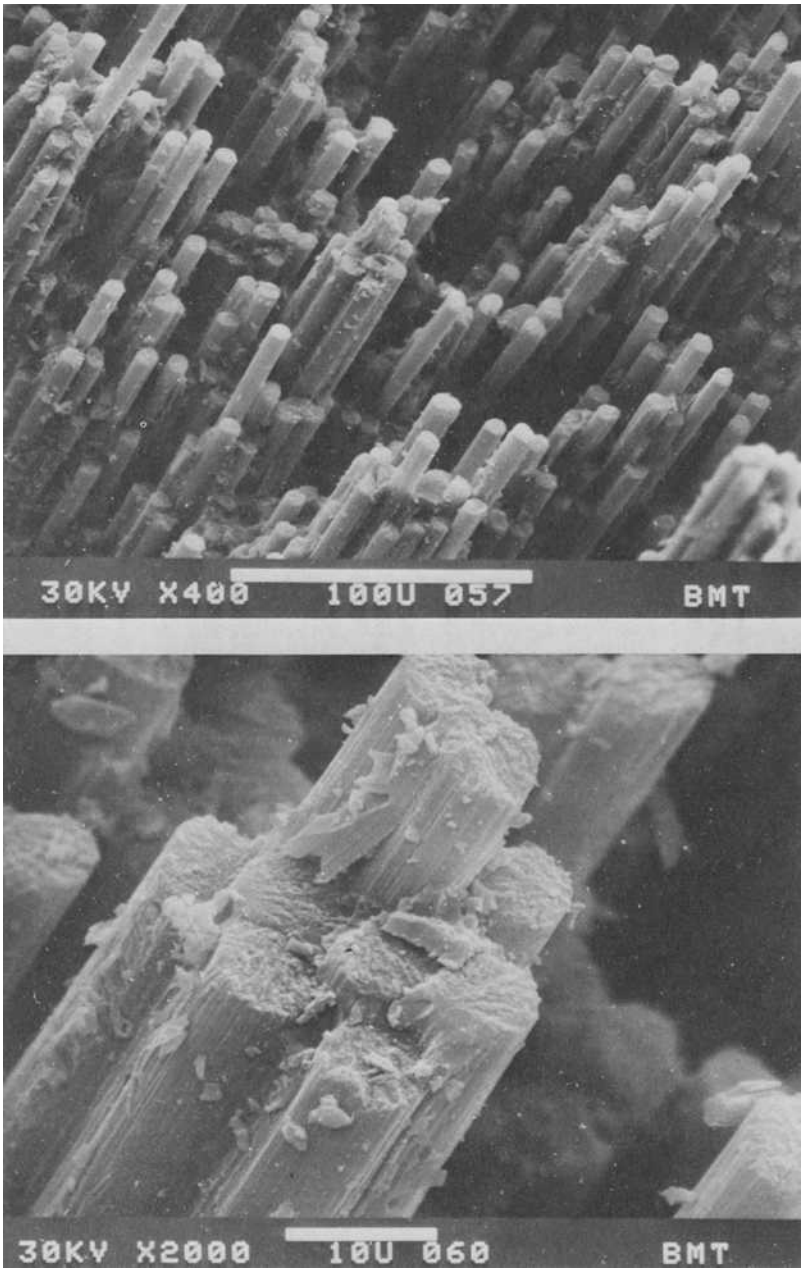

FIG. 15—*Typical microstructures observed for System C specimens at 132°C/dry.*

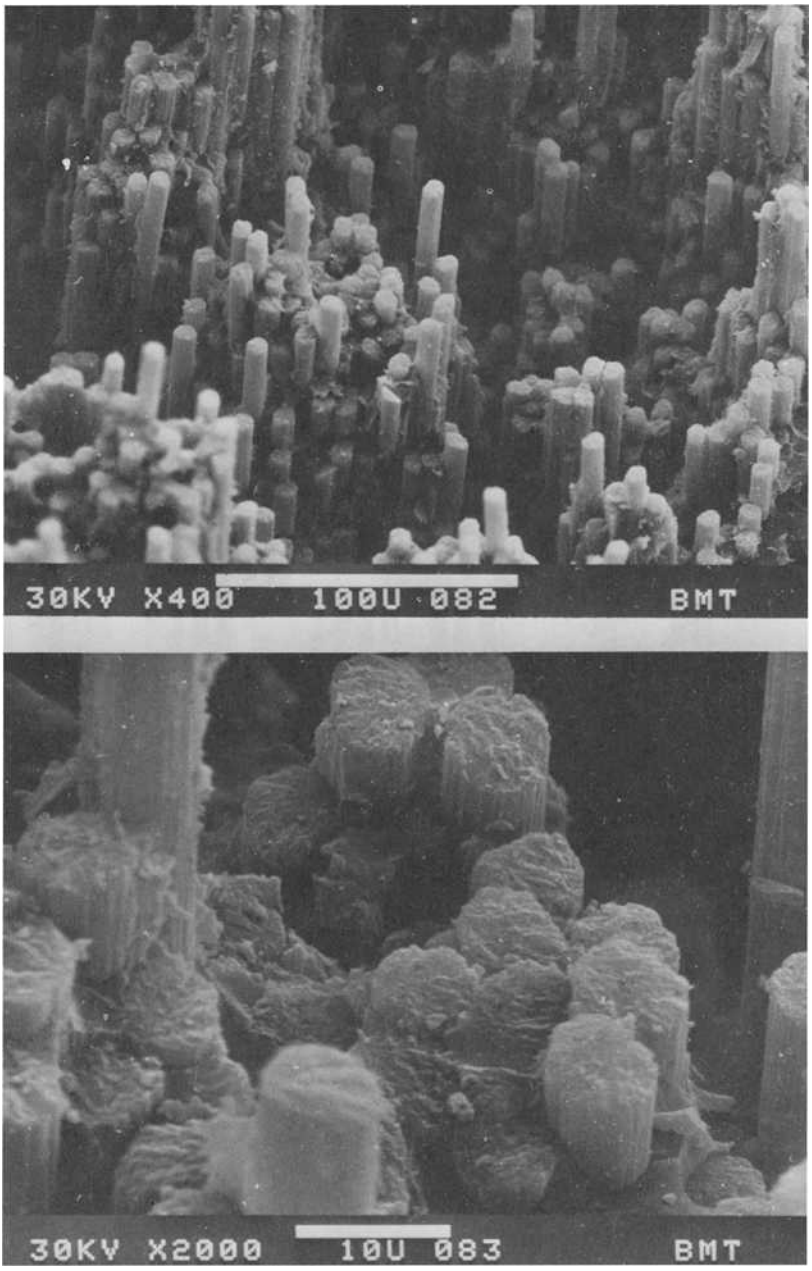

FIG. 16—*Typical microstructures observed for System C specimens at 21°C/wet.*

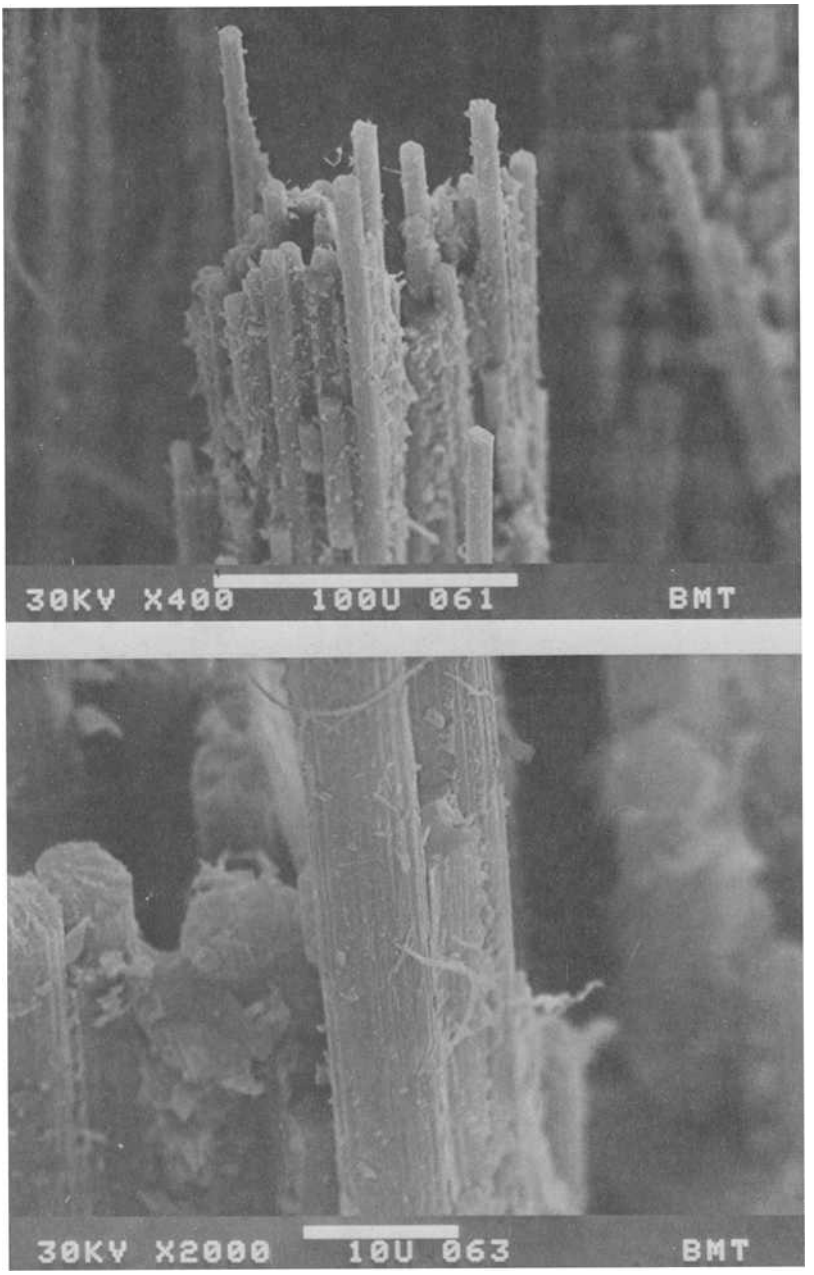

FIG. 17—*Typical microstructures observed for System C specimens at 132°C/wet.*

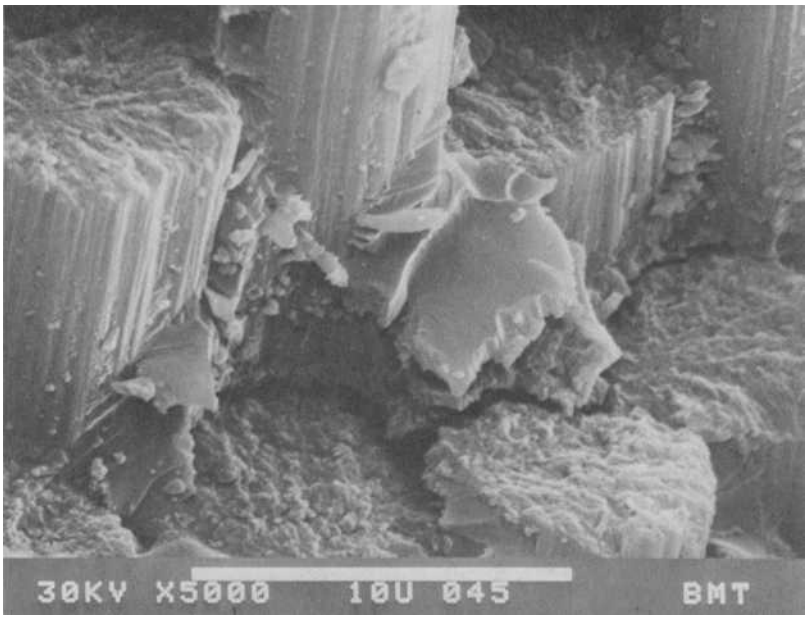

FIG. 18—*An internal fiber flaw which caused a fiber fracture.*

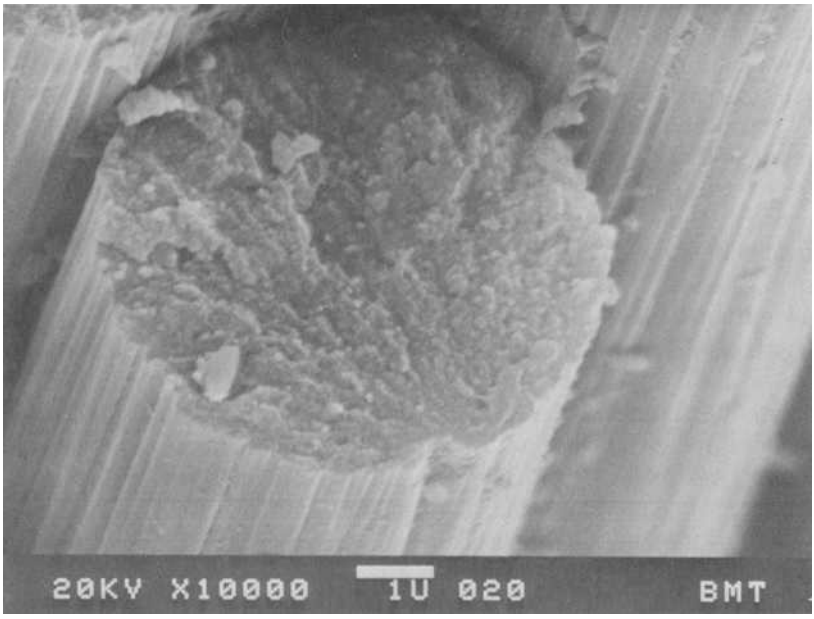

FIG. 19—*An edge flaw which caused a fiber fracture.*

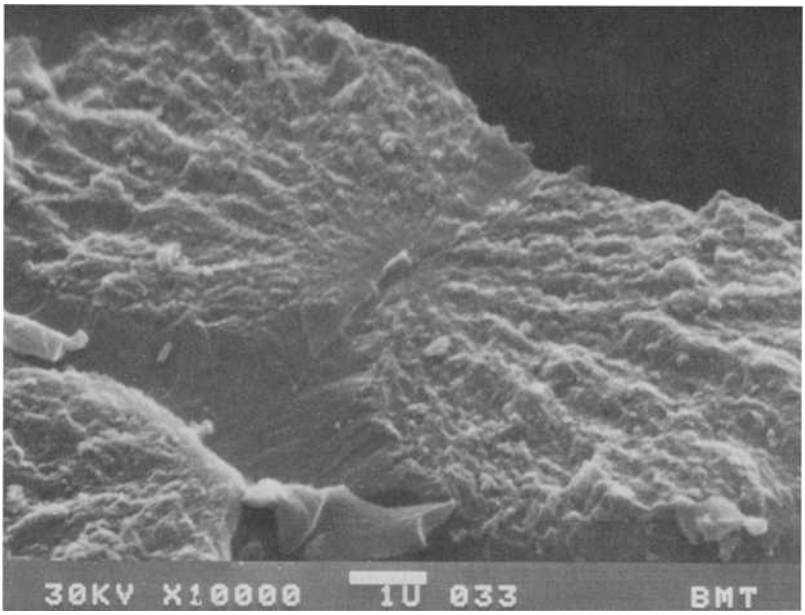

FIG. 20—*A flaw between two adjacent fibers which caused fracture of both fibers. The flaw may be in the matrix phase.*

most fiber. Lastly, crack propagation is not a straightforward process, as shown by Fig. 22. The crack lines in the three fibers in this micrograph show that local fracture occurred in three distinctly different directions.

These observations point to the basic problem of understanding the overall fracture morphology of graphite/epoxy composite materials. Specimen fracture is the cumulative total of a series of nearly independent microstructural fracture events. Extreme caution must be exercised in the extrapolation of isolated microstructural details to the overall fracture process. Local crack initiation and propagation are largely the result of flaw-initiated events in these systems. As is often true for flaw-sensitive materials, the mechanical properties reflect these processes by yielding data with large scatterbands. Despite these limitations, fracture surface analysis does yield information showing fundamental differences between various commercial systems. In addition, the influences of environmental exposure can be observed. Increased study of these types of systems may, therefore, allow development of a coherent approach that would correlate the overall mechanical properties in varying environments with the microstructural details of the fracture process.

Short Beam Shear (SBS)

Figure 23 shows a typical microstructure of an SBS specimen. The

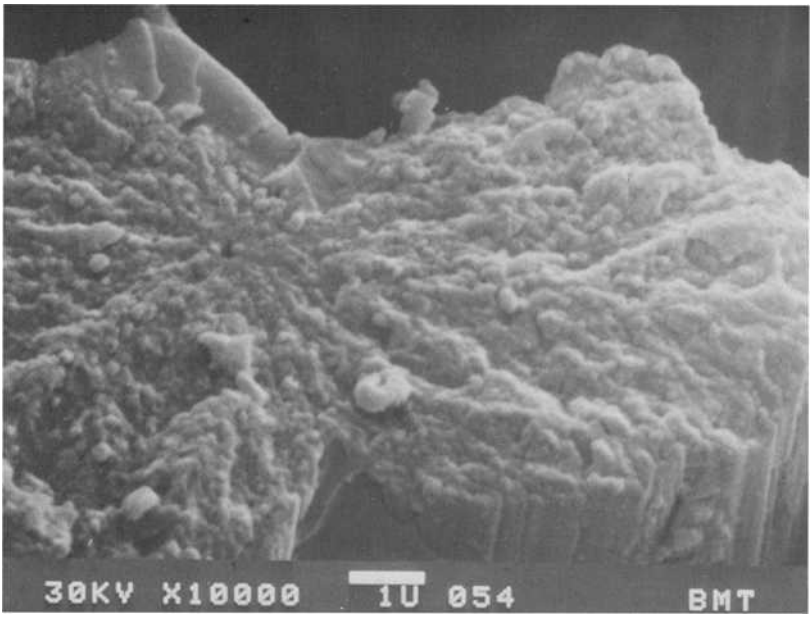

FIG. 21—*Propagation of a crack from a flaw in the left-hand fiber into an adjacent fiber. Note that the fracture lines in the right-hand fiber extend back to the origin in the left-hand fiber.*

view is of the long edge of the specimen with the top of the micrograph representing the tensile stress edge and the bottom of the micrograph representing the compressive stress edge. These specimens are fabrics so that one observes the interweaving of the fiber layers. Different microstructures as presented in the following show different amounts of matrix resin. This does not necessarily imply that the different specimens have varying amounts of matrix, but instead represents the particular cross section examined. In order to relate the microstructural details of these fabrics to the types of microstructures of the tapes discussed earlier, the fibers lying in the plane of the micrograph will be designated as 0-deg fibers and those perpendicular to the plane of the micrograph will be designated as 90-deg fibers.

System A—Figure 24 shows an optical micrograph of the edges of a System A fractured SBS specimen tested at −54°C. The same microstructure is observed for the 21°C case. At these temperatures, the fracture mode is tensile flexure. A crack apparently formed at the tensile stress edge and propagated into the material toward the compressive stress edge. The crack path is a circuitous one, crossing both 0-deg and 90-deg fiber layers. Small subsidiary cracks, which run vertically across the 90-deg layers in the specimen, have formed in areas adjacent to the main crack,

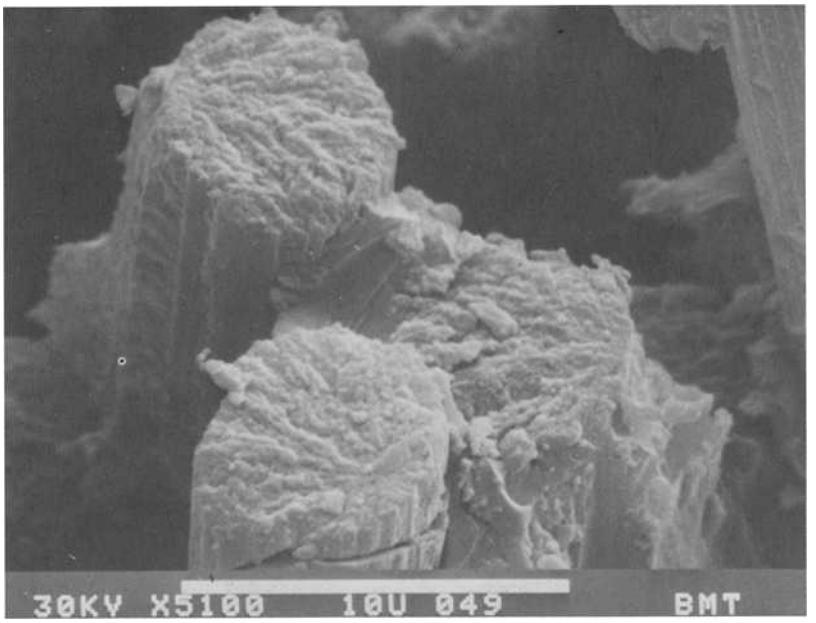

FIG. 22—*Fracture lines on the three fibers indicate that local crack direction occurred in three different directions.*

Fig. 25. In this figure, one notes that the crack fractured through many of the fibers. Because the main crack propagation through an area would have unloaded locally the material at that level, these subsidiary cracks may have formed prior to the main crack propagation through that level.

Alternately, even after the main crack had propagated through an area, continued bending of the specimen may have reapplied load to those areas adjacent to the main crack and caused formation of some of the subsidiary cracks. In addition to the subsidiary cracks, the main crack can also fracture through fibers in the 90-deg layers, Fig. 26.

Figure 27 shows the microstructure of an area where the main crack propagated through a 0-deg fiber layer. The path is a tortuous one which is similar to that observed for the 0-deg tapes loaded in tension, as discussed earlier. As the crack moves toward the compressive edge, large delaminations occur between the 90- and 0-deg fiber layers. The continued crack propagation through a 0-deg layer often occurs a distance away from the previous crack front and, therefore, may be initiated by a flaw in the matrix or in the fiber or in both.

Figures 28 and 29 show the microstructures observed for fracture at 71 and 132°C, respectively. The fracture is characterized by cracks in the 90-deg fiber layers and matrix-rich zones, and by delamination along

FIG. 23—*General microstructure of a short beam shear specimen.*

the 0- and 90-deg fiber layer interfaces. Figure 30 shows a close-up view of one of these cracks that propagated through a 90-deg fiber layer. Note that these cracks uniformly attempt to avoid fracture of the fibers.

Figures 28 and 29 show that the cracks that form at these higher temperatures run at approximately 45 deg to the vertical axis. This orientation represents a conversion of a shear stress acting in a horizontal direction into tensile forces at a 45-deg angle. Thus, the cracks in Figs. 28 and 29 are probably not shear fracture but are instead tensile rupture. This is similar to the view presented earlier that matrix laceration on pulled-out fibers is due to tensile stress resolved from interfacial shear stresses as shown in Figs. 8 and 11. Thus, the tensile strength of the matrix represents the limiting strength factor. However, the intrinsic ultimate strength of the matrix is probably not the key factor. We suggest instead that the flaw sensitivity and flaw distribution function most likely represent the relevant parameters. The matrix materials used in these systems are brittle and

FIG. 24—*Typical microstructure observed for System A specimens at −54 and 21 °C.*

flaw-sensitive, so that the experimentally determined ultimate tensile strength is largely a function of the particular flaw sensitivity and flaw distribution function of the material.

To examine the influence of flaws on these matrix materials, a series of SBS specimens was fabricated using System A resin without any reinforcing fibers. The specimens were carefully outgassed under vacuum and then cured using the same cure cycle as employed for the composites. The specimens were hand-ground and polished to the same dimensions as used for the composite SBS specimens. A total of 36 specimens was tested at room temperature by standard SBS methods. All specimens fractured in tensile flexure at a subsurface location adjacent to the tensile stress edge. Examination of the fracture surfaces showed that all specimens fractured initially at a flaw that was some type of a second-phase particle. The nature and origin of these particles are under investigation. Figure 31 shows several of the particle morphologies observed. Note that the mor-

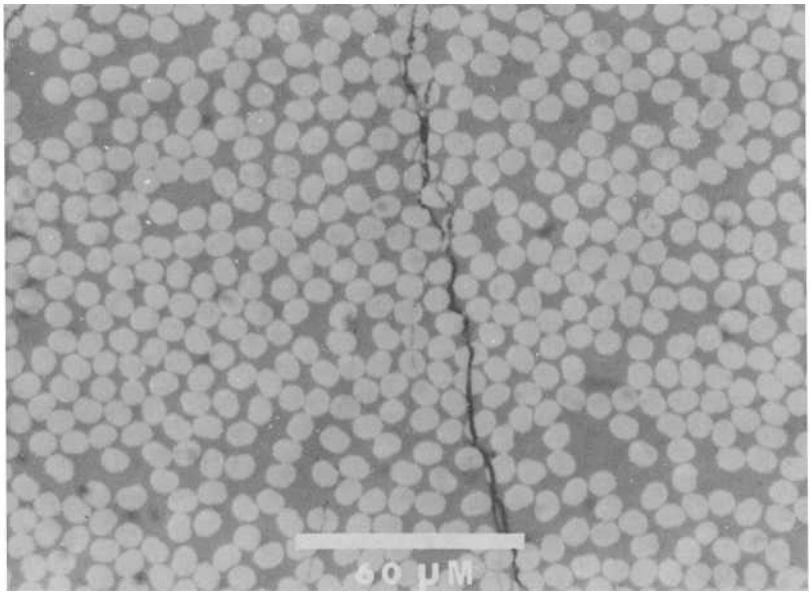

FIG. 25—*Subsidiary crack microstructure seen in System A specimens at −54 and 21°C. Note how the crack propagates through many of the fibers.*

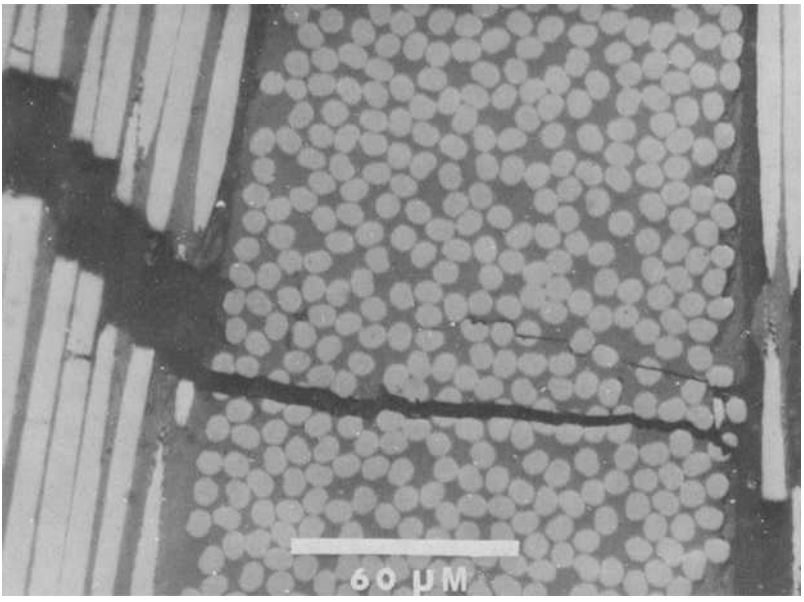

FIG. 26—*Part of the main crack propagation path through a 90-deg layer showing large amounts of fiber fracture.*

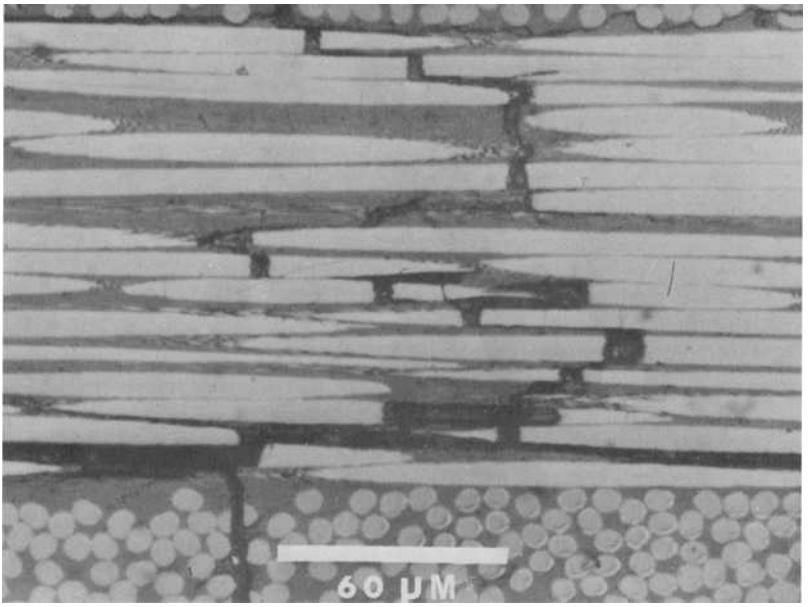

FIG. 27—*Microstructure of crack crossing a 0-deg layer.*

phologies of these particles are not uniform but vary considerably, suggesting that a variety of particulate matter may be present. The number of flaws present may be large, as shown by Fig. 32, a region of secondary crack initiation. The point of these data is that commercial System A resin contains a significant number of flaws and that these flaws appear to cause matrix fracture. Thus, the matrix fracture events of composites formed with these resins may be reasonably expected to be initiated similarly. Matrix flaws may have caused the apparent discontinuity in crack paths and crack initiation sites in the composite specimens for the case of initial matrix fracture events. Although tests have not yet been performed on Matrix Systems B and C, similar results may be expected.

The temperature influence in the System A specimens is large in that fracture occurs at low temperatures by tensile flexure while at higher temperatures an "apparent shear" fracture mode occurs. One may define a transition temperature as the one in which the tensile flexure fracture mode changes to apparent shear. For System A specimens, this transition temperature is between 21 and 71 °C. As discussed earlier, the shear fracture is not a true shear fracture, but is actually a tensile rupture occurring most likely by a flaw-initiated mechanism. The subsidiary cracks observed at low temperature, Fig. 25, run in a nearly vertical fashion and are due to tensile rupture caused by tensile bending stresses. The higher-temperature

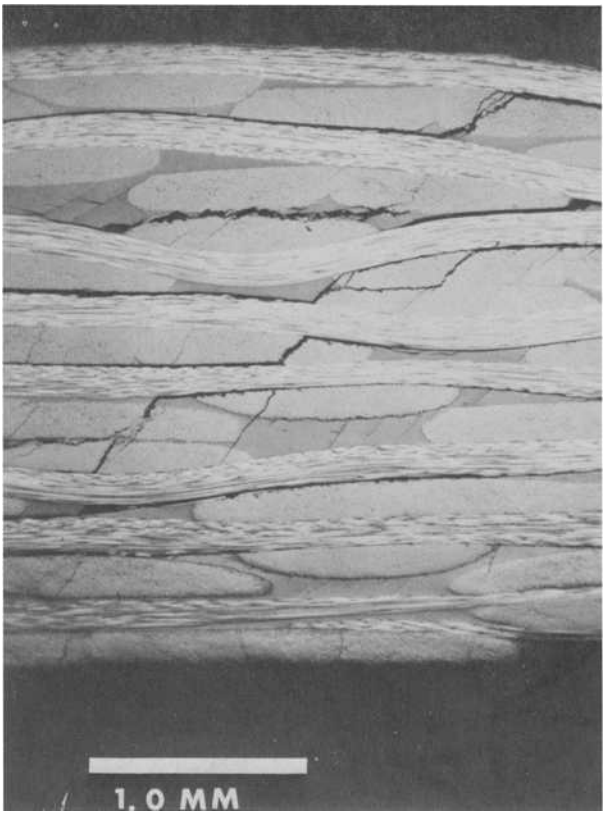

FIG. 28—*Typical microstructure observed for System A specimens at 71 °C.*

specimens also fracture by tensile rupture, but do so due to a resolving of the shear stresses into a tensile mode. Because the higher temperature results in a decrease in modulus of the matrix, that is, softening, a lower-modulus material must promote the apparent shear fracture mode. Although this fracture mode does not appear to fracture across the 0-deg fiber layers, one must remember that only a two-dimensional view is represented by the micrographs. Figure 33 shows a microstructure similar to that observed in Fig. 28, but in a perpendicular view. Thus, the 0-deg fibers in Fig. 28 are 90-deg fibers in Fig. 33, and so on. The 0-deg fiber layers in Fig. 28 are fractured somewhat as shown by Fig. 33, but not in a transfiber mode. The main feature observed in Fig. 33 is the extensive delamination around fiber bundles.

System B—Figure 34 shows one type of microstructure observed for System B SBS specimens tested at −54 °C, while Fig. 35 shows the other

FIG. 29—*Typical microstructure observed for System A specimens at 132°C.*

type of microstructure also observed for this system and temperature. Approximately 20 percent of the System B specimens tested at −54°C displayed the tensile flexure fracture shown in Fig. 34, while the remaining specimens displayed the apparent shear fracture mode shown in Fig. 35. The microstructure of System B specimens tested at 21°C, Fig. 36, displays the apparent shear fracture mode. Thus, the change in temperature from −54 to 21°C was sufficient to change the fracture mode from partially apparent shear and tensile flexure to all apparent shear fracture. This is different from System A specimens, which showed a mode transition between 21 and 71°C. System B specimens have a lower transition temperature between −54 and 21°C than do System A specimens.

Figures 37 and 38 show that the types of fracture behavior observed for System B specimens for the 71 and 132°C cases are similar to those observed for System A specimens. The cracks do not propagate across the 0-deg fiber layers, and they attempt to avoid fibers in the 90-deg fiber

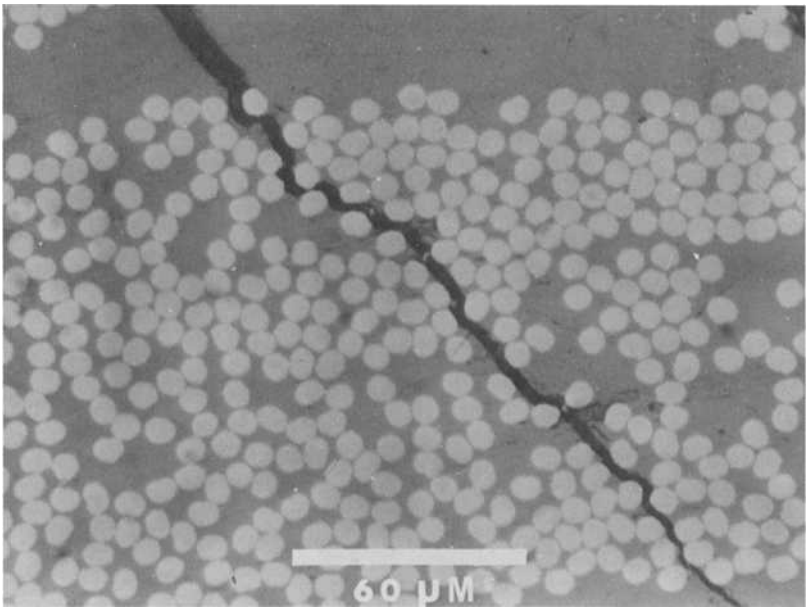

FIG. 30—*Microstructure of crack in System A specimen at 132°C showing crack avoiding fibers.*

layers, Fig. 39. The angles of cracks that form are at approximately 45 deg to the vertical direction, suggesting that actual fracture events represent tensile rupture occurring due to a resolution of shear stresses into normal tensile stresses. The extent of crack formation appears to decrease as temperature increases from 21 to 132°C.

The cause of the change in extent of crack formation may be due in part to an intrinsic material property alteration due to temperature. An increase in temperature causes a decrease in matrix modulus and may also decrease flaw sensitivity. The decreased flaw sensitivity and lower modulus, that is, lower stress for a given strain, may permit formation of fewer cracks at fracture and emphasize delaminations between the 0-deg and 90-deg layers.

System C—Figure 40 shows the fracture mode of System C specimens fractured at −54°C. In all cases, the apparent shear fracture mode is observed. Figures 41, 42, and 43 show that the same fracture mode is observed for the 21, 71, and 132°C cases, respectively. Again, the extent of cracking decreases with increasing temperature. At −54°C, the angular cracks may fracture fibers in the 90-deg layers, but other cracks may avoid the fibers, Fig. 44. At low temperatures, fiber fracture may occur to a limited extent even in an apparent shear fracture mode. By 71°C, the

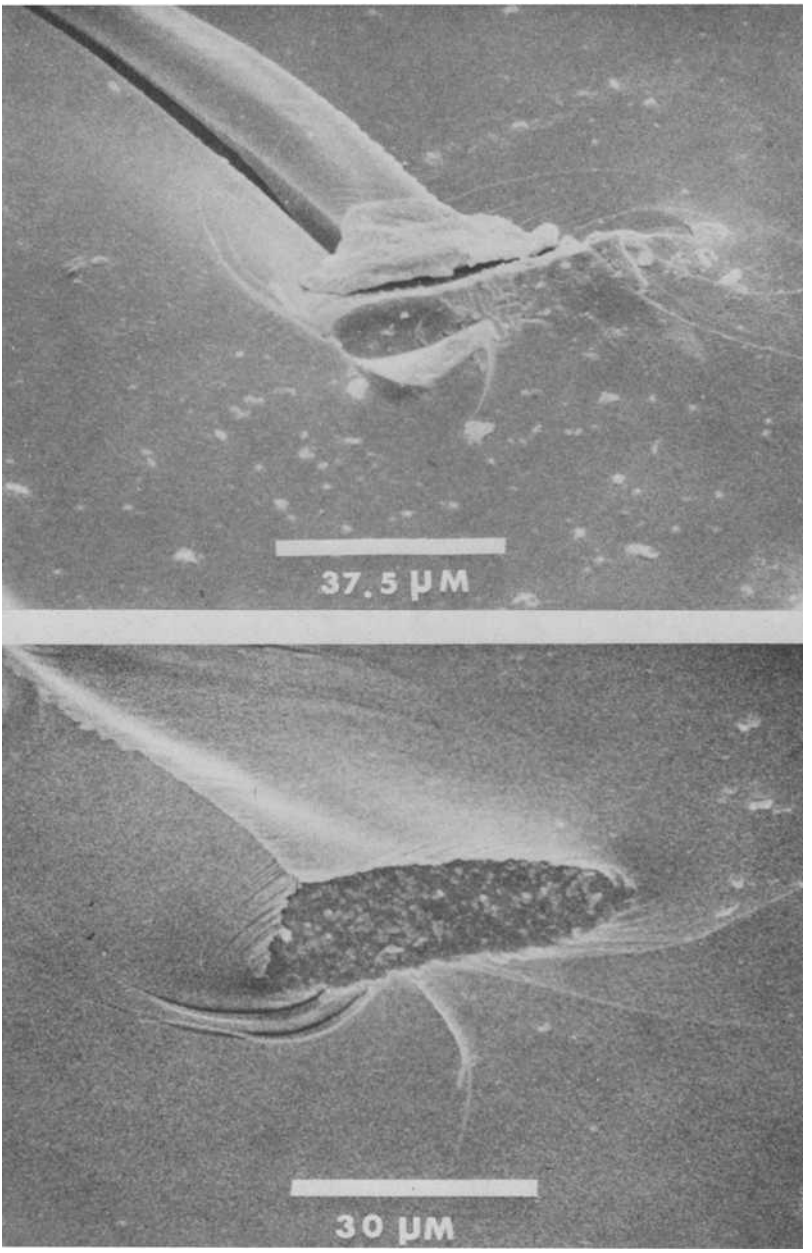

FIG. 31—*Microstructures of three types of flaws found at the fracture origins of System A neat resin SBS specimens.*

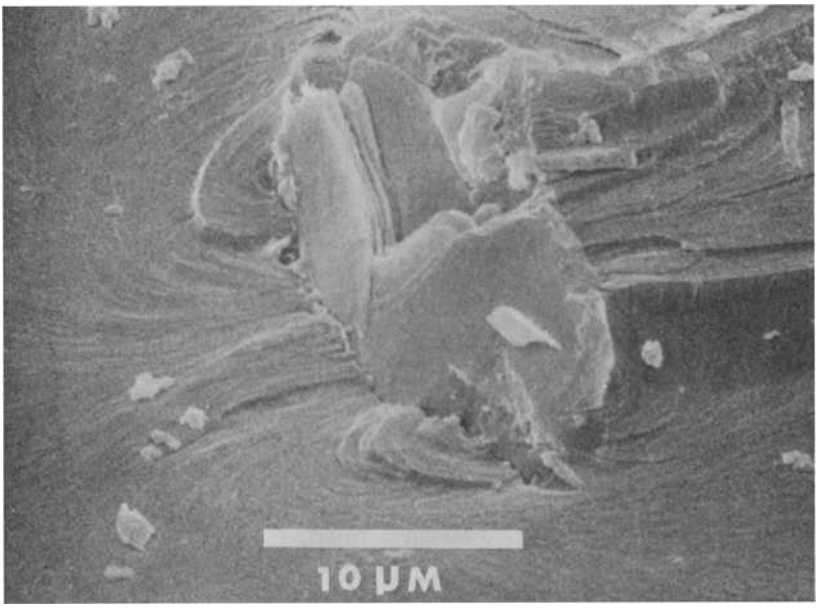

FIG. 31—*Continued.*

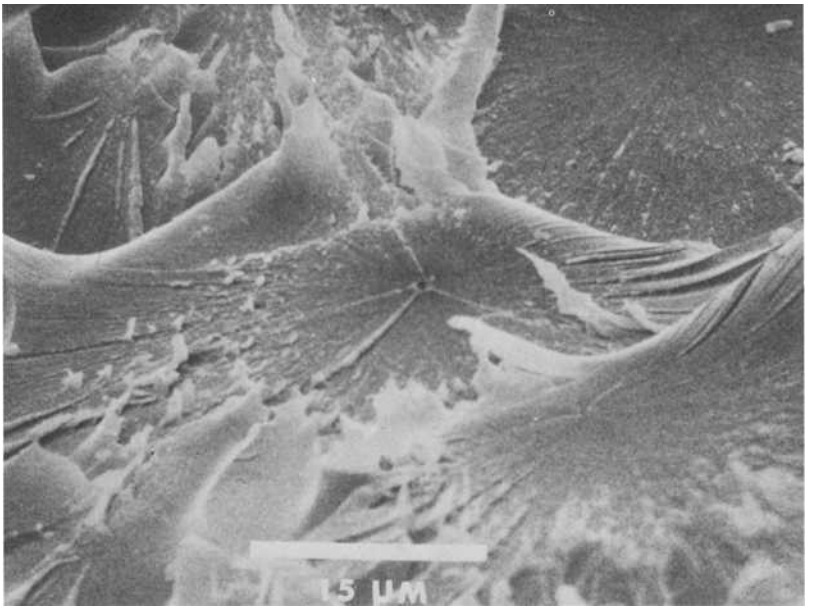

FIG. 32—*Microstructure of area of secondary crack initiation found in System A neat resin SBS specimens.*

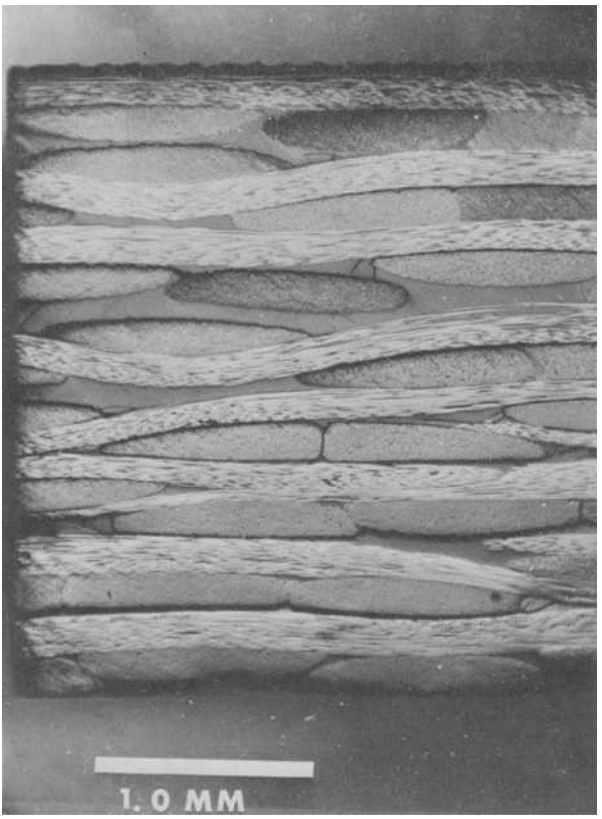

FIG. 33—*Perpendicular views of the SBS microstructure of a System A specimen at 71 °C. Note delaminations around the 90-deg layers which correspond to 0-deg layers in Fig. 28. Some cracking into the 90-deg layers may be seen.*

cracks generally avoid the individual fibers, Fig. 45. At 132°C, cracks may be observed in the matrix phase alone, Fig. 46, in addition to those in the 90-deg layers. System C specimens show no propensity for tensile flexure fracture at any temperature. The transition temperature for System C specimens is below −54°C, which is much lower than was observed for Systems A or B. The cracking again occurred at approximately 45 deg to the vertical, suggesting that matrix fracture occurred due to resolution of shear stresses into tensile stresses.

Discussion

As discussed in the introductory section, the objectives of this study were to (1) develop a rational classification framework by which the fracture

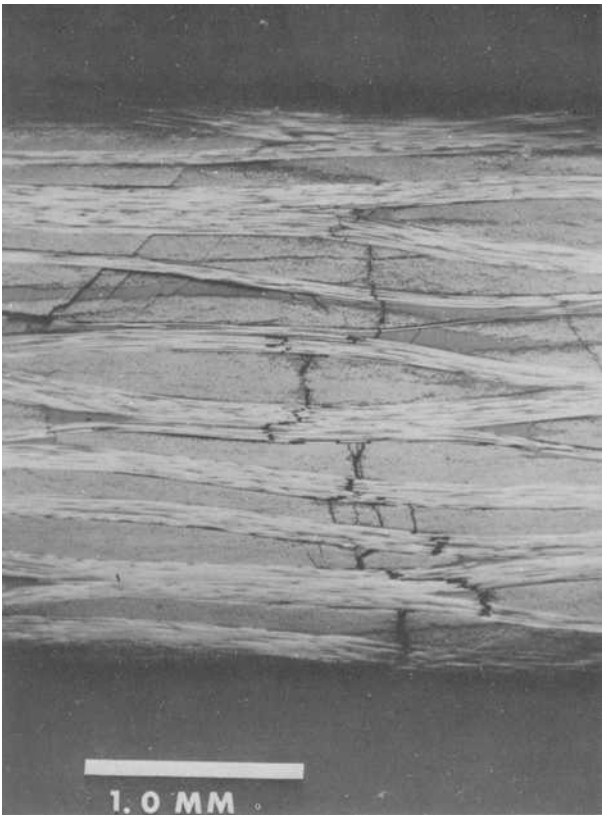

FIG. 34—*Microstructure of tensile flexure fracture mode of System B specimens at −54°C.*

surface morphology could be viewed; (2) determine the influences of load application, material configuration, matrix type, and environmental exposure on fracture surface morphology; and (3) identify crack initiation sites and crack propagation modes. The results of this study have been partially successful in addressing these objectives. However, the extreme complexity of these systems precludes definitive resolution of these questions. Some important observations have been made that will allow, it is hoped, eventual accomplishment of the identified goals.

In terms of a framework of fracture surface characterization, the 0-deg tapes present the most challenging problem. The dominant microstructural feature was the amount and extent of fiber pullout. The pullout fracture process itself was found to be cohesive in almost all cases. The cooperative fiber fracture surface was used to define the small regions in which fibers fractured at the same level in some type of cooperative manner. Character-

FIG. 35—*Microstructure of apparent shear fracture mode of System B specimens at −54°C.*

ization of local fracture events showed that these are generally flaw-initiated events and typically there is no uniform crack propagation direction. This latter aspect makes it difficult to correlate microstructural details with the overall fracture process. As an example of this, a 0-deg tape was edge-notched and then loaded in tension. Under load, the first observable fracture event was a delamination along the fiber axis, which apparently removed the notch from the specimen. The next fracture event occurred on the other side of the specimen without any microstructural linkage to the initial notched area. These types of observations point out the difficulty in trying to describe crack propagation paths in 0-deg tapes loaded in tension. In addition, the flaw-dominated fracture process is the controlling mechanism in these types of specimens. Employment of tougher resin systems may permit more satisfying fracture surface characterization studies.

Short beam shear testing of fabric specimens is an easier system to

FIG. 36—*Microstructure of System B specimens at 21°C.*

characterize in many respects. The competition between bending stresses and shear stresses can be easily documented. Fracture events appear to be controlled by matrix flaw sensitivity. In systems where tensile bending stresses cause fracture, cracks in the 90-deg layers can fracture the reinforcing fibers. Where shear forces are resolved into tensile stresses that cause fracture, the cracks generally attempt to avoid fibers in the 90-deg layers and also will not fracture across the 0-deg layers.

Thus, the morphological criteria for comparing the fracture surfaces of 0-deg tapes are focused on the extent of fiber pullout and on the mechanism of fiber pullout. Attempts to locate crack origins and identify crack propagation paths are probably not feasible for this system. The SBS-tested fabrics indicate that crack origin areas and crack propagation paths can be determined. The type of stress causing fracture, for example, bending versus shear, can be identified. The identification of a specific

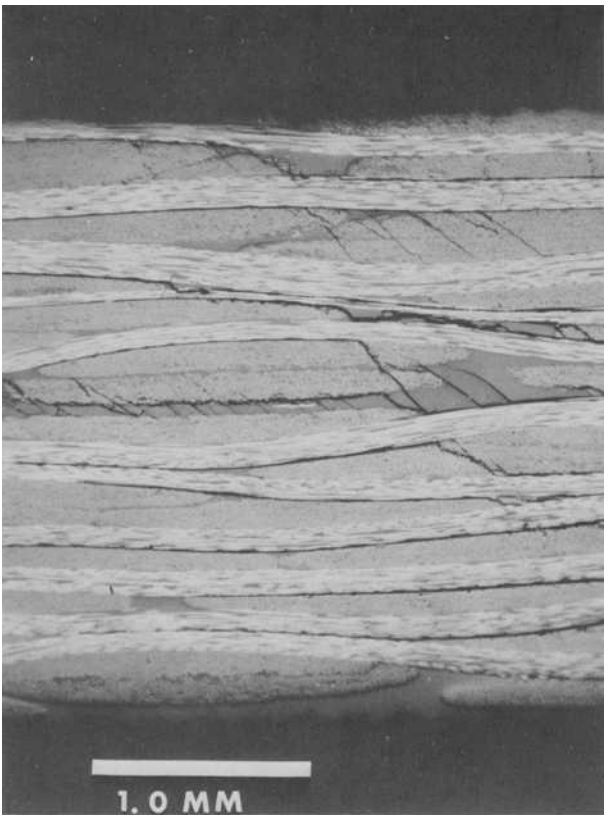

FIG. 37—*Typical microstructure of System B specimens at 71 °C.*

crack origin may be difficult due to the difficulty of observing the specific plane in which it acted.

The effects of environment were easily observed for the 0-deg tapes by the extent of fiber pullout. Increasing temperature increased the amount of pullout. The thermally induced matrix softening appears to increase pullout, although such processes were always found to be cohesive in nature. Thus, the matrix-fiber bond strength was still higher than the internal matrix strength. Thus, one would predict that homogeneous matrix materials of lower modulus would exhibit more fiber pullout than a higher-modulus matrix material.

Moisture exposure caused a modest increase in the amount of fiber pullout at 21 °C. Large amounts of pulled-out fibers were observed for the high-temperature/wet case. Systems A and C displayed a cohesive fracture process for fiber pullout even at the 132 °C/wet environment. Only System

FIG. 38—*Typical microstructure of System B specimens at 132°C.*

B showed evidence of an adhesive fracture process at 132°C/wet. Moisture alone at 21°C or temperature alone at 132°C did not change the pullout fracture mode from cohesive for System B. Thus, only in one case did degradation of the fiber-matrix bond itself by environmental exposure change the observed fracture mode. Cohesive fracture modes are often desirable because they allow a higher confidence in the predicted ultimate stress level. As described in the preceding, this type of fracture mode was generally dominant.

The SBS studies investigated only the role of temperature. System A specimens were characterized by a tensile bending fracture mode at −54 and 21°C. Small subsidiary cracks formed due to bending stresses that quite surprisingly propagated through fibers in the 90-deg layers. The main crack in these specimens also propagated through the 0-deg layers. System A specimens tested at 71 and 132°C showed a change in fracture

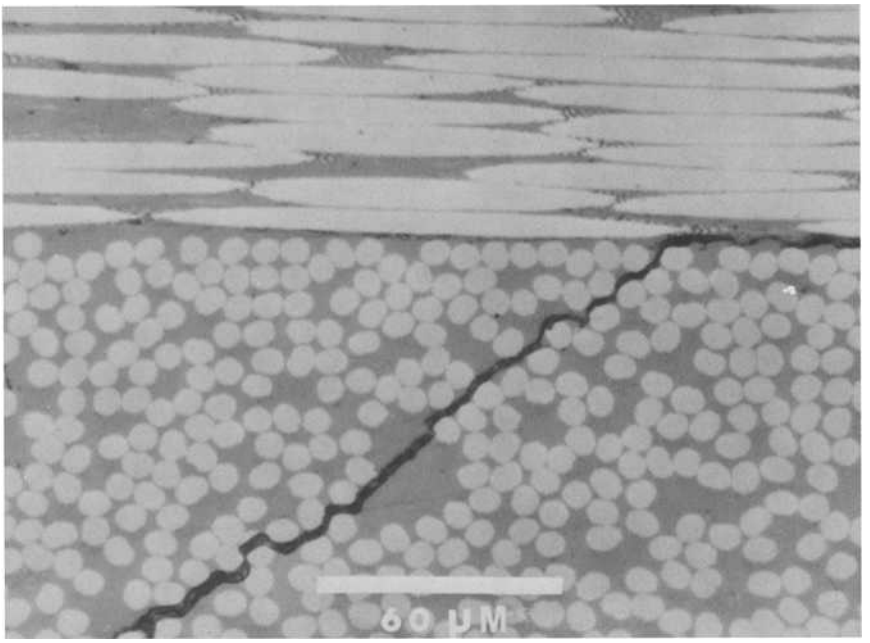

FIG. 39—*Microstructure of crack path of System B specimen at 71°C showing crack attempting to avoid fracture of fibers.*

mode from tensile flexure fracture to apparent shear fracture. The latter was termed apparent shear because the angles of the cracks formed appeared to indicate that they were caused by a resolution of shear stresses into tensile stresses. The cracks no longer crossed the 0-deg layers and avoided fracture of the fibers in the 90-deg layers. Despite the obvious change in fracture mode between −54 and 71°C, System A SBS specimens did not show a large change in ultimate stress, as indicated in Table 3. Either the change in fracture mode does not change the ultimate load-carrying capability of the material or the change is small with respect to the scatter in the results.

System B SBS specimens showed mixed tensile flexure fracture and apparent shear fracture at −54°C. At 21°C, the fracture mode became apparent shear. Thus, the transition temperature for fracture modes was lower for System B than for System A. The higher temperatures of 71 and 132°C showed continued apparent shear fracture. Examination of some matrix-rich areas showed formation of cracks in the matrix, indicating that cracks can form independently of the presence of the fibers.

System C SBS specimen, showed apparent shear fracture at all temperatures from −54 to 132°C. Thus, the transition temperature for System C

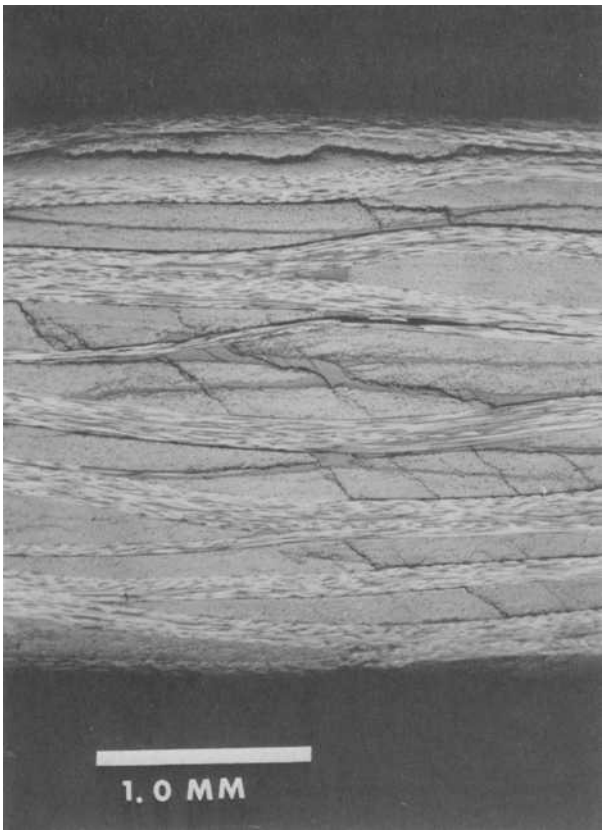

FIG. 40—*Typical microstructures of System C specimens at −54°C.*

was below −54°C. It is interesting to note that System C specimens showed the largest amount of fiber pullout compared with Systems A and B for the −54 and 21°C cases of the 0-deg tapes. Thus, the reasons for the high degree of fiber pullout and the low transition temperature between SBS fracture modes may be related.

Analysis of SBS specimens made of System A resin without fibers showed that matrix fracture occurred at flaws. These flaws appeared to be second-phase particulate matter. Hunter[4] has found by optical microscopy the presence of quartz particles, wood splinters, plant hair, undissolved hardener additives, metallic particles, and diatoms in System A resin. Although studies have not been performed on Systems B and C resin

[4] Hunter, A. B., private communication, Boeing Aerospace Co., Seattle, Wash.

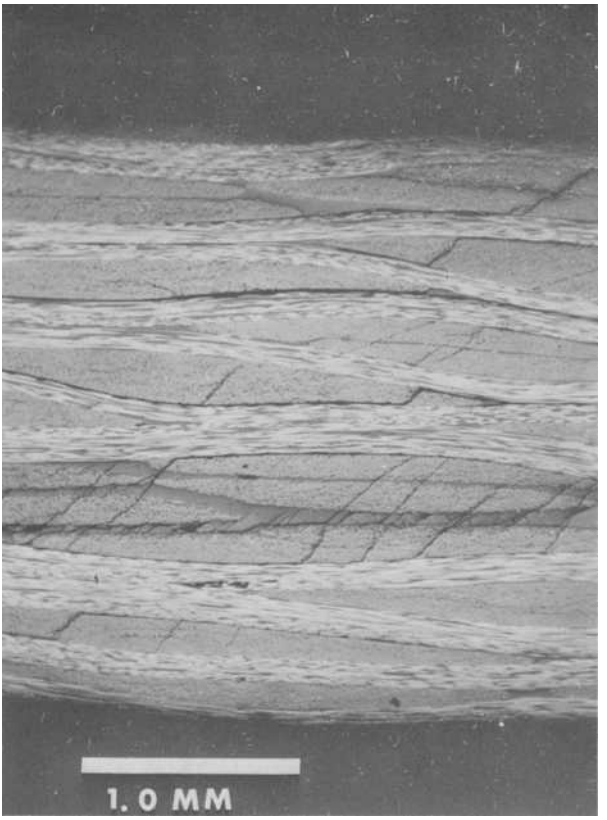

FIG. 41—*Typical microstructure of System C specimens at 21 °C.*

materials, similar results may be expected. Based upon the matrix fracture events observed in the SBS composite specimens, these types of matrix flaws may be important in defining the ultimate stress levels obtained. This is an area in which more work is needed.

The complete correlation between matrix components, fiber type, mechanical properties, and fracture surface morphologies has not yet been achieved. This is because the extreme complexity of each of these areas by itself is multiplied when they are all present. Ultimately, an understanding of these parameters will be necessary for the development of less expensive and more usable composite material applications. The ability to determine the origin and cause of fracture will be essential in order to determine design parameters that will allow the fullest utilization of the high strength-to-weight ratios of these materials.

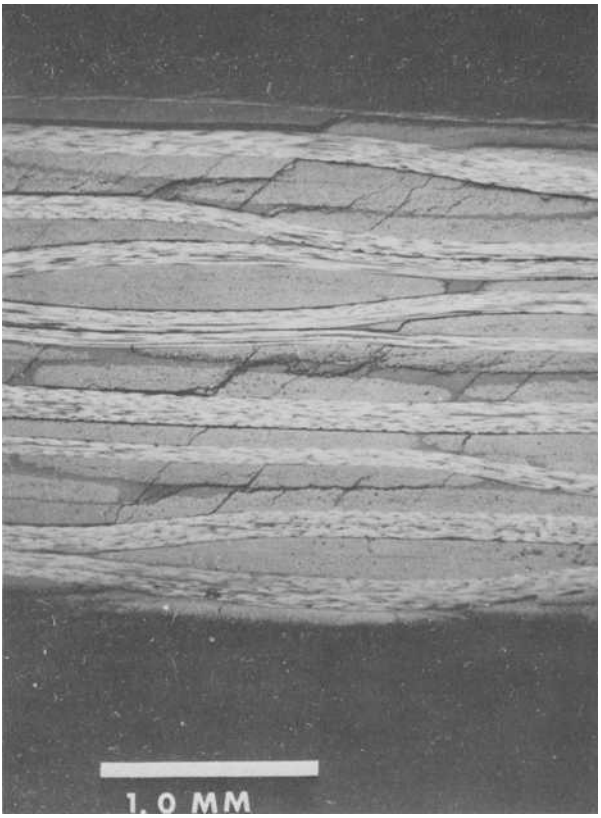

FIG. 42—*Typical microstructure of System C specimens at 71°C.*

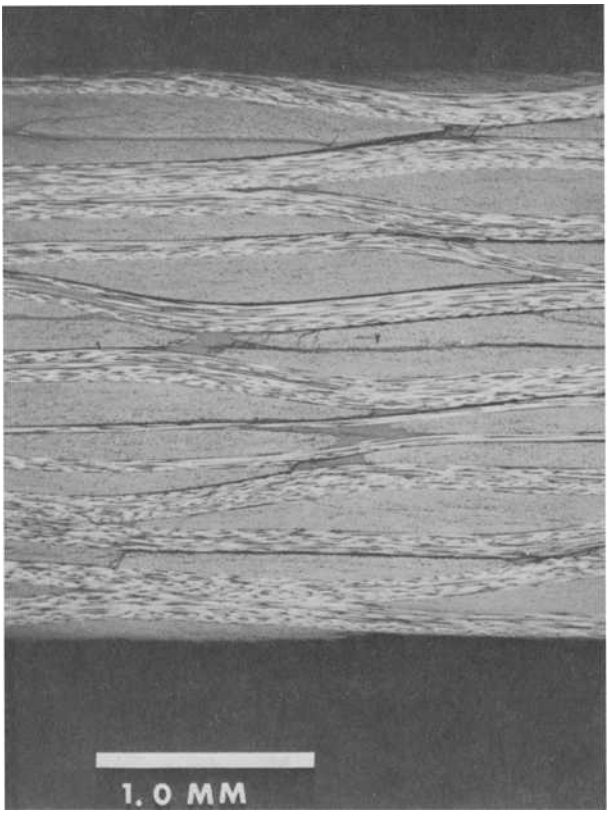

FIG. 43—*Typical microstructure of System C specimens at 132°C.*

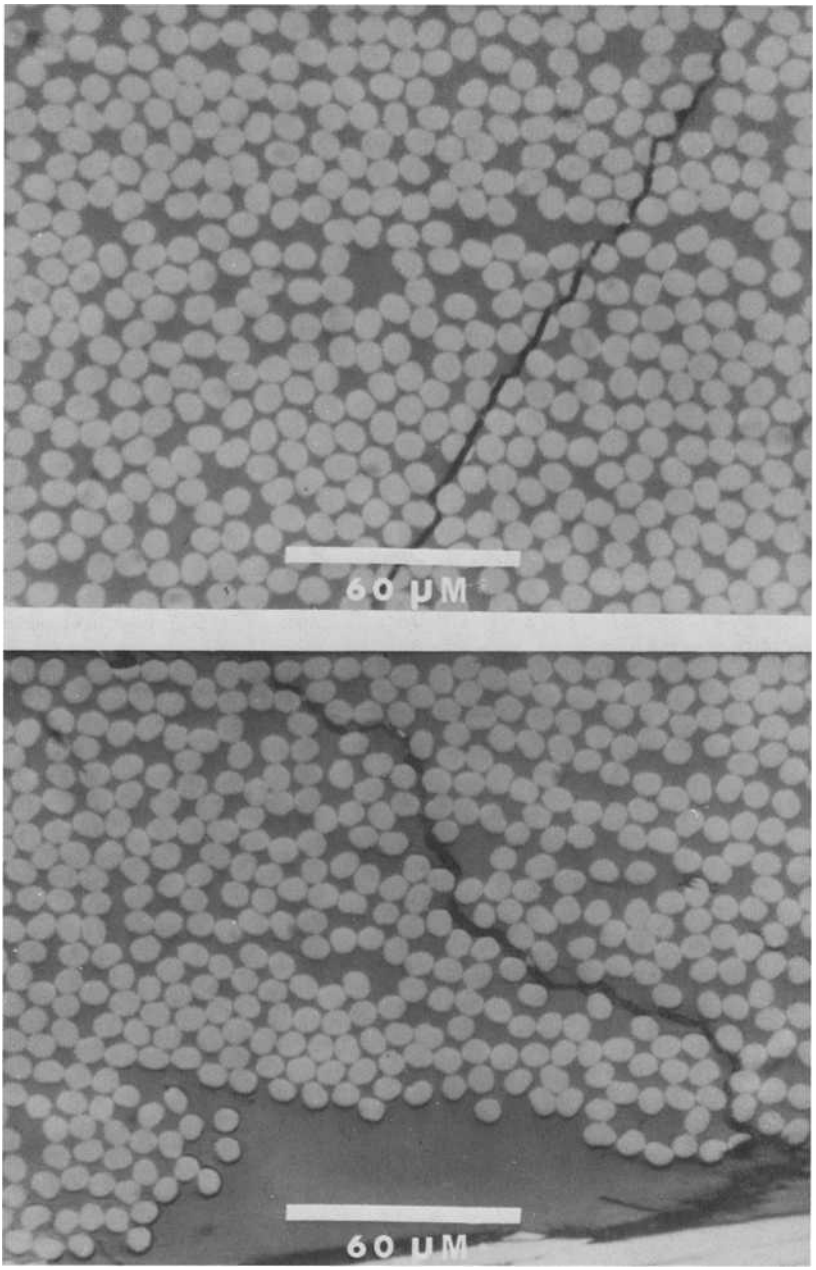

FIG. 44—*Microstructures of cracks in System C specimens at −54°C. Such cracks display mixed behavior in that some cracks fracture through fibers and some do not.*

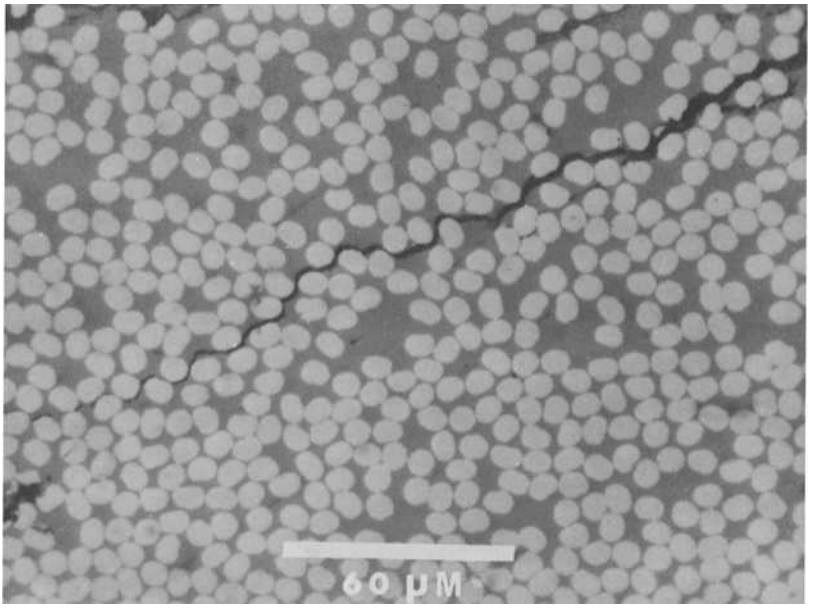

FIG. 45—*Microstructure of a crack in System C specimens at 71 °C. These cracks generally avoid fracture of the fibers.*

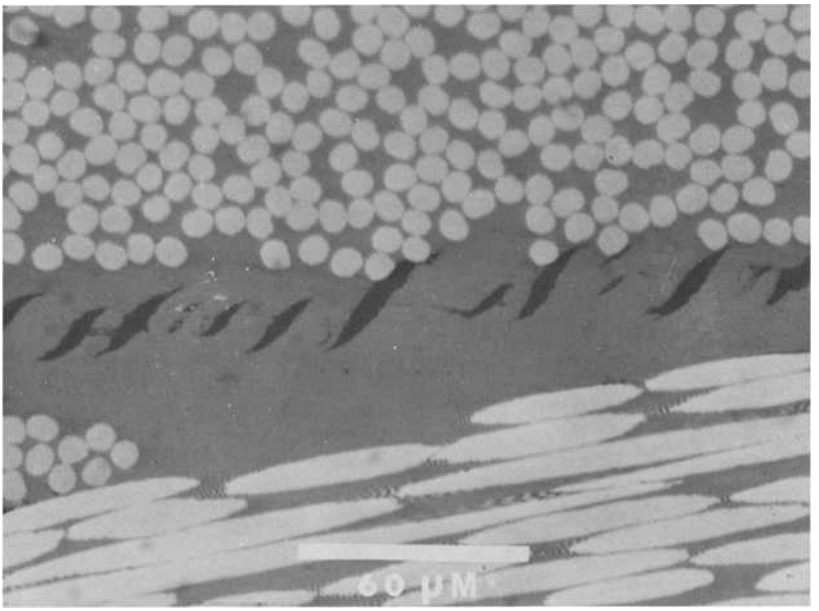

FIG. 46—*Microstructure of cracks found in matrix phase of System C specimens at 132 °C.*

Acknowledgments

We wish to thank D. G. Evans, E. A. Ledbury, and B. W. Smith for assistance in obtaining the micrographs used in this paper. We also acknowledge J. McCarty and A. Viswanathan for guidance and direction during the course of this project. This program was funded by an internal research program at the Boeing Commercial Airplane Co.

G. E. Morris[1]

Determining Fracture Directions and Fracture Origins on Failed Graphite/Epoxy Surfaces

REFERENCE: Morris, G. E., **"Determining Fracture Directions and Fracture Origins on Failed Graphite/Epoxy Surfaces,"** *Nondestructive Evaluation and Flaw Criticality for Composite Materials, ASTM STP 696*, R. B. Pipes, Ed., American Society for Testing and Materials, 1979, pp. 274-297.

ABSTRACT: During this investigation, methods were developed for determining the fracture directions of failed graphite fiber/epoxy resin composite test specimens and structures. Notched test specimens with 90-deg unidirectional fiber orientations were failed in tension by delamination. The resulting fracture surface features consisted of the graphite fiber and epoxy components. Epoxy fracture surface topographic features were identified with a scanning electron microscope (SEM). These features, designated as "hackles," were correlated with the fracture direction. The direction of hackle overlap or tilt reversed when the fracture direction changed. This characteristic can be used to isolate fracture origins on failed test specimens or structures.

Test specimens having cracks with known fracture directions were sectioned, mounted, and polished using standard laboratory techniques and were examined with an optical microscope. A crack tip was detected which provided evidence to support a proposed theory for delamination crack initiation and propagation in graphite/epoxy structures.

Finally, graphite/epoxy test specimens and structural test articles that had been tested to failure in tension and fatigue were examined, and the hackle features were correlated with the fracture directions and origin locations within the specimens.

KEY WORDS: composite materials, fracture (materials), fractography, failure analysis, delamination, fracture direction, graphite/epoxy, nondestructive tests

Fractographic failure analysis techniques for metal structures have existed for over 25 years. These techniques are now routinely used to identify fracture origins and subsequent directions of fracture propagation for components manufactured from any of the common alloys [*1-3*].[2] Failure analysis

[1] Lead engineer, Materials and Physics Laboratories, McDonnell Aircraft Co., St. Louis, Mo. 63166.

[2] The italic numbers in brackets refer to the list of references appended to this paper.

results have become primary considerations when corrective action decisions have had to be made for repairing or redesigning failed metal components.

Epoxy matrix composites, with attractive strength-to-weight ratios, have been developed and, where appropriate, are replacing alloys in various military and commercial aircraft components. These composites have also found many nonmilitary applications in the sporting equipment and automobile industries.

Failure analysis procedures, similar to those that are routinely being used to analyze failed metal parts, are not available for analyzing failed epoxy matrix composites. The most popular failure analysis techniques that are currently available for composites appear to consist of visual examinations that can tell the obvious propagation directions for some cracks, stress analyses of failed components, and stress analyses of failed test specimens that were designed to simulate structural graphite/epoxy components [*4-14*].

Repairs or redesigns of failed composite components often require the incorporation of additional laminate plies with the accompanying weight penalty. By accurately locating failure origins, this penalty can be minimized.

This report describes a technique that has been developed to establish fracture directions and locate fracture origins for graphite/epoxy specimens and structures that fail by delamination.

Procedure

Specimen Fabrication and Testing

Both specimens and structural test articles were studied during this program.

To minimize the variables that could contribute to the fracture surface appearances of the test specimens, initial tests were conducted on specimens that were removed from three 25.4 by 25.4-cm (10 by 10 in.) 40-ply graphite/epoxy panels with either unidirectional 0-deg, unidirectional 90-deg, or an alternate ± 45-deg ply orientation. The panels were laid up using T300 graphite fibers preimpregnated with Narmco 5208 epoxy resin. The laid-up panels were cured in an autoclave for 2 h at a maximum temperature of 177°C (350°F) at 0.69 N/m^2 (100 $lb/in.^2$). They were postcured at 177°C (350°F) for 8 h in an air-circulating oven.

Four test specimens, each measuring 2.54 cm (1 in.) wide by 20.32 cm (8 in.) long, were machined from each panel using diamond-impregnated tools and established machining procedures for graphite/epoxy. An edge crack starter notch was machined at the midlength of each specimen.

Two specimens with each layup configuration were tested with the 0-deg

direction in tension at ambient temperature in air using a universal testing machine. The specimens were loaded to failure at a constant head travel of 0.000021 m/s (0.050 in./min). Since these specimens were tested only to provide fracture surfaces with known origins and fracture directions that resulted from tension overload, mechanical properties data were not recorded.

Another type of test specimen measured approximately 1.27 cm (0.5 in.) thick by 7.62 cm (3 in.) wide by 33.02 cm (13 in.) long and consisted of 1.01-mm-thick (0.04 in.) graphite/epoxy skins bonded to phenolic honeycomb core, Fig. 1. The graphite ply orientations in the skins were 0, ± 45 and 90 deg. This specimen had been damaged intentionally by dropping a 1.27-cm-diameter (0.5 in.) steel ball onto the center area of one graphite/epoxy skin. The resulting delamination damage was measured with an ultrasonic flaw detector and was mapped on the skin surface (Line 1, Fig. 1). Two consecutive axial compression-compression fatigue tests resulted in extensions of the initial damaged area (Lines 2 and 3, respectively, Fig. 1). This specimen provided delaminated graphite plies with different orientations and with fracture surfaces having a known common fracture origin for fracture direction studies.

The third type of specimen examined was a cover panel for a graphite/epoxy wing box beam test article that failed in compression during a four-point bend test. This failed panel provided multiple fracture surfaces to analyze for fracture origins.

Macroexamination and Specimen Preparation

Macroscopic examinations were conducted using a stereo zoom microscope at up to $\times 30$ magnifications. Figure 2 shows views of typical failed notched tension specimens. None of the failed tension specimens exhibited any macroscopic features that revealed the locations of the fracture origins; the 0-deg specimens failed typically by lengthwise shear at the tip of the notch and were not examined further. Specimens containing the fracture surfaces of the 90-deg and ± 45-deg fiber orientations were excised from the failed notched tension specimens for subsequent scanning electron microscope (SEM) examination.

The compression-compression fatigue specimen was sectioned to obtain the six numbered pieces shown in Fig. 3. When pieces of the specimen were viewed obliquely, as shown by the example in Fig. 4, a correlation between some of the interlaminar cracks in the graphite/epoxy skin and the surface map marks was evident. Pieces of the delaminated skin were peeled from each specimen to expose the delaminated fracture surface areas for SEM examination.

Specimens were cut from various locations along the fracture surfaces

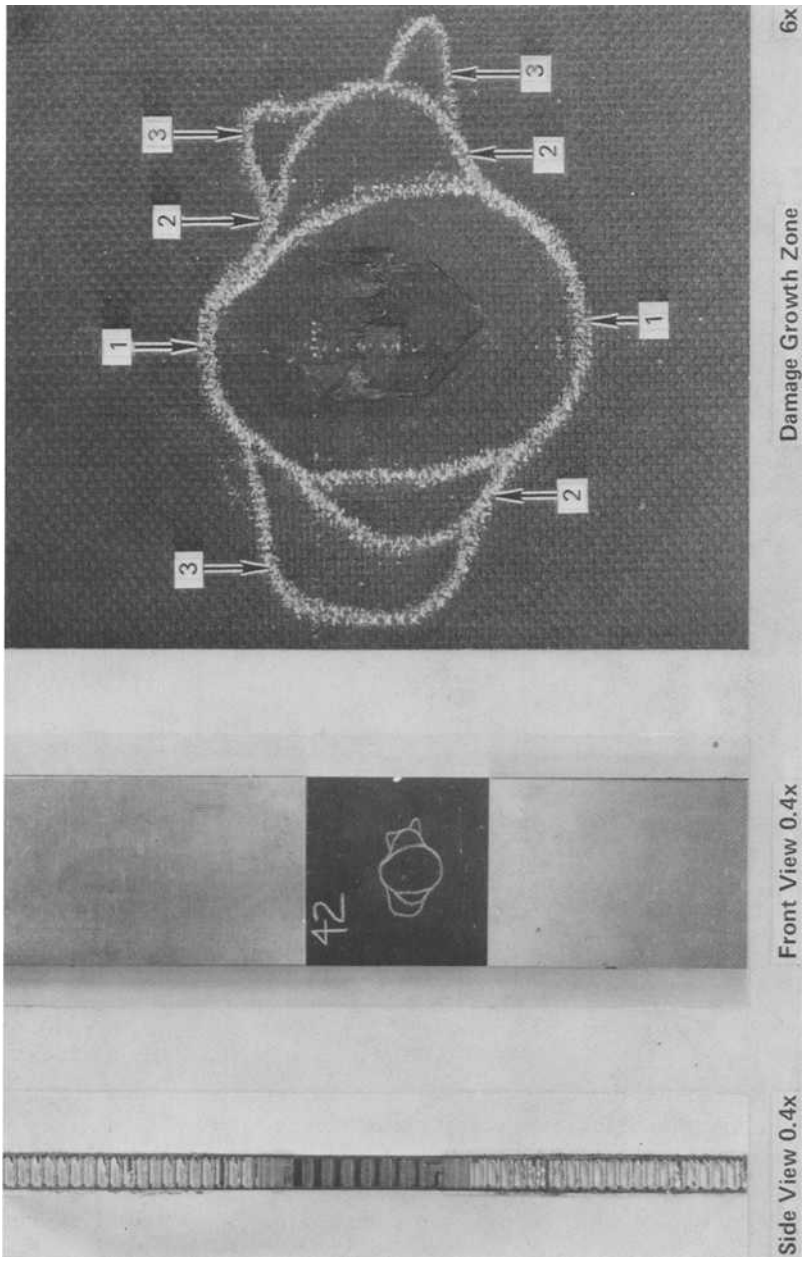

FIG. 1—*Compression-compression fatigue specimen.*

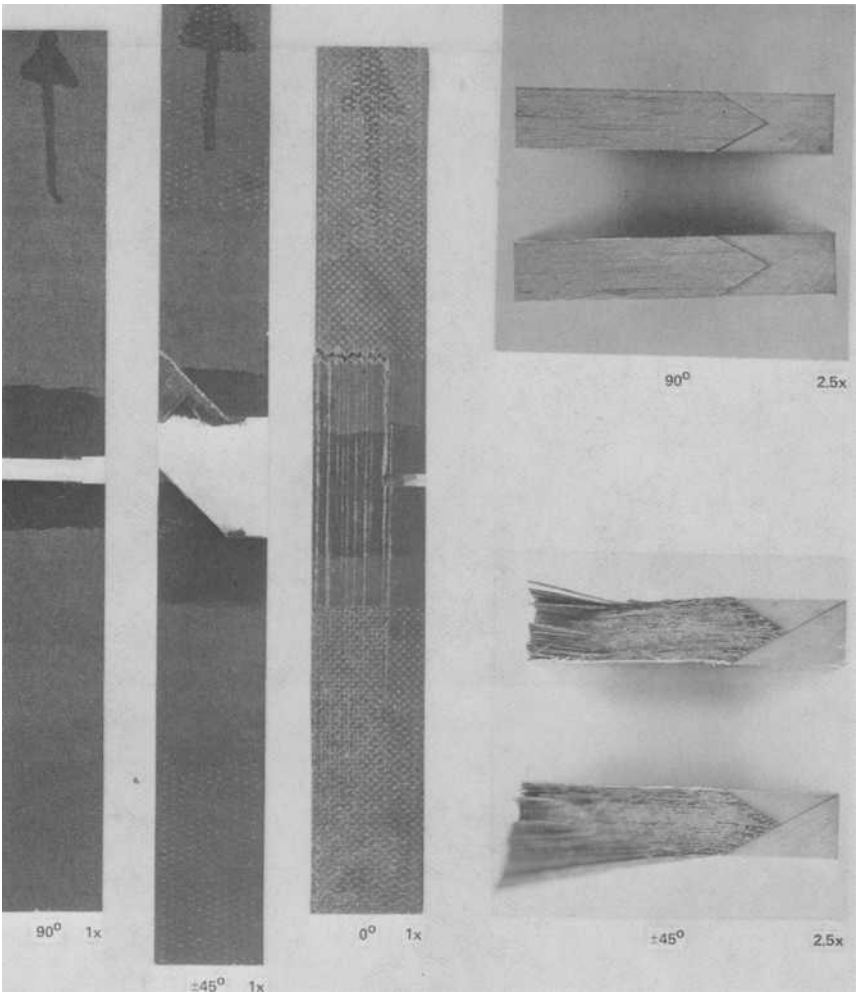

FIG. 2—*Typical failed graphite/epoxy tension specimens and typical fracture surface features of the 90-deg and ±45-deg specimens.*

of the failed graphite/epoxy torque box lower cover component for SEM examination to establish the locations of fracture origins.

Prior to SEM examination, gold was vacuum-evaporated onto the fracture surface of each specimen to obtain optimum resolution of the topographic features and to minimize excessive static charging by the SEM electron beam.

To further study the morphology of graphite/epoxy fracture surfaces, several delamination cracks were created in 40-ply graphite/epoxy specimens

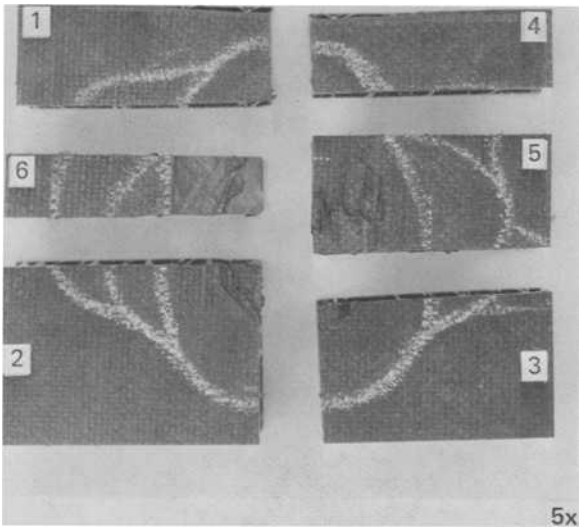

FIG. 3—*Six sectioned pieces of compression-compression fatigue specimen.*

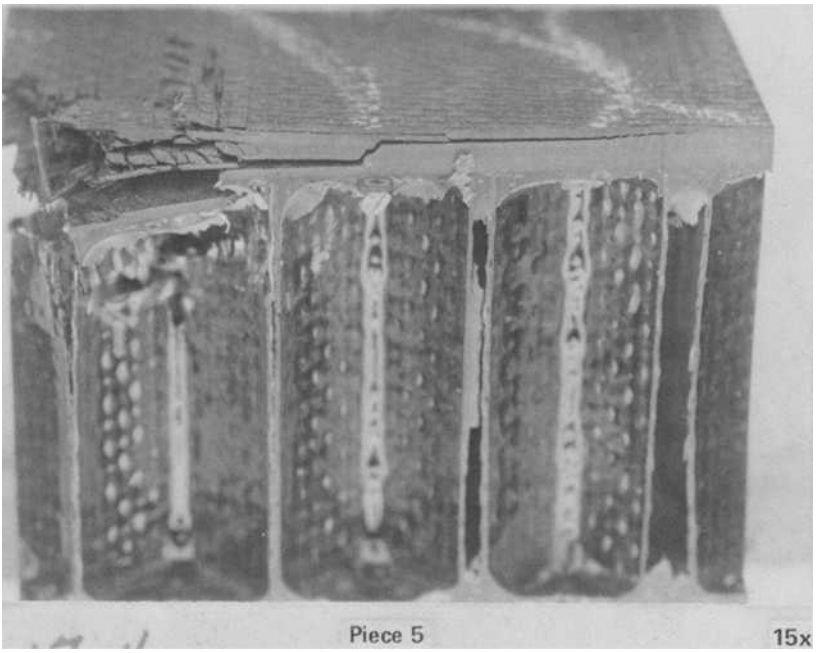

FIG. 4—*Oblique view of Piece 5 showing correlation between interlaminar cracks and mapped surface marks.*

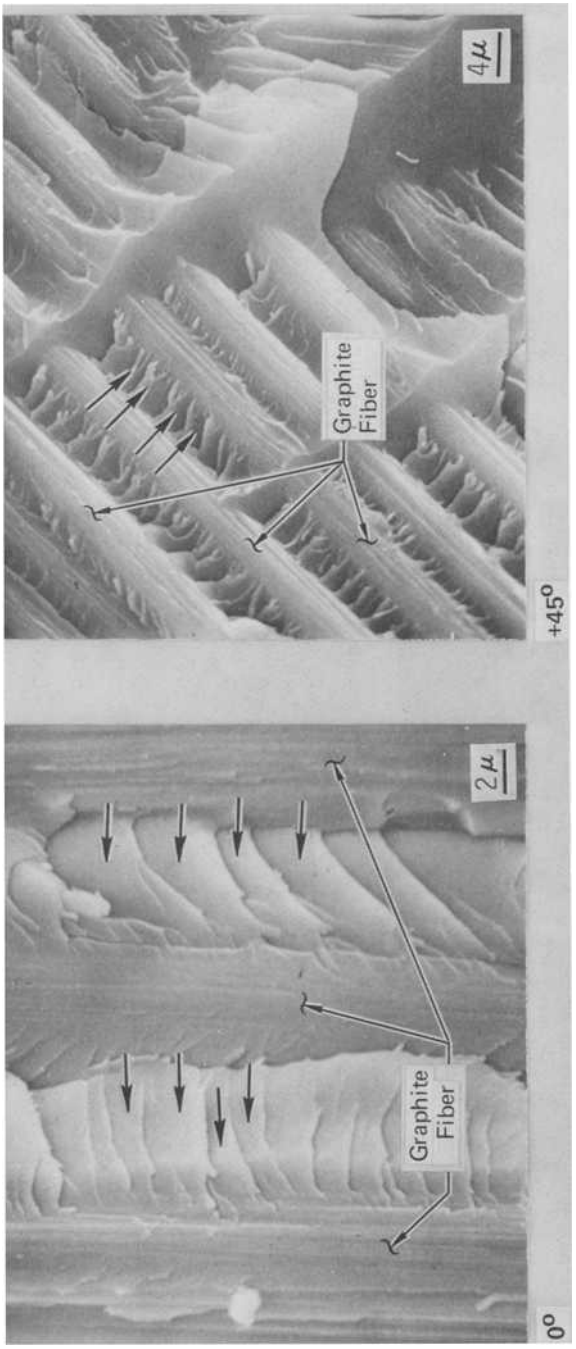
Graphite Fiber
4μ
+45°
Graphite Fiber
2μ
0°

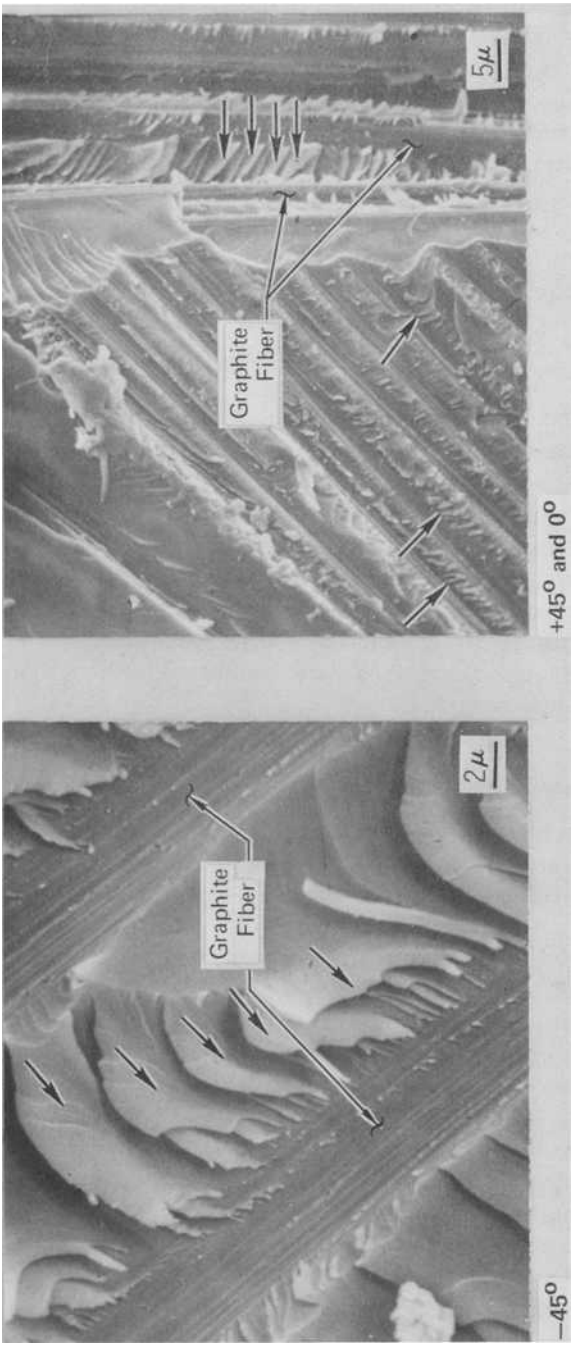

FIG. 5—*SEM fractographs showing hackles (arrows) and differently oriented graphite fibers.*

with unidirectional 0-deg fibers by carefully driving wedges into the ends of the specimens. The lengths of the delaminations were controlled to provide intact crack tips to study. To assure that the mating fracture surfaces did not contact one another, spacers were inserted between them before the wedges were removed. The specimens were coated with a layer of gold using a vacuum evaporator, and were then electroplated with nickel to preserve the fracture surfaces of the epoxy component. The specimens were mounted in cold-mount epoxy mounting material and were polished using standard laboratory polishing techniques. The fracture surface profiles were examined with a metallograph.

Equipment

A JEOL Model JSM-2 scanning electron microscope was used to examine and to document the topographic features of graphite/epoxy test specimen fracture surfaces that were studied during this investigation. The optimum SEM accelerating voltage for examining graphite/epoxy specimens was determined to be 10 kV.

Stereo viewing of stereo pairs of SEM fractographs was determined to be an excellent method for examining and interpreting the fracture surface topographic features of the failed composite specimens.

Metallographic examinations were conducted with a Bausch & Lomb Research II Metallograph.

Test Results and Discussion

The fracture surface topographic features of failed graphite/epoxy composites are composed of graphite fiber and epoxy components. The fractured epoxy component of graphite/epoxy composites exhibits several topographies when examined with an SEM. The fractured epoxy matrix component most often exhibits a topographic feature identified as "hackles" in Fig. 5. Hackles are identified as "lacerations" by Sinclair and Chamis, who relate them to fracture by tearing that results from interlaminar shear [*8*]. Hackles were the most promising topographic feature on the fracture surface of failed graphite/epoxy composites that could be related to fracture direction. As a result, an intensive SEM examination was conducted to characterize hackles.

Individual hackles have different shapes and sizes; however, they do have some common characteristics. The individual hackles are flake-like in appearance and they overlap on top of one another similar to the shingles on the roof of a house, Fig. 6.

Hackle platelets lie between adjacent parallel graphite fibers and are oriented approximately normal to the fiber axes. Hackles are present on both mating surfaces when graphite/epoxy composites fail by delamina-

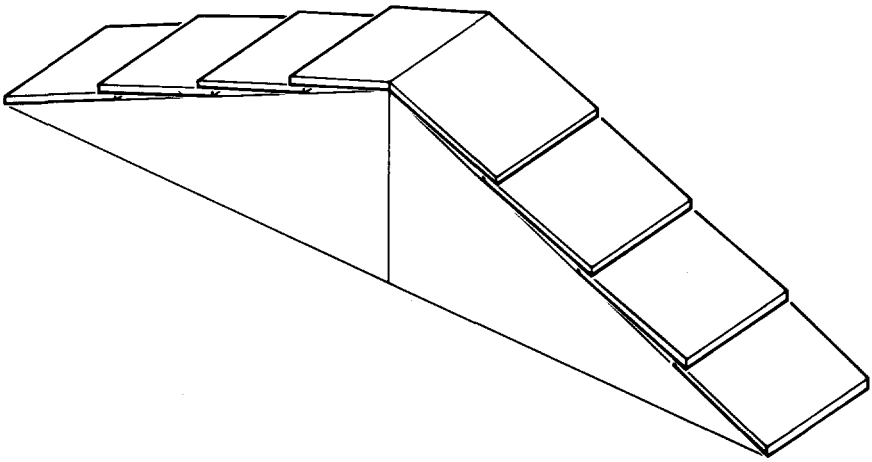

FIG. 6—*Sketch of roof shingles that are analogous to epoxy hackles.*

tion. When the mating fracture surfaces of the unidirectional notched 90-deg tension specimens were examined with the SEM, a consistent hackle pattern was detected, Fig. 7. On one of the fracture surfaces, No. 1, the hackles overlapped one another in the same direction. On the mating fracture surface, No. 2, the hackles again overlapped one another; however, these hackles overlapped in the opposite direction to the hackles on Fracture Surface 1.

Graphite/epoxy composite specimens and panels always fail between more than two adjacent plies of graphite fibers, creating a stepped fracture surface topography. The hackles at various areas on the fracture surfaces overlapped in the same direction even though the fractures propagated between several graphite fiber plies, Fig. 8.

When graphite/epoxy composite materials fail by delamination, and multiple cracks propagate between several adjacent plies of graphite fibers, the hackles on each of the "upper" fracture surfaces overlap in the same direction and the hackles on each of the "lower" fracture surfaces overlap in the opposite direction, Fig. 9. On most delaminated fracture surfaces, however, patches of hackles ordinarily can be detected that overlap one another in the opposite direction to the majority of the hackles on that fracture surface. This local hackle orientation resulted from "reverse-direction" delamination as shown by the sketch in Fig. 10. Forces F1 cause Crack C1 to start in a unidirectional 90-deg graphite/epoxy composite panel. When Crack C1 propagates almost through the width of the panel, a second crack, C2, often begins propagating in the opposite direction due to a second set of forces, F2. Ultimately the two fracture surfaces are

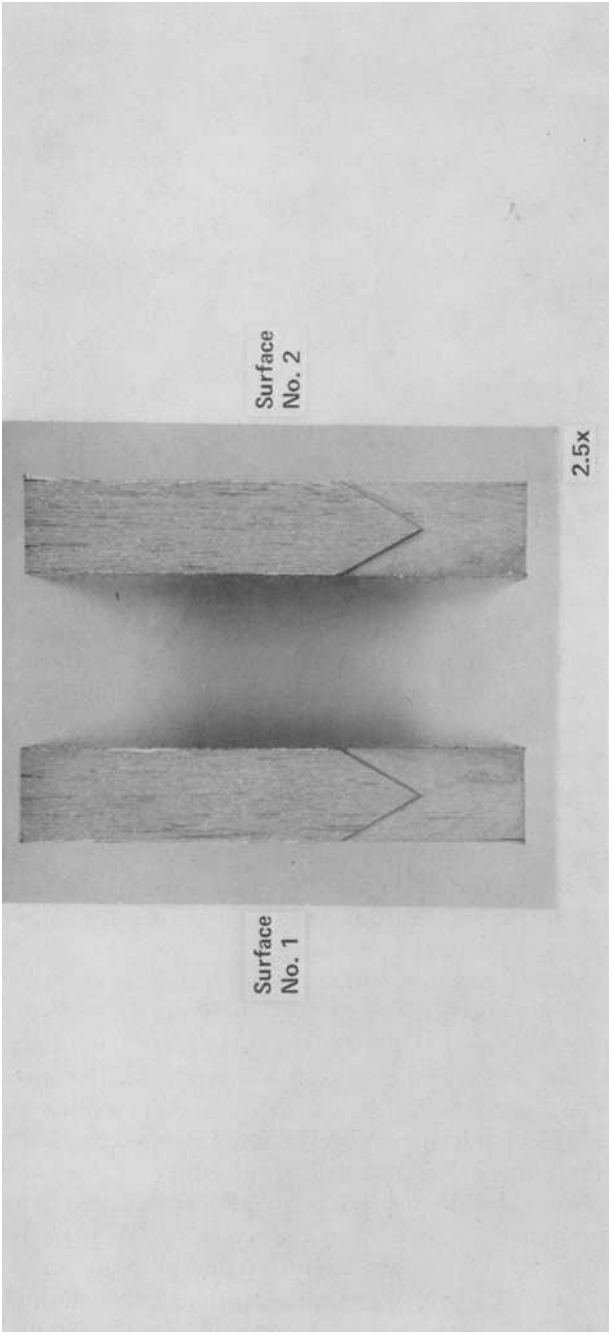
Surface
No. 2
2.5x
Surface
No. 1

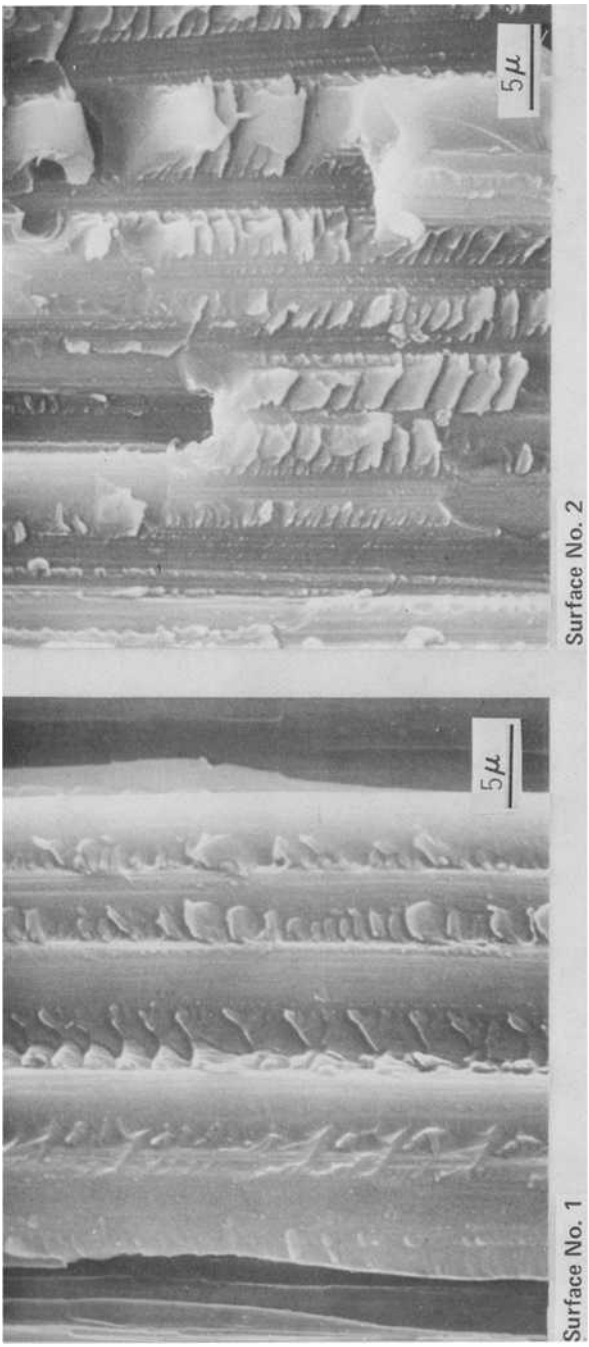

FIG. 7—*SEM fractographs showing hackles oriented in opposite directions on the mating fracture surfaces of a unidirectional 90-deg graphite/epoxy tension specimen.*

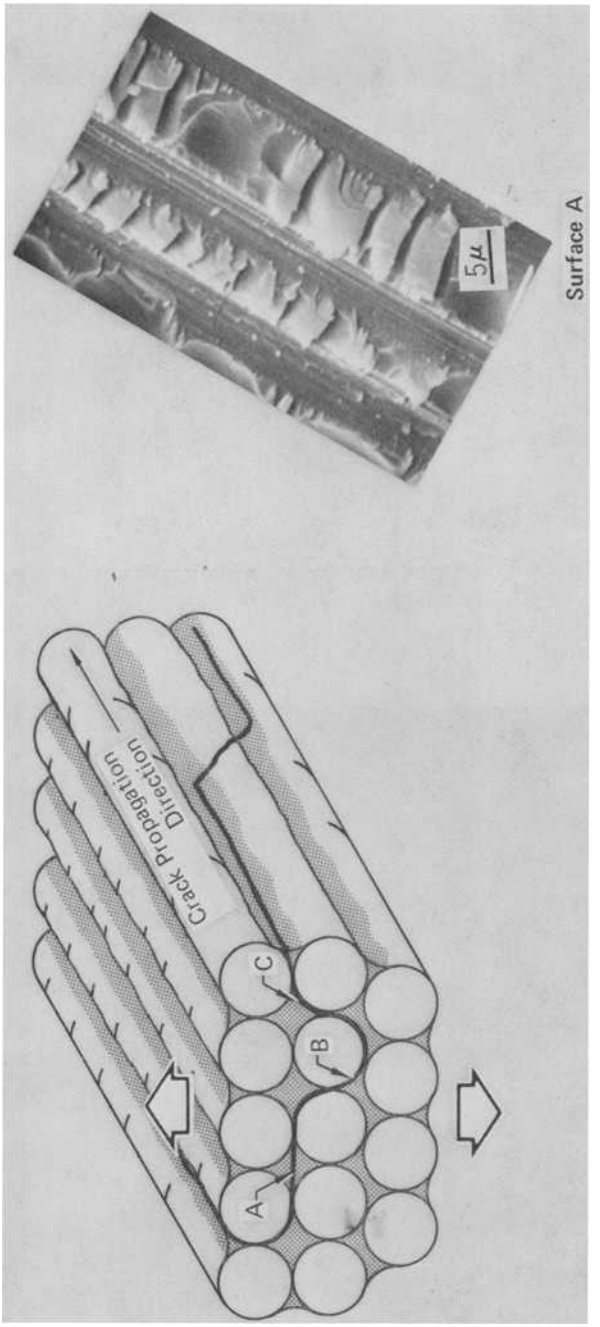
Surface A
5μ
Crack Propagation Direction
A
B
C

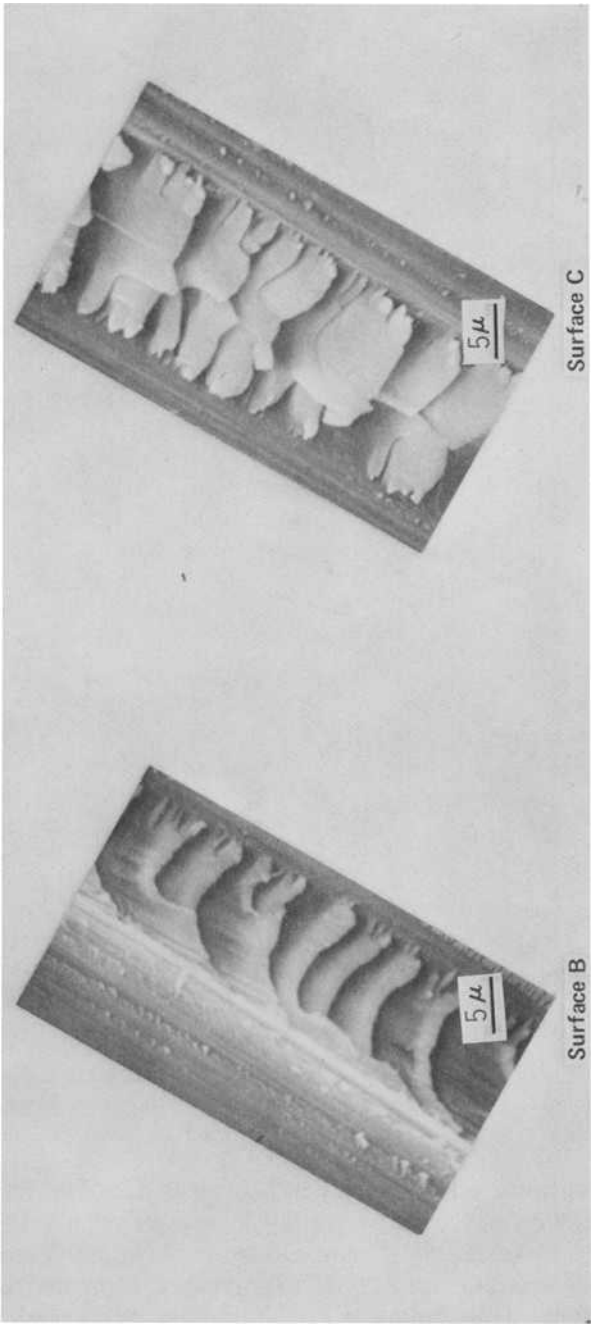

FIG. 8—*Sketch and SEM fractographs showing the common direction of hackle overlap observed for multilayered fractures in graphite/epoxy composites.*

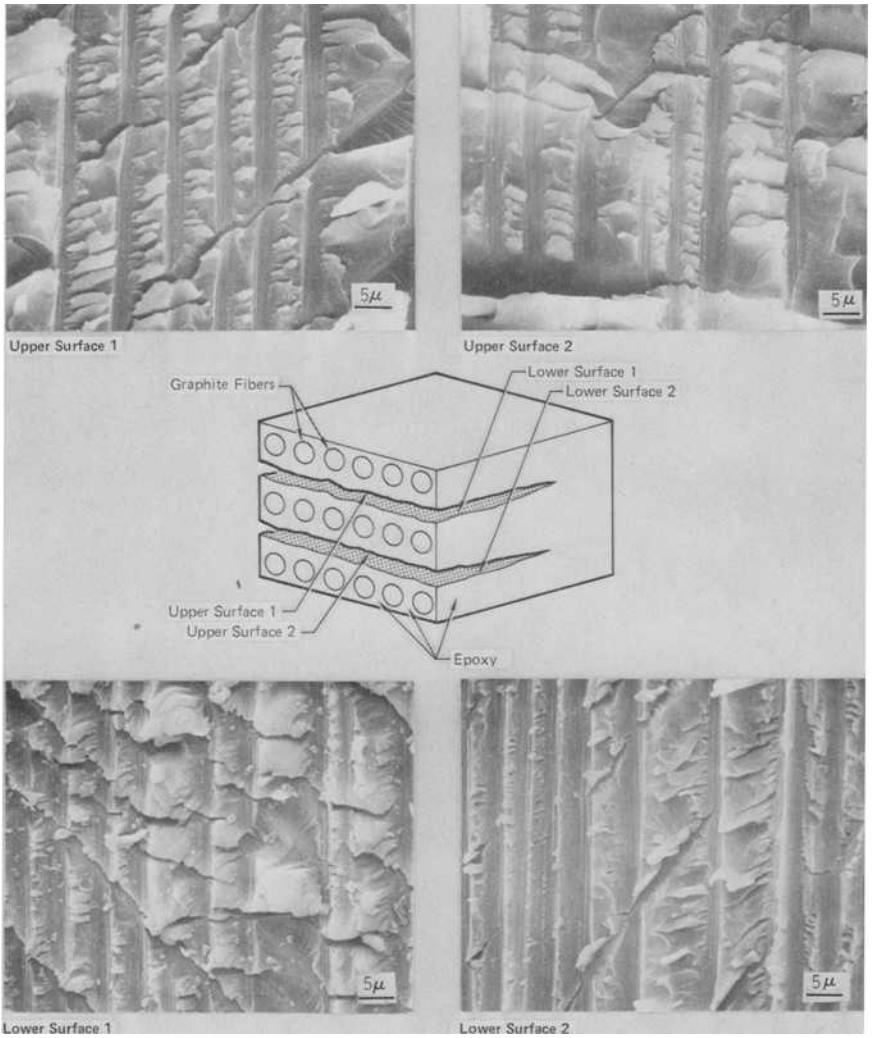

FIG. 9—*Hackle overlap on upper fracture surfaces and hackle overlap in the opposite direction on lower fracture surfaces for multiple-delamination cracks propagating in the same direction.*

linked up by a transverse crack, usually at the tip of C2. The resulting fracture surfaces exhibit hackles that overlap in one direction across the majority of the fracture surface, FS1, and overlap in the opposite direction on the small fracture surface area, FS2, that resulted from the reverse-direction delamination. This change in hackle overlap direction when the fracture direction reverses is the key to determining the locations of fracture origins on a graphite/epoxy fracture surface.

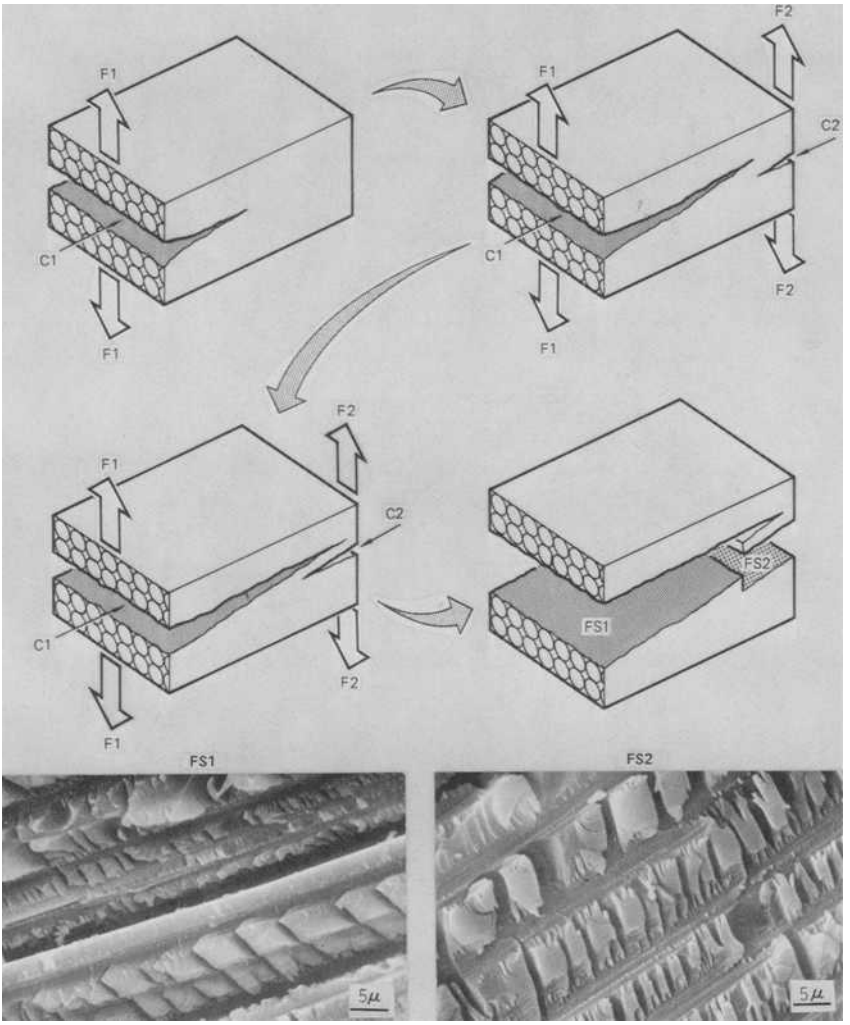

FIG. 10—*Sketches and SEM fractographs showing the orientations of hackle overlaps on fracture surfaces that result from delamination (FS1) and reverse-direction lamination (FS2).*

The term "tilt" is used throughout the remainder of this paper to describe the way hackles overlap on top of one another, and tilt direction arrows are used on photographs or sketches of subject fracture surfaces to describe the hackle tilt directions at various locations on the fracture surface. Hackle tilts are designated by arrows that can be inserted head-first between pairs of successive hackles on SEM fractographs, Fig. 11. Since the orientations of hackle overlaps change when the direction of delamination propagation changes, as shown in Fig. 10, the tilt arrows assigned to the hackles would

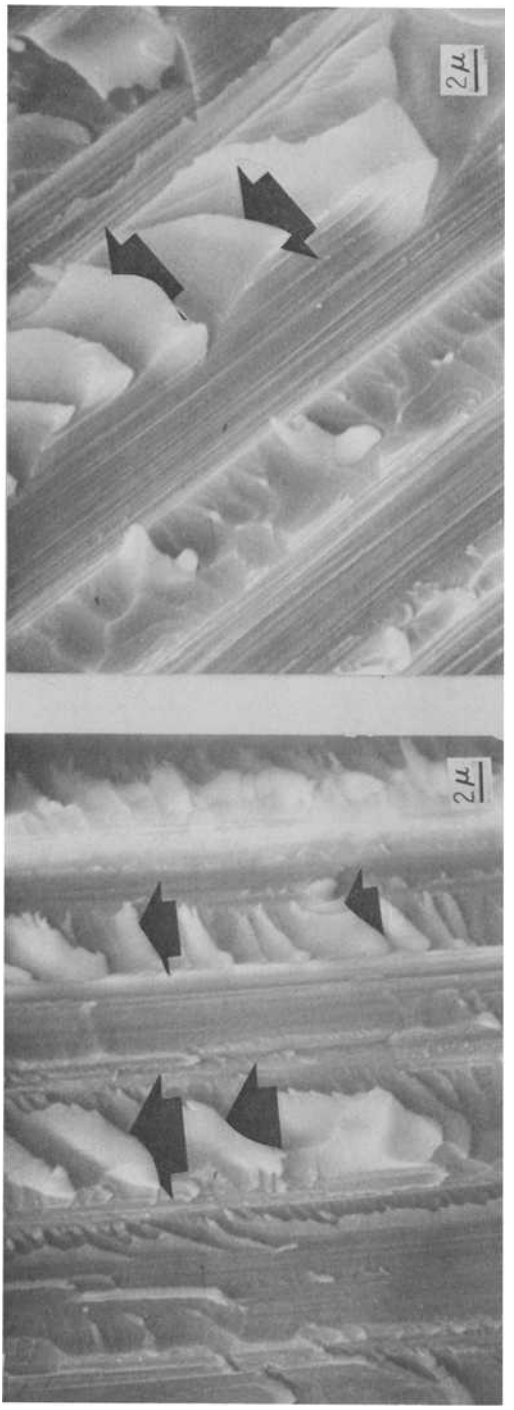

FIG. 11—*SEM fractographs showing hackle tilt arrows inserted between hackles.*

also point in different directions. By assigning hackle tilt arrows to the hackles between the variously oriented fibers on a graphite/epoxy composite delaminated fracture surface, and by studying the resulting pattern, areas where the fracture changed directions of propagation can be determined.

The fracture surfaces of the six pieces from the compression-compression fatigue tested flaw growth specimen were examined in the SEM to establish the tilt directions of the hackles associated with the variously oriented graphite fibers. Figure 12 is a sketch that shows the relative orientations of all of the hackle tilts in the impact-area delaminated zone. The majority of the arrow heads point away from the impact zone, which indicates that the fracture direction changed on opposite sides of the impact zone. At this point, however, it could not be confirmed if the delamination cracks propagated toward the impact zone from all sides or if the delamination cracks propagated away from the impact point. To resolve this question, a strip of 0-deg fibers was peeled from the surface at the location indicated by the two arrows in Piece 3 to produce a delamination fracture surface with a known fracture direction. By determining the hackle tilt for this created fracture surface and then comparing it with the hackle tilts of other 0-deg-oriented fibers, the local fracture directions were determined. The hackle tilt arrows for the 0-deg fibers in Pieces 2 and 3 pointed in the same direction as the hackle tilt arrows on the created fracture surface; therefore, the 0-deg fibers in Pieces 2 and 3 were determined to have delaminated in the same direction as the 0-deg-created fracture. The hackle tilt arrows for the 0-deg fibers in Pieces 1, 4, and 5 pointed in the opposite direction to the hackle tilt arrows of the created fracture, which indicated that the 0-deg fibers in Pieces 1, 4, and 5 had delaminated in the opposite direction to those in Pieces 2 and 3. As a result, it was confirmed that the failure origin was located at the center of the specimen where the steel ball impacted.

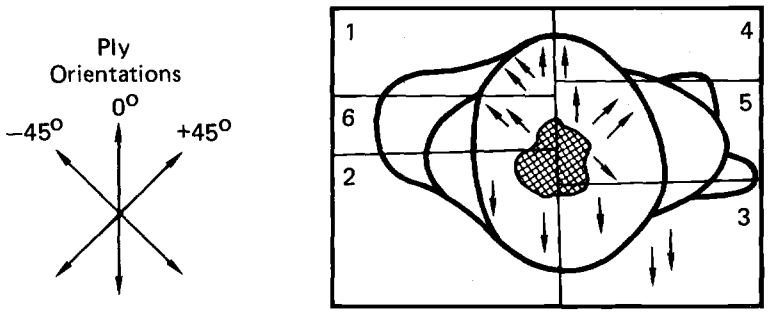

FIG. 12—*Sketch showing hackle tilt directions at various locations in the delaminated impact zone. The cross-hatched area locates the extensively damaged zone at the ball impact point.*

Similarly, using this procedure, hackle tilt direction were established at various locations on the fracture surfaces of the failed graphite/epoxy box beam lower cover test specimen. The fractures were determined to have propagated in the directions indicated by the arrows in Fig. 13.

Hackles have many different shapes and sizes, as seen during the previous fractographic examination. A subsequent metallographic examination was conducted to reveal information about the initiation of delamination cracks, that is, the formation of hackles. The delaminated unidirectional 40-ply graphite/epoxy specimen was polished and examined with a metallograph. Figure 14 presents a photomacrograph and a photomicrograph showing the profiles of hackles near the tip of a crack in the unidirectional 40-ply specimen that delaminated in the 0-deg direction. Some photomicrographs presented in Fig. 15 show cracks and also the profiles of

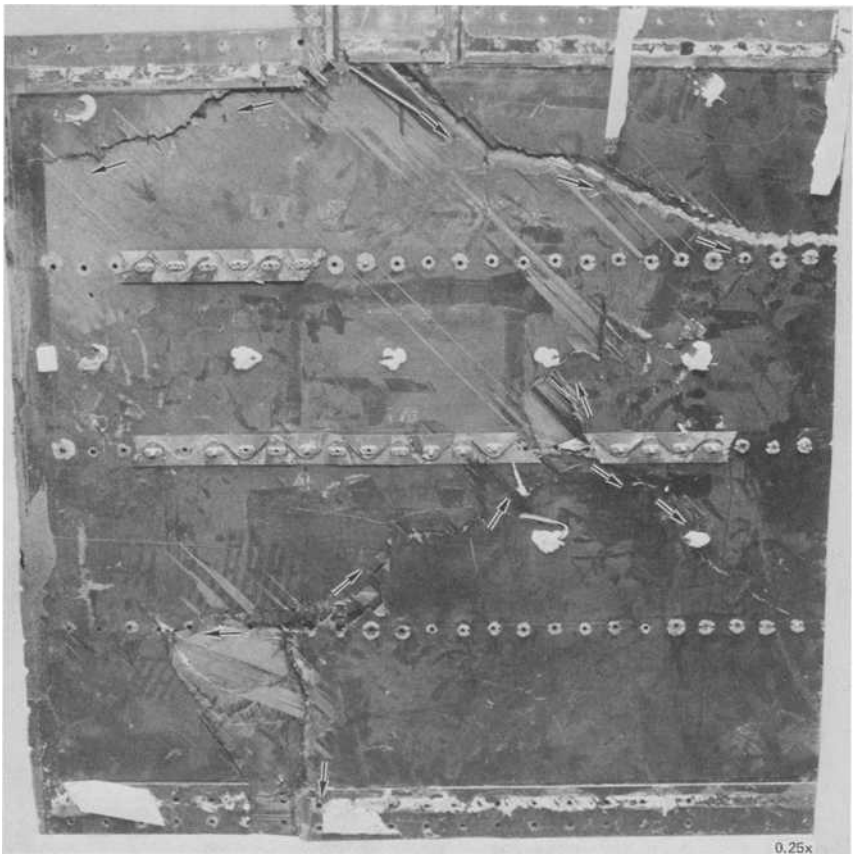

FIG. 13—*Fracture directions of graphite/epoxy box beam lower cover test specimen.*

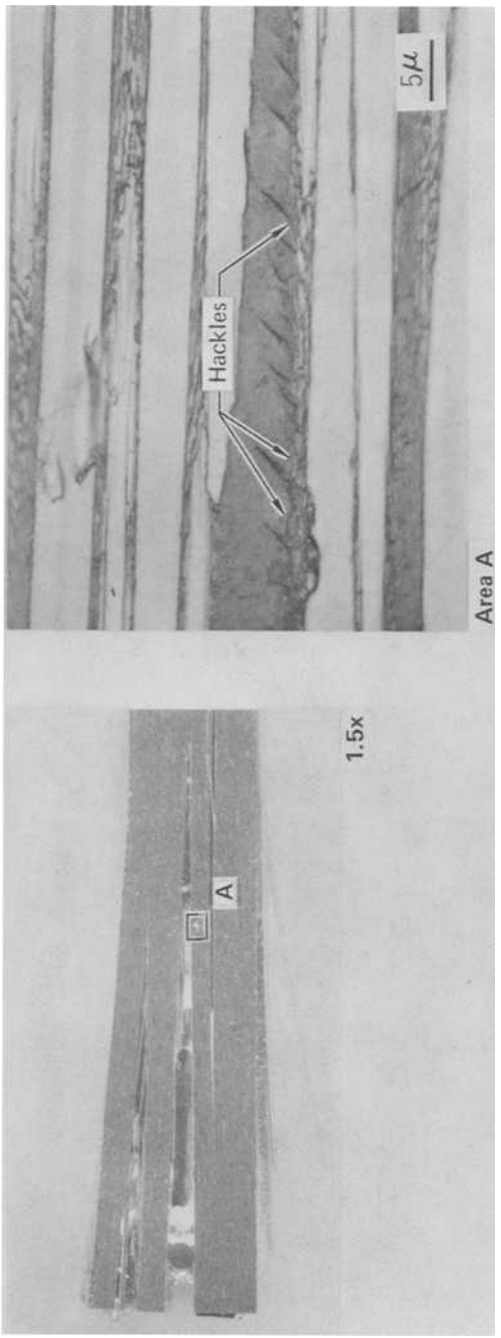

FIG. 14—*Hackle formation at the tip of a delamination crack in a 40-ply 0-deg unidirectional specimen.*

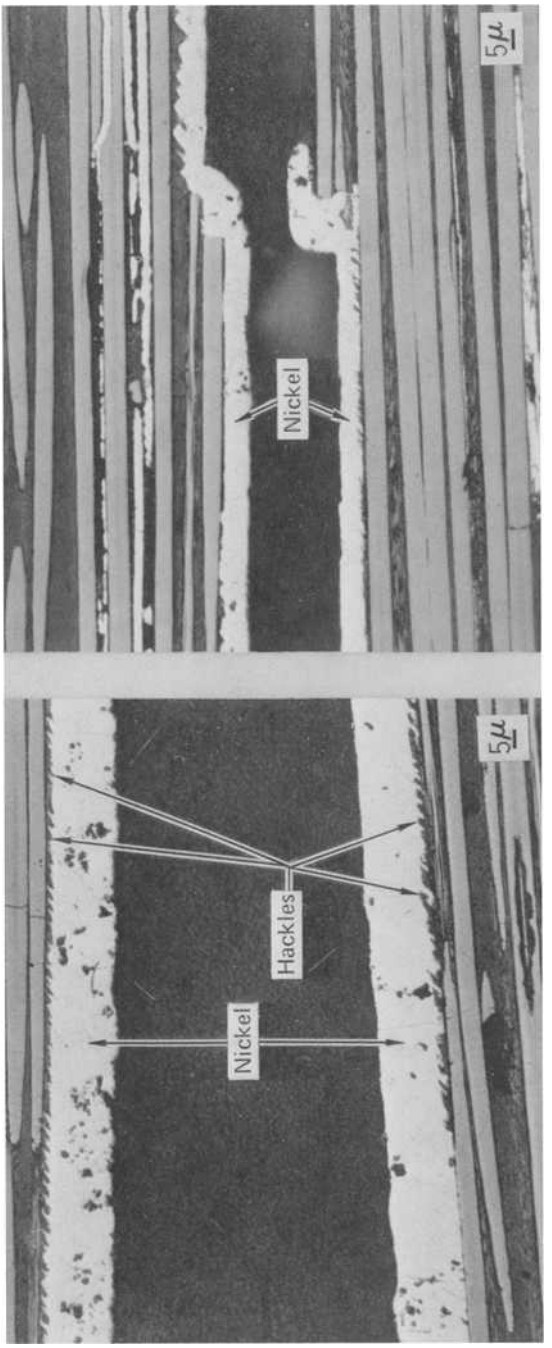
Nickel
5μ
Nickel
Hackles
5μ

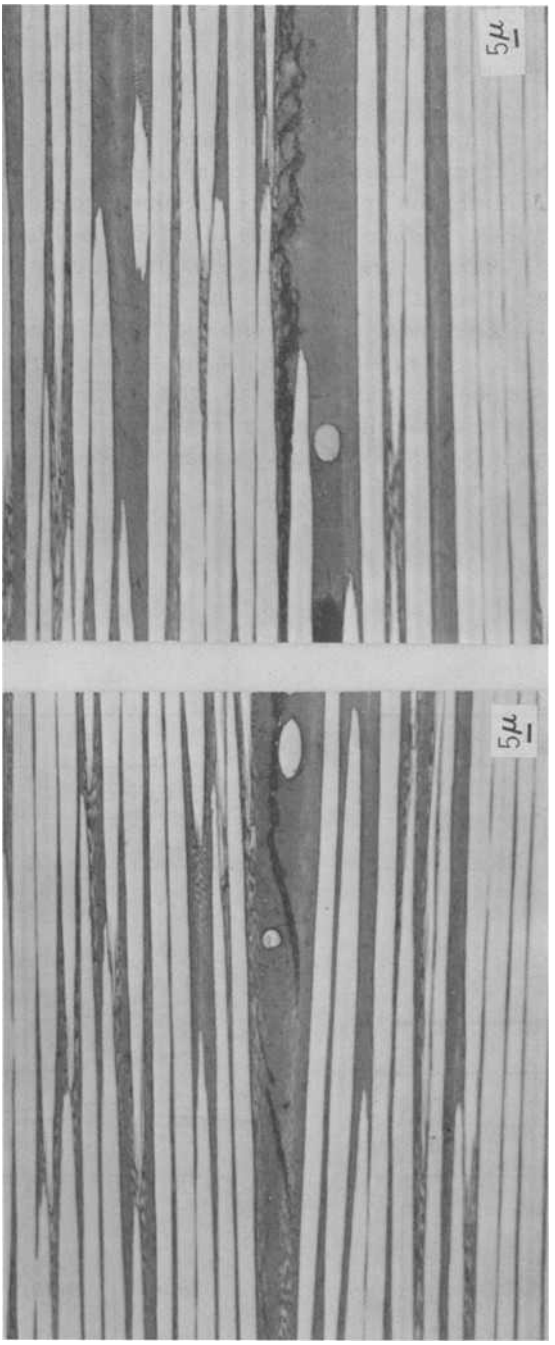

FIG. 15—*Photomicrographs showing hackles tilted in opposite directions on mating delamination fracture surfaces (top photos) and miscellaneous crack profiles (bottom photos).*

hackles that were detected in specimens with delamination fractures propagating between 0-deg fibers. The nickel plating used to prevent edge rounding during polishing is identified in Fig. 15. The exposed hackles on each fracture surface all tilted in the same direction and had overlapping "sawtooth" profiles.

Examination of delamination cracks near their tips indicates that hackles form as indicated by the sketch sequence in Fig. 16. The sequence of delamination crack formation appears to be as follows: (1) Forces F1 cause a delamination crack to initiate proximate to a graphite fiber; (2) as the crack gets longer, tensile forces, F2, concentrate stresses at the top free epoxy surface due to upward bending of the top layer of high-modulus graphite fibers; (3) a secondary crack, initiated by F2, propagates away from the primary crack at an angle of approximately 45 deg and partially relieves the surface tensile stresses, F2; (4) this procedure is repeated, creating a family of cracks. Ultimately, a complete fracture of the composite results, exposing platelets of epoxy material between the secondary cracks; these platelets are hackles.

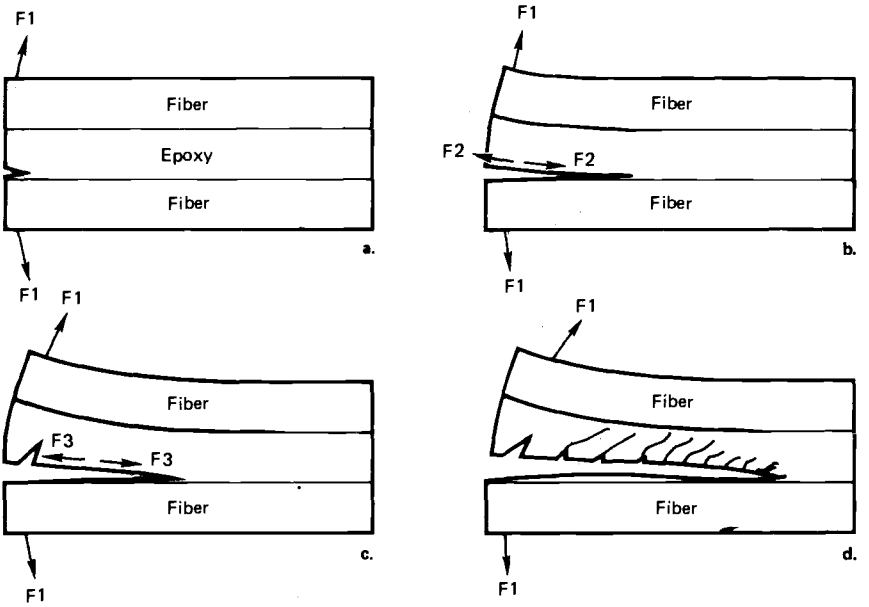

FIG. 16—*Initiation of delamination cracks and the formation of hackles in 0-deg unidirectional composites.*

References

[1] Phillips, A., Kerlins, V., and Whiteson, B. J., *Electron Fractography Handbook,* AFML-TR-64-416, Air Force Materials Laboratory, Wright-Patterson Air Force Base, Ohio, Jan. 1965.

[2] *Fractography and Atlas of Fractographs, ASM Metals Handbook,* American Society for Metals, Metals Park, Ohio, Vol. 9, 1974.

[3] Pittanato, G. F., Kerlins, V., Phillips, A., and Russo, M. A., *SEM/TEM Fractography Handbook,* MCLC-HB-06, Metals and Ceramics Information Center, Battelle Memorial Institute, Columbus, Ohio, Dec. 1975.

[4] Morgan, R. J. and Ames, D. P., *"Relationship Between Physical Structure Failure Modes, and Mechanical Properties of Epoxies."* McDonnell Douglas Corp. Report Q0604, St. Louis, Mo., Oct. 1976.

[5] Morgan, R. J. and O'Neal, J. E., "A Review of the Relation Between the Physical Structure and Mechanical Response of Epoxies," MDRL 76-7, presented at the Symposium on Chemistry and Properties of Crosslinked Polymers of the Division of Organic Coatings and Plastics Chemistry, American Chemical Society, San Francisco, Calif., 29 Aug-3 Sept. 1976.

[6] Toland, R. H., "Failure Modes in Impact-Loaded Composite Materials," presented at Symposium on Failure Modes in Composites, sponsored by the Institute of Metal Division of the Metallurgical Society, American Institute of Mining, Metallurgical, and Petroleum Engineers, May 1972.

[7] Heimbuch, R. A. and Felbeck, D. K., "Tensile Fracture of Boron-Epoxy Composites with Ordered Filament Packing Geometry," presented at Symposium on Failure Modes in Composites, sponsored by the Institute of Metals Division of the Metallurgical Society, American Institute of Mining, Metallurgical, and Petroleum Engineers, May 1972.

[8] Sinclair, J. H. and Chamis, C. C., "Mechanical Behavior and Fracture Characteristics of Off-Axis Fiber Composites I—Experimental Investigation," NASA Technical Paper 1081, National Aeronautics and Space Administration, Washington, D.C., Dec. 1977.

[9] Chamis, C. C. and Sinclair, J. H., "Mechanical Behavior and Fracture Characteristics of Off-Axis Fiber Composites II—Theory and Comparisons," NASA Technical Paper 1082, National Aeronautics and Space Administration, Washington, D.C., Jan. 1978.

[10] Risenfeld, M. S. and Huang, S. L., "Fatigue Characteristics of Graphite/Epoxy Laminates Under Compression Loading," AIAA Paper 473, American Institute of Aeronautics and Astronautics, 1977.

[11] Cook, T. S. and Preston, J. L., Jr., "Impact Behavior of Graphite-Epoxy Simulated Fan Blades," AIAA Paper 365, American Institute of Aeronautics and Astronautics, 1977.

[12] Adams, D. F. and Perry, J. L., *Journal of Testing and Evaluation,* Vol. 5, No. 2, March 1977, pp. 114-123.

[13] Browning, G. V. and Phillips, A., "Review of Graphite Composite Literature and Results of SEM Studies at MDAC," McDonnell Douglas Astronautics Co., West Report MDC G2093, Huntington Beach, Calif., April 1972.

[14] Mills, A. L., "Advanced Composites Production/Service Experience," Interim Technical Report 1 Jan-31 March 1975, Contract No. F33615-73-C5066, prepared for Non-Metals/Composites Branch Manufacturing Technology Division, Air Force Materials Laboratory, Wright-Patterson Air Force Base, Ohio, 1975.

C. L. Leung,[1] *P. J. Dynes,*[1] *and D. H. Kaelble*[1]

Moisture Diffusion Analysis of Microstructure Degradation in Graphite/Expoxy Composites

REFERENCE: Leung, C. L., Dynes, P. J., and Kaelble, D. H., **"Moisture Diffusion Analysis of Microstructure Degradation in Graphite/Epoxy Composites,"** *Nondestructive Evaluation and Flaw Criticality for Composite Materials, ASTM STP 696,* R. B. Pipes, Ed., American Society for Testing and Materials, 1979, pp. 298-315.

ABSTRACT: Directional diffusion coefficients, that is, D_1, D_2 and D_3, for the principal axis $i = 1, 2, 3$ of a unidirectional fibrous composite were determined by moisture absorption measurements. It was shown that the initial moisture absorption of a cured dry composite is non-Fickian and may relate to microstructural relaxation of internal stresses.

Moisture effusion rates of the specimens were also evaluated. Absorption-desorption kinetics over several cycles showed that there exists a damage mechanism in the composite which enhances moisture uptake from the dry state but does not enhance moisture release from the water-equilibrated state.

KEY WORDS: composite materials, diffusion coefficients, hydrothermal aging, moisture profilometry, statistical estimation, nondestructive tests

Hydrothermal aging effects on cured graphite/epoxy composites were determined using (1) acoustic attenuation, α_L; (2) ultrasonic velocity, C_L; and (3) thickness measurements of the composites. Results showed that while ultrasonic acoustic properties, specimen thickness, and moisture diffusion profiles are highly sensitive to structural degradation, ultrasonic inspection becomes insensitive in areas of extensive internal damage, probably due to high acoustic attenuation, which results in loss of signals. Moisture diffusion analysis (MDA), in this case, becomes highly sensitive as a quantitative detection tool.

Presently, analytical methods are developed to quantify the depth profile of moisture penetration in graphite/epoxy composites. Measurement of

[1] Members of the technical staff and senior staff associate, respectively, Rockwell International Science Center, Thousand Oaks, Calif. 91360.

effusion kinetics over a range of time intervals followed by application of statistical estimation theory enables the depth concentration of moisture at initial time $t = 0$ to be calculated. For a particular model in which the specimen is assumed to be exposed to periodically changing environments, the model predicts large fluctuations in moisture concentration near the surfaces while the interior concentration is relatively constant.

The fluctuation in surface moisture gradient during each cycle is assumed to be accumulative, generating deeper cracks into the bulk of the composite. Experimental methods are discussed using both ultrasonic and moisture diffusion techniques for the detection of such cracks. Methods for minimizing these surface cracks by surface modification are also discussed in terms of the aforementioned analytical models for multilayered composites.

Theory

Analytical Profilometry Modeling

A method for determining the depth/concentration profile of moisture in a composite is discussed in terms of mathematical analysis and experiment. This new methodology is termed "moisture profilometry." The experiment involves the heating of the composite to a desired control temperature followed by measurement of the rate of moisture effusion as a function of time. The analytical problem is then to determine the initial distribution of water, that is, the concentration $c_0(x) = c(x,0)$ as a function of x (where x is the distance into the thickness of the composite), from the subsequent history of effusion rate measurements. The attempt to treat this as a deterministic problem leads to difficulties. One of these difficulties is associated with the inevitable incompleteness of the experimental data; namely, any real experiments can yield only a finite set of numbers. A particularly convenient way is to apply statistical estimation theory to the analysis.

The inverse-diffusion system is illustrated in more explicit form in Fig. 1. The material is assumed to be a rectangular block of polymeric material occupying a region of space defined by the inequalities

$$\begin{aligned} 0 \leq x \leq L_x \\ 0 \leq y \leq L_y \\ 0 \leq z \leq L_z \end{aligned} \tag{1}$$

where x, y, and z are the usual Cartesian coordinates. It is also assumed that the material is homogeneous but anisotropic with the principal axes of the diffusion tensor parallel to the coordinate axes. The principal values of

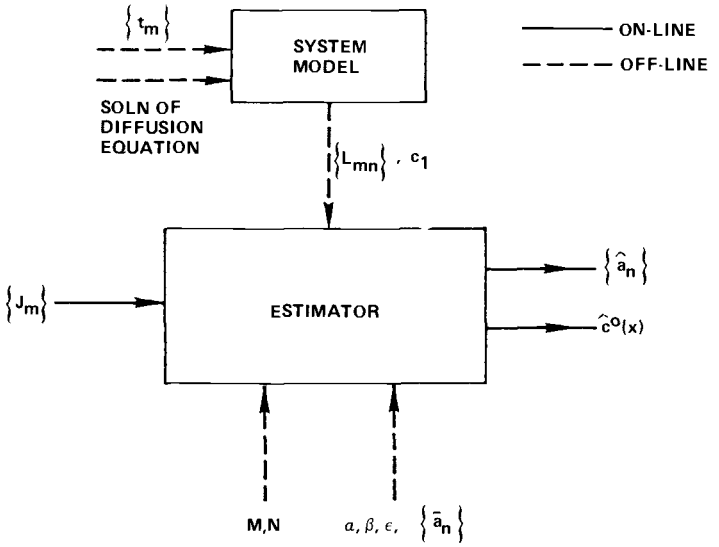

M = NUMBER OF MEASUREMENTS
N = NUMBER OF ESTIMATIONS
c_1 = CONCENTRATION OF WATER IN THE COMPOSITE CORRESPONDING TO THE CHEMICAL POTENTIAL μ_1
α = A PRIORI BIAS AGAINST LARGE AMPLITUDE $c^o(x)$
β = A PRIORI SMOOTHNESS WHICH IS APPLIED TO $c^o x$ IN THE RANGE $\epsilon\pi$, $(1-\epsilon)\pi$
ϵ = NUMERIC RANGE FACTOR $0 \leq \epsilon \leq 0.5$
$\{\bar{a}_n\}$ = OBSERVATIONALLY CONDITIONED AVERAGE FOR a_n

FIG. 1—*Schematic representation of the estimation process.*

the diffusion tensor are denoted by D_x, D_y, and D_z. The initial concentration is assumed to depend only upon x, that is

$$C(x,y,z,\ t = 0) = c_0\,(x) \tag{2}$$

It is further assumed that the measurements involve the total diffusion rate from the entire surface at a specific set of later times. The inversion problem therefore involves a theoretical solution of the foregoing diffusion problem with an arbitrary $c_0\ (x)$ and dry boundary conditions ($c_1 = 0$). The solution is given by Richardson [*1*].[2] The matrix L_{mn} shown in Fig. 1 is then used to obtain from the measured J_m (the total diffusion rate), at times t_m, estimates $\hat{a}_n$ of the coefficients of $\sin(n\pi x/L_x)$, that is

[2]The italic numbers in brackets refer to the list of references appended to this paper.

$$c_0(x) = c_1 + \sum_{n=1}^{N} \hat{a}_n \sin \frac{nx\pi}{L_x} \tag{3}$$

This process of going from the J_m obtained from experimental measurements to the estimates $\hat{a}_n$ is incorporated in the box labeled ESTIMATOR in Fig. 1. The final result of the entire estimation process is presented as a plot of the original moisture concentration with time $t = 0$ on the ordinate and the depth of moisture penetration on the abscissa.

To establish the validity and accuracy of the estimator, called the Inverse Diffusion Solution, a Direct Model is developed [2] which is based on a numerical solution of the Fickian diffusion equation. The Direct Model gives data for

1. moisture profile at any specified time,
2. moisture diffusion rate at each time interval, and
3. moisture content at each time interval.

Theoretical moisture effusion rates obtained from the Direct Model, Item 1, can therefore be analyzed by the Inverse Diffusion Model, yielding moisture profiles which should correlate to those generated directly from Fick's Law, Item 1, thus validating the Inverse Diffusion Model.

Moisture Diffusion and Microdamage

A number of reports show that the mechanical properties of graphite/epoxy reinforced with Hercules Type AS graphite fiber) was fabricated and cured by standard production procedures. The cured composite, called combine as a new methodology for nondestructive evaluation of moisture exposure effects. A logical extension of this is that through moisture diffusion analysis as discussed in the preceding, given a set of diffusion rate data, microdamage can be detected within the bulk of the composite and its location mapped quantitatively.

Experimental

A 48-ply unidirectionally reinforced composite panel (Hercules 3501-5 epoxy reinforced with Hercules Type AS graphite (fiber) was fabricated and cured by standard production procedures. The cured composite, called SC4 in this study, has a fiber volume $V_f = 0.60$ and a volume fraction of voids $V_v \leq 0.01$.

Moisture absorption kinetics were evaluated by measurements of weight change as a function of moisture exposure using a microbalance sensitive to 10^{-5} g. Moisture effusion kinetics were evaluated on the Moisture Evolution Analyzer (DuPont Model 902H) supplemented by weight change

measurements. In the limit of short times for moisture absorption and desorption, the following relation for the initial ϕ versus $t^{1/2}$ was derived [8]

$$\frac{M_t - M_0}{M_\infty - M_0} = \phi_{i=1,2,3} = \frac{4}{x_i}\left[\frac{(D_i\, t)}{\pi}\right]^{1/2} \tag{4}$$

where D_i is the apparent experimental diffusional coefficient as determined from the initial slope of the weight gain curve, ϕ_i versus $t^{1/2}$, for each fiber orientation axis, i.

Thin plate specimens of Composite SC4 were cut to provide dimensions of length by width by thickness (20 by 5 by 1) by 10^{-3} m. They were completely dried in a dessicator and their dry weights determined. Figure 2 details the specimen orientation which respectively exposes the interlaminar, transfibrous, and translaminar faces as the major exposed areas (80 percent of total area) in absorption and effusion measurements.

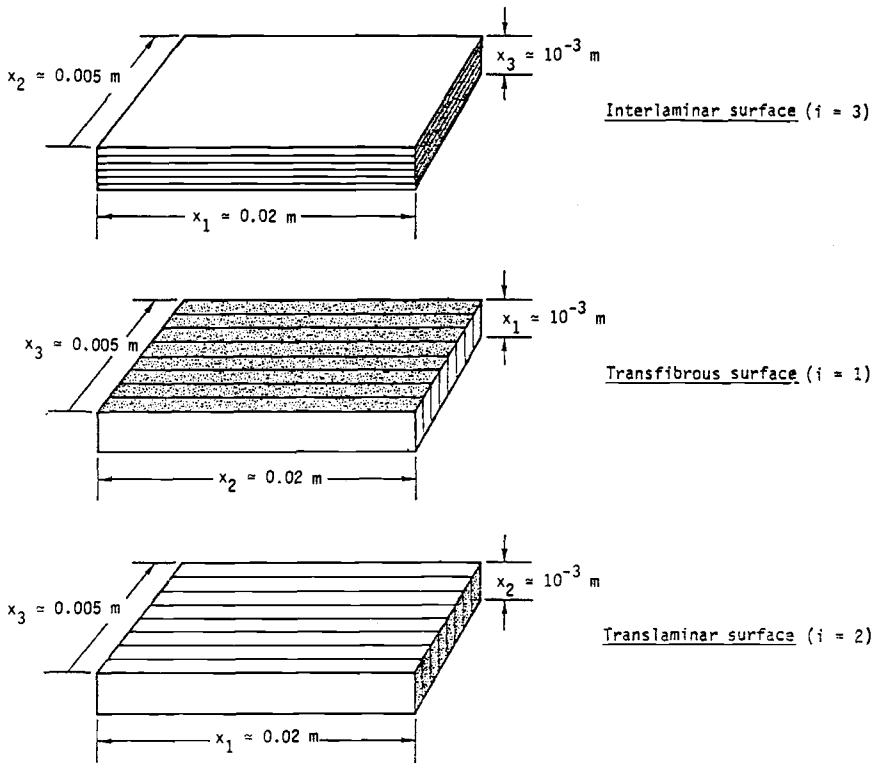

FIG. 2—*Specimen orientations and geometry for kinetics of adsorption and desorption in interlaminar, transfibrous, and translaminar directions of uniaxial reinforced composite (layers represent plies and dots fiber ends).*

To assess the effect of variable moisture exposure on the composite, a separate specimen bar of SC4 was fabricated and aged for 1128 h as shown in Fig. 3, so that the bar was exposed simultaneously to four different moisture environments. Subsequent to aging for 1128 h as described, the bar was characterized by ultrasonic C-scan at 2.25 MHz along its length. The longitudinal sound velocity C_L (Km/s) and spatial attenuation α_L (neper/cm) were determined by the following standard equations

$$C_L = T/t = T/(t_2 - t_1) \tag{5}$$

$$\alpha_L = \ln(A_1/A_2)/T \tag{6}$$

where

T = composite thickness,

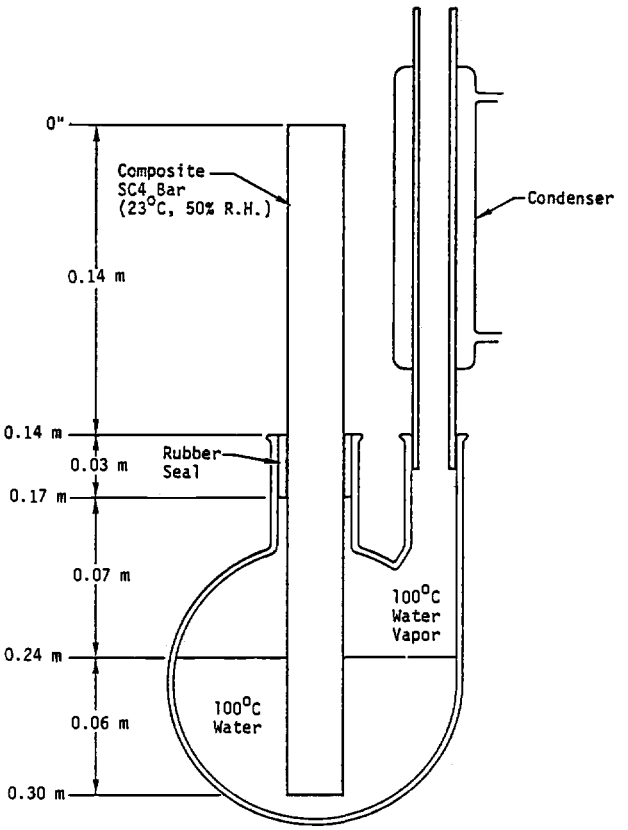

FIG. 3—*Schematic of variable moisture exposure of Composite SC4 aged for 1128 h.*

t = delay time, and
(A_1/A_2) = signal amplitude ratio.

Subsequent to this initial characterization, a series of thermal shocks was imposed on the bar by compressing it between the heated platens of a hydraulic press. After each thermal shock, the thickness, C_L, and α measurements were repeated.

After four thermal shocks, the bar was dried at 110°C in vacuum and sectioned to provide 12 specimens each of dimensions L by W by $T = 0.0015 \times 0.0005 \times 0.0005$ m, taken from regular intervals along the composite bar. These 12 test specimens were first dessicated to provide a common initial condition of zero moisture content. The specimens were then exposed to 1800 min of water immersion at 75°C. After 1800 min of water immersion, the specimens were individually inserted into the specimen chamber of the DuPont Moisture Evolution Analyzer, maintained at 75°C. Measurement of water release rate $dW(H_2O)/dt$ versus time as well as moisture content was automatically carried out by the instrument. (Figure 12 plots the total moisture content $(M_0)_D$ and the time (t_D) required to reduce the effusion rate to an arbitrary constant level of 1.0 μg/s for the 12 specimens along the length of the bar.)

Results and Discussion

Moisture Diffusion Kinetics

The results of moisture diffusional analysis for several successive cycles of absorption (A) and desorption (D) are summarized in Table 1. The upper portion of Table 1 details specimen geometry and maximum moisture content (in percent by weight) for each absorption cycle. Inspection of the experimental values of $(D_i)_A$ in Table 1 for moisture absorption shows that each cycle of full hydration and subsequent drying produces large increases in diffusion coefficients for moisture absorption $(D_i)_A$ over the first three cycles. However, the coefficients for moisture desorption $(D_i)_D$ are essentially constant over the three hydration-dehydration cycles. The results are indicative of a damage mechanism in Composite SC4 microstructure which enhances moisture uptake from the dry state, but does not affect moisture release from the water-equilibrated state. Additionally, data in upper Table 1 show that values of $100^{M_0-1}(M_\infty - M_0)$ for both resin and composite specimens are relatively stable except for Cycle 3, for transfibrous surface specimens, where $100^{M_0-1}(M_\infty - M_0) = 2.56$.

The curves of Fig. 4 graph the moisture release rate dW/dt versus time t for Desorption Cycle 1 of Table 1 as measured by moisture effusion analysis. The higher release rate in the transfibrous specimen is indicative of higher

TABLE 1—*Moisture diffusion kinetics at 75°C.*

	3501-5 Neat Resin	Composite SC4 ($V_f = 0.60$)		
		Transfibrous	Translaminar	Interlaminar
Principal axis (i)	$i = 1 = 2 = 3$	$i = 1$	$i = 2$	$i = 3$
x_1	1.560×10^{-2} m	1.0×10^{-3} m	0.02 m	0.02 m
x_2	0.705×10^{-2} m	0.02 m	0.001 m	0.005 m
x_3	0.0333×10^{-2} m	0.005 m	0.005 m	0.001 m
		$100\, M_0^{-1}(M_\infty - M_0)$		
Cycle No.				
1	6.50	2.29	2.18	2.19
2	6.50	2.26	2.12	2.08
3	...	2.56	2.12	2.22
Experimental result by Eq 4				
Adsorption Cycle No.	$(\bar{D}_r)A$	$(\bar{D}_1)A$	$(\bar{D}_2)A$	$(\bar{D}_3)A$
		(10^{-12} m^2/s)		
1	2.37	1.62	0.0679	0.629
2	3.40	4.89	1.32	1.36
3	...	7.14	1.77	1.75
Desorption Cycle No.	$(\bar{D}_r)D$	$(\bar{D}_1)D$	$(\bar{D}_2)D$	$(\bar{D}_3)D$
		(10^{-12} m^2/s)		
1	3.14	22.0	5.18	4.90
2	5.03	16.0	4.67	4.90
3	...	18.6	5.18	4.90

diffusion along the fiber axis $(D_1)_D = 22.0 \times 10^{-12}$ m^2/s compared with $(D_2)_D \simeq (D_3)_D \simeq 5.04 \pm 0.14 \times 10^{-12}$ m^2/s for transverse diffusion paths.

The lower curves of Fig. 5 plot ϕ_A versus $t^{1/2}$ for the cured matrix epoxy, showing the linear Fickian absorption predicted by Eq 4. The lower curves of Figs. 6-8 show that in the first absorption cycle the curves of ϕ_A versus $t^{1/2}$ for the various fiber orientations are linear but do not extrapolate to the origin at $\phi_A = t = 0$. Since the composite was held dessicated over anhydrous calcium sulphate immediately after cure, thermoelastic stresses generated during curing may not have been relieved [*9,10*]. The linearity and intersection of the ϕ_A versus $t^{1/2}$ curves for Cycles 2 and 3 (Figs. 6-8) suggest that an altered internal stress state is achieved after the first cycle of moisture absorption.

The upper curves of Figs. 5-8 plot values of ϕ_D versus $t^{1/2}$, showing a linear relationship for all drying cycles including Cycle 1. This result reinforces the hypothesis that substantial alteration of an internal stress state in the specimen is accomplished during the first moisture absorption cycle [*11*].

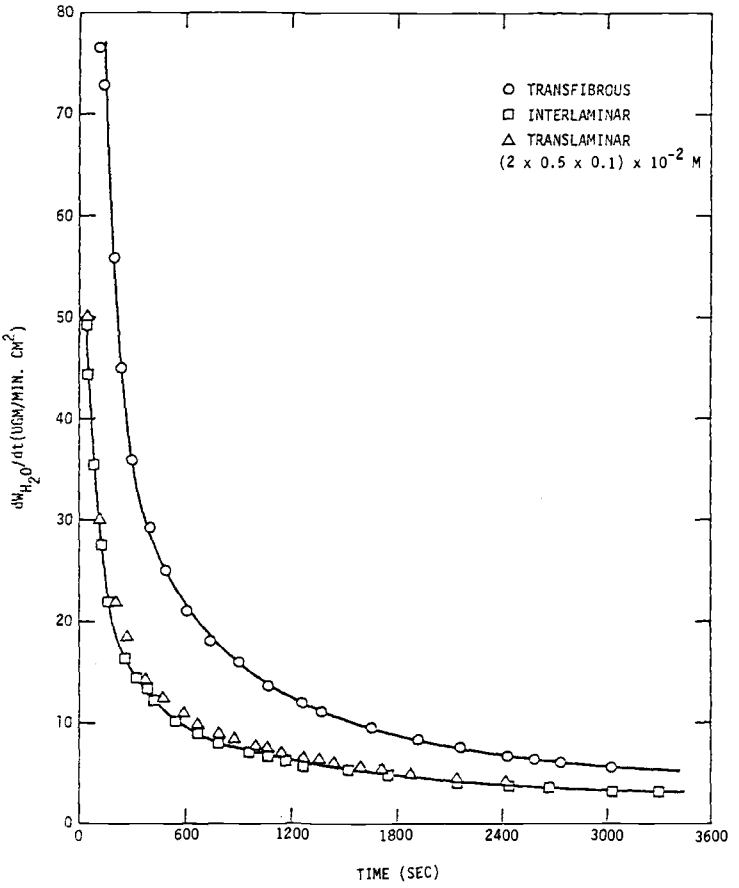

FIG. 4—*Moisture desorption rates of Hercules 3501-AS composite at 75°C.*

Microstructural Degradation

A graphic summary of the effects of variable moisture exposure (Fig. 3) and subsequent thermal cycles on the 73°C values of ultrasonic properties α_L, C_L, and thickness L is shown in Figs. 9-11, respectively. It is seen that with each additional thermal shock cycle the areas of high moisture exposure suffered increased internal damage as evidenced by the rapidly increasing attenuation (Fig. 9) and decreasing ultrasonic velocity (Fig. 10). Swelling of the water-saturated regions also increased (Fig. 11). Thus sound velocity is sensitive to moisture content, and attenuation to the degree of microstructure degradation. Interlaminar dilation as shown by specimen dilation is also indicative of internal damage. Figure 12 shows the length profiles of moisture desorption for the bar, indicating high

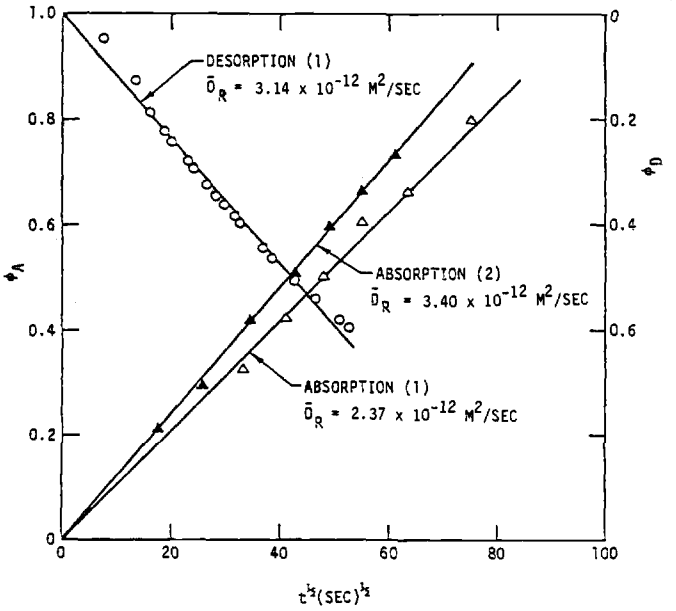

FIG. 5—*Moisture absorption and desorption of Hercules 3501 epoxy at 75°C.*

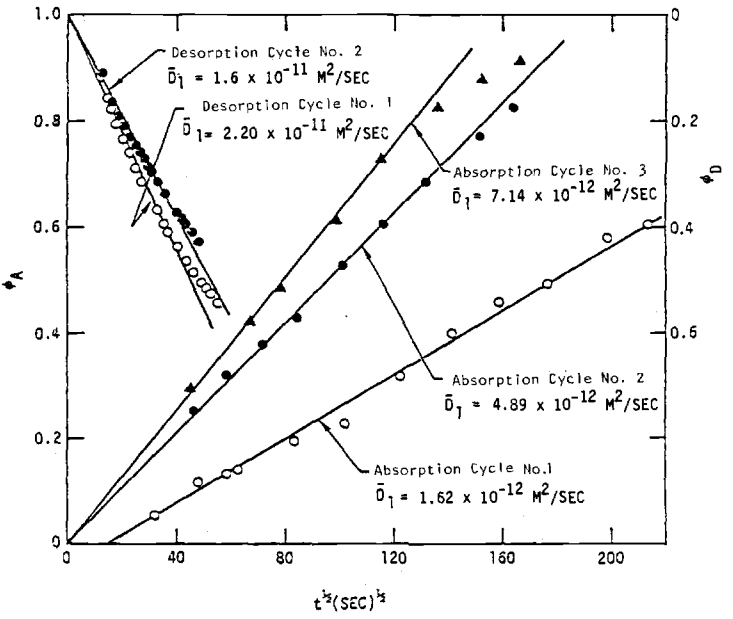

FIG. 6—*Moisture absorption and desorption of Hercules 3501-AS (transfibrous) at 75°C.*

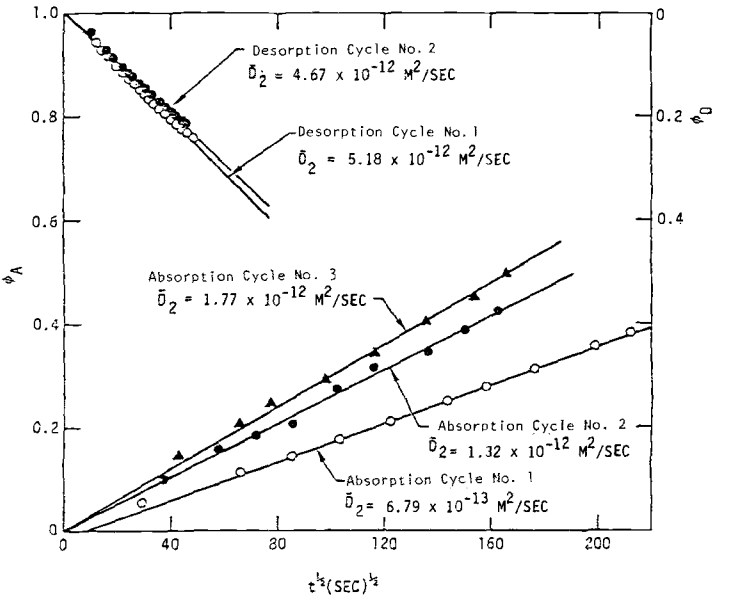

FIG. 7—*Moisture absorption and desorption of Hercules 3501-AS (translaminar) at 75°C.*

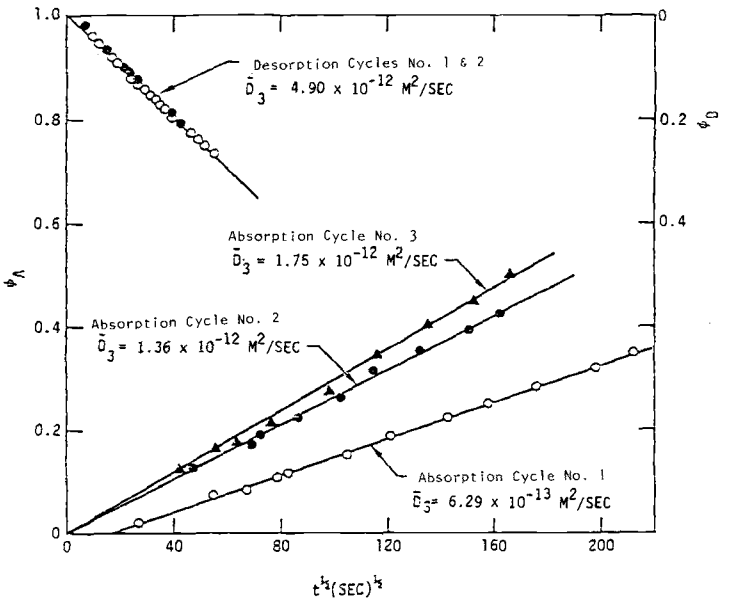

FIG. 8—*Moisture absorption and desorption of Hercules 3501-AS (interlaminar) at 75°C.*

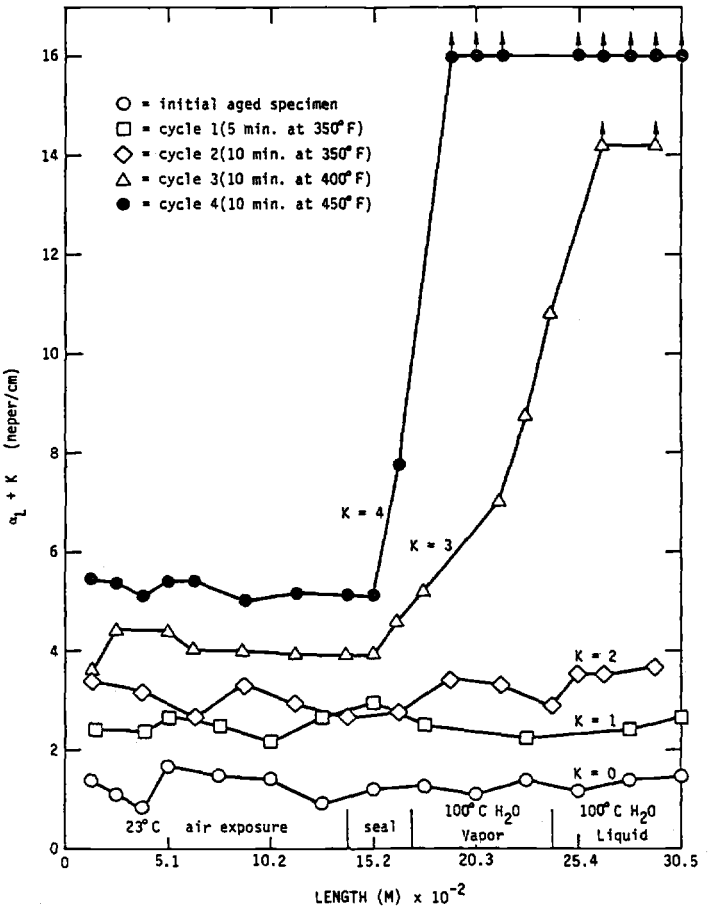

FIG. 9—*Effects of varied moisture exposure and subsequent thermal cycles on the acoustic attenuation* α_L *of Composite SC4.*

moisture content as well as effusion rates in regions of extensive microdamage.

Analytical Profilometry Modeling

A series of the profiles generated by the estimation process is compared in Fig. 13 with the profiles from a direct Fickian solution discussed previously, as assumed to be completely saturated with moisture prior to effusion measurement, and the moisture profiles were calculated at times of 20 and 100 min after effusion started.

A much more severe test of the estimator is for the case of varying

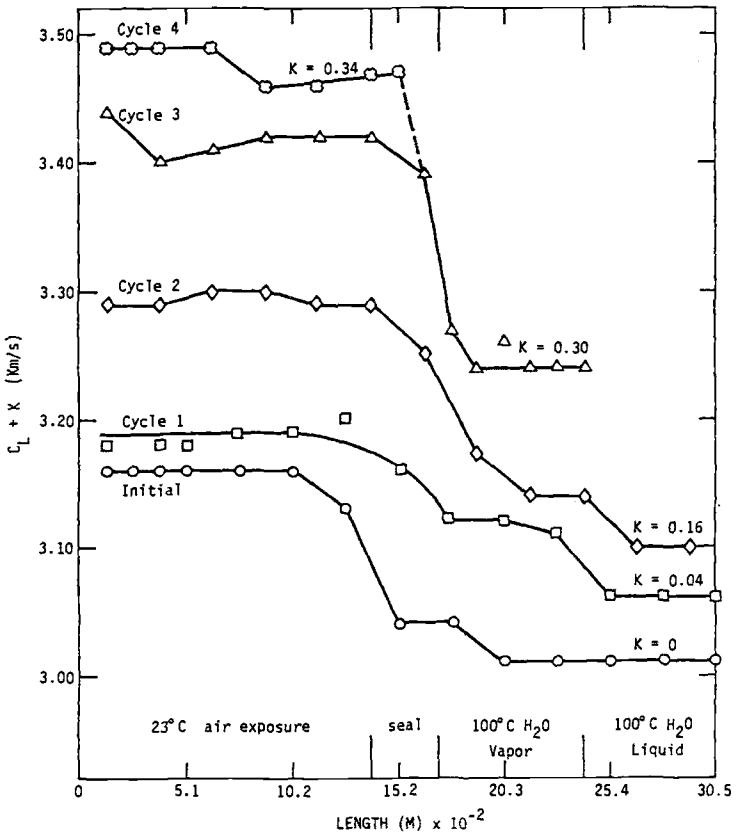

FIG. 10—*Effects of varied moisture exposure and subsequent thermal cycles on the ultrasonic velocity* C_L *of Composite SC4.*

boundary concentrations, in which case the hypothetical specimen is partially saturated, removed from moisture, and the moisture penetration is mapped after various lengths of drying times. Analytical solutions of moisture profiles solved for 20 and 100 min of absorption and various drying times are shown in Fig. 14.

Several important conclusions can be drawn from the results shown in Figs. 13 and 14. In each case, there is excellent agreement between the direct and inverse solutions, thus validating the estimator model. Particularly for Fig. 14, after dehydration has begun, a ridge of high moisture content is present immediately beneath the surface, which is dry. It is entirely feasible that there exists different states of stress to the right (into the center) and to the left (to the surface) of the ridge of water beneath the surface. If a thermal spike is applied to the composite at this time,

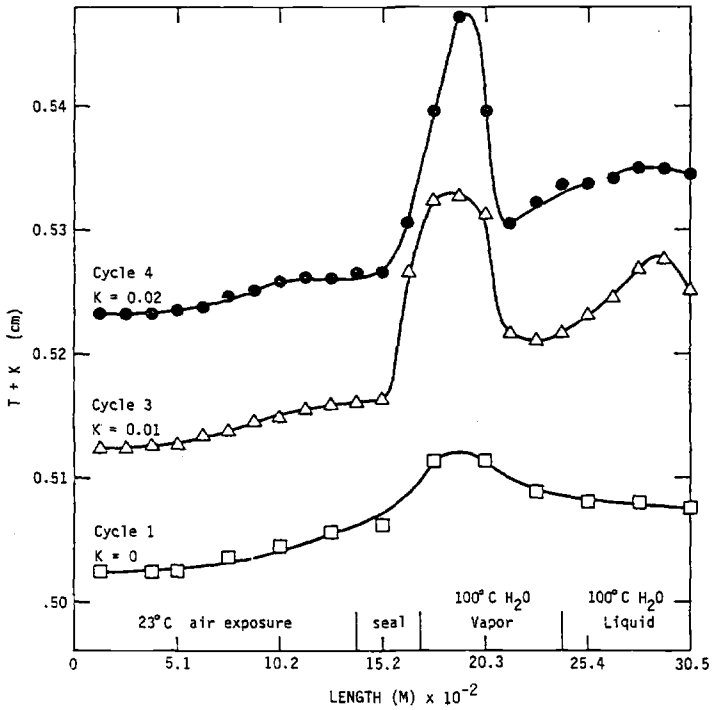

FIG. 11—*Effects of varied moisture exposure and subsequent thermal cycles on the thickness* T *of Composite SC4.*

the different stress states can cause microcracks or delamination beneath the surface of the composite. Experiments [*12*] have been conducted in which subsurface cracks and delamination did occur as postulated.

Summary and Conclusions

This report describes and applies a quantitative methodology to the diffusional kinetics analysis of moisture degradation in graphite/epoxy composites. Diffusional coefficients for water absorption are more sensitive to prior moisture exposure than description coefficients and appear to be sensitive indicators of composite structural degradation.

Ultrasonic acoustic properties, thickness profiles, and moisture diffusion analysis profiles are shown to be sensitive profiling methods. In regions of extensive internal damage, MDA becomes highly sensitive.

The estimator model has been shown to generate correct moisture profiles through the inverse estimation process. Together with automated

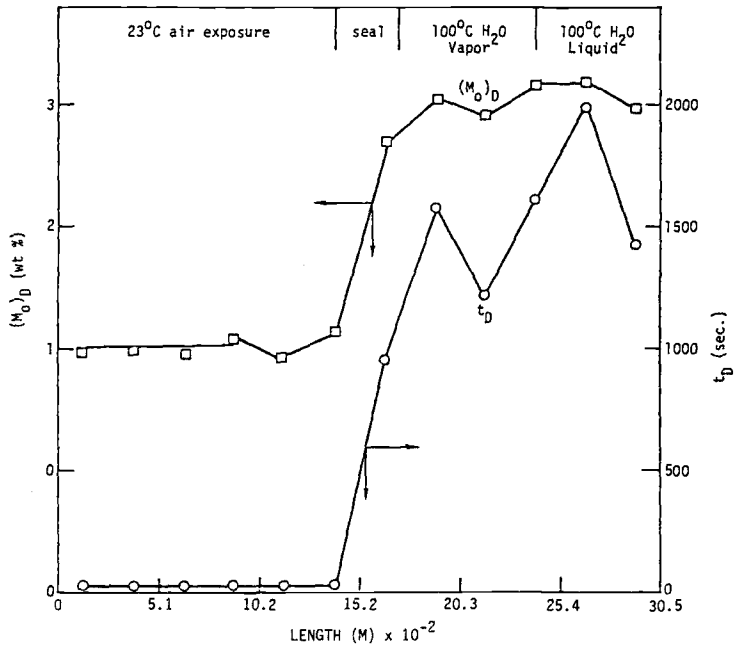

FIG. 12—*Length profiles of moisture desorption.*

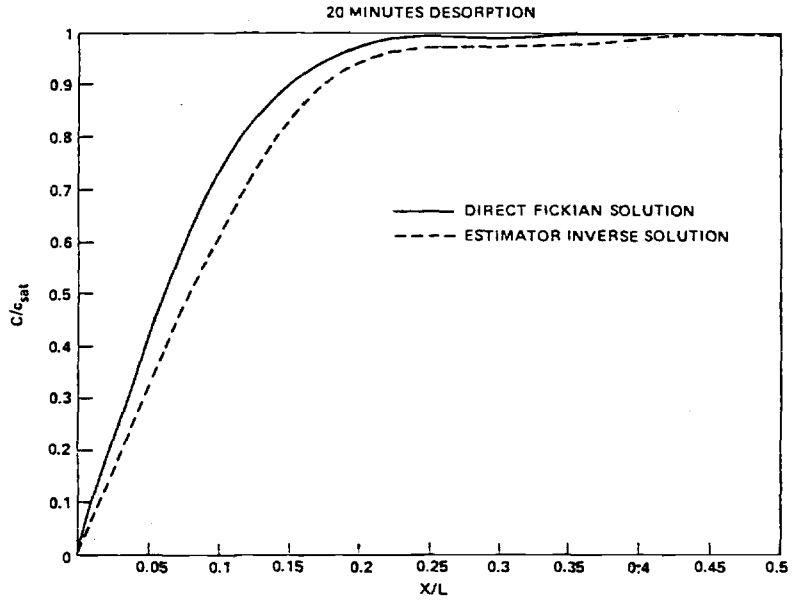

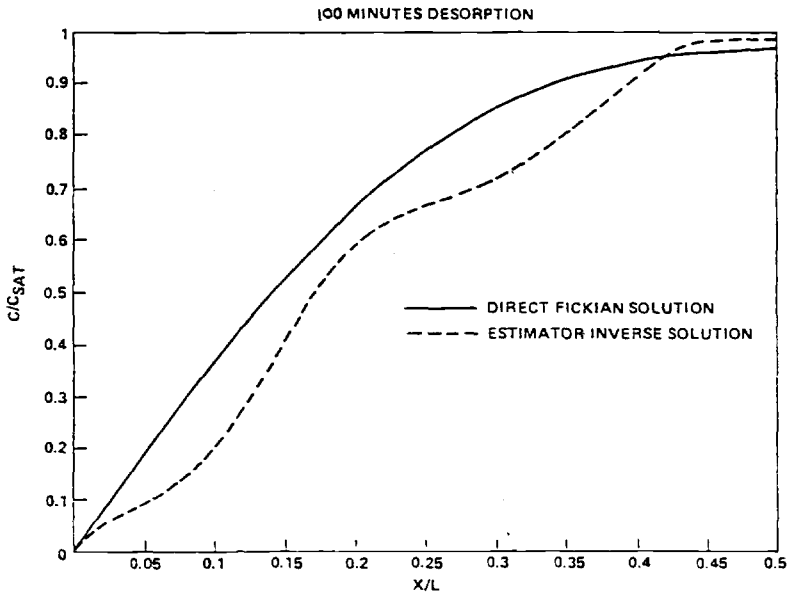

FIG. 13—*Moisture profiles via analytical profilometry modeling of a fully saturated composite after 20-min desorption* (a), *and 100-min desorption* (b).

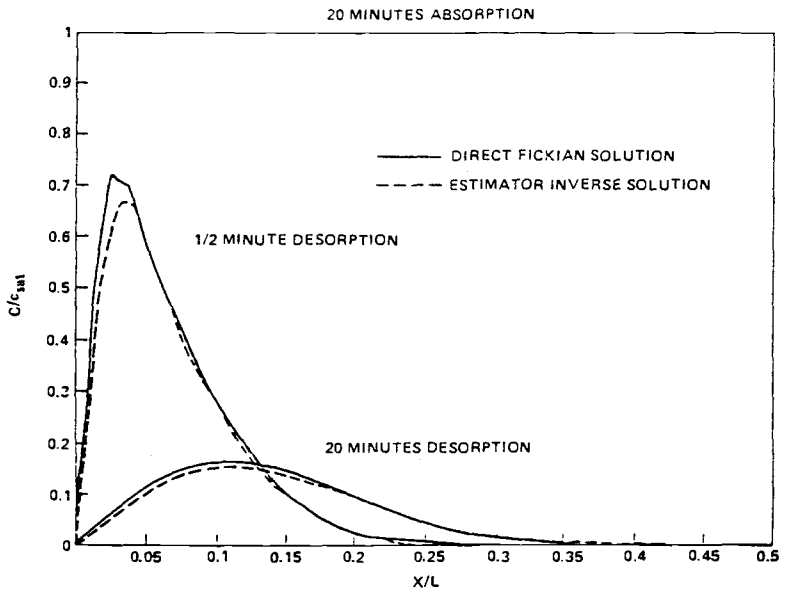

(a)

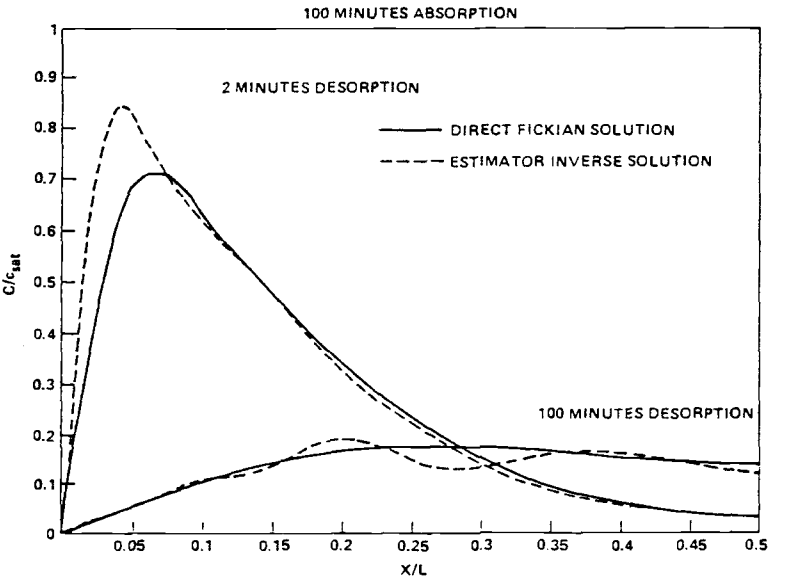

(b)

FIG. 14—*Moisture profile via analytical profilometry modeling of partially saturated composite, after 20-min absorption* (a), *and 100-min absorption* (b).

effusion-rate data collection, the model can become part of a computer-aided moisture-aided moisture detection and profiling nondestructive evaluation (NDE) methodology.

Acknowledgments

This research was sponsored by the Center for Advanced NDE operated by the Science Center Rockwell International for the Advanced Research Projects Agency and the Air Force Laboratory under Contract F33615-74-C-5180.

The authors gratefully acknowledge helpful discussions with Drs. D. O. Thompson and J. M. Richardson during the course of this project.

References

[1] Richardson, J. M., "The Inverse Diffusion Problem," Rockwell International Science Center Internal Letter: "Diffusion with Arbitrary Boundary Concentrations," Thousand Oaks, Calif., Feb. 1978.

[2] Richardson, J. M., Rockwell International Science Center Internal Letter: "Diffusion with Arbitrary Boundary Concentrations," Thousand Oaks, Calif., Feb. 1978.

[3] *Transactions*, Workshop on the Effects of Relative Humidity and Elevated Temperature on Composite Structures, J. R. Vinson, R. B. Pipes, W. J. Walker, and D. R. Ulrich, Eds., Air Force Office of Scientific Research Technical Report AFOSR 77-0030.

[4] Browning, C. E. and Hartness, J. T. in *Composite Materials: Testing and Design (Third Conference)*, *ASTM STP 546*, American Society for Testing and Materials, 1974, pp. 284-302.

[5] Kaelble, D. H., Dynes, P. J., and Maus, L. in *Composite Reliability*, *ASTM STP 580*, American Society for Testing and Materials, 1975, pp. 247-262.

[6] McKague, E. L., Halkais, J. E. and Reynolds, J. D., *Journal of Composite Materials*, Vol. 9, 1975, p. 2.

[7] Kaelble, D. H. and Dynes, P. J. in *Proceedings*, Interdisciplinary Program for Quantitative Flaw Detection, Special Report for Third Year Effort, 1 July 1976-30 June 1977, Contract No. F33615-74-C-5180, Rockwell International Science Center, Thousand Oaks, Calif., pp. 319-363.

[8] Jost, W., *Diffusion in Solids, Liquids, and Gasses*, Academic Press, New York, N.Y., 1960.

[9] Doner, D. R. and Novak, R. C. in *Proceedings*, 24th Annual Technical Conference of the Society of the Plastics Industry, Paper 2D, 1969.

[10] Novak, R. C. and DeCresiente, M. A., *Journal of Engineering for Power*, Vol. 92, 1970, p. 377.

[11] Hahn, H. T., *Journal of Composite Materials*, Vol. 10, 1976, p. 266.

[12] Leung, C. L. and Kaelble, D. H., unpublished results.

P. C. Yeung,[1] *W. W. Stinchcomb,*[1] *and K. L. Reifsnider*[1]

Characterization of Constraint Effects on Flaw Growth

REFERENCE: Yeung, P. C., Stinchcomb, W. W., and Reifsnider, K. L., **"Characterization of Constraint Effects on Flaw Growth,"** *Nondestructive Evaluation and Flaw Criticality for Composite Materials, ASTM STP 696*, R. B. Pipes, Ed., American Society for Testing and Materials, 1979, pp. 316-338.

ABSTRACT: Experimental results have been presented for the case of a flawed unidirectional lamina constrained by off-axis unflawed plies under static and fatigue loading. Flaw growth in the interior of the laminate, around the embedded flaw, was followed by nondestructive testing methods including video-thermographs and ultrasonic C-scan schemes. Two aspects of the results were distinctive. There was an effort of lamination on damage development which was independent of the presence of the notch, and effects which were directly related to the influence of the notch on the local situation. The results are compared with sectioning studies, surface replication, and stiffness change measurements.

KEY WORDS: fatigue (materials), damage, composite materials, nondestructive tests

The ideal elastic behavior of composite laminate is relatively well understood and can be described by laminate theory, some elasticity results, and various numerical methods. However, the nonideal behavior of these materials, consisting of damage initiation, development, and failure, is, at the present time, incompletely described and inadequately understood. Theories of failure for quasi-static loading have been developed and attempts to describe fracture in the presence of a stress raiser such as a hole or notch have been made, but no unified approach such as fracture mechanics for single crack analysis has emerged [*1*].[2] Service conditions encountered by composite structures rarely involve only static loads. The development of damage under oscillating loads is a complex problem, but one which must

[1]Graduate student, associate professor, and professor, respectively, Department of Engineering Science and Mechanics, Virginia Polytechnic Institute and State University, Blacksburg, Va. 24061.

[2]The italic numbers in brackets refer to the list of references appended to this paper.

be approached if proper design leading to service free of disaster is to be a reality.

There is a fairly large body of work covering a wide range of investigations of the fatigue behavior of composite materials [*2*]. The investigations carried out to date show that the state of damage in a composite material is strongly dependent on material, laminate configuration, geometry, stress state, load history, and environment. From an applications viewpoint, one of the most important and, yet, incompletely answered questions concerns the fatigue response of notched composite materials.

One of the major factors controlling the means by which fatigue damage progresses in composite laminates is the constraint imposed on a cracked ply by adjacent plies. The initiation and growth of fatigue damage from a notch depends on the orientation of the major strength and stiffness directions in neighboring plies relative to the local stress state. It would be extremely useful to be able to predict the response of notched laminates from lamina data. At the present time, however, there is a lack of knowledge of the precise details of damage development around a notch in laminates and a corresponding lack of understanding of the influence of one lamina on the response of another lamina when they are bonded together to form a laminate. This paper presents the initial results of an investigation to develop a systematic data base which describes the growth of fatigue damage in notched graphite/epoxy laminae with and without constraining plies. Damage growth in the interior of the laminates, around an embedded flaw, was followed by nondestructive investigative methods including real-time video-thermography and ultrasonic C-scan techniques. The results are compared with sectioning studies, surface replications, and stiffness change measurements.

Experimental Procedures

Specimens

Various types of T-300/5208 graphite/epoxy specimens were selected for testing and investigation [*3*]. Details of ply orientation and notch configuration for the specimens discussed in this paper are given in Table 1.

The specimens were fabricated by Southwest Research Institute. Specimen Types 1 through 4 are 3.81 cm (1.5 in.) by 17.78 cm (7 in.) and Types 5 and 6 are 3.81 cm (1.5 in.) by 25.4 cm (10 in.). The through-the-thickness notches are 0.635 cm (0.25 in.) long by 0.0406 cm (0.016 in.) wide with a 0.02 cm (0.008 in.) radius at the notch tips. The notches were machined in the fabricated specimens using a 0.0406-cm (0.016 in.) high-speed diamond-end mill. The embedded notches are through-the-center two plies of $[0/90]_s$, $[90/0]_s$, $[\pm 45/0]_s$, and $[\pm 45/90]_s$ laminates (Types 3 through 6) and are 0.635 cm (0.25 in.) long by 0.038 cm (0.015 in.) wide. These

TABLE 1—*Graphite/epoxy test specimens.*

Specimen Type	Orientation	Fiber Volume Fraction, %	Notch Configuration
1	$[0]_6$	65.6	through-slit perpendicular to fibers
2	$[90]_6$	64.7	through-slit parallel to fibers
3	$[0/90]_s$	63.6	embedded slit in 90-deg plies parallel to fibers
4	$[90/0]_s$	61.7	embedded slit in 0-deg plies perpendicular to fibers
5	$[\pm 45/90]_s$	65.0	embedded slit in 90-deg plies parallel to fibers
6	$[\pm 45/0]_s$	63.8	embedded slit in 0-deg plies perpendicular to fibers

notches were made by milling the notch in the two prepreg plies simultaneously, filling the void with liquid silicone rubber (RTV-21), and curing. The silicone rubber filler has essentially no tensile or shear strength before or after cure. No damage in the vicinity of the notches was detected by visual and ultrasonic C-scan checks.

Material Testing

All tests were run using a 20-kip MTS testing machine operated in the load-control mode. Load ranges were selected for maximum accuracy and reproducibility.

Static Tests—Three specimens of each type were subjected to static tension tests to determine the mean values of tensile strength, elastic modulus, and fracture strain. Strain data were obtained from strain gages and an extensometer attached to the specimens. Stacked strain rosettes were also attached to the through-the-thickness notched specimens at the notch tips to measure any localized response. Similar gages were mounted on the outside surfaces of specimens with embedded flaws above the tips of the interior flaws. The time-resolved local behavior of the material in the neighborhood of the notch tips was recorded on video tape during the tests. Visual observations of response were made by replaying the tape and noting the change in the damage state during the test.

Fatigue Tests—The tension-tension fatigue tests were run at a stress ratio of $R = 0.1$ and a frequency of 10 Hz. The maximum cyclic stresses were selected using the static tensile strength values as a data base. A slow rate loading ramp was applied to bring the specimen to the desired mean load, and the elastic modulus was determined. A sinusoidal loading function of the desired amplitude was then superimposed on the mean load to achieve a specific cyclic loading condition. The specimens were cycled at a constant maximum stress until fracture or 10^6 cycles, whichever occurred

first. Typically, the test was interruped at ½, 5×10^3, 1×10^4, 5×10^4, 1×10^5, 3×10^5, and 7×10^5 cycles to allow various nondestructive techniques to be applied to determine the damage development in the specimen.

Nondestructive Evaluation and Related Tests

A variety of techniques, some of which were developed in our laboratories, were used to monitor damage development in the specimens during testing. The objectives of these efforts were to establish the nature of damage as precisely as possible and to define the extent of damage. The techniques are outlined briefly in the following. A more detailed description can be obtained from the references.

The method of replication was adapted to composite materials in earlier studies [*4,5*]. Cellulose acetate tape is softened with a diluted acetone solution and pressed against the surface where cracks are thought to exist. The tape flows into the surface detail and hardens. When the tape is removed, a record of the surface detail is obtained. The image on the tape can then be viewed in a microscope or reproduced on film for inspection. The replication process allows magnification of $\times 50$ to $\times 100$ without the depth of field limitations inherent to light microscopy, so that the method is actually preferable to direct observation using a standard microscope. The replicas were made at different load levels or different numbers of loading cycles or both. Replicas were also made of surfaces created by sectioning specimens which had undergone fatigue loading and had developed some damage. These replicas were used to document the damage in the vicinity of an embedded flaw.

Another nondestructive method used to follow fatigue damage growth is thermography [*6*]. Damage events in composite materials dissipate energy as heat, which can easily be detected by a thermographic camera with a 10-color isotherm display unit. By distinguishing between steady-state stress-field-related heat dissipation and transient heat development, it is possible to measure the severity of defect development and monitor the propagation and distribution of flaws by reviewing the real-time display of the thermal patterns of the specimens.

Ultrasonic C-scan pulse echo patterns were also recorded for all specimens before testing to determine the initial state of damage around the embedded flaw region due to the fabrication of these specimens. The specimens were then cycled to various stages of fatigue loading and C-scans were recorded using identical settings on the instrumentation. The patterns were later compared with the actual damage development in the specimens as observed from the sectioning studies.

Finally, stiffness measurements were made throughout the tests at various cyclic intervals through the use of an extensometer. This provides an addi-

tional means of obtaining a quantitative description of the damage growth sustained by the specimens during the fatigue damage process.

Results and Discussions

Static Tests

A summary of the static tensile strength data is given in Table 2. Axial cracks initiated at the notch tips of the transversely notched $[0]_6$ specimens as matrix cracks at approximately 25 percent of the failure load. These cracks then extended along the fiber direction and propagated toward the ends of the specimens as the load was increased. The final failure was usually associated with the complete separation of the specimen into two parts along the longitudinal cracks which developed.

The response of a similarly notched lamina when constrained by unflawed laminae on both sides was quite different. In the case of a Type 4 specimen where the constraining plies were 90-deg plies, transverse cracks in the exterior 90-deg plies were observed to develop at the notch location at stresses of approximately 138 MPa (20 ksi) and grow to a length slightly longer than the notch at 310 MPa (45 ksi). Between 276 MPa (40 ksi) and 483 MPa (70 ksi), creases in the 90-deg plies above and below the notch were observed where cracks developed at the notch tips in the interior 0-deg plies and extended parallel to the fibers. The 90-deg plies then deformed by kinking in the plane of the specimen as the two outside ligaments were displaced relative to the center section as the load increased. The length of the axial cracks in the interior 0-deg plies was different for each specimen and varied from 0.5 to 20 mm. The failure mode of each specimen was a transverse fracture of 0-deg plies initiating at the ends of two axial internal cracks extending from opposite ends of the internal flaw.

When a biaxial state of constraint was imposed, such as in the case of Type 6 specimens, where the constraining plies were oriented at ± 45 deg,

TABLE 2—*Average tensile strength of notched/flawed graphite/epoxy specimens.*

Specimen Type	Orientation	Tensile Strength, ksi
1	$[0]_6$	72.8 ± 11.8^a
2	$[90]_6$	3.44 ± 0.30^a
3	$[0/90]_s$	105.3 ± 9.64
4	$[90/0]_s$	82.0 ± 0.90
5	$[\pm 45/90]_s$	25.6
6	$[\pm 45/0]_s$	51.5

[a]Strength values calculated using net section areas at the notch for through-the-thickness notched specimens (1 ksi = 6.895 MPa).

fractures were through the embedded flaw, with the failure of the 0-deg plies extending away from the notch tip at 45-deg to the fiber direction to within 5 mm of the edge of the specimen. The remaining portion of the specimen failed transverse to the loading direction. Splitting of internal 0-deg plies at the notch tip was detected in only one case; however, it did not act as a major part of the static fracture.

The importance of constraint effects on the behavior of the notched 0-deg plies can be demonstrated by comparing the tensile strength data in Table 2. The notched unidirectional 0-deg laminate failed at an axial net section stress of 502 MPa (72.8 ksi). Using laminated plate analysis, one can calculate the net section stress exerted on the 0-deg plies in the embedded flaw specimens. The net section stresses were 1220 MPa (177 ksi) in the case of 90-deg constraining plies (Type 4 specimen) and 1001 MPa (145.2 ksi) in the case of ± 45-deg constraining plies (Type 6 specimen). It was obvious that some constraint effects were occuring since in both cases the 0-deg ply stresses were higher than those of the unconstrained case. This is possibly due, in part, to the fact that any local stress concentration effect of the notch had been reduced by the presence of the constraining plies. The transverse in-plane tensile stress (σ_y) in the 0-deg plies is greater in the case of the $[90/0]_s$ laminate than for the $[\pm 45/0]_s$ laminate. Hence, the increased effectiveness of the $[90/0]_s$ laminate in constraining the growth of flaws from a notch in the 0-deg plies (at least as indicated by the higher fracture stress) is not due to a local holding together of the 0-deg ply in the direction of vertical crack growth.

The notched $[90]_6$ specimens (Type 2) failed transverse to the load axis through the notch region. In the presence of constraint, however, embedded cracks in the 90-deg plies of Types 3 and 5 specimens had little or no consequence in the final fracture process. The response of these laminates under static loading closely resembled that of the unflawed specimens, and, in many cases, the specimen did not break at the notch region.

In the case of the $[\pm 45/90]_s$ laminate, edge delaminations developed in the 90-deg plies and interacted with transverse cracks in the 90-deg plies by jogging between the $-45/90$-deg interface as the delamination began to grow along the edge of the specimens. The location of the final fracture coincided with initially defective regions away from the notch position in the laminates as detected by ultrasonic C-scans of the specimens made before testing. These regions were probably regions of delaminations between the 90-deg and the ± 45-deg plies, causing a relaxation of the constraint afforded by the normal bonding of these layers.

A simple analytical model, which uses an equilibrium element approach, has been adapted to examine the characteristic spacing of the transverse cracks in the off-angle plies in these laminates [7]. The analytical prediction of the crack spacing agrees well with experimental data obtained from laminates of various stacking sequences.

Fatigue Tests

Fatigue damage of the notched $[0]_6$ specimens initiated at the notch tips and propagated parallel to the fibers in an "H" pattern. The fatigue failures occurred when the axial cracks propagated into and through the gripped region, causing the specimen to pull out of the grips. The fatigue damage was well developed by 5000 cycles and could be followed by thermography. The distance over which the axial cracks traveled varied in length, depending on the maximum load applied.

In the case of the through-thickness notched $[90]_6$ specimens, fatigue failure occurred through the notch parallel to the fiber direction when cycled at a maximum stress of over 55 percent of the static tensile strength. For specimens which survived 10^6 cycles of fatigue loading, no visible damage was observed at the notch tips. It was suspected that, as soon as a crack was initiated at the notch tip, catastrophic failure occurred with the crack running toward the edge of the specimen.

When the notched unidirectional 90-deg laminae are constrained by unflawed plies, the fatigue response of Types 3 and 5 laminates is (embedded) flaw-insensitive. The transverse crack at the notch position in the interior 90-deg plies had little significance on the final failure of the laminates.

When a $[\pm 45/90]_s$ specimen (Type 5) was cycled at high enough stresses, edge delaminations developed in the 90-deg plies and at the $-45/90$ and ± 45-deg interfaces because of the tensile interlaminar normal stress present at the free edge. These delaminations then propagated along the length and through the width of the specimen and final fracture occurred when the nondelaminated section of the specimen could no longer support the load applied. In all cases, no visible damage was detected around the embedded flaw region either by ultrasonic C-scan or by thermography.

A constrained notched 0-deg ply, such as in Types 4 and 6 specimens, presents a more complicated situation. Here, the embedded notch in the laminate becomes the source of damage development and, depending on the orientation of the constraining plies, the interlaminar stresses influence the spread of damage in a complex way since the local stress field in the neighborhood of the flaw is extremely complex.

In order to accurately assess the effect of the different constraining plies on a given flaw situation, a common loading parameter is needed so that the local behavior of different laminates can be compared under at least one identical condition. As a first attempt at identifying an appropriate parameter, the nominal stress in the flawed ply was selected. Specifically, the total applied loads required to produce the same nominal axial stress in the 0-deg plies of Types 4 and 6 specimens were calculated using laminated plate theory, including thermal curing stresses.

C-scan histories of specimens with embedded flaws are presented in Figs.

1-5. The C-scans were made at the cyclic intervals shown in the figures. In all figures, the horizontal arrow locates the position of the embedded flaw.

Figure 1 shows the development of damage as revealed by C-scans of a Type 4 $[90/0]_s$ specimen after 100 000, 300 000, and 700 000 cycles at an applied stress equal to 36 percent of ultimate tensile strength (UTS). By 100 000 cycles, an H-pattern has formed at the flaw. Sectioning studies, to be described in another section of the paper, show that the damage consists of axial cracks at the tips of the notch in the 0-deg plies and delamination of the 90/0 interface. In addition, transverse cracks in the 90-deg constraining plies are also present. Additional cycles at this stress level cause the damage zone to grow in the transverse direction. Between 300 000 and 700 000 cycles, the C-scan reveals little or no growth of the damage zone. All C-scans in this paper are made by gating on the same echo and using the same sensitivity, so that the size of the defective zones in different C-scans can be directly compared and used as a relative measure of the size of the damage zone detectable by the ultrasonic C-scan technique.

Higher applied stresses produce higher damage zone growth rates and larger damage zones. Figure 2 shows that the damage zone in a Type 4 $[90/0]_s$ specimen at 51 percent of UTS continued to grow in the axial direction during the first 100 000 cycles, where the test was stopped and the specimen was sectioned. However, the transverse growth of the damage zone stopped after 5000 cycles. Thermographs recorded during this test show H-shaped hot spots as early as 1000 cycles. Figure 3 shows that after 100 000 cycles at 70 percent UTS, the damage has extended to the grips in the axial direction and additional cycling to 300 000 cycles increases the extent of the damage in the transverse direction. By 300 000 cycles, the

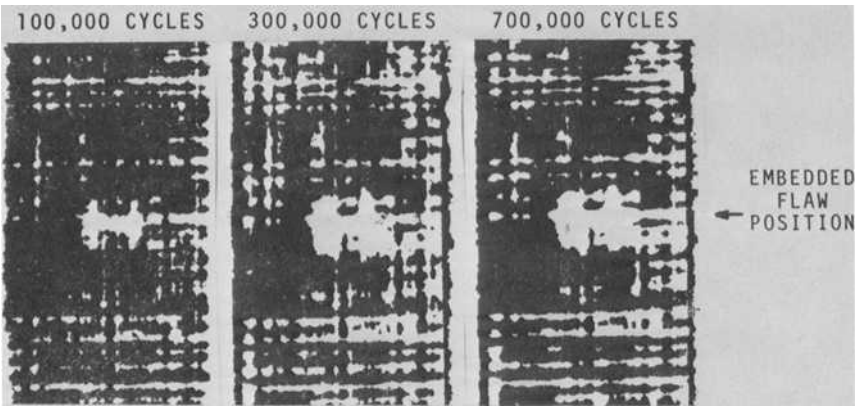

FIG. 1—*C-scan history of a Type 4 $[90/0]_s$ laminate with a notch embedded in the interior 0-deg plies under cyclic loading at 36 percent UTS. The nominal axial stress in the 0-deg plies is 70 percent of the notched tensile strength of Type 1 specimens.*

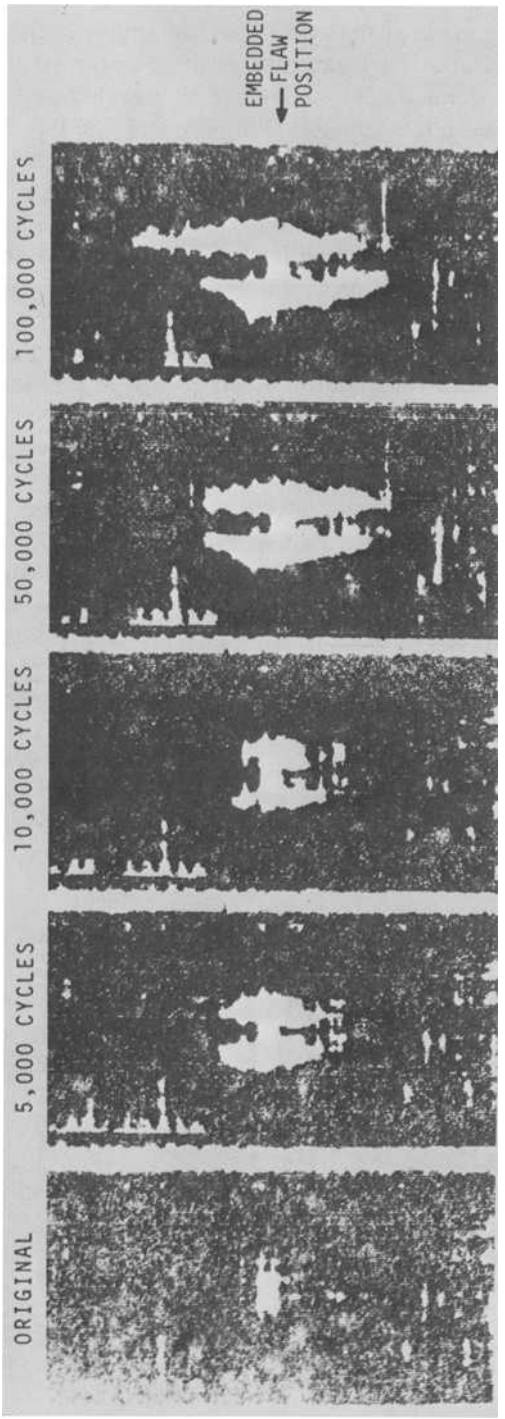

FIG. 2—*C-scan history of a Type 4 $[90/0]_s$ laminate with a notch embedded in the interior 0-deg plies under cyclic loading at 51 percent UTS. The nominal axial stress in the 0-deg plies is 100 percent of the notched tensile strength of Type 1 specimens.*

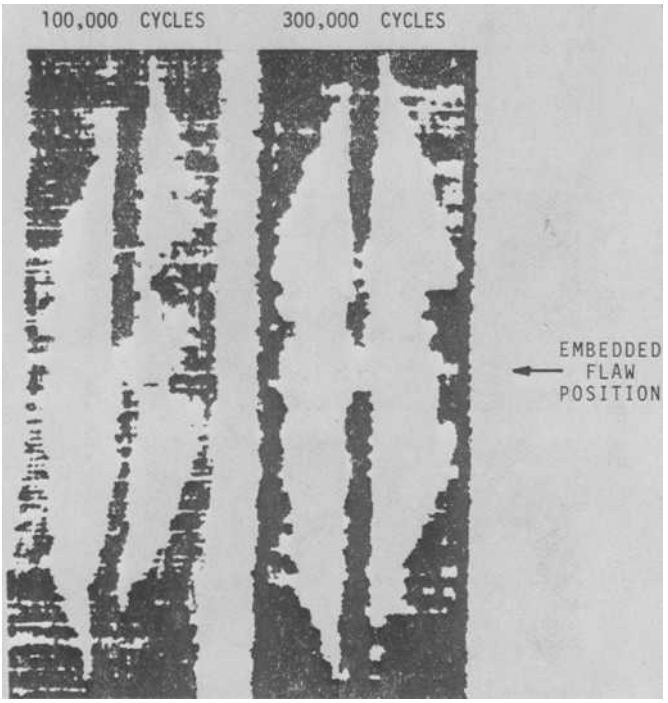

FIG. 3—*C-scan history of a Type 4* $[90/0]_s$ *laminate with a notch embedded in the interior 0-deg plies under cyclic loading at 70 percent UTS. The nominal axial stress in the 0-deg plies is 137 percent of the notched tensile strength of Type 1 specimens.*

90/0 interfaces had delaminated to the extent that the 90-deg plies no longer were effective constraining plies and the test was stopped. Visual inspection showed that the four axial cracks extending from the notch tips in the 0-deg plies had grown into the grip region, creating a "no load" strip of unidirectional material above and below the embedded flaw and two load-carrying strips on each side of the flaw.

Damage zones in Type 6 $[\pm 45/0]_s$ laminates are shown in Figs. 4 and 5. The C-scans in Fig. 4 show the defective region around an embedded flaw in a specimen cycled at a maximum stress of 41 percent UTS. By 100 000 cycles, a damage zone has developed in the flawed region; however, there appears to be little or no growth of the zone after 310 000 cycles. During this test, the thermographic camera detected a hot spot as early as 3300 cycles, although the thermographic pattern was not as distinct as in the Type 4 laminates.

Increasing the applied stress to 63 percent UTS creates a larger damage zone after 100 000 cycles than does cycling at 41 percent UTS. The higher stress also causes the damage zone to increase in size between 5000 and

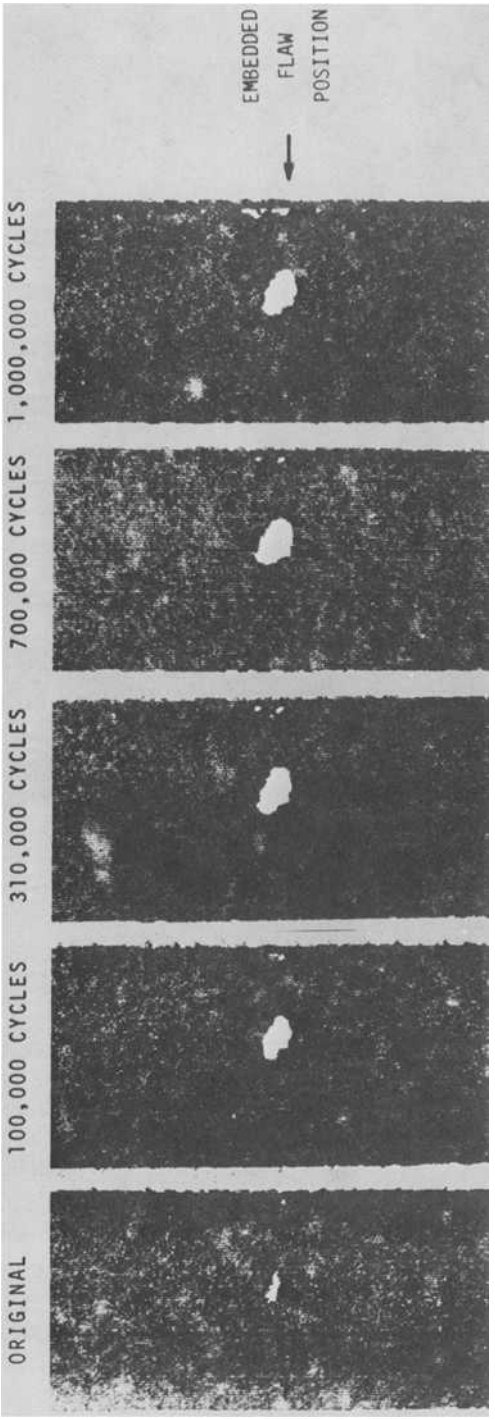

FIG. 4—*C-scan history of a Type 6* $[\pm 45/0]_S$ *laminate with a notch embedded in the interior 0-deg plies under cyclic loading at 41 percent UTS. The nominal axial stress in the 0-deg plies is 70 percent of the notched tensile strength of Type 1 specimens.*

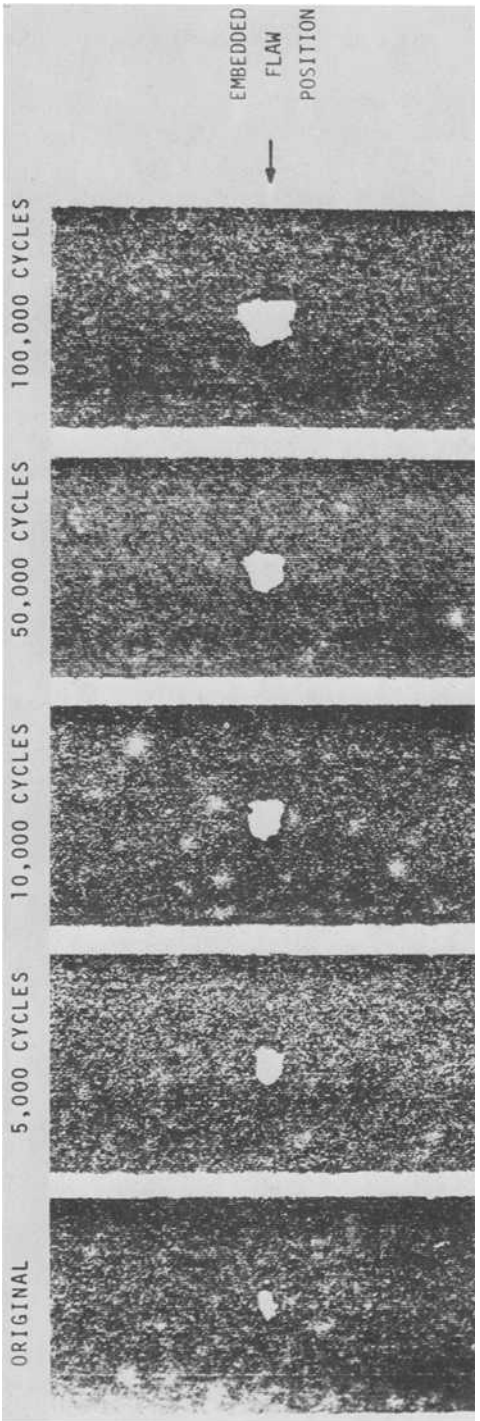

FIG. 5—*C-scan history of a Type 6* $[\pm 45/0]_s$ *laminate with a notch embedded in the interior 0-deg plies under cyclic loading at 63 percent UTS. The nominal axial stress in the 0-deg plies is 100 percent of the notched tensile strength of Type 1 specimens.*

100 000 cycles. The thermographs recorded at a hot spot in the flawed region by 1100 cycles.

Some of the effects of the orientation of the constraining plies on the notched 0-deg plies can be seen in Figs. 6 and 7. Figure 6 compares the C-scans of a Type 4 $[90/0]_s$ laminate and a Type 6 $[\pm 45/0]_s$ laminate after 100 000 cycles. The applied maximum stress is such that the nominal

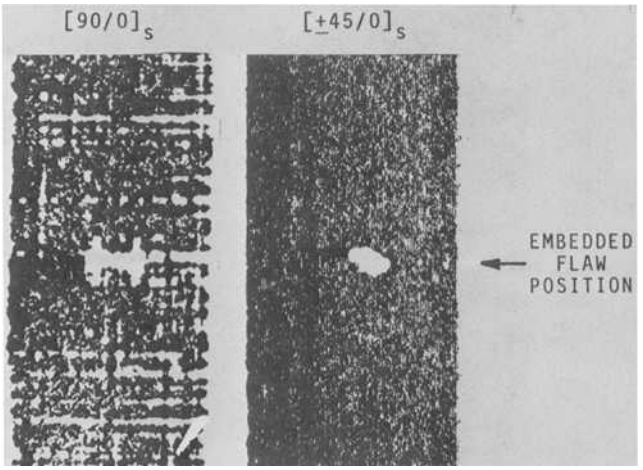

FIG. 6—*Ultrasonic C-scans of a Type 4* $[90/0]_s$ *and a Type 6* $[\pm 45/0]_s$ *laminate after 100 000 cycles of fatigue loading. In each case, the nominal axial stress in the interior 0-deg plies is 70 percent of the notched tensile strength of Type 1 specimens.*

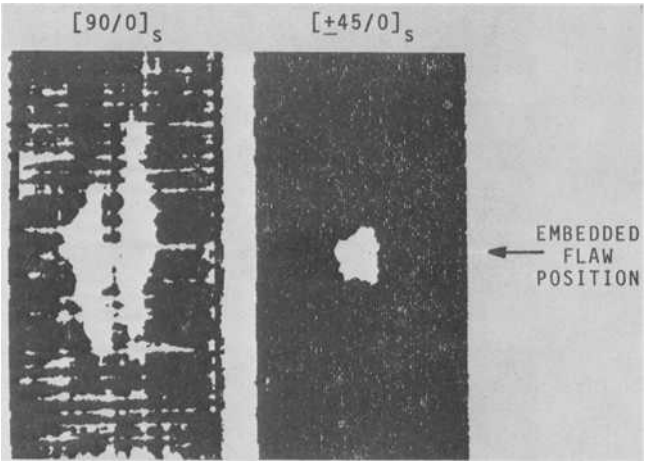

FIG. 7—*Ultrasonic C-scans of a Type 4* $[90/0]_s$ *and a Type 6* $[\pm 45/0]_s$ *laminate after 100 000 cycles of fatigue loading. In each case, the nominal axial stress in the interior 0-deg plies is 100 percent of the notched tensile strength of Type 1 specimens.*

maximum stress in the 0-deg plies is equal to 70 percent of the tensile strength of 0-deg unidirectional laminates with a center notch (Type 1 specimens). The damage zone in the $[90/0]_s$ specimen has the H-shape mentioned previously with damage regions extending away from the notch tips in the 0-deg direction. This C-scan also shows defective areas throughout the $[90/0]_s$ specimen whereas the defective region is confined to the flaw area in the $[\pm 45/0]_s$ specimen. Visual observation of the $[90/0]_s$ specimen shows that these defects are delaminations of the 90/0 interface which allow the exterior 90-deg ply to peel off. The area of the horizontal bar in the H-pattern is approximately equal to the area of the damage zone in the $[\pm 45/0]_s$ specimen. At applied stresses such that the 0-deg ply stress is equal to the notched tensile strength of unidirectional specimens, the damage zone in the $[90/0]_s$ specimen is much larger than in the $[\pm 45/0]_s$ specimen after the same number of cycles, Fig. 7. The H-pattern is extended toward the grip region; however, the damage zone in the $[\pm 45/0]_s$ specimen is again confined to the embedded flaw region. Also as before, delamination of the 90/0 interface is quite extensive in the Type 4 specimen whereas no delaminations outside the damage zone were observed in the Type 6 specimen.

In an attempt to increase the understanding of the effect of local constraint on the state of stress near a flaw, an analysis of the cracked laminate problem has been undertaken [*8*]. The results indicate that positive (tensile) through-the-thickness normal stress develops at the interfaces between lamina where the crack stops. Furthermore, it is also shown that the delamination stress is greater in the $[90/0]_s$ laminate than in the $[\pm 45/0]_s$ laminate, leading one to expect more delamination for the former laminate. This agrees well with the experimental observation of damage growth in these laminates under cyclic loading in our sectioning studies described in the following.

Sectioning Studies

Although the C-scan technique used in making Figs. 1–7 is a useful nondestructive inspection (NDI) method, it gives a two-dimensional plan view of a three-dimensional situation and is sensitive only to area or volume defects. Of the two major damage modes produced in the specimens in this study (matrix cracks parallel to the fiber direction and delaminations), the C-scan method is more capable of detecting delaminations than finding thin cracks. Therefore, in order to determine the extent and interaction of the damage modes, specimens have been sectioned and replicated.

Transverse sections were made (as shown schematically in Fig. 8 for a Type 4 specimen) by sawing the specimen just above the transverse axis of the flaw and polishing the cut surface to the $X = 0$ position. Subsequent sections were made by cutting and polishing at locations above and below

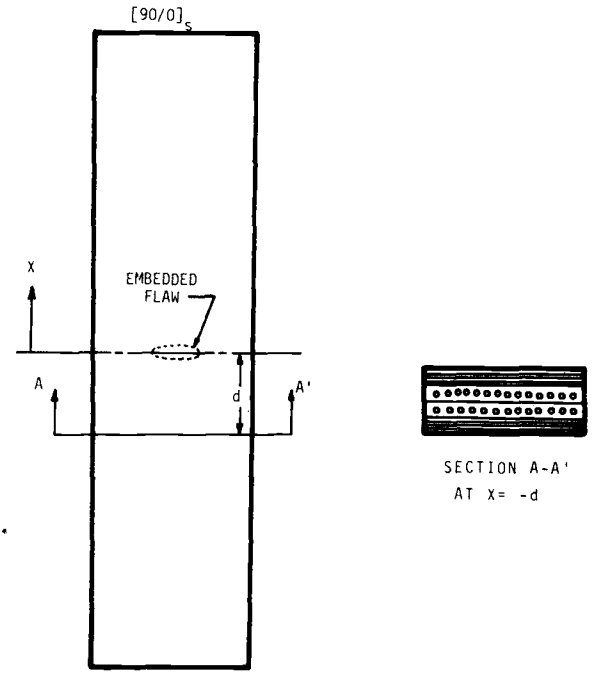

FIG. 8—*Schematic diagram of sectioning studies on a typical* $[90/0]_s$ *type laminate with a flaw embedded in the interior 0-deg plies.*

the horizontal axis. Replicas of the polished surface were formed and studied in a microscope or used to make photographic prints. Photomicrographs were also made in some cases. Reproductions of a series of replicas made on $[90/0]_s$ and $[\pm 45/0]_s$ flawed laminates are shown in Figs. 9 and 10. The specimens represented in these figures were loaded such that the nominal stress in the 0-deg plies was equal to the notched tensile strength of Type 1 specimens.

The $X = 0$ replica shows the transverse section through the embedded flaw, and the arrows indicate the position of the embedded flaw or the axial cracks. The orientation of the constraining plies produces significant differences in the state of damage in the laminates under cyclic loading conditions. The damage state in the Type 4 $[90/0]_s$ specimens consists of axial cracks at the notch tips in the 0-deg plies, delamination of the 90/0 interfaces, and transverse cracks and peeling of the 90-deg plies. Damage starts by transverse cracking of the 90-deg plies at the flaw. The accompanying relaxation of constraint allows the formation of axial cracks at the notch tips in the 0-deg plies, the same damage mode that developed in the unconstrained-notched Type 1 specimens. The delamination of the 90/0

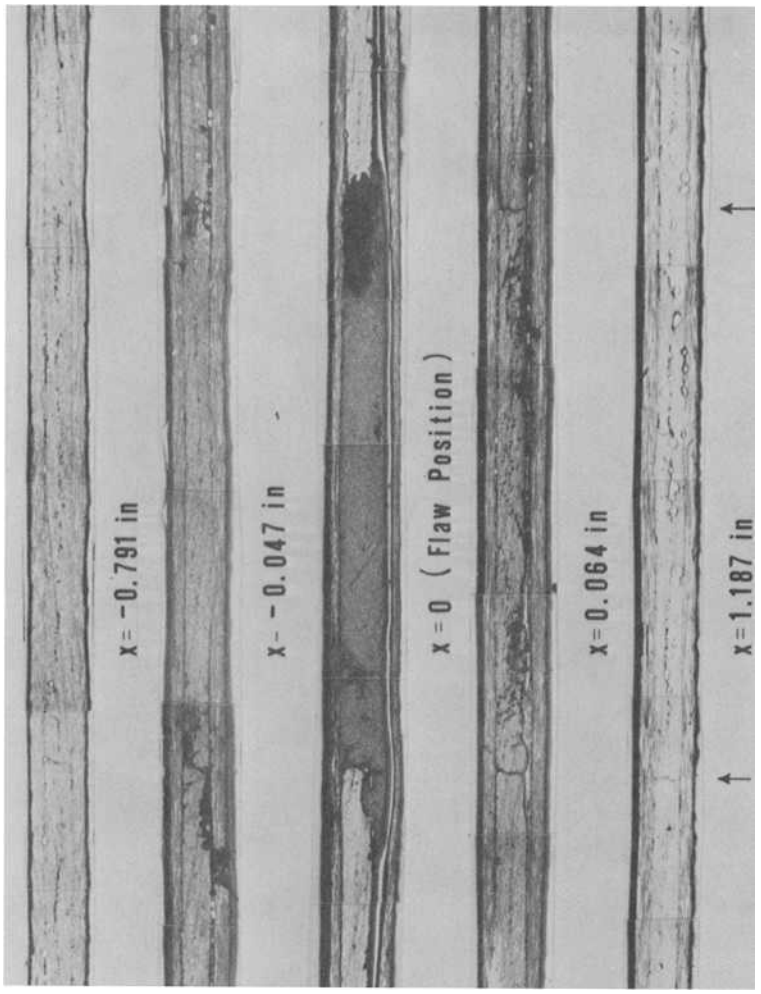

FIG. 9—*Sectioning studies of a Type 4* $[90/0]_s$ *laminate with a notch embedded in the interior 0-deg plies, after 100 000 cycles of fatigue loading at 51 percent UTS. The nominal axial stress in the 0-deg plies is 100 percent of the notched tensile strength of Type 1 specimens.*

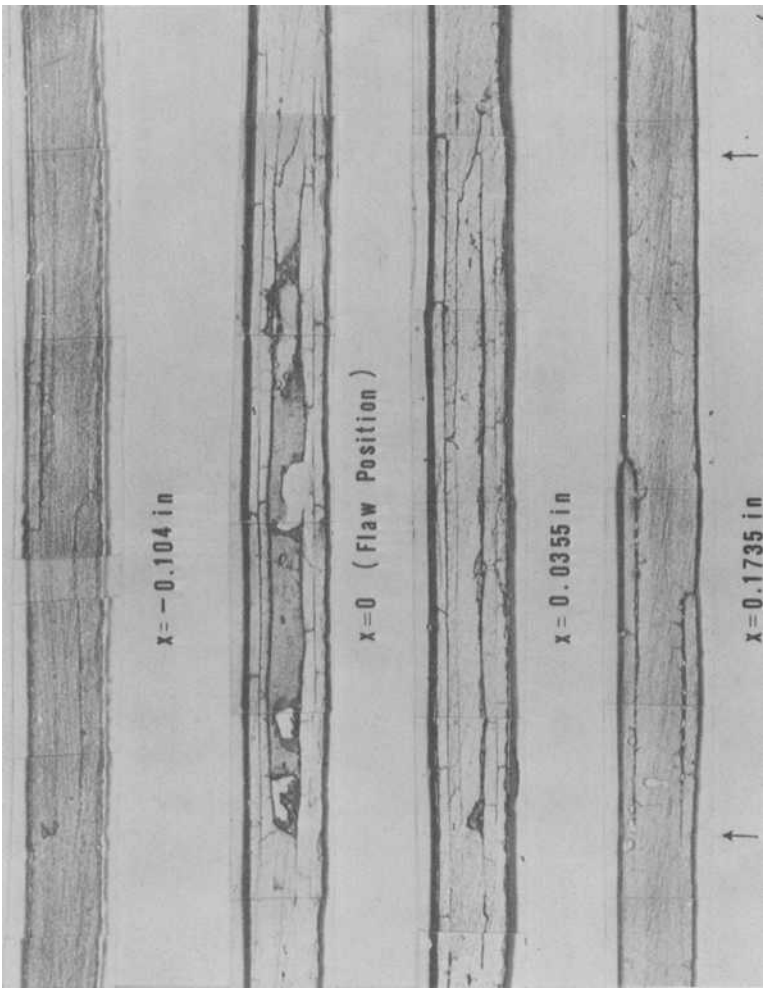

FIG. 10—*Sectioning studies of a Type 6 $[\pm 45/0]_s$ laminate with a notch embedded in the interior 0-deg plies, after 100 000 cycles of fatigue loading at 63 percent UTS. The nominal axial stress in the 0-deg plies is 100 percent of the notched tensile strength of Type 1 specimens.*

interface is caused by the relative displacement of material in the no-load zone above and below the flaw and the material in the adjacent load-carrying strips. The cyclic "kinking" of the 90-deg plies to accommodate the deformation produces delamination of the 90/0 interfaces, which, in turn, further relaxes the constraint on the 0-deg plies. The damage mechanisms for the Type 4 $[90/0]_s$ laminate are the cyclic degradation of the constraining plies and axial cracking of the 0-deg plies as in the unidirectional notched specimens (Type 1).

The behavior of the Type 6 $[\pm 45/0]_s$ and Type 4 laminates is distinctly different. The major damage modes are cracks parallel to the +45-deg and −45-deg fibers and delamination of the ±45 and −45/0 interfaces. The off-axis cracks do not extend out of the delaminated zone as do the axial cracks in the Type 4 specimens. Also, for equal 0-deg ply stresses, the damage zone in the Type 6 specimens is smaller than the damage zone in the Type 4 specimens.

The change in stiffness of each laminate depends upon the orientation of the constraining plies, stress amplitude, and number of cycles, as shown in Fig. 11 for $[90/0]_s$ and $[\pm 45/0]_s$ specimens. For both laminates, the percent change in stiffness, determined from slow ramp loading data, varies directly with the amplitude of applied loading. The two specimens

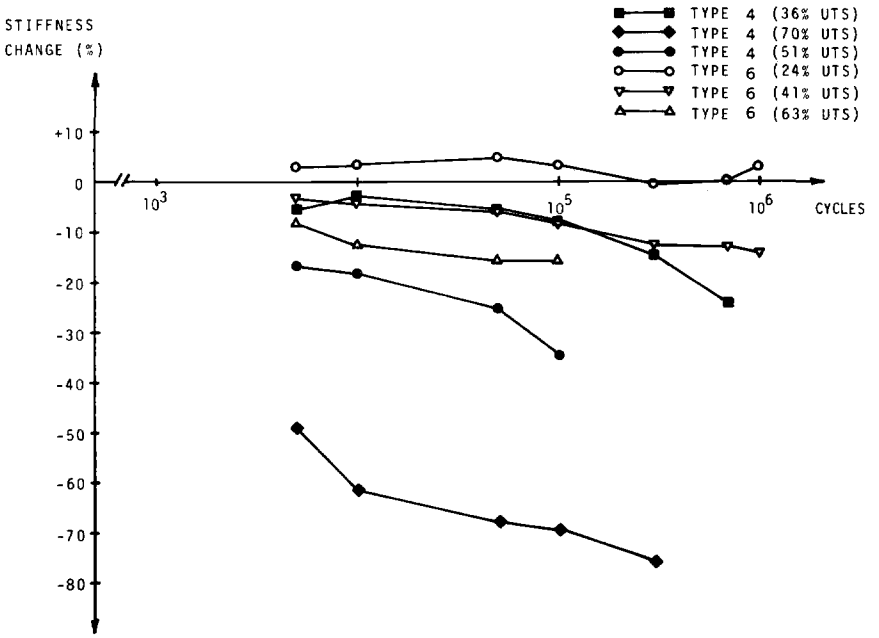

FIG. 11—*Stiffness changes of Type 4 ($[90/0]_s$ with embedded flaw) and Type 6 ($[\pm 45/0]_s$ with embedded flaw) specimens during cyclic fatigue loading.*

with nominal 0-deg ply stresses equal to 70 percent of the notched unidirectional tensile strength (Type 4, 36 percent UTS and Type 6, 41 percent UTS) suffer the same percent degradation of stiffness during the first 300 000 cycles, after which the stiffness of the $[\pm 45/0]_s$ specimen remains constant and the stiffness of the $[90/0]_s$ specimen continues to decrease. At nominal 0-deg ply stresses equal to the notched strength of unidirectional specimens, the percent stiffness change is greater in the 51 percent UTS Type 4 specimen than in the 63 percent UTS Type 6 specimen. Again, the stiffness of the $[\pm 45/0]_s$ specimen initially decreases and remains constant whereas the stiffness of the $[90/0]_s$ specimen continues to decrease to 100 000 cycles. At 70 percent UTS, the damage in the $[90/0]_s$ specimen extended to the grips by 100 000 cycles with a corresponding stiffness decrease of 70 percent. As the damage continued to spread across the width of the specimen, the stiffness also continued to decrease.

In attempting to correlate the ultrasonic C-scan patterns with the actual damage development around the flawed region, the length of delaminations and the extent of cracks were measured on the replicas and original photomicrographs, and the results are presented in Figs. 12*a* and 13*a*, *b*, and *c*. These figures are constructed from the sectioning data with the aid of a Tektronix 4051 computer and graphics system.

The damage revealed by sectioning the $[90/0]_s$ specimen in Fig. 9 is

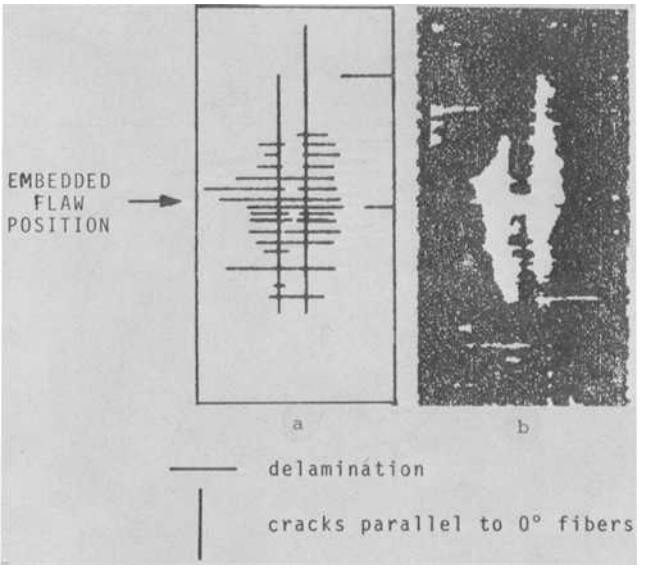

FIG. 12—*Results of sectioning studies on a Type 4 ($[90/0]_s$ with embedded flaw) specimen after 100 000 cycles of fatigue loading at 51 percent UTS:* (a) *delaminations in 90/0 interface and cracks in 0-deg plies:* (b) *C-scan of the same specimen.*

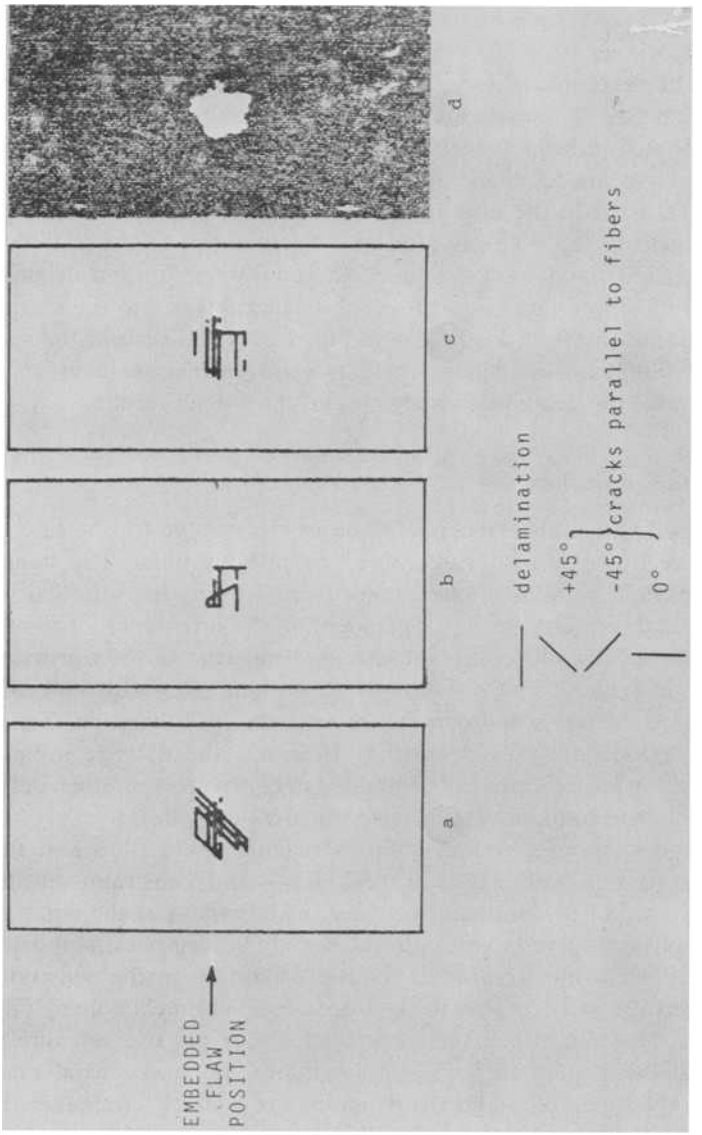

FIG. 13—*Results of sectioning studies on a Type 6* $([\pm 45/0]_s$ *with embedded flaw) specimen after 100 000 cycles of fatigue loading at 63 percent UTS:* (a) *+45-deg ply and +45/−45 interface;* (b) *−45 and 0-deg plies and −45/0 interface;* (c) *combined diagram of delamination at all interfaces; and* (d) *C-scan of the same specimen.*

summarized in Fig. 12*a*, where the long axial lines represent the cracks in the 0-deg plies initiating at the notch tip. The shorter transverse lines show the extent of delaminations of the 90/0 interface in each of the sections. The C-scan of this specimen after 100 000 cycles is shown in Fig. 12*b*. Although the C-scan reveals an extensive zone of damage in the form of the H-pattern associated with the Type 4 specimen, the axial cracks actually extend beyond the damage zone in regions which have not delaminated. The shape and size of the delaminated region described by the sectioning data correlate well with the C-scan results.

The sectioning data for the $[\pm 45/0]_s$ specimen in Fig. 10 are presented in Fig. 13. To assist in the interpretation of the data, the results are presented for cracks in the +45-deg plies and delamination of the ± 45 interface and (Fig. 13*a*), and cracks in the -45 and 0-deg plies and delamination of the $-45/0$ interface (Fig. 13*b*). All delaminations and the single 0-deg ply crack are shown in Fig. 13*c* and Fig. 13*d* is a C-scan of the specimen after 100 000 cycles. Again, there is good correlation between the shape and size of the delamination region and the C-scan results.

Summary and Conclusions

Experimental and analytical results have been presented for the case of a flawed unidirectional lamina constrained by off-axis plies. The damage state that develops in the laminates under cyclic loading is controlled by a complex local stress state which is dependent on the orientation of the flaw in the constrained ply and on the anisotropic properties of the constrained and constraining plies. The response of those laminates with embedded flaws parallel to the fibers and perpendicular to the load direction (Types 3 and 5) was (embedded) flaw-insensitive. However, the damage initiation and development in both types of laminates were sensitive to other defects (inherent and stress induced) in the constrained 90-deg plies.

The damage state in laminates with constrained 0-deg plies and flaws perpendicular to the load axis was both flaw- and constraint-sensitive. Cyclic loading of $[90/0]_s$ laminates produced axial cracks at the notch tips in the 0-deg plies, transverse cracks in the surface 90-deg plies, and delamination of the 90/0 interfaces. The H-pattern damage in the constrained 0-deg plies was the same as that in the unconstrained notched 0-deg (Type 1) specimens. However, when the same cyclic 0-deg ply stresses were imposed on the 0-deg plies in $[\pm 45/0]_s$ laminates, no major axial cracks developed in the 0-deg plies and the delamination zones were smaller than those in the $[90/0]_s$ laminates. In addition to local delamination of the ± 45 and $-45/0$ interfaces, cracks formed parallel to the fibers in the constraining plies but did not extend outside the delamination area. Although the $[90/0]_s$ laminates have higher static strength and stiffness properties, the biaxial constraint imposed by the ± 45-deg plies does not de-

grade as much as the 90-deg constraint during cyclic loading. The general fatigue damage sequence, then, is:

1. Interfibrillose cracks may develop along fiber directions in the flawed ply, beginning at the flaw tip, and in the constraining plies also, depending upon their orientation and the applied stress level. These interfibrillose cracks grow away from the flaw tip.

2. Delamination of constraining plies from the constrained plies follows, driven by differential shearing of the interfibrillose crack faces and by the σ_z stresses that are caused by the crack. The experimental data show that the cracks form before delamination occurs in the $[90/0]_s$ laminates (See Fig. 12).

3. In the delamination region, interfibrillose cracks then may open up further and extend into an undelaminated region, beginning the cycle again, until either fracture occurs or the damage is arrested.

It should be remembered that this sequence occurs for cyclic loading. Delamination plays a much less important role for static loading. It should also be noted that constraining plies act principally on matrix damage, in the direct sense; that is, they provide apparent transverse and shear stiffness to the constrained ply. They prevent cracks in the constrained ply from opening as much as they would otherwise. However, they do not prevent cracks from forming; that is, when the in-plane stress transverse to the fibers reaches the strength of the matrix, cracks will form with or without a constraining ply.

Acknowledgments

The authors gratefully acknowledge the support of the National Aeronautics and Space Administration-Langley Research Center under Grant NSG-1364, monitored by J. Whitcomb. The many helpful suggestions made by E. G. Henneke, II, and assistance by T. K. O'Brien and other members of the Engineering Science and Mechanics Department of Virginia Polytechnic Institute and State University is also appreciated.

References

[1] *Proceedings*, Symposium on Inelastic Behavior of Composite Materials, C. T. Herakovich, Ed., American Institute of Mining, Metallurgical and Petroleum Engineers, Houston, Tex., Nov. 1975.

[2] Stinchcomb, W. W. and Reifsnider, K. L., *Fatigue Mechanisms, ASTM STP 675*, American Society for Testing and Materials, 1979, pp. 762-787.

[3] Stinchcomb, W. W., Reifsnider, K. L., Yeung, P. C., and O'Brien, T. K., "Investigation and Characterization of Constraint Effects on Flaw Growth During Fatigue Loading of Composite Materials," Semi-Annual Status Reports I, II, III, NASA Grant NSG-1364, Virginia Polytechnic Institute and State University, Blacksburg, Va., Dec. 1976-May 1978.

[4] Reifsnider, K. L., Henneke, E. G., II, and Stinchcomb, W. W., "Defect-Property Rela-

tionships in Composite Materials," AFML-TR-76-81, Parts, I, II, III, Air Force Materials Laboratory, Wright-Patterson AFB, Ohio, April 1976, 1977, 1978.

[5] Stalnaker, D. O., "An Investigation of Edge Damage Development in Quasi-Isotropic Graphite-Epoxy Laminates," Thesis, Department of Engineering Science and Mechanics, Virginia Polytechnic Institute and State University, Blackburg, Va., April 1976.

[6] Reifsnider, K. L. and Williams, R. S., *Experimental Mechanics*. Vol. 14, No. 12, Dec. 1974, pp. 479-485.

[7] Reifsnider, K. L. in *Proceedings*, 14th Annual Society of Engineering Science Meeting, Lehigh University, Bethlehem, Pa., 14-16, Nov. 1977.

[8] Talug, A., "Analysis of Stress Fields in Composite Laminates with Interior Cracks," Doctoral Dissertation, Department of Engineering Science and Mechanics, College of Engineering, Virginia Polytechnic Institute and State University, Blacksburg, Va., Aug. 1978.

P. G. Sullivan[1] *and L. W. Davis*[1]

Nondestructive Testing Methods for Graphite/Aluminum Composites

REFERENCE: Sullivan, P. G. and Davis, L. W., **"Nondestructive Testing Methods for Graphite/Aluminum Composites,"** *Nondestructive Evaluation and Flaw Criticality for Composite Materials, ASTM STP 696,* R. B. Pipes, Ed., American Society for Testing and Materials, 1979, pp. 339-354.

ABSTRACT: Development of the C-scan method for nondestructively inspecting graphite/aluminum metal matrix composites is discussed. Specific test results are shown and mechanical properties are correlated with anomalous regions which were detected by the C-scan technique.

KEY WORDS: metal-matrix composite, graphite/aluminum, C-scan, composite materials, nondestructive tests

Some methods for nondestructive inspection/nondestructive testing (NDI/NDT) of materials have been known and in use for many years. These methods have primarily included dimensional checks for compliance with specifications, visual inspection for surface defects, and various penetrant inspection techniques for small discontinuities which originate at or intersect the surface. X-ray and ultrasonic inspection have been used to detect internal defects which do not intersect the surface.

The advent of the use of fracture mechanics in design has made nondestructive inspection by X-ray or ultrasonic methods or both especially important since fracture mechanics deals with predicting and designing for small internal defects. Composites are nonhomogeneous, primarily mechanical mixtures of two or more constituents and can very easily contain defects or flaws. These flaws, not easily seen by ordinary techniques, can adversely affect material performance. Therefore, NDI of parts or their components must be used to detect defects.

Unfortunately, many times NDI/NDT is an afterthought to both the

[1] Project engineer and president, respectively, Nevada Engineering and Technology Corp., Long Beach, Calif. 90806.

material design and hardware design phases. This can lead to problems in selecting and implementing the proper NDT technique for both inspection prior to service and inspection in service. In the field of metal-matrix composites, and primarily in the field of graphite/aluminum composites, NDI/NDT techniques are being developed concurrently with both material development and the design and production of hardware. This paper deals primarily with the ultrasonic C-scan inspection technique as it applies to graphite/aluminum composites, although X-ray techniques are also being used.

Materials

The graphite/aluminum composites used in this development work varied from 0.063 to 0.279 cm thick; the fiber volume varied from 23 to ~35 percent. All material was unidirectional, with all layers oriented in the same direction. All the material had from 0.005 to 0.015 cm of aluminum foils on the top and bottom surfaces. Longitudinal in this discussion refers to the direction parallel to the fiber direction and transverse is perpendicular to the fiber direction. Complete identification of the specific composites is included herein.

Discussion of NDT Techniques Used

Two basic techniques were used, radiography and ultrasonic C-scan. Metallography and destructive tests were used freely to identify and verify anomalous areas and to quantify their effect, if any, on mechanical properties.

X-Ray

Because the densities of the components of graphite/aluminum composites are similar to bulk aluminum (graphite ~1.9 g/cm^3; aluminum ~2.8 g/cm^3), the X-ray techniques used to inspect these composites do not have to be significantly modified from the normal techniques used to inspect bulk aluminum. These techniques are well established in theory and practice [*1,2*].[2]

Ultrasonic

Of historical interest is the fact that it was in the late 1920's and early 1930's when it was recognized that ultrasonic waves could be used for nondestructive inspection of materials by the through-transmission method.

[2]The italic numbers in brackets refer to the list of references appended to this paper.

A rather complete reference list is given at the end of Chapter 43 in Ref *3*. This method, in use today, requires access to both sides of the material to be inspected and is thus limited in application. In the early 1940's Firestone patented a device which used pulsed ultrasonic wave trains reflected from behind the material to detect defects, and therefore the limitation of requiring access to both sides of the material was overcome. Reference *3* gives a detailed presentation of the basic technique available for use. In this work the technique used is immersion-back reflection and the presentation is a C-scan. The result is a plan view of the specimen showing defects from the "top" but not their position through the thickness of the material.

Results and Discussion

In any NDT technique it is almost axiomatic that the technique yields more information than can be interpreted and utilized effectively. In composites this problem is magnified, especially in C-scan work, because the material contains many signal dispersing interfaces. Figure 1 shows a typical cross section of a Th50/201Al Composite diffusion-bonded with 0.015 cm of 2024 aluminum foil on the top and bottom surfaces. This section was taken from an area on a panel that showed "good" in the C-scan. In contrast, Figs. 2 and 3 are photomicrographs of one corner of the same panel that showed anomalies in the C-scan. These serve to illustrate some of the different kinds of defects it is necessary to identify: voids and porosity within the graphite/aluminum, voids in the composite foil, bond defects, and aluminum-rich areas.

The necessity for developing NDT techniques for graphite/aluminum composites was recognized early in the material development cycle. Some of the earliest material was NDT'd without prior knowledge of the kinds of defects which would be found or of their effect on mechanical properties. Figure 4 shows a C-scan of a panel which was originally made to investigate corrosion. Because the C-scan showed an anomalous region in one section, it was redirected for use in investigating NDT techniques. An X-ray of the same panel showed an area of decreased density in the same region shown anomalous in the C-scan. The overlay specimen diagram shows four transverse tension specimens which were used to quantify the effect of the defect on transverse tensile strength. As with any unidirectional composite, transverse strength is the property affected most adversely by any defect. The results of the tests showed that Specimens 1L and 1R fractured in the gage length in the defect region, while Specimens 2L and 2R fractured in the gage length outside the defect region. The fracture strengths of 1L and 1R were ~45 percent of the strength of 2L and 2R, indicating a definite effect on mechanical properties due to the defect region. Subsequent metallography showed that the defect was an unbond region caused by foreign matter of a carbonaceous nature [*4*]. Figure 5

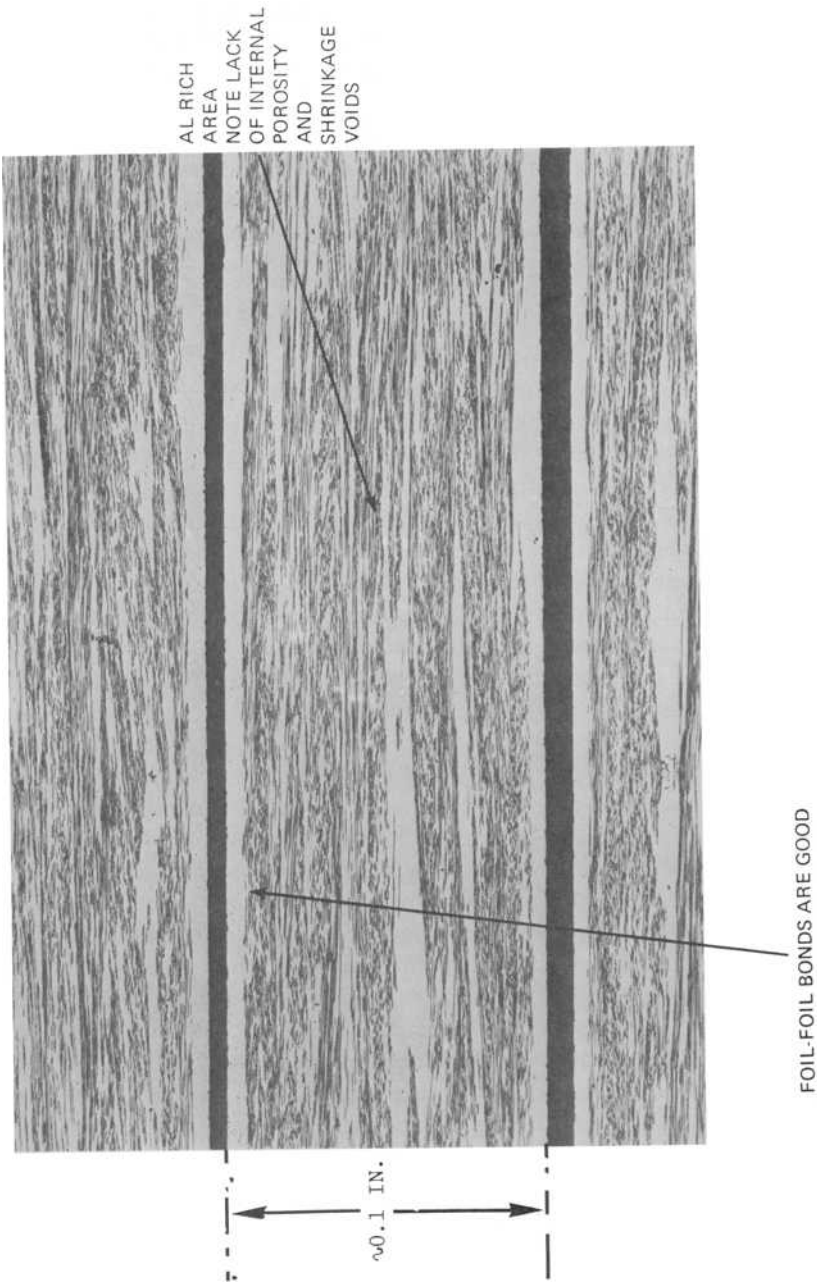

FIG. 1—*Photomicrograph of well-bonded panel (Panel 1-Th50/201A1) (1 in. = 2.54 cm).*

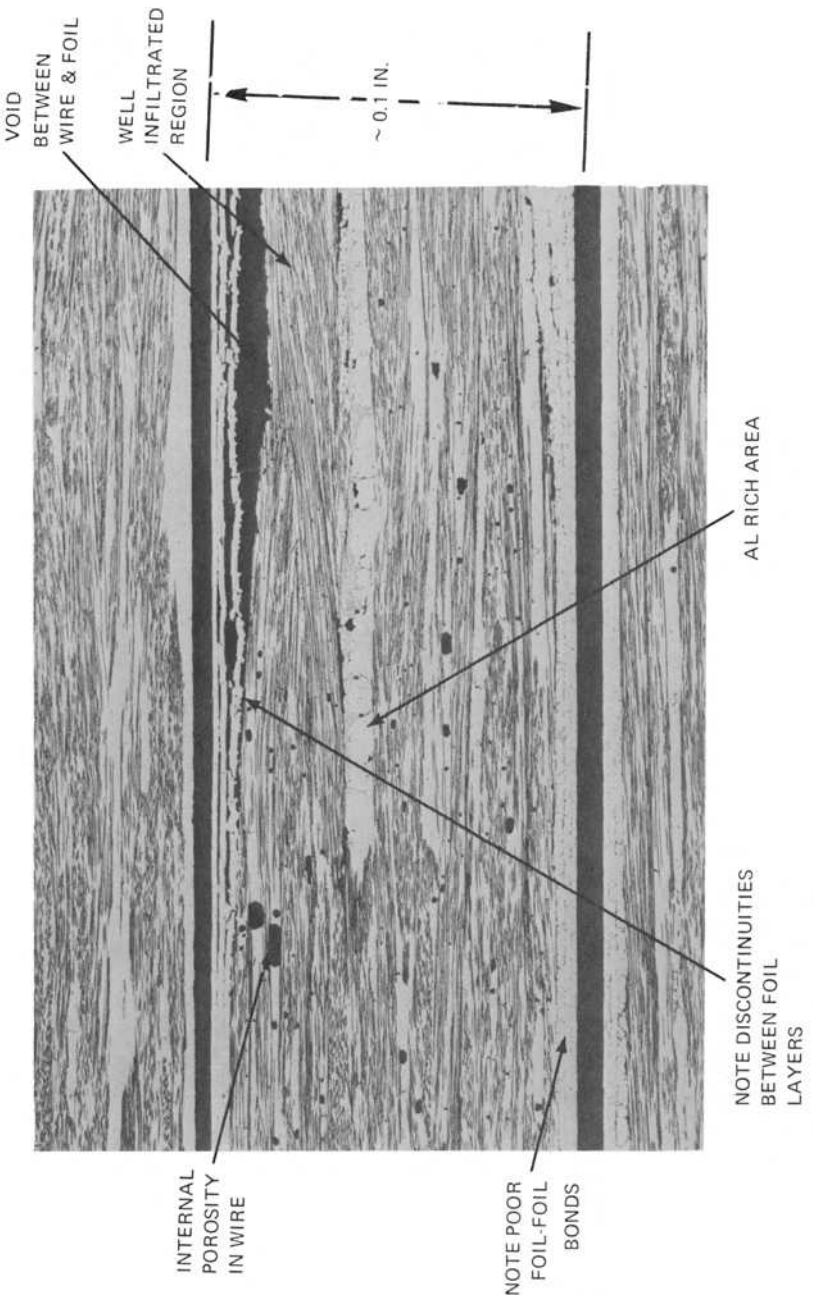

FIG. 2—*Photomicrograph of discontinuities found in Panel 1-Th50/201Al (1 in. = 2.54 cm).*

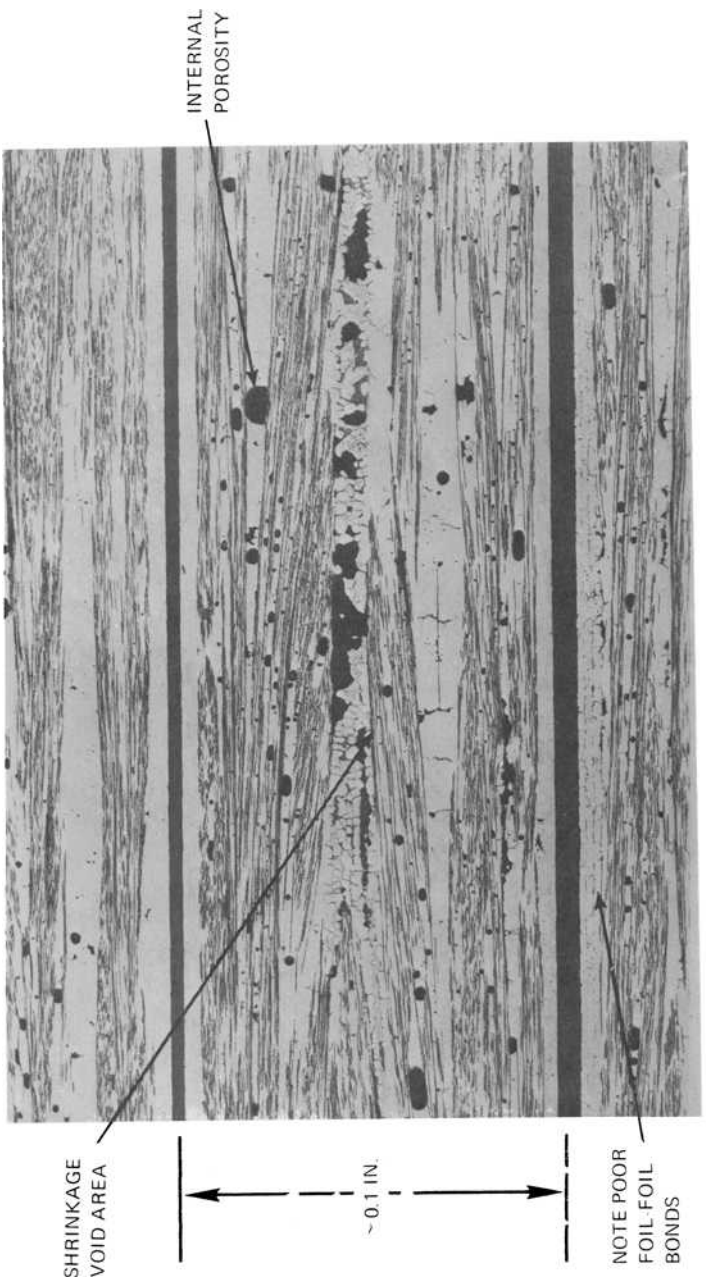

FIG. 3—*Photomicrograph of discontinuities found in Panel 1-Th50/201Al (1 in. = 2.54 cm).*

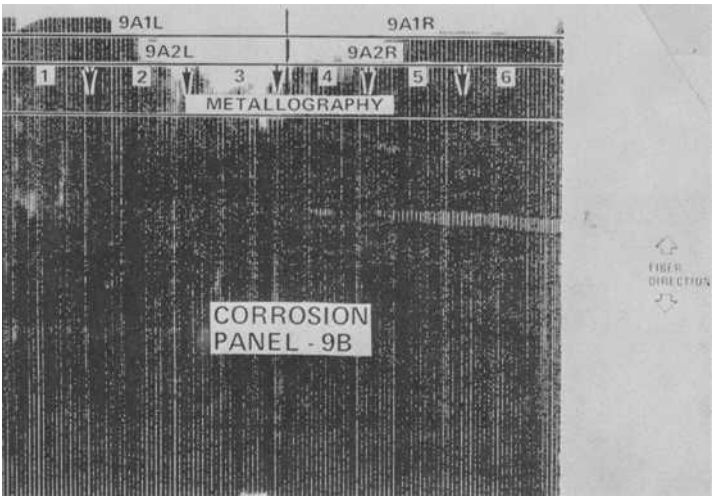

FIG. 4—*C-scan and specimen layout of Panel 9B—Th50/6061A1.*

shows a scanning electron micrograph (SEM) of the foreign matter adhering to the fracture surface of Specimen 1R.

Standard Defect Panel

A schematic of the layout of a panel made with intentional defects is shown in Fig. 6. The panel defects included such things as crossed wires, holes, and foreign material at various places through the thickness. The panel consisted of Th50/201Al, three layers, with 0.015 cm of 2024 aluminum surface foils on both surfaces. It was consolidated by diffusion-bonding by a standard baseline procedure: 30 min at 560°C and 24-MPa pressure. This panel was designated S2. Figure 7 shows one of the initial C-scans of S2. The scan was made using a 1.3 cm-diameter, 7.6-cm-focus lead-zirconate transducer. It was indexed at 0.076 cm per pass with a negative gate ("good" areas are black, "bad" areas are white). In this case 5 MHz, 3 dB, and 50 percent alarm level gain were used. The sound was gated on the glass reflector plate located approximately 2 cm below the composite plate rather than gating on the bottom side of the composite plate. Note in Fig. 7 that the dB level was not sufficient to show the 0.010 cm of extra surface foils in the top right-hand corner of Fig. 6. A higher gain (dB level) showed these foils but also increased the perceived size of the other defects. The use of a standard like this therefore helps in interpreting scans on actual material.

Further scans of Panel S2 were performed using the Erdman Nanoscope 412. The Nanoscope is a very high-resolution instrument and Figs. 8 and

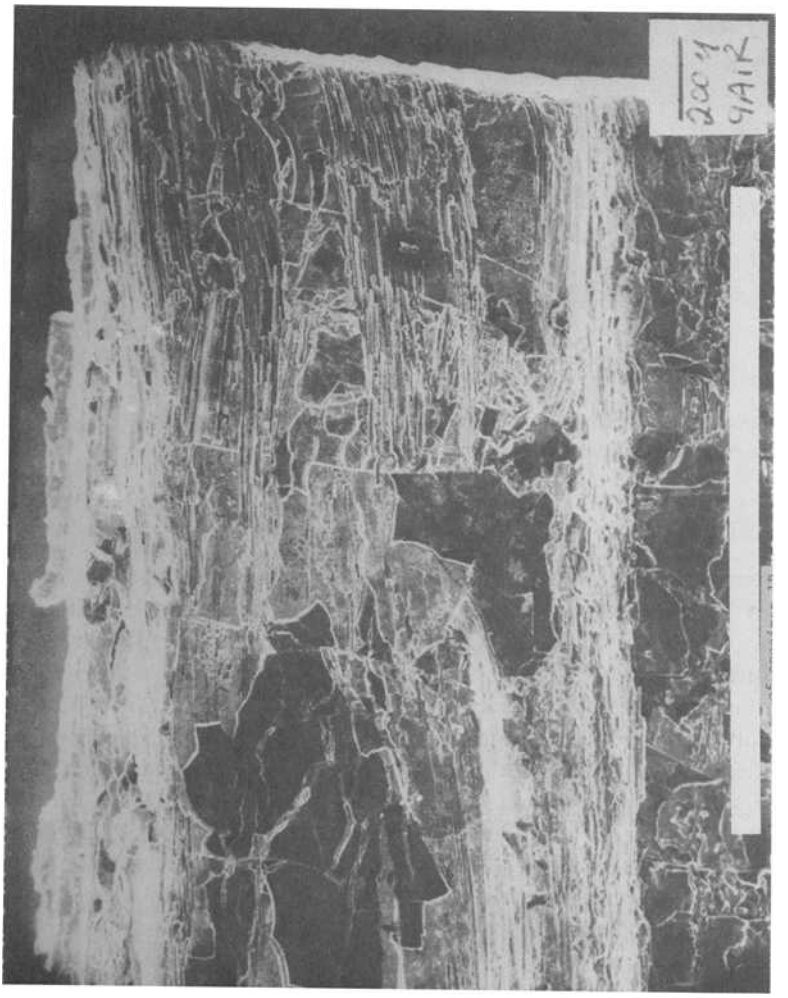

FIG. 5—*SEM of carbonaceous foreign matter in anomalous region of Panel 9B.*

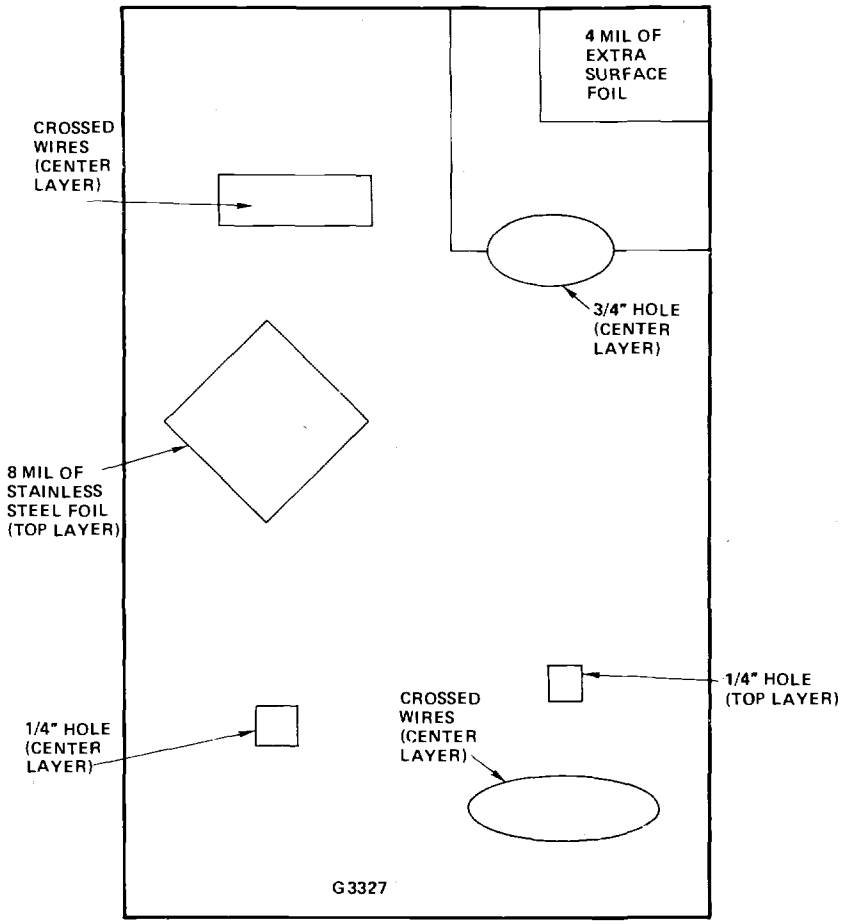

FIG. 6—*Schematic of standard panel (S2) showing intentional defects—Th50/201A1—baseline (1 in. = 2.54 cm).*

9 show the clarity of the resulting C-scans. In Figs. 8 and 9 the scans were run at 5 MHz with a constant gain, and the alarm level (percentage of input/output signal in the toss and catch) was varied. A 5 percent alarm level allowed all return signals greater than 95 percent to be printed. When the return signal fell below 95 percent, no print was indicated on the C-scan. Therefore, in Figs. 8 and 9, "good" is white, and "bad" is black. As the percentage loss is increased, more and more of Panel S2 is shown "bad" in the scan until at 90 percent signal alarm level (5 percent return signal) the panel is shown almost entirely bad. At this point the defects seen in all the other levels become lost in the "spurious" defects. The

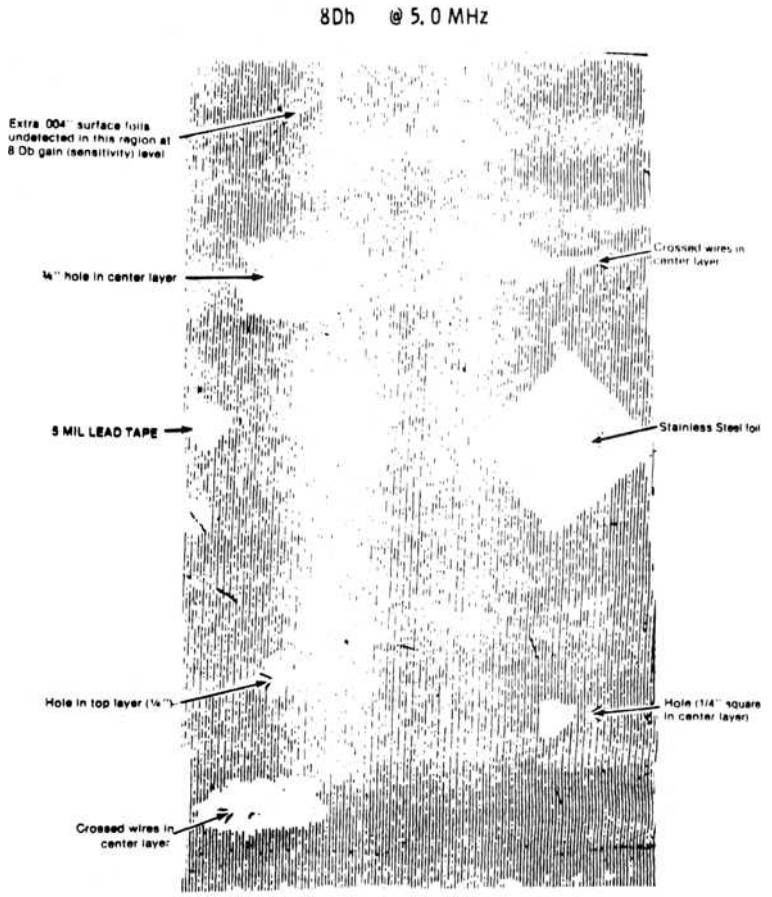

FIG. 7—*Initial C-scan recording of standard panel (S2)—Th50/201A1—baseline; 50 percent alarm level (1 in. = 2.54 cm).*

"spurious" defects almost certainly are just indications that this material has many fiber-matrix interfaces dispersing the signal. It is interesting in Figs. 7-9 that the crossed-wire defects in Fig. 6 do not show as crossed wires. This may be because the crossed wires actually produce a large disbond area which masks the smaller problems.

Panel 216-1, Th50/201Al

Figure 10 shows the C-scan, specimen overlay, and microstructure of defect areas from Panel 216-1[5]. Transverse specimens were placed so that gage length areas were in both "defect" and "good" areas. The defect

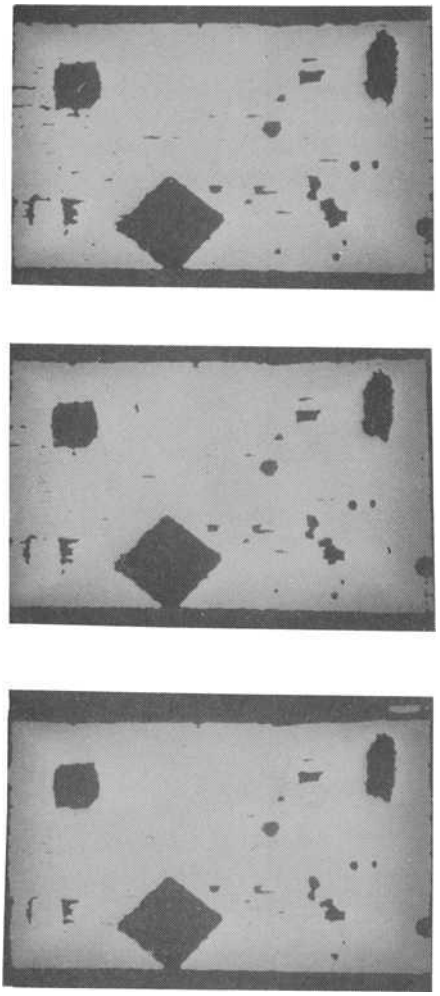

FIG. 8—C-scan of standard panel (S2) using Nanoscope—various alarm levels.

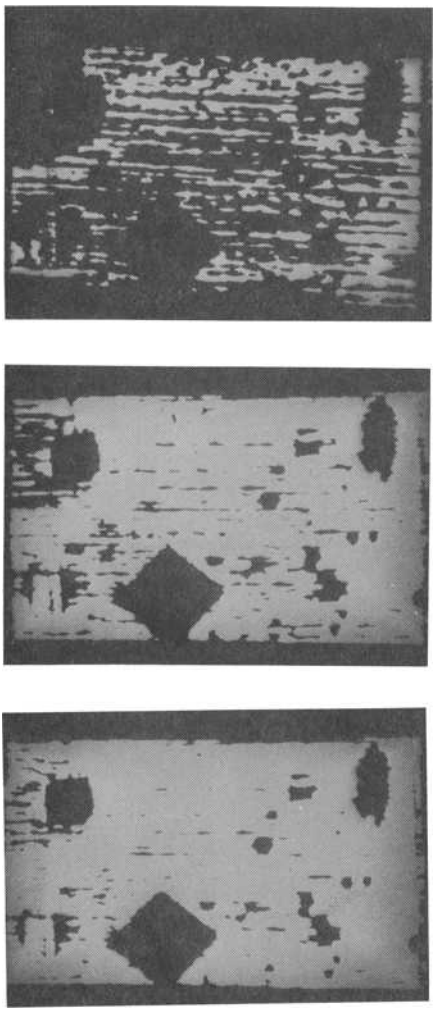

FIG. 9—*C-scan of standard panel (S2) using Nanoscope—various alarm levels.*

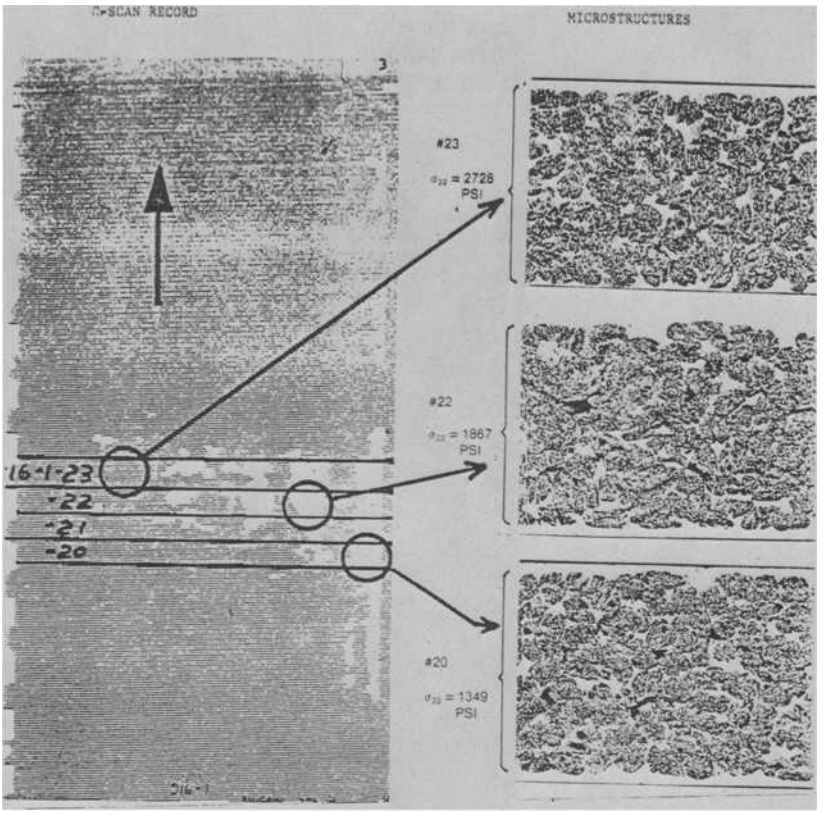

FIG. 10—*C-scan, specimen overlay, and microstructure of Panel 216-1-TH50/201Al baseline; 50 percent alarm level (1 psi = 6.895 kPa).*

specimens exhibited tensile strengths ~50 percent less than the "good" specimens. Microstructures of the "good" and "defect" regions showed that voids/porosity were responsible for the C-scan "defect" indications while "good" regions were well bonded with no voids.

Plate A, Th300/201Al

The C-scan of Plate A [6], Fig. 11, shows a large unbond region. Figure 12 is a schematic of the test specimen layout designed to determine the effect of this unbond on both transverse and longitudinal specimens. As expected, the unbond transverse specimens were 50 percent lower in tensile strength than those from the good region. The longitudinal specimens from the unbond region did not exhibit this decrease in strength. However, the tensile modulus did show a slight (~10 percent) decrease. The mechan-

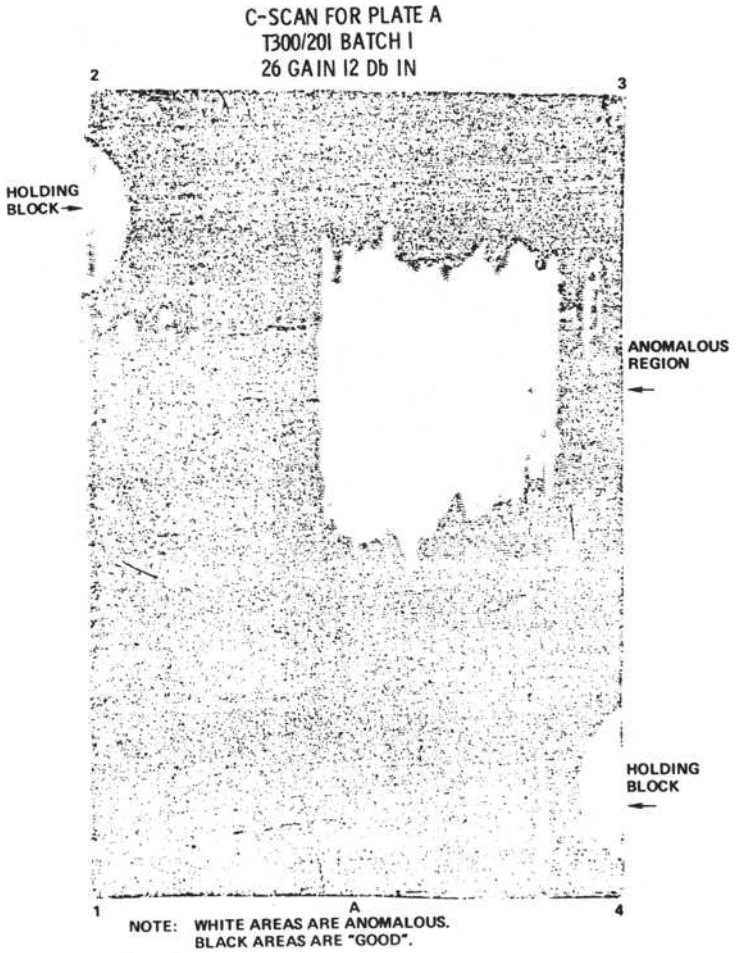

FIG. 11—*C-scan of Plate A showing large anomalous area—Th300/201Al; 50 percent alarm level.*

ical property which is affected most by defect areas in these composites is transverse strength, as would be expected. Most defects are associated with the matrix (unbonds, voids/porosity) and therefore should affect the matrix-dominated properties to a greater extent.

Conclusions

Development work thus far has shown that both X-ray and C-scan NDT can detect those types of anomalies in graphite/aluminum composites which adversely affect material performance. With the use of the ap-

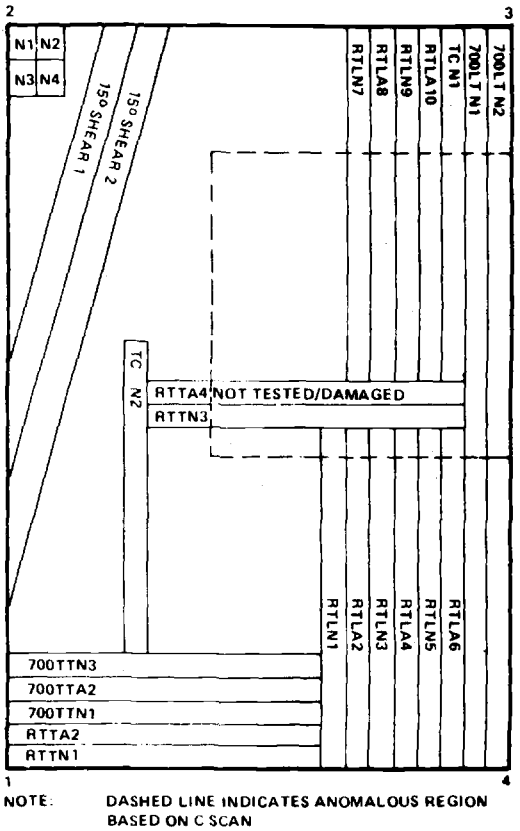

FIG. 12—*Schematic of Plate A (T 300/201) showing specimen locations relative to anomalous area.*

propriate "standards" all material can be inspected to detect suspect regions and, based on previous work, the effect on material performance can be estimated. To date the NDT has been concentrated on flat panels to be used for material property determinations and has helped in avoiding anomalous regions and in interpreting test results. Work has begun on developing NDT methods for curved sections, hats, zees, and other structural shapes and for inspecting attachment methods of various kinds.

References

[1] *Nondestructive Testing Handbook*, R. C. McMaster, Ed., The Ronald Press, New York, Part 1, Chapter 19, 1959.
[2] MIL-STD 453.
[3] *Nondestructive Testing Handbook*, R. C. McMaster, Ed., The Ronald Press, New York, Part 2, Chapters 43 and 44, 1959.

[4] Bascom, W. D., "Corrosive Delamination of Graphite-Aluminum Plate," Letter Report Naval Research Laboratory, 28 July 1976.
[5] Pfeifer, W. H., "Nondestructive Examination of Metal-Matrix Composites," 4th Quarterly Report, N60921-76-C-0216 Naval Surface Weapons Center, Nov. 1977.
[6] Davis, L. W. and Sullivan, P. G., "Exploratory Development of Graphite-Aluminum Composites," Final Report, N00024-76-C-5334, Naval Sea Systems Command, Oct. 1977.

Summary

The types of flaws present in composite materials are numerous and may range from microscopic debonds of the fiber-matrix interface to large through-the-thickness holes. These flaws may be inherent defects in the material, intentional or unintenional defects introduced during fabrication, or damage induced during the service history of the component. Many methods of detecting defects in composite materials are currently used, including ultrasonic C-scan and attenuation, acoustic emission, radiography, thermography, holography, and various types of microscopy. Some of the methods are rather standard techniques adopted from experience with uniform materials while some are highly innovative and novel inspection and evaluation methods developed specifically for composite materials. However, while it is true that many methods are available to detect defects, no single method is currently available to characterize all flaws or to assess the criticality of the damage state in the composite material.

The papers presented in this session attempt to characterize many of the types of flaws frequently encountered in composite materials and to show how these flaws influence the response of the material. The subjects presented include environmentally enhanced surface damage and microstructure degradation in graphite/epoxy, the initiation and growth of damage around embedded flaws in graphite/epoxy, the location of fracture origins and fracture surface characterization in graphite/epoxy, and the detection and characterization of inherent defects in graphite/aluminum. The response of graphite fiber-reinforced composites is shown to be dependent on the type of defect, variations in material systems, environmental and loading history, and stress state. Very difficult but important studies of failures and fracture surface morphology show that it is possible to determine fracture initiation sites and to identify details of the fracture process in some cases.

The collective works on flaw characterization provide useful descriptions of flaws and attendant property changes in composite materials prior to fracture and discuss how postfracture analyses can be used to determine some of the events which occur during the failure process. However, our current understanding of the failure of composite materials is incomplete. Although we can detect, identify, and monitor damage details during the process of failure, we do not understand how the individual details combine to form the damage state which controls the fracture of the material.

Only through assiduous investigations of mechanics and materials interactions throughout the loading history can we hope to more completely characterize flaws and understand their relationship to material response.

W. W. Stinchcomb

Virginia Polytechnic Institute and State University, Blacksburg, Va. 24061; co-editor.

Index